gels

Modification of Hydrogels and Their Applications in Biomedical Engineering

Edited by
Yanen Wang and Qinghua Wei

www.mdpi.com/journal/gels

MDPI

Modification of Hydrogels and Their Applications in Biomedical Engineering

Modification of Hydrogels and Their Applications in Biomedical Engineering

Editors

Yanen Wang
Qinghua Wei

MDPI

Editors

Yanen Wang
School of Mechanical
Engineering
Northwestern Polytechnical
University
Xi'an
China

Qinghua Wei
School of Mechanical
Engineering
Northwestern Polytechnical
University
Xi'an
China

This is a reprint of articles from the Special Issue published online in the open access journal *Gels* (ISSN 2310-2861) (available at: www.mdpi.com/journal/gels/special_issues/hydrogels_biomedical_ engineering).

For citation purposes, cite each article independently as indicated on the article page online and as indicated below:

LastName, A.A.; LastName, B.B.; LastName, C.C. Article Title. *Journal Name* **Year**, *Volume Number*, Page Range.

Contents

About the Editors

Yanen Wang

Yanen Wang is a professor at the School of Mechanical Engineering at Northwestern Polytechnic University. He obtained his Ph.D. degree in aeronautics and astronautics manufacturing engineering from Northwestern Polytechnical University. Currently, he is the vice dean of the School of Mechanical Engineering at Northwestern Polytechnical University, the director of the Shaanxi Biomanufacturing Engineering Research Center, the deputy secretary general of the Shaanxi Additive Manufacturing Committee, and also responsible for the Advanced Manufacturing Bio-Additive Manufacturing. His research interests focus on biofabrication and intelligent manufacturing technology.

Qinghua Wei

Qinghua Wei is an associate professor at the School of Mechanical Engineering at Northwestern Polytechnic University. He has been a faculty member at Northwestern Polytechnical University since he obtained his Ph.D. degree in mechatronics engineering from Northwestern Polytechnical University in 2018. His research interests include biomedical materials, biofabrication, and biomedical engineering.

Preface to "Modification of Hydrogels and Their Applications in Biomedical Engineering"

Hydrogels and hydrophilic polymer networks play an important role in biomedical engineering due to their good biocompatibility, biodegradability, hydrophilicity, and mechanical properties, similar to those of some soft tissues. However, single-component hydrogels usually do not meet the basic functional requirements of biomedical engineering, and modification is an effective way to improve the properties of hydrogels. Currently, a variety of multifunctional hydrogels with excellent performance have been developed, which greatly promotes the application of hydrogels in biomedical engineering.

This reprint focuses on the modification of hydrogels and their applications in biomedical engineering, aiming to provide a reference for scholars in related fields. It mainly involves the applications of hydrogels in biomedical fields such as phantoms, wound healing, skin, cartilage, muscle, and drug loading. We believe this book can provide a valuable reference for scientific and technological workers in the fields of materials science, tissue engineering, biological manufacturing, biomedical engineering, and so on.

We would like to thank all the contributing authors whose expert contributions made the publication of this Special Issue possible. We would also like to express our deepest appreciation to the editorial team, especially Ms. Miranda Song at MDPI, for their encouragement, technical guidance, editing, and publication of this Special Issue. Special thanks go to all reviewers for helping us ensure the quality of each published article.

Yanen Wang and Qinghua Wei
Editors

Editorial on the Special Issue "Modification of Hydrogels and Their Applications in Biomedical Engineering"

Yanen Wang [1,2,*] and Qinghua Wei [1,2,*]

1   Department of Indurstry and Engineering, School of Mechanical Engineering,
Northwestern Polytechnical University, Xi'an 710072, China
2   Bio-Additive Manufacturing University-Enterprise Joint Research Center of Shaanxi Province,
Northwestern Polytechnical University, Xi'an 710072, China
*   Correspondence: wangyanen@nwpu.edu.cn (Y.W.); weiqinghua@nwpu.edu.cn (Q.W.)

Hydrogels and hydrophilic polymer networks play an important role in biomedical engineering due to their good biocompatibility, biodegradability, hydrophilicity, and mechanical properties, similarly to some soft tissues. However, single-component hydrogels usually do not meet the basic functional requirements of biomedical engineering, and modification is an effective way to improve the properties of hydrogels. Currently, a variety of multifunctional hydrogels with excellent performance have been developed and greatly promote the application of hydrogels in biomedical engineering. This Special Issue focuses on the modification of hydrogels and their applications in biomedical engineering, aiming to provide a reference for scholars in related fields. Up until now, ten research articles and one review article have been collected, which mainly involve the application of hydrogels in biomedical fields such as phantoms [1], wound healing [2,3], skin [4], cartilage [5,6], muscle [7], and drug loading [8–10].

The use of phantoms offers a promising solution for the simulation of biological bodies. As tissue phantoms, mimicking the mechanical properties of soft living tissues is the basic requirement. In this regard, Tejo-Otero and his coauthors [1] tested the mechanical properties of a wide range of organs (e.g., liver, heart, kidney, as well as brain), hydrogels (e.g., agarose, polyvinyl alcohol (PVA), Phytagel (PHY), and methacrylate gelatin (GelMA)); the correlation between the mechanical properties of the organs and the different materials was obtained. This provides a reference for the selection of matrix materials for soft tissue models. In terms of wound healing, Chiangnoon et al. [2] used electron beam (EB) irradiation to develop antibacterial hydrogel sheet dressings from poly(vinyl alcohol) (PVA) and silver nanoparticles (AgNPs) in a two-step process and evaluated their bactericidal efficacy, as well as the AgNP's release. This research provides a convenient platform for the preparation of AgNP-loaded hydrogel dressings that can be further developed for wound healing. Meanwhile, Afrin et al. [3] prepared a semi-IPN hydrogel by combining the natural polymer cellulose nanocrystal (CNC) and the synthetic polymer polyethylene glycol (PEG) and poly (N, N′-dimethyl acrylamide) (PDMAA). The semi-IPN hydrogel loaded with the antibiotic drug, gentamicin, also shows excellent wound-healing properties. In a work related to electronic skin, Chen et al. [4] successfully prepared composite hydrogels based on polyvinyl alcohol (PVA), gelatin (GEL), oxidized sodium alginate (OSA), graphene oxide (GO), and single-walled carbon nanotubes (SWNTs). The prepared composite hydrogel exhibits good flexibility, self-healing, and conductive performance, which shows great potential for applications in electronic skin. To obtain an ideal cartilage substitute, Jalageri et al. [5] blended PVA and PVP with a one-dimensional hydroxyapatite nanorod (HNr) and synthesized a PVA/PVP/HNr composite hydrogel via the freeze–thaw method. The experimental results confirm that nanohydroxyapatite-reinforced PVA/PVP hydrogels are promising alternatives for next-generation cartilage substitutes. In another related work, Manferdini et al. [6] analyzed two different concentrations (1:1 and 1:2) of

VitroGel® (VG) hydrogels without (VG-3D) and with arginine–glycine–aspartic acid (RGD) motifs (VG-RGD) and verified their ability to support the chondrogenic differentiation of encapsulated human adipose mesenchymal stromal cells (hASCs). They found that both hydrogels, at different concentrations, and the presence of RGD motifs significantly contributed to the chondrogenic commitment of laden hASCs. Regarding the application of hydrogels in muscle tissue, Mubarok et al. [7] evaluated the influence of physicochemical property dynamics in the gelatin that possess phenol groups (Gelatin-Ph) and hydrogels to regulate the myogenesis in vitro, and the myogenesis was successfully tuned by changes in the physicochemical properties of Gelatin-Ph hydrogel mediated by H_2O_2. This provides a reference for the regeneration and repair of muscle tissue. Hydrogels also have important applications in the controlled release of drugs. Chittasupho et al. [8] developed shape memory gels containing phytosomes as a delivery system for fresh (VFL) and dry (VDL) leaf extracts of *Nicotiana tabacum* var. Virginia. The results showed that the VDL and VFL phytosomes dispersed in shape memory gels could be considered as a promising therapeutic delivery system to protect the skin from oxidation and reactive oxygen species. Kim and his co-authors [9] prepared a hyaluronic acid (HA)–collagen hybrid hydrogel to investigate the effect of fibroblast growth factor (FGF)-2 and platelet-derived growth factor (PDGF)-BB on human pulp regeneration. The results show that the optimal concentration of FGF-2 and PDGF-BB for pulp cell proliferation was 100 ng/mL and that the HA–collagen hybrid hydrogel has the potential as a controlled release delivery system for FGF-2 and PDGF-BB. Srikhao et al. [10] fabricated hydrogel beads for use as a drug delivery system based on basil seed mucilage (BSM), sodium alginate (SA), and magnetic particles (MPs). Based on the results of this work, BSM/SA/MPs hydrogel beads were considered to have the potential to be used as a pH-sensitive alternative material for drug delivery in colon-specific systems. In addition, smart hydrogels based on poly(N-isopropyl acrylamide) (PNIPAM) have been applied in various biomedical applications such as drug delivery, tissue engineering, and wound dressings due to their distinct thermoresponsive features, such as being close to a lower critical solution temperature (LCST). Nevertheless, they have intrinsic shortcomings, such as poor mechanical properties, limited drug loading capacity, and poor biodegradability. Ansari et al. [11] reviewed the latest developments in functional PNIPAM-based smart hydrogels for various biomedical applications and summarized the challenges and opportunities in this emerging field of research.

This Special Issue offers a real insight into the progress made in the application of hydrogel in biomedical engineering. There is every reason to believe that with the efforts of researchers, multifunctional hydrogels will play an increasingly important role in biomedical engineering in the future.

Conflicts of Interest: The authors declare no conflict of interest.

References

1. Tejo-Otero, A.; Fenollosa-Artés, F.; Achaerandio, I.; Rey-Vinolas, S.; Buj-Corral, I.; Mateos-Timoneda, M.Á.; Engel, E. Soft-Tissue-Mimicking Using Hydrogels for the Development of Phantoms. *Gels* **2022**, *8*, 40. [CrossRef] [PubMed]
2. Chiangnoon, R.; Karawak, P.; Eamsiri, J.; Nuchdang, S.; Thamrongsiripak, N.; Neramitmansook, N.; Pummarin, S.; Pimton, P.; Nilgumhang, K.; Uttayarat, P. Antibacterial Hydrogel Sheet Dressings Composed of Poly(vinyl alcohol) and Silver Nanoparticles by Electron Beam Irradiation. *Gels* **2023**, *9*, 80. [CrossRef] [PubMed]
3. Afrin, S.; Shahruzzaman, M.; Haque, P.; Islam, M.S.; Hossain, S.; Rashid, T.U.; Makoto, A.; Takafuji, T.; Rahman, M.M. Advanced CNC/PEG/PDMAA Semi-IPN Hydrogel for Drug Delivery Management in Wound Healing. *Gels* **2022**, *8*, 340. [CrossRef] [PubMed]
4. Chen, X.; Zhang, H.; Cui, J.; Wang, Y.; Li, M.; Zhang, J.; Wang, C.; Liu, Z.; Wei, Q. Enhancing Conductivity and Self-Healing Properties of PVA/GEL/OSA Composite Hydrogels by GO/SWNTs for Electronic Skin. *Gels* **2023**, *9*, 155. [CrossRef] [PubMed]

5. Jalageri, M.B.; Kumar, G.C.M. Hydroxyapatite Reinforced Polyvinyl Alcohol/Polyvinyl Pyrrolidone Based Hydrogel for Cartilage Replacement. *Gels* **2022**, *8*, 555. [CrossRef] [PubMed]
6. Manferdini, C.; Trucco, D.; Saleh, Y.; Gabusi, E.; Dolzani, P.; Lenzi, E.; Vannozzi, L.; Ricotti, L.; Lisignoli, G. RGD-Functionalized Hydrogel Supports the Chondrogenic Commitment of Adipose Mesenchymal Stromal Cells. *Gels* **2022**, *8*, 382. [CrossRef] [PubMed]
7. Mubarok, W.; Elvitigala, K.C.M.L.; Sakai, S. Tuning Myogenesis by Controlling Gelatin Hydrogel Properties through Hydrogen Peroxide-Mediated Cross-Linking and Degradation. *Gels* **2022**, *8*, 387. [CrossRef] [PubMed]
8. Chittasupho, C.; Chaobankrang, K.; Sarawungkad, A.; Samee, W.; Singh, S.; Hemsuwimon, K.; Okonogi, S.; Kheawfu, K.; Kiattisin, K.; Chaiyana, W. Antioxidant, Anti-Inflammatory and Attenuating Intracellular Reactive Oxygen Species Activities of *Nicotiana tabacum* var. Virginia Leaf Extract Phytosomes and Shape Memory Gel Formulation. *Gels* **2023**, *9*, 78. [CrossRef] [PubMed]
9. Kim, M.S.; Hwang, Y.S.; Lee, H.S.; Nam, O.H.; Choi, S.C. Development of Growth Factor Releasing Hyaluronic Acid-Based Hydrogel for Pulp Regeneration: A Preliminary Study. *Gels* **2022**, *8*, 825. [CrossRef] [PubMed]
10. Srikhao, N.; Chirochrapas, K.; Kwansanei, N.; Kasemsiri, P.; Ounkaew, A.; Okhawilai, M.; Likitaporn, C.; Theerakulpisut, S.; Uyama, H. Multi-Responsive Optimization of Novel pH-Sensitive Hydrogel Beads Based on Basil Seed Mucilage, Alginate, and Magnetic Particles. *Gels* **2022**, *8*, 274. [CrossRef] [PubMed]
11. Ansari, M.J.; Rajendran, R.R.; Mohanto, S.; Agarwal, U.; Panda, K.; Dhotre, K.; Manne, R.; Deepak, A.; Zafar, A.; Yasir, M.; et al. Poly(N-isopropylacrylamide)-Based Hydrogels for Biomedical Applications: A Review of the State-of-the-Art. *Gels* **2022**, *8*, 454. [CrossRef] [PubMed]

Mohammad Javed Ansari [1,*] , Rahul R. Rajendran [2] , Sourav Mohanto [3] , Unnati Agarwal [4,†] ,
Kingshuk Panda [5,†] , Kishore Dhotre [6] , Ravi Manne [7] , A. Deepak [8] , Ameeduzzafar Zafar [9] , Mohd Yasir [10]
and Sheersha Pramanik [11,*]

[1] Department of Pharmaceutics, College of Pharmacy, Prince Sattam Bin Abdulaziz University,
Al-Kharj 11942, Saudi Arabia

[2] Department of Mechanical Engineering and Mechanics, Lehigh University, 19 Memorial Drive West,
Bethlehem, PA 18015, USA; rajendranrahulr@gmail.com

[3] Department of Pharmaceutics, Yenepoya Pharmacy College and Research Centre, Yenepoya (Deemed to be
University), Mangalore 575018, Karnataka, India; mohanto111@gmail.com

[4] School of Bioengineering and Biosciences, Lovely Professional University, Jalandhar-Delhi, Grand Trunk
Road, Phagwara 144001, Punjab, India; unnatiaggarwalsmile@gmail.com

[5] Department of Applied Microbiology, Vellore Institute of Technology, School of Bioscience and Technology,
Vellore 632014, Tamilnadu, India; kingshukpanda7@gmail.com

[6] I.C.M.R.—National Institute of Virology, Pune 411021, Maharashtra, India; kishoredhotre27@gmail.com

[7] Chemtex Environmental Lab, Quality Control and Assurance Department, 3082 25th Street,
Port Arthur, TX 77642, USA; ravimannemr@gmail.com

[8] Saveetha School of Engineering, Saveetha Institute of Medical and Technical Sciences,
Chennai 600124, Tamil Nadu, India; deepakarun@saveetha.com

[9] Department of Pharmaceutics, College of Pharmacy, Jouf University, Sakaka 72341, Saudi Arabia;
zzafarpharmacian@gmail.com or azafar@ju.edu.sa

[10] Department of Pharmacy, College of Health Science, Arsi University, Asella 396, Ethiopia;
mohdyasir31@gmail.com

[11] Department of Biotechnology, Bhupat and Jyoti Mehta School of Biosciences, Indian Institute of Technology
Madras, Chennai 600036, Tamil Nadu, India

*   Correspondence: javedpharma@gmail.com (M.J.A.); sheershopramanik24@gmail.com or
bt19d601@smail.iitm.ac.in (S.P.)

†   These authors contributed equally to this work.

Abstract: A prominent research topic in contemporary advanced functional materials science is the production of smart materials based on polymers that may independently adjust their physical and/or chemical characteristics when subjected to external stimuli. Smart hydrogels based on poly(*N*-isopropylacrylamide) (PNIPAM) demonstrate distinct thermoresponsive features close to a lower critical solution temperature (LCST) that enhance their capability in various biomedical applications such as drug delivery, tissue engineering, and wound dressings. Nevertheless, they have intrinsic shortcomings such as poor mechanical properties, limited loading capacity of actives, and poor biodegradability. Formulation of PNIPAM with diverse functional constituents to develop hydrogel composites is an efficient scheme to overcome these defects, which can significantly help for practicable application. This review reports on the latest developments in functional PNIPAM-based smart hydrogels for various biomedical applications. The first section describes the properties of PNIPAM-based hydrogels, followed by potential applications in diverse fields. Ultimately, this review summarizes the challenges and opportunities in this emerging area of research and development concerning this fascinating polymer-based system deep-rooted in chemistry and material science.

Keywords: PNIPAM; hydrogels; drug delivery; tissue engineering; smart polymer; wound healing

1. Introduction

The importance of hydrogels as functional biomaterials in biomedical applications started in the early 19th century [1,2]. As per the report by Wichterle and Lim, hydrogel was initially used in biomedical applications as tissue scaffolds and contact lenses, but later, in the early 20th century, it was also used as high aqueous-swellable crosslinked polymeric networks [3]. Typically, hydrogels are fabricated via physically or chemically crosslinked hydrophilic polymeric macromolecules in a 3D network that can imbibe some water molecules and suspend their movements through physical and/or chemical linkages [4–6]. Hydrogels have become the center of attention in the application of chemical, biological, and pharmaceutical domains during the last two decades due to several intrinsic properties: biocompatibility [7], biodegradability [7], readily adjustable, hydrophilic characteristics [3], high absorption capacity [8], etc. Hydrogels substantially enhance the temporal and spatial delivery of macromolecular drugs, small molecules, and growth factors in several biomedical fields and have also had comprehensive clinical usage [9]. Hydrogel fabrication via natural/synthetic hydrophilic polymers drives the system to be more swellable and enhances the absorption capacity through attachment of hydrophilic functional groups, e.g., amide, amino, carboxyl, hydroxyl, etc.; to the polymeric chain. However, drug delivery using hydrogels has not been free of obstacles, but continuous advancements are helping to settle on a hydrogel design competently conformed to specific drug delivery [10,11]. Due to several limitations of using natural hydrophilic polymers in hydrogel preparation, e.g., low thermal stability [12], absorption capacity [13], gel strength [3], etc.; suitable synthetic polymers are being considered as a biomaterial for hydrogel preparation. Furthermore, several mechanical properties of polymeric hydrogels can be modulated via physicochemical reactions, altering the chains of the polymer with stimuli-responsive functional groups to enhance the physical and mechanical resistance, which are significant attributes to be considered when creating delivery systems [3,14]. In developing an efficient hydrogel system, these characteristics are positively interconnected; from biomaterial selection to developing a gel blueprint, it is typically required to assess the whole system.

Stimuli-responsive hydrogel systems, often known as "smart" or "intelligent" hydrogels, are a unique class of hydrogel due to their high swelling and gelation capacity [15]. Such hydrogels are competent in responding to environmental stimuli, e.g., pH, temperature, light, electrical field, and ionic concentration, by following a reversible change in the volume or a sol–gel phase transition [16–19]. Several thermoresponsive polymers develop gel at temperatures less than lower critical solution temperature (LCST). Positive thermosensitive hydrogels can shrink below and dissolve above the upper critical solution temperature (UCST). The solution formation process is reversible, and there is more swelling in the case of chemically crosslinked polymers when the temperature is lowered below the LCST. Negative thermosensitive hydrogels transform from sol to gel above the LCST, suggesting that they could be exploited to make hydrogels with delayed release, longer skin retention time, and minor systemic side effects [20]. Some previous extensive review articles also summarize the various theories and mechanisms of thermogelation [21–23]. Smart materials have demonstrated numerous promising applications in an aqueous medium. The nature of thermoresponsive hydrogels is similar to living tissue and hence could be utilized as an efficient carrier or delivery system in the biomedical field. This property efficiently simulates the sensitivity and responsiveness of biomolecules in in vivo microenvironments, which is a massive benefit in producing innovative biomedical composites for technical purposes. Thermo-sensitive polymeric materials can incorporate hydrophilic as well as hydrophobic structures of their parts, and the phenomenal temperature responsiveness is acquired from the complex interplay of the monomer's hydrophilic and hydrophobic parts. Temperature alters the association of hydrophilic and hydrophobic components with water molecules, increasing solubility and causing the sol–gel phase transition of the crosslinked polymer [24].

This review concentrates on the specific properties, mechanism of phase transition in thermoresponsive PNIPAM, and the parameters impacting gel behavior. Further, a compre-

hensive review of recent investigations of PNIPAM-based hydrogels in diverse biomedical applications is presented. It focuses on numerous application domains, including tissue engineering, drug delivery, and wound dressing, plus broad fundamentals from material selection to greater efficiency hybridization techniques.

2. Brief on PNIPAM-Based Hydrogel

PNIPAM is a widely utilized negative thermosensitive polymer (as it has increased solubility with lowering of temperature, causing volume phase transition by forming hydrogen bonds) that has currently sparkled a lot of scientific inquisitiveness [25,26]. In the aqueous medium, PNIPAM assembles a stretched spiral elastic shape; polymer molecules form hydrogen bonds with each other due to hydrogen bonding with molecules of water. It has both hydrophobic isopropyl ($-CH(CH3)_2$) side groups and hydrophilic amide ($-CONH-$) groups in the structure. PNIPAM has an LCST of 32 °C, which is somewhat lower than human body temperature of 37 °C, and it can be modified by copolymerizing with some distinct hydrophobic or hydrophilic polymers to develop thermo-sensitive, in situ hydrogels. [27–29]. The temperature-responsive behaviors are primarily due to connections between these groups and solvent molecules. As a result, PNIPAM converts from solution to gel state as the LCST reaches human body temperature [30–34]. Additional hydrophilic monomers increase the polymer's hydrophilicity and lead to more significant interactions with water, resulting in a higher LCST, whereas copolymerization with more hydrophobic monomers reduces LCST [35]. This property makes PNIPAM suitable for biomedical applications, e.g., controlled wound dressings, tissue engineering scaffolds, and drug delivery systems [36,37]. Notwithstanding these appealing benefits, PNIPAM-based hydrogels nevertheless have certain drawbacks, including limited biodegradability [38], weak mechanical strength [39], insufficient drug loading capacity [40], and immediate release [39,41,42], etc.; limiting the feasibility in drug delivery.

Several drugs can be efficiently encapsulated into the hydrophilic polymers by using a lower temperature to dissolve the drug in the solvent to ensure efficient delivery, raising the temperature slightly above the LCST for hydrogel appearance. Furthermore, maintaining precise temperature control permits site-specific drug delivery and delayed release. The PNIPAM solution can be rapidly applied to the skin and activated by utilizing body temperature to create a 3D hydrogel that can help restore tissues by encouraging cell proliferation and differentiation while preserving the homeostatic activity of cells. The temperature-dependent modulation of gel coating and reversible sol-to-gel can be utilized to develop adherence to the skin and its dissociation for wound treatment. Other features of PNIPAM, in conjunction with thermosensitivity, include adjustable geometries and nontoxicity, both of which are advantageous for biological applications [43]. Wound dressings play a crucial part in lesion care, and their effectiveness impacts how quickly a wound heals [44]. That a warm, moist environment promotes faster healing has been widely demonstrated in several empirical investigations in both in vivo and in vitro wound healing [45,46]. Various medical studies also recommend that dressings should be translucent to allow easy observation, and that they have the ability to retain fluids [47–49]. Aside from the properties described above, zwitterionic hydrogels have lately gained popularity as nonadherent wound dressings due to their high resistance to cell attachment, protein adsorption, and microbial adherence [50,51]. For wound dressing, PNIPAM can be utilized to retain the skin adhesion and differentiation of gel coatings. Its thermosensitivity is complemented by LCST adjustability, low toxicity, and [48] variable structure. [52], making it suitable for biomedical applications [43].

Many contemporary tissue engineering techniques rely on the use of a material scaffold. These scaffolds act as an artificial extracellular matrix (ECM), allowing cells to be organized into a three-dimensional framework and stimulating the growth and creation of desirable tissue [53]. The scaffold material and qualities required vary greatly depending on the tissue of concern and the individual application [54]. Thermoresponsive polymers are

extensively employed in tissue engineering in two ways: platforms for cell proliferation and injectable solutions for in situ scaffolding [55].

The primary disadvantage of PNIPAM-based hydrogels in drug delivery is the incorporation of hydrophobic drugs in the water-loving polymeric core [56], since mostly hydrophobic drugs are typically and effectively used in disease treatment. Along with this, the tensile strength [39] of these hydrogels is weak, which may sometimes lead to early drug release before arrival at the specific site [57]. Several researchers are working painstakingly to improve the mechanical characteristics of PNIPAM hydrogels to fix the reported shortcomings. Hybridization of PNIPAM-based composite hydrogels with appropriate materials such as inorganic/metal nanoparticles [58], organic self-assemblies [40], and several other polymeric material incorporations/composite formations are some reported viable techniques for achieving this goal [59,60]. A novel polymeric block could regulate the thermal sensitivity of the resulting hydrogel by adjusting the hydrophilic/hydrophobic equilibrium of PNIPAM. Alternatively, a novel polymeric component can affect the hydrogel network's chemical rigidity and morphology, modulating the copolymeric hydrogel's mechanical properties [61–63]. The successful composite formation of PNIPAM with various materials, e.g., hyaluronic acid (HA) [64,65], zinc oxide (ZnO) nanoparticles [66], silver nanoparticles [67], hydroxyapatite (HAp) nanoparticles [68], carbon nanoparticles [69], etc.; for tissue engineering and wound healing has been reported in several investigations [70–72]. Adequate biocompatibility, higher tensile strength, customizable temperature responsiveness, multi-drug loading capability, targeted drug delivery, and controlled drug delivery are among the unique and/or improved features of composite hydrogels [43]. The inclusion of some other polymer inside the hydrogel matrix to make interpenetrating polymeric network system (IPN) hydrogels for biomedical application [73] is another useful way to alter the functionalities of a hydrogel. The polymeric networks in IPN hydrogels can efficiently adjust mechanical characteristics, swelling/deswelling behavior, and drug loading/release pattern [74].

3. Unique Properties of PNIPAM

Physically crosslinked hydrogels can be assembled via ionic/hydrogen bond formation, Van der Waals forces, hydrophobic interactions, crystalline structure, etc. [75]. The strong hydrogen bonding between the polymeric chains in the hydrogel may promote drug release, which can be further controlled via the type of solvent, degree of sonication, solution temperature, polymer concentration, etc.; in hydrogel formulation. Another method, crosslinking, has been most commonly utilized to overcome biomaterial physicochemical and mechanical limitations via strong interconnections between the reaction molecules. Furthermore, ionic interactions can be initiated at room temperature and physiological pH to overcome constraints [76]. Bifunctional crosslinking agent-initiated hydrogels are generally developed via several techniques, e.g., condensation polymerization, irradiation using high-energy ionizing radiation such as electron beams, gamma rays, or X-rays, chain-growth polymerization, etc. [76].

In biomedical science, PNIPAM-based hydrogels have versatile applications for the effective therapeutic delivery of molecules by modulating substance movement in a medium, altering thermo-controlled dimensions [77]. A monomeric structure of PNIPAM commonly identified by isopropyl and amide moieties maintains LCST at ~32 °C in aqueous conditions. PNIPAM hydrogels are developed by crosslinking themselves or their derivates, exhibiting a reversible and extreme volume phase transition towards LCST through swelling/shrinking [78]. Along with the changes in size during the transition phase, there are also several other changes in many properties, such as hydrophilicity [79,80], transparency [81], and apparent electrostatic permittivity [82]. The mixing of polymer in a solvent leads to polymeric dissolution at a specific temperature (T), which the negative ΔG_{mix} of the Gibbs free energy equation can well indicate. The involvement of thermodynamics in the method forms hydrogen bonds that create significant negative enthalpy change of mixing ($\Delta H_{mix} < 0$), contributing to dissolution. Lowering PNIPAM's

temperature below LCST develops a counterbalance between the hydrogen bonds of hydrophilic amide groups and molecules of water, leading to hydrophobic interactions among isopropyl groups and hence collapsing the PNIPAM chain to avoid water contact [78].

PNIPAM hydrogels exhibit a slow response to environmental temperature variations due to the formation of the thick skin surface, decreasing the outward diffusion of water molecules and causing hydrogel collapse at temperatures above LCST [83–85]. Likewise, the swelling rate of hydrogels is relatively slower at temperatures lower than LCST. Therefore, improving the rate of thermoresponsiveness of established PNIPAM hydrogels has become a research subject [86]. Some physical strategies have been involved in enhancing the thermal responsiveness of PNIPAM hydrogels, such as phase separation [87], porogen [88], freezing [83], vacuum-synthesis [89], and interpenetrating polymer networks [90]. Along with these, alternate chemical approaches have also been introduced, which include the addition of hydrophilic moieties [91], grafting freely mobile hydrophilic moieties [92], and reversible addition–fragmentation chain transfer (RAFT) polymerization [93] to attain a rapid response rate. Stimuli-responsive hydrogels require mechanical properties for various applications. Hence, to improve the PNIPAM hydrogel's mechanical properties, some techniques have been implemented, such as an interconnected polymer network [94], a hydrogel with two networks [95], a hydraulic ring for slides [96], nanoporous PNIPAM hydrogel [97], and copolymerized PNIPAM hydrogel [98]. Free radical redox polymerization of PNIPAM hydrogels is relatively weak and can even be affected using standard mechanical testing equipment [99].

Takigawa et al. determined PNIPAM hydrogel's Young's modulus (E0) for the first time in 1997. They found a stress–strain graph of the collapsed and swelled gel to be linear in a specific hardness strength test, where the E0 was a hundred times more for the collapsed state. The swelled and collapsed conditions were found to have fracture strains of 35% and 75%, respectively [99]. The collapsed state was found to have a higher E0 than the swollen state, as the collapsed gels had an increased number of crosslinks. The change in E0 at the initial stage of the scaffold was probably due to rapid relaxation shown by the macroporous hydrogel, which remains constant for a more extended period during cellular growth [100].

PNIPAM hydrogel has inadequate mechanical performance in the highly swelled state, prominently identified as a disadvantage in drug delivery. Its nonbiodegradable nature has led to surgical excision after the release of the drug. Removing the device by typical surgical operations is also challenging if it is too light, as it might break down during handling. However, PNIPAM hydrogel's lack of controlled release capability, i.e.; leading to the release of impregnated drugs within 24 h, is a severe reason for the possibility of being restricted as a drug carrier [101–103]. A swelled PNIPAM hydrogel with a decreased polymeric mass per unit volume explains its poor mechanical characteristics and increased drug release rate. The decreased polymeric mass per unit volume results in the fast release of impregnated drugs because of the gel's open pores and low mechanical characteristics. Rapid drug release from the drug reservoir is because of the weak intermolecular bonds of swelled PINPAM hydrogel [90].

In an aqueous phase at a certain temperature range of about 32 °C, for drug delivery, the PNIPAM hydrogel could be combined with bioactive components to form a solution. The introduction of polymers becomes possible in that particular physical condition. The subcutaneous injection of the polymer-loaded gel leads to sustained release and an immediate increase in physiological temperature (to about 36.5–37.5 °C). The biodegradability of the hydrogel leads to the release of encapsulated bioactive compounds, initially in the body via diffusion and later on by a mixture of diffusion and mechanical breakdown [104]. Both physical and chemical properties (melting point, temperature, glass transition storage modulus, crystallinity, etc.) are responsible for the biodegradability of the polymer [105]. The reduced biodegradability of PNIPAM hydrogel has restricted its use in clinical practice. Different crosslinking agents and/or biodegradable polymers or native polymers, including poly(amino acids) [106], polysaccharides [107], proteins [108], and synthetic polymers

including poly(esters) [109], poly(caprolactone) [38], and poly(ethylene glycol) [110], have now been analyzed for the development of biodegradable PNIPAM hydrogels [104]. PNIPAM is also highly biocompatible with animal cells [104]. Cao et al. explored the use of PNIPAM–chitosan copolymers for ophthalmic drug delivery. The copolymer was utilized for encapsulation of timolol maleate molecules for around 12 h to effectively lower intraocular pressure (IOP). The in vivo study of PNIPAM–chitosan for thermo-sensitive hydrogels confirmed non-cytotoxicity, hence furnishing new insights into glaucoma therapy along with several other eye illnesses [111].

Biopolymers or artificially degradable compounds help alter the chemical composition of PNIPAM to obtain biodegradability and biocompatibility effectively. In a study by Das et al.; covalently crosslinked PNIPAM hydrogels utilizing NIPAM as the monomer, dextrin as the biopolymer, potassium persulfate (KPS) N,N′-methylene bisacrylamide (MBA) as the promoter, and N,N′-methylene bisacrylamide (MBA) as the crosslinker were effectively synthesized. Ciprofloxacin and ornidazole could be administered in a controlled manner by the novel PNIPAM hydrogel, as it is nontoxic and biodegradable [112].

4. Phase Transition for PNIPAMs

The polyacrylamide structure is mostly crafted with a hydrophilic amide group (almost 90%) and -C-C- hydrophobic portion. However, poly(*N*-isopropyl-acrylamide) and other N-substituted acrylamide polymers (PNIPAM) have balanced hydrophilic and hydrophobic regions below LCST. The gel-polymer/water system's total energy is lowered due to hydrophobic polymers enveloped by water molecules below LCST [113]. The solvation and transition capacity of PNIPAM in cold water increases when the temperature is raised off its LCST (LCST $\approx$ 32–34 °C), leading to the "coil to globule" of the polymeric chain's (CG) transition. The CG transition is in charge of phase inversion into rich layers. Polymeric/water phases further exhibit volume phase transition (VPT) [114]. A loss in entropy of water molecules enveloping the hydrophilic polymeric chain is counterbalanced by an increase in enthalpy owing to hydrogen bonding between the hydroxyl groups surrounding the polymeric chain's hydrophobic sections. Hydrophobic hydration is a process that allows a hydrophobic polymer to stay hydrated in an aqueous environment. If the temperature is increased above LCST, water molecules leave the polymer chain and form a globule structure. As a result, the PNIPAM–polymer is hydrated, and a definite volume phase transition is observed. The phase separation initially occurs due to PNIPAM molecule incorporation into larger aggregates [115,116] via several mechanisms and factors, e.g., dewetting caused by solvent fluctuations, cooperative hydration [117–119], the aqueous medium's energy state [120], endothermic heat [121], precipitation polymerization [122], etc. The hydrogen bond between water molecules and PNIPAM is weaker due to the temperature rising above LCST, leading to the formation of an unstable solution. Further, the transitions of the PNIPAM–polymer can be confirmed by FTIR spectroscopy; the hydrodynamic diameter of PNIPAM gel affects the volume phase transition, causing dehydration of the polymeric gel [114].

The dependency of LCST on molecular weight and concentration of PNIPAM polymer in H2O and D2O can be confirmed via dielectric relaxation spectroscopy with small- and wide-angle x-ray scattering (SWAXS) (DRS) to show phase transition. Several investigations have reported a strong effect of interpenetration between the diverse chains of PNIPAM at high concentration decreasing correlation length (ξ). The molecular weight of PNIPAM is entirely independent of ξ at higher concentrations due to PNIPAM chains' crammed state [116]. Interface formation and interchange aggregation are reported to be higher as a result of lowering the molecular weight of the polymer [116]. Several investigations have studied the phase transition effect due to LCST and confirmed peculiar behavior prevails with hydration [118,123–125]. The phase transition of the PNIPAM network can also be modulated by precipitation polymerization at 37−45 °C (near the LCST). Several analytical studies, e.g., atomic force microscopy (AFM) with photon correlation spectroscopy (PCS), etc.; have reported narrow, dispersed, spherical microgel and hydrogel

volume phase transition behaviors [126,127]. Moreover, the phase transition property of PNIPAM-based hydrogel systems is advantageous due to its high mechanical strength and encapsulation capability, which has gained more attention in biomedical and tissue engineering applications [128].

5. Preparation of PNIPAM-Based Hydrogel Systems

The ideal hydrophilic polymer-based hydrogel possesses good biocompatibility and cell viability, excellent mechanical strength (especially stiffness for tissue engineering), high adhesion, moisture retention, promotion of cell proliferation, and high absorption capacity of the fluid for tissue engineering and wound healing [129]. Hydrogels are hydrophilic/hydrophobic monomeric unit-based systems that can be crosslinked via several techniques (e.g., physical and chemical crosslinking) to produce an elastic structure that can be affected/modulated via monomer, initiator, and crosslinker selection [130]. The synthesis or preparation of hydrogels with various functional properties can be initiated with physical and chemical crosslinking [129]. Several physical crosslinking methods (as displayed in Figure 1), e.g., ionic interaction, hydrophobic bonds, protein interaction, etc.; may improve the toughness and self-healing ability of the hydrogel system, which is further required for biomedical application. The hydrogels formed by ionic interaction, i.e.; dynamic interaction of the negatively charged groups or metal-ligand interactions, have improved self-healing, ionic conductivity, biological properties, etc. However, various limitations have also been reported, e.g., poor mechanical characteristics, complex/strong bonds between polymers, etc.; limiting the preparation technique's usage [129]. Several investigations have been reported e.g., alginate/N-isopropylacrylamide (NIPAM) hydrogel [131], PNIPAM/poly(sodium acrylate) hydrogel [132], methacryloylchitosan/PNIPAM hydrogel [133], polyacrylamide/sodium alginate IPN hydrogel [134], etc.; based on ionic interaction of PNIPAM-based hydrogel systems for improving stiffness, cell viability, and mechanical integrity of the hydrogel system. Another physical crosslinking method involves the usage of dynamic hydrogen bond interaction, which is often unstable in an aqueous environment but is possible to rebuild after breaking; it can improve self-healing, cell biocompatibility, biodegradability, etc.; properties [135] via an IPN hydrogel preparation effective in wound-healing dressing. Several investigations, e.g., chitosan-poly (vinyl alcohol) (PVA) DN (double network) hydrogel [135], sodium alginate (SA)/polyacrylamide (PAM) semi-IPN hydrogel [136], hydrazide-functionalized PNIPAM/dialdehyde dextrin thermoresponsive hydrogel [137], etc.; have reported, based on dynamic hydrogen bond mechanistic, PNIPAM hydrogel preparations for biomedical application. Another commonly utilized physical crosslinking method, freeze–thaw, can form ice crystal and fabricate the polymeric chain around the crystals, followed by fabrication of a microporous structure while melting the crystals [138]. The freeze–thaw method can proliferate stem cells and ECM deposition [139], cell compatibility, and biodegradability [140] in the biomedical application based on the modulation of temperature, time, number of cycles, polymer contents, etc. [140,141]. Some recent investigations, e.g., PNIPAM hydrogel [142], PNIPAM/cellulose nanocrystal hybrid hydrogel [143], chitosan-graft-PNIPAM/PVA hydrogel [144], etc.; utilized the freeze–thaw physical crosslinking method and were reported to have high encapsulation efficiency, stimuli-responsive, adsorption capacity, etc. Hydrophilic polymers with hydrophobic end groups/side chains/monomers can be associated via physical crosslinking, resulting in high mechanical strength via strong hydrophobic interaction [129]. Several studies e.g., polyacrylamide (PAAm)/polyacrylic acid (PAAc)/PNIPAM hydrogel [145], poly(N-isopropylacrylamide) hydrogel [146,147], etc.; have been successfully prepared and reported high mechanical strength for biomedical application. The low mechanical stability and strength of physically crosslinked, reversible hydrogels may improve the utilization of chemical crosslinkers connected via covalent interactions. Diverse chemical crosslinking mechanisms have been reported, e.g., conjugation reaction, free radical polymerization, enzymatic reaction, etc.; where the hydrogel was formed via covalent bonds [148]. Conjugation occurred in mild conditions in the presence of Michael addition,

Schiff's base, Diels–Alder addition, etc.; which are green methods in the presence of condensate functional groups to improve biodegradability, transparency, and adhesiveness of the hydrogel system [129,148]. To overcome the limitations associated with the mechanical properties of hydrogel prepared by conjugation, free radical polymerization was reinforced via heating, ultraviolet radiation, energy radiation, electrolysis, etc.; to improve the swelling, porosity, and mechanical strength of the hydrogel system for biomedical application [148]. Several studies, e.g., PNIPAM/magnetite nanoparticles hydrogel [149], poly(*N*-isopropylacrylamide) hydrogel [150], PNIPAM–Ln(DPA)3 hydrogels [151], PNIPAM/gold nanocluster hydrogel [152], etc.; have utilized free radical polymerization for PNIPAM-based hydrogel preparation to improve mechanical strength and stability. The enzymatic reaction of natural polysaccharides in the presence of several enzymes, e.g., transglutaminase, tyrosinase, urease, horseradish peroxidase, etc.; occurs in very mild conditions and can retain the biological properties and improve the mechanical strength of the polymers utilized for hydrogel preparation. In various reports, e.g., *N*-isopropylacrylamide (NIPAM) and acrylic acid (AAc) hydrogel [153], vinylimidazole/PNIPAM) hydrogel [154], NaCMC/PNIPAM hydrogels [155], etc.; enzymatic crosslinking was seen to be effective for improving the mechanical stability and strength of PNIPAM-based hydrogels.
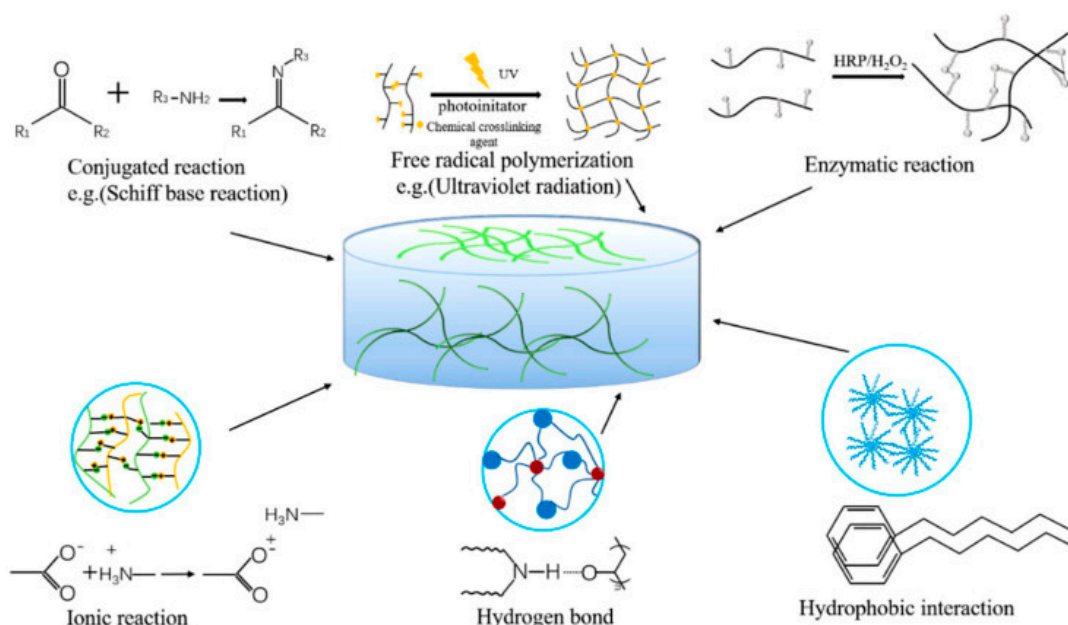
Figure 1. Physical and chemical crosslinking methods to prepare hydrogel systems for biomedical application [128].

6. Formulation Approaches for Tailoring the Mechanical Behavior of PNIPAM Composite Hydrogel

The biomedical application of PNIPAM composite hydrogel must be considered based on biodegradability, stimuli-responsiveness, encapsulation efficiency, drug release behavior, mechanical strength, self-healing properties, etc.; which further depends on the selection of biomaterials, formulation strategy, and incorporation of other materials inside the hydrogel system, especially for drug delivery, tissue engineering, and wound healing. Several common crosslinking strategies have been utilized for hydrogel preparation to improve mechanical strength, but when it comes to the incorporation of drugs/molecules in the hydrogel system, the mechanical properties raise concern. Therefore, several techniques have been adopted to fabricate PNIPAM composite hydrogel, e.g., copolymerization with other monomers, fabrication/incorporation of polymeric nanoparticles, formation of IPN or nanocomposite hydrogel, etc.; where temperature, reaction conditions, chain functionality, drying method, degree of crosslinking, pH, and ionic strength can be tuned to improve the mechanical strength of the PNIPAM composite hydrogel [40,74]. Interpenetrating

polymer networks (IPNs) are strong, noncovalently attached polymer networks consisting of more than two natural/synthetic polymers at a molecular scale and are difficult to separate without breaking chemical bonds. Semi-IPNs are the linear polymeric chain penetrating another crosslinked network, whereas in full IPNs, both the polymeric networks are crosslinked. The higher mechanical strength of IPN hydrogels is mostly via polymerization consisting of natural hydrophilic polymers alone or in a combination of synthetic polymers and natural proteins [40,74]. Double network (DN) hydrogels are a new category of IPN hydrogel with high mechanical strength (tensile strength: 1–10 MP, compressive fracture stress: 20–60 MPa, etc.) and higher moisture absorption capacity, effective for wound dressing [74]. IPN hydrogel may be crosslinked to such an extent that drug release will be retarded, and the degree of crosslinking also affects particle size, polydispersity, degree of polymerization, etc.; these are considered the main limitations [104,156] of the IPN hydrogel. Some recent investigations have reported that the PNIPAM IPN hydrogel improved various mechanical properties e.g., chitosan/PNIPAM IPN hydrogels [157], poly(acrylic acid)/PNIPAM IPN hydrogel [158], luteolin/hyaluronic acid (HA)/PNIPAM IPN hydrogel [29], etc. Another strategy to improve the mechanical properties of PNIPAM hydrogel is copolymerization by optical or chemical crosslinkers in the presence of an initiator in the solvent system. The copolymeric hydrogel had tuned biological and mechanical properties, especially the swelling ability of the polymeric networks, but was a poor bacterial barrier [159] and had weak tensile stress [160], unstable functional groups [161], noncovalent bonds [161], etc.; which may cause concern in biomedical application. A few recent investigations were reported on PNIPAM-based copolymeric hydrogel systems, e.g., Laponite® platelets/PNIPAM hydrogel [162], polypyrrole/PNIPAM hydrogel [163], polyethylene glycol diacrylate (PEGDA)/chitosan (CS)/PNIPAM hydrogel [164], chitosan–*N*-2-hydroxypropyl trimethylammonium chloride (HACC)/PNIPAM hydrogel [165] etc.; where biological properties and mechanical properties were improved. Recently, nanoparticle-loaded composite hydrogels gained significant consideration due to high stimuli responsiveness, reversible deformation, one-pot synthesis method, notable biological and mechanical properties (i.e.; more elongation strength and higher compression); they were prepared via physical crosslinking or covalent integration. Several inorganic/metallic nanoparticles, e.g., ceramic, hydroxyapatite, carbon-based nanoparticles, etc.; can also be loaded into the PNIPAM-based hydrogel system due to their biological abilities and modulating mechanical strength, making them effective for tissue engineering and wound healing [74]. Despite several biological advancements of PNIPAM-based nanocomposite hydrogels, a few limitations have been reported, e.g., low biosorption in vivo, poor stimulation for the proliferation of new tissue, mechanical degradability in tissue engineering, etc.; which may limit utilization, especially in tissue engineering application [166]. Some recent studies, e.g., silver nanoparticles/(PNIPAM166-co-n-butyl acrylate9)-poly(ethylene glycol)-(PNIPAM166-co-n-butyl acrylate9) copolymeric hydrogel [167], cellulose nanocrystals/PNIPAM hydrogel [168], fibroblast growth factor/sodium alginate (SA)/PNIPAM nanogel [169], polydopamine nanoparticles/PNIPAM hydrogel, etc.; showed high stimuli responsiveness [167], encapsulation efficiency [168], storage modulus, and water absorption capacity [169] in tissue engineering and wound healing applications. Therefore, choosing the best material to form a hybrid system with PNIPAM requires extensive materials study, which can further modulate the properties and functionalities of PNIPAM-based hydrogels in biomedical applications.

7. PNIPAM-Based Hydrogels in Drug Delivery

Considering the thermoresponsive polymer poly (*N*-isopropylacrylamide) (PNIPAM) for its precise structure as well as properties, mainly because of temperature feedback that is close to human body temperature and that it can be fine-tuned to meet the imperative temperature–pH dual responsiveness of drug delivery systems [39], thermosensitive polymer free-radical polymerization was used to make PNIPAM. When exposed to organic solvents, the risk of drug denaturation and aggregation increases because hydrogels are

made up of a substantial amount of water, and the crosslinked polymer network is decreased [170,171]. As a result of the polymer network containing crosslinks, hydrogels are solid-like and can possess various mechanical properties, for example, tunable stiffness, allowing their physical qualities to be harmonized with the human body's different soft tissues; additionally, the stimuli-responsive hydrogels adjust their structural properties in response to peripheral stimuli and are also conditional based on environmental changes Stimulus-responsive hydrogels can alter phase or volume in response to stimuli and perform specified activities. A hydrogel that responds to stimuli such as near-infrared (NIR) may be modulated error-free by regulating the radiation intensity, light exposure time, and irradiation sites [172]. The crosslinked network can hinder the infiltration of several proteins; therefore, it protects against premature degradation of bioactive therapeutics by the inward diffusion of the enzymes. This is critically valuable for highly labile macromolecular therapeutics (meant for monoclonal antibodies and recombinant proteins), consisting of an escalating proportion of newly approved and under development drugs [171]. Interaction of PNIPAM with various other molecules comes up with many leads in therapeutic as well as biomedical studies. Strategies have been established to enhance the weak reaction to NIR irradiation of PNIPAM hydrogels, for instance by introducing NIR-responsive nanocomponents, including Fe_3O_4 nanoparticles, carbon nanotubes, graphene oxide nanosheets, and many more, into the hydrogel system.

Khan et al. utilized PNIPAM and carboxymethyl chitosan to create cytocompatible in situ crosslinked pH/thermo-dual sensitive injectable hydrogels (CMCS-g-NIPAM) via combining cold and free radical polymerization techniques. After subcutaneous injection in vivo, the produced formulations were intended to be utilized as drug depots for 5-fluorouracil (5-FU). Tube titling and optical transmittance studies were used to examine and validate the phase transition from the sol–gel state to the physiological range of temperature. The produced formulations had the most significant release in acidic pH at 25 °C, according to an in vitro release profile. An MTT assay was used to assess the toxicity of empty gel expressions on L929 cell lines, and the results verified cytocompatibility with no observable toxicity. In vitro cytotoxicity of drug-loaded hydrogel against HeLa and MCF-7 cancer cell lines demonstrated that 5-FU in depot state had controlled cytotoxicity compared to free 5-FU solution. In contrast to the loaded form, the IC50 values for free 5-FU (21.05 g/mL and 18.66 g/mL) were more significant. The results showed that the suggested porous in situ hydrogel formulations are pH/temperature-sensitive and capable of delivering regulated drug release systemically and intratumorally [173].

Kim et al. developed a double-crosslinked permeating polymer network (IPN) hydrogel with pH-sensitive hyaluronic acid (HA) and PNIPAM via radical polymerization and Michael addition, which aids in transdermal administration of luteolin while suppressing keratinocyte hyperproliferation in psoriasis. According to texture analysis and rheometry, the most adherent and stable crosslinked networks were found in an IPN hydrogel with a 3% crosslinking agent concentration. HA-PNIPAM IPN hydrogel successfully delivered luteolin to the epidermis and dermis, and monitoring the cytotoxic effects of the hydrogel for topical application revealed no toxicity. Therefore, IPN hydrogels might be used for luteolin transdermal administration for psoriasis skin alleviation [29].

Dynamic hydrogels are kept together by transiently stable connections, giving gels different features such as self-healing and shear-thinning [174]. They allow controlled regional and systemic delivery after treatment via a subcutaneous method for ongoing therapy in various disorders [173]. In this context, McInnes et al. investigated the long-term and temperature-dependent drug delivery of biodegradable porous silicon (pSi) loaded with fluorescent anticancer drug camptothecin (CPT) and coated with poly (*N*-isopropyl acrylamide-co-diethylene glycol divinyl ether) (PNIPAM-co-DEGDVE) or non-stimulus-responsive poly (amino styrene) (pAS) via long-term and temperature-dependent drug delivery by initiating chemical vapor deposition (iCVD). The pSi coated with non-stimulus-responsive poly (amino styrene) (pAS) also exhibited continual drug distribution profiles and independent of the release temperature. CPT was released in a burst form from

the uncoated oxidized pSi control (21 nmol/(cm^2 h)), and this was nearly comparable at temperatures between 25 °C to 37 °C, the LCST of the switchable polymer employed, PNIPAM-co-DEGDVE (28.5 °C). At 25 °C and 37 °C, the burst drug release of the pSi-PNIPAM-co-DEGDVE section was much more sluggish, at 6.12 and 9.19 nmol/(cm^2 h), respectively. The total quantity of CPT distributed in 16 h was 10% greater at 37 °C compared to 25 °C for pSi coated with PNIPAM-co-DEGDVE (46.29% vs. 35.67%), showing that this polymer may be utilized to deliver drugs at high temperatures. The drug delivery patterns of pSi coated with pAS were likewise sustainable, although they were unaffected by the release temperature. These findings indicate that by functionalizing pSi using iCVD polymer films, it is possible to create long-lasting and temperature-responsive drug delivery. The iCVD method has several advantages, including applying the iCVD coating following drug loading to avoid triggering drug deterioration, which is frequently caused by being exposed to variables such as solvents or high temperatures. Importantly, because the iCVD approach is not affected by the surface chemistry or pore size of the nanoporous matrix being coated, it can be used on a wide variety of surfaces [175].

Surface introduced reversible addition-fragmentation chain-transfer (SI-RAFT) polymerization was used by Zheng et al. to produce a dual-responsive thermal- and pH-sensitive nanocarrier, where the core is silica and the shell is a block copolymer of poly (methacrylic acid) (PMAA) and PNIPAM. At extreme temperatures, the resultant SiO$_2$-PMAA-b-PNIPAM elements are distributed independently in an aqueous solution, yet they are reversibly aggregated under acidic circumstances or at increased temperatures. These dual-responsive nanoparticles were used as carriers to transport the model drug doxorubicin (DOX) with excellent entrapment efficacy and loading capacity because of their small size (15 nm), lightweight cores, and high graft density (0.619 chains/nm^2) generated using SI-RAFT polymerization. Both the temperature and pH of the surrounding media also influenced the rate of drug release. Furthermore, these nanoparticles preferentially precipitated under an acidic environment with rising temperatures, suggesting that they may be more capable of accumulating at tumor locations. Cytotoxicity investigation indicated that DOX-loaded nanoparticles were far more efficient against Hela cells, unlike free DOX at the same dosage. According to a cellular uptake experiment, SiO$_2$-PMAA-b-PNIPAM nanoparticles may efficiently transport DOX molecules into the nucleus of Hela cells. These characteristics suggested that SiO$_2$-PMAA-b-PNIPAM nanoparticles are a viable therapeutic option [176].

Additionally, Peralta et al. synthesized magnetic mesoporous silica nanoparticles with thermoresponsive polymer grafting for regulated drug delivery. For this purpose (PNIPAM-co-MPS), iron oxide nanoparticles with mesoporous silica shells were grafted with PNIPAM-co-3-(methacryloxypropyl)trimethoxysilane). Grafting and polymerization of as-prepared nanoparticles was achieved in a single step, followed by a radical polymerization technique. Using this approach, the polymer was effectively grafted onto the silica shell, leaving the mesopores empty for drug loading. To evaluate the efficacy of the fused nanoparticles as a thermosensitive drug delivery vehicle, ibuprofen was employed as a standard drug. In vitro drug delivery experiments were performed between 25 °C to 40 °C on the polymer's LCST (PNIPAM-co-MPS). There was a significant contrast of 80% in ibuprofen release at these two temperatures, with the drug being released quickly and completely at 40 °C. These results suggest that the thermoresponsive copolymer acts as a barrier to the temperature-controlled release of the drug encapsulated within the mesopores. As a result, co-MPSs are thus promising magnetic and thermoresponsive nanocarriers for regulated medication delivery [177].

In another investigation, Li et al. widely studied a PNIPAM-MAPOSS hybrid hydrogel established on the presentation of acrylolsobutyl polyhedral oligomer silsesquioxane (MAPOSS) into the PNIPAM matrix in the presence of polyethylene glycol, which was prepared via radical polymerization (as shown in Figure 2A). To alter the pore size, PEG was employed as a pore-forming agent. MAPOSS lowered gel swelling ratios (as shown in Figure 2B) and reduced the LCST, triggering the hydrogels to shrink away at reduced

temperatures (as shown in Figure 2C). However, its hydrophobicity aided in increasing the temperature reliability. The insertion of stiff MAPOSS into the polymer network raised the compressive modulus of the hydrogel by around tenfold [178]. The fused hydrogel can operate as a drug carrier for 5-fluorouracil (as shown in Figure 2D) and might have prospective applications in additional biomedical fields. 5-fluorouracil (5-FU) is an essential anti-cancer agent and perhaps the most extensively used in clinical anti-pyrimidine therapies [179]. It has an excellent therapeutic impact on gastrointestinal cancer and other malignant tumors. However, its fast metabolism in the body may diminish its therapeutic implications [180].
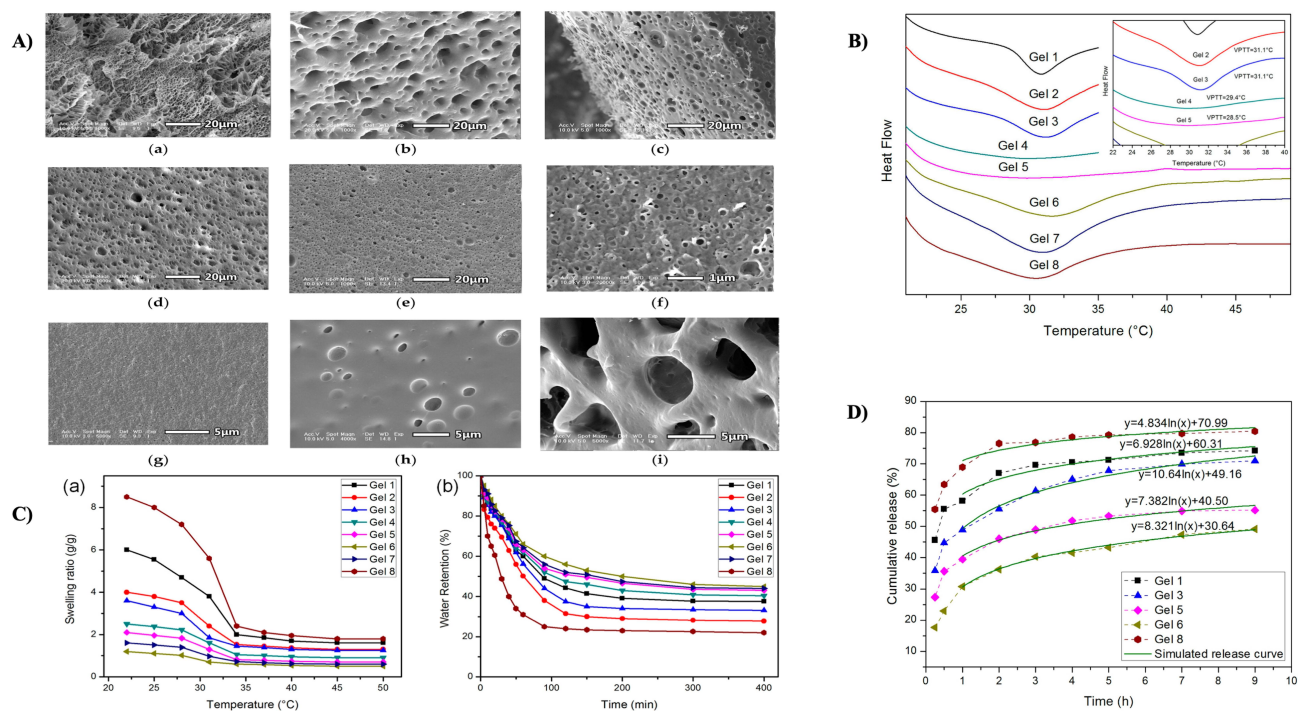
Figure 2. (**A**) SEM images of (a) Gel 1; (b) Gel 2; (c) Gel 3; (d) Gel 4; (e) Gel 5; (f,g) Gel 6; (h) Gel 7; and (i) Gel 8. (**B**) DSC analysis of gel phase transition characteristics. (**C**) (a) Temperature-dependent swelling ratios of gels between 20 and 50 degrees Celsius; (b) gel deswelling behavior at 60 degrees Celsius. (**D**) The simulated release curves and release behaviors of 5-FU from gels in PBS (pH 7.4) at 37 °C [177].

Accordingly, systems such as, PNIPAM@ magnetic NPs (Fe_3O_4)/5-fluorouracil (5FU) and oxaliplatin (OXA)- acrylic acid (AA), 3-butenoic acid (3BA) or allylamine (AL) (pNIPAM@ Fe_3O_4/5FU/OXA-AA, 3BA, AL) [181], doxorubicin(DOX)-gold nanorods (GNRs)-PNIPAM@poly (d, l-lactide)-poly (ethylene glycol) (PLA-PEG) (DAPP)micelles (DOX-GNRs-PNIPAM@PEG-PLA,DAPP) [182], vancomycin (VANCO)/SF-Na Alg NPs/PNIPAM @epidermal growth factor (EGF) (VANCO/SF-Na Alg NPs/PNIPAM@EGF) [183], PNIPAM-superparamagnetic iron oxide nanoparticles (SPION)- etoposide (SPION-PNIPAM-Etoposide) [184], NaALG-g-P(NIPAM$_{80}$-*co*-NtBAM$_{20}$)/Dulbecco's modified Eagle's medium (DMEM) (NaALG-g-P(NIPAM$_{80}$-*co*-NtBAM$_{20}$)/DMEM) [185] and many more have been designed by researchers in order to intensify the use of PNIPAM polymer in the field of drug delivery [186,187]. Table 1 depicts the latest investigations of PNIPAM-based hydrogels in drug delivery.

Table 1. Current studies on PNIPAM-based hydrogel in drug delivery.

Hydrogel Composition	Drug	Preparation Technique	Key Features	References
PNIPAM/poly (ε-caprolactone) 8 dimethacrylate (PCLDMA)/bisacryloylcystamine (BACy)	Levofloxacin	Polymerization	The thermosensitive and biodegradable hydrogels were made from PCLDMA as a hydrolytically degradable unit along with a hydrophobic unit, with BACy as reducible degradation combined with a hydrophilic unit. The advantages of both thermoresponsive and biodegradable polymer systems was amalgamated.	[38]
PNIPAM/PPCN	Chemokine SDF-1 alpha	Sequential polycondensation and radical polymerization	The thermosensitive and biodegradable hydrogels with inherent antioxidant properties for the effective distribution of therapeutics was observed.	[110]
PNIPAM/Hyaluronic acid (HA)	Melatonin	Copolymerization	PNIPAM with HA increased the interrelatedness in microscopic structure with mechanical and chemical properties, and the hydrogels were highly adaptable to liquid/gel conversion temperatures which aid the improved support of the microenvironment for cell expansions and aggregates.	[188]
PNIPAM/Hydroxypropyl guar-graft-poly(N-vinyl caprolactam)	Ciprofloxacin	Graft polymerization	In situ covalent crosslinking of HPG-g-PNVCL copolymer with nano-hydroxyapatite (n-HA) by using divinyl sulfone (DVS) as a crosslinking agent to achieve HPG-g-PNVCL/n-HA/DVS composite material.	[189]
PNIPAM/poly(methacrylic acid)	Doxorubicin	Distillation precipitation or emulsion precipitation copolymerization	The PMAA/PNIPAM-1 microgel, prepared with the moderately-swollen PMAA cores for thicker PNIPAM shells via distillation precipitation copolymerization in acetonitrile, displayed more efficient pH and temperature-independent dual-stimuli responsive controlled releasing performance, while the PMAA/PNIPAM-2 microgels prepared with the fully swollen PMAA cores for thicker PNIPAM shells, via emulsion precipitation copolymerization in water, influenced higher drug-loading capability.	[190]
PNIPAM/HOOC-PNIPAM)-b-poly(2-(dimethylamino) ethyl acrylate)-C$_{12}$H$_{25}$ (HOOC-PNIPAM-b-PDMAEA-C$_{12}$H$_{25}$)/HOOC-poly(2-dimethylamino)ethyl acrylate)-b-PNIPAM)-C$_{12}$H$_{25}$ (HOOC-PDMAEA-b-PNIPAM-C$_{12}$H$_{25}$)	-	Sequential reversible addition-fragmentation chain transfer (RAFT) polymerization	The diblock copolymers were chemically modified to strong cationic, double hydrophilic, block polyelectrolytes via quaternization reaction on the PDMAEA block. The quaternized block copolymers form larger aggregates than the amine-based block copolymers because of the electrostatic repulsions of the positively charged quaternary amine groups.	[191]
PNIPAM/chitosan-poly(methacrylic acid) Cs-PMAA	-	Free radical emulsion polymerization	Copolymerized chitosan with MAA along with NIPAM is an improved version of chitosan gel to be further receptive to the atmosphere of the human body, including different pH, ionic strength, temperature, electric field, and enzyme activities. The small size of the particles is essential to ensure that the particles get through to the target site, especially in drug delivery.	[192]

Table 1. *Cont.*

Hydrogel Composition	Drug	Preparation Technique	Key Features	References
PNIPAM/carboxymethyl chitosan/multiwalled carbon nanotube	Doxorubicin	In situ crosslinking polymerization	The hydrogels demonstrated dual-responsiveness of pH and temperature, and high maximal swelling ratios were possessed by multiwalled carbon nanotubes (MWCNTs)–COOH. The hydrogel could be utilized for the site-specific direct delivery of protein or hydrophilic anticancer drugs.	[193]
PNIPAM/3-(methacryloxypropyl)trimethoxysilane)	ibuprofen	Grafting and polymerization	The hybrid nanoparticles were monodispersed in an aqueous medium and displayed temperature dependency of standard hydrodynamic diameter, promoting them as drug nanocarriers. They demonstrated the exceptional temperature-regulated delivery of the model drug. Specifically, a low % release of ibuprofen below LCST along with a complete and fast ibuprofen delivery at higher than LCST contrasted the earlier report.	[177]
PNIPAM/poly(2-(dimethylamino) ethyl acrylate)20-b-PNIPAM)11-b-poly(oligo ethylene glycol methyl ether acrylate)18 (PDMAEA20-b-PNIPAM11-b-POEGA18)	-	Sequential reversible addition-fragmentation chain transfer polymerization	The thermoresponsive behavior was displayed by amine-based triblock terpolymer, despite the low amount of PNIPAM block in comparison to other comprising blocks. The chemically altered triblock terpolymers self-assemble into larger aggregates in the whole temperature scale compared to the amine-functionalized triblock terpolymer as a result of electrostatic repulsions of the permanently charged quaternary amine groups of the modified PDMAEA blocks.	[191]
PNIPAM/N,N-dimethylacrylamide (DMA)	-	Reversible addition-fragmentation chain transfer (RAFT) polymerization	The synthesis of six NIPAM and DMA-based statistical, ABA triblock, and ABABA pentablock copolymers for each comprised one or two dodecyl hydrocarbon end-groups. The results demonstrated extraordinary and carefully balanced tradeoffs among short non-polar end groups and customized hydrophobicity in the nanoscale self-fabrication of PNIPAm-based copolymers in the water near the LCST.	[194]
PNIPAM/poly(2-(4-formylbenzoyloxy) ethyl methacrylate)	Doxorubicin	Disulfide linkages	Shells of disulfide-bonded temperature-sensitive block copolymers act as gatekeepers to control drug release. The developed multifunctional materials do not produce premature release in blood circulation but accelerate drug release inside cancer cells.	[195]
PNIPAM/polyglutamic acid (γ-PGA)/polyethylene glycol (PEG)	-	Polymerization	The optimal mass ratio of comonomers (NIPAM, γ-PGA, and PEG), crosslinker, and initiator was secured at 1:0.2:1:0.01:0.01, defined by the response surface method (RSM). It was also discovered by RSM that the ESR was considerably reliant on the crosslinker along with the collaboration amongst the initiator and γ-PGA.	[196]

Table 1. *Cont.*

Hydrogel Composition	Drug	Preparation Technique	Key Features	References
PNIPAM/polystyrene (PS)	-	Anionic polymerization	Thermoresponsive wetting performance as a role of substrate micromorphology with the surface. PS/PNIPAM films of various fusions were spin-casted on microstructured silicon substrates together with or devoid of a native SiO_2 layer, and take up the benefit of the large specific area of the silicon substrates to enrich the film thermoresponsiveness.	[197]
PNIPAM/poly (stearyl methacrylate)	-	Reversible addition-fragmentation chain-transfer (RAFT) polymerization	The triblock copolymer micelles demonstrated a distinctive evolution, initially developing into small, then developing into larger, and finally stable. The transition process was fast as well as reversible with temperature. The hydrophobic PSMA chain segment dropped the LCST of the diblock copolymer micelles.	[198]

8. Gene Delivery

The introduction of transiently active nucleic acids for genetic engineering is a promising approach with prospective uses in the therapy of ailments ranging from tumors to communicable diseases to genetic syndromes. Reviving the expression of a defective protein, repairing faulty transcript splicing, and suppressing or regulating the expression of genes are all strong techniques that might have significant implications in biological discovery and treatment. In the last decade, substantial progress in enhancing gene delivery has been accomplished, and numerous products have entered the market [199]. While utilizing a polymeric transporter, the critical phases of gene delivery (correspondingly known as transfection) are (1) polymer with DNA complexation; (2) insertion of polymer/DNA composite (also known as polyplex) on top of cells for a duration of time frequently known as the transfection period; (3) elimination of composite from cells; and (4) incubation time. In most cases, complexation occurs at ambient temperature, while transfection and incubation occur at 37 °C (the cells' body temperature to survive). Remarkably, thermoresponsive polymers are being utilized to improve transfection effectiveness by varying the temperature during the complexation, incubation, and/or transfection period [20].

Hydrogels constitute a class of biomaterials formed by self-assembling or crosslinking water-soluble polymers into a network [200]. Hydrogels' porous and hydratable structure causes them to gel and swell in the biological milieu, allowing them to be injected locally without invasive surgery [201]. Hydrogels can be engineered via physical (such as ionic and hydrogen bonding and hydrophobic interactions) or chemical (such as Michael-type addition reaction or photo polymerization) crosslinking processes [202]. Additionally, they are designed to demonstrate modified properties to the tissue to be refurbished as 3D-bioprinted constructs [203,204] and/or injectable [205], stimuli-responsive [206], or adhesive systems [207–209]. Self-assembled PNIPAM-co-dAAc nanogels fused with GFP-green fluorescent protein remained extremely expressed in human mesenchymal stem cells (hMSCs) and are also a prospective material for gene delivery [178]. When a stimulus is applied to responsive gels, their properties change. The disruption or development of both chemical and physical crosslinks can cause this alteration, which may or may not be reversible [174]. Unique materials that respond to certain stimuli can be used to encapsulate drugs, proteins, and organisms on a macro and micro scale. Sensory factors such as pH and temperature modify these materials' phases and hydrophobic interactions reversibly. These changes can lead to self-assembly of the materials, which enables controlled drug release and safe gene delivery into cells and tissues [210].

In a study by Zhang et al.; it was revealed that in comparison to traditional PNI-PAM hydrogel, the swelling fractions of PNIPAM hydrogels with extremely permeable microstructures, organized utilizing hydrophobic polydimethylsiloxane (PDMS) along with sodium dodecyl sulfate, were better at room temperature. Their response rates were amplified intensely with the temperature above the LCST. For instance, an innovative hydrogel made in conjunction with a 40% PDMS template lost nearly 95% of its water in five minutes, but standard PNIPAM gel dropped just about 14% simultaneously. When liquid PDMS templates are added to reaction solutions, porous structures are created during polymerization/crosslinking, resulting in improved properties. Bovine serum albumin (BSA) and lysozyme as protein templates were physically absorbed into these micro-structured smart hydrogels. The experimental results revealed that—owing to the size exclusion effect, because BSA with a significant molecular weight has a lower loading efficacy than lysozyme—the loading effectiveness of both peptides in the porous hydrogel was significantly higher than that of the standard PNIPAM hydrogel. For instance, the load-up efficacy of BSA in the porous hydrogel is 0.114, which is around 200% more than the loading efficiency in traditional hydrogel (0.035). At 22 C, both BSA and lysozyme were totally liberated from the permeable hydrogel. Moreover, the rates of protein release from the porous hydrogel may be controlled by adjusting the ambient temperature. These newly developed porous materials exhibited excellent potential for protein or gene therapy since they present a mechanism to improve loading efficiency and manage the release patterns of macromolecular medications from hydrogels [211].

In another study, Chalanqui et al. developed Alg-g-PNIPAM hydrogel via free radical polymerization for the local release of nanoparticles of DNA as a possible medicinal mechanism for men diagnosed with castrate-resistant prostate cancer (CRPC). Considering that CRPC often spreads to the bone, initiating discomfort and death, combined with a slew of other skeletal-associated complications, a copolymer-based hydrogel was developed to extend curative DNA nanoparticles' extended delivery. In milder circumstances, alginate grafted poly(*N*-isopropylacrylamide) hydrogels (Alg-g-PNIPAM)) develop 3D frameworks, making them ideal for the insertion of fragile biomolecules such as DNA. The effect of PNIPAM on copolymer qualities has been thoroughly explored, though the impact of alginate backbone features on copolymer properties has yet to be addressed. Six distinct Alg-g-PNIPAM hydrogels were created using 10% alginate, which differed in terms of molecular weight (MW) and mannuronate/guluronate (M/G) monomer ratio, and 90% NIPAM to create an injectable highly thermoresponsive hydrogel preparation for localized gene delivery (as shown in Figure 3A). Hydrogels with high MW or low M/G ratio alginate backbone tend to have higher stiffness than hydrogels with low MW alginate and a high M/G ratio. A complexed and meshed hydrogel network was also generated by hydrogels with a high M/G ratio, whereas hydrogels with a low M/G ratio developed a simpler architecture with the juxtaposition of Alg-g-PNIPAM sheets. These nanoparticles were made using plasmid DNA (pDNA) functionalized in conjunction with RALA, an amphipathic cell-penetrating peptide intended to penetrate cells efficiently. The rigidity, morphology, injectability, and deterioration of the Alg-g-PNIPAM hydrogel were all influenced by the alginate MW and M/G ratio. Algogel 3001, filled with RALA/pDNA NPs, exhibited the best properties for long-term use. According to the release profiles, RALA preserved the pDNA from degradation over 30 days (as shown in Figure 3C) and provided a persistent and regulated release from hydrogels when matched to pDNA alone (as shown in Figure 3B). After incubating it for 15 days in Alg-g-PNIPAM hydrogel, the efficacy of DNA transfection was evaluated. Flow cytometry analysis of the NPs incubated inside algogel 3001-g-PNIPAM hydrogel demonstrated constant transfection effectiveness of 10%, which was independent of the time of incubation (as shown in Figure 3D) [212].
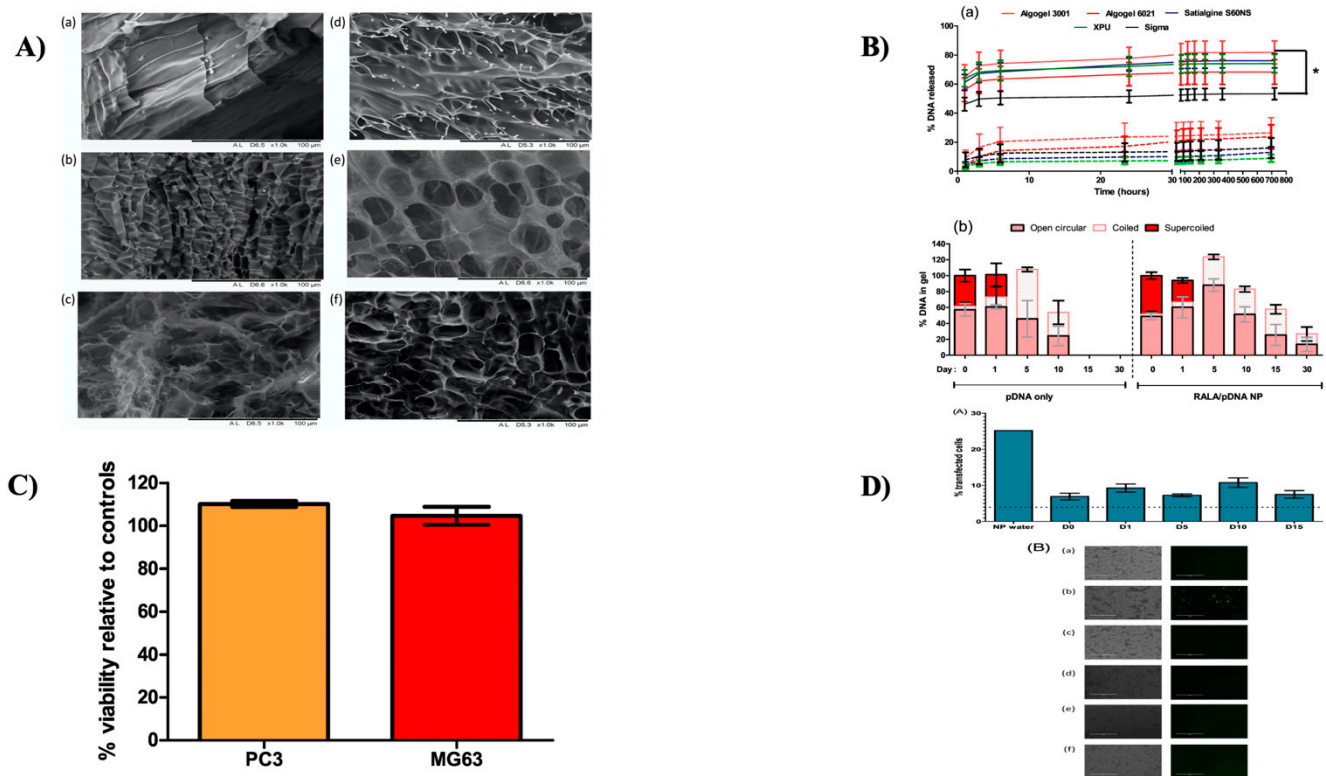
Figure 3. (**A**) SEM structural analysis of Alg-g-P (NIPAAm) hydrogels premised on (a) Algogel3001, (b) Algogel6021, (c) Satialgine S60NS, (d) SatialgineS900NS, (e) Sigma, and (f) XPU alginate. (**B**) As a pDNA and RALA/pDNA NPs delivery device, Alg-g-PNIPAM hydrogel was used. (a) For up to one month in DDW at 37 °C, hydrogels discharged pDNA (continuous line) at a faster rate (burst release) than RALA/pDNA NPs (dashed line). (b) DNA stability was sustained in algogel 3001-g-P (NIPAAm) hydrogels for uncomplexed pDNA for up to 10 days and complexed RALA NPs for up to 30 days; * $p < 0.05$. (**C**) Degradation of algogel 3001-g-PNIPAM hydrogel at 70 °C in cell medium for 3 days caused cytotoxicity in PC3 and MG63 cells. (**D**) Evaluation of DNA transfection effectiveness after 15 days of incubation in Alg-g-PNIPAM hydrogel (A) flow cytometry analysis for transfection efficiency (B) The prevalence of green fluorescent protein-expressing cells for the various treatment groups. Reproduced with permission from [211], copyright Elsevier, 2017.

In another study, Cao et al. utilized conventional radical graft copolymerization to integrate the thermosensitive polymer PNIPAM in the side chain of low-molecular-weight PEI to form an amphiphilic graft copolymer at 80 °C reaction temperature and encapsulated the TRP53 gene, a tumor suppressor gene involved in cell cycle regulation and programmed cell death [213]; pH-sensitive nanogels are ideal for delivering integrated payloads to specific target locations with altered environmental conditions caused by disease processes [214].

In another investigation, Fliervoet et al. conducted a study for offsetting electrostatic and hydrophobic interactions in thermosensitive plasmid DNA (pDNA)-loaded polyplexes for nucleic acid delivery. By using a hetero-functional PEG macroinitiator, NPD triblock copolymers composed of a thermosensitive poly(*N*-isopropylacrylamide) (PNIPAM, N), along with a cationic poly(2-(dimethylamino)ethyl methacrylate) (PDMAEMA, D) and a hydrophilic poly (ethylene glycol) (PEG, P) block with variable block dimensions were formulated. According to dynamic light scattering, the NPD polymers self-assembled into polyplex nanostructures with hydrodynamic diameters ranging from 150 to 205 nm at room temperature in HBS buffer. Polyplexes with a low-down N/P charge ratio of 1 accumulated when heated to 37 °C, whereas greater N/P charge ratios did not. Throughout all N/P ratios and extreme temperatures, stable polyplexes were produced when the cationic D block was comparatively lengthy compared to the thermosensitive N block. The overall

viability of these polyplexes at 37 °C was further supported by H-NMR studies, static light scattering, and possible dimensions. Furthermore, the addition of thermosensitive blocks to NPD-based polyplexes increased cytocompatibility in HeLa cells when associated with PD-based polyplexes with comparable cargo delivery competencies [215].

Correspondingly, HOOC-PNIPAM -*b*-poly(2-(dimethylamino) acrylate)-$C_{12}H_{25}$/DNA (HOOC-PNIPAM-*b*-QPDMAEA-$C_{12}H_{25}$/DNA) [191], chitosan-*g*-PNIPAM) (CPN)@graphene oxide (GO)-cetuximab (CET)/irinotecan (CPT-11)@short hairpin RNA (shRNA) hydrogel (CPN@GO-CET/CPT11@shRNA) [216] and siRNA@poly(2-dimethylaminoethyl methacrylate) (PDMAEMA)/PNIPAM-PEG-PNIPAM hydrogel (siRNA@PDMAEMA/PNIPAM-PEG-PNIPAM) [217] systems were formulated by researchers and demonstrated promising results in gene delivery. Table 2 demonstrates the latest studies on PNIPAM-based hydrogels in gene delivery.

Table 2. Current investigations on PNIPAM-based hydrogels in gene delivery.

Device	Model Drug	Composition	Preparation Technique	Applications	Results	References
Hydrogels	RALA, plasmid DNA (p-DNA)	Alginate (Alg) grafted PNIPAM (Alg-g-PNIPAM)	Free radical polymerization	Castrate-resistant prostate cancer (CRPC)	The copolymer's alginate backbone significantly influenced the mechanical and structural properties of hydrogels. At 37 °C, high-pitched MW alginate improved the copolymer's rigidity, and the M/G ratio affected rigidity as well as the molecular network. In contrast to uncomplexed pDNA, which had a significant rupture release during the first six hours in Alg-g-PNIPAM hydrogels, RALA/pDNA NPs had a prolonged and controlled release over time. This offers up a slew of possibilities for remedial pDNA delivery from this thermoresponsive hydrogel, which proved to have a wide range of medical applications.	[212]
Thermoresponsive hydrogel	RALA/pEGFP–N1	Chitosan-g-PNIPAM crosslinked with genipin	Free radical polymerization	-	The proportion of chitosan in the copolymer affected the hydrogel's breakdown, swelling, NP release level, and storage modulus. The Cs-g-injectability PNIPAM's at room temperature suggested that it may be delivered to the target site in a minimally invasive manner. The hydrogel's ability to provide long-acting drugs to target tissues was demonstrated by sustained NP release and breakdown over three weeks. More crucially, the nucleic acid payload remained active, as evidenced by the NCTC-929 fibroblast cell line's excellent transfection.	[218]

Table 2. *Cont.*

| Device	Model Drug	Composition	Preparation Technique	Applications	Results	References
Thermosensitive hydrogel	Irinotecan (CPT-11)/cetuximab (CET) conjugate graphene oxide (GO) (GO-CET/CPT11), stomatin like protein 2 (SLP2), and short heparin RNA (shRNA)	Chitosan-g-PNIPAM (CPN)	Free radical polymerization	Glioblastoma multiforme	Controlled drug release and increased mechanical strength of the in situ-produced hydrogel were achieved by combining a negatively charged nanocarrier and a positively charged CPN. CPT-11 release from a drug-loaded hydrogel exhibited a 28-day continuous release pattern, whereas the intricate shear modulus rose fivefold after entrapping GO-CET in the hydrogel. The formulation increased anti-tumor activity in vitro by eliciting a 53% apoptotic rate in 2 days. A xenograft tumor model was used to illustrate treatment efficacy, with a 40% reduction in tumor size after 12 days compared to the untreated control group.	[216]
Thermosensitive mesoporous silica nanoparticles (MSN)	microRNA-222 and aspirin (ASP)	Poly(ethylene glycol)-b-poly(lactic-co-glycolic acid)-b-PNIPAM (PEG-PLGA-PNIPAM)	Atom transfer radical polymerization and ring-opening copolymerization	Bone tissue engineering	As previously reported, ASP stimulated bone production, and miR222 triggered Wnt/-catenin/nemo-like kinase signaling to drive differentiation of bone mesenchymal stem cells to neural-like cells. Injection of co-delivered MSN hydrogel into a rat mandibular bone defect resulted in neurogenesis and faster bone development, suggesting that the injectable ASP and miR222co-delivering colloid hydrogel has potential for vascularized BTE.	[219]
Thermoresponsive hydrogels	SiRNA, glyceraldehyde-3-phosphate dehydrogenase (GAPDH)	PNIPAM/MgAl-layered double hydroxides (LDHs) (MgAl-LDH)	Radical polymerization	Degenerative disease of cartilaginous tissues	When the temperature of the hybrid hydrogel was increased from 25 to 37 degrees Celsius, it transitioned from a fluid to viscous gel phase in less than 10 s. The introduction of siRNA against a housekeeping gene into an in vitro model of cartilaginous tissue degeneration comprised of osteoarthritic cells was reported to achieve gene silencing in situ for 6 days with a high gene silencing efficacy (>80%). Providing extracellular matrix scaffolds and interfering with degenerative factor expression, therapeutic RNA oligonucleotides with supporting hydrogel material may offer promises in treating cartilaginous tissue degeneration.	[220]
Nanogels	Green fluorescence protein (GFP) gene, amine functional magnetic iron oxide nanoparticles (NH2-MNP)	PNIPAM-co-acrylic acid (p(NiPAAm-co-AAc)) coated with poly (ethyleneimine) (PEI)	Free radical polymerization	Gene delivery	Treatment with 20 mg/mL PEI-coated nanogels resulted in the maximum EGFP expression. After 24 h of transfection, EGFP expression was found for the first time, lasting up to 72 h. In hMSCs, self-assembled p(NiPAAm-co-dAAc) nanogels conjugated with the GFP gene were strongly expressed, suggesting they may be used for gene delivery.	[210]

9. PNIPAMs Hydrogel in Tissue Engineering

9.1. Cartilage Tissue Engineering

Cartilage is a smooth, elastic tissue membrane that covers the heads of the bones in articulating joints and allows smooth joint motion. It is composed of chondrocytes that are involved in producing collagen fibers and proteoglycans (PG) [221]. Due to its avascular structure, cartilages possess a low rate of healing capacity [222]. Cartilage damage leads to arthritis, the most common cause of disabilities caused by cartilage-related disease in recent years [223]. A scaffold can be a biological or a synthetic microstructure that can provide a niche to accelerate cell growth and trans-differentiation into various phenotypes. Currently, scientists are interested in exploring new and more biocompatible scaffolds for tissue engineering and delivery systems. Thermosensitive hydrogels are the most preferred hydrogels in tissue engineering, and PNIPAM is the one that has been extensively studied [224].

Irregular degenerative cartilage defects are also accompanied by osteoarthritis. Osteoarthritis is a significant disease characterized by pain, cartilage degradation, and inflammation. The uneven composition of injured cartilage further complicates the engineering of appropriate scaffolds for fabrication. Hydrogels are extensively employed for three-dimensional (3D) stem cell culture, but hardly any are utilized for stimulating in situ cell aggregation for specific applications. In this context, Zhang et al. reported the synthesis of a neo-cartilage patch by examining the mechanism of mesenchymal stem cell aggregation within the p(NIPAM-AA) and forcing aggregates onto electrospun film [225]. These cell aggregates promoted chondrogenesis by increasing endogenous growth factor production and extracellular matrix (ECM) deposition inside the p(NIPAM-AA) hydrogel. These in situ-generated cell aggregates were bioengineered into a neo-cartilage patch that might be used to repair superficial irregular cartilage lesions.

Many attempts have been made to develop hydrogel-based synthetic cartilage, but unfortunately, none have achieved cartilage-like properties. In this context, Means et al. concocted a double network (DN) PNIPAM hydrogel that possessed superior mechanical properties similar to cartilage, with a thermal transition temperature adjusted beyond the physiological scale. They prepared the DN PNIPAM hydrogel by using poly (2-acrylamido-2-methylpropanesulfonic acid) (PAMPS) as a primary network and poly(*N*-isopropylacrylamide-co-acrylamide) [P(NIPAM-co-AM)] as another network [226]. PAMPS/P(NIPAM-co-AM)-DN hydrogels exhibited an outstanding cartilage-like characteristic, making them a good choice for cartilage replacement as synthetic cartilage grafts.

For tissue engineering applications, injectable thermoresponsive hydrogels enable excellent cell transport and low invasion. The ability of recently designed thermoresponsive poly(*N*-isopropylacrylamide) (HA-PNIPAM-CL) hydrogels modified with hyaluronic acid (HA) to enrich rabbit ADSC (rADSC) chondrogenesis in the synovial cavity of rabbits as well as in vitro was examined in a study by Wang et al. Physical interaction and chemical crosslinking were used to make HA-crosslinked PNIPAM (HA-PNIPAM-CL) and HA-mixed PNIPAM (HA-PNIPAM-CP) (as shown in Figure 4a). In vitro studies demonstrated that the HA-modified hydrogels equally dramatically boosted cell survival, chondrogenic marker gene expression (aggrecan and type II collagen), and sulfide glycosaminoglycan (sGAG) production in implanted rADSCs as compared to original PNIPAM. HA-PNIPAM-CL, on the other hand, had the best rADSC survivability and chondrogenesis (as shown in Figure 4b,c). The chondrogenic activities of HA-modified hydrogels on rADSCs were validated in vivo by injecting hydrogel-embedded rADSC assemblies into rabbit synovial cavities for three weeks and mapping using CM-DiI labeling. Type II collagen and GAG histomorphological staining were used to detect neocartilage development in the hydrogels. In the synovial cavity of rabbits, rADSC/HA-PNIPAM-CL induced greater hyaline cartilage development than rADSC/HA-PNIPAM-CP and rADSC/PNIPAM constructs (as shown in Figure 4d). These findings implied that the HA-PNIPAM-CL milieu was suited for enhancing ADSC chondrogenesis in articular cartilage tissue regeneration [227].
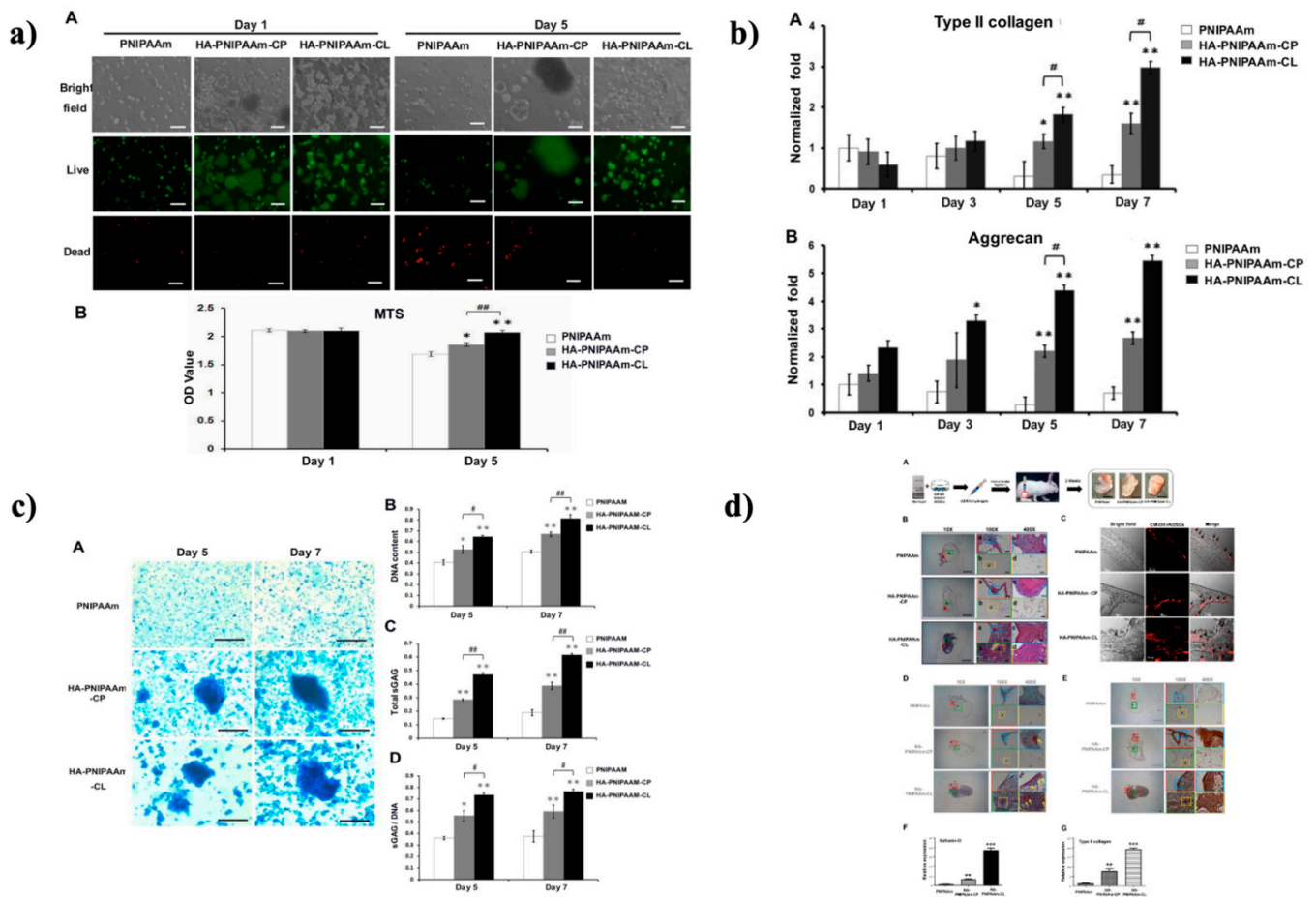
Figure 4. (**a**) The cytocompatibility and cell survival of rADSCs were improved by HA-modified PNIPAM hydrogels. Using (A) live and dead staining and (B) an MTS assay, cell survival of rADSCs encapsulated in PNIPAM, HA-PNIPAM-CP, and HA-PNIPAM-CL hydrogels was determined during days 1 and 5. (**b**) In rADSCs cultivated in PNIPAM, HA-PNIPAM-CP, and HA-PNIPAM-CL hydrogels for 1, 3, 5, and 7 days, the chondrogenic indicators of gene expression of (A) type II collagen and (B) aggrecan were detected. Collagen type II and aggrecan mRNA expression levels in rADSCs cultivated in HA-modified hydrogels are expressed and normalized in comparison to rADSCs cultured in PNIPAM hydrogels, which is designated as 1. (**c**) At days 5 and 7, there was enhanced cell aggregation and cartilaginous matrix sGAG production in rADSC cultured HA-modified PNIPAM hydrogels in vitro. (A) Glycosaminoglycans stained with Alcian blue (sGAG). (B) The DMMB assay was used to quantify the production of sGAG. (**d**) In vivo evaluation of the increase of neocartilage development in rADSCs/HA- PNIPAM-CL constructions using a rabbit model. (A) Illustration of the intraarticular injection of the rADSC/hydrogel constructions into the synovial cavity of rabbit knees. After 3 weeks, injected rADSC/hydrogel constructions were collected from rabbit synovial cavities and analyzed using (B) H&E staining, (C) confocal microscopy for pictures of bright fields, and CM-DiI-labeled rADSCs (red, arrows), (D) safranin-O fast green staining showing sGAG deposition (arrows), and (E) IHC staining for type II collagen synthesis (brown). Normalized relative to the PNIPAM group, which is defined as 1. Quantification examination of safranin-O staining (F) and type II collagen staining (G). Scale bar: 100 μm. (*), (**), and (***) represented $p < 0.05$, $p < 0.01$, and $p < 0.005$ respectively, in contrast with the PNIPAM group. (#), and (##) represented $p < 0.05$, and $p < 0.01$, respectively in contrast with the HA-PNIPAM-CP group [226].

Recent advances in photocrosslinkable hydrogel synthesis have enabled the fabrication of native articular cartilage. However, various aspects, including selecting appropriate cell sources and biocompatible scaffolds for hosting cell support and proliferation, remain to be addressed. Chitosan is widely used as a bio-macromolecular adhesive [228]. It not

only possesses a similar molecular structure to hyaluronic acid and glycosaminoglycans (GAG) but also mimics the natural microenvironment to improve chondrogenesis and modulates cell proliferation and differentiation [229]. In this regard, Mellati et al. described the potential role of chitosan-graft-poly(*N*-isopropylacrylamide) (CS-g-PNIPAM) hydrogel and micropatterning of 3D cell-laden as a technique for manipulating the cell shape and multi-zonal cartilage tissue engineering [230]. The hydrogel was capable of mimicking the superficial zone of cartilage and tended to be a suitable candidate for chondrogenic differentiation of mesenchymal stem cells (MSCs).

Electrospun hydrogels were used to make fibrous scaffolds. However, they tend to collapse when cells are seeded into them. An electrospun hybrid scaffold composed by integrating PEG-PNIPAM in conjunction with a biodegradable, eco-friendly polymer such as poly (ε-caprolactone) (PCL) might overcome this limitation. This hybrid scaffold had improved mechanical properties and enhanced the chondrogenic demarcation of human mesenchymal stem cells (hMSCs) [231]. In another analysis, Saghebasl et al. demonstrated a biodegradable thermosensitive hydrogel scaffold (PNIPAM-PCL-PEG-PCL-PNIPAM)/gelatin fabricated by TIPS (thermally induced phase separation). The in vitro study found that the scaffold provided a better survival rate for encapsulated cells and expressed cartilage-related genes. Hence, it serves as a potential approach to encourage the development of cartilage tissue [232].

Apart from this, other formulations that researchers have synthesized are Au NPs/chitosan/k-carrageenan/poly(NIPAm) [233] and vancomycin-loaded cellulose nanocrystals/Fe_3O_4/PNIPAm [168], which showed promising results in cartilage tissue engineering.

9.2. Bone Tissue Engineering

Bone is a hard tissue comprised of different bone cells containing osteoblasts and osteocytes [234]. The structural integrity of bone is threatened by physical injury. Gold standard medication for bone defects is an autologous bone graft. Nevertheless, the scope of autologous bone grafting is restricted by irregular shape, donor number, and immunogenicity. Therefore, bone tissue engineering (BTE) becomes crucial to overcome these limitations. Hydrogels are applied for bone regeneration, and various studies reported using modified hydrogels to increase new bone formation [235].

Due to the avascular nature of bone, the vitality of cells after implantation is a critical concern in bone tissue engineering. Trans-differentiation of human bone marrow-derived mesenchymal stem cells (hBMSCs) to an endothelial cell phenotype is achievable. This can be accomplished by combining the delayed distribution of vascular endothelial growth factor (VEGF) with osteogenic stimuli to increase both angiogenic and osteogenic differentiation [236]. Osteoclasts are involved in the secretion of bone morphogenetic proteins (BMPs) into the extracellular matrix during bone development. BMP-2, a member of the transforming growth factor (TGF) class, controls the development of chondrocytes and osteoblasts [234]. Following this, Muller et al. suggested the use of poly (NIPAM-co-DMEAEMA)/cellulose sulfate complex hydrogel for switchable release of bone morphogenetic protein (BMP-2) on demand for local bone healing and regeneration [237]. The authors reported that with the introduction of a thermoinducible delivery system, the release of BMP-2 from PNIPAM-DMAEMA/CS increases with increasing temperature. Overall results demonstrated that the delivery system has the potential to treat acute bone defects such as osteoporosis.

Hydroxyapatite (Hap) is an inorganic component of bone; synthetic HAP, $Ca_{10}(PO_4)_6(OH)_2$, a calcium phosphate, shows structural along with chemical similarities with the mineral phase of human bone and teeth [238]. HAP has been extensively used with hydrogel scaffolds for bone regeneration studies [239]. Thorpe et al. developed a laponite (crosslinked PNIPAM-co-DMAc) hydrogel delivery arrangement stacked with hydroxyapatite nanoparticles (HAPna) [240]. The study focused on the efficacy and in vivo safety of the hydrogel in rats. This resulting delivery system was biocompatible while promoting enhanced bone formation and assisting cell movement to stimulate incorporation with encircling bone. The

in vivo and in vitro studies exhibited the induction of osteogenic differentiation without the need for supplementary growth elements in mesenchymal stem cells (MSCs).

Postmenopausal osteoporosis (PO) is caused by estrogen deficiency with age in females, which is distinguished by minimal bone mineral density (BMD) loss, causing bone fragility. Estrogen affects bone by increasing calcitonin production, which in turn inhibits bone resorption and lowers the sensitivity of bone mass to parathyroid hormone (PTH), sequentially reducing bone resorption. Menopause leads to estrogen deficiency, which impairs the normal bone turnover cycle. Therefore, the quantity of bone reabsorbed surpasses the total of bone deposited, ultimately leading to the net loss of bone [241]. Mesoporous hydroxyapatite (MHA) possesses meticulous pore size and optimized pore volume as well as exhibiting excellent biocompatibility [242]. Simvastatin (SIM), commonly employed in the treatment of hyperlipidemia, has recently gained popularity as a bone development medication. However, the hydrophobicity of SIM makes it challenging to release SIM sustainably and locally in vivo. Wu et al. fabricated PNIPAM brush-modified MHA nanoparticles loaded with simvastatin [243]. This system delivered a constant release of hydrophobic SIM and exhibited great potential for promoting osteogenesis.

In contrast, graphene derivatives have been shown to support stem cell attachment and differentiation [244]. Graphene oxide as a scaffold shows excellent biocompatibility, with its exceptional physicochemical properties, comprising brilliant hydrophilicity with hydrophilic functional groups. To exploit this property, Amiryaghoubi et al. invented a temperature-sensitive injectable hydrogel employing poly (*N*-isopropylacrylamide)-based copolymer/graphene oxide (GO) through chitosan (CS) as a natural polymer. The study found that prepared hydrogel was highly biocompatible for hDPSCs by providing a biomimetic ECM microenvironment for hDPSC proliferation, and thus could be used as a potential bioactive material for transplantation of hDPSCs. Developing an injectable bone-forming hydrogel would have broad clinical and economic benefits. Calcium phosphate cements (CPCs) are frequently used for bone regeneration applications. CPCs possess excellent biocompatibility with bone tissue. Unfortunately, CPCs are highly brittle and their usage is limited in load-bearing skeletal sites. To improve their toughness, Petre et al. suggested the incorporation of fibers as the enforcing component for CPCs by covalently modifying the surface of poly (vinyl alcohol) with PNIPAM brushes [245].

Likewise, many such formulations have been designed by researchers, which displayed promising results, such as (PNIPAM)/hydroxyapatite (HAp) scaffold [246], carboxymethyl xylan (CMX)-PNIPAm (CMX-PNIPAm) [247], etc.

9.3. Cardiac Tissue Engineering

In the current scenario, tissue engineering becomes a ray of hope for cardiac regeneration. Several studies have reported cardiac regeneration, such as providing mechanical support, cardio-protective molecule delivery, and others [248]. Hydrogels are an essential therapeutic approach in cardiac tissue engineering for various reasons. Concerning the cardiac environment, the properties of injectable hydrogels can be altered to provide physical, chemical, and electrical compatibility. To provide structural support to continuously contracting cardiac muscles, hydrogels with varying stiffness can be synthesized to enable their biocompatibility. Hydrogels may serve as a controlled delivery system for injecting genes directly into damaged cardiac tissue for tissue regeneration [248].

Myocardial infarction (MI), typically referred to as a heart attack, is a condition in which the heart muscle is permanently damaged. Fibrin-rich thrombus development, which inhibits blood flow in coronary arteries, is a significant cause of MI. When oxygenated blood flow returns to the tissue after a period of ischemia, ischemia reperfusion injury (IRI) occurs (hypoxia). This restoration causes inflammation and oxidative damage, which contributes to cardiac fibrosis, and lack of energy for cardiomyocytes leads to death. Cardiac function can be improved after an MI by injecting biomaterials into the infarcted heart's ventricular wall and by reducing stress on the left ventricular wall of cardiomyocytes by mechanical load shielding.

In an investigation, Mihalko et al. used fibrin-specific poly (*N*-isopropylacrylamide) nanogel in a projected dual-delivery technique capable of reestablishing blood flow and simultaneously inhibiting cardiac fibrosis. This system consisted of tissue plasminogen activator (tPA) combined with a cell contractibility inhibitor (Y-27632); tPA, is an enzyme responsible for clot breakdown, and Y-27632 is essential in rho-associated protein kinase (ROCK) signaling pathway inhibition. Strategically, the dual delivery system design allowed for a preliminary release of tPA to soften the prime MI fibrin deposition, trailed by an additional constant release of Y-27632 (as shown in Figure 5a) to avert cardiac scarring through obstructive critical cellular replies intricated into the onset plus development of fibrosis. The in vitro studies showed fibrin degradation with decreased cardiac cell fiber formation (as shown in Figure 5b,c). In contrast, in vivo studies demonstrated improved ventricular ejection fraction and reduced infarct size (as shown in Figure 5d), advocating the value of this therapy for improving cardiac function after a heart attack [249].
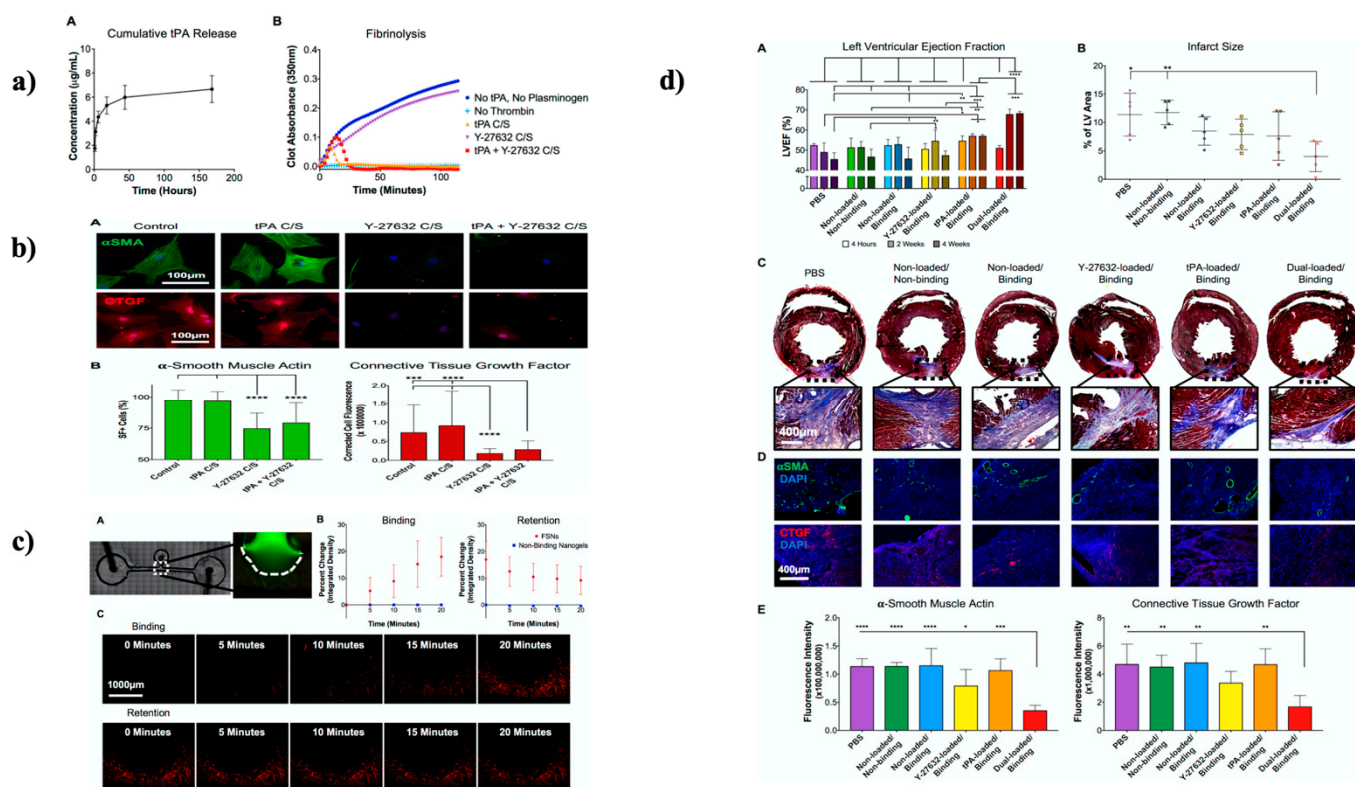
Figure 5. (**a**) Effective burst release of tPA is indicated by cumulative tPA release from C/S nanogels (A) and examination of fibrinolysis in the existence of drug-loaded nanogels (B). (**b**) The expression of fibrotic markers such as -SMA and CTGF on neonatal rat cardiac fibroblasts is reduced by introducing drug-loaded C/S particles in vitro (A). Percentage of stress fiber-positive cells for -SMA and adjusted total cell fluorescence for CTGF were used to quantify the results (B). (**c**) In vitro, FSNs adhere to and are maintained at fibrin clot borders at 1 sec-1 wall shear rates. A fibrin clot (green) was polymerized along the channel using PDMS molds (A). Particle binding (red) throughout 20 min and retention (C) during a 20 min buffer wash demonstrate deposition at fibrin clot sites, as measured by fluorescence intensity at the clot boundary (B). (**d**) In vivo dual-loaded FSNs augment left ventricular ejection fraction 2 and 4 weeks after I/R (A). Dual-loaded FSNs dramatically reduce infarct size (B) 4 weeks after damage, as measured by Masson's trichrome staining and measuring blue collagen stain as a percent of the left ventricular area (C). Four weeks after I/R (D), dual-loaded FSNs significantly reduce -SMA (top, green) and CTGF (bottom, red) expression in vivo, as measured by immunofluorescence intensity (E). (*), (**), (***), and (****) represented $p < 0.05$, $p < 0.01$, $p < 0.001$, and $p < 0.0001$, respectively. Reproduced with permission from [248], copyright ACS, 2018.

Another technique that scientists explore is therapeutic angiogenesis. Angiogenic factors are used as therapeutic proteins to treat myocardial ischemia and increase perfusion to the surviving cardiomyocytes. Angiogenesis is triggered when angiogenic molecules such as VEGF (vascular endothelial growth factor) attach to the endothelial cell receptor, causing new blood vessels to develop. Due to rapid diffusion from the target site, poor constancy, and short half-lives of angiogenic factors, several dosages are required, which has the disadvantage of unrestrained vascular development at undesirable spots. In this context, Lee et al. coupled poly (serinol hexamethylene urea) (PSHU) with PNIPAM, and sulfonated groups were used to create an injectable sulfonated reversible thermal gel [250]. The electrostatic interaction amongst heparin sulfate coupled with angiogenic agents is exploited in this hydrogel. Heparin sulfate's electrostatic interaction with angiogenic factors provides long-term transport, drug binding, receptor stability, and proteolysis protection while maintaining the bioactivity of the angiogenic factors. This blend was established for intramyocardial injection in conjunction with angiogenic factors such as VEGF to safeguard cardiac function following myocardial infarction. In vivo study exhibited promising results with the localized release of VEGF, improved vascularization, and potential role of anti-apoptotic impacts of the thermal gel.

It is complicated to select the optimal techniques for preventing myocardial necrosis and optimizing cardiac healing after a heart attack. Revascularization of the injured myocardium was the focus of the investigation. To avoid the MI–heart failure vicious cycle, it is also critical to limit overreactive and protracted inflammatory responses following cardiac injury, in addition to increasing vascularization (HF). In this regard, Rocker et al. proposed the use of multiple angiogenic factors (PDGF (platelet-derived growth factor) and VEGF) and anti-inflammatory cytokine (IL-10) to promote angiogenesis and restrict the detrimental impacts of MI [251]. Sulfonated reverse thermal gel (SRTG), a polymeric distribution system, is created from poly (serinol hexamethylene urea) (PSHU) coupled with PNIPAM with sulfonate groups. The system could sequentially deliver VEGF to initiate the angiogenesis process, followed by IL-10, which could suppress proinflammatory mediators to protect the heart from unnecessary inflammatory damage, and the final delivery of PDGF to stabilize newly formed vesicles and reduce their regression.

Further, following MI, injured tissue does not mend spontaneously, as mature cardiomyocytes have limited capacity to proliferate, and scar tissue is formed instead. The scar tissue that has replaced it is unable to conduct electrical or mechanical impulses, reducing pumping capacity even more. Vasoconstriction, hypertrophy, or enlargement of the cardiac muscles for increased pumping force and left ventricle enlargement help to stabilize reduced output. This extra complication may weaken the heart and lead to worsening cardiac function, eventually leading to heart collapse. Patients with end-stage heart failure have only two options for treatment: heart transplantation or mechanical ventricular assist devices (VADs). Lately, cardiac tissue engineering (CTE) has been widely investigated. Cui et al. evaluated the biocompatibility of PNIPAM-based-microgels to provide an optimized microenvironment for cardiac stromal cells (CSCs) with different surface charges and degrees of hydrophilicity and functional groups [252]. The study reported that a negative charge and more hydrophilic microenvironment of PNIPAM exhibited higher viability and proliferation of human cardiac stromal cells (hCSCs) and neonatal rat cardiomyocytes (NRCMs). Nanofibrous gelling microspheres (NF-GMS) are a copolymer of poly (l-lactic acid)-b-poly (ethylene glycol)-b-poly (*N*-iso-propylacrylamide). NF-GMS mimicked the extracellular matrix (ECM) and showed promising results for transplantation of human embryonic stem cell (hESC)-derived cardiomyocytes (CMs) for reducing infarct size in rats, leading to the substantial recovery of cardiac function [253].

Heart tissue possesses a complex three-dimensional (3D) structure. The myocardium chamber possesses a helical fiber with curved and hollow lumen organization. With few available fabrication techniques, it becomes difficult to recreate such complex carved structures in vitro. To address this need, Williams et al. established a fabrication technique for patterning the 3D structure of heart tissue by layering numerous layers of cells onto

adaptable scaffoldings combined with casting them into cavity tubular hydrogels [253]. The complex 3D tubular hydrogels were constructed by layering individual sheets of cardiomyocytes on flexible thermoresponsive nanofabricated substrates (fTNFS), layer-by-layer stacking, and casting them into 3D tubular geometries with twisted molds. The resulting pre-patterned cell sheets after tissue casting promoted cellular configuration in 3D tissues. The results suggest that a mixture of internal as well as external signals may be essential to extend mature tissues. The flexible TNFS approach can be used for fabricating more advanced engineered tissues. In another investigation, PNIPAM- gelatin-based injectable hydrogel proved a prominent candidate for cardiac tissue engineering [254].

9.4. Lymphoid Tissue Engineering

The lymphatic system is made up of lymphoid tissue, which is majorly associated with fluid homeostasis and internal fluid drainage, lipid absorption, and immune cell surveillance [255]. Several complications related to the lymphatic system include lymphedema, cancer progression and metastasis, cardiovascular disease, impaired wound healing, and obesity. Tissue engineering has become an essential tool for providing both ex vivo research models and a therapeutic for alleviating lymphatic deficiencies [256]. Several studies have been done on engineering lymphatic capillaries, lymph nodes, and other nonspecific lymphoid organoids [257]. Hydrogels are majorly associated with lymphoid tissue engineering during the 3D cell culture matrices for modeling the lymphoid tissue, expanding hematopoietic–lymphoid cells, and incorporating growth factors during vascular network formation in in vivo and in vitro conditions. Thermo-responsive inverted colloidal crystal (ICC) hydrogel scaffolds are used for mimicking lymphoid cells as they consist of fully interlinked, tunable pore arrays, which provide both a large area and multicellular communications [258]. PNIPAM is used to create several thermoresponsive hydrogels for designing ICC hydrogel scaffolds which will undergo a volumetric change over a physiological temperature range. Thermoresponsive cell culture dish helps control cell adhesion in various temperature ranges [259]. PNIPAM-based hydrogels help deter mechanical and chemical disintegration of the hydrogel scaffold, allowing the pore-entrapped hematopoietic-lymphoid cell to be released without breaking the scaffold [258]. Recently, Kwak et al. designed a thermoresponsive ICC hydrogel scaffold by polymerization between PNIPAM hydrogel scaffolds and a nanogel crosslinker as a potent strategy for releasing pore-entrapped hematopoietic-lymphoid cells without breaking the scaffold [258]. According to the findings, ICC PNIPAM-NG allowed the recapitulation of bone marrow microenvironment function, which created an environment for hematopoietic cell proliferation and retrieval via temperature changes.

9.5. Intestinal Tissue Engineering

The gastrointestinal tract is associated with various functions such as ingestion, digestion, nutritional element absorption, and waste excretion [257]. Tissue engineering for intestinal tissues has become an emerging field as it is majorly associated with replacing functional tissue containing biological activity and biodegradability. Intestinal stem cells also possess great potential for tissue engineering and are widely grown for biological research and several applications. Lately, Dosh et al. investigated alternative hydrogels that could support Caco-2 plus HT29-MTX cells and the development of a small intestine villi 3D model under in vitro conditions [260]. They found that l-PNIPAM hydrogel scaffolds maintained the 3D culture of two human colon adenocarcinoma cells, stimulated the cells to form villus-like structures, and helped with differentiation into native small intestinal epithelium. This research indicates the potentiality of PNIPAM hydrogel to deliver a 3D culture and could be used to investigate several diseases. A different approach was used by the authors in another experiment, where they used PNIPAM hydrogel to design a 3D coculture model of Caco-2 and HT29-MTX cells to regulate its possibility in exploring inflammatory bowel disease [261]. The study demonstrated that PNIPAM hydrogel helped maintain the 3D model even after treating the cell with IL-1β, TNF-α, and hypoxia for

1 week [261]. Later, in another study set, Dosh et al. showed the potential of i-PNIPAM hydrogels in providing support for the formation of enteroids in vitro as a scaffold, and of cell differentiation of mice isolated small intestinal crypts along with Lgr5^{+} stem cells [262]. Previously, different materials had been used, such as PLA, Matrigel, PGA, and collagen type 1 as a cellular scaffold, but those showed several limitations in various areas. This study showed that synthetic i-PNIPAM has many advantages, such as supporting crypt cell seeding and adhesion, cellular survival and differentiation, and others [262]. Table 3 demonstrates the latest studies on PNIPAM-based hydrogels in various tissue engineering.

Table 3. Recent investigations on PNIPAM-based hydrogels for tissue engineering.

Device Type	Model Drug	Polymer Formulation	Preparation Method	Applications	Results	References
Injectable hydrogel	Melatonin	PNIPAM/hyaluronic acid (HA) loaded chitosan-g-acrylic acid-coated PLGA (ACH/PLGA)	Single emulsion solvent evaporation	Cartilage tissue engineering	This system demonstrated excellent integration with genuine cartilage, and scanning electron microscopy pictures revealed an interconnected permeable structure. The hydrogels had exceptional MTT plus biocompatibility, and the live–dead assay demonstrated that WJMSCs could proliferate and survive. Overall, this injectable hydrogel proved to be an encouraging system for cartilage tissue engineering due to its increased mechanical properties, reduced synersis, ability to sustain drug release, and high bioactivity.	[188]
Hydrogels	Mesenchymal stem cells (MSCs)	PNIPAM/chitosan	Freeze drying	Cartilage tissue engineering	The hydrogel solution's residence duration inside the scaffold was determined to be 6 min for CSNI100 and 9 min for CSNI400. The swelling ratio of hybrid scaffolds was larger than that of chitosan-only scaffolds, and CSNI400 had a greater swelling ratio than CSNI100. In CSNI100 and CSNI400, the number of MSCs climbed by 58 and 108%. These findings imply that chitosan solid and PNIPAM hydrogels with a polymerization degree of 400 are found to be encouraging for cartilage tissue engineering.	[263]
Injectable hydrogel	Human dental pulp stem cells (hDPSCs)	PNIPAM-based copolymer/graphene oxide (GO)/chitosan (CS) crosslinked by beta glycerol phosphate (beta-GP) and genipin (GN)	Free radical copolymerization	Bone tissue engineering	Based on MTT, DAPI staining, and cell survival findings, the produced hydrogels provided a biomimetic ECM milieu for hDPSC proliferation and can be used as a novel BTE scaffold with good biocompatibility. The hydrogels ramped up the expression of osteogenic genes such as OCN and Runx 2, and activity of ALP and calcium deposition was enhanced.	[264]

Table 3. *Cont.*

Device Type	Model Drug	Polymer Formulation	Preparation Method	Applications	Results	References
Hydrogel	Oxacillin	PNIPAM/ hydroxyapatite (HAp)	Electrochemical polymerization	Bone tissue engineering	The PNIPAM-HAp scaffolds were found to be very porous using SEM, and the HAp concentration appeared to govern the composite's porosity. The scaffolds had original ingredients (no new chemical compounds were produced), and the ECP procedure did not affect the crystallinity of the HAp, according to XRD and FTIR analyses. Compared to the scaffolds with limited HAp content, the PNIPAM-HAp scaffolds with higher HAp content had a decreased oxacillin drug release rate. The oxacillin delivered from scaffolds maintained bacterial activity against P. aeruginosa and S. aureus for an extensive period. ECP seems to be a favorable methodology for producing PNIPAM-HAp scaffolds for BTE based on the data acquired from the above results.	[246]
Hydrogel	-	PNIPAM/ cardiosphere derived cells (CDCs)	Free radical polymerization	Cardiac tissue engineering	Under static and dynamic stretching, the CDCs validated elastic modulus-dependent cardiac diversity, as revealed by gene and protein expressions of cardiac markers such as cTnI, Connexin43, CACNA1c, and MYH6. The expression of cardiac markers CACNA1c and MYH6 was considerably enhanced after 1 Hz frequency was applied to murine CDCs, indicating that they were driven to differentiate into cardiac lineage. In 40 kPa and 21 kPa hydrogels, the strain promoted CDC cardiac differentiation. These findings suggest that employing a 40 kPa hydrogel to transplant CDCs could result in optimum cardiac regeneration and differentiation.	[265]
Thermosensitive hydrogel	Brown adipose-derived stem cells (BASCs)	PNIPAM/ single wall carbon nanotubes (SWCNTs)	Lyophilization	Cardiac tissue engineering	In vitro, SWCNTs with PNIPAM hydrogel demonstrated significantly more bioactivities to encapsulated cells than onefold PNIPAM. When utilized as a carrier, the technique improved seeded cell engraftment and survival in infarct myocardium, showing therapeutic efficacy following myocardial infarction.	[266]

Table 3. *Cont.*

| Device Type	Model Drug	Polymer Formulation	Preparation Method	Applications	Results	References
Stimuli-responsive hydrogel	5-amino salicylic acid (5-ASA) and ornidazole	PNIPAM/glycogen (Gly) (cl-Gly/PNIPAM) and crosslinked by ethylene glycol dimethacrylate (EGDMA)	Free radical polymerization	Intestinal tissue engineering	The produced hydrogel's LCST was reported to be in the spectrum of 32.5–34 °C. The hydrogel was shown to be compatible with human mesenchymal stem cells (hMSCs). The medications were efficiently loaded into the hydrogel system, which released both medications in a controlled manner, with 96–97% of the medications remaining stable after two months. The created hydrogel could be used for colon-focused delivery because of the nature and component stability of the medications.	[267]
Thermoresponsive hydrogel	-	Polyacrylic acid (PAA)/norbornene-functionalized chitosan (CsNb) crosslinked by bistetrazine-PNIPAM (bisTz-PNIPAM)	reversible addition–fragmentation chain transfer (RAFT) polymerization	Intestinal tissue engineering	The Tz-Nb click reaction between bisTz-PNIPAM crosslinker and CsNb created chemical crosslinks that improved the hydrogel structure's durability and produced pores in the hydrogel grid that allowed high drug load capacity and release. Because of the pH responsiveness of PAA, shrinkage behavior, and hydrogel porosity of PNIPAM, the hydrogel only gave a restricted medication release (8.5%) of 5-ASA at pH 2.2, but then it showed practically perfect delivery (92%) at pH 7.4 and 37 °C within 48 h. The hydrogels were nontoxic to human fibroblast cells and were biodegradable, indicating that they have a lot of potential as a medication delivery mechanism for the colon.	[268]
Hybrid hydrogel	Chlorhexidine diacetate	P-methacrylate arginine (M-Arg)/*N*-isopropylacrylamide (NIPAAm)/polyhexamethylene guanidinie phosphate (PHMG) [P(M-Arg/NIPAAm/PHMG)] crosslinked by N-N'methylene bisacrylamide.	Free radical copolymerization.	Wound dressing	Changing the monomer's mass ratio controlled the hydrogels' mechanical characteristics, swelling manner, and CHX release in vitro. The zwitterionic M-Arg monomer validated the hydrogel device's resilience to protein adsorption. The hydrogels' wound healing performance and safety were validated in an in vivo and cytotoxicity investigation. Ultimately, this research showed that hydrogels that possess long-term, anti-protein adsorption and antibacterial capabilities could effectively heal wounds.	[269]

Table 3. *Cont.*

Device Type	Model Drug	Polymer Formulation	Preparation Method	Applications	Results	References
Thermosensitive hydrogel	Superoxide dismutase (SOD)	PNIPAM/poly (γ-glutamic acid)	Free radical polymerization.	Wound dressing	The hydrogels had thermo-sensitivity at physiological temperature, and the phase transition temperature was 28.2 °C according to results from a differential scanning calorimeter and gelling action. SOD activity in vitro reached up to 85% after 10 h, which seemed beneficial in eradicating the superoxide anion. MTT experiments ensured that this hydrogel was biocompatible. The thermo-sensitive hydrogels had a longer-lasting SOD release, improved moisture retention, and higher water absorption. The device has significant application potential for wound repair and may effectively stimulate healing.	[270]

10. PNIPAM Hydrogels for Wound Dressings

Wound dressings are a conventional clinical treatment to keep the wound moist and warm to help with healing. Although there is no ideal wound dressing material, cotton wools, gauzes, and adhesive bandages are generally used. These materials merely offer general safeguard of wounds but do not help in a speedy recovery [40]. A significant problem associated with these materials is that they can dry out and harden, which can cause secondary injury upon removal [40]. Currently, many wound-healing materials have been developed, but hydrogels have been identified as an ideal wound dressing component. PNIPAM hydrogels have some additional advantages for wound dressing, as these hydrogels are thermosensitive. Maintaining the moisture level in the wound area with maximum mechanical strength is an essential criterion for a wound dressing component. Due to its transparency, PNIPAM hydrogel allows supervision of the healing process [40]. It also helps keeping a moist environment in the wound area.

Recently, Zubik et al. synthesized thermoresponsive hydrogels comprised of poly(*N*-isopropylacrylamide) (PNIPAM) using free-radical polymerization and strengthened both noncovalent and covalent connections with cellulose nanocrystals (CNC) devoid of any added crosslinkers (as shown in Figure 6A). The quantity of CNC introduced determined the characteristics of PNIPAM-CNC hybrid hydrogels. The hydrogels' thermal stability deteriorated as the CNC concentration increased. The viscous and elastic moduli of hydrogels rose with increasing levels of CNC, indicating greater mechanical capabilities of the hydrogels according to rheological measurements. Furthermore, hydrogel incorporation validated the idea that CNC strengthened the hydrogels, as enhanced CNC content improved the material properties after injection. The PNIPAM-CNC hybrid hydrogels had a volume phase transition temperature (VPTT) of 36° to 39° Celsius, equivalent to human body temperature (as shown in Figure 6B,C). To investigate drug loading and release for wound dressing applications, researchers used metronidazole, an antiprotozoal and antibiotic frequently employed in topical infections. At room temperature, the hydrogels had a significant drug-loading efficiency and a rushed drug delivery, accompanied by a steady and continuous release at 37 °C (as demonstrated in Figure 6D). These findings indicated that recently discovered therapeutics incorporated in injectable hydrogels could be helpful to wound dressing materials [143]. Hathway et al. also designed a PNIPAM-co-allylamine grafted material on nonwoven fabric that had increased mechanical strength and became more prominent for use as a bandage [271].
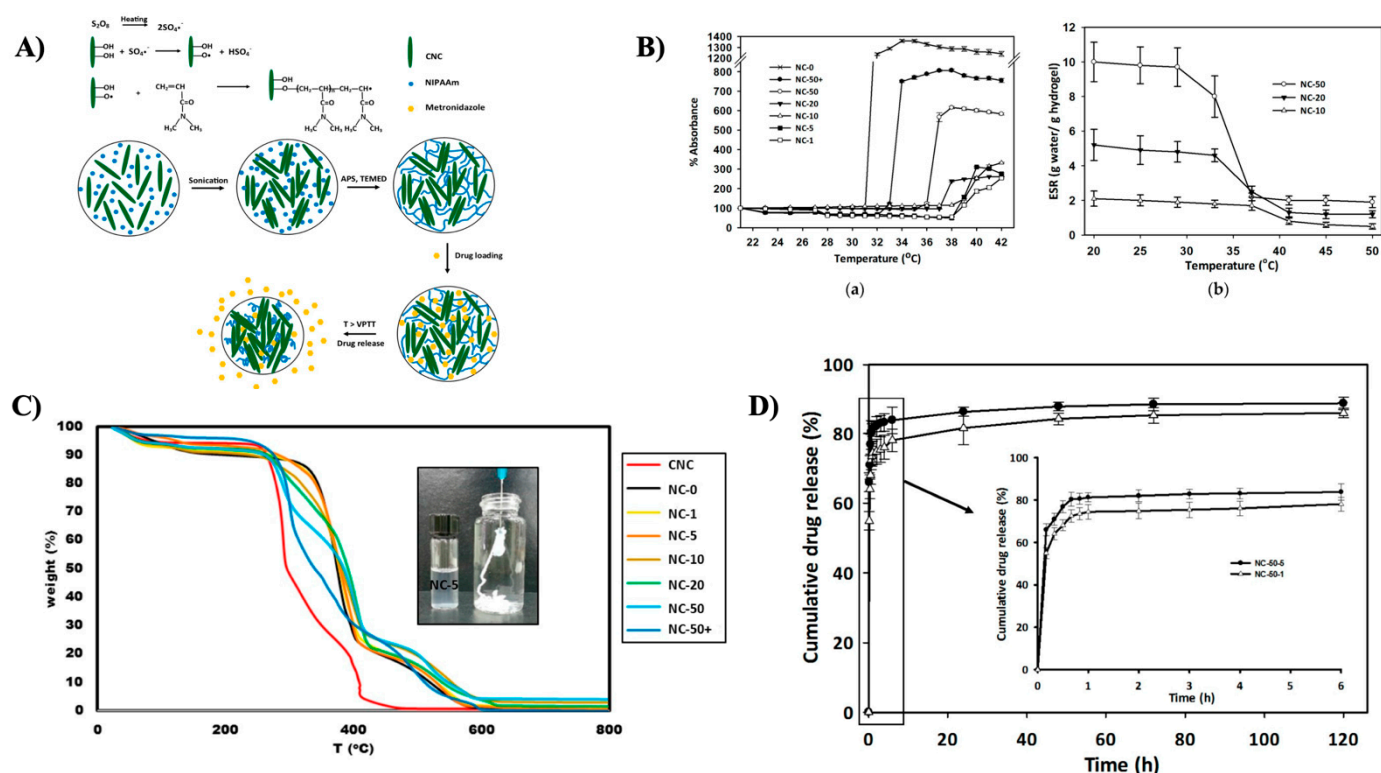
Figure 6. (**A**) The synthesis of thermoresponsive poly(*N*-isopropylacrylamide) (PNIPAM)-cellulose nanocrystal (CNC) hybrid hydrogels and a graphic depiction of the structural framework of drug release and drug load. (**B**) Thermoresponsive characteristics of PNIPAM-CNC hybrid hydrogels: (a) volume phase transition temperature (VPTT) profiles of hydrogels NC-0, NC-50+, NC-50, NC-20, NC-10, NC-5, and NC-1, with temperatures of 32, 34, 36.2, 37.5, 38.5, 39, and 39 degrees Celsius, correspondingly; (b) equilibrium swelling ratio (ESR) of PNIPAM-CNC hybrid hydrogels at various temperatures. (**C**) TGA thermograms of a pure CNC sample and produced PNIPAM-CNC hybrid hydrogels with varied levels of CNC content revealing thermal degradation characteristics. (**D**) Metronidazole (MZ) release profile from NC-50 hydrogels in phosphate-buffered saline (PBS) with pH 7.4 at 37 °C in vitro [142].

In another investigation, Li et al. tried to prepare alginate Ca^{2+}/PNIPAM interpenetrating hydrogels onto a cotton fabric surface using three different grafting methods [272]. They found that fabric-supported hydrogels have the ability to maintain wound area breathability and comfort. They also supported the moist environment and controlled drug release [272].

Previously, some studies reported the bacteriostatic property of AgNPs. Although proper care should be taken for using AgNPs, high exposure of AgNPs to cells can be toxic and cause serious damage. Recently, AgNPs have been incorporated into PNIPAM hydrogels to make a wound dressing with antimicrobial activity. This strategy also reduces the direct exposure of AgNPs into the cell, resulting in less cytotoxicity. In that context, Qasimet et al. encapsulated AgNPs within PNIPAM and pNIPAM-NH2 polymeric nanoparticles via the reduction of silver nitrate. The result exhibited substantial bacteriostatic activity against both Gram positive and Gram negative bacteria on a quantitative basis of both nanoparticle size and silver nitrate used [273].

In another study, Gao et al. synthesized an Ag@PNIPAM nanocomposite that demonstrated highly effective antibacterial activity against *Staphylococcus aureus* and a high recovery rate against burn wounds [274]. Antimicrobial resistance is a primary focus of biological science in this situation. Recently, Liu et al. designed a first aid wound dressing component by combining sodium polyacrylate with triangular AgNPs@PNIPAM, which could be an effective strategy for microbial resistance. The dressings were created in an

intelligent way in that they can regulate temperature, antibacterial properties, and the release of nanoparticles [275]. The race for developing methods of speedy wound recovery is still ongoing or under investigation. Lately, Blacklow et al. developed a PNIPAM-based hybrid hydrogel that could heal the wound in a natural process [276]. They prepared an active adhesive dressing (AAD) using PNIPAM, alginate, carbodiimide, silver nanoparticles (AgNPs), and chitosan. The components showed several advantages such as high stretchability, toughness, strong tissue adhesion, high antimicrobial activity, and speedy skin wound healing [276].

11. PNIPAM for Bioelectronics

Many bioelectronic technologies require seamless integration onto the surfaces of vital organs, where the interfaces provide soft mechanical coupling and efficient electrical/optical/thermal and chemical exchange. PNIPAM has been widely used to develop next-generation bioelectronic interfaces in recent years.

Electronic devices and computers can be used to create therapeutic body–machine interfaces using electrically active tissues such as the brain, heart, and skeletal muscle. In 2012, Tiwari et al. developed a PNIPAM-CNT-polyaniline-based three-dimensional nonwoven scaffold to check the effect on cell growth and viability [277]. They reported that the microfabric scaffold provides an excellent surface for cell growth and proliferation. This finding opened a new path in the field of tissue regeneration. Recently, Bagherifard et al. designed a PNIPAM-based drug delivery system that allowed drug release and growth factors to treat skin disorders [278]. They developed the platform using thermoresponsive microparticles, a flexible hydrogel layer, a heater for microparticle stimulation, a controller, and a power source. PNIPAM was used in this study due to its thermoresponsive behavior, increasing the possibility of modulating drug release rate through a temperature-dependent manner. A dermal patch that utilizes thermoresponsive drug microcarriers encapsulated within a hydrogel layer was attached to a flexible heater with integrated electronic heater control circuitry. The engineered patch covered the wound and allowed drug delivery by electronically adjusting the temperature of the hydrogel layer. In another study, Chen C. et al. developed a hydrogel patch for diabetic wound treatment [279]. Due to its thermoresponsive nature, they used PNIPAM-based hydrogel loaded with vascular endothelial cell growth factor as a filler, which could be released in response to temperature stimulus. Few studies report the association of PNIPAM with nucleic acid, as it consists of hydrophilic amido and hydrophobic isopropyl groups. A study by Lee A.W. et al. generated PNIPAM-DNA supramolecular complexes, transforming the PNIPAM into a semiconductive matter [280]. In another investigation, PNIPAM was used to generate PIPAAM-nucleobase supramolecular complexes (PSCs) by hybridizing with five different nucleobase units (adenine, thymine, uracil, guanine, and cytosine) [281]. Similarly, neat PNIPAM was transformed into a semiconductor from an insulator after hybridizing with nucleobases. Such improvements in the conductivity of hydrogels could lead PNIPAM's use as a novel material in bioelectronics.

Recent development in bioelectronics has provided tremendous opportunities to allow diverse methods for monitoring and treating long-term disease. However, current electronics–tissue biosystems are characterized by weak physical interactions, rigidity, and dislocation during long-term application. Electrically conductive hydrogels exhibit flexibility (arising from hydrogel) and electrical conductivity (arising from conductive components) [282]. Further, electrically conductive hydrogels are divided into polymer-based (PPY, PANI, and PT) [283–287], metal-based (silver nanowires and gold nanoparticles) c [286,288–290], ionic (lithium chloride and sulfonate) [291–293], and carbon materials based (carbon nanotubes and graphene) [290,294–296]. Polypyrrole (PPy), being a conducting polymer, is extensively studied as an electrochemical actuator. It demonstrates outstanding potential in a variety of applications, including electrochemical sensors [297], mechanical actuators [298], supercapacitors [299–301], and artificial muscles [302–304]. However, despite the wide applications, its brittle and rigid nature may not suit its applica-

tion in biological systems. The use of pNIPAM hydrogel provides more than x2 actuation and exhibits better optimization, bending, and out-of-plane deformations. In another study, Xue et al. demonstrated the use of hydrogel-based bioelectronics to enable implantable bio-electronics for monitoring and treating long-term diseases such as hypertension, diabetes, and Parkinson's. Moreover, in vivo reports indicate promising results by exhibiting applicability. This hydrogel-based bioelectronic interface enabled recording of physiological parameters (blood pressure and electromyograph) while also showing trigger-detachable properties without causing skin, tissue, or organ damage [304].

12. Conclusions and Future Perspectives

According to the literature review, PNIPAM is the most explored and preferred thermoresponsive polymer, with applications ranging from tissue engineering to medication delivery and wound dressings. The significant advantage of PNIPAM is that it has an LCST of about 32° and is easily triggered by body temperature to give a phase transition. This unique property makes PNIPAM-based hydrogels highly suitable for various applications. PNIPAM hydrogels still have a few drawbacks, including low mechanical strength, limited drug loading capacity, low biodegradability, etc. Their slow response speed and low mechanical strength have hindered further development. Recently, scientists have tried designing PNIPAM-based hydrogels for tissue repair and regeneration. However, they remain unsuccessful because of their nonbiodegradable nature, which poses the problem of long-term bioaccumulation. The development of PNIPAM-based cell sheeting has also encountered complications. The chain length and film thickness of PNIPAM and its copolymers vary depending on the type of cells. As a result, further development is restricted to achieving a stable condition suitable for many cell types. Researchers have devised several effective strategies to overcome these challenges, including improving biocompatibility, mechanical strength, and biodegradability, initiating multi-stimulus interactions, or enabling multidrug encapsulation and advanced drug loading amounts. Polymerization methods such as live radical polymerization, ATRP, EB-irradiation-induced polymerization, and RAFT or light-induced polymerization have been used to create a range of thermoresponsive PNIPAM-modified surfaces. Another strategy focused on producing copolymeric hydrogels by linking PNIPAM with other polymer blocks with unique properties. Additionally, random or block copolymerization of ionic or hydrophobic monomers with PNIPAM provides additional functionality to the thermoresponsive interfaces. Such thermoresponsive surfaces provide a microenvironment for fabricating cell sheets, followed by modulating cell adhesion and detachment. The layer-by-layer technique has recently emerged as a potential surface modification technique. To deliver medications, a porous hydrogel structure can act as a matrix for drug loading while also protecting drugs from the environment. Furthermore, the porosity of the gel matrix can be adjusted by altering crosslinking density. Copolymerization is an essential approach in the context of the delivery system. A new drug delivery system can be developed by creating a surface with different adhesion kinetics. However, the most state-of-the-art PNIPAM-based hydrogels are still at the developmental stage and far from clinical practice.

The invention of a successful, intelligent hydrogel delivery system requires excellent material engineering and, more than ever, an interdisciplinary approach involving polymer scientists, medical practitioners, chemists, and pharmacists.

Author Contributions: Conceptualization and supervision: M.J.A., R.R.R. and S.P.; Resources: R.M., A.Z., M.Y. and S.P.; Literature review and writing—original draft preparation: M.J.A., R.R.R., S.M., U.A., K.P., K.D., A.D., R.M. and S.P.; writing—review and editing: M.J.A., R.R.R., S.M., K.P., K.D., A.Z., M.Y. and S.P. All authors have read and agreed to the published version of the manuscript.

Data Availability Statement: No new data were created or analyzed in this study. Data sharing is not applicable to this article.

References

1. Pramanik, S.; Sali, V. Connecting the dots in drug delivery: A tour d'horizon of chitosan-based nanocarriers system. *Int. J. Biol. Macromol.* **2021**, *169*, 103–121. [CrossRef] [PubMed]
2. Shrivastav, P.; Pramanik, S.; Vaidya, G.; Abdelgawad, M.A.; Ghoneim, M.M.; Singh, A.; Abualsoud, B.M.; Amaral, L.S.; Abourehab, M.A. Bacterial cellulose as a potential biopolymer in biomedical applications: A state-of-the-art review. *J. Mater. Chem. B* **2022**, *10*, 3199–3241. [CrossRef] [PubMed]
3. Ferreira, N.N.; Ferreira, L.M.B.; Cardoso, V.M.O.; Boni, F.I.; Souza, A.L.R.; Gremião, M.P.D. Recent advances in smart hydrogels for biomedical applications: From self-assembly to functional approaches. *Eur. Polym. J.* **2018**, *99*, 117–133. [CrossRef]
4. Darge, H.F.; Andrgie, A.T.; Tsai, H.C.; Lai, J.Y. Polysaccharide and polypeptide based injectable thermo-sensitive hydrogels for local biomedical applications. *Int. J. Biol. Macromol.* **2019**, *133*, 545–563. [CrossRef]
5. Jonker, A.M.; Löwik, D.W.P.M.; van Hest, J.C.M. Peptide- and protein-based hydrogels. *Chem. Mater.* **2012**, *24*, 759–773. [CrossRef]
6. Di, X.; Kang, Y.; Li, F.; Yao, R.; Chen, Q.; Hang, C.; Xu, Y.; Wang, Y.; Sun, P.; Wu, G. Poly(*N*-isopropylacrylamide)/polydopamine/clay nanocomposite hydrogels with stretchability, conductivity, and dual light- and thermo- responsive bending and adhesive properties. *Colloids Surf. B Biointerfaces* **2019**, *177*, 149–159. [CrossRef]
7. Bashir, S.; Hina, M.; Iqbal, J.; Rajpar, A.H.; Mujtaba, M.A.; Alghamdi, N.A.; Wageh, S.; Ramesh, K.; Ramesh, S. Fundamental Concepts of Hydrogels: Synthesis, Properties, and Their Applications. *Polymers* **2020**, *12*, 2702. [CrossRef]
8. Klouda, L. Thermoresponsive hydrogels in biomedical applications A seven-year update. *Eur. J. Pharm. Biopharm.* **2015**, *97*, 338–349. [CrossRef]
9. Hoare, T.R.; Kohane, D.S. Hydrogels in drug delivery: Progress and challenges. *Polymer* **2008**, *49*, 1993–2007. [CrossRef]
10. Abourehab, M.A.; Ansari, M.J.; Singh, A.; Hassan, A.; Abdelgawad, M.A.; Shrivastav, P.; Abualsoud, B.M.; Amaral, L.S.; Pramanik, S. Cubosomes as an emerging platform for drug delivery: A state-of-the-art review. *J. Mater. Chem. B* **2022**, *10*, 2781–2819. [CrossRef]
11. Pramanik, S.; Mohanto, S.; Manne, R.; Rajendran, R.R.; Deepak, A.; Edapully, S.J.; Patil, T.; Katari, O. Nanoparticle-Based Drug Delivery System: The Magic Bullet for the Treatment of Chronic Pulmonary Diseases. *Mol. Pharmaceutics* **2021**, *18*, 3671–3718. [CrossRef] [PubMed]
12. Catoira, M.C.; Fusaro, L.; di Francesco, D.; Ramella, M.; Boccafoschi, F. Overview of natural hydrogels for regenerative medicine applications. *J. Mater. Sci. Mater. Med.* **2019**, *30*, 115. [CrossRef] [PubMed]
13. Bao, Z.; Xian, C.; Yuan, Q.; Liu, G.; Wu, J. Natural Polymer-Based Hydrogels with Enhanced Mechanical Performances: Preparation, Structure, and Property. *Adv. Healthc. Mater.* **2019**, *8*, 1900670. [CrossRef] [PubMed]
14. Chai, Q.; Jiao, Y.; Yu, X. Hydrogels for Biomedical Applications: Their Characteristics and the Mechanisms behind Them. *Gels* **2017**, *3*, 6. [CrossRef] [PubMed]
15. Guragain, S.; Bastakoti, B.P.; Malgras, V.; Nakashima, K.; Yamauchi, Y. Multi-Stimuli-Responsive Polymeric Materials. *Chem.-A Eur. J.* **2015**, *21*, 13164–13174. [CrossRef] [PubMed]
16. Liu, F.; Kozlovskaya, V.; Medipelli, S.; Xue, B.; Ahmad, F.; Saeed, M.; Cropek, D.; Kharlampieva, E. Temperature-Sensitive Polymersomes for Controlled Delivery of Anticancer Drugs. *Chem. Mater.* **2015**, *27*, 7945–7956. [CrossRef]
17. Fundueanu, G.; Constantin, M.; Bucatariu, S.; Ascenzi, P. pH/thermo-responsive poly(*N*-isopropylacrylamide-co-maleic acid) hydrogel with a sensor and an actuator for biomedical applications. *Polymer* **2017**, *110*, 177–186. [CrossRef]
18. Karimi, M.; Ghasemi, A.; Zangabad, P.S.; Rahighi, R.; Basri, S.M.M.; Mirshekari, H.; Amiri, M.; Pishabad, Z.S.; Aslani, A.; Bozorgomid, M.; et al. *Smart Micro/Nanoparticles in Stimulus-Responsive Drug/Gene Delivery Systems*; Royal Society of Chemistry: London, UK, 2016; Volume 45. [CrossRef]
19. Schmaljohann, D. Thermo- and pH-responsive polymers in drug delivery. *Adv. Drug Deliv. Rev.* **2006**, *58*, 1655–1670. [CrossRef]
20. Ward, M.A.; Georgiou, T.K. Thermoresponsive polymers for biomedical applications. *Polymers* **2011**, *3*, 1215–1242. [CrossRef]
21. Jeong, B.; Kim, S.W.; Bae, Y.H. Thermosensitive sol-gel reversible hydrogels. *Adv. Drug Deliv. Rev.* **2002**, *54*, 37–51. [CrossRef]
22. Klouda, L.; Mikos, A.G. Thermoresponsive hydrogels in biomedical applications. *Eur. J. Pharm. Biopharm. Off. J. Arb. Fur Pharm. Verfahr. E.V.* **2008**, *68*, 34–45. [CrossRef] [PubMed]
23. Ruel-Gariépy, E.; Leroux, J.-C. In situ-forming hydrogels—Review of temperature-sensitive systems. *Eur. J. Pharm. Biopharm. Off. J. Arb. Fur Pharm. Verfahr. E.V.* **2004**, *58*, 409–426. [CrossRef]
24. Bajpai, A.K.; Shukla, S.K.; Bhanu, S.; Kankane, S. Responsive polymers in controlled drug delivery. *Prog. Polym. Sci.* **2008**, *33*, 1088–1118. [CrossRef]

25. Karimi, M.; Sahandi Zangabad, P.; Ghasemi, A.; Amiri, M.; Bahrami, M.; Malekzad, H.; Ghahramanzadeh Asl, H.; Mahdieh, Z.; Bozorgomid, M.; Ghasemi, A.; et al. Temperature-responsive smart nanocarriers for delivery of therapeutic agents: Applications and recent advances. *ACS Appl. Mater. Interfaces* **2016**, *8*, 21107–21133. [CrossRef]

26. Sang, Y.; Li, W.; Liu, H.; Zhang, L.; Wang, H.; Liu, Z.; Ren, J.; Qu, X. Construction of Nanozyme-Hydrogel for Enhanced Capture and Elimination of Bacteria. *Adv. Funct. Mater.* **2019**, *29*, 1900518. [CrossRef]

27. Wang, G.; Chen, X.; Liu, S.; Wong, C.; Chu, S. Copolymer Brushes with Temperature-Triggered, Reversibly Switchable Bactericidal and Antifouling Properties for Biomaterial Surfaces. *ACS Appl. Mater. Interfaces* **2016**, *8*, 27207–27217. [CrossRef]

28. Zhao, D.; Ma, W.; Wang, R.; Yang, X.; Li, J.; Qiu, T.; Xiao, X. The preparation of green fluorescence-emissioned carbon dots/poly(*N*-isopropylacrylamide) temperature-sensitive hydrogels and research on their properties. *Polymers* **2019**, *11*, 1171. [CrossRef]

29. Kim, A.R.; Lee, S.L.; Park, S.N. Properties and in vitro drug release of pH-and temperature-sensitive double cross-linked interpenetrating polymer network hydrogels based on hyaluronic acid/poly (*N*-isopropylacrylamide) for transdermal delivery of luteolin. *Int. J. Biol. Macromol.* **2018**, *118*, 731–740. [CrossRef]

30. Kim, S.; Lee, K.; Cha, C. Refined control of thermoresponsive swelling/deswelling and drug release properties of poly (*N*-isopropylacrylamide) hydrogels using hydrophilic polymer crosslinkers. *J. Biomater. Sci. Polym. Ed.* **2016**, *27*, 1698–1711. [CrossRef]

31. Oak, M.; Mandke, R.; Singh, J. Smart polymers for peptide and protein parenteral sustained delivery. *Drug Discov. Today Technol.* **2012**, *9*, e131–e140. [CrossRef]

32. Turturro, S.B.; Guthrie, M.J.; Appel, A.A.; Drapala, P.W.; Brey, E.M.; Pérez-Luna, V.H.; Mieler, W.F.; Kang-Mieler, J.J. The effects of cross-linked thermo-responsive PNIPAAm-based hydrogel injection on retinal function. *Biomaterials* **2011**, *32*, 3620–3626. [CrossRef]

33. Gupta, M.K.; Martin, J.R.; Dollinger, B.R.; Hattaway, M.E.; Duvall, C.L. Thermogelling, ABC Triblock Copolymer Platform for Resorbable Hydrogels with Tunable, Degradation-Mediated Drug Release. *Adv. Funct. Mater.* **2017**, *27*, 1–14. [CrossRef]

34. McCune, J.A.; Mommer, S.; Parkins, C.C.; Scherman, O.A. Design Principles for Aqueous Interactive Materials: Lessons from Small Molecules and Stimuli-Responsive Systems. *Adv. Mater.* **2020**, *32*, 1–14. [CrossRef]

35. Qiu, Y.; Park, K. Environment-sensitive hydrogels for drug delivery. *Adv. Drug Deliv. Rev.* **2001**, *53*, 321–339. [CrossRef]

36. Zhao, Y.; Shi, C.; Yang, X.; Shen, B.; Sun, Y.; Chen, Y.; Xu, X.; Sun, H.; Yu, K.; Yang, B.; et al. PH- and Temperature-Sensitive Hydrogel Nanoparticles with Dual Photoluminescence for Bioprobes. *ACS Nano* **2016**, *10*, 5856–5863. [CrossRef]

37. Ziane, S.; Schlaubitz, S.; Miraux, S.; Patwa, A.; Lalande, C.; Bilem, I.; Lepreux, S.; Rousseau, B.; Le Meins, J.F.; Latxague, L. A thermosensitive low molecular weight hydrogel as scaffold for tissue engineering. *Eur. Cells Mater.* **2012**, *23*, 147–160. [CrossRef]

38. Gan, J.; Guan, X.; Zheng, J.; Guo, H.; Wu, K.; Liang, L.; Lu, M. Biodegradable, thermoresponsive PNIPAM-based hydrogel scaffolds for the sustained release of levofloxacin. *RSC Adv.* **2016**, *6*, 32967–32978. [CrossRef]

39. Haq, M.A.; Su, Y.; Wang, D. Mechanical properties of PNIPAM based hydrogels: A review. *Mater. Sci. Eng. C* **2017**, *70*, 842–855. [CrossRef]

40. Xu, X.; Liu, Y.; Fu, W.; Yao, M.; Ding, Z.; Xuan, J.; Li, D.; Wang, S.; Xia, Y.; Cao, M. Poly (*N*-isopropylacrylamide)-based thermoresponsive composite hydrogels for biomedical applications. *Polymers* **2020**, *12*, 580. [CrossRef]

41. Tokarev, I.; Minko, S. Stimuli-responsive hydrogel thin films. *Soft. Matter.* **2009**, *5*, 511–524. [CrossRef]

42. Alexander, A.; Khan, J.; Saraf, S.; Saraf, S. Polyethylene glycol (PEG)-Poly(*N*-isopropylacrylamide) (PNIPAAm) based thermosensitive injectable hydrogels for biomedical applications. *Eur. J. Pharm. Biopharm.* **2014**, *88*, 575–585. [CrossRef] [PubMed]

43. Graham, S.; Marina, P.F.; Blencowe, A. Thermoresponsive polysaccharides and their thermoreversible physical hydrogel networks. *Carbohydr. Polym.* **2019**, *207*, 143–159. [CrossRef] [PubMed]

44. Balakrishnan, B.; Mohanty, M.; Umashankar, P.R.; Jayakrishnan, A. Evaluation of an in situ forming hydrogel wound dressing based on oxidized alginate and gelatin. *Biomaterials* **2005**, *26*, 6335–6342. [CrossRef] [PubMed]

45. Guo, S.; DiPietro, L.A. Critical review in oral biology & medicine: Factors affecting wound healing. *J. Dent. Res.* **2010**, *89*, 219–229. [CrossRef]

46. Gurtner, G.C.; Werner, S.; Barrandon, Y.; Longaker, M.T. Wound repair and regeneration. *Nature* **2008**, *453*, 314–321. [CrossRef]

47. Ghobril, C.; Grinstaff, M.W. The chemistry and engineering of polymeric hydrogel adhesives for wound closure: A tutorial. *Chem. Soc. Rev.* **2015**, *44*, 1820–1835. [CrossRef]

48. Ghavaminejad, A.; Park, C.H.; Kim, C.S. In Situ Synthesis of Antimicrobial Silver Nanoparticles within Antifouling Zwitterionic Hydrogels by Catecholic Redox Chemistry for Wound Healing Application. *Biomacromolecules* **2016**, *17*, 1213–1223. [CrossRef]

49. Singer, A.J.; Dagum, A.B. Current Management of Acute Cutaneous Wounds. *N. Engl. J. Med.* **2008**, *359*, 1037–1046. [CrossRef]

50. Chang, Y.; Yandi, W.; Chen, W.Y.; Shih, Y.J.; Yang, C.C.; Chang, Y.; Ling, Q.D.; Higuchi, A. Tunable bioadhesive copolymer hydrogels of thermoresponsive poly(*N*-isopropyl acrylamide) containing zwitterionic polysulfobetaine. *Biomacromolecules* **2010**, *11*, 1101–1110. [CrossRef]

51. Mi, L.; Xue, H.; Li, Y.; Jiang, S. A thermoresponsive antimicrobial wound dressing hydrogel based on a cationic betaine ester. *Adv. Funct. Mater.* **2011**, *21*, 4028–4034. [CrossRef]

52. Vihola, H.; Laukkanen, A.; Valtola, L.; Tenhu, H.; Hirvonen, J. Cytotoxicity of thermosensitive polymers poly(*N*-isopropylacrylamide), poly(N-vinylcaprolactam); amphiphilically modified poly(N-vinylcaprolactam). *Biomaterials* **2005**, *26*, 3055–3064. [CrossRef] [PubMed]

53. Yang, S.; Leong, K.F.; Du, Z.; Chua, C.K. The design of scaffolds for use in tissue engineering. Part I. Traditional factors. *Tissue Eng.* **2001**, *7*, 679–689. [CrossRef] [PubMed]

54. Drury, J.L.; Mooney, D.J. Hydrogels for tissue engineering: Scaffold design variables and applications. *Biomaterials* **2003**, *24*, 4337–4351. [CrossRef]

55. Cunliffe, D.; Alarcón, C.d.; Peters, V.; Smith, J.R.; Alexander, C. Thermoresponsive surface-grafted poly(*N*-isopropylacrylamide) copolymers: Effect of phase transitions on protein and bacterial attachment. *Langmuir* **2003**, *19*, 2888–2899. [CrossRef]

56. Nie, L.; Li, J.; Lu, G.; Wei, X.; Deng, Y.; Liu, S.; Zhong, S.; Shi, Q.; Hou, R.; Sun, Y.; et al. Temperature responsive hydrogel for cells encapsulation based on graphene oxide reinforced poly(*N*-isopropylacrylamide)/hydroxyethyl-chitosan. *Mater. Today Commun.* **2022**, *31*, 103697. [CrossRef]

57. Narayanaswamy, R.; Torchilin, V.P. Hydrogels and their applications in targeted drug delivery. *Molecules* **2019**, *24*, 603. [CrossRef]

58. Zhang, C.L.; Cao, F.H.; Wang, J.L.; Yu, Z.L.; Ge, J.; Lu, Y.; Wang, Z.H.; Yu, S.H. Highly Stimuli-Responsive Au Nanorods/Poly(*N*-isopropylacrylamide) (PNIPAM) Composite Hydrogel for Smart Switch. *ACS Appl. Mater. Interfaces* **2017**, *9*, 24857–24863. [CrossRef]

59. Wang, C.; Flynn, N.T.; Langer, R. Controlled structure and properties of thermoresponsive nanoparticle-hydrogel composites. *Adv. Mater.* **2004**, *16*, 1074–1079. [CrossRef]

60. Gaharwar, A.K.; Peppas, N.A.; Khademhosseini, A. Nanocomposite hydrogels for biomedical applications. *Biotechnol. Bioeng.* **2014**, *111*, 441–453. [CrossRef]

61. He, C.; Kim, S.W.; Lee, D.S. In situ gelling stimuli-sensitive block copolymer hydrogels for drug delivery. *J. Control. Release* **2008**, *127*, 189–207. [CrossRef]

62. Singh, N.K.; Lee, D.S. In situ gelling pH- and temperature-sensitive biodegradable block copolymer hydrogels for drug delivery. *J. Control. Release* **2014**, *193*, 214–227. [CrossRef] [PubMed]

63. Wu, S.W.; Liu, X.; Miller, A.L.; Cheng, Y.S.; Yeh, M.L.; Lu, L. Strengthening injectable thermo-sensitive NIPAAm-g-chitosan hydrogels using chemical cross-linking of disulfide bonds as scaffolds for tissue engineering. *Carbohydr. Polym.* **2018**, *192*, 308–316. [CrossRef] [PubMed]

64. Tan, H.; Ramirez, C.M.; Miljkovic, N.; Li, H.; Rubin, J.P.; Marra, K.G. Thermosensitive injectable hyaluronic acid hydrogel for adipose tissue engineering. *Biomaterials* **2009**, *30*, 6844–6853. [CrossRef] [PubMed]

65. Dadoo, N.; Gramlich, W.M. Spatiotemporal Modification of Stimuli-Responsive Hyaluronic Acid/Poly(*N*-isopropylacrylamide) Hydrogels. *ACS Biomater. Sci. Eng.* **2016**, *2*, 1341–1350. [CrossRef]

66. Zhang, J.; Huang, Q.; Du, C.; Peng, R.; Hua, Y.; Li, Q.; Hu, A.; Zhou, J. Preparation and Anti-Mold Properties of Nano-ZnO/Poly(*N*-isopropylacrylamide) Composite Hydrogels. *Molecules* **2020**, *25*, 4135. [CrossRef]

67. Bajpai, S.K.; Bajpai, M.; Sharma, L. In Situ Formation of Silver Nanoparticles in Poly(*N*-isopropyl Acrylamide) Hydrogel for Antibacterial Applications. *Des. Monomers Polym.* **2011**, *14*, 383–394. [CrossRef]

68. Wei, J.; He, P.; Liu, A.; Chen, X.; Wang, X.; Jing, X. Surface Modification of Hydroxyapatite Nanoparticles with Thermal-Responsive PNIPAM by ATRP. *Macromol. Biosci.* **2009**, *9*, 1237–1246. [CrossRef]

69. Liu, X.; Song, T.; Chang, M.; Meng, L.; Wang, X.; Sun, R.; Ren, J. Carbon Nanotubes Reinforced Maleic Anhydride-Modified Xylan-g-Poly(*N*-isopropylacrylamide) Hydrogel with Multifunctional Properties. *Materials* **2018**, *11*, 354. [CrossRef]

70. Zhao, F.; Yao, D.; Guo, R.; Deng, L.; Dong, A.; Zhang, J. Composites of Polymer Hydrogels and Nanoparticulate Systems for Biomedical and Pharmaceutical Applications. *Nanomaterials* **2015**, *5*, 2054–2130. [CrossRef]

71. Han, X.; Xu, H.; Che, L.; Sha, D.; Huang, C.; Meng, T.; Song, D. Application of Inorganic Nanocomposite Hydrogels in Bone Tissue Engineering. *iScience* **2020**, *23*, 101845. [CrossRef]

72. Wahid, F.; Zhao, X.-J.; Jia, S.-R.; Bai, H.; Zhong, C. Nanocomposite hydrogels as multifunctional systems for biomedical applications: Current state and perspectives. *Compos. Part B Eng.* **2020**, *200*, 108208. [CrossRef]

73. Matricardi, P.; di Meo, C.; Coviello, T.; Hennink, W.E.; Alhaique, F. Interpenetrating polymer networks polysaccharide hydrogels for drug delivery and tissue engineering. *Adv. Drug Deliv. Rev.* **2013**, *65*, 1172–1187. [CrossRef] [PubMed]

74. Vedadghavami, A.; Minooei, F.; Mohammadi, M.H.; Khetani, S.; Kolahchi, A.R.; Mashayekhan, S.; Sanati-Nezhad, A. Manufacturing of hydrogel biomaterials with controlled mechanical properties for tissue engineering applications. *Acta Biomater.* **2017**, *62*, 42–63. [CrossRef] [PubMed]

75. Sosnik, A.; Seremeta, K.P. Polymeric hydrogels as technology platform for drug delivery applications. *Gels* **2017**, *3*, 25. [CrossRef] [PubMed]

76. Reddy, N.; Reddy, R.; Jiang, Q. Crosslinking biopolymers for biomedical applications. *Trends Biotechnol.* **2015**, *33*, 362–369. [CrossRef]

77. Hoffman, A.S. Applications of thermally reversible polymers and hydrogels in therapeutics and diagnostics. *J. Control. Release* **1987**, *6*, 297–305. [CrossRef]

78. Tang, L.; Wang, L.; Yang, X.; Feng, Y.; Li, Y.; Feng, W. Poly(*N*-isopropylacrylamide)-based smart hydrogels: Design, properties and applications. *Prog. Mater. Sci.* **2021**, *115*, 100702. [CrossRef]

79. Ju, G.; Cheng, M.; Xiao, M.; Xu, J.; Pan, K.; Wang, X.; Zhang, Y.; Shi, F. Smart Transportation Between Three Phases Through a Stimulus-Responsive Functionally Cooperating Device. *Adv. Mater.* **2013**, *25*, 2915–2919. [CrossRef]

80. Sun, T.; Song, W.; Jiang, L. Control over the responsive wettability of poly(*N*-isopropylacrylamide) film in a large extent by introducing an irresponsive molecule. *Chem. Commun.* **2005**, *13*, 1723–1725. [CrossRef]

81. Füllbrandt, M.; Ermilova, E.; Asadujjaman, A.; Hölzel, R.; Bier, F.F.; von Klitzing, R.; Schönhals, A. Dynamics of Linear Poly(*N*-isopropylacrylamide) in Water around the Phase Transition Investigated by Dielectric Relaxation Spectroscopy. *J. Phys. Chem. B* **2014**, *118*, 3750–3759. [CrossRef]

82. Wang, M.; Gao, Y.; Cao, C.; Chen, K.; Wen, Y.; Fang, D.; Li, L.; Guo, X. Binary Solvent Colloids of Thermosensitive Poly(*N*-isopropylacrylamide) Microgel for Smart Windows. *Ind. Eng. Chem. Res.* **2014**, *53*, 18462–18472. [CrossRef]

83. Zhang, X.Z.; Yang, Y.Y.; Chung, T.S. The influence of cold treatment on properties of temperature-sensitive poly(*N*-isopropylacrylamide) hydrogels. *J. Colloid Interface Sci.* **2002**, *246*, 105–111. [CrossRef] [PubMed]

84. Matsuo, E.S.; Tanaka, T. Kinetics of discontinuous volume-phase transition of gels. *J. Chem. Phys.* **1988**, *89*, 1695–1703. [CrossRef]

85. Li, Y.; Tanaka, T. Kinetics of swelling and shrinking of gels. *J. Chem. Phys.* **1990**, *92*, 1365–1371. [CrossRef]

86. Zhang, X.Z.; Xu, X.D.; Cheng, S.X.; Zhuo, R.X. Strategies to improve the response rate of thermosensitive PNIPAAm hydrogels. *Soft. Matter.* **2008**, *4*, 385–391. [CrossRef]

87. Sayil, C.; Okay, O. Macroporous poly (*N*-isopropylacrylamide) networks. *Polym. Bull.* **2002**, *506*, 499–506. [CrossRef]

88. Zhang, J.T.; Cheng, S.X.; Huang, S.W.; Zhuo, R.X. Temperature-sensitive poly (*N*-isopropylacrylamide) hydrogels with macroporous structure and fast response rate. *Macromol. Rapid Commun.* **2003**, *24*, 447–451. [CrossRef]

89. Zhang, X.Z.; Wang, F.J.; Chu, C.C. Thermoresponsive hydrogel with rapid response dynamics. *J. Mater. Sci. Mater. Med.* **2003**, *14*, 451–455. [CrossRef]

90. Zhang, X.Z.; Wu, D.Q.; Chu, C.C. Synthesis, characterization and controlled drug release of thermosensitive IPN-PNIPAAm hydrogels. *Biomaterials* **2004**, *25*, 3793–3805. [CrossRef]

91. Zhang, X.Z.; Yang, Y.Y.; Wang, F.J.; Chung, T.S. Thermosensitive poly(*N*-isopropylacrylamide-co-acrylic acid) hydrogels with expanded network structures and improved oscillating swelling-deswelling properties. *Langmuir* **2002**, *18*, 2013–2018. [CrossRef]

92. Ju, H.K.; Kim, S.Y.; Lee, Y.M. pH/temperature-responsive behaviors of semi-IPN and comb-type graft hydrogels composed of alginate and poly(*N*-isopropylacrylamide). *Polymer* **2001**, *42*, 6851–6857. [CrossRef]

93. Vázquez-Dorbatt, V.; Tolstyka, Z.P.; Maynard, H.D. Synthesis of aminooxy end-functionalized pnipaam by raft polymerization for protein and polysaccharide conjugation. *Macromolecules* **2009**, *42*, 7650–7656. [CrossRef] [PubMed]

94. Zhang, J.T.; Cheng, S.X.; Zhuo, R.X. Poly(vinyl alcohol)/poly(*N*-isopropylacrylamide) semi-interpenetrating polymer network hydrogels with rapid response to temperature changes. *Colloid Polym. Sci.* **2003**, *281*, 580–583. [CrossRef]

95. Li, Z.; Shen, J.; Ma, H.; Lu, X.; Shi, M.; Li, N.; Ye, M. Preparation and characterization of pH- and temperature-responsive nanocomposite double network hydrogels. *Mater. Sci. Eng. C* **2013**, *33*, 1951–1957. [CrossRef] [PubMed]

96. Bin Imran, A.; Esaki, K.; Gotoh, H.; Seki, T.; Ito, K.; Sakai, Y.; Takeoka, Y. Extremely stretchable thermosensitive hydrogels by introducing slide-ring polyrotaxane cross-linkers and ionic groups into the polymer network. *Nat. Commun.* **2014**, *5*, 1–8. [CrossRef] [PubMed]

97. Ma, X.; Li, Y.; Wang, W.; Ji, Q.; Xia, Y. Temperature-sensitive poly(*N*-isopropylacrylamide)/graphene oxide nanocomposite hydrogels by in situ polymerization with improved swelling capability and mechanical behavior. *Eur. Polym. J.* **2013**, *49*, 389–396. [CrossRef]

98. Lencina, M.S.; Iatridi, Z.; Villar, M.A.; Tsitsilianis, C. Thermoresponsive hydrogels from alginate-based graft copolymers. *Eur. Polym. J.* **2014**, *61*, 33–44. [CrossRef]

99. Takigawa, T.; Yamawaki, T.; Takahashi, K.; Masuda, T. Change in Young's modulus of poly(*N*-isopropylacrylamide) gels by volume phase transition. *Polym. Gels Netw.* **1998**, *5*, 585–589. [CrossRef]

100. Rivero, R.E.; Capella, V.; Liaudat, A.C.; Bosch, P.; Barbero, C.A.; Rodríguez, N.; Rivarola, C.R. Mechanical and physicochemical behavior of a 3D hydrogel scaffold during cell growth and proliferation. *RSC Adv.* **2020**, *10*, 5827–5837. [CrossRef]

101. Zhang, X.Z.; Zhuo, R.X.; Cui, J.Z.; Zhang, J.T. A novel thermo-responsive drug delivery system with positive controlled release. *Int. J. Pharm.* **2002**, *235*, 43–50. [CrossRef]

102. Gutowska, A.; Bark, J.S.; Kwon, I.C.; Bae, Y.H.; Cha, Y.; Kim, S.W. Squeezing hydrogels for controlled oral drug delivery. *J. Control. Release* **1997**, *48*, 141–148. [CrossRef]

103. Alvarez-Lorenzo, C.; Concheiro, A. Reversible adsorption by a pH- and temperature-sensitive acrylic hydrogel. *J. Control. Release* **2002**, *80*, 247–257. [CrossRef]

104. Lanzalaco, S.; Armelin, E. Poly(*N*-isopropylacrylamide) and Copolymers: A Review on Recent Progresses in Biomedical Applications. *Gels* **2017**, *3*, 36. [CrossRef] [PubMed]

105. Tokiwa, Y.; Calabia, B.P.; Ugwu, C.U.; Aiba, S. Biodegradability of plastics. *Int. J. Mol. Sci.* **2009**, *10*, 3722–3742. [CrossRef]

106. Boere, K.W.M.; Soliman, B.G.; Rijkers, D.T.S.; Hennink, W.E.; Vermonden, T. Thermoresponsive injectable hydrogels cross-linked by native chemical ligation. *Macromolecules* **2014**, *47*, 2430–2438. [CrossRef]

107. Gao, C.; Ren, J.; Zhao, C.; Kong, W.; Dai, Q.; Chen, Q.; Liu, C.; Sun, R. Xylan-based temperature/pH sensitive hydrogels for drug controlled release. *Carbohydr. Polym.* **2016**, *151*, 189–197. [CrossRef]

108. Charan, H.; Kinzel, J.; Glebe, U.; Anand, D.; Garakani, T.M.; Zhu, L.; Bocola, M.; Schwaneberg, U.; Böker, A. Grafting PNIPAAm from β-barrel shaped transmembrane nanopores. *Biomaterials* **2016**, *107*, 115–123. [CrossRef]

109. Li, Z.; Guo, X.; Matsushita, S.; Guan, J. Differentiation of cardiosphere-derived cells into a mature cardiac lineage using biodegradable poly(*N*-isopropylacrylamide) hydrogels. *Biomaterials* **2011**, *32*, 3220–3232. [CrossRef]

110. Yang, J.; van Lith, R.; Baler, K.; Hoshi, R.A.; Ameer, G.A. A thermoresponsive biodegradable polymer with intrinsic antioxidant properties. *Biomacromolecules* **2014**, *15*, 3942–3952. [CrossRef]

111. Cao, Y.; Zhang, C.; Shen, W.; Cheng, Z.; Yu, L.; Ping, Q. Poly(*N*-isopropylacrylamide)-chitosan as thermosensitive in situ gel-forming system for ocular drug delivery. *J. Control. Release* **2007**, *120*, 186–194. [CrossRef]

112. Das, D.; Ghosh, P.; Ghosh, A.; Haldar, C.; Dhara, S.; Panda, A.B.; Pal, S. Stimulus-Responsive, Biodegradable, Biocompatible, Covalently Cross-Linked Hydrogel Based on Dextrin and Poly(N -isopropylacrylamide) for in Vitro/in Vivo Controlled Drug Release. *ACS Appl. Mater. Interfaces* **2015**, *7*, 14338–14351. [CrossRef] [PubMed]

113. Ono, Y.; Shikata, T. Hydration and dynamic behavior of poly (*N*-isopropylacrylamide) s in aqueous solution: A sharp phase transition at the lower critical solution temperature. *J. Am. Chem. Soc.* **2006**, *128*, 10030–10031. [CrossRef] [PubMed]

114. Yanase, K.; Buchner, R.; Sato, T. Microscopic insights into the phase transition of poly (*N*-isopropylacrylamide) in aqueous media: Effects of molecular weight and polymer concentration. *J. Mol. Liq.* **2020**, *302*, 112025. [CrossRef]

115. P.R. ten Wolde; Chandler, D. Drying-induced hydrophobic polymer collapse. *Proc. Natl. Acad. Sci. USA* **2002**, *99*, 6539–6543. [CrossRef]

116. Futscher, M.H.; Philipp, M.; Müller-Buschbaum, P.; Schulte, A. The Role of Backbone Hydration of Poly(*N*-isopropyl acrylamide) Across the Volume Phase Transition Compared to its Monomer. *Sci. Rep.* **2017**, *7*, 17012. [CrossRef]

117. Hou, L.; Wu, P. LCST transition of PNIPAM-b-PVCL in water: Cooperative aggregation of two distinct thermally responsive segments. *Soft. Matter.* **2014**, *10*, 3578–3586. [CrossRef]

118. Kojima, H.; Tanaka, F. Cooperative Hydration Induces Discontinuous Volume Phase Transition of Cross-Linked Poly(*N*-isopropylacrylamide) Gels in Water. *Macromolecules* **2010**, *43*, 5103–5113. [CrossRef]

119. Grinberg, V.Y.; Burova, T.V.; Grinberg, N.V.; Moskalets, A.P.; Dubovik, A.S.; Plashchina, I.G.; Khokhlov, A.R. Energetics and Mechanisms of poly(*N*-isopropylacrylamide) Phase Transitions in Water–Methanol Solutions. *Macromolecules* **2020**, *53*, 10765–10772. [CrossRef]

120. Shan, J.; Chen, J.; Nuopponen, M.; Tenhu, H. Two phase transitions of poly(*N*-isopropylacrylamide) brushes bound to gold nanoparticles. *Langmuir ACS J. Surf. Colloids* **2004**, *20*, 4671–4676. [CrossRef]

121. Rey, M.; Hou, X.; Tang, J.S.J.; Vogel, N. Interfacial arrangement and phase transitions of PNiPAm microgels with different crosslinking densities. *Soft. Matter.* **2017**, *13*, 8717–8727. [CrossRef]

122. Okada, Y.; Tanaka, F.; Kujawa, P.; Winnik, F.M. Unified model of association-induced lower critical solution temperature phase separation and its application to solutions of telechelic poly(ethylene oxide) and of telechelic poly(*N*-isopropylacrylamide) in water. *J. Chem. Phys.* **2006**, *125*, 244902. [CrossRef] [PubMed]

123. Pham, Q.-T.; Yao, Z.-H.; Chang, Y.-T.; Wang, F.-M.; Chern, C.-S. LCST phase transition kinetics of aqueous poly(*N*-isopropylacrylamide) solution. *J. Taiwan Inst. Chem. Eng.* **2018**, *93*, 63–69. [CrossRef]

124. Bischofberger, I.; Trappe, V. New aspects in the phase behaviour of poly-*N*-isopropyl acrylamide: Systematic temperature dependent shrinking of PNiPAM assemblies well beyond the LCST. *Sci. Rep.* **2015**, *5*, 15520. [CrossRef] [PubMed]

125. Werner, P.; Münzberg, M.; Hass, R.; Reich, O. Process analytical approaches for the coil-to-globule transition of poly(*N*-isopropylacrylamide) in a concentrated aqueous suspension. *Anal. Bioanal. Chem.* **2017**, *409*, 807–819. [CrossRef] [PubMed]

126. Hu, X.; Tong, Z.; Lyon, L.A. Control of poly(*N*-isopropylacrylamide) microgel network structure by precipitation polymerization near the lower critical solution temperature. *Langmuir ACS J. Surf. Colloids* **2011**, *27*, 4142–4148. [CrossRef]

127. Ashraf, S.; Park, H.-K.; Park, H.; Lee, S.-H. Snapshot of phase transition in thermoresponsive hydrogel PNIPAM: Role in drug delivery and tissue engineering. *Macromol. Res.* **2016**, *24*, 297–304. [CrossRef]

128. Su, J.; Li, J.; Liang, J.; Zhang, K.; Li, J. Hydrogel Preparation Methods and Biomaterials for Wound Dressing. *Life* **2021**, *11*, 1016. [CrossRef] [PubMed]

129. Ahmed, E.M. Hydrogel: Preparation, characterization, and applications: A review. *J. Adv. Res.* **2015**, *6*, 105–121. [CrossRef]

130. Choi, E.J.; Ha, S.; Lee, J.; Premkumar, T.; Song, C. UV-mediated synthesis of pNIPAM-crosslinked double-network alginate hydrogels: Enhanced mechanical and shape-memory properties by metal ions and temperature. *Polymer* **2018**, *149*, 206–212. [CrossRef]

131. Zarzyka, I.; Pyda, M.; di Lorenzo, M.L. Influence of crosslinker and ionic comonomer concentration on glass transition and demixing/mixing transition of copolymers poly(*N*-isopropylacrylamide) and poly(sodium acrylate) hydrogels. *Colloid Polym. Sci.* **2014**, *292*, 485–492. [CrossRef]

132. Ma, X.M.; Li, R.; Ren, J.; Lv, X.C.; Zhao, X.H.; Ji, Q.; Xia, Y.Z. Restorable high-strength poly(*N*-isopropylacrylamide) hydrogels constructed through chitosan-based dual macro-cross-linkers with rapid response to temperature jumps. *RSC Adv.* **2017**, *7*, 47767–47774. [CrossRef]

133. Li, Y.; Wang, C.; Zhang, W.; Yin, Y.; Rao, Q. Preparation and characterization of PAM/SA tough hydrogels reinforced by IPN technique based on covalent/ionic crosslinking. *J. Appl. Polym. Sci.* **2015**, *132*. [CrossRef]

134. Bi, S.; Pang, J.; Huang, L.; Sun, M.; Cheng, X.; Chen, X. The toughness chitosan-PVA double network hydrogel based on alkali solution system and hydrogen bonding for tissue engineering applications. *Int. J. Biol. Macromol.* **2020**, *146*, 99–109. [CrossRef] [PubMed]

135. Zhao, D.; Feng, M.; Zhang, L.; He, B.; Chen, X.; Sun, J. Facile synthesis of self-healing and layered sodium alginate/polyacrylamide hydrogel promoted by dynamic hydrogen bond. *Carbohydr. Polym.* **2021**, *256*, 117580. [CrossRef] [PubMed]

136. Wang, D.; Xia, Y.; Zhang, D.; Sun, X.; Chen, X.; Oliver, S.; Shi, S.; Lei, L. Hydrogen-Bonding Reinforced Injectable Hydrogels: Application as a Thermo-Triggered Drug Controlled-Release System. *ACS Appl. Polym. Mater.* **2020**, *2*, 1587–1596. [CrossRef]

137. Xiao, J.; Zhou, Y.; Ye, M.; An, Y.; Wang, K.; Wu, Q.; Song, L.; Zhang, J.; He, H.; Zhang, Q.; et al. Freeze-Thawing Chitosan/Ions Hydrogel Coated Gauzes Releasing Multiple Metal Ions on Demand for Improved Infected Wound Healing. *Adv. Healthc. Mater.* **2021**, *10*, e2001591. [CrossRef]

138. Oh, S.H.; An, D.B.; Kim, T.H.; Lee, J.H. Wide-range stiffness gradient PVA/HA hydrogel to investigate stem cell differentiation behavior. *Acta Biomater.* **2016**, *35*, 23–31. [CrossRef]

139. Genevro, G.M.; de Moraes, M.A.; Beppu, M.M. Freezing influence on physical properties of glucomannan hydrogels. *Int. J. Biol. Macromol.* **2019**, *128*, 401–405. [CrossRef]

140. Figueroa-Pizano, M.D.; Vélaz, I.; Peñas, F.J.; Zavala-Rivera, P.; Rosas-Durazo, A.J.; Maldonado-Arce, A.D.; Martínez-Barbosa, M.E. Effect of freeze-thawing conditions for preparation of chitosan-poly (vinyl alcohol) hydrogels and drug release studies. *Carbohydr. Polym.* **2018**, *195*, 476–485. [CrossRef]

141. Liu, J.; Fan, X.; Tao, Y.; Deng, C.; Yu, K.; Zhang, W.; Deng, L.; Xiong, W. Two-Step Freezing Polymerization Method for Efficient Synthesis of High-Performance Stimuli-Responsive Hydrogels. *ACS Omega* **2020**, *5*, 5921–5930. [CrossRef]

142. Zubik, K.; Singhsa, P.; Wang, Y.; Manuspiya, H.; Narain, R. Thermo-responsive poly(*N*-isopropylacrylamide)-cellulose nanocrystals hybrid hydrogels for wound dressing. *Polymers* **2017**, *9*, 119. [CrossRef] [PubMed]

143. Cheaburu-Yilmaz, C.N.; Yilmaz, O.; Kose, F.A.; Bibire, N. Chitosan-Graft-Poly(*N*-isopropylacrylamide)/PVA Cryogels as Carriers for Mucosal Delivery of Voriconazole. *Polymers* **2019**, *11*, 1432. [CrossRef] [PubMed]

144. Su, Q.; Duan, L.; Zou, M.; Chen, X.; Gao, G.H. The tough allograft adhesive behavior between polyacrylamide and poly(acrylic acid) hydrophobic association hydrogels. *Mater. Chem. Phys.* **2017**, *193*, 57–62. [CrossRef]

145. Cho, E.C.; Lee, J.; Cho, K. Role of Bound Water and Hydrophobic Interaction in Phase Transition of Poly(*N*-isopropylacrylamide) Aqueous Solution. *Macromolecules* **2003**, *36*, 9929–9934. [CrossRef]

146. Custodio, K.K.S.; Claudio, G.C.; Nellas, R.B. Structural Dynamics of Neighboring Water Molecules of *N*-isopropylacrylamide Pentamer. *ACS Omega* **2020**, *5*, 1408–1413. [CrossRef]

147. Ullah, A.; Lim, S.I. Bioinspired tunable hydrogels: An update on methods of preparation, classification, and biomedical and therapeutic applications. *Int. J. Pharm.* **2022**, *612*, 121368. [CrossRef]

148. Lee, E.; Kim, D.; Kim, H.; Yoon, J. Photothermally driven fast responding photo-actuators fabricated with comb-type hydrogels and magnetite nanoparticles. *Sci. Rep.* **2015**, *5*, 15124. [CrossRef]

149. Rana, M.M.; Rajeev, A.; Natale, G.; Siegler, H.D. Effects of synthesis-solvent polarity on the physicochemical and rheological properties of poly(*N*-isopropylacrylamide) (PNIPAm) hydrogels. *J. Mater. Res. Technol.* **2021**, *13*, 769–786. [CrossRef]

150. Li, Q.-F.; Du, X.; Jin, L.; Hou, M.; Wang, Z.; Hao, J. Highly luminescent hydrogels synthesized by covalent grafting of lanthanide complexes onto PNIPAM via one-pot free radical polymerization. *J. Mater. Chem. C* **2016**, *4*, 3195–3201. [CrossRef]

151. Zhu, S.; Wang, X.; Cong, Y.; Liu, L.; Li, L. Free Radical Polymerization of Gold Nanoclusters and Hydrogels for Cell Capture and Light-Controlled Release. *ACS Appl. Mater. Interfaces* **2021**, *13*, 19360–19368. [CrossRef]

152. Kim, S.; Healy, K.E. Synthesis and Characterization of Injectable Poly(*N*-isopropylacrylamide-co-acrylic acid) Hydrogels with Proteolytically Degradable Cross-Links. *Biomacromolecules* **2003**, *4*, 1214–1223. [CrossRef] [PubMed]

153. Schachschal, S.; Adler, H.-J.; Pich, A.; Wetzel, S.; Matura, A.; van Pee, K.-H. Encapsulation of enzymes in microgels by polymerization/cross-linking in aqueous droplets. *Colloid Polym. Sci.* **2011**, *289*, 693–698. [CrossRef]

154. Yi, G.; Huang, Y.; Xiong, F.; Liao, B.; Yang, J.; Chen, X. Preparation and swelling behaviors of rapid responsive semi-IPN NaCMC/PNIPAm hydrogels. *J. Wuhan Univ. Technol.-Mater. Sci. Ed.* **2011**, *26*, 1073–1078. [CrossRef]

155. Ghasemiyeh, P.; Mohammadi-Samani, S. Hydrogels as Drug Delivery Systems; Pros and Cons. *Trends Pharm. Sci.* **2019**, *5*, 7–24. [CrossRef]

156. Wiwatsamphan, P.; Chirachanchai, S. Persistently reversible pH-/thermo-responsive chitosan/poly (*N*-isopropyl acrylamide) hydrogel through clickable crosslinked interpenetrating network. *Polym. Degrad. Stab.* **2022**, *198*, 109874. [CrossRef]

157. Gwon, S.; Park, S. Preparation of uniformly sized interpenetrating polymer network polyelectrolyte hydrogel droplets from a solid-state liquid crystal shell. *J. Ind. Eng. Chem.* **2021**, *99*, 235–245. [CrossRef]

158. Menegatti, T.; Žnidaršič-Plazl, P. Copolymeric Hydrogel-Based Immobilization of Yeast Cells for Continuous Biotransformation of Fumaric Acid in a Microreactor. *Micromachines* **2019**, *10*, 867. [CrossRef]

159. Kondiah, P.J.; Choonara, Y.E.; Kondiah, P.P.; Marimuthu, T.; Kumar, P.; Du Toit, L.C.; Pillay, V. A Review of Injectable Polymeric Hydrogel Systems for Application in Bone Tissue Engineering. *Molecules* **2016**, *21*, 1580. [CrossRef]

160. Vinchhi, P.; Rawal, S.U.; Patel, M.M. Chapter 19—Biodegradable hydrogels. In *Drug Delivery Devices and Therapeutic Systems*; Chappel, E., Ed.; Academic Press: Cambridge, MA, USA, 2021; pp. 395–419. [CrossRef]

161. Boyes, V.L.; Janani, R.; Partridge, S.; Fielding, L.A.; Breen, C.; Foulkes, J.; Le Maitre, C.L.; Sammon, C. One-pot precipitation polymerisation strategy for tuneable injectable Laponite®-pNIPAM hydrogels: Polymerisation, processability and beyond. *Polymer* **2021**, *233*, 124201. [CrossRef]

162. Ting, M.S.; Vella, J.; Raos, B.J.; Narasimhan, B.N.; Svirskis, D.; Travas-Sejdic, J.; Malmström, J. Conducting polymer hydrogels with electrically-tuneable mechanical properties as dynamic cell culture substrates. *Biomater. Adv.* **2022**, *134*, 112559. [CrossRef]

163. Xiao, Q.; Cui, Y.; Meng, Y.; Guo, F.; Ruan, X.; He, G.; Jiang, X. PNIPAm hydrogel composite membrane for high-throughput adsorption of biological macromolecules. *Sep. Purif. Technol.* **2022**, *294*, 121224. [CrossRef]

164. Liu, J.; Miao, J.; Zhao, L.; Liu, Z.; Leng, K.; Xie, W.; Yu, Y. Versatile Bilayer Hydrogel for Wound Dressing through PET-RAFT Polymerization. *Biomacromolecules* **2022**, *23*, 1112–1123. [CrossRef]

165. Rafieian, S.; Mirzadeh, H.; Mahdavi, H.; Masoumi, M.E. A review on nanocomposite hydrogels and their biomedical applications. *Sci. Eng. Compos. Mater.* **2019**, *26*, 154–174. [CrossRef]

166. Chakraborty, I.; Bodurtha, K.J.; Heeder, N.J.; Godfrin, M.P.; Tripathi, A.; Hurt, R.H.; Shukla, A.; Bose, A. Thermoresponsive in Situ Forming Hydrogel with Sol–Gel Irreversibility for Effective Methicillin-Resistant Staphylococcus aureus Infected Wound Healing. *ACS Nano* **2019**, *13*, 10074–10084. [CrossRef]

167. Chen, T.; Yang, Y.; Peng, H.; Whittaker, A.K.; Li, Y.; Zhao, Q.; Wang, Y.; Zhu, S.; Wang, Z. Cellulose nanocrystals reinforced highly stretchable thermal-sensitive hydrogel with ultra-high drug loading. *Carbohydr. Polym.* **2021**, *266*, 118122. [CrossRef]

168. Lin, X.; Guan, X.; Wu, Y.; Zhuang, S.; Wu, Y.; Du, L.; Zhao, J.; Rong, J.; Zhao, J.; Tu, M. An alginate/poly(*N*-isopropylacrylamide)-based composite hydrogel dressing with stepwise delivery of drug and growth factor for wound repair. *Mater. Sci. Engineering. C Mater. Biol. Appl.* **2020**, *115*, 111123. [CrossRef]

169. Han, L.; Zhang, Y.; Lu, X.; Wang, K.; Wang, Z.; Zhang, H. Polydopamine nanoparticles modulating stimuli-responsive PNIPAM hydrogels with cell/tissue adhesiveness. *ACS Appl. Mater. Interfaces* **2016**, *8*, 29088–29100. [CrossRef]

170. Geng, S.; Zhao, H.; Zhan, G.; Zhao, Y.; Yang, X. Injectable in situ forming hydrogels of thermosensitive polypyrrole nanoplatforms for precisely synergistic photothermo-chemotherapy. *ACS Appl. Mater. Interfaces* **2020**, *12*, 7995–8005. [CrossRef]

171. Li, J.; Mooney, D.J. Designing hydrogels for controlled drug delivery. *Nat. Rev. Mater.* **2016**, *1*, 1–17. [CrossRef]

172. Khan, S.; Akhtar, N.; Minhas, M.U.; Badshah, S.F. pH/Thermo-Dual Responsive Tunable In Situ Cross-Linkable Depot Injectable Hydrogels Based on Poly (*N*-isopropylacrylamide)/Carboxymethyl Chitosan with Potential of Controlled Localized and Systemic Drug Delivery. *AAPS PharmSciTech* **2019**, *20*, 119. [CrossRef]

173. Spicer, C.D. Hydrogel scaffolds for tissue engineering: The importance of polymer choice. *Polym. Chem.* **2020**, *11*, 184–219. [CrossRef]

174. McInnes, S.J.; Szili, E.J.; Al-Bataineh, S.A.; Vasani, R.B.; Xu, J.; Alf, M.E.; Gleason, K.K.; Short, R.D.; Voelcker, N.H. Fabrication and Characterization of a Porous Silicon Drug Delivery System with an Initiated Chemical Vapor Deposition Temperature-Responsive Coating. *Langmuir* **2016**, *32*, 301–308. [CrossRef] [PubMed]

175. Zheng, Y.; Wang, L.; Lu, L.; Wang, Q.; Benicewicz, B.C. PH and Thermal Dual-Responsive Nanoparticles for Controlled Drug Delivery with High Loading Content. *ACS Omega* **2017**, *2*, 3399–3405. [CrossRef] [PubMed]

176. Peralta, M.E.; Jadhav, S.A.; Magnacca, G.; Scalarone, D.; Mártire, D.O.; Parolo, M.E.; Carlos, L. Synthesis and in vitro testing of thermoresponsive polymer-grafted core-shell magnetic mesoporous silica nanoparticles for efficient controlled and targeted drug delivery. *J. Colloid Interface Sci.* **2019**, *544*, 198–205. [CrossRef]

177. Li, P.; Hou, X.; Qu, L.; Dai, X.; Zhang, C. PNIPAM-MAPOSS hybrid hydrogels with excellent swelling behavior and enhanced mechanical performance: Preparation and drug release of 5-fluorouracil. *Polymers* **2018**, *10*, 137. [CrossRef]

178. Li, L.; Chen, L.; Zhang, H.; Yang, Y.; Liu, X.; Chen, Y. Temperature and magnetism bi-responsive molecularly imprinted polymers: Preparation, adsorption mechanism and properties as drug delivery system for sustained release of 5-fluorouracil. *Mater. Sci. Eng. C* **2016**, *61*, 158–168. [CrossRef]

179. Blanco, M.D.; Guerrero, S.; Benito, M.; Fernández, A.; Teijón, C.; Olmo, R.; Katime, I.; Teijón, J.M. In vitro and in vivo evaluation of a folate-targeted copolymeric submicrohydrogel based on *N*-isopropylacrylamide as 5-fluorouracil delivery system. *Polymers* **2011**, *3*, 1107–1125. [CrossRef]

180. Garcia-Pinel, B.; Ortega-Rodríguez, A.; Porras-Alcalá, C.; Cabeza, L.; Contreras-Cáceres, R.; Ortiz, R.; Díaz, A.; Moscoso, A.; Sarabia, F.; Prados, J.; et al. Magnetically active pNIPAM nanosystems as temperature-sensitive biocompatible structures for controlled drug delivery. *Artif. Cells Nanomed. Biotechnol.* **2020**, *48*, 1022–1035. [CrossRef]

181. Wang, N.; Shi, J.; Wu, C.; Chu, W.; Tao, W.; Li, W.; Yuan, X. Design of DOX-GNRs-PNIPAM@PEG-PLA Micelle With Temperature and Light Dual-Function for Potent Melanoma Therapy. *Front. Chem.* **2021**, *8*, 1181. [CrossRef]

182. Rezaei, F.; Damoogh, S.; Reis, R.L.; Kundu, S.C.; Mottaghitalab, F.; Farokhi, M. Dual drug delivery system based on pH-sensitive silk fibroin/alginate nanoparticles entrapped in PNIPAM hydrogel for treating severe infected burn wound. *Biofabrication* **2020**, *13*, 15005. [CrossRef]

183. Erkisa, M.; Ari, F.; Ulku, I.; Khodadust, R.; Yar, Y.; Yagci Acar, H.; Ulukaya, E. Etoposide Loaded SPION-PNIPAM Nanoparticles Improve the in vitro Therapeutic Outcome on Metastatic Prostate Cancer Cells via Enhanced Apoptosis. *Chem. Biodivers.* **1974**, *17*, 109867. [CrossRef] [PubMed]

184. Safakas, K.; Saravanou, S.-F.; Iatridi, Z.; Tsitsilianis, C. Alginate-g-PNIPAM-Based Thermo/Shear-Responsive Injectable Hydrogels: Tailoring the Rheological Properties by Adjusting the LCST of the Grafting Chains. *Int. J. Mol. Sci.* **2021**, *22*, 3824. [CrossRef] [PubMed]

185. Hernández-Téllez, C.N.; Luque-Alcaraz, A.G.; Plascencia-Jatomea, M.; Higuera-Valenzuela, H.J.; Burgos-Hernández, M.; García-Flores, N.; Álvarez-Ramos, M.E.; Iriqui-Razcon, J.L.; Gonzalez, R.E.; Hernández-Abril, P.A. Synthesis and Characterization of a Fe$_3$O$_4$@PNIPAM-Chitosan Nanocomposite and Its Potential Application in Vincristine Delivery. *Polymers* **2021**, *13*, 1704. [CrossRef] [PubMed]

186. Shin, H.H.; Choi, H.W.; Lim, J.H.; Kim, J.W.; Chung, B.G. Near-Infrared Light-Triggered Thermo-responsive Poly(*N*-isopropylacrylamide)-Pyrrole Nanocomposites for Chemo-photothermal Cancer Therapy. *Nanoscale Res. Lett.* **2020**, *15*, 214. [CrossRef] [PubMed]

187. Atoufi, Z.; Kamrava, S.K.; Davachi, S.M.; Hassanabadi, M.; Garakani, S.S.; Alizadeh, R.; Farhadi, M.; Tavakol, S.; Bagher, Z.; Motlagh, G.H. Injectable PNIPAM/Hyaluronic acid hydrogels containing multipurpose modified particles for cartilage tissue engineering: Synthesis, characterization, drug release and cell culture study. *Int. J. Biol. Macromol.* **2019**, *139*, 1168–1181. [CrossRef]

188. Parameswaran-Thankam, A.; Parnell, C.M.; Watanabe, F.; RanguMagar, A.B.; Chhetri, B.P.; Szwedo, P.K.; Biris, A.S.; Ghosh, A. Guar-based injectable thermoresponsive hydrogel as a scaffold for bone cell growth and controlled drug delivery. *ACS Omega* **2018**, *3*, 15158–15167. [CrossRef]

189. Liu, L.; Zeng, J.; Zhao, X.; Tian, K.; Liu, P. Independent temperature and pH dual-responsive PMAA/PNIPAM microgels as drug delivery system: Effect of swelling behavior of the core and shell materials in fabrication process. *Colloids Surf. A Physicochem. Eng. Asp.* **2017**, *526*, 48–55. [CrossRef]

190. Giaouzi, D.; Pispas, S. PNIPAM-b-PDMAEA double stimuli responsive copolymers: Effects of composition, end groups and chemical modification on solution self-assembly. *Eur. Polym. J.* **2020**, *135*, 109867. [CrossRef]

191. Rasib, S.Z.M.; Akil, H.M.; Yahya, A. Effect of different composition on particle size chitosan-PMAA-PNIPAM hydrogel. *Proc. Chem.* **2016**, *19*, 388–393. [CrossRef]

192. Luo, Y.L.; Zhang, X.Y.; Fu, J.Y.; Xu, F.; Chen, Y.S. Novel Temperature and pH Dual Sensitive PNIPAM/CMCS/MWCNTs semi-IPN Nanohybrid Hydrogels: Synthesis, Characterization and DOX Drug Release. *Int. J. Polym. Mater. Polym. Biomater.* **2017**, *66*, 398–409. [CrossRef]

193. Ohnsorg, M.L.; Ting, J.M.; Jones, S.D.; Jung, S.; Bates, F.S.; Reineke, T.M. Tuning PNIPAm self-assembly and thermoresponse: Roles of hydrophobic end-groups and hydrophilic comonomer. *Polym. Chem.* **2019**, *10*, 3469–3479. [CrossRef]

194. Zhang, R.Q.; Liu, Z.Q.; Luo, Y.L.; Xu, F.; Chen, Y.S. Tristimuli responsive carbon nanotubes covered by mesoporous silica graft copolymer multifunctional materials for intracellular drug delivery. *J. Ind. Eng. Chem.* **2019**, *80*, 431–443. [CrossRef]

195. Zhang, K.; Li, F.; Wu, Y.; Feng, L.; Zhang, L. Construction of ionic thermo-responsive PNIPAM/γ-PGA/PEG hydrogel as a draw agent for enhanced forward-osmosis desalination. *Desalination* **2020**, *495*, 114667. [CrossRef]

196. Kanidi, M.; Papagiannopoulos, A.; Matei, A.; Dinescu, M.; Pispas, S.; Kandyla, M. Functional surfaces of laser-microstructured silicon coated with thermoresponsive PS/PNIPAM polymer blends: Switching reversibly between hydrophilicity and hydrophobicity. *Appl. Surf. Sci.* **2020**, *527*, 146841. [CrossRef]

197. Zhao, X.; Shan, G. PSMA-b-PNIPAM copolymer micelles with both a hydrophobic segment and a hydrophilic terminal group: Synthesis, micelle formation, and characterization. *Colloid Polym. Sci.* **2019**, *297*, 1353–1363. [CrossRef]

198. Lostalé-Seijo, I.; Montenegro, J. Synthetic materials at the forefront of gene delivery. *Nat. Rev. Chem.* **2018**, *2*, 258–277. [CrossRef]

199. McCrary, M.R.; Jesson, K.; Wei, Z.Z.; Logun, M.; Lenear, C.; Tan, S.; Gu, X.; Jiang, M.Q.; Karumbaiah, L.; Yu, S.P.; et al. Cortical Transplantation of Brain-Mimetic Glycosaminoglycan Scaffolds and Neural Progenitor Cells Promotes Vascular Regeneration and Functional Recovery after Ischemic Stroke in Mice. *Adv. Healthc. Mater.* **2020**, *9*, 1900285. [CrossRef]

200. Cui, Z.; Lee, B.H.; Pauken, C.; Vernon, B.L. Degradation, cytotoxicity, and biocompatibility of NIPAAm-based thermosensitive, injectable, and bioresorbable polymer hydrogels. *J. Biomed. Mater. Res. Part A* **2011**, *98*, 159–166. [CrossRef] [PubMed]

201. Krebs, M.D.; Salter, E.; Chen, E.; Sutter, K.A.; Alsberg, E. Calcium phosphate-DNA nanoparticle gene delivery from alginate hydrogels induces in vivo osteogenesis. *J. Biomed. Mater. Res. Part A Off. J. Soc. Biomater. Jpn. Soc. Biomater. Aust. Soc. Biomater. Korean Soc. Biomater.* **2010**, *92*, 1131–1138.

202. Vijayavenkataraman, S.; Yan, W.-C.; Lu, W.F.; Wang, C.-H.; Fuh, J.Y. 3D bioprinting of tissues and organs for regenerative medicine. *Adv. Drug Deliv. Rev.* **2018**, *132*, 296–332. [CrossRef]

203. Singh, S.; Choudhury, D.; Yu, F.; Mironov, V.; Naing, M.W. In situ bioprinting–Bioprinting from benchside to bedside? *Acta Biomater.* **2020**, *101*, 14–25. [CrossRef] [PubMed]

204. Liu, M.; Zeng, X.; Ma, C.; Yi, H.; Ali, Z.; Mou, X.; Li, S.; Deng, Y.; He, N. Injectable hydrogels for cartilage and bone tissue engineering. *Bone Res.* **2017**, *20175*, 1–20. [CrossRef] [PubMed]

205. Sood, N.; Bhardwaj, A.; Mehta, S.; Mehta, A. Stimuli-responsive hydrogels in drug delivery and tissue engineering. *Drug Deliv.* **2016**, *23*, 748–770. [CrossRef] [PubMed]

206. Zhang, Y.; Yu, J.; Ren, K.; Zuo, J.; Ding, J.; Chen, X. Thermosensitive hydrogels as scaffolds for cartilage tissue engineering. *Biomacromolecules* **2019**, *20*, 1478–1492. [CrossRef] [PubMed]

207. Deng, Z.; Guo, Y.; Zhao, X.; Du, T.; Zhu, J.; Xie, Y.; Wu, F.; Wang, Y.; Guan, M. Poly (*N*-isopropylacrylamide) Based Electrically Conductive Hydrogels and Their Applications. *Gels* **2022**, *8*, 280. [CrossRef] [PubMed]

208. Chaudhari, A.A.; Vig, K.; Baganizi, D.R.; Sahu, R.; Dixit, S.; Dennis, V.; Singh, S.R.; Pillai, S.R. Future prospects for scaffolding methods and biomaterials in skin tissue engineering: A review. *Int. J. Mol. Sci.* **2016**, *17*, 1974. [CrossRef]

209. Park, J.S.; Yang, H.N.; Woo, D.G.; Jeon, S.Y.; Park, K.-H. Poly (*N*-isopropylacrylamide-co-acrylic acid) nanogels for tracing and delivering genes to human mesenchymal stem cells. *Biomaterials* **2013**, *34*, 8819–8834. [CrossRef]

210. Zhang, J.T.; Petersen, S.; Thunga, M.; Leipold, E.; Weidisch, R.; Liu, X.; Fahr, A.; Jandt, K.D. Micro-structured smart hydrogels with enhanced protein loading and release efficiency. *Acta Biomater.* **2010**, *6*, 1297–1306. [CrossRef]

211. Chalanqui, M.J.; Pentlavalli, S.; McCrudden, C.; Chambers, P.; Ziminska, M.; Dunne, N.; McCarthy, H.O. Influence of alginate backbone on efficacy of thermo-responsive alginate-g-PNIPAM hydrogel as a vehicle for sustained and controlled gene delivery. *Mater. Sci. Eng. C* **2019**, *95*, 409–421. [CrossRef]

212. Ghaeini-Hesaroeiye, S.; Bagtash, H.R.; Boddohi, S.; Vasheghani-Farahani, E.; Jabbari, E. Thermoresponsive Nanogels Based on Different Polymeric Moieties for Biomedical Applications. *Gels* **2020**, *6*, 20. [CrossRef]

213. Kandil, R.; Merkel, O.M. Recent progress of polymeric nanogels for gene delivery. *Curr. Opin. Colloid Interface Sci.* **2019**, *39*, 11–23. [CrossRef] [PubMed]

214. Fliervoet, L.A.L.; van Nostrum, C.F.; Hennink, W.E.; Vermonden, T. Balancing hydrophobic and electrostatic interactions in thermosensitive polyplexes for nucleic acid delivery. *Multifunct. Mater.* **2019**, *2*, 024002. [CrossRef]

215. Lu, Y.J.; Lan, Y.H.; Chuang, C.C.; Lu, W.T.; Chan, L.Y.; Hsu, P.W.; Chen, J.P. Injectable thermo-sensitive chitosan hydrogel containing CPT-11-loaded EGFR-targeted graphene oxide and SLP2 shRNA for localized drug/gene delivery in glioblastoma therapy. *Int. J. Mol. Sci.* **2020**, *21*, 7111. [CrossRef] [PubMed]

216. Fliervoet, L.A.; Zhang, H.; van Groesen, E.; Fortuin, K.; Duin, N.J.; Remaut, K.; Schiffelers, R.M.; Hennink, W.E.; Vermonden, T. Local release of siRNA using polyplex-loaded thermosensitive hydrogels. *Nanoscale* **2020**, *12*, 10347–10360. [CrossRef] [PubMed]

217. Ziminska, M.; Wilson, J.J.; McErlean, E.; Dunne, N.; McCarthy, H.O. Synthesis and evaluation of a thermoresponsive degradable chitosan-grafted PNIPAAm hydrogel as a 'smart' gene delivery system. *Materials* **2020**, *13*, 2530. [CrossRef] [PubMed]

218. Lei, L.; Liu, Z.; Yuan, P.; Jin, R.; Wang, X.; Jiang, T.; Chen, X. Injectable colloidal hydrogel with mesoporous silica nanoparticles for sustained co-release of microRNA-222 and aspirin to achieve innervated bone regeneration in rat mandibular defects. *J. Mater. Chem. B* **2019**, *7*, 2722–2735. [CrossRef]

219. Yang, H.Y.; van Ee, R.J.; Timmer, K.; Craenmehr, e.g., Huang, J.H.; Öner, F.C.; Dhert, W.J.; Kragten, A.H.; Willems, N.; Grinwis, G.C.; et al. A novel injectable thermoresponsive and cytocompatible gel of poly(*N*-isopropylacrylamide) with layered double hydroxides facilitates siRNA delivery into chondrocytes in 3D culture. *Acta Biomater.* **2015**, *23*, 214–228. [CrossRef]

220. Mansour, J.M. Biomechanics of cartilage. *Kinesiol. Mech. Pathomechanics Hum. Mov.* **2003**, *2*, 69–83.

221. Yuan, T.; Zhang, L.; Li, K.; Fan, H.; Fan, Y.; Liang, J.; Zhang, X. Collagen hydrogel as an immunomodulatory scaffold in cartilage tissue engineering. *J. Biomed. Mater. Res. Part B: Appl. Biomater.* **2014**, *102*, 337–344. [CrossRef]

222. Keeney, J.A.; Eunice, S.; Pashos, G.; Wright, R.W.; Clohisy, J.C. What is the evidence for total knee arthroplasty in young patients?: A systematic review of the literature. *Clin. Orthop. Relat. Res.* **2011**, *469*, 574–583. [CrossRef]

223. Hunt, J.A.; Chen, R.; van Veen, T.; Bryan, N. Hydrogels for tissue engineering and regenerative medicine. *J. Mater. Chem. B.* **2014**, *2*, 5319–5338. [CrossRef] [PubMed]

224. Zhang, J.; Yun, S.; Du, Y.; Zannettino, A.C.W.; Zhang, H. Fabrication of a cartilage patch by fusing hydrogel-derived cell aggregates onto electrospun film. *Tissue Eng. Part A* **2020**, *26*, 863–871. [CrossRef] [PubMed]

225. Means, A.K.; Shrode, C.S.; Whitney, L.V.; Ehrhardt, D.A.; Grunlan, M.A. Double network hydrogels that mimic the modulus, strength, and lubricity of cartilage. *Biomacromolecules* **2019**, *20*, 2034–2042. [CrossRef] [PubMed]

226. Wang, C.Z.; Eswaramoorthy, R.; Lin, T.H.; Chen, C.H.; Fu, Y.C.; Wang, C.K.; Wu, S.C.; Wang, G.J.; Chang, J.K.; Ho, M.L. Enhancement of chondrogenesis of adipose-derived stem cells in HA-PNIPAAm-CL hydrogel for cartilage regeneration in rabbits. *Sci. Rep.* **2018**, *8*, 10526. [CrossRef]

227. Yang, J.; Bai, R.; Suo, Z. Topological adhesion of wet materials. *Adv. Mater.* **2018**, *30*, 1800671. [CrossRef] [PubMed]

228. Kim, I.Y.; Seo, S.J.; Moon, H.S.; Yoo, M.K.; Park, I.Y.; Kim, B.C.; Cho, C.S. Chitosan and its derivatives for tissue engineering applications. *Biotechnol. Adv.* **2008**, *26*, 1–21. [CrossRef]

229. Mellati, A.; Fan, C.M.; Tamayol, A.; Annabi, N.; Dai, S.; Bi, J.; Jin, B.; Xian, C.; Khademhosseini, A.; Zhang, H. Microengineered 3D cell-laden thermoresponsive hydrogels for mimicking cell morphology and orientation in cartilage tissue engineering. *Biotechnol. Bioeng.* **2017**, *114*, 217–231. [CrossRef]

230. Brunelle, A.R.; Horner, C.B.; Low, K.; Ico, G.; Nam, J. Electrospun thermosensitive hydrogel scaffold for enhanced chondrogenesis of human mesenchymal stem cells. *Acta Biomater.* **2018**, *66*, 166–176. [CrossRef]

231. Saghebasl, S.; Davaran, S.; Rahbarghazi, R.; Montaseri, A.; Salehi, R.; Ramazani, A. Synthesis and in vitro evaluation of thermosensitive hydrogel scaffolds based on (PNIPAAm-PCL-PEG-PCL-PNIPAAm)/Gelatin and (PCL-PEG-PCL)/Gelatin for use in cartilage tissue engineering. *Polym. Ed.* **2018**, *29*, 1185–1206. [CrossRef]

232. Pourjavadi, A.; Doroudian, M.; Ahadpour, A.; Azari, S. *Injectable Chitosan/κ-Carrageenan Hydrogel Designed with au Nanoparticles: A Conductive Scaffold for Tissue Engineering Demands*; Elsevier: Amsterdam, The Netherlands, 2019; Volume 126. [CrossRef]

233. Mohamed, A.M.F.S. An overview of bone cells and their regulating factors of differentiation. *Malays. J. Med. Sci.* **2008**, *15*, 4–12.

234. Park, J.-B. The use of hydrogels in bone-tissue engineering. *Biomater. Bioeng. Dent.* **2011**, *16*, e115–e118. [CrossRef] [PubMed]

235. Adibfar, A.; Amoabediny, G.; Eslaminejad, M.B.; Mohamadi, J.; Bagheri, F.; Doulabi, B.Z. VEGF delivery by smart polymeric PNIPAM nanoparticles affects both osteogenic and angiogenic capacities of human bone marrow stem cells. *Mater. Sci. Eng. C* **2018**, *93*, 790–799. [CrossRef] [PubMed]

236. Müller, M.; Urban, B.; Reis, B.; Yu, X.; Grab, A.L.; Cavalcanti-Adam, E.A.; Kuckling, D. Switchable Release of Bone Morphogenetic Protein from Thermoresponsive Poly (NIPAM-co-DMAEMA)/Cellulose Sulfate Particle Coatings. *Polymers* **2018**, *10*, 1314. [CrossRef]

237. Prasadh, S.; Suresh, S.; Wong, R. Osteogenic potential of graphene in bone tissue engineering scaffolds. *Materials* **2018**, *11*, 1430. [CrossRef] [PubMed]

238. Thorpe, A.A.; Creasey, S.; Sammon, C.; le Maitre, C.L. Hydroxyapatite nanoparticle injectable hydrogel scaffold to support osteogenic differentiation of human mesenchymal stem cells. *Eur. Cells Mater.* **2016**, *32*, 1–23. [CrossRef] [PubMed]

239. Thorpe, A.A.; Freeman, C.; Farthing, P.; Callaghan, J.; Hatton, P.V.; Brook, I.M.; Sammon, C.; Le Maitre, C.L. In vivo safety and efficacy testing of a thermally triggered injectable hydrogel scaffold for bone regeneration and augmentation in a rat model. *Oncotarget* **2018**, *9*, 18277. [CrossRef] [PubMed]

240. Ji, M.-X.; Yu, Q. Primary osteoporosis in postmenopausal women. *Chronic. Dis. Transl. Med.* **2015**, *1*, 9–13. [CrossRef]

241. Oberbek, P.; Bolek, T.; Chlanda, A.; Hirano, S.; Kusnieruk, S.; Rogowska-Tylman, J.; Nechyporenko, G.; Zinchenko, V.; Swieszkowski, W.; Puzyn, T. Characterization and influence of hydroxyapatite nanopowders on living cells. *Beilstein J. Nanotechnol.* **2018**, *9*, 3079–3094. [CrossRef]

242. Wu, T.; Sun, J.; Tan, L.; Yan, Q.; Li, L.; Chen, L.; Liu, X.; Bin, S. Enhanced osteogenesis and therapy of osteoporosis using simvastatin loaded hybrid system. *Bioact. Mater.* **2020**, *5*, 348–357. [CrossRef]

243. Zhou, K.; Yu, P.; Shi, X.; Ling, T.; Zeng, W.; Chen, A.; Yang, W.; Zhou, Z. Hierarchically porous hydroxyapatite hybrid scaffold incorporated with reduced graphene oxide for rapid bone ingrowth and repair. *ACS Nano* **2019**, *13*, 9595–9606. [CrossRef]

244. Petre, D.G.; Nadar, R.; Tu, Y.; Paknahad, A.; Wilson, D.A.; Leeuwenburgh, S.C. Thermoresponsive brushes facilitate effective reinforcement of calcium phosphate cements. *ACS Appl. Mater. Interfaces* **2019**, *11*, 26690–26703. [CrossRef] [PubMed]

245. Ribeiro, C.A.; Martins, M.V.S.; Bressiani, A.H.; Bressiani, J.C.; Leyva, M.E.; de Queiroz, A.A.A. Electrochemical preparation and characterization of PNIPAM-HAp scaffolds for bone tissue engineering. *Mater. Sci. Eng. C* **2017**, *81*, 156–166. [CrossRef] [PubMed]

246. Sun, X.-F.; Zeng, Q.; Wang, H.; Hao, Y. Preparation and swelling behavior of pH/temperature responsive semi-IPN hydrogel based on carboxymethyl xylan and poly(*N*-isopropyl acrylamide). *Cellulose* **2018**, *26*, 1909–1922. [CrossRef]

247. Shumer, D.E.; Natalie, J.; Nokoff, N.P.S. 乳鼠心肌提取 HHS Public Access. *Physiol. Behav.* **2017**, *176*, 139–148. [CrossRef]

248. Mihalko, E.; Huang, K.; Sproul, E.; Cheng, K.; Brown, A.C. Targeted treatment of ischemic and fibrotic complications of myocardial infarction using a dual-delivery microgel therapeutic. *ACS Nano* **2018**, *12*, 7826–7837. [CrossRef]

249. Lee, D.J.; Cavasin, M.A.; Rocker, A.J.; Soranno, D.E.; Meng, X.; Shandas, R.; Park, D. An injectable sulfonated reversible thermal gel for therapeutic angiogenesis to protect cardiac function after a myocardial infarction. *J. Biol. Eng.* **2019**, *13*, 6. [CrossRef]

250. Rocker, A.J.; Lee, D.J.; Shandas, R.; Park, D. Injectable Polymeric Delivery System for Spatiotemporal and Sequential Release of Therapeutic Proteins To Promote Therapeutic Angiogenesis and Reduce Inflammation. *ACS Biomater. Sci. Eng.* **2020**, *6*, 1217–1227. [CrossRef]

251. Cui, X.; Tang, J.; Hartanto, Y.; Zhang, J.; Bi, J.; Dai, S.; Qiao, S.Z.; Cheng, K.; Zhang, H. NIPAM-based microgel microenvironment regulates the therapeutic function of cardiac stromal cells. *ACS Appl. Mater. Interfaces* **2018**, *10*, 37783–37796. [CrossRef]

252. Zhao, C.; Tian, S.; Liu, Q.; Xiu, K.; Lei, I.; Wang, Z.; Ma, P.X. Biodegradable Nanofibrous Temperature-Responsive Gelling Microspheres for Heart Regeneration. *Adv. Funct. Mater.* **2020**, *30*, 2000776. [CrossRef]

253. Navaei, A.; Truong, D.; Heffernan, J.; Cutts, J.; Brafman, D.; Sirianni, R.W.; Vernon, B.; Nikkhah, M. PNIPAAm-based biohybrid injectable hydrogel for cardiac tissue engineering. *Acta Biomater.* **2016**, *32*, 10–23. [CrossRef]

254. Breslin, J.W.; Yang, Y.; Scallan, J.P.; Sweat, R.S.; Adderley, S.P.; Murfee, W.L. Lymphatic vessel network structure and physiology. *Compr. Physiol.* **2019**, *9*, 207–299. [CrossRef]

255. Wu, C.; Schneider, T.; Zeigler, M.; Yu, J.; Schiro, P.G.; Burnham, D.R.; McNeill, J.D.; Chiu, D.T. Bioconjugation of ultrabright semiconducting polymer dots for specific cellular targeting. *J. Am. Chem. Soc.* **2010**, *132*, 15410–15417. [CrossRef] [PubMed]

256. Sierra, H.; Cordova, M.; Chen, C.S.J.; Rajadhyaksha, M. Confocal imaging-guided laser ablation of basal cell carcinomas: An ex vivo study. *J. Investig. Dermatol.* **2015**, *135*, 612–615. [CrossRef] [PubMed]

257. Kwak, J.; Lee, J. Thermoresponsive Inverted Colloidal Crystal Hydrogel Scaffolds for Lymphoid Tissue Engineering. *Adv. Healthc. Mater.* **2020**, *9*, 1901556. [CrossRef]

258. Nagase, K.; Yamato, M.; Kanazawa, H.; Okano, T. Poly (*N*-isopropylacrylamide)-based thermoresponsive surfaces provide new types of biomedical applications. *Biomaterials* **2018**, *153*, 27–48. [CrossRef]

259. Dosh, R.H.; Essa, A.; Jordan-Mahy, N.; Sammon, C.; le Maitre, C.L. Use of hydrogel scaffolds to develop an in vitro 3D culture model of human intestinal epithelium. *Acta Biomater.* **2017**, *62*, 128–143. [CrossRef]

260. Dosh, R.H.; Jordan-Mahy, N.; Sammon, C.; le Maitre, C.L. Long-term in vitro 3D hydrogel co-culture model of inflammatory bowel disease. *Sci. Rep.* **2019**, *9*, 1–15. [CrossRef]

261. Dosh, R.H.; Jordan-Mahy, N.; Sammon, C.; le Maitre, C.L. Use of L-pNIPAM hydrogel as a 3D-scaffold for intestinal crypts and stem cell tissue engineering. *Biomater. Sci.* **2019**, *7*, 4310–4324. [CrossRef]

262. Mellati, A.; Valizadeh, M.; Madani, S.H.; Dai, S.; Bi, J. Poly (*N*-isopropylacrylamide) hydrogel/chitosan scaffold hybrid for three-dimensional stem cell culture and cartilage tissue engineering. *J. Biomed. Mater. Res. Part A* **2016**, *104*, 2764–2774. [CrossRef]

263. Amiryaghoubi, N.; Pesyan, N.N.; Fathi, M.; Omidi, Y. Injectable thermosensitive hybrid hydrogel containing graphene oxide and chitosan as dental pulp stem cells scaffold for bone tissue engineering. *Int. J. Biol. Macromol.* **2020**, *162*, 1338–1357. [CrossRef]

264. Li, Z.; Fan, Z.; Xu, Y.; Niu, H.; Xie, X.; Liu, Z.; Guan, J. Thermosensitive and Highly Flexible Hydrogels Capable of Stimulating Cardiac Differentiation of Cardiosphere-Derived Cells under Static and Dynamic Mechanical Training Conditions. *ACS Appl. Mater. Interfaces* **2016**, *8*, 15948–15957. [CrossRef] [PubMed]

265. Li, X.; Zhou, J.; Liu, Z.; Chen, J.; Lü, S.; Sun, H.; Li, J.; Lin, Q.; Yang, B.; Duan, C.; et al. A PNIPAAm-based thermosensitive hydrogel containing SWCNTs for stem cell transplantation in myocardial repair. *Biomaterials* **2014**, *35*, 5679–5688. [CrossRef] [PubMed]

266. Patra, P.; Rameshbabu, A.P.; Das, D.; Dhara, S.; Panda, A.B.; Pal, S. Stimuli-responsive, biocompatible hydrogel derived from glycogen and poly(: N -isopropylacrylamide) for colon targeted delivery of ornidazole and 5-amino salicylic acid. *Polym. Chem.* **2016**, *7*, 5426–5435. [CrossRef]

267. Hoang, H.T.; Jo, S.H.; Phan, Q.T.; Park, H.; Park, S.H.; Oh, C.W.; Lim, K.T. Dual pH-/thermo-responsive chitosan-based hydrogels prepared using 'click' chemistry for colon-targeted drug delivery applications. *Carbohydr. Polym.* **2021**, *260*, 117812. [CrossRef] [PubMed]

268. Wu, D.Q.; Zhu, J.; Han, H.; Zhang, J.Z.; Wu, F.F.; Qin, X.H.; Yu, J.Y. Synthesis and characterization of arginine-NIPAAm hybrid hydrogel as wound dressing: In vitro and in vivo study. *Acta Biomater.* **2018**, *65*, 305–316. [CrossRef]

269. Dong, Y.; Zhuang, H.; Hao, Y.; Zhang, L.; Yang, Q.; Liu, Y.; Qi, C.; Wang, S. Poly(*N*-isopropyl-acrylamide)/poly(γ-glutamic acid) thermo-sensitive hydrogels loaded with superoxide dismutase for wound dressing application. *Int. J. Nanomed.* **2020**, *15*, 1939–1950. [CrossRef]

270. Hathaway, H.; Alves, D.R.; Bean, J.; Esteban, P.P.; Ouadi, K.; Sutton, J.M.; Jenkins, A.T.A. Poly (*N*-isopropylacrylamide-co-allylamine)(PNIPAM-co-ALA) nanospheres for the thermally triggered release of Bacteriophage K. *Eur. J. Pharm. Biopharm.* **2015**, *96*, 437–441. [CrossRef]

271. Li, B.; Li, D.; Yang, Y.; Zhang, L.; Xu, K.; Wang, J. Study of thermal-sensitive alginate-Ca^{2+}/poly (*N*-isopropylacrylamide) hydrogels supported by cotton fabric for wound dressing applications. *Text. Res. J.* **2019**, *89*, 801–813. [CrossRef]

272. Qasim, M.; Udomluck, N.; Chang, J.; Park, H.; Kim, K. Antimicrobial activity of silver nanoparticles encapsulated in poly-*N*-isopropylacrylamide-based polymeric nanoparticles. *Int. J. Nanomed.* **2018**, *13*, 235. [CrossRef]

273. Paquin, F.; Rivnay, J.; Salleo, A.; Stingelin, N.; Silva, C. Multi-phase semicrystalline microstructures drive exciton dissociation in neat plastic semiconductors. *J. Mater. Chem. C* **2015**, *3*, 10715–10722. [CrossRef]

274. Liu, M.; Zhang, H.; Min, D.; Miao, X.; Li, F.; Dong, L.; Xing, J.; Guo, G.; Wang, X. Dual layered wound dressing with simultaneous temperature {\&} antibacterial regulation properties. *Mater. Sci. Eng. C* **2019**, *94*, 1077–1082. [CrossRef]

275. Blacklow, S.O.; Li, J.; Freedman, B.R.; Zeidi, M.; Chen, C.; Mooney, D.J. Bioinspired mechanically active adhesive dressings to accelerate wound closure. *Sci. Adv.* **2019**, *5*, eaaw3963. [CrossRef] [PubMed]

276. Tiwari, A.; Sharma, Y.; Hattori, S.; Terada, D.; Sharma, A.K.; Turner, A.P.; Kobayashi, H. Influence of poly(*N*-isopropylacrylamide)-CNT-polyaniline three-dimensional electrospun microfabric scaffolds on cell growth and viability. *Biopolymers* **2013**, *99*, 334–341. [CrossRef] [PubMed]

277. Bagherifard, S.; Tamayol, A.; Mostafalu, P.; Akbari, M.; Comotto, M.; Annabi, N.; Ghaderi, M.; Sonkusale, S.; Dokmeci, M.R.; Khademhosseini, A. Dermal Patch with Integrated Flexible Heater for on Demand Drug Delivery. *Adv. Healthc. Mater.* **2016**, *5*, 175–184. [CrossRef] [PubMed]

278. Chen, C.; Wang, Y.; Zhang, H.; Zhang, H.; Dong, W.; Sun, W.; Zhao, Y. Responsive and self-healing structural color supramolecular hydrogel patch for diabetic wound treatment. *Bioact. Mater.* **2022**, *15*, 194–202. [CrossRef] [PubMed]

279. Lee, A.-W.; Hsu, C.-C.; Liu, Y.-Z.; Wei, P.-L.; Chen, J.-K. Supermolecules of poly(*N*-isopropylacrylamide) complexating Herring sperm DNA with bio-multiple hydrogen bonding. *Colloids Surf. B Biointerfaces* **2016**, *148*, 422–430. [CrossRef] [PubMed]

280. Yang, H.-W.; Lee, A.-W.; Huang, C.-H.; Chen, J.-K. Characterization of poly(*N*-isopropylacrylamide)–nucleobase supramolecular complexes featuring bio-multiple hydrogen bonds. *Soft. Matter.* **2014**, *10*, 8330–8340. [CrossRef]

281. Someya, T.; Bao, Z.; Malliaras, G.G. The rise of plastic bioelectronics. *Nature* **2016**, *540*, 379–385. [CrossRef]

282. Jin, X.; Jiang, H.; Li, G.; Fu, B.; Bao, X.; Wang, Z.; Hu, Q. Stretchable, conductive PAni-PAAm-GOCS hydrogels with excellent mechanical strength, strain sensitivity and skin affinity. *Chem. Eng. J.* **2020**, *394*, 124901. [CrossRef]

283. Chen, J.; Peng, Q.; Thundat, T.; Zeng, H. Stretchable, Injectable, Self-Healing Conductive Hydrogel Enabled by Multiple Hydrogen Bonding toward Wearable Electronics. *Chem. Mater.* **2019**, *31*, 4553–4563. [CrossRef]

284. Wu, T.; Cui, C.; Huang, Y.; Liu, Y.; Fan, C.; Han, X.; Yang, Y.; Xu, Z.; Liu, B.; Fan, G.; et al. Coadministration of an Adhesive Conductive Hydrogel Patch and an Injectable Hydrogel to Treat Myocardial Infarction. *ACS Appl. Mater. Interfaces* **2020**, *12*, 2039–2048. [CrossRef] [PubMed]

285. Deng, Z.; Wang, H.; Ma, P.X.; Guo, B. Self-healing conductive hydrogels: Preparation, properties and applications. *Nanoscale* **2020**, *12*, 1224–1246. [CrossRef] [PubMed]

286. Ting, M.S.; Narasimhan, B.N.; Travas-Sejdic, J.; Malmström, J. Soft conducting polymer polypyrrole actuation based on poly(*N*-isopropylacrylamide) hydrogels. *Sens. Actuators B Chem.* **2021**, *343*, 130167. [CrossRef]

287. Zhou, Y.; Wan, C.; Yang, Y.; Yang, H.; Wang, S.; Dai, Z.; Ji, K.; Jiang, H.; Chen, X.; Long, Y. Highly Stretchable, Elastic, and Ionic Conductive Hydrogel for Artificial Soft Electronics. *Adv. Funct. Mater.* **2019**, *29*, 1806220. [CrossRef]

288. Green, R. Elastic and conductive hydrogel electrodes. *Nat. Biomed. Eng.* **2019**, *3*, 9–10. [CrossRef]

289. Deng, Z.; Yu, R.; Guo, B. Stimuli-responsive conductive hydrogels: Design, properties, and applications. *Mater. Chem. Front.* **2021**, *5*, 2092–2123. [CrossRef]

290. Sui, X.; Guo, H.; Cai, C.; Li, Q.; Wen, C.; Zhang, X.; Wang, X.; Yang, J.; Zhang, L. Ionic conductive hydrogels with long-lasting antifreezing, water retention and self-regeneration abilities. *Chem. Eng. J.* **2021**, *419*, 129478. [CrossRef]

291. Kong, W.; Wang, C.; Jia, C.; Kuang, Y.; Pastel, G.; Chen, C.; Chen, G.; He, S.; Huang, H.; Zhang, J.; et al. Muscle-Inspired Highly Anisotropic, Strong, Ion-Conductive Hydrogels. *Adv. Mater.* **2018**, *30*, 1801934. [CrossRef]

292. Zhang, H.; Gao, T.; Zhang, S.; Zhang, P.; Li, R.; Ma, N.; Wei, H.; Zhang, X. Conductive and Tough Smart Poly(N -isopropylacrylamide) Hydrogels Hybridized by Green Deep Eutectic Solvent. *Macromol. Chem. Phys.* **2021**, *222*, 2000301. [CrossRef]

293. Han, L.; Liu, K.; Wang, M.; Wang, K.; Fang, L.; Chen, H.; Zhou, J.; Lu, X. Mussel-Inspired Adhesive and Conductive Hydrogel with Long-Lasting Moisture and Extreme Temperature Tolerance. *Adv. Funct. Mater.* **2018**, *28*, 1704195. [CrossRef]

294. Park, J.; Jeon, J.; Kim, B.; Lee, M.S.; Park, S.; Lim, J.; Yi, J.; Lee, H.; Yang, H.S.; Lee, J.Y. Electrically Conductive Hydrogel Nerve Guidance Conduits for Peripheral Nerve Regeneration. *Adv. Funct. Mater.* **2020**, *30*, 2003759. [CrossRef]

295. Jo, H.; Sim, M.; Kim, S.; Yang, S.; Yoo, Y.; Park, J.H.; Yoon, T.H.; Kim, M.G.; Lee, J.Y. Electrically conductive graphene/polyacrylamide hydrogels produced by mild chemical reduction for enhanced myoblast growth and differentiation. *Acta Biomater.* **2017**, *48*, 100–109. [CrossRef] [PubMed]

296. Wang, T.; Farajollahi, M.; Choi, Y.S.; Lin, I.T.; Marshall, J.E.; Thompson, N.M.; Kar-Narayan, S.; Madden, J.D.W.; Smoukov, S.K. Electroactive polymers for sensing. *Interface Focus.* **2016**, *6*, 20160026. [CrossRef]

297. Khan, A.; Alamry, K.A.; Jain, R.K. Polypyrrole nanoparticles-based soft actuator for artificial muscle applications. *RSC Adv.* **2019**, *9*, 39721–39734. [CrossRef] [PubMed]

298. Raza, W.; Ali, F.; Raza, N.; Luo, Y.; Kim, K.H.; Yang, J.; Kumar, S.; Mehmood, A.; Kwon, E.E. Recent advancements in supercapacitor technology. *Nano Energy* **2018**, *52*, 441–473. [CrossRef]

299. Snook, G.A.; Kao, P.; Best, A.S. Conducting-polymer-based supercapacitor devices and electrodes. *J. Power Sources* **2011**, *196*, 1–12. [CrossRef]

300. Ren, X.; Fan, H.; Ma, J.; Wang, C.; Zhang, M.; Zhao, N. Hierarchical Co3O4/PANI hollow nanocages: Synthesis and application for electrode materials of supercapacitors. *Appl. Surf. Sci.* **2018**, *441*, 194–203. [CrossRef]

301. Harjo, M.; Järvekülg, M.; Tamm, T.; Otero, T.F.; Kiefer, R. Concept of an artificial muscle design on polypyrrole nanofiber scaffolds. *PLoS ONE* **2020**, *15*, e0232851. [CrossRef]

302. Balint, R.; Cassidy, N.J.; Cartmell, S.H. Conductive polymers: Towards a smart biomaterial for tissue engineering. *Acta Biomater.* **2014**, *10*, 2341–2353. [CrossRef]

303. Guo, B.; Ma, P.X. Conducting Polymers for Tissue Engineering. *Biomacromolecules* **2018**, *19*, 1764–1782. [CrossRef]

304. Xue, Y.; Xue, Y.; Zhang, J.; Chen, X.; Zhang, J.; Chen, G.; Zhang, K.; Lin, J.; Guo, C.; Liu, J. Trigger-Detachable Hydrogel Adhesives for Bioelectronic Interfaces. *Adv. Funct. Mater.* **2021**, *31*, 2106446. [CrossRef]

Soft-Tissue-Mimicking Using Hydrogels for the Development of Phantoms

Aitor Tejo-Otero [1,*], Felip Fenollosa-Artés [1,2], Isabel Achaerandio [3], Sergi Rey-Vinolas [4], Irene Buj-Corral [2], Miguel Ángel Mateos-Timoneda [4,5] and Elisabeth Engel [4,6,7]

1. Centre CIM, Universitat Politècnica de Catalunya (CIM UPC), Carrer de Llorens i Artigas, 12, 08028 Barcelona, Spain; ffenollosa@cimupc.org
2. Departament of Mechanical Engineering, Barcelona School of Industrial Engineering (ETSEIB), Universitat Politècnica de Catalunya, Av. Diagonal, 647, 08028 Barcelona, Spain; irene.buj@upc.edu
3. Department d'Enginyeria Agroalimentària i Biotecnologia, Escola d'Enginyeria Agroalimentària i de Biosistemes de Barcelona, Universitat Politècnica de Catalunya, Carrer Esteve Terradas, 8, 08860 Barcelona, Spain; maria.isabel.achaerandio@upc.edu
4. Institute for Bioengineering of Catalonia (IBEC), The Barcelona Institute of Science and Technology (BIST), c/Baldiri Reixac 15-21, 08028 Barcelona, Spain; srey@ibecbarcelona.eu (S.R.-V.); mamateos@ibecbarcelona.eu (M.Á.M.-T.); eengel@ibecbarcelona.eu (E.E.)
5. Bioengineering Institute of Technology, Universitat Internacional de Catalunya (UIC), c/Josep Trueta s/n, 08195 Barcelona, Spain
6. CIBER en Bioingeniería, Biomateriales y Nanotecnología (CIBER-BBN), 28029 Madrid, Spain
7. IMEM-BRT Group, Departament de Ciència i Enginyeria de Materials, Universitat Politècnica de Catalunya, Av. Eduard Maristany 10-14, 08019 Barcelona, Spain
* Correspondence: atejo@cimupc.org; Tel.: +34-934-01-71-71

Abstract: With the currently available materials and technologies it is difficult to mimic the mechanical properties of soft living tissues. Additionally, another significant problem is the lack of information about the mechanical properties of these tissues. Alternatively, the use of phantoms offers a promising solution to simulate biological bodies. For this reason, to advance in the state-of-the-art a wide range of organs (e.g., liver, heart, kidney as well as brain) and hydrogels (e.g., agarose, polyvinyl alcohol –PVA–, Phytagel –PHY– and methacrylate gelatine –GelMA–) were tested regarding their mechanical properties. For that, viscoelastic behavior, hardness, as well as a non-linear elastic mechanical response were measured. It was seen that there was a significant difference among the results for the different mentioned soft tissues. Some of them appear to be more elastic than viscous as well as being softer or harder. With all this information in mind, a correlation between the mechanical properties of the organs and the different materials was performed. The next conclusions were drawn: (1) to mimic the liver, the best material is 1% wt agarose; (2) to mimic the heart, the best material is 2% wt agarose; (3) to mimic the kidney, the best material is 4% wt GelMA; and (4) to mimic the brain, the best materials are 4% wt GelMA and 1% wt agarose. Neither PVA nor PHY was selected to mimic any of the studied tissues.

Keywords: dynamic mechanical analysis; hardness; hydrogels; materials; mimicking; soft tissues; tissue scaffolding; viscoelasticity; Warner–Braztler shear test

1. Introduction

Hydrogels are hydrophilic gels, polymer networks that are swollen with water as the dispersion medium. They are an excellent solution for different medical applications such as bone regeneration [1,2], tissue engineering [3,4] or, soft-tissue-mimicking [5].

Regarding the latter application, studying the mechanical characterization of real soft tissues is an important approach to understanding how they are deformed during different clinical scenarios such as surgeries. In this way, different solutions could be developed to reduce soft tissue damage. Nonetheless, using real biological tissues can be difficult

for two reasons: (1) accessibility, and (2) ethics [6]. In this way, a possible solution could be to use surgical planning prototypes, also known as phantoms, which are simulated biological bodies.

Surgeons only have a short period to carry out complex technical tasks during the operation. Therefore, it could be vital to know in advance what exactly must be done, during surgery to shorten the operation duration and thereby reduce surgical-related risks. However, to date doctors have not received enough training and methods to face this problem [7]. Additionally, different studies demonstrated that surgeons who trained with physical models had better skills in comparison with those who did not have the same opportunity [8].

Considering this, it is necessary to find materials that mimic the properties of biological tissues. Until now, different materials such as silicones, hydrogels, or photopolymer resins were studied [6,9–23]: PVA, PHY, agar, gelatine, alginate, hydrogels or Sylgard 527 (PDMS) and Sylgard 184 (Silicone Elastomer), as well as photopolymer resins for Additive Manufacturing (e.g., VeroWhite+, a rigid general purpose, high resolution, opaque white material; and TangoPlus+, which simulates thermoplastic elastomers with flexible, rubber-like qualities; both of them developed by Stratasys®). Additionally, it is worth mentioning that there are other biopolymeric materials such as aerogels that can be used for tissue engineering and regenerative medicine [24,25]. For example, Yahya et al. [24] highlighted the main challenges of biopolymer-based scaffolds and the prospects of using these materials in regenerative medicine.

Of these materials, hydrogels (hydrophilic water-based gels [26]) were mainly used in different studies; yet they only focused on one or two organs. For example, Forte et al. [18] and Leibinger et al. [17] mimicked the brain tissue by developing a composite hydrogel (6% wt PVA/0.85% wt PHY [18] and 5% wt PVA/0.59% wt PHY [17]). Additionally, Tan et al. [6] mimicked three soft living tissues (brain, lung, and liver) by molding in a petri dish using different compositions of PVA and PHY. It was determined that the best compositions for each organ were the following: (1) to mimic the brain, 2.5% wt PVA + 1.2% wt PHY; (2) to mimic the lung, 11% wt PVA; and (3) to mimic the liver, 14% wt PVA + 2% wt PHY. This study was the first important step for the realization of surgical planning training devices and tools. Dister et al. [23] measured similar viscoelastic properties of the brain tissue by developing a 0.5% wt alginate/0.5% wt gelatine. Adams et al. [9] used the molding technique for obtaining different soft kidney phantoms using silicone elastomer, agarose gel, or PDMS.

Among these studies, not all of them covered in-depth viscoelastic properties as well as the Shore hardness of the materials. These two properties are important parameters that are normally measured in soft-tissue-biomechanics.

Regarding the viscoelastic properties, few studies covered the viscoelasticity of soft tissues in recent years. For instance, Chatelin et al. [27] reviewed the viscoelastic properties of the brain tissue studied during the last 50 years. Then, Estermann et al. [28] studied the viscoelasticity of the liver tissue using DMA. It was found that at a frequency of 1 Hz the storage and loss modulus measured at porcine and bovine liver were extremely high. For example, the storage and loss modulus for the porcine is 488.3 ± 163.9 kPa and 52.23 ± 28.91 kPa, respectively. Other studies [29–31], on the other hand, showed lower values in the range of 0.5–9 kPa and 0.07–1 kPa for the storage and loss modulus, respectively. Focusing on the kidney, as it happened with the liver, some discrepancy was seen [32,33]. For example, Charles [32] measured high values: for E', around 40 kPa; and for E'', around 17 kPa whereas Amador [33] got lower values for storage and loss modulus: 4.5–5.5 kPa (for $\eta = 10$ Pa·s) and 4.5–9 kPa (for $\eta = 100$ Pa·s) and 0.026–1.08 kPa (for $\eta = 10$ Pa·s) and 0.25–2.2 kPa (for $\eta = 100$ Pa·s), respectively. The heart [34] has a storage modulus (E'), which varies from 20 KPa at 0.5 Hz to 40 KPa at 3.5 Hz. On the other hand, the loss modulus (E'') values are between 3 kPa at 0.5 Hz and 8 kPa at 3.5 Hz.

On the other hand, another important parameter is hardness, which can be measured either by indentation or abrasion. For the soft biological tissues, macroindentation

has been previously used to measure the organs' hardness. The hardness is a tactile property, which is useful by manual palpation to distinguish healthy from pathological tissues [22]. In this way, it is an important parameter to take into consideration. There are various types of hardness tests for hard materials such as Vickers (HV), Brinell (HB), or Rockwell (HR). Regarding the characterization of the soft tissues, Shore hardness is the most commonly used [5,13,22,35–37]. As an example of this, Yoon et al. [35] measured a 15.06 ± 2.64 Shore 00 in a healthy human liver. Additionally, Estermann et al. [22] measured a 30.52 ± 1.52 Shore 00 for a porcine liver, whereas for a bovine liver was 25.67 ± 2.61 Shore 00. Additionally, with the Shore hardness test, the shear stiffness of the soft tissue can be obtained as described in [38]. Regarding the pancreas, Belyaev et al. [13] and Foitzik et al. [36] measured a 20 Shore 00 and 26.3 ± 2.5 Shore 00, respectively. Then, Riedle et al. [37] obtained different values, even harder: for the arcus aortae, 13.4 ± 1.9 Shore A; for the thoracic aorta, 17.1 ± 1.4 Shore A; and for the aorta abdominalis, 17.6 ± 1.2 Shore A.

Additionally, from the authors' knowledge, less research has been carried out studying the cut feeling (related to shear strength), a crucial factor to be considered during surgical procedures [39]. Quantifying this property can be vital in the tissue-mimicking field to achieve more realistic phantoms. Warner-Bratzer (WB) shear test is used widely in food science to evaluate meat or animal muscle tenderness. The test is considered as an empirical method; however, some authors have found a statistical correlation between the maximum tensile force (mechanical property) and WB shear force in beef muscle, related to the strength of the muscle fibers [40].

Overall, the present paper aims to address several soft living tissues mimicking using different hydrogels. For that, the measurement of the viscoelastic properties will be carried out using the DMA (Dynamic Mechanical Analysis) technique and the hardness using a Shore Hardness durometer as well as the cut feeling concept by carrying out the Warner–Bratzler shear test. In this way, the mimicking between six hydrogels (based on agarose, PVA, PHY, and GelMA) and four soft living tissues (liver, heart, kidney, and brain) can be achieved. The reason for the large extent of organs and materials, which is a novelty in this research field, is both the wide range of values detected in previous articles and the intention to be able to use the mimicking data obtained to address, in a future stage, the 3D printing of multi-material prototypes. Therefore, this study offers originality not only because the Warner–Bratzler Shear test can be used as a new mimicking method, but also due to the wide range of soft living tissues and materials that are analyzed.

2. Results and Discussion

In this study, we aimed to mimic several soft living tissues with different materials taking into consideration several parameters: (1) viscoelastic properties using compression tests (E' and E''); (2) Shore hardness; and (3) the "cut feeling" concept by carrying out the Warner–Bratzler shear test, which measured the forces (shear strength) profile along the cut. The materials that are out of range of the soft-tissue-biomechanics are not included in the different plots.

2.1. Liver

Firstly, the liver Shore hardness obtained in our experiments is 13 ± 4.5 Shore 00, which has been measured as is described in Section 4.3.2. This value is similar to the result obtained by Yoon et al. [35], which is 15.06 ± 2.64 Shore 00 in a healthy liver. Additionally, Estermann et al. [22] measured a 30.52 ± 1.52 Shore 00 for a porcine liver, whereas for a bovine liver was 25.67 ± 2.61 Shore 00. Higher numbers on the scale indicate a greater resistance to indentation and, hence, harder materials. In this study, the material which matched more closely the hardness of the liver tissue is 1% wt agarose gel (14 ± 2.5 Shore 00). Regarding this material, Oflaz et al. [13] obtained a value of 27.25 ± 2.72 Shore 00 for 1% wt agarose gel. Secondly, this study measured a liver tissue storage and loss modulus of 1.2 ± 0.5 kPa and 0.27 ± 0.17 kPa, respectively. These results were similar to other studies [29–31] which showed values in the range of 0.5–9 kPa and 0.07–1 kPa for the

storage and loss modulus, respectively. On the other hand, Estermann et al. [28] also studied the viscoelasticity of the liver tissue. However, it was found that at a frequency of 1 Hz the storage and loss modulus measured at porcine and bovine liver were extremely high, which is not common for soft tissues. For example, the storage and loss modulus for the porcine liver is 488.3 ± 163.9 kPa and 52.23 ± 28.91 kPa, respectively [28]. Then, Figure 1 shows the best materials for mimicking the viscoelastic properties of the liver. In both storage and loss modulus, the 6% wt PVA/1% wt PHY-1FT hydrogel that undergoes one freeze-thaw cycle seemed to be the best option. This composite hydrogel was also used with similar PVA and PHY amounts by Tan et al. [6]. In terms of the Warner–Bratzler shear test, Figure 1C shows the liver tissue cutting profile. The peaks observed might be related to the presence of internal blood vessels as are veins and arteries. Additionally, it might also be because it is a heterogeneous organ. Regarding the mimicking, among all materials, no hydrogel was able to match its cutting profile. Finally, it is important to highlight the mimicking achieved in other studies. For example, de Jong et al. investigated that a 4% wt PVA hydrogel that undergoes two freeze-thaw cycles can mimic the liver tissue. For instance, Tan et al. [6] studied a composition hydrogel of 14% wt PVA/2.1% wt PHY that undergoes one freeze-thaw cycle was determined to mimic the liver.
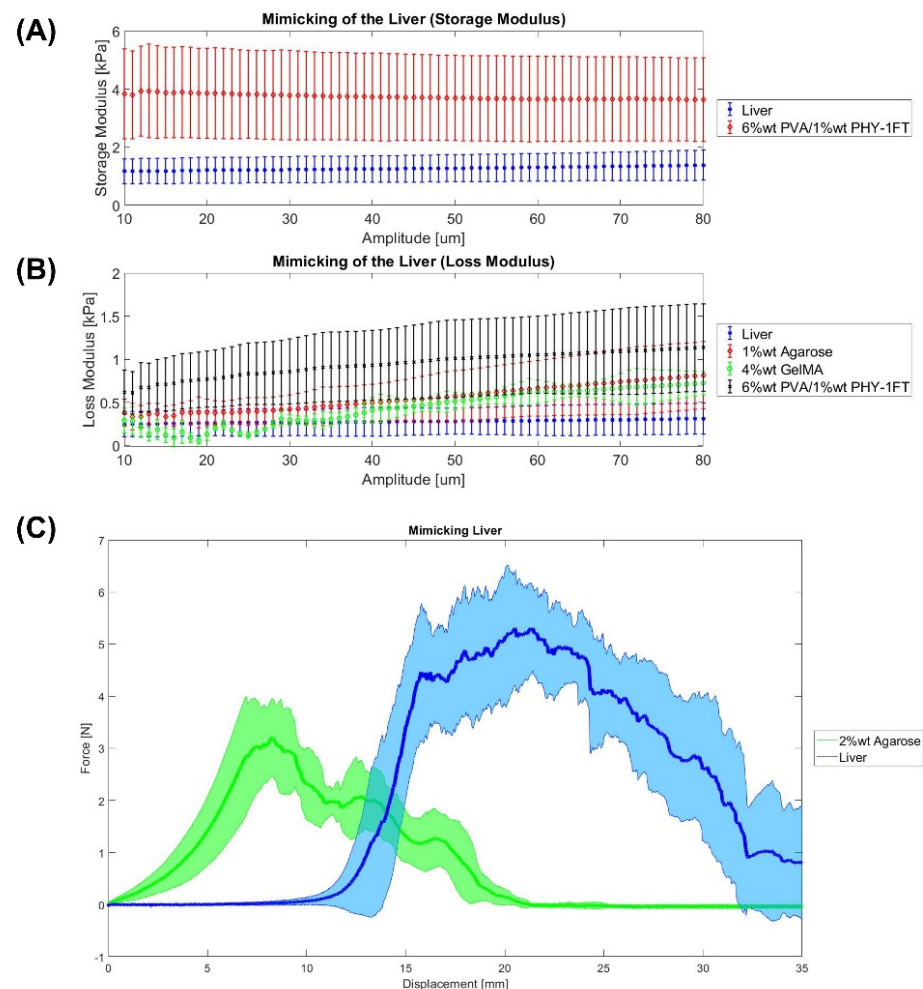
Figure 1. Mimicking the liver. (**A**,**B**) DMA results. (**C**) Warner–Bratzler shear test results. Data were represented as mean $\pm$ SEM values. Each sample has an *n* = 6.

A statistical analysis was carried out to clarify the effectiveness of the present tissue-mimicking analysis. Table 1 shows the statistical analysis of the liver and the closest materials using the *t*-test. If the *p*-value is higher than 0.05, the null hypothesis stated before is not rejected and the material matches the organ.
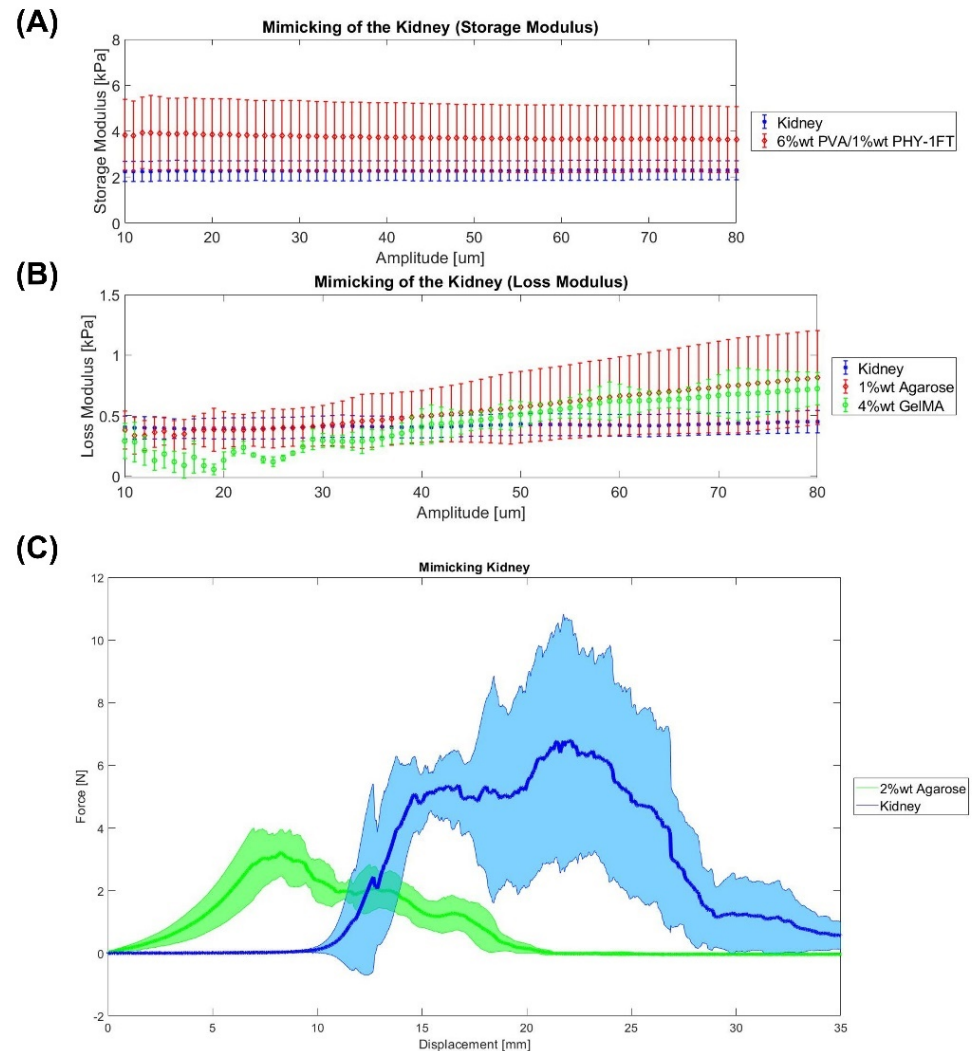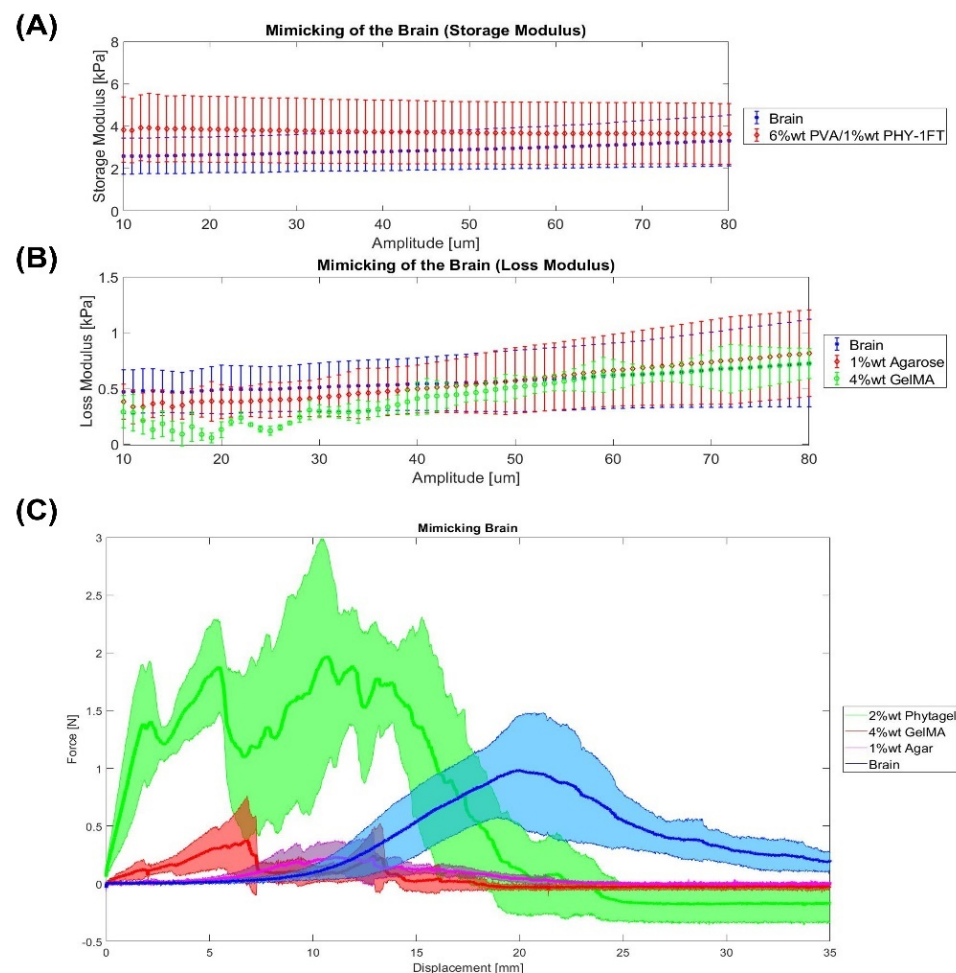
Table 1. Statistical analysis of the liver (*p*-value). SH: Shore Hardness. E′: Storage Elastic Modulus. E″: Loss Elastic Modulus. WB: Warner–Bratzler shear test. X states that this material is not able to mimic the tissue and, that is why no statistical analysis is carried out.

	SH	E′	E″	WB
1% wt agarose	0.044	X	0.069	X
2% wt agarose	X	X	X	X
4% wt GelMA	X	X	0.01	X
2% wt PHY	X	X	X	X
6% wt PVA/1% wt PHY-1FT	X	0.016	0.008	X
6% wt PVA/1% wt PHY-2FT	X	X	X	X

2.2. Heart

Firstly, the heart Shore hardness is 20 ± 7.5 Shore 00, which means that it is harder than the liver. This might be because the heart is a muscle. Riedle et al. [38] obtained different values, even harder: for the arcus aortae, 13.4 ± 1.9 Shore A; for the thoracic aorta, 17.1 ± 1.4 Shore A; and for the aorta abdominals, 17.6 ± 1.2 Shore A. In this study, the material which matched more closely the hardness of the heart tissue is 1% wt agarose gel (14 ± 2.5 Shore 00). Secondly, this study measured a heart tissue storage and loss modulus of 14.5 ± 5.5 kPa and 3.40 ± 1.87 kPa, respectively. Regarding the storage modulus, the values of our study are lower than the values measured by Ramadan et al. [34] from 20 kPa at 0.5 Hz to 40 kPa at 3.5 Hz. On the other hand, the loss modulus (E″) values are between 3 kPa at 0.5 Hz and 8 kPa at 3.5 Hz, which are close to our results. In addition, the stiffness lies from 400 to 800 N/m with a phase shift around 0.175. In our study, the phase shift is 0.22, which means that a more vicious behavior was obtained. Then, Figure 2A,B show the best materials for mimicking the viscoelastic properties of the heart. In both storage and loss modulus, 2% wt agarose gel seemed to be the best material for mimicking the viscoelastic behavior of the heart. In terms of the Warner–Bratzler shear test, Figure 2C shows the heart tissue seems to have a straight slope at the beginning of the cutting profile since the samples used did not take into consideration the possible holes in which the blood flows. Additionally, it is interesting to see that the maximum is higher than some of the other soft tissues, which might due to the presence of the cardiac muscles. Regarding the "cut feeling" mimicking, 2% wt agarose is the material that more closely resembles the mechanical properties of native heart tissue. Although as can be seen in Figure 2C, it is still far from the heart tissue. This means a higher amount of agarose would be needed. In the literature, however, different materials have been used for the mimicking of the heart tissue. For instance, Yoo et al. [41] used the material jetting technology for 3D printing the heart. For that, the most flexible material (TangoPlus FullCure resin) for the heart, a solid material (VeroWhite) for the platform and stools, and a mixture of the 2 print materials for valvar annuli were used. In another study, Riedle et al. [42] 3D printed in red translucent silicone with a Shore A hardness of 20 (ACEO® Silicone GP Shore A 20, Wacker Chemie AG) using the ACEO®-technology.

A statistical analysis was carried out to clarify the effectiveness of the present tissue-mimicking analysis. Table 2 shows the statistical analysis of the heart and the closest materials using the *t*-test. If the *p*-value is higher than 0.05, the null hypothesis stated before is not rejected and this means that the material matches the real organ.
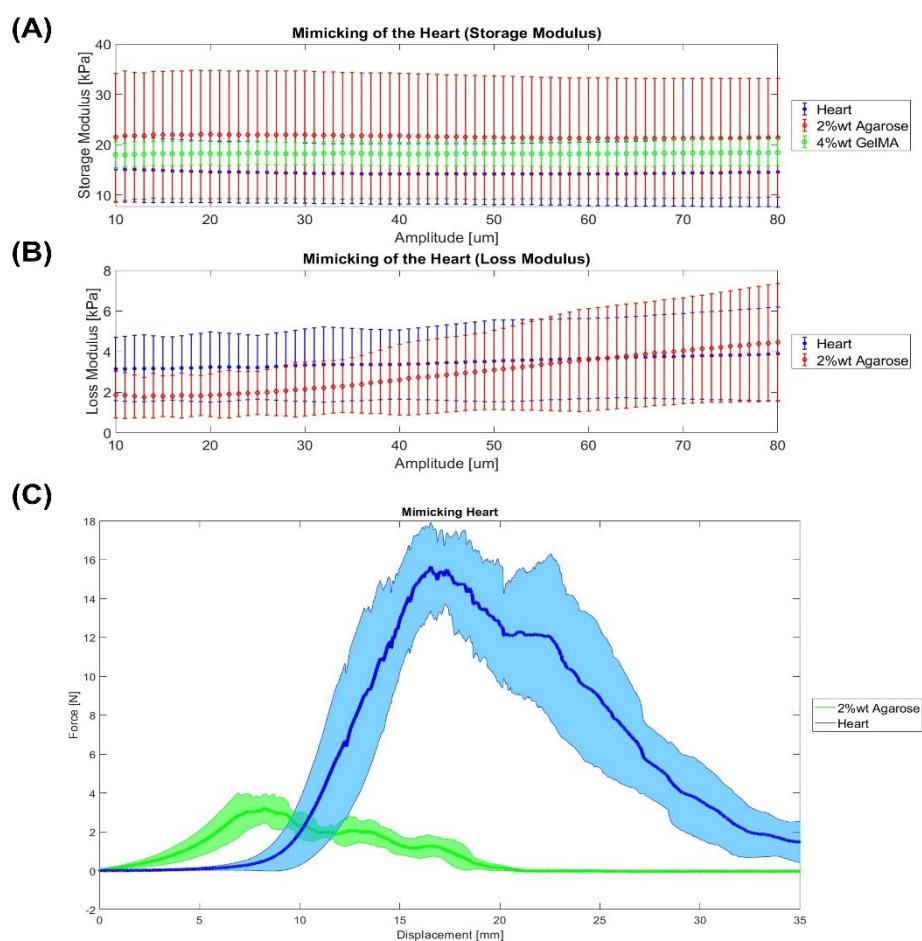
Figure 2. Mimicking the heart. (**A**,**B**) DMA results. (**C**) Warner–Bratzler shear test results. Data were represented as mean $\pm$ SEM values. Each sample has an $n = 6$.

Table 2. Statistical analysis of the heart (*p*-value). SH: Shore Hardness. E′: Storage Elastic Modulus. E″: Loss Elastic Modulus. WB: Warner–Bratzler shear test. X states that this material is not able to mimic the tissue and, that is why no statistical analysis is carried out.

	SH	**E′**	**E″**	**WB**
1% wt agarose	0.42	X	X	X
2% wt agarose	X	0.28	0.98	X
4% wt GelMA	X	0.18	X	X
2% wt PHY	X	X	X	X
6% wt PVA/1% wt PHY-1FT	X	X	X	X
6% wt PVA/1% wt PHY-2FT	X	X	X	X

2.3. Kidney

Firstly, the kidney Shore hardness is 36 ± 10 Shore 00, which is the hardest soft tissue measured, and the materials which matched more closely are 2% wt agarose (37 ± 5 Shore 00) and 4% wt GelMA (32 ± 4 Shore 00). Secondly, a kidney tissue storage and loss modulus of 2.38 ± 0.43 kPa and 0.40 ± 0.08 kPa were obtained, respectively. Then, Figure 3A,B show the best materials for mimicking the viscoelastic properties of the kidney. In both storage and loss modulus, different materials appear to be the best option. On the one hand, the storage modulus of 6% wt PVA/1% wt PHY-1FT makes it the best material to mimic the elastic part of the kidney. On the other hand, in terms of the loss modulus part vicious, the closest materials are 1% wt agarose as well as 4% wt GelMA. Concerning the Warner–Bratzler shear test, Figure 3C shows that the best material is 2% wt agarose.

Finally, Adams et al. [9] 3D printed different kidney models using the molding technique. The kidney models were made of silicone elastomer, agarose gel, and PDMS. For example, the agarose gel we developed would be an option.

(A)

(B)

(C)

Figure 3. Mimicking the kidney. (**A**,**B**) DMA results. (**C**) Warner–Bratzler shear test results. Data were represented as mean $\pm$ SEM values. Each sample has an *n* = 6.

A statistical analysis was carried out to clarify the effectiveness of the present tissue-mimicking analysis. Table 3 shows the statistical analysis of the kidney and the closest materials using the *t*-test. If the *p*-value is higher than 0.05, the null hypothesis stated before is not rejected and the material matches the organ.

Table 3. Statistical analysis of the kidney (*p*-value). SH: Shore Hardness. E′: Storage Elastic Modulus. E″: Loss Elastic Modulus. WB: Warner–Bratzler shear test. X states that this material is not able to mimic the tissue and, that is why no statistical analysis is carried out.

	SH	**E′**	**E″**	**WB**
1% wt agarose	X	X	0.10	X
2% wt agarose	0.59	X	X	0.02
4% wt GelMA	0.42	X	0.03	X
2% wt PHY	X	X	X	X
6% wt PVA/1% wt PHY-1FT	X	0.02	X	X
6% wt PVA/1% wt PHY-2FT	X	X	X	X

2.4. Brain

Firstly, the brain Shore hardness is 4.5 ± 1.5 Shore 00, which matches the hardness of 2% wt Phytagel (8 ± 2 Shore 00) more closely. Secondly, a brain tissue storage and loss modulus of 2.6 ± 0.84 kPa and 0.47 ± 0.19 kPa were measured, respectively. Then, Figure 4A,B show the best materials for mimicking the viscoelastic properties of the brain. In both storage and loss modulus, different materials appear to be the best option. On the one hand, the storage modulus of 6% wt PVA/1% wt PHY-1FT is the best material to mimic the elastic part of the brain. On the other hand, in terms of the loss modulus part (vicious part), the closest materials are 1% wt agarose and 4% wt GelMA. Then, Dister et al. [23] measured similar viscoelastic properties of the brain tissue by developing a 0.5% wt alginate/0.5% wt gelatine. Concerning the Warner–Bratzler shear test, Figure 4C shows that there are several options: 1% wt agarose, 4% wt GelMA, and 2% wt PHY. Finally, Forte et al. [18] mimicked the brain tissue by developing a composite hydrogel (6% wt PVA/0.85% wt PHY), which then was used for manufacturing a phantom.

Figure 4. Mimicking the brain. (**A**,**B**) DMA results. (**C**) Warner–Bratzler shear test results. Data were represented as mean $\pm$ SEM values. Each sample has an $n = 6$.

A statistical analysis was carried out to clarify the effectiveness of the present tissue-mimicking analysis. Table 4 shows the statistical analysis of the brain and the closest materials using the *t*-test. If the *p*-value is higher than 0.05, the null hypothesis stated before is not rejected and the material matches the organ.

Table 4. Statistical analysis of the brain (*p*-value). SH: Shore Hardness. E′: Storage Elastic Modulus. E″: Loss Elastic Modulus. WB: Warner–Bratzler shear test. X states that this material is not able to mimic the tissue and, that is why no statistical analysis is carried out.

	SH	E′	E″	WB
1% wt agarose	X	X	0.70	0.02
2% wt agarose	X	X	X	X
4% wt GelMA	X	X	0.61	0.12
2% wt PHY	X	X	X	3.89×10^{-3}
6% wt PVA/1% wt PHY-1FT	X	0.34	X	X
6% wt PVA/1% wt PHY-2FT	X	X	X	X

2.5. Qualitative Summary

According to the previous results, Table 5 summarizes all values of the tissue-mimicking study.

Table 5. Qualitative summary of the mimicking. SH: shore hardness; DMA (E″); DMA (E″); WB (Warner–Bratzler). ✔ corresponds that a material can mimic a certain organ in terms of a certain property.

	Liver				Heart				Kidney				Brain			
	SH	E′	E″	WB	SH	E′	E″	WB	SH	E′	E″	WB	SH	E′	E″	WB
1% wt Agar	✔		✔		✔						✔				✔	✔
2% wt Agar						✔	✔		✔							
4% wt GelMA			✔			✔			✔		✔				✔	✔
2% wt PHY																✔
6% wt PVA/1% wt PHY-1FT		✔	✔							✔				✔		
6% wt PVA/1% wt PHY-1FT																

3. Conclusions

In the present work, different materials were tested regarding their viscoelastic behavior, and hardness, as well as their non-linear elastic mechanical response.

All in all, it was seen that the mimicking of soft living tissues is a difficult task, due to the high complexity of organs. Most of them are composed of different tissues that play a key role in terms of structure and mechanical behavior.

According to all the mimicking results that are summarized in the qualitative summary (see Table 5) and statistics, the following are the best materials for mimicking each organ: (1) to mimic the liver, the best materials are 1% wt agarose and CH-1FT; (2) to mimic the heart, the best material is 2% wt agarose; (3) to mimic the kidney, the best material is 4% wt GelMA; and (4) to mimic the brain, the best material is 4% wt GelMA and 1% wt agarose.

Among the different materials, hydrogels are an option for the molding technique, since they offer a good consistency. Additionally, they are soft as well as mostly transparent. In this way, the implications of the current research are interesting for the manufacture of phantoms to be used in medical imaging, preoperative surgical planning in hospitals by doctors, etc.

There is still a lot of work to do in the present field, but this is an excellent starting point for continuing with future research studies in the mimicking of soft living tissues.

4. Materials and Methods

4.1. Biological Tissue Sample Preparation

Lamb organ (liver, heart, brain, and pancreas) specimens were procured from a local supplier within 24 hours' post-mortem. These organs were chosen for three different reasons: (1) they cover a high range of different mechanical properties; (2) surgeons often

need to accomplish complex surgical tasks in these organs (for example, with the liver a hepatectomy for the tumor removal or very delicate operations in the heart or brain); and (3) there is a lack of knowledge in the mimicking of these four. On the other hand, for the DMA and Warner–Bratzler shear testing, the biological tissues (n = 6) were cut using a biopsy punch (16 mm in diameter) to get cylindrical samples: 16 mm diameter and 8 mm height. Regarding the Shore hardness (n = 6), no sample preparation was needed as it was directly measured on the tissue's surface.

4.2. Hydrogels Sample Preparation

The hydrogels that were synthetized are: 1% wt and 2% wt agarose gels, 4% wt GelMA, 2% wt PHY, and 6% wt PVA/ 1% wt PHY with one or two freeze-thaw -FT- cycles. These materials were chosen because of their softness. For the DMA and Warner–Bratzler shear testing, the materials' samples (n = 6) were cut using a biopsy punch (16 mm in diameter) to get cylindrical samples: 16 mm diameter and 8 mm height. Regarding the Shore hardness (n = 6), no sample preparation was needed.

4.2.1. Agarose Gels

Agarose is a linear polymer with a molecular weight of about 120,000, consisting of alternating D-galactose and 3,6-anhydro-L-galactopyranose linked by α-(1$\rightarrow$3) and β-(1$\rightarrow$4) glycosidic bonds [43]. The 1% wt and 2% wt agarose gels were produced by mixing deionized water and agarose powder (supplied by Químics Dalmau, Barcelona, Spain). The 1% wt and 2% wt agarose powder amounts were added to the deionized water and magnetically stirred and heated at 90 °C until fully mixed.

4.2.2. GelMA

Gelatine consists of a large number of glycine, proline, and 4-hydroxy proline residues [44]. Methacrylate gelatine (GelMA) was synthesized following a previously described protocol [44]. In short, type A porcine skin gelatin (Sigma Aldrich, San Lui, USA) was mixed at 10% (*w/v*) into phosphate-buffered saline (PBS) at 60 °C and stirred until fully dissolved. Methacrylic anhydride was added at a rate of 0.5 mL/min to the gelatin solution under stirred conditions at 50 °C and allowed to react for 1 h. Following a 5 dilution with additional warm (40 °C) PBS to stop the reaction, the mixture was dialyzed against distilled water using 12–14 kDa cutoff dialysis tubing for 1 week at 40 °C. The solution was lyophilized to generate a porous white foam. GelMA was dissolved into deionized water at 4% (*w/v*) at 37 °C, and Irgacure 2959® (BASF, Mannheim, Germany) was used as a photoinitiator at 0.7% *w/v*. The photoinitiator was dissolved into ethanol absolute (1:2 *w/v*), and then added to GelMA solution. To crosslink GelMA, UV light (365 nm, RegenHU, Villaz-Saint-Pierre, Switzerland) was used.

4.2.3. PHY Gels

Phytagel is produced from a bacterial substrate that is composed of rhamnose, glucuronic acid, and glucose. This polymer is composed of repeating tetrasaccharide units that will form a gel in the presence of mono- or divalent cations [45]. A 2% wt PHY solution was prepared by mixing deionized water and PHY powder, supplied by Sigma Aldrich, San Luis, AR, USA. A 2% wt PHY powder was added to the deionized water and magnetically stirred and heated at 90 °C for 1 h until fully mixed. Then, the solution could cool down.

4.2.4. PVA/PHY Composite Hydrogel (CH)

The composite hydrogel (CH) was produced by mixing PVA (molecular weight 85–124 Da) and PHY, both supplied by Sigma Aldrich, San Luism USA. See Figure 5. PVA is an atactic material that is composed of the 1,3-diol linkages, some of them occur depending on the conditions for the polymerization of the vinyl ester precursor [46]. Solutions were prepared separately with the corresponding amount of powder and deionized water as described in Tan et al. [46]. Amounts of 6% wt PVA and 1% wt PHY powder

amounts were added to the deionized water and magnetically stirred and heated at 93 °C for 1 h. Then, when the particles and deionized water were mixed, the solutions could cool down. Afterward, the separate solutions were combined at a 1:1 weight ratio and stirred at 70 °C for 1h. Finally, the samples were physically cross-linked by undergoing one or two freeze-thaw (FT) cycles (24 h) of −18 °C for 16 h, and then the samples were thawed at room temperature for 8 h.
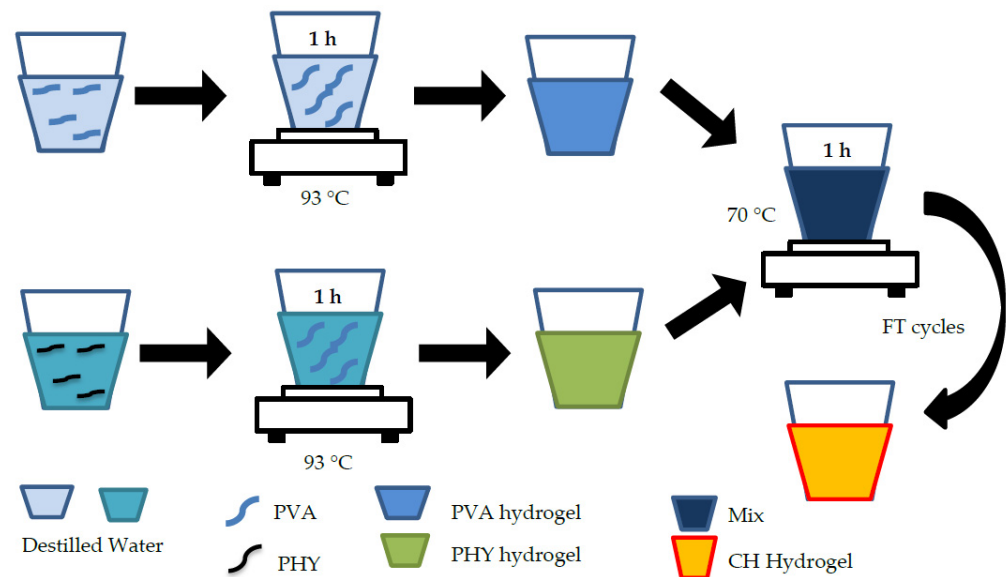
Figure 5. PVA/PHY hydrogel synthesis process.

4.3. Parameters for the Mimicking of Soft Tissues

4.3.1. Dynamic Mechanical Analysis (DMA)

DMA is a technique that applies an oscillating force to a material/tissue sample and analyzes the response of the sample to that force [47]. The samples were tested using a DMA Q800 equipment of TA Instruments at 37 °C, 1 Hz and a pre-load force of 0.001 N. DMA in compression calculate the storage modulus (E′), which is the elastic part of the sample; and the loss modulus (E″), which is the vicious part of the sample.

4.3.2. Shore Hardness Test

Shore hardness is a measurement of the resistance of a sample to indentation. There are different scales based on ASTM D2240 testing standards [48]: A, B, C, D, DO, E, M, O, OO, OOO, OOO-S, and R. Each scale results in having values between 0 and 100, where higher values indicate that a sample is harder. The shore is a key parameter for the mimicking of soft living tissues because it measures the consistency of the samples. This is an important aspect of the perception of surgeons.

STM D2240-Durometer Hardness method was used [48]. For that, Shore Durometer Type 00 and 000, supplied by Baxlo, Instrumentos de Medida y Precisión, S.L., Barcelona, Spain, were used for measuring the hardness of the biological tissues (different measurements were done at different parts of the anatomical structure) and material samples. Shore Durometer Type A was also used, but only showed values in the heart.

4.3.3. Warner–Bratzler Shear Test

Warner–Bratzler shear test is commonly used in the food industry as a standard characterization method. For example, it has been used to determine the best meat tenderness (toughness) for various types of meat. The Warner–Bratzler consists of a steel frame which is supporting a triangular shear blade (see Figure 6A).
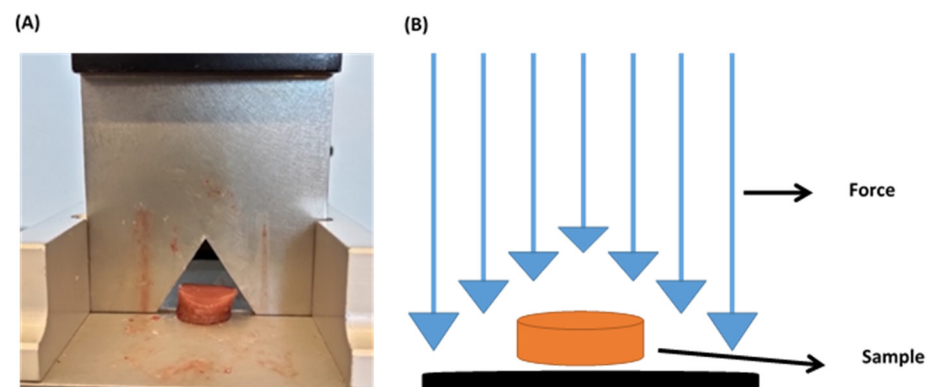
Figure 6. (**A**) Liver sample ready for being cut using the Warner–Bratzler. (**B**) Warner–Bratzler shear test method.

The analysis of the Warner–Bratzler shear test was carried out by focusing on four different parameters: (1) breaking force is the force peak where the cut starts (it is either before the curve is starting to flatten and reaching the maximum force or when there is a change in the curve like a small hole); (2) maximum cutting force is the maximum force of the plot when the sample is being cut; (3) adjustment area is the area under curve until the braking force, and (4) cutting area is the area under the curve from the breaking force until the end.

For creating a tissue-mimicking material for surgical training, the Warner–Bratzler shear test was carried out. This technique is related to the surgeon's cut feeling operating. A texturometer Texture Analyser TA.XT.plus (Stable Micro Systems, Surrey, UK) was used with a 50 N load cell (Figure 2A). Maximum shear force (N) and area under the curve (J) were measured using the Warner–Bratzler probe. The speed is 1 mm/s during 35 mm of cut. The height of the sample was measured with a digital micrometer.

4.4. Statistical Analysis

Statistics were performed using MATLAB R20. Organs mimicking using different materials was assessed using paired sample *t*-test to compare if the material can mimic the organ by focusing on the parameters of the Warner–Bratzler Shear test (maximum force), DMA, and Shore hardness. Data are represented as mean $\pm$ SEM (Standard Error of the Mean). $p \leq 0.05$ (*), $p \leq 0.01$(**), and $p \leq 0.001$ (***). The null hypothesis states that an organ and a material are equal. If the *p*-value is lower than 0.05, the hypothesis is rejected; and consequently, it is confirmed that the material cannot mimic the organ. This analysis was only carried out with the most similar materials that can be seen in Figures 1–4.

References

1. Derkus, B.; Okesola, B.O.; Barrett, D.W.; D'Este, M.; Chowdhury, T.T.; Eglin, D.; Mata, A. Multicomponent hydrogels for the formation of vascularized bone-like constructs in vitro. *Acta Biomater.* **2020**, *109*, 82–94. [CrossRef]

2. Gupta, S.; Teotia, A.K.; Qayoom, I.; Shiekh, P.A.; Andrabi, S.M.; Kumar, A. Periosteum-Mimicking Tissue-Engineered Composite for Treating Periosteum Damage in Critical-Sized Bone Defects. *Biomacromolecules* **2021**, *22*, 3237–3250. [CrossRef] [PubMed]

3. Rodríguez-Vázquez, M.; Vega-Ruiz, B.; Ramos-Zúñiga, R.; Saldaña-Koppel, D.A.; Quiñones-Olvera, L.F. Chitosan and Its Potential Use as a Scaffold for Tissue Engineering in Regenerative Medicine. *BioMed Res. Int.* **2015**, *2015*. [CrossRef] [PubMed]

4. Lin, W.; Kluzek, M.; Iuster, N.; Shimoni, E.; Kampf, N.; Goldberg, R.; Klein, J. Cartilage-inspired, lipid-based boundary-lubricated hydrogels. *Science* **2020**, *338*, 335–338. [CrossRef] [PubMed]

5. Tejo-Otero, A.; Lustig-Gainza, P.; Fenollosa-Artés, F.; Valls, A.; Krauel, L.; Buj-Corral, I. 3D printed soft surgical planning prototype for a biliary tract rhabdomyosarcoma. *J. Mech. Behav. Biomed. Mater.* **2020**, *109*, 103844. [CrossRef] [PubMed]

6. Tan, Z.; Dini, D.; Rodriguez y Baena, F.; Forte, A.E. Composite hydrogel: A high fidelity soft tissue mimic for surgery. *Mater. Des.* **2018**, *160*, 886–894. [CrossRef]

7. Chikwe, J.; de Souza, A.C.; Pepper, J.R. No time to train the surgeons. *BMJ* **2004**, *328*, 418–419. [CrossRef]

8. Sekhar, A.; Sun, M.R.; Siewert, B. A tissue phantom model for training residents in ultrasound-guided liver biopsy. *Acad. Radiol.* **2014**, *21*, 902–908. [CrossRef]

9. Adams, F.; Qiu, T.; Mark, A.; Fritz, B.; Kramer, L.; Schlager, D.; Wetterauer, U.; Miernik, A.; Fischer, P. Soft 3D-Printed Phantom of the Human Kidney with Collecting System. *Ann. Biomed. Eng.* **2017**, *45*, 963–972. [CrossRef]

10. de Jong, T.L.; Pluymen, L.H.; van Gerwen, D.J.; Kleinrensink, G.J.; Dankelman, J.; van den Dobbelsteen, J.J. PVA matches human liver in needle-tissue interaction. *J. Mech. Behav. Biomed. Mater.* **2017**, *69*, 223–228. [CrossRef]

11. van Oosten, A.S.G.; Chen, X.; Chin, L.K.; Cruz, K.; Patteson, A.E.; Pogoda, K.; Shenoy, V.B.; Janmey, P.A. Emergence of tissue-like mechanics from fibrous networks confined by close-packed cells. *Nature* **2019**, *573*, 96–101. [CrossRef] [PubMed]

12. Falland-Cheung, L.; Scholze, M.; Hammer, N.; Waddell, J.N.; Tong, D.C.; Brunton, P.A. Elastic behavior of brain simulants in comparison to porcine brain at different loading velocities. *J. Mech. Behav. Biomed. Mater.* **2018**, *77*, 609–615. [CrossRef]

13. Oflaz, H.; Baran, O. A new medical device to measure a stiffness of soft materials. *Acta Bioeng. Biomech.* **2014**, *16*, 125–131. [CrossRef] [PubMed]

14. Meisel, N.A.; Dillard, D.A.; Williams, C.B. Impact of material concentration and distribution on composite parts manufactured via multi-material jetting. *Rapid Prototyp. J.* **2018**, *24*, 872–879. [CrossRef]

15. Bezek, L.B.; Cauchi, M.P.; De Vita, R.; Foerst, J.R.; Williams, C.B. 3D printing tissue-mimicking materials for realistic transseptal puncture models. *J. Mech. Behav. Biomed. Mater.* **2020**, *110*, 103971. [CrossRef]

16. Mueller, J.; Courty, D.; Spielhofer, M.; Spolenak, R.; Shea, K. Mechanical Properties of Interfaces in Inkjet 3D Printed Single- and Multi-Material Parts. *3D Print. Addit. Manuf.* **2017**, *4*, 193–199. [CrossRef]

17. Leibinger, A.; Forte, A.E.; Tan, Z.; Oldfield, M.J.; Beyrau, F.; Dini, D.; Rodriguez y Baena, F. Soft Tissue Phantoms for Realistic Needle Insertion: A Comparative Study. *Ann. Biomed. Eng.* **2016**, *44*, 2442–2452. [CrossRef]

18. Forte, A.E.; Galvan, S.; Manieri, F.; Rodriguez y Baena, F.; Dini, D. A composite hydrogel for brain tissue phantoms. *Mater. Des.* **2016**, *112*, 227–238. [CrossRef]

19. Forte, A.E.; Galvan, S.; Dini, D. Models and tissue mimics for brain shift simulations. *Biomech. Model. Mechanobiol.* **2018**, *17*, 249–261. [CrossRef]

20. Forte, A.E.; Gentleman, S.M.; Dini, D. On the characterization of the heterogeneous mechanical response of human brain tissue. *Biomech. Model. Mechanobiol.* **2017**, *16*, 907–920. [CrossRef]

21. Jiang, S.; Liu, S.; Feng, W. PVA hydrogel properties for biomedical application. *J. Mech. Behav. Biomed. Mater.* **2011**, *4*, 1228–1233. [CrossRef]

22. Estermann, S.J.; Pahr, D.H.; Reisinger, A. Quantifying tactile properties of liver tissue, silicone elastomers, and a 3D printed polymer for manufacturing realistic organ models. *J. Mech. Behav. Biomed. Mater.* **2020**, *104*, 103630. [CrossRef]

23. Distler, T.; Schaller, E.; Steinmann, P.; Boccaccini, A.R.; Budday, S. Alginate-based hydrogels show the same complex mechanical behavior as brain tissue. *J. Mech. Behav. Biomed. Mater.* **2020**, *111*, 103979. [CrossRef]

24. Yahya, E.B.; Amirul, A.A.; Abdul Khalil, H.P.S.; Olaiya, N.G.; Iqbal, M.O.; Jummaat, F.; Atty Sofea, A.K.; Adnan, A.S. Insights into the role of biopolymer aerogel scaffolds in tissue engineering and regenerative medicine. *Polymers* **2021**, *13*, 1612. [CrossRef] [PubMed]

25. Chandrasekaran, R.; Hillgärtner, M.; Ganesan, K.; Milow, B.; Itskov, M.; Rege, A. Computational design of biopolymer aerogels and predictive modelling of their nanostructure and mechanical behavior. *Sci. Rep.* **2021**, *11*, 10198. [CrossRef] [PubMed]

26. Tejo-Otero, A.; Ritchie, A.C. Biological and mechanical evaluation of mineralized-hydrogel scaffolds for tissue engineering applications. *J. Biomater. Appl.* **2021**, *36*, 460–473. [CrossRef] [PubMed]

27. Chatelin, S.; Constantinesco, A.; Willinger, R. Fifty years of brain tissue mechanical testing: From in vitro to in vivo investigations. *Biorheology* **2010**, *47*, 255–276. [CrossRef]

28. Estermann, S.J.; Pahr, D.H.; Reisinger, A. Hyperelastic and viscoelastic characterization of hepatic tissue under uniaxial tension in time and frequency domain. *J. Mech. Behav. Biomed. Mater.* **2020**, *112*, 104038. [CrossRef]

29. Mattei, G.; Tirella, A.; Gallone, G.; Ahluwalia, A. Viscoelastic characterisation of pig liver in unconfined compression. *J. Biomech.* **2014**, *47*, 2641–2646. [CrossRef]

30. Kiss, M.Z.; Varghese, T.; Hall, T.J. Viscoelastic characterization of in vitro canine tissue. *Phys. Med. Biol.* **2004**, *49*, 4207–4218. [CrossRef]

31. Chatelin, S.; Oudry, J.; Périchon, N.; Sandrin, L.; Allemann, P.; Soler, L.; Willinger, R. In vivo liver tissue mechanical properties by transient elastography: Comparison with dynamic mechanical analysis. *Biorheology* **2011**, *48*, 75–88. [CrossRef]

32. Barnes, S.C. Viscoelastic Properties of the Bladder and Design of a Surgical Instrument for the Removal of Bladder Tumours. Ph.D. Thesis, University of Birmingham, Birmingham, UK, 2016; p. 164.

33. Amador Carrascal, C. Measurement of Kidney Viscoelasticity with Shearwave Dispersion Ultrasound Vibrometry. Ph.D. Thesis, College of Medicine-Mayo Clinic, Rochester, MN, USA, 2011; p. 167.

34. Ramadan, S.; Paul, N.; Naguib, H.E. Standardized static and dynamic evaluation of myocardial tissue properties. *Biomed. Mater.* **2017**, *12*, 25013. [CrossRef]

35. Yoon, Y.C.; Lee, J.S.; Park, S.U.; Kwon, J.H.; Hong, T.H.; Kim, D.G. Quantitative assessment of liver fibrosis using shore durometer. *Ann. Surg. Treat. Res.* **2017**, *93*, 300. [CrossRef]

36. Foitzik, T.; Gock, M.; Schramm, C.; Prall, F.; Klar, E. Octreotide hardens the pancreas. *Langenbeck Arch. Surg.* **2006**, *391*, 108–112. [CrossRef] [PubMed]

37. Riedle, H.; Molz, P.; Franke, J. Determination of the mechanical properties of cardiac tissue for 3D printed surgical models. In Proceedings of the 2018 IEEE-EMBS Conference on Biomedical Engineering and Sciences (IECBES), Sarawak, Malaysia, 3–6 December 2018; pp. 171–176. [CrossRef]

38. Arani, A.; Lanzino, G.; Ehman, R. Higher-Resolution Magnetic Resonance Elastography in Meningiomas to Determine Intratumoral Consistency. *Neurosurgery* **2015**, *77*, 653–659. [CrossRef]

39. Tibbits, S. 4D printing: Multi-material shape change. *Archit. Des.* **2014**, *84*, 116–121. [CrossRef]

40. Lu, R.; Solomon, M.B.; Berry, B.W. Tensile properties and warner-bratzler tenderness measurement of raw and cooked beef. *Trans. ASAE* **1998**, *41*, 1431–1439. [CrossRef]

41. Yoo, S.J.; Spray, T.; Austin, E.H.; Yun, T.J.; van Arsdell, G.S. Hands-on surgical training of congenital heart surgery using 3-dimensional print models. *J. Thorac. Cardiovasc. Surg.* **2017**, *153*, 1530–1540. [CrossRef]

42. Riedle, H.; Ghazy, A.; Seufert, A.; Seitz, V.; Dorweiler, B.; Franke, J. Generic design of an anatomical heart model optimized for additive manufacturing with silicone. *Rapid Prototyp. J.* **2020**, *27*, 217–222. [CrossRef]

43. Gustavsson, P.-E. Per-OlofLars Son Journal of Chromatography Library. In *Journal of Chromatography Library*; Elsevier: Amsterdam, The Netherlands, 1993; Volume 55, pp. 797–800.

44. Nichol, J.W.; Koshy, S.; Bae, H.; Hwang, C.M.; Khademhosseini, A. 2010 Biomaterials Ali. Cell-laden microengineered gelatin methacrylate hydrogels. *Biomaterials* **2011**, *31*, 5536–5544. [CrossRef]

45. Phyto Technology Laboratories ®Product Information Sheet Coconut Powder Phyto Technology Laboratories®. Available online: https://phytotechlab.com/mwdownloads/download/link/id/59/ (accessed on 25 November 2021).

46. Tan, Z.; Parisi, C.; Di Silvio, L.; Dini, D.; Forte, A.E. Cryogenic 3D Printing of Super Soft Hydrogels. *Sci. Rep.* **2017**, *7*, 16293. [CrossRef] [PubMed]

47. Menard, K.P. *Dynamic Mechanical Analysis: A Practical Introduction*, 2nd ed.; CRC Press: Boca Raton, FL, USA, 1999.

48. ASTM D2240-15e1: Standard Test Method for Rubber Property—Durometer Hardness. Available online: https://www.astm.org/d2240-15e01.html (accessed on 25 November 2021).

Antibacterial Hydrogel Sheet Dressings Composed of Poly(vinyl alcohol) and Silver Nanoparticles by Electron Beam Irradiation

Rattanakorn Chiangnoon [1], Pennapa Karawak [1], Jarurattana Eamsiri [1], Sasikarn Nuchdang [1], Nuatawan Thamrongsiripak [2], Naruemon Neramitmansook [2], Siwanut Pummarin [3,4], Pimchanok Pimton [3,5], Kewalee Nilgumhang [6] and Pimpon Uttayarat [1,*]

1   Nuclear Technology Research and Development Center, Thailand Institute of Nuclear Technology (Public Organization), Ongkarak, Nakhon Nayok 26120, Thailand
2   Irradiation Center, Thailand Institute of Nuclear Technology (Public Organization), Ongkarak, Nakhon Nayok 26120, Thailand
3   Department of Biology, School of Science, Walailak University, Nakhon Si Thammarat 80160, Thailand
4   Program in Medical Sciences, Faculty of Medicine, Chulalongkorn University, Bangkok 10330, Thailand
5   Functional Materials and Nanotechnology Center of Excellence, Walailak University, Nakhon Si Thammarat 80160, Thailand
6   Advanced Engineering and Nuclear Technology Center, Thailand Institute of Nuclear Technology (Public Organization), Ongkarak, Nakhon Nayok 26120, Thailand
*   Correspondence: pimponu@tint.or.th; Tel.: +66-80-585-8245

Abstract: Advanced wound dressings that can deliver potent antibacterial action are still much in need, especially for treating wound infections caused by drug-resistant bacteria. In this research, we utilized electron beam (EB) irradiation to develop antibacterial hydrogel sheet dressings from poly(vinyl alcohol) (PVA) and silver nanoparticles (AgNPs) in a two-step processing and evaluated their bactericidal efficacy, as well as the AgNP release. The effect of the irradiation dose on the swelling, gel fraction, network parameters, and mechanical properties of the hydrogels was first determined to establish the optimal doses for the two-step processing. The prototypic hydrogel sheets were then formed in the first EB irradiation and served as a matrix for the AgNP synthesis by the reduction of the silver nitrate precursors during the second EB irradiation. The diffusion assay showed that the minimal inhibition concentration (MIC) of the AgNP-load hydrogels was 0.25 and 0.5 mg/cm^2 against *Escherichia coli* and *Staphylococcus aureus*, respectively. At these MIC levels, the released AgNPs increased sharply before reaching the maximum, ~950 and 1800 ppb, at 24 h as analyzed by atomic absorption. Therefore, we successfully demonstrated that this two-step processing by EB irradiation provides a convenient platform to fabricate AgNP-loaded hydrogel dressings that can be further developed for wound healing.

Keywords: hydrogel sheet dressings; poly(vinyl alcohol); silver nanoparticles; electron beam irradiation; antibacterial

1. Introduction

Annually, millions of people worldwide suffer from the loss of skin due to the fact of injuries, such as burns, chemical exposure, and diseases [1]. The lack of proper wound treatment can cause serious dehydration and wound infection that becomes life-threatening to the patients and poses major burdens for wound care [2,3]. With drug-resistant bacteria currently threatening the treatment of infected wounds, it is desirable to develop wound dressings that can maintain the appropriate moisture at the wound interface, prevent infection, and be easily removed without causing trauma [4].

Hydrogels have emerged as a new class of dressing materials capable of providing a necessary moist environment for wound healing [2,3,5]. Having three-dimensional (3D)

networks of crosslinked hydrophilic polymers that can swell a large amount of water without being disintegrated [6], hydrogels can donate hydration to the wounds in addition to absorbing excess exudate into the structure. The soft consistency and smooth surface of hydrogels also enable them to easily conform to the skin [2] and become nonadherent upon removal [7]. The crosslinked networks of hydrogels can be constructed by physical, chemical, and radiation methods [6,8]. Among these approaches, ionizing radiation from high-energy sources, such as gamma rays or an electron beam (EB), offers many unique advantages, as the crosslinking of polymer chains into a gel can be performed without the use of harmful chemical crosslinkers or initiators at room temperature [9,10]. At the same time, sterilization of the final products can be combined within the processing step [9,10]. Therefore, the radiation processing itself is considered a "green" technology and environmentally friendly. In aqueous polymer systems, the generation of hydroxyl radicals (•OH) and hydrogen atoms (•H) during radiolysis of water by gamma or EB irradiation serve as the key agents that induce intermolecular crosslinking of polymer chains into a permanent 3D network [11].

With the increasing demands for advanced wound dressings to treat infected wounds without the overuse of antibiotics, silver nanoparticles (AgNPs) have gained considerable attention, since they exhibit potency across a broad spectrum of bacteria [12,13]. When bound to proteins of cell membranes, internal organelles, and reaction pathways, AgNPs can disrupt protein function which, in turn, lead to bacterial cell death [14]. A recent study by Liu et al. [3] also showed that AgNPs could serve as an agent for photothermal effects to further enhance bacterial cell death via locally elevated temperature. Incorporation of AgNPs into hydrogels can be performed either by synthesizing AgNPs separately before mixing with hydrogel precursors [3] or by combining the formation of AgNPs within the hydrogel crosslinking process [15]. Using the latter approach, Leawhiran et al. [15] demonstrated that AgNP/gelatin/poly(vinyl alcohol) hydrogels could be processed within a single exposure to gamma irradiation. During irradiation, the hydrated electrons (e^-_{aq}) generated by radiolysis reduced Ag^+ in the starting $AgNO_3$ to Ag^0 that later aggregated to form AgNPs. However, the mechanical strength of the hydrogels was compromised, as the reduction in AgNPs also decreased the extent of the crosslinked polymer matrix [15].

The two-step processing of AgNP-loaded hydrogels has previously been explored by Eid et al. [16] in which the hydrogels were first formed by radiation-induced crosslinking of poly(vinyl alcohol) (PVA) and polyvinyl pyrrolidone, followed by the addition of silver precursor, which was finally reduced into AgNPs by sodium borohydride. As the resulting AgNP-loaded hydrogels will be interfaced with body tissue, caution and consideration is required concerning any remaining harmful chemicals within hydrogels, as well as the sterilization of final products. Therefore, the ability to produce sterilized AgNP-loaded hydrogels with an environmentally friendly method is advantageous and of great interest.

In the present study, we demonstrated for the first time the use of EB irradiation to develop antibacterial hydrogel dressings in a two-step processing in which AgNPs were formed by the reduction of silver nitrate ($AgNO_3$) precursors during the second irradiation at the sterilization dose (Figure 1). PVA was chosen due to the fact of its biocompatibility, nontoxicity, and water solubility [17]. To elucidate the effect of the irradiation dose on the water absorption, crosslinking, and mechanical properties of the hydrogels, gamma irradiation was first applied to fabricate hydrogel sheet models at doses that ranged from 10 to 80 kGy. The effect of repeated irradiation at a sterilization dose of 25 kGy was then investigated regarding the hydrogels' swelling and mechanical properties to establish the optimal doses for the two-step processing by EB irradiation. Finally, the antibacterial efficacy, release of AgNPs, and cytocompatibility of the AgNP-loaded hydrogel sheet dressings were evaluated.

I. Irradiation-induced crosslinking of PVA and synthesis of AgNPs
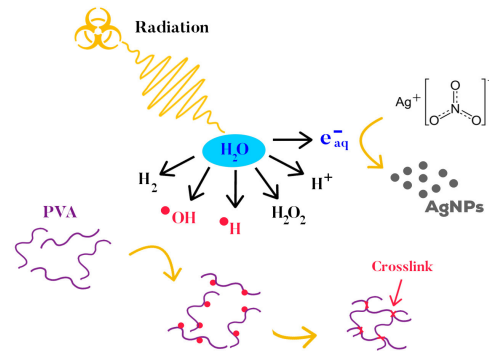
II. A two-step processing of AgNP-loaded hydrogel by EB irradiation
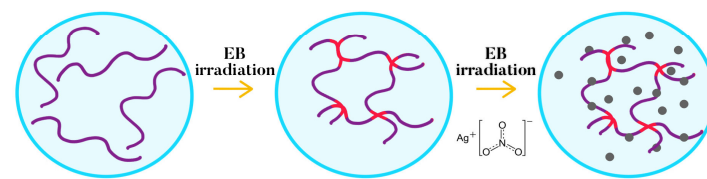
Figure 1. Preparation scheme of antibacterial AgNP-loaded hydrogel sheets by EB irradiation.

2. Results and Discussion

2.1. Structural Characterization of the Hydrogels

To elucidate the effect of the irradiation dose on the swelling, gel fraction, and crosslinked network parameters of the hydrogels, we first applied gamma irradiation to form hydrogel models from starting PVA solutions at varied doses. Table 1 shows that the gel fraction and EDS of the hydrogels were at opposing trends with the increase in gamma doses. The gel fraction was first measurable (~25%) at a dose of 10 kGy before it increased significantly to 86% when the dose was raised to 25 kGy. At higher doses, the gel fraction further increased to above 90% and remained relatively constant up to the highest dose of 80 kGy. Regarding the swelling capacity of the hydrogels compared to their dried weights, a sharp reduction of the EDS from 2500% to 1300% as the gamma dose was raised from 25 to 40 kGy. A further increase in the doses caused a slight reduction in the EDS to 890% at the highest dose of 80 kGy. The samples formed at 10 kGy were not included in the EDS study due to the fact of their flowable, paste-like appearance that was difficult to handle. Based on these results, the increase in the irradiation dose induced more linking of PVA chains into 3D networks, resulting in the smaller space between the crosslink units to accommodate water molecules.

In addition to the gel fraction and EDS obtained by the experiments, the basic network parameters of the hydrogels, including the average molecular weight between the crosslinks (M_c), crosslink density (ρ_x), and mesh size (ε), could also be elucidated by calculation. Using the modified equilibrium swelling theory of Flory and Rehner, assuming an isotropic swelling of the neutral polymer networks in which four polymer chains are joined at one crosslink point [18], M_c can be calculated by the following equation:

$$\frac{1}{M_c} = \frac{2}{M_n} - \frac{v/V_1 [\ln(1 - V_{2,s}) + V_{2,s} + \mu V_{2,s}^2]}{V_{2,r}[(V_{2,s}/V_{2,r})^{1/3} - 0.5\left(\frac{V_{2,S}}{V_{2,R}}\right)]} \tag{1}$$

where M_n is the number of the average molecular weight (~52,800 based on the manufacturer's data), v is the specific volume of PVA (0.788 cm^3/g), V_1 is the molar volume of water (18 cm^3/mol), m is the Flory–Huggins interaction parameter (0.494 for PVA-water) [19], and $V_{2,r}$ and $V_{2,s}$ are polymer fractions of hydrogel in a relaxed state and swollen state at equilibrium, respectively. These polymer fractions can be derived from the weights of the original hydrogel, swollen hydrogel, and dried hydrogel, assuming the volume

additivity of water and PVA [18,20]. Subsequently, ρ_x and ε can be calculated by the following equations [21]:

$$\rho_x = \frac{1}{vM_c},$$ (2)

$$\varepsilon = (V_{2,s})^{-\frac{1}{3}} \left[C_n \left(\frac{2M_c}{M_r} \right) \right]^{\frac{1}{2}} l$$ (3)

where C_n is the Flory characteristics ratio (8.3 for PVA), M_r is the average molecular weight of repeating unit (44 g/mol for VOH), and l is the C-C bond length (1.54 Å) [19].

Table 1 shows that the calculated M_c and ρ_x values are also at opposing trends with an irradiation dose similar to the EDS and gel fraction data. These M_c and ρ_x values obtained in our study were also within the same range as those previously reported in a similar PVA hydrogel system formed by EB irradiation [22]. Following the same trend of M_c with the irradiation doses, the ε values also decreased from 358 to 130 Å as the gamma dose increased from 25 to 80 kGy. Based on the calculation of these network parameters, it was clear that as ρ_x increased with the number of crosslink units induced by irradiation, the space or mesh size to accommodate water molecules inside the hydrogel matrix became smaller, resulting in a lowered swelling capacity. Although the values of the gel fraction remained near its maximum at doses of 25–60 kGy, ρ_x continued to increase within this dose range. It may be deduced that despite having most of the polymer chains already joined together by crosslinking at a dose of 25 kGy, more linking of the chains continued to proceed at higher doses. However, at the highest dose of 80 kGy, we observed that our hydrogel sheets became easily torn at the edges during the release from molds. This could be attributed to other modes of radical interaction, such as chain scissions that start to compete with crosslinking [11].

Table 1. Gel fraction, equilibrium degree of swelling (EDS), and network parameters (M_c, ρ_x, and ε) of crosslinked PVA hydrogels as a function of irradiation doses. Each value of the EDS and gel fraction data represents the mean ± SD (n = 4).

Dose (kGy)	Gel Fraction (%)	EDS (%)	M_c (g/mol)	ρ_x (10^{-4} mol/cm^3)	ε (Å)
10	25.1 ± 16.1	-	-	-	-
25	86.6 ± 5.1	2554 ± 294	16,240	0.8	358
40	93.5 ± 2.9	1348 ± 222	6770	1.9	173
60	92.0 ± 7.0	1311 ± 133	6250	2.0	163
80	93.8 ± 1.0	892 ± 17	3300	3.9	130

Note: The EDS at 10 kGy was not obtainable due to the difficulties in the sample handling.

2.2. Thermal Properties of the Crosslinked Hydrogels

The extent of the crosslinked 3D networks inside the hydrogel sheets could also be detected by changes in the thermal properties (Figure 2). A large and sharp endodermic curve that peaked at approximately 227 °C was observed in the nonirradiated samples (0 kGy). After irradiation at increasing doses from 10 to 80 kGy, the melting enthalpies and melting points decreased with broader endodermic peaks, especially at doses greater than 25 kGy. These changes in the thermal properties could be due to the decrease in PVA molecules that were arranged orderly into crystallite domains through hydrogen bonding of the -OH side chains, as they were instead chemically joined into 3D networks. These thermal properties of our crosslinked hydrogels are in agreement with previous studies [23,24] that reported a noticeable drop in the melting enthalpies and melting points of PVA hydrogels crosslinked by irradiation.
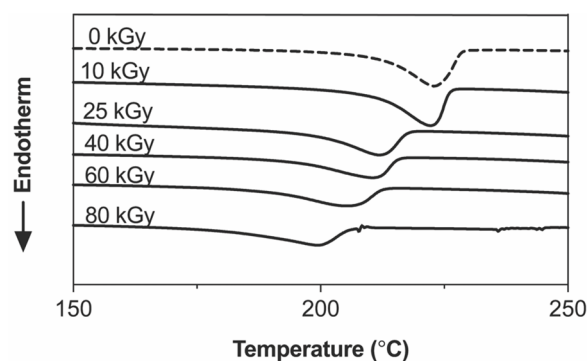
Figure 2. DSC analysis of the crosslinked PVA hydrogel sheets at varied irradiation doses.

2.3. Morphology of the Hydrogels

In our study, gamma doses of 25, 40, and 60 kGy led to the formation of hydrated and pliable hydrogel sheets that could be easily released from the mold without tearing. Figure 3a,b show that the hydrogel sheets were stretchable and conformal over the skin with ease upon removal. Among the three gamma doses, the doses of 40 and 60 kGy resulted in hydrogel sheets that could maintain their expanded, flat shape during handling, while the sheets that formed at 25 kGy appeared floppy and easily rolled or curled from the sides.

To further investigate the microstructure of 3D networks, the hydrogels were cold fractured and visualized by SEM. Irregular pores with sizes that ranged from ~100 to 500 mm were shown to be distributed throughout the hydrogel matrices (Figure 3c–e) in contrast to the as-cast hydrogels (Figure 3f). The size of the pores observed in SEM images was much larger than the average pore size values calculated by the Flory–Rehner modeling approach (Table 1). Such discrepancies have previously been reported in dextran [10,18] and other PVA [25] hydrogel systems in which the actual size of the macropores was underestimated. Although the modeling approach provides a useful description of the crosslinked network structure inside the hydrogels that varied with irradiation doses, the analysis by SEM had to be used in conjunction to obtain an accurate picture of the pore size.
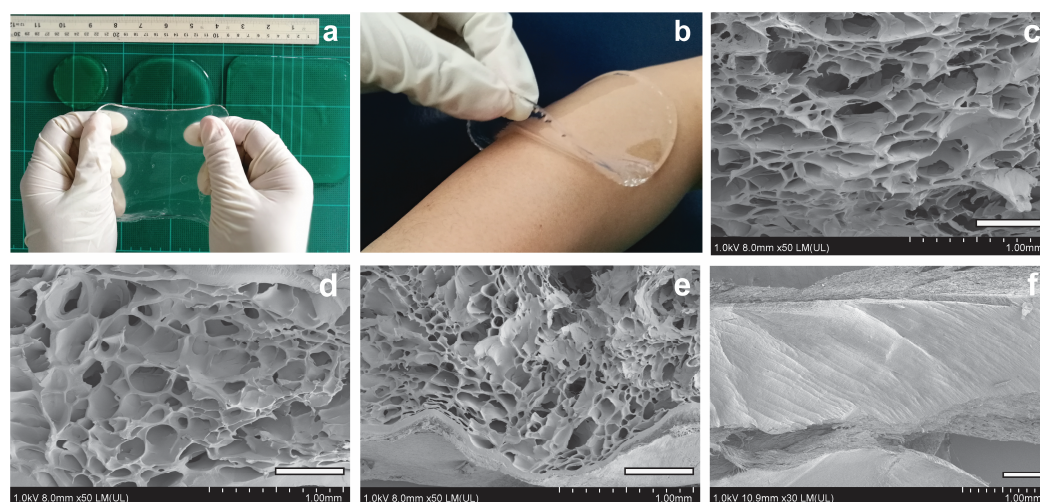
Figure 3. Morphology of the crosslinked PVA hydrogel sheets. Representative digital images of (**a**) stretchable and (**b**) conformal hydrogel sheets fabricated by irradiation at 40 kGy. SEM images showing a porous microstructure inside the hydrogel matrices crosslinked at doses of (**c**) 25, (**d**) 40, and (**e**) 60 kGy compared to the (**f**) as-cast hydrogel sheet. Scale bars are 500 mm in (**c**–**f**).

2.4. Effect of Repeated Irradiation on the Sterility, Swelling, and Mechanical Properties of the Hydrogel Sheets

As the second irradiation was conducted at 25 kGy, a dose level that was commonly used to sterilize medical devices [15], our test of the sterility confirmed the absence of the microorganism in broths containing bare hydrogel sheets without AgNPs. We then tested if such repeated irradiation would affect the swelling and mechanical properties of the hydrogels. Previously, we demonstrated that both the gel strength and tensile strength of the hydrogel sheets increased with the irradiation doses used to crosslink the hydrogels having the similar 10% (*w/v*) PVA system and gamma doses ranging from 25 to 80 kGy [26]. Therefore, based on our current data on swelling, hydrogel sheets that formed at 25 and 40 kGy were selected for the repeated irradiation experiments, as the swelling became saturated at higher doses. The repeatedly irradiated samples were termed 25r and 40r, respectively.

In terms of the swelling, the 25r hydrogels showed a significant reduction in EDS from ~2500 to 1400% after the second exposure to irradiation, whereas the EDS of 40r samples remained relatively the same (Figure 3a). For the tensile properties, both the 25r and 40r samples exhibited a two-fold increase in the tensile strength from ~5 to 10 kPa and ~8 to 18 kPa, respectively. By contrast, the elongation at break showed a slight increase for the 25r and a slight decrease for the 40r samples (Figure 4c). Similar to the tensile strength, the Young's moduli of both the 25r and 40r samples showed a significant two-fold and three-fold increase, respectively, compared to those without repeated irradiation. Based on these results, the 40 kGy dose was chosen to produce the prototypic hydrogel sheets in the first irradiation step, as their swelling capacity and stretchability were not significantly changed after the second exposure to irradiation at 25 kGy.
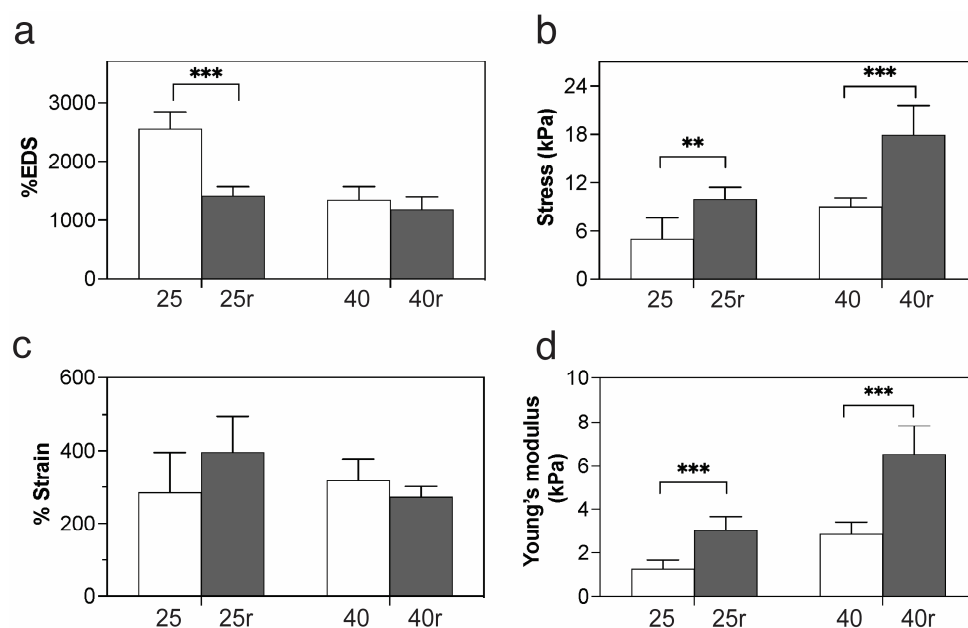
Figure 4. Effect of repeated irradiation on the (**a**) swelling, (**b**) tensile strength, (**c**) elongation at break, and (**d**) Young's modulus of the hydrogel sheets. Symbols ** and *** correspond to *p*-values of less than 0.01 and 0.001, respectively.

2.5. Antibacterial Properties of the AgNP-Loaded Hydrogel Sheets

Based on the optimized irradiation doses obtained from the repeated irradiation experiments, the formation of prototypic hydrogel sheet dressings loaded with AgNPs was performed in the two-step processing by electron beam irradiation. This latter irradiation platform could support the further up-scale fabrication of AgNP-loaded hydrogel sheet dressings within a shorter processing time. The presence of the AgNPs in the AgNP-loaded hydrogel sheets was confirmed by SEM (Supplementary Materials Figure S1). For the

evaluation of the AgNP-loaded hydrogel sheets for their antibacterial efficacy, we selected *S. aureus* and *E. coli* out of the 28 bacteria species [13] commonly found in infected wounds as the representatives of Gram-positive and Gram-negative bacteria. Using the agar diffusion assay (Figure 5), a clear zone formed around each sample with a distinct boundary from the hydrogel's edge indicating the zone of inhibited bacterial growth. Between the two strains of bacteria, the larger and more prominent clear zones were observed around the AgNP-loaded hydrogels on the *E. coli* plate (Figure 5A). As a control, no clear zone or halo was observed around the hydrogels (*control*) against both *E. coli* and *S. aureus*.
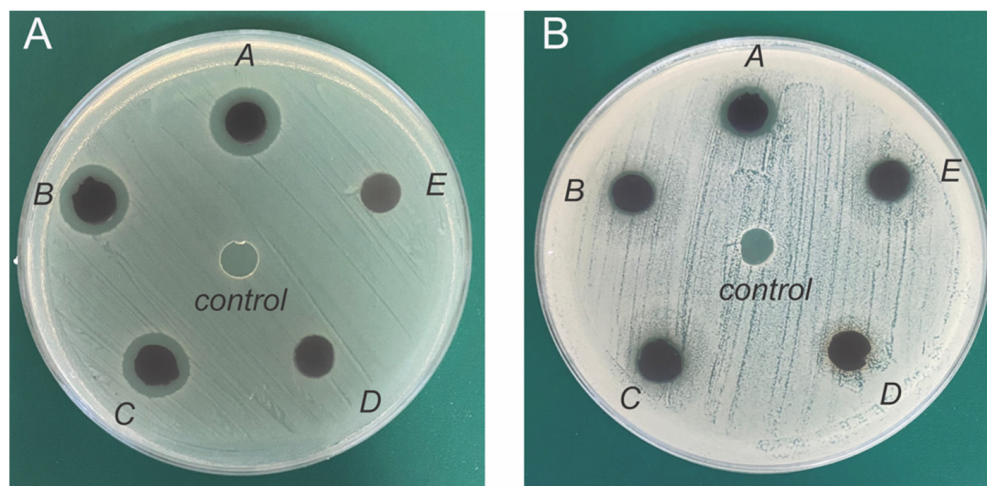
Figure 5. Disc diffusion assay of the AgNP-loaded hydrogels against (**A**) *E. coli* and (**B**) *S. aureus*. Hydrogels A, B, C, D, and E contained AgNPs at 1.0, 0.5, 0.25, 0.125, and 0.0625 mg/cm^2, respectively. *Control* refers to the hydrogel without AgNPs.

The quantitative analysis of the clear zone and its implication for the antibacterial efficacy of the AgNP-loaded hydrogels was performed by manually measuring the diameter of the clear zone that formed around each sample. The inhibition ratio, which was defined as the diameter of the clear zone normalized by the diameter of the hydrogel, was then calculated in which a ratio above "1" indicated the ability of the AgNP-loaded hydrogel in inhibiting bacterial growth. Table 2 shows that the inhibition ratios against *E. coli* and *S. aureus* increased with the amount of AgNPs loaded in the hydrogels. The total amount of AgNPs on each hydrogel was calculated based on the concentration of the starting AgNO$_3$ solution (Table 3 in Section 4 Materials and Methods) at 50 μL per 4 cm^2 area of hydrogel. For *E. coli*, the amount of AgNPs at the minimal level of 0.25 mg/cm^2 on the hydrogel could effectively inhibit bacterial growth.

In contrast, it required at least 0.5 mg/cm^2 of AgNPs on the hydrogels to inhibit the growth of *S. aureus*. Based on these data, *E. coli* was more sensitive to the AgNPs at a lower concentration than *S. aureus*, which was consistent with a previous report [27]. Regarding the antibacterial efficacy against *S. aureus*, the amounts of AgNPs loaded in our hydrogels, 0.5 and 1.0 mg/cm^2, were within the same range as the commercial dressing coated with silver nanocrystalline at 0.69–1.64 mg/cm^2 [28]. As we serially varied the amount of AgNPs at a two-fold dilution, the minimal inhibition concentration (MIC) of AgNPs against *S. aureus* and *E. coli* was found to be 0.5 and 0.25 mg/cm^2, respectively. In terms of the sensitivity of the different bacteria to the AgNPs, our findings also agreed with a previous report that the MIC of AgNPs against *S. aureus* was higher than the level required for *E. coli* [29].

Table 2. The inhibition ratios of the AgNP-loaded hydrogels against *E. coli* and *S. aureus*. The data are represented by the mean $\pm$ standard deviation from 3 replicates, each measured in 3 directions. The dash indicates the absence of a clear zone.

Sample	Total AgNPs (mg/cm^2)	Inhibition Ratio	
		E. coli	*S. aureus*
Hydrogel A	1.0	1.78 ± 0.09	1.50 ± 0.01
Hydrogel B	0.5	1.66 ± 0.01	1.26 ± 0.02
Hydrogel C	0.25	1.50 ± 0.17	-
Hydrogel D	0.125	-	-
Hydrogel E	0.0625	-	-

Based on our previous study, the release of AgNPs from the hydrogels was qualitatively confirmed by UV-Vis spectrophotometry [30]. In the present study, the amount of released AgNPs at varied AgNO$_3$ loadings was quantitatively measured in the form of ionized Ag$^+$ by ICP-MS (Figure 6), which decreased proportionally from treatments A–E. For hydrogels A, B, and C incorporated with AgNPs at 1, 0.5, and 0.25 mg/cm^2, respectively, the amount of released AgNPs increased sharply by approximately two-fold between 2 and 24 h. After, the level of the released AgNPs remained relatively unchanged for up to 72 h. Interestingly, for treatments D and E, with a much lower initial AgNO$_3$ loading, the released AgNPs continued to rise linearly with the incubation time from 2 up to 72 h. Regarding the AgNP levels of 1775 ± 151 ppb for hydrogel B and 948 ± 45 ppb for hydrogel C measured by ICP at 24 h, it can be derived from our experiment that at least ~1000–2000 ppb of AgNPs is required for effective antibacterial action against *S. aureus* and *E. coli*, respectively.
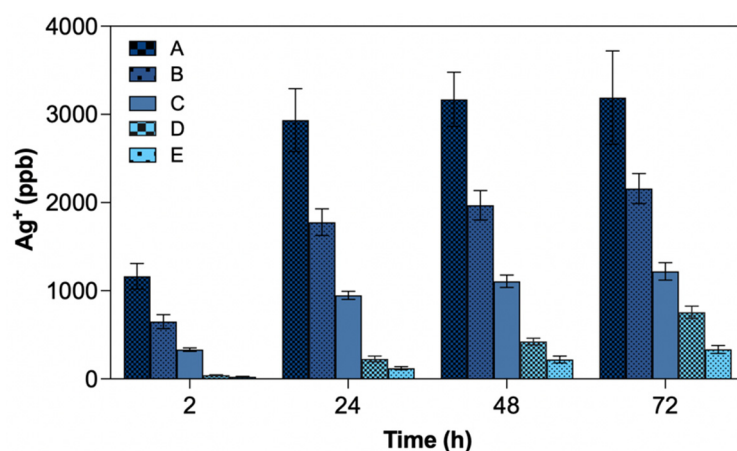
Figure 6. Release of Ag$^+$ from the AgNP-embedded hydrogels measured by ICP.

2.6. Cytocompatibility

The MTT-based extract test was used to evaluate the cytocompatibility of the nontreated hydrogels and AgNP-loaded hydrogels. For the nontreated hydrogels, a cytotoxicity evaluation was performed in both L929 and HDFB cells compared to positive and negative controls (Figure 7A). After being cultured in extracts derived from hydrogels, the L929 cells showed viability at 80%, similar to the negative control and above the 70% threshold of non-cytotoxicity for medical devices [31]. By contrast, the viability of L929 cells in extract derived from the positive control was below 10%. In addition to L929 cells, the viability of HDFB in extracts derived from the hydrogels was also well above 70%, suggesting that our prototypic hydrogel sheets could be applied for dermal application, such as wound dressings.
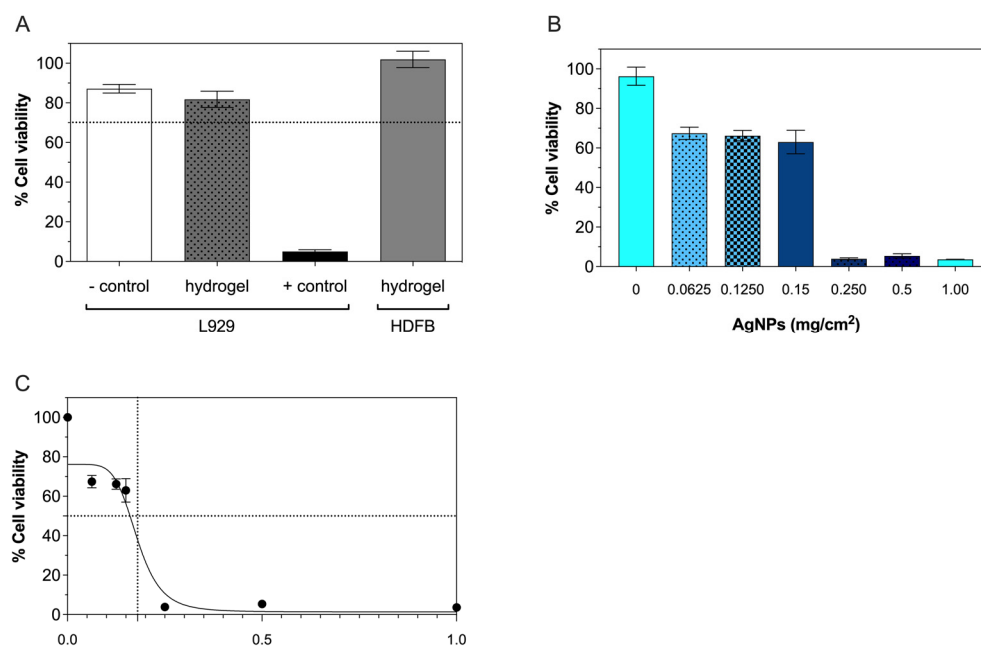
Figure 7. Cytocompatibility evaluation of (**A**) hydrogel sheets with both L929 and HDFB cells and (**B**) AgNP-loaded hydrogel sheets at varied amounts of AgNPs with L929 cells. The dashed line at a cell viability of 70% in (**A**) presents the threshold of non-cytotoxicity. (**C**) Dose–response curve shows the estimation of the IC_{50} by the nonlinear regression analysis with the four-parameter logistic curve fit.

For the AgNP-loaded hydrogel sheets, the viability of the L929 cells decreased with the amounts of AgNPs present on the hydrogels (Figure 7B). Over a range of AgNPs from 0.0625 to 0.15 mg/cm^2, the cell viability gradually decreased from ~96% to 60%. However, the cell viability was sharply reduced to ~5% when the AgNPs increased from 0.25 to 1 mg/cm^2. To estimate the AgNP concentration required to inhibit the cell viability to 50% (IC_{50}), a nonlinear regression analysis was performed on the dose–response curve. Based on the four-parameter logistic curve fit, the calculated IC_{50} value for the AgNPs in hydrogel was 0.18 mg/cm^2 (Figure 7C).

In this study, we found that AgNPs at the bactericidal level was toxic not only to bacteria but also to mammalian cultured cells. This finding agreed with previous studies that reported the cytotoxic effect of AgNPs in mammalian cells when used at its bactericidal concentration [32–34]. Based on these data, it is possible to have both the antibacterial benefit of AgNPs and also the cytotoxic effect of AgNPs on mammalian cells at the same time. Therefore, the antibacterial benefits and potential health risks of AgNPs need to be weighed for further use in clinical application [29]. One promising strategy is to apply AgNPs at the cytocompatible dose in combination with other antibacterial agents to gain a synergistic antibacterial effect. Recently, Ipe et al. [29] successfully demonstrated in both disc diffusion and broth microdilution assays that AgNPs at the cytocompatible dose could enhance the bactericidal effects of the antibiotics against several bacterial species, including antibiotic-resistant bacteria. Therefore, the use of AgNPs in combination with other antibacterial agents, each at their respective cytocompatible thresholds, to gain synergistic antibacterial activity can provide a new approach for the design of wound dressings with antibacterial properties.

3. Conclusions

In this study, we demonstrated that the two-step processing by EB irradiation provided an environmentally friendly and convenient platform to fabricate AgNP-loaded hydrogel sheet dressings that can be further developed for wound healing. The basic properties and structure of the crosslinked hydrogels showed that the swelling and M_c, but not the gel fraction and ρ_x, decreased with the increase in the irradiation dose. The optimal doses

for the two-step processing were established based on the swelling and stretchability of the hydrogel sheets. While the disc diffusion assay showed that the antibacterial efficacy scaled with the AgNPs loaded in the hydrogels with a stronger effect against *E. coli* than *S. aureus*, the cytotoxicity evaluation showed a sharp decrease in the cell viability. At the minimal inhibition concentration levels, the release of AgNPs from hydrogels followed an immediate increase before remaining relatively unchanged after 24 h. Using this two-step processing approach by EB irradiation, sterilized and antibacterial AgNP-loaded hydrogel sheet dressings were successfully fabricated. The possibility of combining AgNPs with other antibacterial agents still needs to be explored to lower the cytotoxicity effect.

4. Materials and Methods

4.1. Materials

PVA (MW 89,000–98,000 Da, 99% hydrolysis), sodium carbonate (Na_2CO_3), calcium chloride ($CaCl_2$), nitric acid (HNO_3), 3-(4,5-dimethylthiazol-2-yl)-2,5-diphenyl tetrazolium bromide (MTT), isopropanol, ICP-grade silver nitrate ($AgNO_3$) standard, fetal bovine serum (FBS), Eagle's minimal essential medium (MEM), tissue-culture grade water, L-glutamine, and penicillin–streptomycin, Mueller–Hinton agar, and nutrient broth were purchased from Sigma-Aldrich. The L929 mouse fibroblasts (NCTC clone 929) and HDFB (PCS-201-012) were purchased from ATCC. Reagent-grade $AgNO_3$ was purchased from Merck. Polyurethane containing 0.1% zinc (RM-A) and high-density polyethylene (RM-C) were purchased from Hatano. *S. aureus* (ATCC 25923) and *E. coli* (ATCC 25922) were purchased from ATCC (ATCC, USA). Deionized water was used to prepare all solutions.

4.2. Preparation of the PVA Hydrogels

The PVA powder was dissolved in boiling water at a concentration of 10% (*w/v*) and thoroughly mixed by a magnetic stirrer for 1 h. The solution was de-aerated with N_2 gas, transferred to 8 × 8 cm square Petri dishes or round dishes with a 5.5 cm diameter and then sealed inside plastic bags. The samples were irradiated in a multipurpose gamma irradiator at a dose rate of 4.3 kGy/h to the final doses of 10, 25, 40, 60, and 80 kGy at the Gem Irradiation Center facility, Thailand Institute of Nuclear Technology (Public Organization). As-cast PVA sheets served as a control. For the fabrication of the prototypic hydrogel sheets at a selected dose for further studies, EB irradiation generated by an electron accelerator (MB10–50) with an energy of 10 MeV at 50 kW was applied instead of gamma irradiation.

4.3. Hydrogel Characterization

4.3.1. Swelling

Round hydrogel sheets from the 5.5 cm dishes were first rinsed with DI water to remove unreacted PVA. The samples were then fully immersed for 24 h in an aqueous solution containing 142 mmol NaCl and 2.5 mM $CaCl_2$, which simulated the discharge at the wound site [26], before being dried at 60 °C to a constant weight. The equilibrium degree of the swelling was calculated as follows:

$$EDS\ (\%) = (W_s - W_d)/W_d \times 100 \qquad (4)$$

where W_s is the swollen weight at 24 h, and W_d is the dried weight. The experiments were performed in quadruplicate.

4.3.2. Gel Fraction

Based on the previously reported protocol [35], the round hydrogel samples were cut in half to an approximately equal weight. One-half of the samples was boiled in DI water for 15 min to extract any loose, non-crosslinked PVA molecules. They were then dried with the remaining half of the samples at 60 °C to a constant weight. The stable gel portion was calculated by the following equation:

$$Gel\ fraction\ (\%) = W_f/W_o \times 100 \qquad (5)$$

where W_f is the dried weight of the hydrogels after boiling, and W_o is the dried weight of the starting hydrogels. The lumpy, paste-like samples formed at 10 kGy were first dried at 60 °C to a constant weight (W_o) before being boiled and finally dried to a final constant weight (W_f). The experiments were performed in quadruplicate.

4.3.3. Thermal Analysis

The melting enthalpy and melting point of each sample (approximately 3 mg) was analyzed by differential scanning calorimetry with a DSC 822^e (Metler Toledo, Columbus, OH, USA), and an empty crucible served as a reference. The heating cycle was set between 25 and 255 °C with a heating/cooling rate of 10 °C/min under a flow of N_2 at 60 mL/min. The experiments were performed in triplicate.

4.3.4. Morphology Analysis

The hydrogel sheets, with thicknesses of 5 mm, were first prepared and then frozen at −80 °C in their swollen state overnight. After lyophilization at −49 °C and 0.08 mbar (Christ Alpha 2–4 LD plus, Germany) for 72 h, the samples were immersed in liquid N_2 for at least 30 min before being quickly fractured. The cut surface was coated with gold palladium and examined by scanning electron microscopy (SEM, Hitachi SU8020, Ibaraki, Japan) at a 1 kV and 10.5 μA setting.

4.4. Analysis of the Tensile Properties

The hydrogel sheets were cut into dumbbell shape (ASTM D-1822) with a narrow section 9.53 mm long and 3.18 mm wide. The tensile tests were performed on a texture analyzer (Lloyd LS1, AMETEK, Largo, FL, USA) equipped with 50 N load cell and a crosshead speed set at 50 mm/min. The data were recorded as the load and displacement in quintuplicate per irradiation dose.

4.5. Synthesis of the AgNPs by EB Irradiation on the Hydrogel Sheets

The solutions of $AgNO_3$ were first prepared at four different concentrations (A–D), as shown in Table 3. Briefly, $AgNO_3$ powder was dissolved in DI water and sonicated for 15 min. Then, 50 μL of $AgNO_3$ solution was pipetted onto 2 × 2 cm hydrogel sheets that were preformed by EB irradiation at 40 kGy. The hydrogel samples were allowed to fully absorb the $AgNO_3$ solution for 3 h in the dark. Next, all of the coated samples were exposed to EB irradiation at 25 kGy to convert the starting $AgNO_3$ into AgNPs. The distribution of AgNPs inside the lyophilized AgNP-loaded hydrogel sheet was confirmed by field emission SEM (Hitachi SU5000, Japan) operated at 5 kV using the EDS mode.

Table 3. Concentrations of the $AgNO_3$ solutions used in the preparation of the AgNP-loaded hydrogels.

Solution	Concentration of $AgNO_3$ (mg/mL)
A	80
B	40
C	20
D	10
E	5

4.6. Antibacterial Properties

The antibacterial activities of the AgNPs loaded hydrogel sheets were first evaluated by the agar diffusion method against *S. aureus* and *E. coli.* The concentration of the bacterial suspension was determined by absorbance at 600 nm with an optical density (OD) of 0.2, corresponding to 10^7 colony forming units (CFUs) per milliliter. The hydrogel samples were cut by an 8 mm diameter puncher under aseptic conditions and then placed on the agar plates inoculated with 10^6 CFU of either *S. aureus* or *E. coli.* After 20 h incubation

at 35 °C, the clear areas that formed around the samples were recorded and measured in three directions. The experiments were performed in triplicate.

4.7. In Vitro Cytotoxicity Test

The cytotoxicity was determined by the MTT-based extract test. The hydrogel sheets, AgNP-loaded hydrogel sheets, and negative and positive controls were first extracted in MEM supplemented with 100 IU mL^{-1} penicillin streptomycin, 4 mM L-glutamine, and 10% (*v/v*) FBS (complete media) inside 15 mL centrifuge tubes for 24 h. Complete media in tubes without sample served as the blank control. The L929 and HDFB cells were seeded in 96-tissue culture plates at a density of 1×10^4 cells per well in complete MEM and incubated in a humidified incubator at 5% CO_2 and 37 °C for 24 h before being refreshed with 100 µL of extracts and further incubated for 24 h. The extracts were then removed, and 50 µL of freshly prepared MTT solution in MEM without phenol red at a concentration of 10% (*w/v*) was added to each well. After 3 h of incubation, the resulting formazan crystals formed inside the cells were dissolved in 50 µL of isopropanol. The absorbance of the purple solution was measured with a microplate reader (SpectraMax M3, Molecular Devices, San Jose, CA, USA) at 570 nm. The cell viability was determined based on the absorbance ratio of each sample over the blank control. The experiments were performed in quadruplicate.

4.8. Inductively Couple Plasma-Mass Spectrometry Analysis

The release of AgNPs was quantitated by ICP-MS. The AgNP-loaded hydrogels were digested in 6 mL of 1% (*v/v*) HNO_3 for 4 h to covert silver to Ag^+. To construct the calibration curve, Ag solution in 2% (*v/v*) HNO_3 (ICP-grade) was diluted to 5, 25, 50, 75, 100, and 250 µg/L. The samples were analyzed on an ICP-MS (Agilent 7900, Agilent Technologies Japan, Ltd., Tokyo, Japan).

4.9. Test of Sterility

The hydrogel sheets without AgNPs (square sheets: 8 × 8 cm and 2 × 2 cm; circular sheets: 5.5 cm diameter) were immersed in 250 mL of Modified Letheen Broth and incubated at 30 °C for 14 days. Any occurrence of turbidity, sediment, flocculation, and color changed indicated the growth of microorganisms in the broth and would be interpreted as nonsterile. If the broth remained clear after 14 days, the pour plate method was further performed by incubating the plate count agar containing 1 mL of broth at 30 °C for 4 days. The absence of a microorganism colony on the plate count agar would be interpreted as sterile. Finally, the suitability test was performed by inoculation of 10–100 CFUs of *Escherichia coli* in the medium containing the product. The suitability test was qualified if the presence of microorganisms was observed.

4.10. Statistical Analysis

The data are presented as the mean ± standard deviation. All statistical analyses were performed using GraphPad Prism version 9.2.0 (GraphPad Software, San Diego, CA, USA). The normality of the data distribution was performed using the Sharpiro–Wilk test. For the EDS, tensile strength, Young's modulus, and elongation at break data, a comparison between the two means was carried out using the unpaired Student's *t*-test. For the gel fraction data, the Mann–Whitney test was used for comparison between two means. The nonlinear regression analysis was performed on the dose–response curve using four-parameter logistic curve fitting to estimate the IC$_{50}$. The *p*-value < 0.05 was considered statistically significant.

References

1. Sun, B.K.; Siprashvili, Z.; Khavari, P.A. Advances in Skin Grafting and Treatment of Cutaneous Wounds. *Science* **2014**, *346*, 941–945. [CrossRef] [PubMed]
2. Hou, Y.; Jiang, N.; Sun, D.; Wang, Y.; Chen, X.; Zhu, S.; Zhang, L. A Fast UV-Curable PU-PAAm Hydrogel with Mechanical Flexibility and Self-Adhesion for Wound Healing. *RSC Adv.* **2020**, *10*, 4907–4915. [CrossRef] [PubMed]
3. Liu, Y.; Li, F.; Guo, Z.; Xiao, Y.; Zhang, Y.; Sun, X.; Zhe, T.; Cao, Y.; Wang, L.; Lu, Q.; et al. Silver Nanoparticle-Embedded Hydrogel as a Photothermal Platform for Combating Bacterial Infections. *Chem. Eng. J.* **2020**, *382*, 122990. [CrossRef]
4. Massarelli, E.; Silva, D.; Pimenta, A.F.R.; Fernandes, A.I.; Mata, J.L.G.; Armês, H.; Salema-Oom, M.; Saramago, B.; Serro, A.P. Polyvinyl Alcohol/Chitosan Wound Dressings Loaded with Antiseptics. *Int. J. Pharm.* **2021**, *593*, 120110. [CrossRef] [PubMed]
5. Yang, R.; Liu, X.; Ren, Y.; Xue, W.; Liu, S.; Wang, P.; Zhao, M.; Xu, H.; Chi, B. Injectable Adaptive Self-Healing Hyaluronic Acid/Poly (γ-Glutamic Acid) Hydrogel for Cutaneous Wound Healing. *Acta Biomater.* **2021**, *127*, 102–115. [CrossRef]
6. Rodríguez-Rodríguez, R.; Espinosa-Andrews, H.; Velasquillo-Martínez, C.; García-Carvajal, Z.Y. Composite Hydrogels Based on Gelatin, Chitosan and Polyvinyl Alcohol to Biomedical Applications: A Review. *Int. J. Polym. Mater. Polym. Biomater.* **2020**, *69*, 1–20. [CrossRef]
7. Jaffe, L.; Wu, S.C. Dressings, Topical Therapy, and Negative Pressure Wound Therapy. *Clin. Podiatr. Med. Surg.* **2019**, *36*, 397–411. [CrossRef]
8. Rosiak, J.M.; Ulański, P. Synthesis of Hydrogels by Irradiation of Polymers in Aqueous Solution. *Radiat. Phys. Chem.* **1999**, *55*, 139–151. [CrossRef]
9. Rosiak, J.M.; Yoshii, F. Hydrogels and Their Medical Applications. *Nucl. Instrum. Methods Phys. Res. B* **1999**, *151*, 56–64. [CrossRef]
10. Hennink, W.E.; van Nostrum, C.F. Novel crosslinking methods to design hydrogels. *Adv. Drug Deliv. Rev.* **2002**, *54*, 13–36. [CrossRef]
11. Ashfaq, A.; Clochard, M.-C.; Coqueret, X.; Dispenza, C.; Driscoll, M.; Ulański, P.; Al-Sheikhly, M. Polymerization Reactions and Modifications of Polymers by Ionizing Radiation. *Polymers* **2020**, *12*, 2877. [CrossRef] [PubMed]
12. Nešporová, K.; Pavlík, V.; Šafránková, B.; Vágnerová, H.; Odráška, P.; Žídek, O.; Císařová, N.; Skoroplyas, S.; Kubala, L.; Velebný, V. Effects of wound dressings containing silver on skin and immune cells. *Sci. Rep.* **2020**, *10*, 15216. [CrossRef] [PubMed]
13. Paladini, F.; Pollini, M. Antimicrobial Silver Nanoparticles for Wound Healing Application: Progress and Future Trends. *Materials* **2019**, *12*, 2540. [CrossRef] [PubMed]
14. Prasher, P.; Singh, M.; Mudila, H. Silver nanoparticles as antimicrobial therapeutics: Current perspectives and future challenges. *3 Biotech* **2018**, *8*, 411. [CrossRef]
15. Leawhiran, N.; Pavasant, P.; Soontornvipart, K.; Supaphol, P. Gamma irradiation synthesis and characterization of AgNP/gelatin/PVA hydrogels for antibacterial wound dressings. *J. Appl. Polym. Sci.* **2014**, *131*. [CrossRef]
16. Eid, M.; El-Arnaouty, M.B.; Salah, M.; Soliman, E.-S.; Hegazy, E.-S.A. Radiation synthesis and characterization of poly(vinyl alcohol)/poly(N-vinyl-2-pyrrolidone) based hydrogels containing silver nanoparticles. *J. Polym. Res.* **2012**, *19*, 9835. [CrossRef]
17. Kamoun, E.A.; Kenawy, E.-R.S.; Chen, X. A review on polymeric hydrogel membranes for wound dressing applications: PVA-based hydrogel dressings. *J. Adv. Res.* **2017**, *8*, 217–233. [CrossRef]
18. Ferreira, L.; Figueiredo, M.M.; Gil, M.H.; Ramos, M.A. Structural analysis of dextran-based hydrogels obtained chemoenzymatically. *J. Biomed. Mater. Res. B Appl. Biomater.* **2006**, *77*, 55–64. [CrossRef]
19. Ruiz, J.; Mantecón, A.; Cádiz, V. Synthesis and properties of hydrogels from poly (vinyl alcohol) and ethylenediaminetetraacetic dianhydride. *Polymer* **2001**, *42*, 6347–6354. [CrossRef]
20. Benamer, S.; Mahlous, M.; Boukrif, A.; Mansouri, B.; Youcef, S.L. Synthesis and characterisation of hydrogels based on poly(vinyl pyrrolidone). *Nucl. Instrum. Methods Phys. Res. B* **2006**, *248*, 284–290. [CrossRef]

21. Kumar, M.; Varshney, L.; Francis, S. Radiolytic formation of Ag clusters in aqueous polyvinyl alcohol solution and hydrogel matrix. *Radiat. Phys. Chem.* **2005**, *73*, 21–27. [CrossRef]

22. Peppas, N.A.; Merrill, E.W. Poly(vinyl alcohol) hydrogels: Reinforcement of radiation-crosslinked networks by crystallization. *J. Polym. Sci. Polym. Chem. Ed.* **1976**, *14*, 441–457. [CrossRef]

23. Zhao, L.; Mitomo, H.; Zhai, M.; Yoshii, F.; Nagasawa, N.; Kume, T. Synthesis of antibacterial PVA/CM-chitosan blend hydrogels with electron beam irradiation. *Carbohydr. Polym.* **2003**, *53*, 439–446. [CrossRef]

24. Zhai, M.; Yoshii, F.; Kume, T.; Hashim, K. Syntheses of PVA/starch grafted hydrogels by irradiation. *Carbohydr. Polym.* **2002**, *50*, 295–303. [CrossRef]

25. Reinhart, C.T.; Peppas, N.A. Solute diffusion in swollen membranes. Part II. Influence of crosslinking on diffusive properties. *J. Membr. Sci.* **1984**, *18*, 227–239. [CrossRef]

26. Uttayarat, P.; Chiangnoon, R.; Eamsiri, J.; Senawongse, W. Processing and Characterization of Antibacterial Hydrogel Sheet Dressings Composed of Poly(vinyl alcohol) and Silk Fibroin for Wound Healing Application. *Walailak J. Sci. Technol.* **2019**, *16*, 349–359. [CrossRef]

27. Domínguez, A.V.; Algaba, R.A.; Canturri, A.M.; Villodres, R.; Smani, Y. Antibacterial Activity of Colloidal Silver against Gram-Negative and Gram-Positive Bacteria. *Antibiotics* **2020**, *9*, 36. [CrossRef]

28. Alinejad, F.; Momeni, M.; Fatemi, M.J.; Dahmardehei, M.; Naderi, S.; Akhoondinasab, M.R.; Zayedly, M.; Mahboubi, O.; Rahbar, H. Comparing the effect of two types of silver nano-crystalline dressings (acticoat and agcoat) in the treatment of full thickness burn wound. *Iran. J. Microbiol.* **2018**, *10*, 378–384.

29. Ipe, D.S.; Kumar, P.T.S.; Love, R.M.; Hamlet, S.M. Silver Nanoparticles at Biocompatible Dosage Synergistically Increases Bacterial Susceptibility to Antibiotics. *Front. Microbiol.* **2020**, *11*, 1074. [CrossRef]

30. Pimton, P.; Ratphibun, P.; Tassaneesuwan, N.; Chiangnoon, R.; Uttayarat, P. Cytotoxicity Evaluation of Hydrogel Sheet Dressings Fabricated by Gamma Irradiation: Extract and Semi-Direct Contact Tests. *Trends Sci.* **2022**, *19*, 4583. [CrossRef]

31. Srivastava, G.K.; Alonso-Alonso, M.L.; Fernandez-Bueno, I.; Garcia-Gutierrez, M.T.; Rull, F.; Medina, J.; Coco, R.M.; Pastor, J.C. Comparison between direct contact and extract exposure methods for PFO cytotoxicity evaluation. *Sci. Rep.* **2018**, *8*, 1425. [CrossRef] [PubMed]

32. Liao, C.; Li, Y.; Tjong, S.C. Bactericidal and Cytotoxic Properties of Silver Nanoparticles. *Int. J. Mol. Sci.* **2019**, *20*, 449. [CrossRef] [PubMed]

33. Botha, T.L.; Elemike, E.E.; Horn, S.; Onwudiwe, D.C.; Giesy, J.P.; Wepener, V. Cytotoxicity of Ag, Au and Ag-Au bimetallic nanoparticles prepared using golden rod (*Solidago canadensis*) plant extract. *Sci. Rep.* **2019**, *9*, 4169. [CrossRef] [PubMed]

34. Shi, T.; Sun, X.; He, Q.-Y. Cytotoxicity of silver nanoparticles against bacteria and tumor cells. *Curr. Protein Pept. Sci.* **2018**, *19*, 525–536. [CrossRef]

35. Varshney, L. Role of natural polysaccharides in radiation formation of PVA–hydrogel wound dressing. *Nucl. Instrum. Methods Phys. Res. B* **2007**, *255*, 343–349. [CrossRef]

Advanced CNC/PEG/PDMAA Semi-IPN Hydrogel for Drug Delivery Management in Wound Healing

Samia Afrin [1,2], Md. Shahruzzaman [1,*], Papia Haque [1], Md. Sazedul Islam [1,3], Shafiul Hossain [1,4,5], Taslim Ur Rashid [1,6], Tanvir Ahmed [1], Makoto Takafuji [7] and Mohammed Mizanur Rahman [1]

1 Department of Applied Chemistry and Chemical Engineering, Faculty of Engineering and Technology, University of Dhaka, Dhaka 1000, Bangladesh; saa292@pitt.edu (S.A.); papiahq@du.ac.bd (P.H.); sazid.acce@du.ac.bd (M.S.I.); shossain2@huskers.unl.edu (S.H.); turashid@ncsu.edu (T.U.R.); tanvirahmed@du.ac.bd (T.A.); mizanur.rahman@du.ac.bd (M.M.R.)
2 Department of Chemistry, University of Pittsburgh, Pittsburgh, PA 15260, USA
3 Department of Chemistry and Biochemistry, Florida State University, Tallahassee, FL 32306, USA
4 Department of Chemical Engineering and Polymer Science, Shahjalal University of Science and Technology, Sylhet 3114, Bangladesh
5 Department of Chemistry, University of Nebraska-Lincoln, Lincoln, NE 68588, USA
6 Fiber and Polymer Science, North Carolina State University, Campus Box 7616, Raleigh, NC 27695, USA
7 Department of Applied Chemistry and Biochemistry, Kumamoto University, Kumamoto 860-8555, Japan; takafuji@kumamoto-u.ac.jp
* Correspondence: shahruzzaman@du.ac.bd

Abstract: A Semi Interpenetrating Polymer Network (semi-IPN) hydrogel was prepared and loaded with an antibiotic drug, gentamicin, to investigate the wound healing activity of this system. The semi-IPN hydrogel was synthesized by combining natural polymer cellulose nanocrystal (CNC) and synthetic polymer polyethylene glycol (PEG) and poly (N,N'-dimethyl acrylamide) (PDMAA), which was initially added as a monomer dimethyl acrylamide (DMAA). CNC was prepared from locally obtained jute fibers, dispersed in a PEG-NaOH solvent system and then mixed with monomer DMAA, where polymerization was initiated by an initiator potassium persulphate (KPS) and cross-linked by N,N'-methylenebisacrylamide (NMBA). The size, morphology, biocompatibility, antimicrobial activity, thermal and swelling properties of the hydrogel were investigated by different characterization techniques. The biocompatibility of the hydrogel was confirmed by cytotoxicity analysis, which showed >95% survival of the BHK-21, Vero cell line. The drug loaded hydrogel showed antimicrobial property by forming 25 and 23 mm zone of inhibition against *Staphylococcus aureus* (gram-positive) and *Escherichia coli* (gram-negative) bacteria, respectively, in antimicrobial analysis. At pH 5.5, 76% of the drug was released from the hydrogel within 72 h, as observed in an in vitro drug release profile. In an in vivo test, the healing efficiency of the drug loaded hydrogel was examined on a mice model with dorsal wounds. Complete healing of the wound without any scar formation was achieved in 12 days, which revealed excellent wound healing properties of the prepared drug loaded semi-IPN hydrogel. These results showed the relevance of such a system in the rapid healing of acute wounds.

Keywords: semi-IPN; hydrogel; drug delivery; wound healing

1. Introduction

Hydrogels are soft, wet and cross-linked three-dimensional networks of hydrophilic polymeric materials that are capable of absorbing large amounts of water or biological fluids, and thus resemble, to a large extent, a biological tissue [1]. These hydrogels have been studied for a wide range of pharmaceutical, biomedical and daily care applications, such as drug delivery, contact lenses, tissue engineering and superabsorbent agents [2]. However, they can be hard to handle, may be difficult to load with drugs and sterilize and usually have low mechanical strength [3]. To overcome this type of problem, an

Interpenetrating Polymer Network (IPN) is introduced, which is a category of such newly developed bioactive materials that are significantly used in the pharmaceutical industry [4].

IPN, in general, is a combination of two polymers in a physically cross-linked network where chains of one polymer are entangled with or penetrate the network of another polymer. Among different types of IPNs, semi-IPNs are the new systems for application in drug delivery [5]. In semi-IPN, two polymers are independent of each other while being physically interlocked and, hence, the improvement in mechanical stability of the hydrogel is possible due to physical entanglement and network interactions. Hydrogels prepared from natural polymers may offer great advantages including outstanding biocompatibility, biodegradability and low toxicity. However, these polymers also show poor mechanical properties and brittleness and, hence, cannot withstand the forces imposed in vivo, which may restrict their use in different biomedical applications. On the other hand, hydrogels synthesized from synthetic polymers generally present good mechanical properties, good process ability, easily tunable molecular weight and chemical composition. Relatively long response times, however, were required by most of them for external environment change due to slow diffusion of water. In addition, they may lack informational structure for biological response. However, the fusion of natural and synthetic polymers in the form of semi-Interpenetrating polymer network (semi-IPN) hydrogels may combine the most useful characteristics of both the systems and may address the individual drawbacks [6].

Cellulose nanocrystal (CNC) attracts a wide variety of applications in drug delivery system by incorporating a suitable drug blended with any synthetic polymer. Poly (N,N′-dimethyl acrylamide) (PDMAA), a hydrophilic synthetic biocompatible polymer, finds various applications in DNA sequencing, molecular biology, medical and pharmaceutical fields, including contact lenses and drug delivery [7]. Another polymer, polyethylene glycol (PEG), can be used as a solvent system for dispersion of CNC by grafting of PEG onto the CNC surface as PEG is a steric stabilizer in the preparation of dispersible nanoparticles [8]. Thus, the fusion of these polymers forming semi-IPN can be a great development for drug delivery systems, as it will decrease the brittleness of the corresponding CNC and, with synthetic PEG and PDMAA, it forms a matrix for semi-IPN which results in better drug loading.

Wounds occur when a tissue is disrupted or the cellular integrity is compromised due to mechanical, physical or metabolism-related issues [9]. In recent years, different bacterial contaminations of skin wounds have become very common, with high rates of morbidity and mortality [10]. Therefore, an ideal antibacterial wound dressing is necessary for this purpose. In ideal wound dressing, a moist environment around the wound is maintained and the exudates from the wound surface are absorbed. As semi-IPN hydrogels absorb a high quantity of water, a moist environment can be provided to the wound area and, moreover, hydrogels can easily absorb the exudates [11]. To improve antimicrobial properties of the wound dressing, different antibiotics can be incorporated into the hydrogel. As an antimicrobial agent, the antibiotic gentamicin sulphate can be incorporated in hydrogel. The aminoglycoside gentamicin has been the most widely used antibiotic as it exhibits broad spectrum antimicrobial activity, excellent solubility and stability at elevated temperatures [12]. Gentamicin has been extensively used in the superficial infections of skin as it shows high effectiveness against aerobic gram-negative and some aerobic gram-positive bacteria [11]. Besides antibacterial activity, hemostasis is an important factor for rapid wound healing because, if not managed properly, the hemorrhage from the wounded area can increase the need for blood transfusion, hypovolemic shock and hypothermic coagulopathy [13]. Using a proper semi-IPN system can improve the hemostasis process, which is the first stage of wound healing. As the polymers are independent of each other while being physically interlocked to form semi-IPN, the linear polymer chains can be eluted from the network [14]. If one of the linear polymer chains in the semi-IPN has hemostatic property, e.g., collagen, gelatin, chitosan, starch, oxidized cellulose, alginate and PEG, etc. [15], it enhances hemostasis when the semi-IPN network breaks down at the

site of wound. Thus, a semi-IPN hydrogel containing appropriate polymers can have huge impact on the rapid wound healing process.

In the present work, a semi-IPN CNC/PEG/PDMAA hydrogel is synthesized where PDMAA is cross-linked with N,N′-methylenebisacrylamide (NMBA), and the polymerization is supported by an initiator potassium per sulphate (KPS). The prepared hydrogel is loaded with gentamicin sulphate to observe the wound healing activity in a mice model. The significance of this research is to support wound healing by eliminating bacterial infections while releasing gentamicin in a controlled manner which can indicate better hemostatic property for faster wound healing. This hydrogel will deliver drugs to the target pathological cells to increase the effectiveness and reduce undesirable side effects.

2. Experimental

2.1. Materials

The jute fiber was collected from the local market of Tangail district, Bangladesh. The monomer Dimethyl acrylamide (DMAA), cross-linker N,N′-Methylene bisacrylamide and initiator Potassium per Sulphate (KPS) were obtained from Sigma Aldrich, Germany. Polyethylene glycol (PEG) with a molar mass of 6000 and sulphuric acid (H_2SO_4) were supplied by Merck, Jabalpur, Madhya Pradesh, India. The other chemicals such as ninhydrin, sodium hydroxide (NaOH), sodium chlorite ($NaClO_2$), dipotassium hydrogen phosphate (K_2HPO_4) and potassium dihydrogen phosphate (KH_2PO_4) were purchased from the supplier of Loba Chemicals, Mumbai, India. The water soluble antibiotic gentamicin sulphate was obtained from Square Pharmaceuticals Limited, Dhaka, Bangladesh. The highest quality available for the chemicals was ensured, and they were used without further purification.

2.2. Preparation of Cellulose Nanocrystal (CNC) from Jute Fiber

The preparation of jute fiber from cellulose nanocrystal was followed as per our previous report [16]. At first, the jute fibers were washed to remove impurities. The fibers were then cut into a small size (about 2 cm) by using scissors and then milled into a fine size by using a mechanical milling machine. These fibers (25 g) were dispersed in distilled water (500 mL) for 10 min at room temperature and stirred for 2 h at 50 °C using a glass rod. There might be some extractives present in water and filtration was conducted to remove those extracts. The fibers were dried later. The dried fiber was then mercerized with 2% NaOH solution at 80 °C for 6 h with mechanical stirring followed by thorough washing. After continuous washing, when the fibers were neutralized completely, drying of those fibers was completed. After that, the dried fibers were bleached with 2 wt% $NaClO_2$ at 80 °C for 4 h with mechanical stirring, washed and dried in an oven.

The bleached fibers were additionally treated in a concentrated sulfuric acid solution (45 wt% sulfuric acid in water) at 45 °C for 10 h with mechanical stirring. The ratio of fibers to acid solution was 1:15 gL^{-1}. After the treatment, the hydrolyzed cellulose samples were neutralized by 30 wt% NaOH solution in water and washed multiple times. The crystals were separated and washed by centrifugation at 8000 rpm for 10 min until the solution was completely neutralized. Finally, the cellulose nanocrystal was obtained after freeze drying for 48 h.

2.3. Dissolution of CNC in PEG/NaOH Solvent System

CNC powder was mixed into 20 mL of aqueous solution, containing PEG (2% *w/v*) and NaOH as a solvent system. The dispersion formed was allowed to be put in a deep freezer (Haier, Camden, SC, USA) at −10 °C for a period of 24 h. The next day, the obtained solid frozen mass was kept at room temperature under vigorous stirring for a period of 3 h until the solution became completely transparent. This resulting transparent solution was used to prepare the semi-IPN hydrogels.

2.4. Synthesis of CNC/PEG/PDMAA Semi-IPN Hydrogel

The dispersed CNC-PEG was then used to prepare the ternary hydrogel system. Different compositions of CNC 0.3, 0.8 and 1% (*w/v*) were used to prepare the hydrogel for comparison and the best result of formation of hydrogel was seen in the solution containing 1% *w/v* CNC [1]. Dimethyl acrylamide monomer (2 mL) was added to the solution followed by the addition of cross-linker NMBA (0.05 g) under constant stirring. The solution was placed in an ice bath during the addition of KPS (0.1 g) as an initiator. The mixture was stirred vigorously to ensure complete dissolution of all components. Then, the solution was transferred to a petri dish and kept in an oven at 60 °C for 2 h. After the polymerization was completed, the resulting hydrogels were taken out of the oven in film form and freeze dried (Supporting Information, Figure S1). The gel was then used for a further characterization process. The possible structure of the hydrogel is shown in Figure 1, and the cross-linking of monomer with cross linker NMBA [2] is given in Supporting Information (Figure S2).
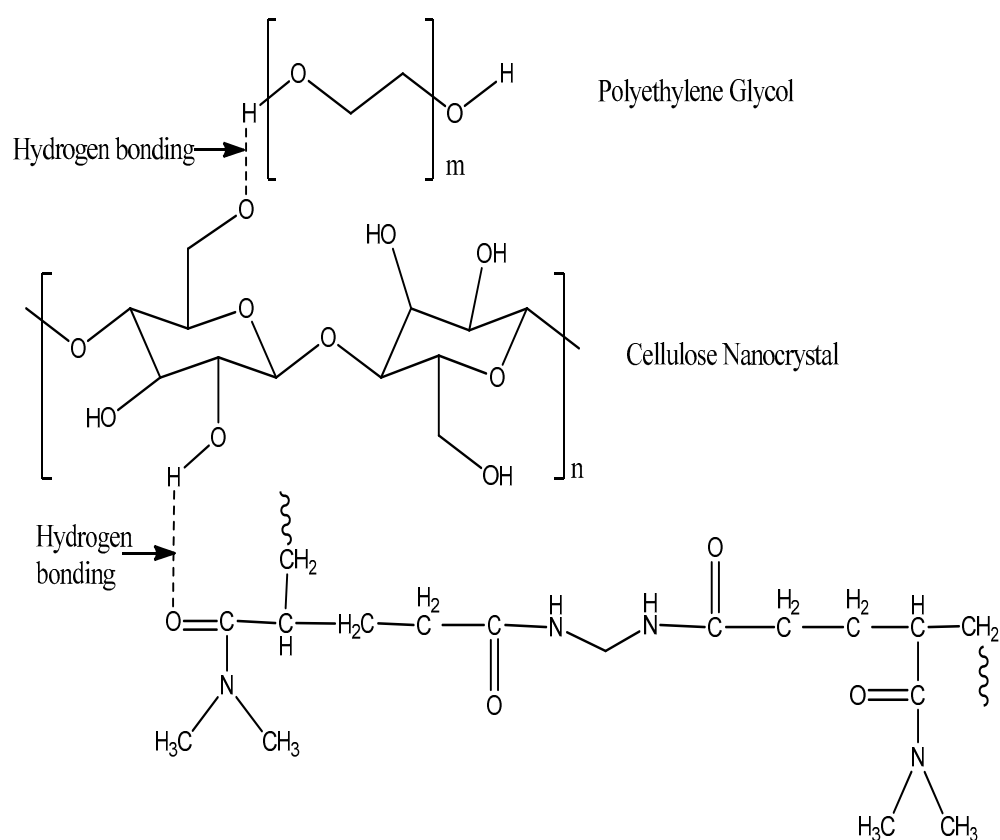
Figure 1. Proposed structure of semi-IPN hydrogel.

2.5. Characterization Techniques

Attenuated Total Reflectance (ATR) spectra of the samples were obtained using the IR spectrophotometer (IR prestige-21, Shimadzu Corporation, Kyoto, Japan) in the range of 4000–400 cm^{-1}. The particle size of CNC was observed by Transmission Electron Microscope (TEM) (JEM-1400 Plus, Tokyo, Japan). Thermal properties of the samples were carried out by thermo gravimetric analysis (TGA) (TGA-50, Shimadzu, Tokyo, Japan) under nitrogen atmosphere in aluminum cell with a temperature rate of 10 °C/min up to 600 °C from room temperature. X-ray powder diffraction (XRD) analysis was investigated in a Rigaku Ultima IV X-ray diffractometer (Rigaku Americas Corporation, Tokyo, Japan) using Cu-Kα radiation with a scan speed of 5°/min ranging from 20° to 80°.

To observe the surface morphology of hydrogel and CNC, The Carry Scope JCM-5700 Scanning Electron Microscope (JEOL, Tokyo, Japan) was used and, for observing the morphology of the drug loaded hydrogel, JEOL JSM-6490LA, an analytical scanning

electron microscope was used. The sputtering machine used for this machine was a JEOL JFC 1600 auto fine coater.

The UV-1700 Pharmaspec (Shimadzu, Kyoto, Japan) was used for the determination of drug concentration in solution. For gentamicin drug, a wavelength of 400 nm was used.

2.6. Swelling Test of CNC/PEG/PDMAA Semi-IPN Hydrogel

The swelling behavior of the hydrogel was determined at first by completely drying the hydrogel and by immersion of the hydrogel both in distilled water at room temperature and in pH 7.4 at 37 °C, to compare the swelling property in both of the cases. About 20 mg of the sample (1.5 cm × 1.5 cm) was weighed and immersed in around 20 mL of solution for observation of swelling property. The gel was gently wiped and weighed at various time intervals for the test.

The swelling studies were carried out until equilibrium in swelling was reached. The swelling percentage was calculated using the following equation:

$$S\% = ((M_t - M_0)/M_0) \times 100\% \tag{1}$$

Here, M_t and M_0 refer to the weight of the swollen hydrogel at time t and initial time, respectively.

The equilibrium percent swelling S_{eq} after the hydrogel had swollen to equilibrium in the swelling media was calculated using the following formula:

$$S_{eq}\% = ((M_{eq} - M_0)/M_0) \times 100\% \tag{2}$$

where M_{eq} is the mass of the swollen hydrogel sample at equilibrium.

The water absorbed by CNC/PEG/PDMAA Semi-IPN hydrogel is quantitatively represented by equilibrium water content (EWC) [3,4], where

$$EWC = (M_{eq} - M_0)/M_{eq} \tag{3}$$

2.7. Gentamicin–Ninhydrin Assay

Gentamicin poorly absorbs ultraviolet and visible light, and so the indirect spectrophotometric method was used for assaying the gentamicin sulphate standard curve and loading the drug onto the gel. Here, ninhydrin was used to form a complex with gentamicin which is basically based on a ninhydrin reaction with primary and secondary amines present in the gentamicin, producing a colored solution [5]. In this method, a clear spectrum was shown whereas, in the case of using only gentamicin, no significant spectrum was observed.

The standard curve was prepared using this gentamicin–ninhydrin complex, where seven different concentrations of gentamicin (20, 40, 80, 100, 200, 400 and 500 mg/L) were used. The phosphate buffer solution (PBS) was prepared in the lab following the standard of the European Pharmacopoeia and mixed with ninhydrin by heating, to form ninhydrin PBS reagent. In each case, 5 mL of antibiotic solution was mixed with 1.5 mL of ninhydrin PBS reagent by vortexing (30 s) and then heated at 95 °C for 15 min in a water bath [6]. The solutions were then cooled in an ice water bath and the required amount of the solutions was subjected to UV reading at 400 nm against the ninhydrin PBS reagent as a background reading, and thus the standard calibration curve was prepared. The loading and release profile of the drug was quantified in UV visible spectrophotometer using the same method of forming the ninhydrin complex with the antibiotic, and then the efficiencies were calculated.

2.8. Loading of Gentamicin Sulphate on CNC/PEG/PDMAA Semi-IPN Hydrogel Film

The loading of the antibiotic gentamicin sulphate was performed by soaking the hydrogel film in the gentamicin solution. In this experiment, 10 mg of prepared hydrogel film were soaked in gentamicin sulphate solution of varying concentrations (20, 40, 100, 200 and 300 mg/L). The solutions were placed in a reciprocating shaker at 90 rpm for 24 h [7]

for facilitating the drug uptake. The absorbance values of unloaded drug measured by UV Visible Spectrophotometer at 400 nm, examined by ninhydrin assay, helped to determine the efficiency of the drug. The percentage of loading efficiency was calculated using the following formula [8]:

$$\text{Loading Efficiency \%} = \frac{\text{Initial Drug Concentration} - \text{Drug concentration in supernatant}}{\text{Initial Drug Concentration}} \times 100\% \qquad (4)$$

2.9. In Vitro Cytotoxicity and Biocompatibility Study by Cell Culture

A cytotoxicity test was designed to determine the toxicity of a compound to cells, either qualitatively or quantitatively. For the prepared hydrogel, two cell lines were used for testing cytotoxicity. They were BHK-21, a baby hamster kidney fibroblast cell line, and Vero cell line, kidney epithelial cells extracted from an African green monkey.

In brief, BHK-21 cells and Vero cells were maintained separately in DMEM (Dulbecco's Modified Eagles medium) containing 1% penicillin–streptomycin (1:1) and 0.2% gentamycin and 10% fetal bovine serum (FBS). Both cells (3×10^4/200 μL) were seeded onto 48-well plate and incubated at 37 °C + 5% in a CO_2 (CO_2 Incubator, Nuaire, Plymouth, MN, USA) environment for 24 h. The next day, 50 μL of sample (autoclave) was added to each well. Cytotoxicity was examined under an inverted light microscope (trinocular microscope with camera, Optika, Ponteranica, Italy) after 48 h of incubation. Duplicate cells were used for each sample.

2.10. Antimicrobial Activity and In Vitro Release Profile

The analysis of antibacterial activity was studied using the agar diffusion method by Kirby-Bauer, 1985 [7]. In this method, generally, the test agar plate was wiped by a standardized concentration of test where paper disks with different concentration samples were placed on the lawn of bacteria. After overnight incubation, the zone of inhibition was identified and the diameter of the zone around the disk was measured.

The antibacterial activity was examined for both gram-positive *Staphylococcus aureus* and gram-negative *Escherichia coli* bacteria. A hole was made in the Agar broth to keep the drug loaded sample, and the bacterial colonies were swabbed in the agar broth and, after that, left for 24 h for incubation. The inhibition zones were checked after 24 h. The measurement of the inhibition zones was made with a ruler under the surface of the plate without opening the lid.

For determining the in vitro release profile, the optimum drug loaded hydrogel (1.5 cm × 1.5 cm) was placed in a phosphate buffer solution of pH 5.5 and pH 6.0 in a conical flask. The buffer solutions of pH 5.5 and 6.0 were prepared in the lab using the European Pharmacopoeia guideline. The flask was placed in a shaker which was maintained at 37 °C and 100 rpm. After a predetermined time interval, 3 mL of the aliquots were withdrawn from the solution, which was replaced by the same amount of freshly prepared buffer solution. The aliquots represent the released amount of gentamicin in the solution, which was quantified using ninhydrin assay by UV Visible spectrophotometer at 400 nm wavelength range.

2.11. In Vivo Wound Healing Evaluation

Experiments of in vivo wound healing evaluation were conducted in two groups: a normal surgical gauge (control group) and a drug loaded hydrogel in mice model where each mouse weighed around 20–25 gm. The mice were maintained under standard pellet and water conditions along with controlled environmental conditions. The mice were anesthetized by Ketamin HCl injection (10 mg/kg), injected into the lower abdomen to make them unconscious for about 15 min. An electric trimmer was used to shave the dorsal fur 5 mm away from the ears of the mice and a wound approximately 1 cm × 1 cm was cut [17] in each mouse. For creating a full thickness wound with minimal bleeding, both

the epidermal and dermal layers were removed. The wound areas were sterilized using 70% ethanol.

Before placing the gel onto the wounded area, the gel (1.5 cm × 1.5 cm) was immersed in saline solution for a certain period of time. The efficacy of the wound healing was determined by observing wound morphology, re-epithelialization and wound contraction with naked eye observation [9]. The evaluation of the healing process was examined on the fourth, eighth and twelfth day, consecutively, and photographs were taken for examining the size of the wound. The relative wound size reduction was calculated using the following equation [10]:

$$\text{Relative wound size reduction (\%)} = \frac{A_0 - A_t}{A_0} \times 100 \tag{5}$$

Here, A_o is wound size at initial time, and A_t is the wound size at any time 't'.

3. Results and Discussion

3.1. ATR Spectra Analysis

The ATR spectra of CNC, PEG, DMAA and the semi-IPN hydrogel are shown in Figure 2.
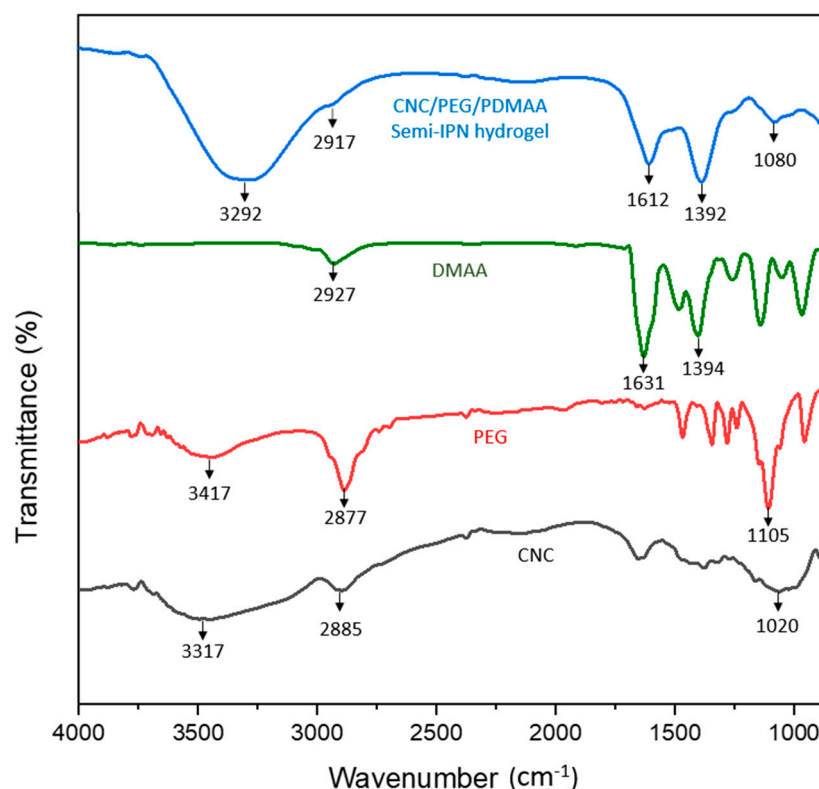
Figure 2. ATR Spectra of CNC/PEG/PDMAA semi-IPN hydrogel, DMAA, PEG, CNC.

The major characteristic peaks for cellulose were at 3317 cm^{-1}, due to –OH stretching, 2885 cm^{-1}, which corresponded to C-H stretching in sp^3 hybridized bond, 1420 cm^{-1} due to symmetric bending in –CH$_2$ and 1020 cm^{-1}, which corresponded to C-O-C asymmetric vibration that was associated with cellulose. The major characteristic peaks for PEG were at 3417 cm^{-1} due to –OH stretching, 2877 cm^{-1} for stretching vibration of the –CH group, 1465 cm^{-1}, which corresponded to the deformation vibration of the C-H group, 1385 cm^{-1} due to –OH bending vibration and 1105 cm^{-1}, which was due to C-O stretching. Moreover, the major characteristic peaks for DMAA were at 2927 cm^{-1} due to C-H stretching in sp^3 hybridized bond, 1631 cm^{-1}, which corresponded to C=O stretching vibration of amide,

1394 cm^{-1}, due to the C-N stretching vibration of amide and a medium strong peak at 1500 cm^{-1} for the C=C group [11].

The ATR spectrum of the semi-IPN hydrogel contained a major characteristic peak of CNC, PEG and DMAA. Some shifting of the peaks had occurred, which might prove H-bonding and complete polymerization of the monomer. There was a broad absorption peak at 3292 cm^{-1} due to hydrogen bonding in the –OH group because the peak was slightly shifted and broadened from the raw material CNC and PEG, and hence this confirmed the hydrogen bonding between CNC and PEG in the semi-IPN hydrogel. There was a slight absorption peak at 2917 cm^{-1} region due to C-H stretching in sp^3 hybridized bond. The C=O stretching vibration of amide shifted from 1631 cm^{-1} to 1612 cm^{-1} after the formation of hydrogel, which suggested the existence of an inter- or intra-molecular interaction of DMAA with other raw materials. The C-N stretching of the amide group showed that the absorbance peak at 1392 cm^{-1} and absorbance peak at 1080 cm^{-1} was due to the C-O-C asymmetric vibration, which might be associated with cellulose. In the hydrogel, the peak of the C-H group at 1465 cm^{-1}, shown in the PEG spectrum, disappears completely because this peak has merged with the nearest C-N stretching peak (1392 cm^{-1}) of the amide group. In DMAA, there was a medium weak peak at 1500 cm^{-1} for the C=C group which disappeared in the hydrogel, confirming the complete polymerization of the monomer.

3.2. X-ray Diffraction Pattern Analysis

Figure 3 shows the XRD pattern of CNC, PEG and CNC/PEG/PDMAA semi-IPN hydrogel.
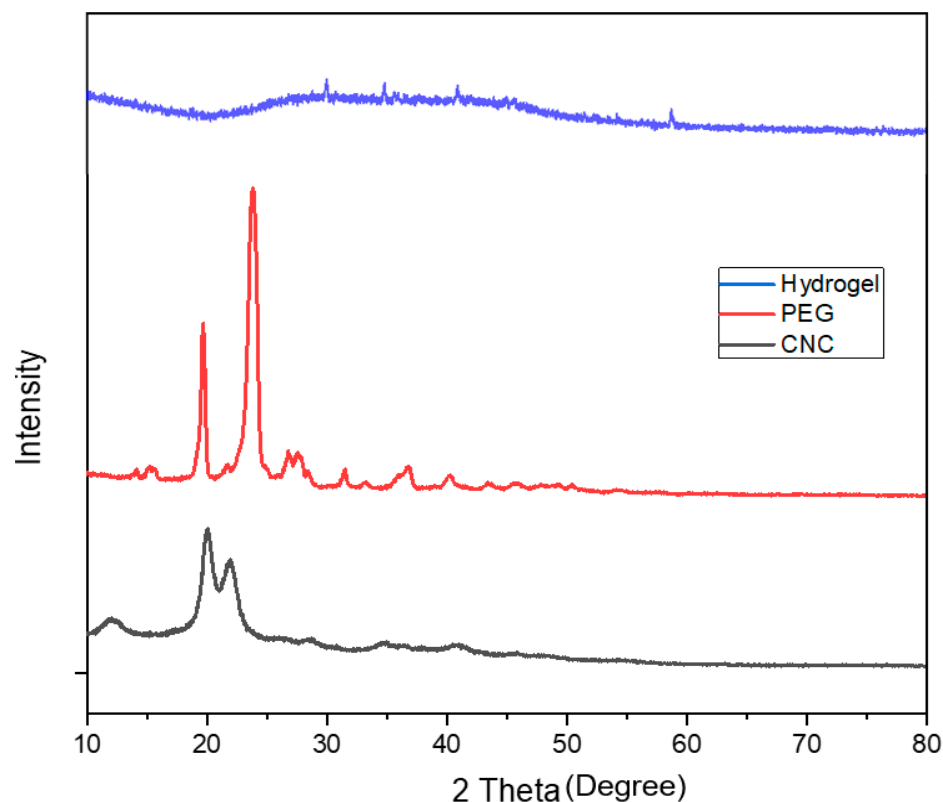
Figure 3. XRD pattern of CNC/PEG/PDMAA semi-IPN Hydrogel, PEG and CNC.

The characteristic crystalline peak for CNC centered at 2 theta = 20.5°; 23° was observed in the diffractogram of CNC [12]. Cellulose shows orderly hydrogen bonding arrangement among the molecules, and hence during acid hydrolysis, acid could not penetrate and hydrolyze the crystalline region. Therefore, it cleaved only the amorphous

region, leaving the crystalline area intact, which resulted in high degree of crystallinity of CNC [18,19]. PEG was observed to show major XRD peaks at 2 theta = 19.39°, 23.56° and a few minor peaks at 2 theta = 27.2°, 36.4°, 39° and 45.2°, respectively, which was similar to the data in the previous literature [20].

The X-ray diffraction pattern in the semi-IPN hydrogel showed no characteristic major peak of CNC or PEG due to the small amount of the constituent polymers. No peaks of CNC were observed in the hydrogel and some minor peaks of PEG were shown. After forming semi-IPN, a drastic change in the typical characteristic peak of the crystalline CNC was seen, which indicated that the crystal structure of CNC was changed after the formation of semi-IPN and confirmed the uniform dispersion of the constituent polymers [21].

3.3. Thermogravimetric Analysis

The thermograms of the samples CNC, PEG, PDMAA and CNC/PEG/PDMAA semi-IPN hydrogel are shown in Figure 4.
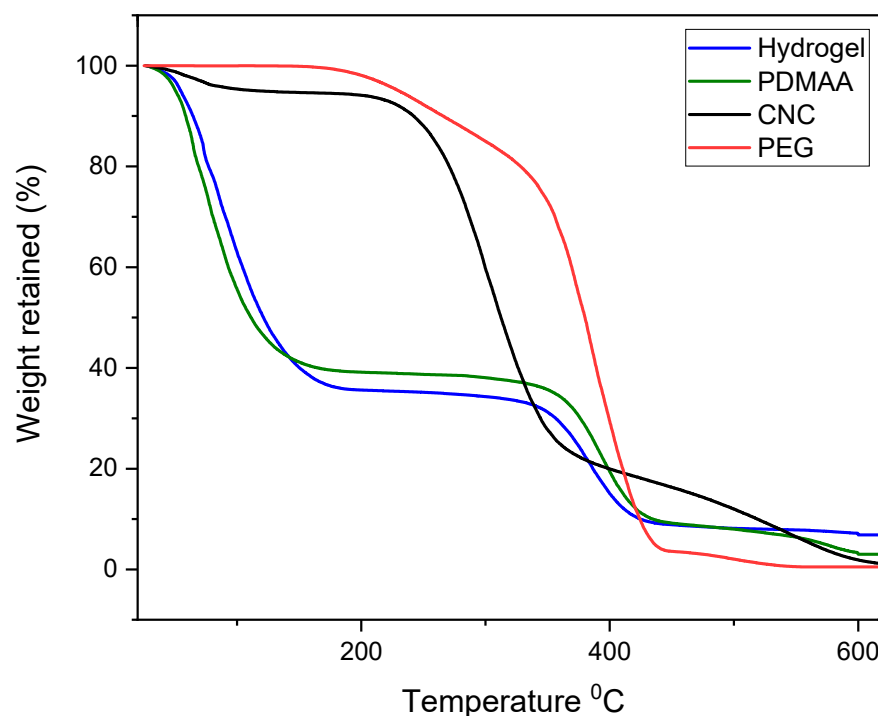
Figure 4. TGA curves of CNC, PEG, PDMAA and CNC/PEG/PDMAA semi-IPN hydrogel.

In the thermogram of CNC, first thermal degradation or weight loss of nearly 5% is in the range of 25 °C to 150 °C was seen. This degradation might be due to the moisture evaporation of the CNC. Afterwards, a sharp thermal degradation could be seen in the temperature range of 210 °C to 400 °C due to the pyrolysis of the cellulose. In this phase, volatile hydrocarbon might be liberated from the cellulose. Here, the weight loss was nearly 65%. Finally, frequent weight loss was observed. This could be attributed to the fact of the decomposition of the remaining heavy component in cellulose, mainly from lignin [22]. Here, almost all weight of CNC was lost. PEG had a single thermal degradation stage. It started to degrade at around 320 °C and ended at 420 °C. In this degradation, almost 95% of the weight loss of PEG was observed, and with higher temperature, complete weight loss was observed.

The TGA curve of the ternary hydrogel system showed multistage degradation due to the presence of different polymers in the system. The first stage degradation was seen approximately at 150 °C, which might be due to the moisture evaporation of the polymeric constituents. After that, the second stage degradation was up to 350 °C and, here, around

67% weight loss was observed. Successive cleaving of the backbone of the polymeric hydrogel could be the reason for this degradation stage [23].

The third stage degradation occurred from 350 °C to 420 °C, which was due to the presence of a small amount of PEG. From the TGA curve of pure PEG it could be seen that the degradation started from 320 °C. However, in this hydrogel, it started to degrade at 350 °C, which might ensure the improvement of the thermal stability of PEG. The weight loss remained nearly constant when the temperatures were higher than 420 °C. From the thermogram of PDMAA, it can be clearly seen that the thermal stability of the hydrogel is mainly governed by the PDMAA, as this polymer is highest in composition compared to other polymers present in hydrogel. If we could compare the overall stability of the hydrogel and the constituent polymers individually, then it was seen that overall weight loss is approximately 90% at 600 °C for the hydrogel sample, whereas the polymer constituents exhibited almost 100% weight loss at this temperature.

3.4. Morphology and Particle Size Analysis

The surface morphology of the samples was identified by SEM analysis, shown in Figure 5. The SEM image of CNC (Figure 5a) gave a clear external appearance of the cellulose nanocrystal by showing the Nano-rod-like structure. The hydrogel was prepared first with three different compositions of CNC (0.3, 0.8 and 1%), which are shown in Figure 5 b, c, d1, d2). The SEM images indicated that the hydrogel prepared with 1% CNC had three-dimensional porous structure. The pores and spongy surface in the hydrogel helped to increase the swelling property of the product. The pores could be the region of water permeation and interaction site of the water molecules with hydrophilic groups of the hydrogel. Thus, this composition was used for further analysis as it could be easier to load drugs in this composition. The SEM image of hydrogel after gentamicin drug loading at its optimum loading efficiency is shown in Figure 5e. This image clearly shows the entrapment filling the pores, compared to the SEM image of the hydrogel in Figure 5d.1. The comparison clearly shows that the structure of the gel was not affected by the incorporation of the drug onto the hydrogel [10].
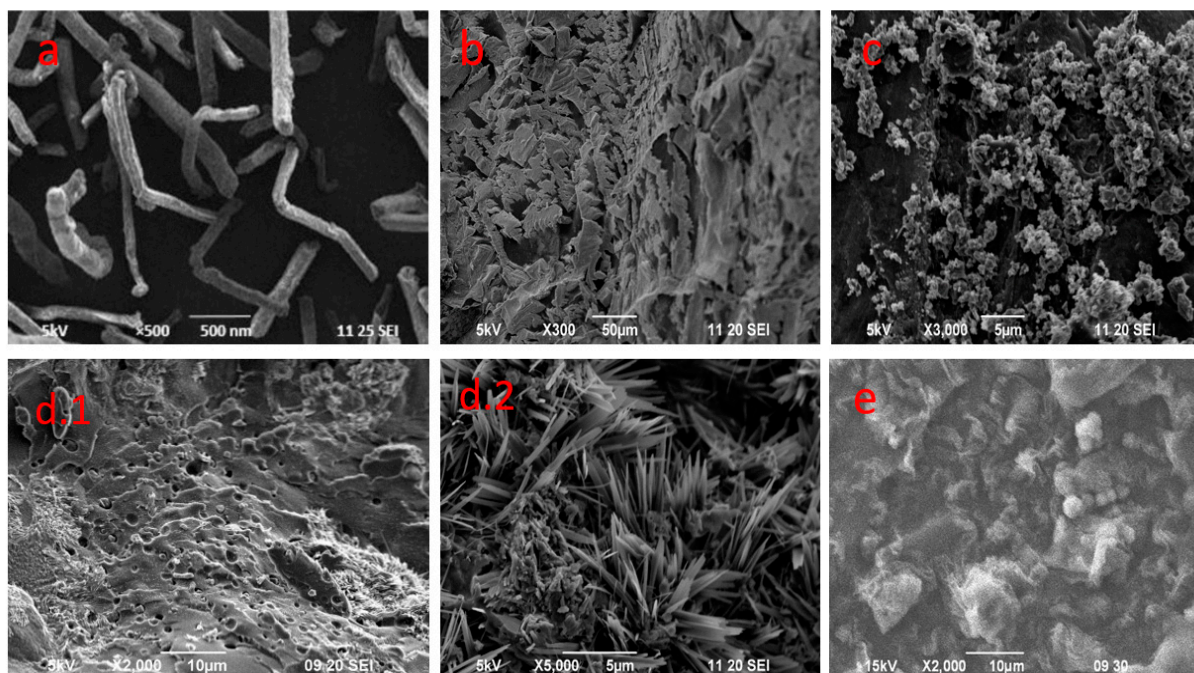
Figure 5. SEM image of (**a**) CNC, (**b**) hydrogel with 0.3% CNC, (**c**) hydrogel with 0.8% CNC, (**d1**) hydrogel with 1% CNC 2000×, (**d2**) hydrogel with 1% CNC 5000× and (**e**) gentamicin loaded hydrogel with 1% CNC.

The particle size for CNC was determined by TEM analysis, which is shown in Figure 6. The particle size of the nanocrystal was found to be 40–80 nm.
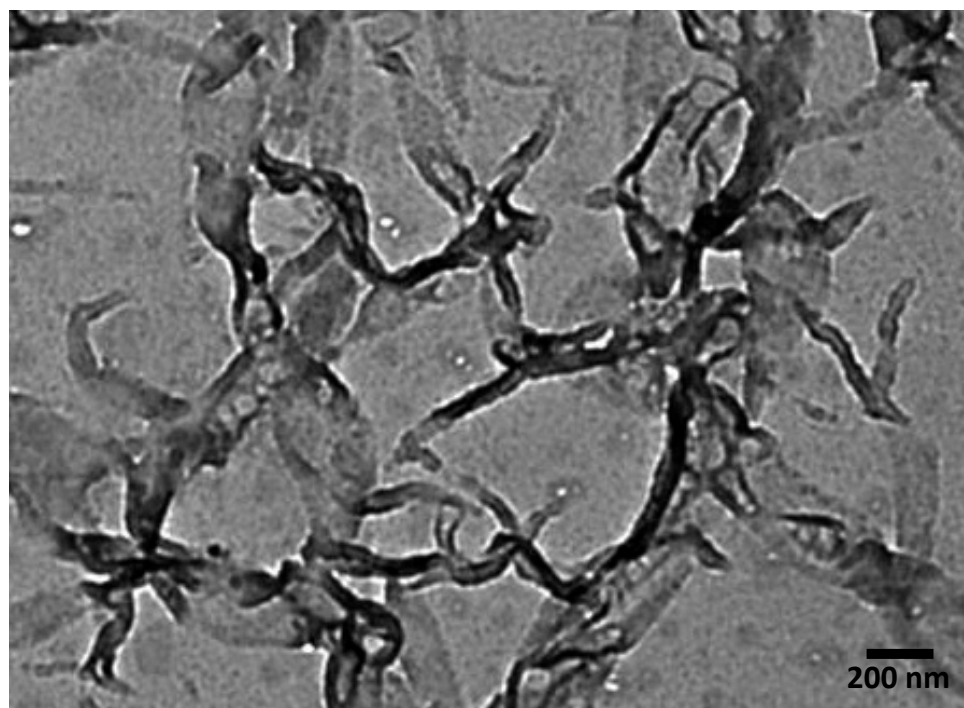
Figure 6. TEM image of CNC.

3.5. Swelling Study

The swelling behavior of the hydrogel had been studied as a function of time and is shown in Figure 7. The figure shows that the percent of swelling in distilled water was 605%, and in phosphate buffer it was 308%, and the equilibrium was reached within 4–5 h. The hydrophilic ability of the functional groups and effective crosslink density of the hydrogel mainly governed the swelling property of any hydrogel. Cellulose acted as a multifunctional cross-linker to form more junctions in hydrogel, followed by an increase in crosslinking density in hydrogel. This could result in the decrease in swelling capacity. The increased number of crosslinks in the polymer segments could reduce free space available for accommodation of the incoming solvent. This was because of the rigidity of the chain that resulted by the crosslinking and, hence, restricted their relaxation [24]. In this system, all the components were hydrophilic and, for this reason, the water absorption behavior of the hydrogel was governed by the concentration of the components in the feed mixture.

The value of equilibrium water content (EWC) was found in the range of 0.8, which showed that the synthesized hydrogels could be used as biomaterials on any biomedical application, because EWC was bigger than the percent of water content value of the body, about 0.6 [25].

3.6. Cytotoxic Effect Analysis

Cytotoxicity of the hydrogel was examined under an inverted light microscope after 48 h of incubation to both the BHK-21 and Vero cell line. Cytotoxicity of the control was also measured for each cell. The two cell lines were observed for 48 h to examine any possible morphological changes, areas of cellular lysis and cell death [26]. Table 1 shows the results of the cytotoxicity tests conducted using the BHK-21 cell line and Vero cell line. No cytotoxicity was observed for the hydrogel sample after 48 h observation on both the BHK-21 cell line and Vero cell lines, as the percentage of survival for both the cells was greater than 95% (Figure 8). The prepared gel survived the cell line and, therefore, the hydrogel could be applied to animal cell wound healing.
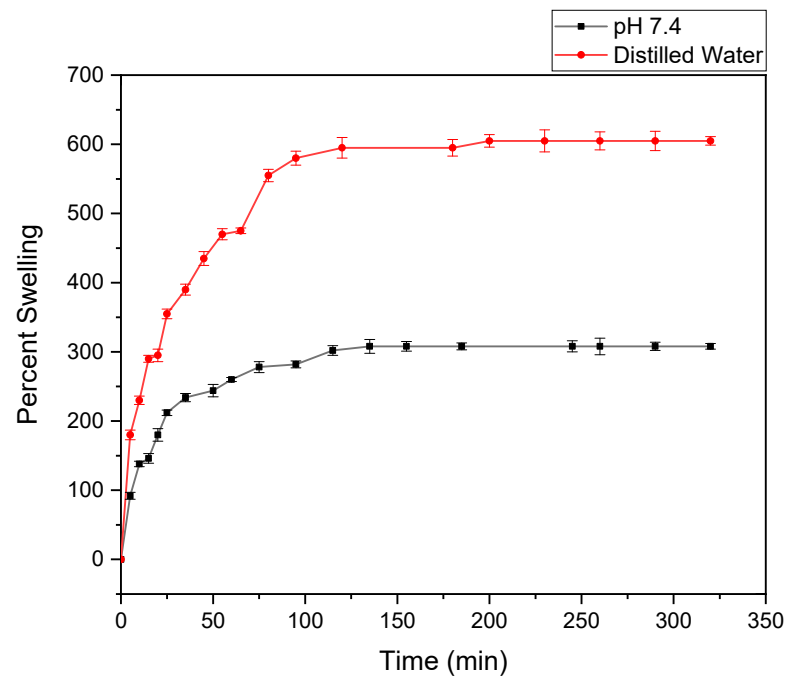
Figure 7. Percent swelling vs. time curve of CNC/PEG/PDMAA semi-IPN hydrogel in water and pH 7.4 phosphate buffer.

Table 1. Cytotoxic effect analysis of CNC/PEG/PDMAA semi-IPN hydrogel.

Sample ID	Survival of BHK-21 Cell	Survival of Vero Cell	Remarks
Control (−)	100%	100%	No cytotoxicity
Control (+)	>95%	>95%	No cytotoxicity
Hydrogel sample	>95%	>95%	No cytotoxicity
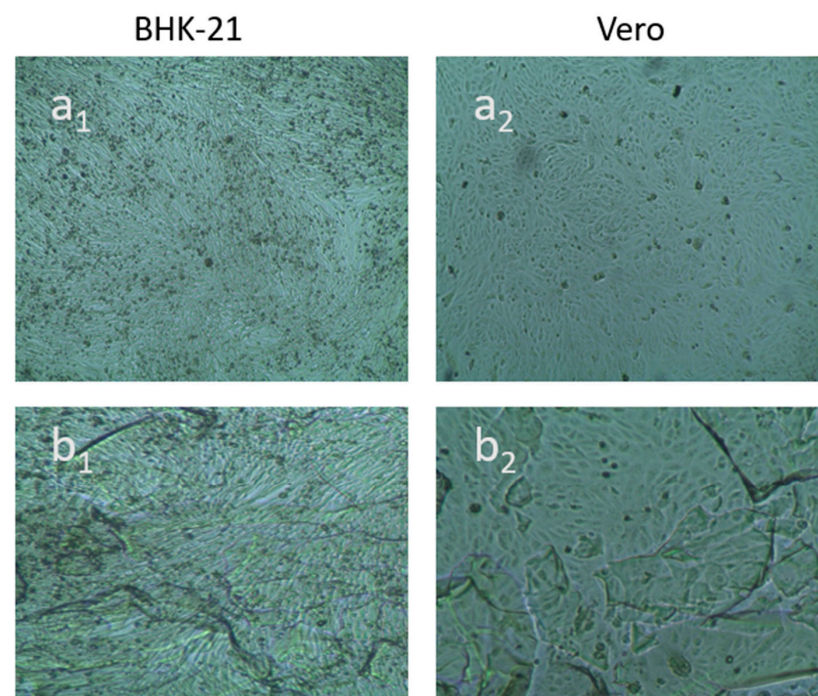
Figure 8. Optical microscopic images of BHK-21 and Vero cell lines treated with semi-IPN hydrogel; (**a1**) control and (**b1**) hydrogel after 48 h for BHK-21 cell, (**a2**) control and (**b2**) hydrogel after 48 h for Vero cell.

3.7. Gentamicin Drug Loading

3.7.1. Standard Curve of Gentamicin Sulphate

The standard curve of the gentamicin sulphate was prepared by forming gentamicin ninhydrin complex at first because gentamicin alone does not show a significant spectrum in the UV-Visible spectrophotometer. Five mL of gentamicin sulphate solution (400 mg/L) were mixed with 1.5 mL of ninhydrin reagent (2 mg/mL) to form a complex which shows nearly three maxima in the spectrum (Figure 9). Figure 9 shows three maxima near 320, 400 and 550 nm in the gentamicin–ninhydrin complex where, as in the gentamicin solution, no spectrum was observed. The absorbance values at 400 nm of the complex mixtures remained virtually unchanged for at least 4 h, and hence this wavelength was taken as standard [5]. Then, at the 400 nm range, the standard calibration curve was drawn.
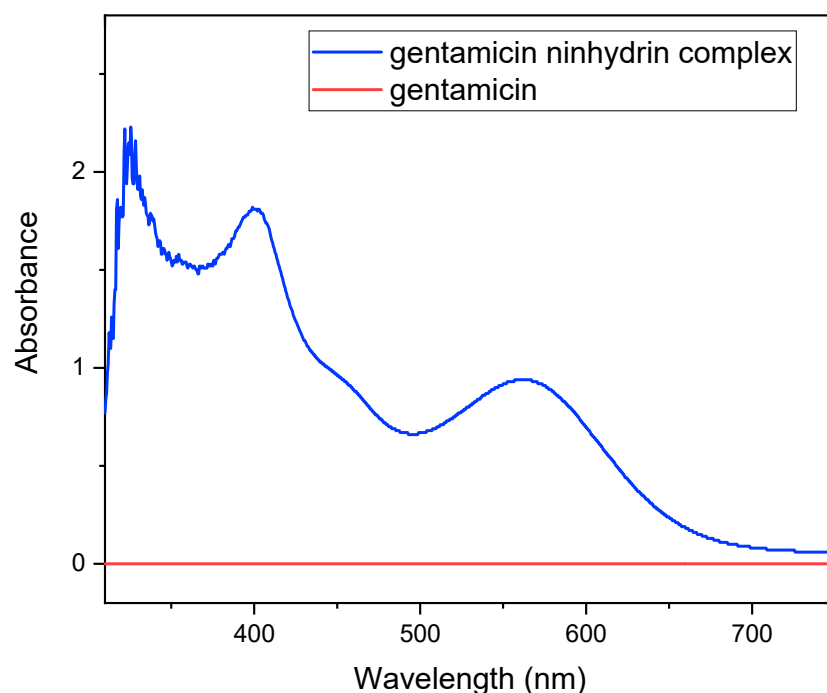
Figure 9. Spectrophotometric curve of gentamicin and the gentamicin–ninhydrin complex.

Seven different known concentrations of gentamicin sulphate (20, 40, 80, 100, 200, 400 and 500 mg/L) were prepared by forming the ninhydrin complex and were subjected to 400 nm to obtain the absorbance values, and thus was the standard curve obtained (Figure 10) (R^2 value = 0.9899), which was further used for quantifying the drug loading and release profile.

3.7.2. Drug Loading Performance and Optimum Drug Loading Efficiency

The suitable loading of gentamicin sulphate could be quantified by loading different concentrations of drugs onto the hydrogel film. The images of hydrogels before and after drug loading are presented in the Supporting Information (Figure S1). The hydrogel film was soaked in a gentamicin sulphate solution of varying concentrations (20, 40, 100, 200 and 300 mg/L). Then, the absorbance values of unloaded drugs in the supernatant solution helped to quantify the loading efficiency of the drug. These absorbance values were measured with a UV-Visible spectrophotometer at 400 nm compared to the standard calibration curve of gentamicin sulphate. The loading efficiencies of 20, 40, 100, 200 and 300 mg/L gentamicin sulphate were 87.17, 62.5, 61.16, 40.15 and 32.19%, respectively. Table 2 shows the loading performance of gentamicin sulphate for varying concentrations.
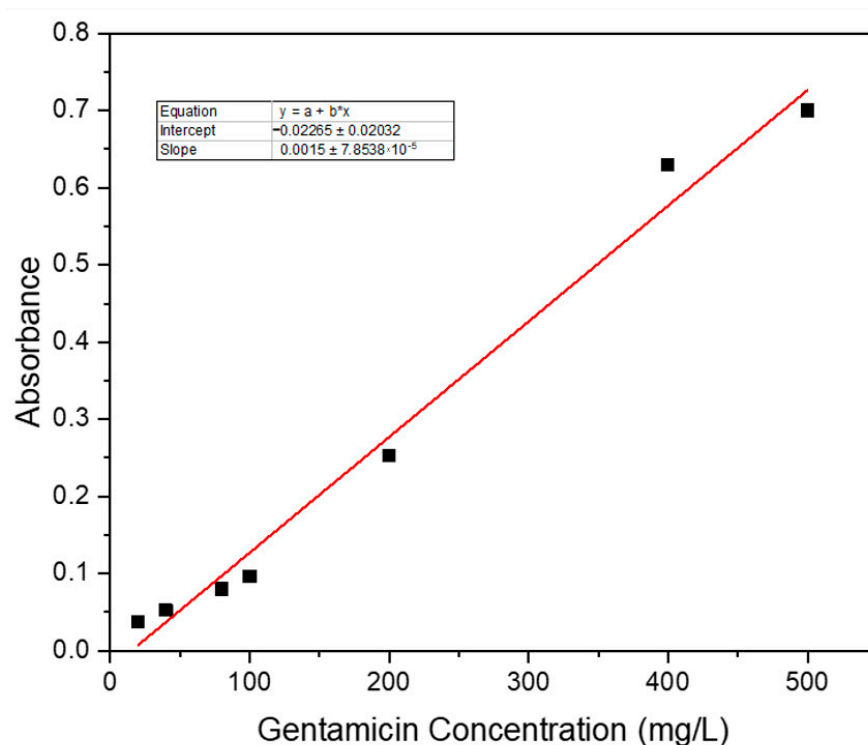
Figure 10. Standard calibration curve for gentamicin sulphate.

Table 2. Drug loading performance of hydrogel film in different concentrations.

Gentamicin Sulphate Concentration (mg/L)	Loaded Amount of Gentamicin Sulphate in 24 h (mg)	Loading Efficiency (%)	Standard Deviation($\pm$ %)
20	17.43	87.17	3.26
40	25	62.5	2.44
100	61.16	61.16	2.04
200	80.3	40.15	2.67
300	96.57	32.19	4.08

The optimum loading efficiency was identified as 61.16% with a gentamicin sulphate concentration of 100 mg/L (Figure 11). The optimum loading efficiency was determined to be 61.16% because, in this percentage, the maximum amount of drug was loaded with the highest efficiency. The crosslinking of this semi-IPN hydrogel film resulted in some void spaces for the physical entrapment of the drug in these spaces [27]. After 100 mg/L concentration, a sharp decrease in drug loading efficiency was seen, and hence it could be concluded that the highest drug entrapment inside the void spaces occurred in this efficiency.
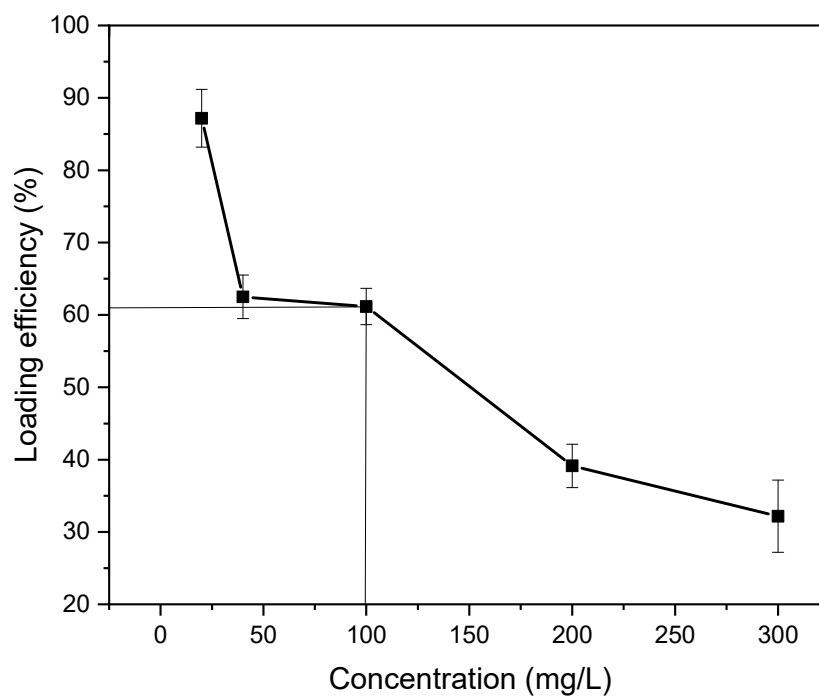
Figure 11. Optimum drug loading efficiency determination.

3.8. Antimicrobial Activity Study

Antibacterial study was observed in one gram-negative (*E. coli*) and one gram-positive (*S. aureus*) bacteria. For assessing the activity pattern, strains of the bacteria were swabbed in the agar broth and left for incubation for 24 h, resulting in an inhibition zone in both cases (Figure 12), which was measured using a millimeter scale. The zone of inhibition observation showed antibacterial activity for the gentamicin loaded hydrogel film, and hence it could be concluded that the hydrogel film could be used for wound healing purposes, which could inhibit the bacterial growth in the wound exposure. The zone of inhibition for both the bacteria is listed in Table 3.
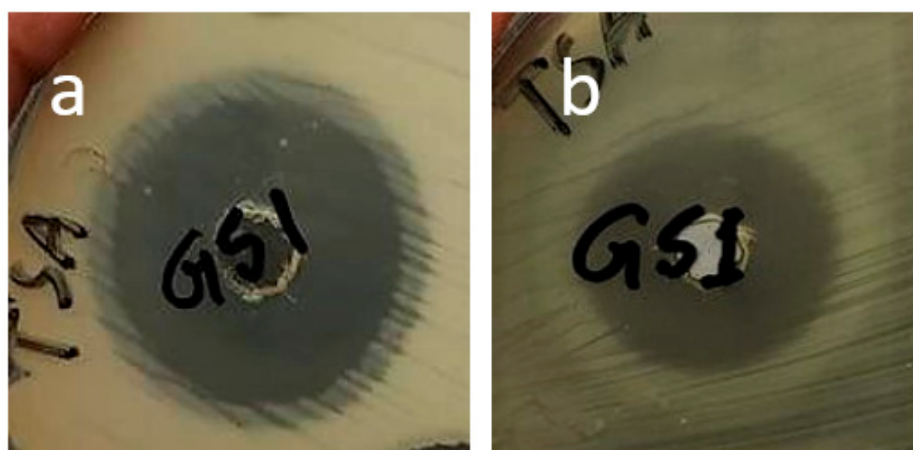
Figure 12. Antibacterial activity of drug loaded hydrogel film showing the inhibition zone for (**a**) *S. aureus* and (**b**) *E. coli* bacteria.

Table 3. Zone of inhibition (mm) in drug loaded hydrogel sample.

Sample	Bacteria Specific Diameter (mm) of Inhibition Zone	
	Staphylococcus aureus	*Escherichia coli*
Drug loaded hydrogel film	25	23

3.9. In Vitro Release Profile

Slightly acidic solutions were used for determining the release profile because, during the healing of acute wounds, generally, a temporary physiological acidosis is seen due to the generation of different organic acids and increased demand for oxygen during the healing process combined with a stasis of tissue perfusion, increasing the local carbon dioxide in wounds [28]. Therefore, at acidic pH 5.5 and 6.0, a better release profile could be understood.

The release of the drug under in vitro conditions at various time intervals, up to an 80 h period, showed the highest percentage of release of 76% within 72 h (Figure 13) at pH 5.5 and release of 63% within 72 h at pH 6.0. Figure 13 shows drug release in a manner which indicated homogeneous dispersion of the drug in the polymer matrix, which resulted in a sustained drug release in acidic pH and confirmed that the drug could be released in the acidic environment of the wounded area.
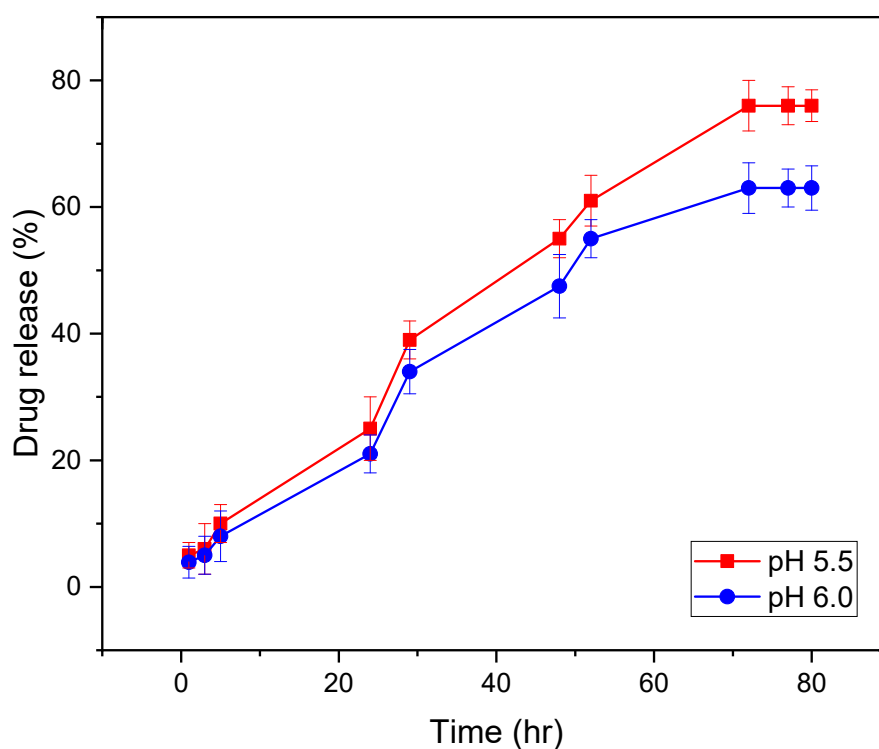
Figure 13. In vitro drug release profile of gentamicin sulphate from hydrogel in phosphate buffer solution at pH 5.5 and pH 6.0.

3.10. In Vivo Wound Healing in Mice Model

The efficacy of the prepared hydrogel film was determined by the responsiveness of the faster wound healing which had been observed using the 12 day mice model experiment [29]. The wound closure observation continued on day 0, 4, 8 and 12, both for the control mouse which was treated without drugs and another mouse with optimum drug loaded hydrogel film. The results are shown in Figure 14a,b with a comparison of relative wound size reduction. The control mouse which was treated with normal gauze showed no significant size reduction in the wound. Within this 12-day experiment period, only 40% wound closure was observed for the control mouse, whereas the mouse treated

with optimum drug loaded semi-IPN hydrogel indicated noteworthy wound closure within this time period. On the eighth day, the hydrogel loaded with drug showed a wound size reduction of 75%, which was significantly higher compared to the control. Less scabbing was observed in the case of the wound treated with drug loaded hydrogel and, on the twelfth day, complete wound closure of 100% was exhibited with complete growth of the skin tissues.
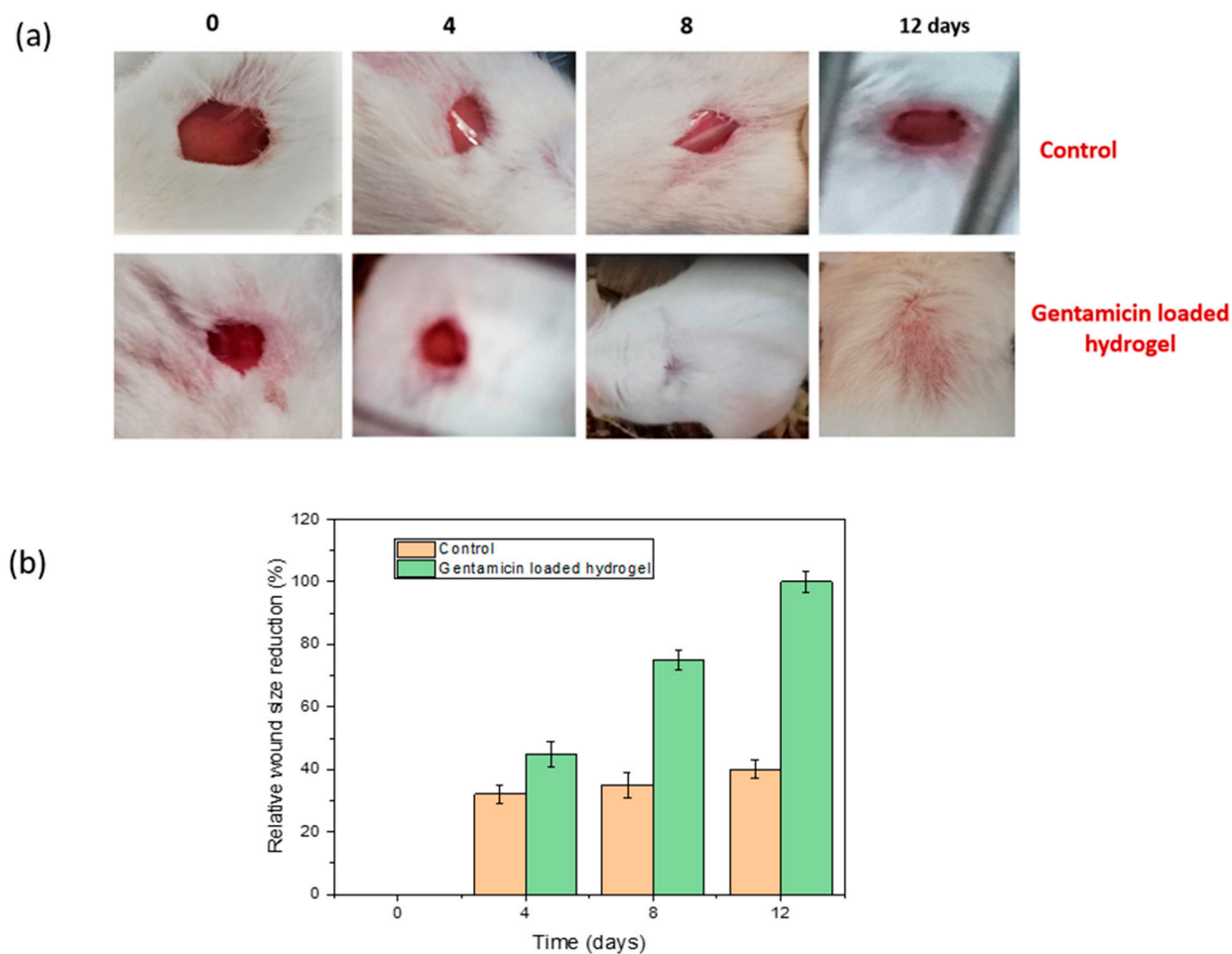
Figure 14. (**a**) Photographs of wounds treated with normal gauze and gentamicin loaded hydrogel. (**b**) Evaluation of relative wound size reduction.

4. Conclusions

In this research work, we tried to develop a biocompatible hydrogel which could be in contact with bodily organs with minimum damage to the surrounding tissues and without triggering undesirable immune responses. The biocompatibility of the semi-IPN hydrogel along with the faster wound healing response, which was confirmed by the in vivo testing, and lack of toxicity have been taken advantage of in wound dressings, and hence this gentamicin loaded CNC/PEG/PDMAA semi-IPN hydrogel can be successfully used in various wound healing purpose. The complete polymerization and formation of semi-IPN was confirmed by ATR analysis. The morphological studies showed their efficacy in drug loading, with an optimum gentamicin sulphate loading efficiency of 61.16% and with a drug concentration of 100 mg/L. The antibacterial activity against *S. aureus* and *E. coli* bacteria confirms their suitability for wound healing. In vitro drug release of 76% at pH 5.5 within 72 h followed by a successful in vivo testing in a mice model, with a recovery within 12 days, give this work a possible scope for wound healing management. Overall, the easy

preparation method, low operational cost and outstanding wound healing properties of this advanced hydrogel compound have made it a potential biomaterial for wound dressing.

References

1. Yang, J.; Han, C.R.; Duan, J.F.; Ma, M.G.; Zhang, X.M.; Xu, F.; Sun, R.C. Synthesis and characterization of mechanically flexible and tough cellulose nanocrystals–polyacrylamide nanocomposite hydrogels. *Cellulose* **2013**, *20*, 227–237. [CrossRef]
2. Mardali, M.; Sarraf-Mamoory, R.; Sadeghi, B.; Safarbali, B. Acrylamide route for the co-synthesis of tungsten carbide–cobalt nanopowders with additives. *Ceram. Int.* **2016**, *42*, 9382–9386. [CrossRef]
3. Saraydın, D.; Karadag, E.; Işıkver, Y.; Şahiner, N.; Güven, O. The influence of preparation methods on the swelling and network properties of acrylamide hydrogels with crosslinkers. *J. Macromol. Sci. Part A* **2004**, *41*, 419–431. [CrossRef]
4. Lee, S.J.; Kim, S.S.; Lee, Y.M. Interpenetrating polymer network hydrogels based on poly (ethylene glycol) macromer and chitosan. *Carbohydr. Polym.* **2000**, *41*, 197–205. [CrossRef]
5. Thakur, A.; Wanchoo, R.K.; Singh, P. Hydrogels of poly (acrylamide-co-acrylic acid): In-vitro study on release of gentamicin sulfate. *Chem. Biochem. Eng. Q.* **2011**, *25*, 471–482.
6. Zarida, C.N.; Fauziah, O.; Arifah, A.K.; Nazri, M.Y.; Rusnah, M.; GK, M.A.K. In vitro elution and dissolution of tobramycin and gentamicin from calcium phosphate. *Afr. J. Pharm. Pharmacol.* **2011**, *5*, 2283–2291.
7. Murray, P.R. Mandell, Douglas and Bennett's Principles and Practice of Infectious Diseases. *Clin. Microbiol. Rev.* **2015**, *1*, 191–223.
8. Sarwar, M.S.; Huang, Q.; Ghaffar, A.; Abid, M.A.; Zafar, M.S.; Khurshid, Z.; Latif, M. A smart drug delivery system based on biodegradable chitosan/poly (allylamine hydrochloride) blend films. *Pharmaceutics* **2020**, *12*, 131. [CrossRef]
9. Balakrishnan, B.; Mohanty, M.; Umashankar, P.R.; Jayakrishnan, A. Evaluation of an in situ forming hydrogel wound dressing based on oxidized alginate and gelatin. *Biomaterials* **2005**, *26*, 6335–6342. [CrossRef]
10. Hwang, M.R.; Kim, J.O.; Lee, J.H.; Kim, Y.I.; Kim, J.H.; Chang, S.W.; Jin, S.G.; Kim, J.; Lyoo, W.S.; Han, S.S.; et al. Gentamicin-loaded wound dressing with polyvinyl alcohol/dextran hydrogel: Gel characterization and in vivo healing evaluation. *AAPS Pharm. Sci. Tech.* **2010**, *11*, 1092–1103. [CrossRef]
11. Baek, S.; Kim, D.; Jeon, S.L.; Seo, J. Preparation and characterization of pH-responsive poly (N, N-dimethyl acrylamide-co-methacryloyl sulfadimethoxine) hydrogels for application as food freshness indicators. *React. Funct. Polym.* **2017**, *120*, 57–65. [CrossRef]
12. Kargarzadeh, H.; Ahmad, I.; Abdullah, I.; Dufresne, A.; Zainudin, S.Y.; Sheltami, R.M. Effects of hydrolysis conditions on the morphology, crystallinity, and thermal stability of cellulose nanocrystals extracted from kenaf bast fibers. *Cellulose* **2012**, *19*, 855–866. [CrossRef]
13. Pourshahrestani, S.; Zeimaran, E.; Kadri, N.A.; Mutlu, N.; Boccaccini, A.R. Polymeric hydrogel systems as emerging biomaterial platforms to enable hemostasis and wound healing. *Adv. Healthc. Mater.* **2020**, *9*, 2000905. [CrossRef] [PubMed]
14. Sahiner, M.; Sagbas, S.; Bitlisli, B.O. p (AAm/TA)-based IPN hydrogel films with antimicrobial and antioxidant properties for biomedical applications. *J. Appl. Polym. Sci.* **2015**, *132*, 41876. [CrossRef]
15. Cidreira, A.C.M.; de Castro, K.C.; Hatami, T.; Linan, L.Z.; Mei, L.H.I. Cellulose nanocrystals-based materials as hemostatic agents for wound dressings: A review. *Biomed. Microdevices* **2021**, *23*, 1–23. [CrossRef]

16. Hossain, S.; Shahruzzaman, M.; Kabir, S.F.; Rahman, M.S.; Sultana, S.; Mallik, A.K.; Haque, P.; Takafuji, M.; Rahman, M.M. Jute cellulose nanocrystal/poly (N, N-dimethylacrylamide-co-3-methacryloxypropyltrimethoxysilane) hybrid hydrogels for removing methylene blue dye from aqueous solution. *J. Sci. Adv. Mater. Devices* **2021**, *6*, 254–263. [CrossRef]

17. Zou, J.; Bao, D.; Ma, R.; Zhu, Z.; Chen, X.; Zhu, J.; Fan, X.; Zhang, K.; Zheng, H.; Li, F.; et al. Green and sustainable self-assembly nanocomposite from gentamicin sulfate/lignosulfonate with efficient antibacterial and wound-healing activity. *ACS Sustain. Chem. Eng.* **2020**, *8*, 4931–4940. [CrossRef]

18. Alemdar, A.; Sain, M. Isolation and characterization of nanofibers from agricultural residues–Wheat straw and soy hulls. *Bioresour. Technol.* **2008**, *99*, 1664–1671. [CrossRef]

19. Rosli, N.A.; Ahmad, I.; Abdullah, I. Isolation and characterization of cellulose nanocrystals from Agave angustifolia fibre. *BioResources* **2013**, *8*, 1893–1908. [CrossRef]

20. Bhattacharyya, R.; Ray, S.K. Removal of congo red and methyl violet from water using nano clay filled composite hydrogels of poly acrylic acid and polyethylene glycol. *Chem. Eng. J.* **2015**, *260*, 269–283. [CrossRef]

21. Liu, M.; Wang, L.; Su, H.; Cao, H.; Tan, T. pH-sensitive IPN hydrogel based on poly (aspartic acid) and poly (vinyl alcohol) for controlled release. *Polym. Bull.* **2013**, *70*, 2815–2827. [CrossRef]

22. Zabaniotou, A.; Ioannidou, O.; Antonakou, E.; Lappas, A. Experimental study of pyrolysis for potential energy, hydrogen and carbon material production from lignocellulosic biomass. *Int. J. Hydrog. Energy* **2008**, *33*, 2433–2444. [CrossRef]

23. Ali, A.E.H.; Shawky, H.A.; Abd El Rehim, H.A.; Hegazy, E.A. Synthesis and characterization of PVP/AAc copolymer hydrogel and its applications in the removal of heavy metals from aqueous solution. *Eur. Polym. J.* **2003**, *39*, 2337–2344.

24. Hiremath, J.N.; Vishalakshi, B. Effect of Crosslinking on swelling behaviour of IPN hydrogels of Guar Gum & Polyacrylamide. *Der. Pharma. Chem.* **2012**, *4*, 946–955.

25. Ibrahim, A.G.; Hai, F.A.; Wahab, H.A.; Mahmoud, H. Synthesis, characterization, swelling studies and dye removal of chemically crosslinked acrylic acid/acrylamide/N, N-dimethyl acrylamide hydrogels. Am. *J. Appl. Chem.* **2016**, *4*, 221–234.

26. Hasan, M.M.; Khan, M.N.; Haque, P.; Rahman, M.M. Novel alginate-di-aldehyde cross-linked gelatin/nano-hydroxyapatite bioscaffolds for soft tissue regeneration. *Int. J. Biol. Macromol.* **2018**, *117*, 1110–1117. [CrossRef] [PubMed]

27. Islam, M.; Haque, P.; Rashid, T.U.; Khan, M.N.; Mallik, A.K.; Khan, M.N.I.; Khan, M.; Rahman, M.M. Core–shell drug carrier from folate conjugated chitosan obtained from prawn shell for targeted doxorubicin delivery. *J. Mater. Sci. Mater. Med.* **2017**, *28*, 1–10. [CrossRef]

28. Schneider, L.A.; Korber, A.; Grabbe, S.; Dissemond, J. Influence of pH on wound-healing: A new perspective for wound-therapy? *Arch. Dermatol.* **2007**, *298*, 413–420. [CrossRef]

29. Dwivedi, C.; Pandey, H.; Pandey, A.C.; Patil, S.; Ramteke, P.W.; Laux, P.; Luch, A.; Singh, A.V. In vivo biocompatibility of electrospun biodegradable dual carrier (antibiotic+ growth factor) in a mouse model—Implications for rapid wound healing. *Pharmaceutics* **2019**, *11*, 180. [CrossRef]

Enhancing Conductivity and Self-Healing Properties of PVA/GEL/OSA Composite Hydrogels by GO/SWNTs for Electronic Skin

Xiaohu Chen [1,2], Haonan Zhang [1,2], Jiashu Cui [1,2], Yanen Wang [1,2,*], Mingyang Li [1,2], Juan Zhang [1,2], Changgeng Wang [1,2], Zhisheng Liu [1,2] and Qinghua Wei [1,2,*]

[1] Department of Indurstry and Engineering, School of Mechanical Engineering, Northwestern Polytechnical University, Xi'an 710072, China

[2] Bio-Additive Manufacturing University-Enterprise Joint Research Center of Shaanxi Province, Northwestern Polytechnical University, Xi'an 710072, China

* Correspondence: wangyanen@nwpu.edu.cn (Y.W.); weiqinghua@nwpu.edu.cn (Q.W.); Tel./Fax: +86-029-88493232 (Y.W.)

Abstract: The use of flexible, self-healing conductive hydrogels as a type of typical electronic skin with the function of transmitting sensory signals has attracted wide attention in the field of biomaterials. In this study, composite hydrogels based on polyvinyl alcohol (PVA), gelatin (GEL), oxidized sodium alginate (OSA), graphene oxide (GO), and single-walled carbon nanotubes (SWNTs) were successfully prepared. The hydrogen and imine bonding of the composite hydrogels gives them excellent self-healing properties. Their self-healing properties restore 68% of their breaking strength and over 95% of their electrical conductivity. The addition of GO and SWNTs enables the PGO-GS hydrogels to achieve a compressive modulus and conductivity of 42.2 kPa and 29.6 mS/m, which is 8.2 times and 1.5 times that of pure PGO, respectively. Furthermore, the PGO-GS hydrogels can produce profound feedback signals in response to deformation caused by external forces and human movements such as finger flexion and speech. In addition, the PGO-GS hydrogels exhibit superior biocompatibility compared to PGO. All of these results indicate that the PGO-GS hydrogels have great potential with respect to future applications in the field of electronic skin.

1. Introduction

The skin is the largest organ of the human body, and has the characteristics of flexibility, self-repairability, and tactile sensitivity [1–3]. Bionic tactile sensor devices that mimic the characteristics and functions of human skin are referred to as electronic skin [4]. With the rapid development of electronic technology in recent years, increasingly more electronic devices are developing towards the directions of achieving miniaturization, flexibility, and lightweight properties [5,6]. Electronic skin has also been widely used in wearable devices, health monitoring, intelligent robots, and bionic prostheses [7–10].

In order to perceive deformations in real time, electronic skin must be highly flexible and resilient, and should be able to generate specific response signals to stimuli and provide timely feedback [11,12]. Conductive hydrogels are soft materials with good flexibility and biocompatibility, whose structure is similar to natural living tissue [13–15]. Conductive hydrogels are considered to constitute an ideal material for the preparation of bionic electronic skin due to their functional designability [16–18]. Bionic electronic skin requires a high level of electrical conductivity and sensitivity, which are often achieved by introducing conductive filling materials [19]. Examples of such incorporations include the addition of conductive polymers (polypyrrole (PPy) and polyaniline (PANI)) and inorganic nanomaterials (carbon nanotubes, graphene, and metal nanoparticles) [13,20–22]. Among

them, graphene and carbon nanotubes have excellent electrical, mechanical, and surface properties, and have shown the greatest potential for use in bionic electronic skin [23,24]. Compared with conductive polymers, the excellent mechanical properties of graphene and carbon nanotubes can improve the overall mechanical properties (especially the toughness) of hydrogels, while building stable conductive networks within the hydrogels [25–27]. For example, Wu et al. [28] prepared polyvinyl alcohol (PVA)/graphene oxide (GO) composite hydrogels by introducing metal ion coordination bonds. The tensile strength of the PVA-GO hydrogel could reach 11.10 MPa, which is 175% higher than that of pure PVA. Wu et al. [29] successfully prepared a composite hydrogel based on PVA, carboxymethyl chitosan (CMCS), oxidized sodium alginate (OSA), and oxidized multi-walled carbon nanotubes (OMWCNTs). The addition of OMWCNTs increased the fracture strength and electrical conductivity of the hydrogel to 0.8 MPa and 70.2 mS/m, respectively, which were 2.5 and 4 times higher than those of the previous hydrogel. The change in the resistance of the composite hydrogel after 200 cycles of 20% constant strain was almost identical to the initial value, thus demonstrating the excellent stability of the composite hydrogel. Li et al. [30] successfully constructed gelatin (GEL)-OSA-PVA ternary hydrogels by mixing PVA with GEL and OSA. By adjusting the concentration of PVA and the degree of oxidation of OSA, the hydrogel obtained adjustable mechanical properties with a maximum compressive modulus of 75 kPa. In the 300 s fatigue compression test, a large amount of PVA only reduced the stress of the hydrogel by 30.99%. In addition, the hydrogel exhibits good electrical conductivity (10.68 mS/m) due to the presence of free ions.

In addition to the mechanical and electrical properties mentioned above, the self-healing properties and biocompatibility of hydrogels are also of interest. Self-healing hydrogels can spontaneously repair damage without any external stimulation, which can effectively extend the lifetime of hydrogel electronic skins and expand their applications in extreme environments [31,32]. Self-healing is mainly achieved by constructing reversible dynamic bonds (non-covalent and dynamic covalent bonds) in hydrogel networks. The non-covalent bonds include hydrogen bonds, metal coordination bonds, etc. Dynamic covalent bonds include imine/hydrazone bonds, Diels–Alder reactions, borate ester bonds, and disulfide bonds [33,34]. In addition, electronic skin needs to be biocompatible to avoid damaging human skin when employed as health-monitoring devices [25,35]. Therefore, a kind of hydrogel with excellent properties (conductivity, mechanics, self-healing, biocompatibility, etc.) used for electronic skin still needs to be found, and this pursuit is attracting a considerable amount of attention.

Herein, we report the construction of a conductive and self-healing composite hydrogel using PVA, GEL, OSA, GO, and single-walled carbon nanotubes (SWNTs). The formation of imine bonds between GEL and OSA allows the hydrogel to heal itself without any external stimulation. Two kinds of nanomaterials, GO and SWNTs, were applied to enhance the properties of the composite hydrogel, such as effecting a higher compression modulus, better elastic behavior, and enhanced electrical conductivity. Finally, the prepared composite hydrogel proved to have excellent biocompatibility and sensitivity. These characteristics show that the prepared composite hydrogel has great potential in application scenarios regarding electronic skin such as wearable devices, health monitoring, and voice recognition.

2. Results and Discussion

2.1. Microtopography of Hydrogels

As shown in Figure 1, which presents scanning electron microscopy (SEM) images of the freeze-dried PGO and PGO-GA hydrogels, it can be seen that all the freeze-dried hydrogels show the characteristics of a porous structure. Particularly, the GO sheets and SWNTs were evenly distributed without agglomeration in the PGO-GS3 hydrogel framework (Figure 1c). Compared with the PGO hydrogel, the PGO-GS3 hydrogel has a porous three-dimensional network structure and more uniform pore size, which is conducive to the conductivity and mechanical strength of hydrogels.
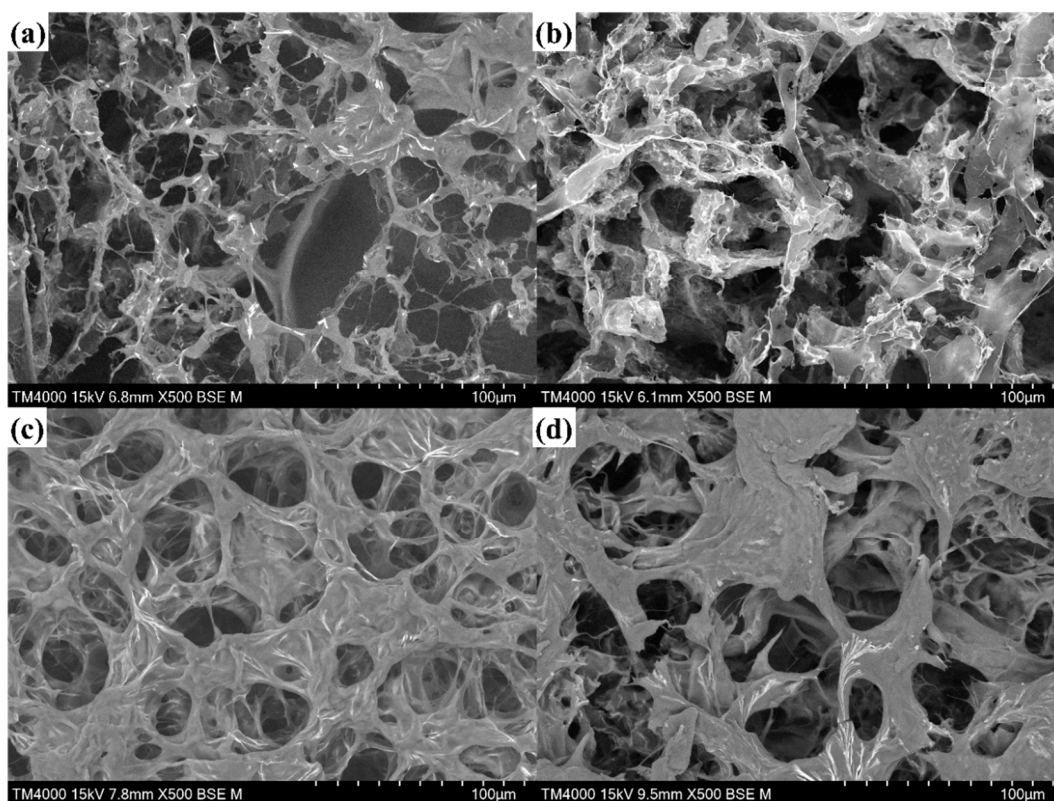
Figure 1. The SEM images of (**a**) PGO hydrogel, (**b**) PGO-GS1 hydrogel, (**c**) PGO-GS3 hydrogel, and (**d**) PGO-GS5 hydrogel.

The density and porosity of the hydrogels were also calculated, as shown in Table 1. Notably, the PGO-GS3 hydrogel has the highest porosity and the lowest density; this is because they are closely related to the structure of the hydrogel. This result is consistent with the results observed using electron microscopy.

Table 1. Density and porosity of hydrogels.

Hydrogel Samples	Density (g/cm^3)	Porosity (%)
PGO	0.205 ± 0.009	40.59 ± 2.71
PGO-GS1	0.109 ± 0.003	60.77 ± 3.65
PGO-GS3	0.101 ± 0.019	62.28 ± 7.30
PGO-GS5	0.114 ± 0.012	58.58 ± 6.82

Figure S1 shows the swelling ratios of the hydrogels. The swelling ratio of the PGO hydrogel reaches 13.91, which is significantly higher than that of the PGO-GS hydrogel. This indicates that the PGO hydrogel has large internal pores and loose structures, and this finding is consistent with the SEM images. The reason behind this is that the addition of GO and SWNTs may increase the viscosity of the hydrogel, resulting in a denser network, and the denser hydrogel network prevents water molecules from diffusing into the hydrogel.

2.2. Chemical Structure of the Hydrogels

The spectra of SA and OSA are shown in Figure 2a. The peak located at 1736 cm^{-1} in OSA spectra is the characteristic peak of -CHO [29,36], which is caused by the symmetric stretching vibration of C=O, indicating that the oxidation reaction was successful. Meanwhile, the peak of SA at 3430 cm^{-1} is wider than that in OSA, which also indicates that the content of -OH decreased in OSA.
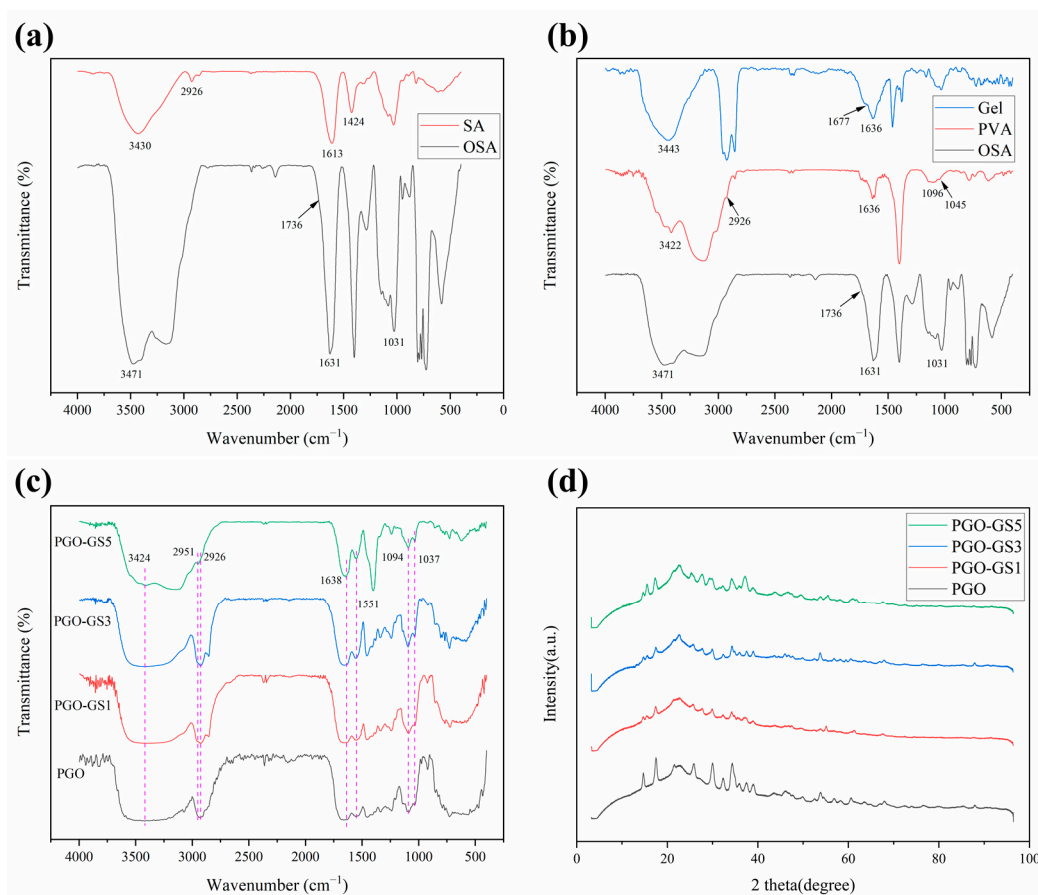
Figure 2. The FTIR spectrum of (**a**) SA and OSA; (**b**) GEL, PVA, and OSA; (**c**) PGO and PGO-GS hydrogels. (**d**) The XRD patterns of PGO and PGO-GS hydrogels.

Figure 2b shows the spectra of PVA and GEL. The peak at 3422 cm^{-1} in the PVA spectrum was generated by hydrogen bonding between hydroxyl groups. The C-O stretching vibration in the crystalline region and amorphous region of PVA produced peaks at 1096 cm^{-1} and 1045 cm^{-1}, respectively. In GEL's spectrum, the stretching vibration and deformation vibration of -NH$_2$ are at the 3443 cm^{-1} and 1677 cm^{-1} peaks, respectively.

Figure 2c shows the spectrum of the PGO hydrogel with different GO and SWNTs fractions. The enhancement peak at 3424 cm^{-1} was caused by the overlap of hydrogen bonds. The peak of PGO-GS5 at 3424 cm^{-1} is significantly weaker than the other samples. This may be attributable to the high content of GO and SWNTs, which leads to a certain degree of agglomeration of the two materials, thus affecting the formation of hydrogen bonds in the hydrogel. The peaks at 1636 cm^{-1} and 1547 cm^{-1} belong to C=N vibration, which occurred due to the formation of imine bonds. The peak at 1094 cm cm^{-1} is stronger than that at 1037 cm^{-1}, indicating that PVA has higher crystallinity and forms hydrogen bonds with the other two macromolecules. The peak at 1094 cm^{-1} of the PGO-GS5 spectrum is weak, which further indicates that high GO and SWNTs fractions will hinder the formation of hydrogen bonds between three macromolecules. In general, the addition of GO and SWNT does not significantly change the composition of the organic functional groups in the PGO hydrogel.

The formation of the PGO-GS hydrogel was also analyzed by XRD. Figure 2d shows the XRD patterns of the hydrogels with different GO and SWNTs fractions. PGO-GS formed a low-intensity diffraction peak at 2θ = 15.4°, which is the characteristic peak of GO. The curve shows distinct peaks at 2θ = 15°, 22°, and 34°, which are typical XRD patterns for OSA [29]. The XRD pattern of the PGO and PGO-GS hydrogel shows a wide, amorphous diffraction peak centered at 2θ = 22.7°. It is well known that GEL and PVA express their ordered structure at around 2θ = 20° [28,37,38], and that amorphous PVA phase produces

a weak band at 2θ = 42° [39]. The PGO-GS composite hydrogel has a weaker diffraction peak at 2θ = 14.75° than the PGO hydrogel, indicating that the addition of GO and SWNTs attenuates the crystallization of PVA. In addition, there is no significant difference between the PGO and PGO-GS hydrogels. All the samples have similar curves, which shows that the incorporation of GO sheets and SWNTs has no obvious effect on the crystallinity of PVA and GEL. It has been confirmed that there is no significant phase separation appearing in this system, indicating that GO and SWNTs are well dispersed in the PGO-GS hydrogel.

2.3. Mechanical Properties of Hydrogels

The mechanical strength of the hydrogels was further quantified with compressive tests. The compressive stress–strain curves of the PGO and PGO-GS hydrogels are shown in Figure 3a. It can be seen that the mechanical properties of the PGO-GS hydrogel are better than those of the PGO hydrogel. This is because the sheet-like shape of the GO molecule, tubular shape of the SWNT molecule, and three kinds of macromolecular chains are intertwined to form a tighter, more stable network structure thanks to hydrogen bonding. During the compression process, part of the compression stress was transferred to the GO and SWNTs dispersed in the hydrogel, ultimately increasing in the compression strength of the PGO-GS hydrogel. However, the compressive strength of PGO-GS5 shows a decrease compared to PGO-GS3 (Figure 3b). This is mainly due to the agglomeration of GO and SWNT caused by the electrostatic force and van der Waals forces between the nanoparticles, resulting in a decrease in the mechanical properties of the hydrogel [40,41]. Notably, the addition of GO and SWNTs resulted in a compressive modulus of 42.2 kPa for the PGO-GS3 hydrogel, which is as much as eight times higher than that of PGO.
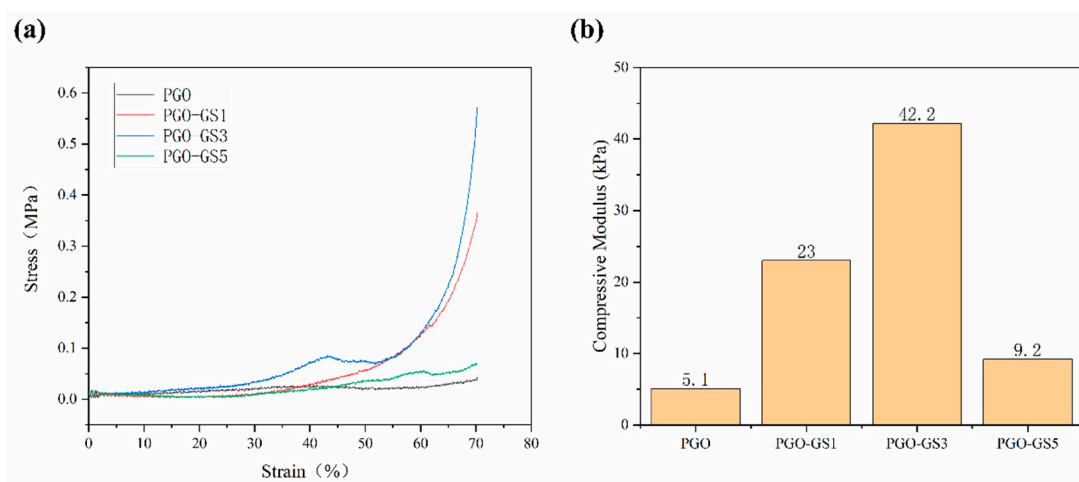
Figure 3. (**a**) The compression stress–strain curves of PGO and PGO-GS hydrogels. (**b**) The compressive modulus of PGO and PGO-GS hydrogels.

2.4. Conductive Properties of Hydrogels

Figure 4a shows the brightness of an LED when the hydrogel was connected to the displayed circuit. It can be seen that the conductivity of the PGO hydrogel improves with the increasing content of GO and SWNTs. Figure 4b shows the resistance curves for 500 measurements of the different hydrogels. It can be seen that the resistance of the hydrogel measured when it was first connected to the circuit has a large deviation. Therefore, the resistance values of the first 100 measurements were discarded, and only the last 400 measurements were kept to calculate the mean value and determine the standard deviation in this paper (the subsequent resistance measurements are treated in the same way). The conductivity of the PGO-GS3 hydrogel reached 29.6 mS/m, which is 1.5 times that of the PGO hydrogel. This is mainly attributed to the conductive network formed by the GO sheets and SWNTs inside the hydrogel. The increasing content of GO and SWNTs can significantly promote the density of the conductive network, resulting in higher

conductivity. However, when the sum of the two fillers divided by the mass of GEL is more than 4.5%, the growth rate of the conductivity is significantly reduced. This phenomenon may be caused by the uneven dispersion of GO and SWNTs.

Interestingly, we found that when the wires were placed on either side of the PGO and PGO-GS hydrogels, the brightness of the LED would gradually darken with the folding of the hydrogel (Figure 4c). Therefore, the electrical conductivity of the hydrogel was also tested at different degrees of bending (Table S1). When the distance between the two electrodes decreased from 5 cm to 1 cm, the conductivity of the PGO hydrogel decreased from 19.11 to 18.73 mS/m, and the conductivity of the PGO-GS3 hydrogel decreased from 29.13 to 26.60 mS/m. The variation range of the PGO-GS3 hydrogel is about 8.6%, which demonstrates the PGO-GS3 hydrogel's potential as a flexible, electronic sensing skin.
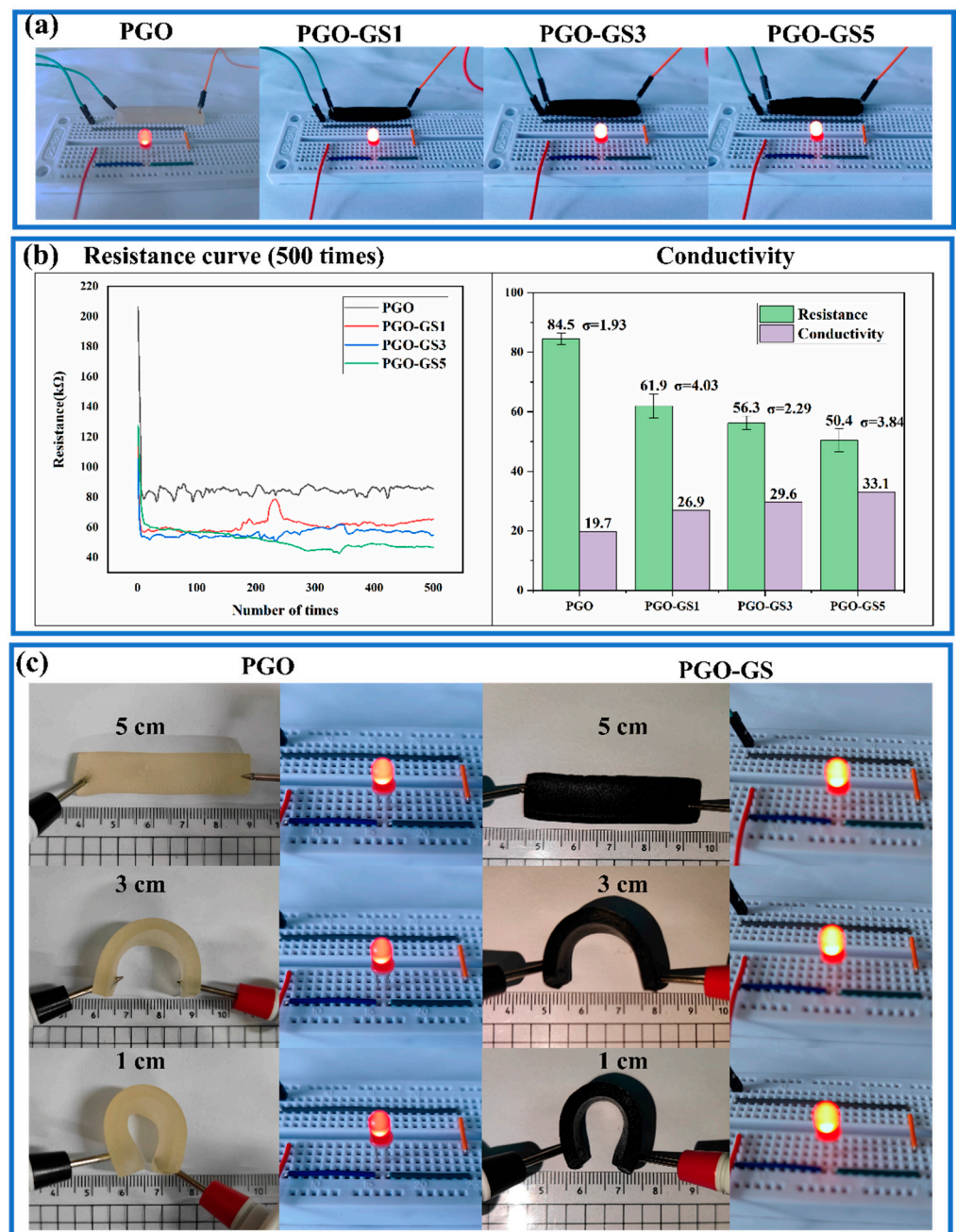
Figure 4. (**a**) The brightness of LED when hydrogel was connected to the circuit. (**b**) The conductivity and resistance of hydrogels. (**c**) The brightness of the LED when bending the hydrogel. (The applied voltage of all displayed circuits is 10 V.)

2.5. Self-Healing Property of Hydrogels

It can be seen that the PGO-GS3 hydrogel has superior comprehensive properties by analyzing the swelling, mechanical, and conductive properties of the different hydrogels. Therefore, the PGO-GS3 hydrogel was selected to evaluate the self-healing performance and other subsequent performances and applications.

Figure 5a shows that both the PGO and PGO-GS3 hydrogels have good self-healing properties. After 24 h of self-healing, both hydrogels were able to bear their own weights. After 48 h, although the cut marks were still visible, the hydrogels had completely healed and could withstand various tensile forces.
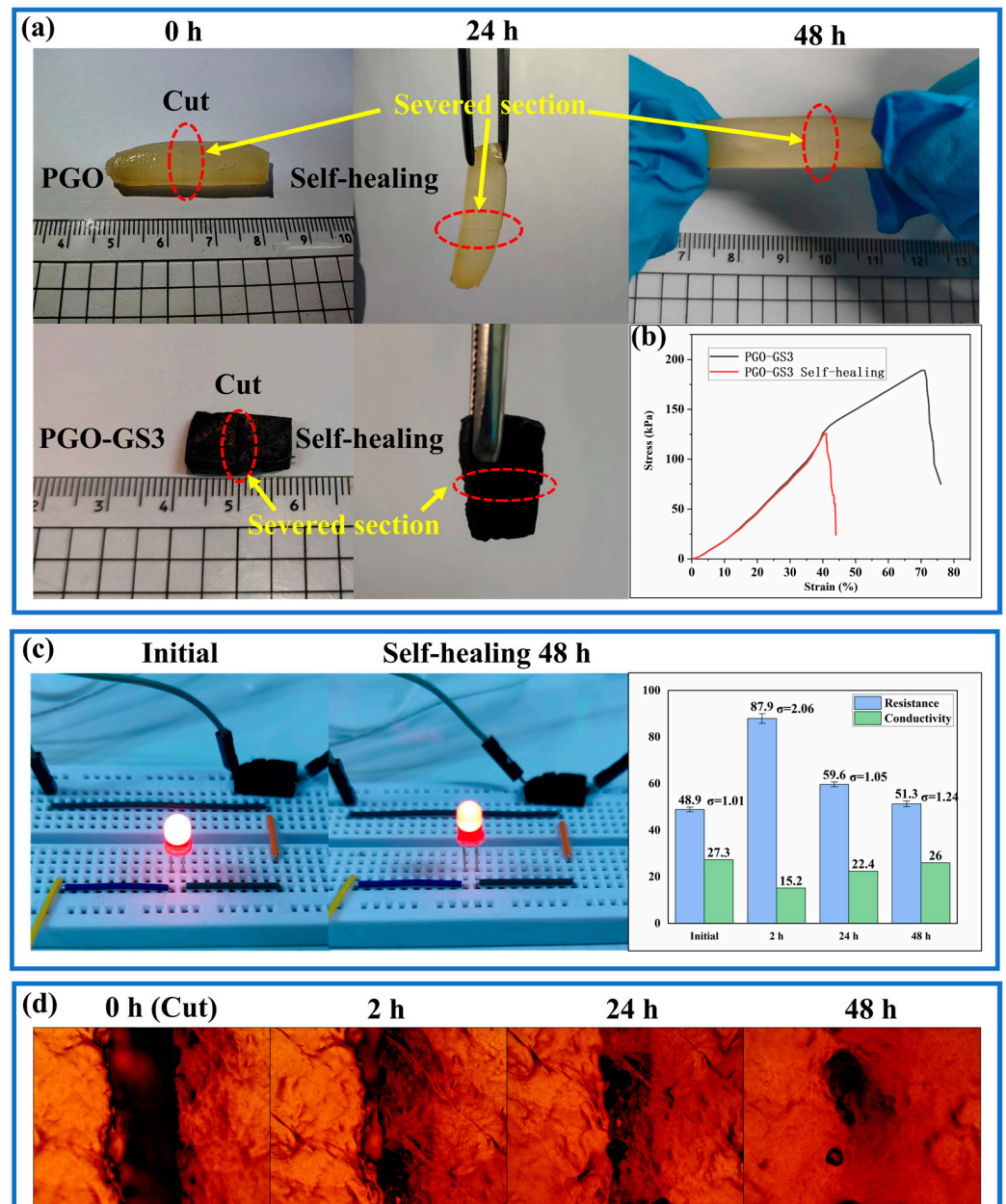
Figure 5. (**a**) Photos of the self-healing process of hydrogels. (**b**) The tensile curves of the initial hydrogel and the 48 h self-healing hydrogel (PGO-GS3). (**c**) Conductivity of initial hydrogel and the 48 h self-healing process of the hydrogel (PGO-GS3). (**d**) The self-healing process of the PGO hydrogel under optical microscope.

The typical stress–strain data of the original PGO-GS3 hydrogel and the self-healing hydrogel are shown in Figure 5b. After 48 h of healing, the fracture strength and elongation at break reached 0.13 MPa and 40.9%, respectively, which were 68% and 57% of the initial hydrogel (0.19 MPa and 71.2%). This is the result of hydrogen bonds and imine bonds formed between the molecular chains of PVA and GEL on the fracture's surface.

The conductivity-related self-healing performance of the hydrogels was also verified, as shown in Figure 5c. Although the brightness of the LED decreased slightly after 48 h of self-healing, its conductivity recovered to more than 95% of the initial value. This also suggests that the imine bonds and hydrogen bonds help the hydrogel reconstruct the network structure during the self-healing process.

For further investigation, the PGO hydrogel was selected to observe the self-healing process under an optical microscope (Figure 5d). It can be seen that most of the gaps between the cut areas of the PGO hydrogel disappeared after 48 h of self-healing.

2.6. Electronic Skin

To explore the ability of the PGO-GS3 hydrogel to monitor human movement and recognize speech, the PGO-GS3 hydrogel was attached to the fingers and throat of a subject to detect the signals generated by finger bending and speaking. Figure 6a shows the real-time resistance change of the hydrogel during finger bending. Obviously, the bending of fingers can sufficiently stimulate the hydrogel so as to generate regular electrical signals. In addition, the throat vibrations caused by human speech can also be accurately captured (Figure 6b–d). It can be seen from the comparison that the feedback signal of the PGO-GS3 hydrogel is different for different words, which proves that the PGO-GS3 hydrogel has the potential to be used in speech recognition.
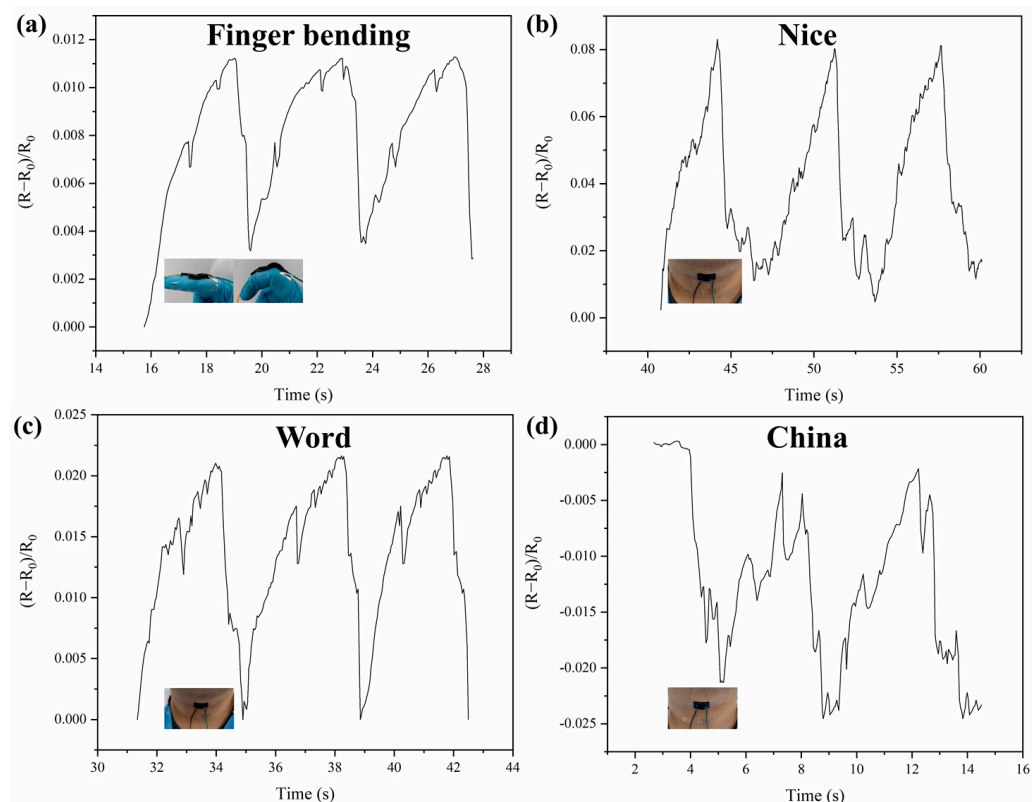
Figure 6. Sensing signals of encapsulated hydrogel corresponding to (**a**) finger bending, (**b**) the vocalization of the word "Nice", (**c**) the vocalization of the word "LOVE," and (**d**) the vocalization of the word "China".

2.7. Cytocompatibility

A CCK8 assay was performed to determine the L929 cells' viability after being cultured in 10% hydrogel leach liquor solution. The experimental results are shown in Table 2.

Table 2. The viability of cells incubated with hydrogel leach liquor for 48 h.

Group Name	Absorbance	Sur %
Blank group	0.35469	N/A
Control group	1.19736	100
PGO-GS3	0.99315	75.8
PGO	1.15768	95.3

Although the survival rate of the cells cultured in 10% leach liquor solution is lower than that of the control group, the cell survival rates in both groups are much higher than 50% after 48 h of incubation. This indicates that both the PGO and PGO-GS3 hydrogels have good cell capability.

As a comparison, the cell survival rate of PGO-GS3 group (95.3%) was significantly higher than that of PGO experimental group (75.8%). This indicates that the addition of GO and SWNTs has a potential effect on cell proliferation. In this study, the activity levels may be related to the good mechanical properties and porosity of the PGO-GS3 hydrogel.

Overall, the above biological evaluations prove that the PGO-GS3 hydrogel possess good potential for use as a biomaterial for flexible bionic electronic skin that does not cause cellular inflammation.

3. Conclusions

In this study, a series of conductive composite hydrogels were successfully constructed by introducing GO and SWNTs into a PVA/GEL/OSA ternary hydrogel system. The SA was successfully oxidized and formed dynamic imine bonds with the GEL, which gave the hydrogel good self-healing properties. The obtained self-healing properties restored 68% of the hydrogels' original breaking strength and over 95% of their electrical conductivity. The addition of PVA effectively improves the toughness of the hydrogels, and the introductions of GO and SWNTs effectively enhance the electrical and mechanical properties of the hydrogels. The compressive modulus and electrical conductivity of the PGO-GS hydrogel are 42.2 kPa and 29.6 mS/m, respectively, i.e., 8.2 and 1.5 times higher than those of pure PGO. In addition, the cytocompatibility tests not only demonstrated the good biocompatibility of the PGO-GS hydrogels but also showed that GO and SWNTs have a potentially positive effect on cell proliferation. Notably, PGO-GS conductive hydrogels can quickly capture external stimulations, including human movement and speech, and give correspondingly accurate and timely electrical signal feedback. Compared to similar studies [29,30,37], PGO-GS hydrogels have better self-healing properties (conductivity and tensile properties), higher electrical conductivity, and better biocompatibility. These properties indicate that PGO-GS hydrogels have promising applications in the field of electronic skin, such as voice recognition, human movement, and health monitoring.

4. Materials and Methods

4.1. Materials

GO and SWNTs were purchased from Jiacai Technology Co., Ltd. (Chengdu, China). Sodium alginate (SA) (1.05~1.15 Pa·S) was purchased from Fuchen Chemical Reagent Co., Ltd. (Tianjin, China). GEL (BR, jelly strength $\geq$ 220) was purchased from Qiansheng Biotechnology Co., Ltd. (Hefei, China). Sodium chloride (NaCl) (AR) was purchased from Sinopharm Chemical Reagent Co., Ltd. (Beijing, China). PVA (polymerization degree 1799, 98% alcoholysis), Ethanol (C_2H_6O) (99.7%), Sodium periodate ($NaIO_4$, AR, 99.5%), and Ethylene glycol ($C_2H_6O_2$) (GC, >99%) were obtained from McLean Biochemical Technology Co., Ltd. (Shanghai, China). Potassium bromide (KBr) was purchased from Tianguang

Optical Instrument Co., Ltd. (Tianjin, China). Deionized (DI) water was obtained using the pure water machine in our laboratory.

4.2. Preparation of OSA

The oxidation of SA was carried out according to a previously reported method, as shown in Figure 7a [42,43]. In brief, SA (10 g) was dispersed in ethanol (50 mL) in a water bath at 40 °C. Then, 50 mL $NaIO_4$ solution (5 g) was added into the SA solution to react for 4 h, which was put on a magnetic stirrer in the dark at 25 °C. Then, 7.5 mL of $C_2H_6O_2$ and 5 g of NaCl were added and quenched for 0.5 h under stirring. The sediment was filtered out through a vacuum filtration device. The final product was washed with C_2H_6O three times and then vacuum-dried at 35 °C for 24 h to obtain OSA.
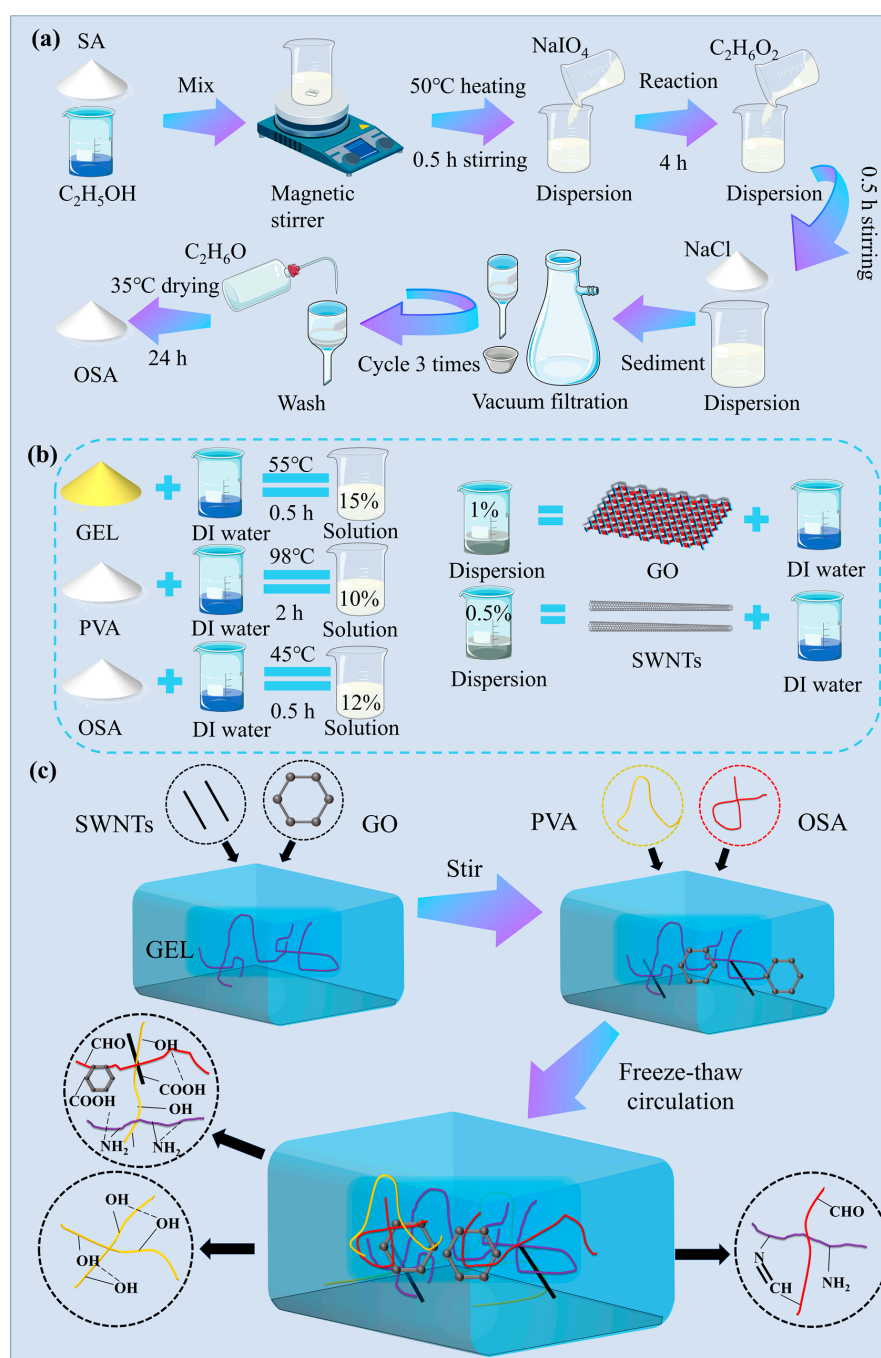
Figure 7. (**a**) Preparation process of OSA. (**b**) Mass fraction of each component solution of composite hydrogel. (**c**) Preparatory process for PGO-GS hydrogel.

4.3. Preparation of Hydrogel

In order to prepare PVA–GEL–OSA–GO–SWNT hydrogels with different compositions (Figure 7b,c), GEL (15 wt %) was dissolved in DI water at 55 °C and stirred for 0.5 h. The prepared OSA (12 wt %) was dissolved in DI water at 45 °C and stirred for 0.5 h. PVA (10 wt %) was dispersed in DI water in a 98 °C water bath with stirring for 2 h to form a solution. After defoaming at 20 °C for 5 h, 10 mL PVA solution was added to 10 mL GEL solution; then, the mixed solution was magnetically stirred at 40 °C for 0.5 h. Subsequently, the same volumes of GO (1 wt %) and SWNT (0.5 wt %) dispersions were added to PVA–GEL mixed solution in corresponding proportions and stirred for 1 h. Finally, 10 mL of OSA solution was added to the above mixed solution and stirred at 40 °C for 0.5 h. The final solution was poured into a mold and left at 20 °C for 1.5 h. Then, the mold was frozen at −20 °C for 12 h and thawed at 20 °C for 2 h, which is known as a freeze–thaw cycle. The freeze–thaw cycle was repeated 3 times to obtain PVA–GEL–OSA–GO–SWNT hydrogel. The hydrogel is named PGO-GSx, where x represents the mass fraction of GO relative to gelatin. Pure PVA–GEL–OSA hydrogel was prepared by the same method (it was named PGO hydrogel).

4.4. Characterization

4.4.1. Constituent Analysis

FT-IR spectroscopic measurements were performed using an infrared spectrometer (ALPHA II, BRUKER, Salbruken, GER). The hydrogel sample was placed in an oven (DGG-9140A; LINPIN, Shanghai, CHN) at 35 °C for 36 h to dehydrate it completely. Then, the sample was placed into an agate mortar and ground into powder by adding liquid nitrogen. Finally, the FT-IR spectrum of the sample was analyzed using the KBr method [44].

The diffraction patterns of PGO-GS hydrogels were detected by an X-ray diffractometer (D8 DISCOVER A25, BRUKER, Salbruken, GER) using Co K radiation. The range of 2θ was 5~90°. The scanning rate was 0.1°/s, and the scanning step was 0.02°.

4.4.2. Structural Analysis

The surface morphologies of hydrogels were observed by a scanning electron microscope (SEM) (TM4000PLUS, HITACHI, Tokyo, Japan). The hydrogel samples were freeze-dried for 24 h with a freeze dryer (TF-FD-27, Tianfeng, Shanghai, China), and then the surfaces of the samples were sprayed with gold for observation.

The density of hydrogels was calculated by dividing the mass of the freeze-dried hydrogel by its volume. Cylindrical hydrogels were obtained by molding and freeze-drying for 24 h. The diameter and height of each hydrogel were measured, using a vernier caliper to calculate the volume. Each sample was measured 5 times and the mean value was reported.

The porosity of hydrogels was measured according to the alcohol displacement method [45]. Briefly, the freeze-dried hydrogels were weighed (W_d) and immersed in anhydrous ethanol at 25 °C for 12 h. The wet hydrogels (W_w) were then weighed again. The porosity was determined by the following equation:

$$\text{Porosity} = \frac{W_w - W_d}{\rho V}$$

where ρ is the absolute ethyl alcohol density (0.789 g/cm^3), and V is the volume of freeze-dried hydrogel.

The swelling behavior of PGO-GS hydrogel was studied in phosphate buffer solution (PBS) at 25 °C. The freeze-dried hydrogels were immersed in the PBS (pH = 7.4) for 24 h. After the sample was taken out, the water on the swollen hydrogel's surface was wiped off with absorbent paper, and then the hydrogel was weighed with an electronic balance (PKM124ZH; OHAUS, Pine Brook, NJ, USA). The swelling ratio was calculated by the following equation:

$$\text{Swelling ratio} = (W_s - W_d)/W_d$$

where W_d and W_s are the weights of dried and swollen samples, respectively.

4.4.3. Mechanical Performance

The mechanical tests were carried out using a universal testing machine (CTM2500; Liangong, Dezhou, Shandong Province, China). The compressive mechanical properties of PGO-GS hydrogels were measured with cylindrical samples (H = 50 mm and d = 10 mm). The compressive speed was set as 1 mm/min and the compressive modulus was calculated from the approximate linear fitting values of the stress–strain curves within the strain range of 30~40%. The tensile test used to evaluate the self-healing property of PGO-GS3 was carried out with a rectangular sample (L = 50 mm, W = 12 mm, and H = 5 mm) at a speed of 5 mm/min.

In the previous specifications, L is the length of the hydrogel, W is the width of the hydrogel, H is the height of the hydrogel, and d is the diameter of the hydrogel. The meanings of the three letters provided below are the same.

4.4.4. Conductive Property Measurement

The conductivity of the hydrogel was determined through observing the brightness of an LED bulb in the entire circuit when the hydrogels with different deformations were connected. The circuit was powered by DC stabilized constant current power supply (SPD3303C, Dingyang Technology, Shenzhen, Guangdong Province, CHN).

The electric resistance of the hydrogel (L = 50 mm, W = 8 mm, and H = 4 mm) was tested with a digital source meter (Keithley 6500, Beaverton, OR, USA). The conductivity (σ) of the sample was calculated using the following formula:

$$\sigma = \frac{l}{Rs}$$

where l and s are the length and cross-sectional area of the hydrogel sample, respectively. R is the measured resistance.

4.4.5. Self-Healing Behaviors

In order to study the self-healing behavior of PGO-GS hydrogels at room temperature, the hydrogel samples were cut into two halves using a knife. Then, the two hydrogels were placed together without any external stimulation. After 48 h, the tensile stress–strain curves of the self-healing PGO-GS3 hydrogels (L = 20 mm, W = 12 mm, and H = 5 mm) were measured again with a universal testing machine. The self-healing process of the PGO hydrogel at different time points was observed using an orthostatic metallographic microscope (9XB-PC, Shangguang, Shanghai, CHN). The PGO-GS3 hydrogel is black and thus could not be observed under an optical microscope.

4.4.6. Cytocompatibility Test

Mouse epithelioid fibroblast cells (L929) were used to evaluate the biocompatibility of the hydrogels. All cell culture-related reagents were purchased from Bojin Biotechnology Co., Ltd. (Xi'an, Shaanxi Province, China).

Both PGO and PGO-GS3 hydrogel pieces (L = 5 mm, W = 5 mm, and H = 5 mm) were placed in a glass petri dish and sterilized under ultraviolet radiation for 4 h. Then, one part of PGO and PGO-GS3 hydrogels was immersed in 10 mL PBS for 48 h to extract the leach solution.

To test CCK8, 4 testing groups were created and each group included 10 wells of a 96-well plate. No cells were seeded in the first group for blank well absorption value measurements. The cells were seeded at a density of 7×10^4 cells/mL per well in the second, third, and fourth groups. For all groups, 90 μL cell media (first group) or cell suspension (other groups, ~6×10^3 cells per well) were added in each well. For each

well in all groups, each surrounding well was filled with 100 μL of PBS if it was empty. This ensured that all the wells in all groups were surrounded by wells filled with the same amount of solution. The cells were incubated at 5% CO_2 and 37 °C for 12 h for cell attachment. Then, the 10 μL PBS leach liquors of PGO and PGO-GS3 were added into each well in the third and fourth groups (PGO and PGO-GS3 experimental groups), respectively. A total of 10 μL of PBS was added into each well in the first (blank group) and the second group (control group).

After incubation for 48 h, the cell viability was evaluated through CCK-8 (EnoGene Biotechnology Co., Ltd., Nanjing, Jiangsu Province, China) assay. Briefly, 10 μL CCK-8 solution and 90 μL cell culture medium were added into each well and incubated at 37 °C for 3 h. The light absorbance at the wavelength of 450 nm was measured using a microplate reader (Multiskan Go, Thermal fisher, Massachusetts, USA) for each well to calculate the cell viability. The cell survival rate was calculated using the equation below:

$$\text{Sur } \% = \frac{(A_s - A_b)}{(A_c - A_b)} \times 100\%$$

where Sur % is the cell survival rate, A_s is the absorbance of the experimental group, A_b is the absorbance of the blank group, and A_c is the absorbance of the control group.

References

1. Tobin, D.J. Biochemistry of human skin—Our brain on the outside. *Chem. Soc. Rev.* **2006**, *35*, 52–67. [CrossRef]
2. Xu, K.; Lu, Y.; Takei, K. Multifunctional Skin-Inspired Flexible Sensor Systems for Wearable Electronics. *Adv. Mater. Technol.* **2019**, *4*, 1800628. [CrossRef]
3. Yang, T.; Xie, D.; Li, Z.; Zhu, H. Recent advances in wearable tactile sensors: Materials, sensing mechanisms, and device performance. *Mater. Sci. Eng. R Rep.* **2017**, *115*, 1–37. [CrossRef]
4. Chen, S.; Jiang, K.; Lou, Z.; Chen, D.; Shen, G. Recent Developments in Graphene-Based Tactile Sensors and E-Skins. *Adv. Mater. Technol.* **2018**, *3*, 1700248. [CrossRef]
5. Zhang, Y.; Zhang, L.; Cui, K.; Ge, S.; Cheng, X.; Yan, M.; Yu, J.; Liu, H. Flexible Electronics Based on Micro/Nanostructured Paper. *Adv. Mater.* **2018**, *30*, 1801588. [CrossRef]
6. He, Z.; Gao, B.; Li, T.; Liao, J.; Liu, B.; Liu, X.; Wang, C.; Feng, Z.; Gu, Z. Piezoelectric-Driven Self-Powered Patterned Electrochromic Supercapacitor for Human Motion Energy Harvesting. *ACS Sustain. Chem. Eng.* **2019**, *7*, 1745–1752. [CrossRef]
7. Zhao, J.; Zhang, C.; Zou, D.; Liu, X.; Cai, L.; Li, X.; Shi, M. A Structured Design for Highly Stretchable Electronic Skin. *Adv. Mater. Technol.* **2019**, *4*, 1900492. [CrossRef]

8. Zhang, Y.-F.; Guo, M.-M.; Zhang, Y.; Tang, C.Y.; Jiang, C.; Dong, Y.; Law, W.-C.; Du, F.-P. Flexible, stretchable and conductive PVA/PEDOT:PSS composite hydrogels prepared by SIPN strategy. *Polym. Test.* **2020**, *81*, 106213. [CrossRef]

9. Huang, H.; Han, L.; Fu, X.; Wang, Y.; Yang, Z.; Pan, L.; Xu, M. Multiple Stimuli Responsive and Identifiable Zwitterionic Ionic Conductive Hydrogel for Bionic Electronic Skin. *Adv. Electron. Mater.* **2020**, *6*, 2000239. [CrossRef]

10. Li, Z.; Zhu, M.; Shen, J.; Qiu, Q.; Yu, J.; Ding, B. All-Fiber Structured Electronic Skin with High Elasticity and Breathability. *Adv. Funct. Mater.* **2020**, *30*, 1908411. [CrossRef]

11. Nie, B.; Liu, S.; Qu, Q.; Zhang, Y.; Zhao, M.; Liu, J. Bio-inspired flexible electronics for smart E-skin. *Acta Biomater.* **2022**, *139*, 280–295. [CrossRef] [PubMed]

12. Zhang, J.; Li, J.; Cheng, W.; Zhang, J.-H.; Zhou, Z.; Sun, X.; Li, L.; Liang, J.-G.; Shi, Y.; Pan, L. Challenges in Materials and Devices of Electronic Skin. *ACS Mater. Lett.* **2022**, *4*, 577–599. [CrossRef]

13. Tran, V.V.; Lee, K.; Nguyen, T.N.; Lee, D. Recent Advances and Progress of Conducting Polymer-Based Hydrogels in Strain Sensor Applications. *Gels* **2023**, *9*, 12. [CrossRef]

14. Tang, L.; Wu, S.; Qu, J.; Gong, L.; Tang, J. A Review of Conductive Hydrogel Used in Flexible Strain Sensor. *Materials* **2020**, *13*, 3947. [CrossRef] [PubMed]

15. Hong, Y.; Lin, Z.; Luo, Z.; Jiang, T.; Shang, J.; Yang, Y. Development of conductive hydrogels: from design mechanisms to frontier applications. *Bio-Design Manuf.* **2022**, *5*, 729–756. [CrossRef]

16. Wei, H.; Wang, Z.; Zhang, H.; Huang, Y.; Wang, Z.; Zhou, Y.; Xu, B.B.; Halila, S.; Chen, J. Ultrastretchable, Highly Transparent, Self-Adhesive, and 3D-Printable Ionic Hydrogels for Multimode Tactical Sensing. *Chem. Mater.* **2021**, *33*, 6731–6742. [CrossRef]

17. Guo, Y.; Wei, X.; Gao, S.; Yue, W.; Li, Y.; Shen, G. Recent Advances in Carbon Material-Based Multifunctional Sensors and Their Applications in Electronic Skin Systems. *Adv. Funct. Mater.* **2021**, *31*, 2104288. [CrossRef]

18. Yang, J.; Sun, X.; Kang, Q.; Zhu, L.; Qin, G.; Chen, Q. Freezing-tolerant and robust gelatin-based supramolecular conductive hydrogels with double-network structure for wearable sensors. *Polym. Test.* **2021**, *93*, 106879. [CrossRef]

19. Jing, Y.; Wang, A.; Li, J.; Li, Q.; Han, Q.; Zheng, X.; Cao, H.; Bai, S. Preparation of conductive and transparent dipeptide hydrogels for wearable biosensor. *Bio-Design Manuf.* **2022**, *5*, 153–162. [CrossRef]

20. Chen, K.; Hu, Y.; Liu, M.; Wang, F.; Liu, P.; Yu, Y.; Feng, Q.; Xiao, X. Highly Stretchable, Tough, and Conductive Ag@Cu Nanocomposite Hydrogels for Flexible Wearable Sensors and Bionic Electronic Skins. *Macromol. Mater. Eng.* **2021**, *306*, 2100341. [CrossRef]

21. Hammock, M.L.; Chortos, A.; Tee, B.C.-K.; Tok, J.B.-H.; Bao, Z. 25th Anniversary Article: The Evolution of Electronic Skin (E-Skin): A Brief History, Design Considerations, and Recent Progress. *Adv. Mater.* **2013**, *25*, 5997–6038. [CrossRef]

22. Liu, C.; Huang, N.; Xu, F.; Tong, J.; Chen, Z.; Gui, X.; Fu, Y.; Lao, C. 3D Printing Technologies for Flexible Tactile Sensors toward Wearable Electronics and Electronic Skin. *Polymers* **2018**, *10*, 629. [CrossRef] [PubMed]

23. Nie, P.; Wang, R.; Xu, X.; Cheng, Y.; Wang, X.; Shi, L.; Sun, J. High-Performance Piezoresistive Electronic Skin with Bionic Hierarchical Microstructure and Microcracks. *ACS Appl. Mater. Interfaces* **2017**, *9*, 14911–14919. [CrossRef] [PubMed]

24. Wang, L.; Jiang, K.; Shen, G. Wearable, Implantable, and Interventional Medical Devices Based on Smart Electronic Skins. *Adv. Mater. Technol.* **2021**, *6*, 2100107. [CrossRef]

25. Zhang, Z.; Zheng, Z.; Zhao, Y.; Hu, J.; Wang, H. Highly stretchable porous composite hydrogels with stable conductivity for strain sensing. *Compos. Sci. Technol.* **2021**, *213*, 108968. [CrossRef]

26. Wen, N.; Jiang, B.; Wang, X.; Shang, Z.; Jiang, D.; Zhang, L.; Sun, C.; Wu, Z.; Yan, H.; Liu, C.; et al. Overview of Polyvinyl Alcohol Nanocomposite Hydrogels for Electro-Skin, Actuator, Supercapacitor and Fuel Cell. *Chem. Rec.* **2020**, *20*, 773–792. [CrossRef] [PubMed]

27. Peng, Z.; Zhong, W. Facile Preparation of an Excellent Mechanical Property Electroactive Biopolymer-Based Conductive Composite Film and Self-Enhancing Cellulose Hydrogel to Construct a High-Performance Wearable Supercapacitor. *ACS Sustain. Chem. Eng.* **2020**, *8*, 7879–7891. [CrossRef]

28. Wu, X.; Xie, Y.; Xue, C.; Chen, K.; Yang, X.; Xu, L.; Qi, J.; Zhang, D. Preparation of PVA-GO composite hydrogel and effect of ionic coordination on its properties. *Mater. Res. Express* **2019**, *6*, 075306. [CrossRef]

29. Wu, L.; Li, L.; Pan, L.; Wang, H.; Bin, Y. MWCNTs reinforced conductive, self-healing polyvinyl alcohol/carboxymethyl chitosan/oxidized sodium alginate hydrogel as the strain sensor. *J. Appl. Polym. Sci.* **2021**, *138*, 49800. [CrossRef]

30. Li, K.; Wang, J.; Li, P.; Fan, Y. Ternary hydrogels with tunable mechanical and self-healing properties based on the synergistic effects of multiple dynamic bonds. *J. Mater. Chem. B* **2020**, *8*, 4660–4671. [CrossRef]

31. Zhang, J.; Wang, Y.; Wei, Q.; Wang, Y.; Lei, M.; Li, M.; Li, D.; Zhang, L.; Wu, Y. Self-Healing Mechanism and Conductivity of the Hydrogel Flexible Sensors: A Review. *Gels* **2021**, *7*, 216. [CrossRef] [PubMed]

32. Deng, Z.; Wang, H.; Ma, P.X.; Guo, B. Self-healing conductive hydrogels: Preparation, properties and applications. *Nanoscale* **2020**, *12*, 1224–1246. [CrossRef] [PubMed]

33. Strandman, S.; Zhu, X.X. Self-Healing Supramolecular Hydrogels Based on Reversible Physical Interactions. *Gels* **2016**, *2*, 16. [CrossRef]

34. Zhang, J.; Wang, Y.; Wei, Q.; Wang, Y.; Li, M.; Li, D.; Zhang, L. A 3D printable, highly stretchable, self-healing hydrogel-based sensor based on polyvinyl alcohol/sodium tetraborate/sodium alginate for human motion monitoring. *Int. J. Biol. Macromol.* **2022**, *219*, 1216–1226. [CrossRef] [PubMed]

35. Chen, Y.; Lu, B.; Chen, Y.; Feng, X. Biocompatible and Ultra-Flexible Inorganic Strain Sensors Attached to Skin for Long-Term Vital Signs Monitoring. *IEEE Electron Device Lett.* **2016**, *37*, 496–499. [CrossRef]

36. He, Y.; Li, Y.; Sun, Y.; Zhao, S.; Feng, M.; Xu, G.; Zhu, H.; Ji, P.; Mao, H.; He, Y.; et al. A double-network polysaccharide-based composite hydrogel for skin wound healing. *Carbohydr. Polym.* **2021**, *261*, 117870. [CrossRef]

37. Zhang, L.; Wang, Z.; Xu, C.; Li, Y.; Gao, J.; Wang, W.; Liu, Y. High strength graphene oxide/polyvinyl alcohol composite hydrogels. *J. Mater. Chem.* **2011**, *21*, 10399–10406. [CrossRef]

38. Cong, H.-P.; Wang, P.; Yu, S.-H. Highly Elastic and Superstretchable Graphene Oxide/Polyacrylamide Hydrogels. *Small* **2014**, *10*, 448–453. [CrossRef]

39. Ionita, M.; Crica, L.E.; Tiainen, H.; Haugen, H.J.; Vasile, E.; Dinescu, S.; Costache, M.; Iovu, H. Gelatin–poly(vinyl alcohol) porous biocomposites reinforced with graphene oxide as biomaterials. *J. Mater. Chem. B* **2015**, *4*, 282–291. [CrossRef]

40. Lin, J.; Yao, X.; Basquiroto de Souza, F.; Sagoe-Crentsil, K.; Duan, W. Mechanisms of dispersion of nanoparticle-decorated graphene oxide nanosheets in aqueous media: Experimental and molecular dynamics simulation study. *Carbon* **2021**, *184*, 689–697. [CrossRef]

41. Atif, R.; Inam, F. Reasons and remedies for the agglomeration of multilayered graphene and carbon nanotubes in polymers. *Beilstein J. Nanotechnol.* **2016**, *7*, 1174–1196. [CrossRef] [PubMed]

42. Fan, L.-H.; Pan, X.-R.; Zhou, Y.; Chen, L.-Y.; Xie, W.-G.; Long, Z.-H.; Zheng, H. Preparation and characterization of crosslinked carboxymethyl chitosan–oxidized sodium alginate hydrogels. *J. Appl. Polym. Sci.* **2011**, *122*, 2331–2337. [CrossRef]

43. Wang, L.; Deng, F.; Wang, W.; Li, A.; Lu, C.; Chen, H.; Wu, G.; Nan, K.; Li, L. Construction of Injectable Self-Healing Macroporous Hydrogels via a Template-Free Method for Tissue Engineering and Drug Delivery. *ACS Appl. Mater. Interfaces* **2018**, *10*, 36721–36732. [CrossRef] [PubMed]

44. Geng, W.; Nakajima, T.; Takanashi, H.; Ohki, A. Analysis of carboxyl group in coal and coal aromaticity by Fourier transform infrared (FT-IR) spectrometry. *Fuel* **2009**, *88*, 139–144. [CrossRef]

45. Liu, Y.; Xiao, Y.; Cao, Y.; Guo, Z.; Li, F.; Wang, L. Construction of Chitosan-Based Hydrogel Incorporated with Antimonene Nanosheets for Rapid Capture and Elimination of Bacteria. *Adv. Funct. Mater.* **2020**, *30*, 2003196. [CrossRef]

Article

Hydroxyapatite Reinforced Polyvinyl Alcohol/Polyvinyl Pyrrolidone Based Hydrogel for Cartilage Replacement

Mallikarjun B. Jalageri * and **G. C. Mohan Kumar ***

Polymer Composites Laboratory, Department of Mechanical Engineering, National Institute of Technology Karnataka, Surathkal, Mangalore 575025, India
* Correspondence: mallikarjunbjalageri.187me008@nitk.edu.in (M.B.J.); mkumargc@nitk.edu.in (G.C.M.K.)

Abstract: Polyvinyl alcohol (PVA) and Polyvinyl Pyrrolidone (PVP) hydrogels are desirable biomaterials for soft tissue repair and replacement. However, the bio-inertness and poor cell adhesive potency of the PVA and PVP hinder the wide range of biomedical applications. In the present work, PVA and PVP were blended with a one-dimensional hydroxyapatite nanorod (HNr), and PVA/PVP/HNr composite hydrogel was synthesized by the freeze-thaw process. The developed hydrogels were characterized by Scanning Electron Microscope (SEM). The bio-ceramic nanohydroxyapatite content was optimized, and it was found that reinforcement improves mechanical strength as well as bioactivity. The compression strength values are 2.47 ± 0.73 MPa for the composite having 2 wt% of nanohydroxyapatite. The storage modulus was much higher than the loss modulus, which signifies the elastic dominancy similar to cartilage. Besides, the antimicrobial activity of nanohydroxyapatite reinforced PVA hydrogel towards bacterial species, *Escherichia coli* (*E. Coli*), *Staphylococcus aureus* (*S. aureus*) was satisfactory, and the in vitro biocompatibility response towards Human Mesenchymal stem cells(hMSC) after 72 h of culture confirms nanohydroxyapatite reinforced PVA/PVP hydrogels are the promising alternatives for next-generation cartilage substitutes.

Keywords: biomaterial; ceramic; freeze-drying; polymer; tissue

1. Introduction

Hydrogels are a three-dimensional water-swollen polymeric material, and these hydrogels are the first biomaterials used for the human body [1]. In recent years, hydrogels utilization increased due to the applicability of hydrogels in biomedical developments and their unique ability to engineer materials that closely match natural tissues such as artificial cartilage [2], intraocular and contact lenses [3], nucleus pulposus [4] and soft actuators [5]. Hydrogels are also used in pharma industries as a drug delivery vehicle, wound dressing, care products, etc. [6]. Hydrogels can be developed from synthetic, natural, or hybrid polymers. The development of hydrogel involves Physical and chemical cross-linking. Crosslinking can be formed in different ways, including solution casting, solution mixing, and interpenetrating network formation [7]. ide reactions such as unreacted pendant groups and entanglement lead hydrogels to exert less mechanical stability and delayed response to external stimuli. Revolutionary ideas in designing hydrogels exhibit numerous opportunities within biomaterials research—new thought associated with the design of hydrogels that enhance mechanical stability and porosity. Recently, quite a few developments have widened the applicability of hydrogel materials [8]. Moreover, there are three major approaches to enhancing hydrogels' mechanical stability and porosity, mainly by adding cross-linking agents, double network, or hybrid hydrogel synthesis, and reinforcing nanoparticles to the hydrogels.

Polyvinyl alcohol is a biocompatible, water-soluble polymeric synthetic material that has been used extensively in the fabrication of biomaterials due to its favorable properties such as nontoxicity, biocompatibility, and ease of fabrication [9]. PVA hydrogels synthesized via a freeze-thaw process and characterized to examine various physicochemical

properties are compared to meniscal and artificial cartilage [10]. These biomaterials can mimic the function of human tissue. Polyvinyl pyrrolidone is a hydrogel with distinct properties such as good water solubility, nontoxicity, and high viscoelastic strength, which improves the mechanical properties of PVP composites, and good quality biocompatibility. Polyvinyl pyrrolidone is a membrane additive and pore former agent used in biomedical applications [11]. PVA hydrogel has been identified as a fascinating and promising material for articular cartilage replacement. The most significant limitation of PVA hydrogels is that their mechanical properties are difficult to match the requirements of articular cartilage [12].

Polyvinyl alcohol hydrogels are excellent biomaterials for cartilage scaffolds due to their structural similarities with biological tissues and inherent hydrophilicity [13]. However, their bioinertness and increased flexibility severely limit their applications to mechanical strength-required fields [14]. To improve performance, an appropriate modification is required. As a result, numerous efforts have been made to develop high-strength hydrogels. For example, consider double network hydrogels [15,16], hydrophobic associated hydrogels [17], ionically crosslinked hydrogels [18], and nanocomposite hydrogels [19]. Furthermore, various metallic and ceramic reinforcements such as silver [20], titanium dioxide [21], calcium phosphate [22], and zirconium [23,24] have been incorporated to create mechanically robust hydrogels. PVA/PVP blend hydrogels have been extensively studied as cartilage replacement materials. Functional compressive mechanics of a PVA/PVP nucleus pulposus replacement [4]. Embedding a small quantity of PVP molecules into the PVA improves network stability via interchain hydrogen bonding between both the PVA hydroxyl group and the PVP carbonyl groups, increasing crystallinity and decreasing PVA hydrogel degradation [25]. The mechanical and tribological properties of the PVP/PVA hydrogels were significantly dependent on the amount of PVP content, according to the results of the developed PVP/PVA composite hydrogel by repeated freeze and thaw process [26]. The inclusion of PVP into the PVA hydrogel enhances its mechanical properties and reduces the friction coefficient, which makes it to be one of the most promising alternatives for artificial cartilage [27].

Many nanohydroxyapatite syntheses are currently limited to chemical methods, which may impact cell proliferation in vivo. Furthermore, most nanohydroxyapatite research focuses on orthopedic and dental implant coating, with very few studies on the morphological influence of reinforcement on soft tissue scaffolds [28]. Optimizing the morphology and particle size of bioceramics used in biomedical applications is critical. Developing one-dimensional hydroxyapatite nanorods is an effective method for improving hydroxyapatite's mechanical and biological properties. The polar modulus of elongated nanohydroxyapatite provides structural stability and a larger surface area in contact with osteoblasts. Furthermore, human bone is composed of rod-like nanohydroxyapatite with diameters of 20–50 nm and lengths of 100–300 nm. Under physiological conditions such as temperature, pH, and fluid composition, nano-hydroxyapatite is one of the most stable forms of calcium phosphate. It also has a larger surface area and high adversity, which aids in the adsorption and differentiation of osteoblast cells in a biological environment [29,30]. A thorough investigation has been made over calcium phosphate-based bioceramics due to their utilization in biomedical application (tissue engineering and pharmaceutical industries). Due to its favorable characteristics such as biocompatibility and osteoconductive, hydroxyapatite is regarded as the most promising biomaterial in orthopedic medicine. Its chemical composition is similar to that of natural bone [31].

Articular cartilage is a soft tissue layer covering diarthrodial joints' surfaces. Cartilage damage caused by aging or physical injury leads to joint diseases such as osteoarthritis [32]. Its advanced composition and architecture allow it to withstand complex joint stresses. When cartilage is injured, it loses its ability to self-heal, which leads to osteoarthritis (OA), which causes severe pain and mobility loss [33]. Articular cartilage injury is a chronic and growing issue that affects millions of people around the world. Polyvinyl alcohol (PVA) biomaterials are promising transplants because they have properties similar to soft tissue; however, their low mechanical resistance and durability, as well as their

inability to integrate with surrounding tissue, limit their application in this area [12]. Knee arthroplasty is a surgical procedure that uses cobalt-chromium alloys and high-density polyethylene to reconstruct a damaged knee. It has a few drawbacks, such as removing healthy bone during surgery for scaffold fixation, and if the first surgery fails, making the second attempt much more difficult. Nonetheless, cartilage regeneration is primarily intended to address three issues. Holds the compressive load first, then generates flow. Second, the reconstructed zone could induce stem cells in the subchondral bone. Third, the reconstructed zone promotes cartilage tissue regeneration by inducing the formation of osteoblasts, chondrocytes, and stromal cells from bone marrow [34,35]. There is an urgent need to create an advanced biomaterial that has the physical, mechanical, and biological properties of natural cartilage.

From our observation so far, very few reports were found on hydroxyapatite nanorod-reinforced PVA/PVP nanocomposite hydrogel for tissue-engineered cartilage scaffold. By taking into account, it was planned to synthesize hydroxyapatite nanorods using cuttlefish bone through a simple mechanochemical route. It was then blended with PVA/PVP to develop nanocomposite hydrogel using the freeze and thaw route. The main objective of this work was to investigate the influence of hydroxyapatite nanorods over the PVA/PVP-based double network hydrogel used to replace cartilage. The general idea behind this work is that the addition of phosphate group improves the mechanical property, bioactivity, and morphological characteristics of the PVA/PVP-based hydrogel.

2. Results and Discussion

2.1. Hydroxyapatite Nanorods Characterization

The morphology of the hydroxyapatite nanorods was analyzed using FESEM. Figure 1a exhibits nanorod structure and spread in various arrangements and has a diameter ranging from 100 nm to 600 nm was analyzed using Image J software. XRD spectrum demonstrates a hexagonal crystal system, a common form of calcium phosphate. The hydroxyapatite phase was verified with JCPDS CARD:09-432, and significant peaks were observed between 20–35°, which indicates the better crystallinity of hydroxyapatite as shown in Figure 1b.

(**a**)   (**b**)
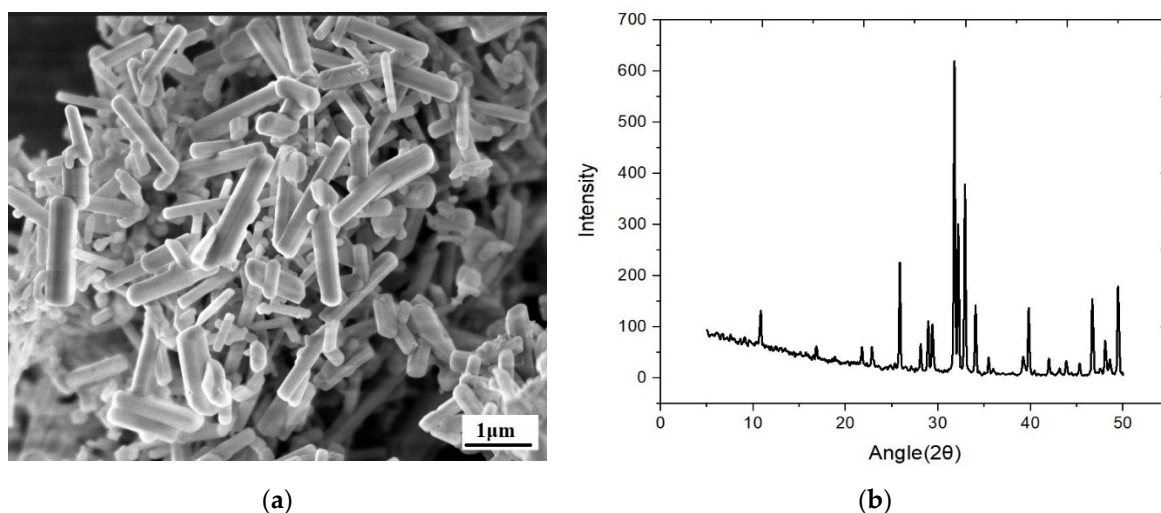
Figure 1. (**a**) SEM image of Hydroxyapatite nanorods, (**b**) X-ray diffraction spectrum.

2.2. Morphological Study of Nanocomposite Hydrogel

Figure 2 displays SEM images of the hydrogel scaffolds in a cross-sectional view. A porous structure with well-connected porosity is present in all lyophilized hydrogels, which is necessary for the cartilage scaffold to transport nutrients and metabolic wastes to the biological system. Table 1 provides an overview of the hydrogels' average porosity. The average porosity of PVA/PVP scaffolds is 84.77 ± 0.41. Incorporating Inorganic hydroxyapatite causes the ordered microstructure and pore boundaries in the composite

hydrogel to collapse and disappear. According to SEM pictures, adding hydroxyapatite to the PVA/PVP matrix transforms the microstructure from an undefined porous structure to a rounded porous structure. This porosity is beneficial for nutrient transfer and the extracellular matrix that provides for cell adhesion, cell-to-cell communication, and dedifferentiation. On the other hand, the structure, pore size, and porosity can be controlled.


(**a**)   (**b**)
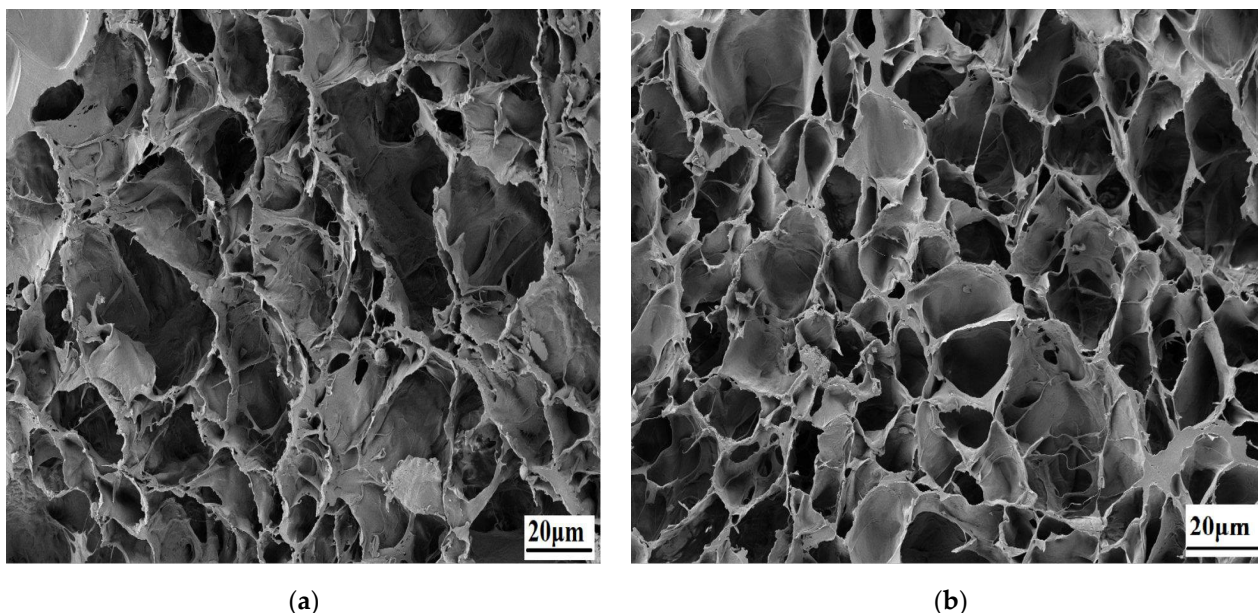
Figure 2. Scanning electron micrographs of (**a**) PVA/PVP and (**b**) PVA/PVP/2HNr hydrogel.

Table 1. PVA/PVP/HNr composite hydrogel physical properties.

Hydrogel	Swelling Ratio	Contact Angle (°)	Porosity (%)
PPH0%	209.03 ± 4.95	64.96 ± 0.94	84.77 ± 0.41
PPH1%	194.23 ± 4.45	60.25 ± 0.30	81.12 ± 0.24
PPH1.5%	184.07 ± 4.41	59.42 ± 0.79	76.12 ± 0.95
PPH2%	167.23 ± 4.97	53.77 ± 1.0	73.63 ± 0.51
PPH2.5%	139.16 ± 5.12	51.78 ± 1.4	71.12 ± 1.11
PPH3%	125.54 ± 3.13	48.60 ± 1.2	70.06 ± 0.41

2.3. Swelling Behaviour

Swelling studies are preliminary in vitro tests for the hydrogels; swelling studies are performed for PVA/PVP with different compositions of HNr reinforcement. Swelling strength is a very important metric for biomaterials in tissue engineering applications [36]. Pore size and interconnectivity play a key role in body fluid absorption, nutrient transport, and metabolite exchange [37]. Furthermore, swelling expands the pore volume, thus increasing the inner surface area/volume and increasing the likelihood of cell infusion from the surface to the interior. However, a higher swelling ratio negatively affects the mechanical stability of the scaffold. Composites with higher reinforcement concentrations have lesser swelling abilities, so the swelling strength gradually decreases, as shown in Figure 3. Previous research suggests that as reinforcement increases, water absorption will get decrease. This could be caused by secondary electrostatic bonds between the reinforcement and polymer structure [38]. We determined the porous structure of the scaffold with interconnected porosity using SEM analysis, as shown in Figure 2. The swollen hydrogel macroscopic image is shown in Figure 4. The abbreviations are used in the figures. PP0 denotes a combination of pure PVA/PVP similarly. PPH1%, PPH 1.5%, PPH2%, PPH 2.5%, PPH3% denotes PVA/PVP fortified with different concentrations of hydroxyapatite (1, 1.5, 2, 2.5, 3)%.
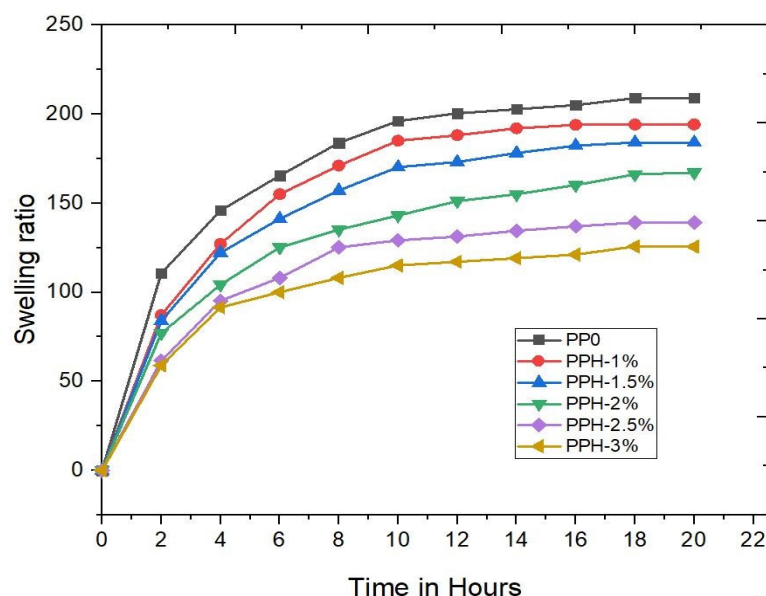
Figure 3. Swelling behaviors of PVA/PVP/HA hydrogels.

Figure 4. Macroscopic view of the swollen hydrogel.

Similarly, surface wettability affects the protein, essential nutrient adsorption, and cell differentiation on the surface scaffold. Surface wetting characteristics of PVA/PVP/HA composites are examined by contact angle measurement. The contact angle data are summarised in Table 1, and the reduction of contact angles is observed as an increment in reinforcement from 0 to 3%. Pure PVA/PVP hydrogel exhibit a contact angle of $64.96 \pm 0.94°$. The surface hydrophilicity of composite hydrogel increases with increases in the concentration of HA.this result reveals the hydrophilic nature of the hydrogel.

2.4. Compression Strength

The stress-strain graph of the hydrogel materials is depicted in Figure 5. the obtained graph corresponds to the nature of viscoelastic solids. The behavior of hydrogel under compression is strongly influenced by the polymer structure, which is similar to the cartilage under compression [38]. When a polymeric hydrogel is loaded, the load is absorbed, and the polymeric chains are reoriented, causing the interstitial fluid to flow out of the hydrogel.

During this, a load is sufficient for significant deformation. When the application of load continues, the reorientation leads to uniformity, and friction from interstitial fluids causes the gelly materials to harden and need extra effort to improve the additional strain. In the present data, adding 2 wt% of hydroxyapatite gives good compressive strength of (2.47 MPa), as shown in Figure 5. this result is matched with the compression strength of the healthy cartilage, which lies between 0.1 to 2 MPa [39]. Furthermore, hydrogels above 2%HA decrease compressive strength. This may be possible due to the agglomeration of hydroxyapatite nanoparticles. As the load is applied, the agglomeration point itself acts as

a crack generator; as loading increases, the crack propagates and damages the hydrogel sample. All the hydrogels stress, strain and young's modulus details are tabulated in Table 2.
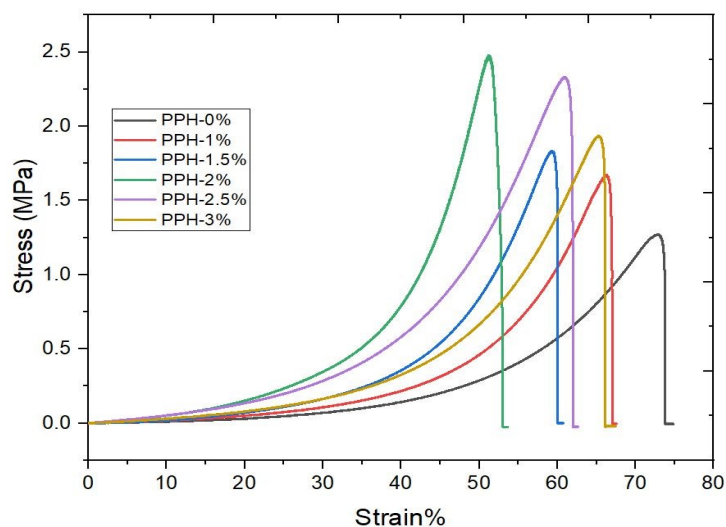
Figure 5. Mechanical characterization of composite hydrogels under unconfined compression.

Table 2. Properties of PVA/PVP/HNr hydrogel under unconfined compression.

Material Combination	Stress in MPa	Strain ε (%)	Modulus (E), in Mpa
PPH0%	1.27 ± 0.09	72.74 ± 0.44	0.24 ± 0.07
PPH1%	1.67 ± 0.15	66.19 ± 0.52	0.36 ± 0.06
PPH1.5%	1.83 ± 0.026	59.17 ± 1.83	0.44 ± 0.018
PPH2%	2.47 ± 0.73	51.11 ± 1.63	0.69 ± 0.034
PPH2.5%	2.33 ± 0.96	60.81 ± 1.39	0.54 ± 0.002
PPH3%	1.93 ± 0.74	65.15 ± 3.13	0.42 ± 0.003

2.5. Rheological Behavior of Hydrogel

The viscoelastic nature of the hydrogels was investigated by oscillatory frequency sweep using MCR 702 Anton-Paar rheometer. The storage modulus (G′) and loss modulus (G″) of hydrogels with Nano hydroxyapatite mass fractions are shown in the figures. The G′ (storage modulus) represents hydrogel sample elasticity, defined as energy stored due to elasticity, and G″ represents hydrogel sample viscosity. From the figures, it was observed that the storage modulus of all the samples is not dependent on the frequency. Still, the increment followed by increases in mass fractions of hydroxyapatite nanoparticles until 2%Hap then decrement observed until 3%Hap is the loss modulus (G″) situation in Figure 6b. Pan et al. reported similar output, indicating that storage and loss modulus increased to a maximum value when nano-hydroxyapatite mass fraction was 6%, then decreased as the hydroxyapatite increased to 9% [40].

This phenomenon is subjected relationship between rheometer angular frequency and chain segment oscillation. Storage modulus is independent of the frequency, implying macromolecular chains can keep up with changes in angular frequency, and the effect of hysteresis is significantly less. The trend of increasing storage modulus with increasing hydroxyapatite amount suggests that hydroxyapatite can adapt hydrogel to higher movement frequency, which can be used in extreme conditions. When the hydrogel is loaded with external loads, the matrix transfers the load to the hydroxyapatite nanoparticle, increasing the hydrogel's strength.

Figure 6a depicts the relationship between storage and loss modulus of PVA/PVP/HNr composites. The storage modulus (G′) for all hydrogels is always greater than the loss modulus (G″), indicating that composites are elastic in nature rather than in a fluid-like

state. The elastic modulus of all composite hydrogels is greater than that of PVA/PVP. Demonstrates that the matrix and reinforcement have a good interaction. The fluid in the nanopores, on the other hand, interlocks the polymer network and provides mechanical stiffness to resist shear deformation.
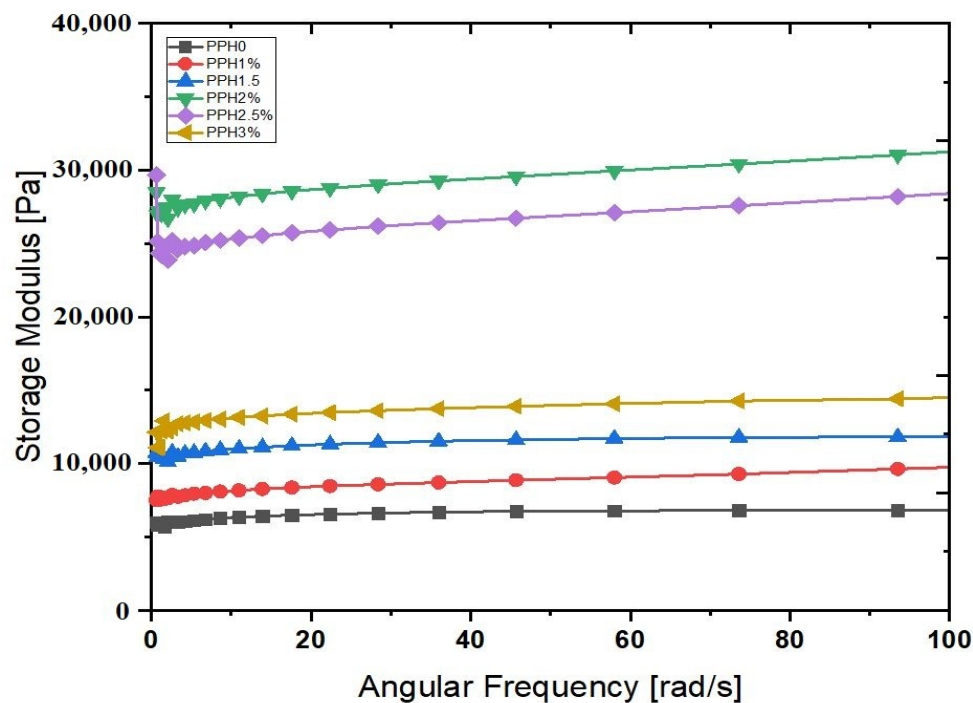

(**a**)
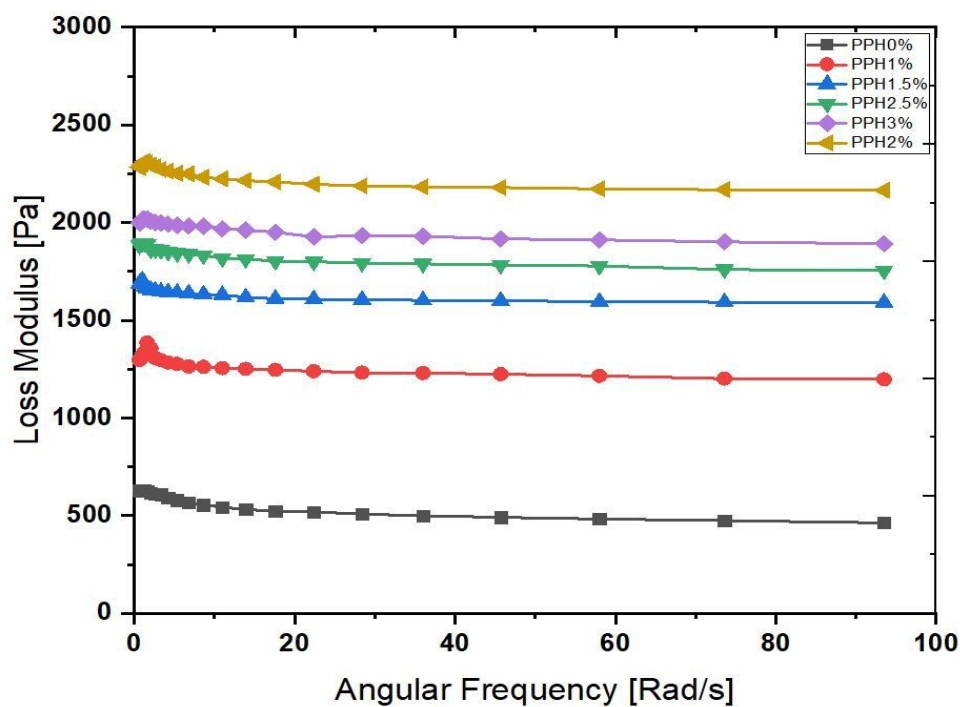
(**b**)

**Figure 6.** Rheological properties of PVA/PVP/HNr Composite hydrogel. (**a**) StorageModulus, (**b**) Loss modulus.

2.6. Antimicrobial and Cytotoxic Assay

The antimicrobial efficacy of bioactive material is crucial to resisting post-surgical infections and film formation. The growth inhibition of microbes on PVA/PVP and composite hydrogel are as shown in Figure 7. As expected, composite hydrogels PVA/PVP/2HNr show superior antimicrobial properties than the PVA/PVP hydrogel and they are more effective for *E. coli* than *S. aureus*, since 8% more inhibition was found for PVA/PVP/2HNr after 24 h of culture. This could be explained by the difference in the cellular cladding of Gram-negative and Gram-positive bacteria. Typically gram negative *E. coli* has a thin wall structure consisting of peptidoglycans and lipopolysaccharide, whereas Gram-positive bacteria such as *S. aureus* has a thick layer made of muco peptides murein and lipoteichoic acid, which resist the cytoplasmic leakage [41]. On the other hand, the Ca^{2+} ions of hydroxyapatite destabilize the cell membranes by reactive oxygen species (ROS) generation [42].
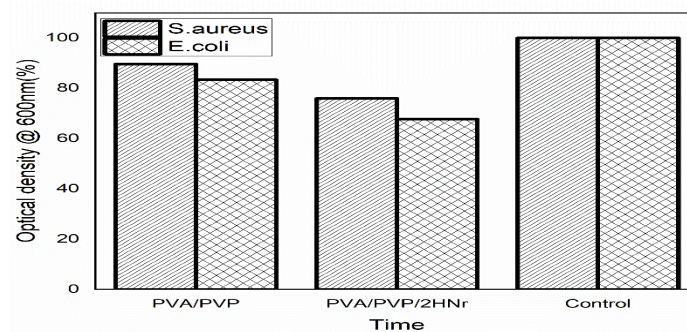
Figure 7. Antibiogram of PVA/PVP and PVA/PVP/2HNr hydrogel against Gram-negative *Escherichia coli*, Gram-positive *Staphylococcus aureus*.

The in-vitro toxicity assay for the PVA/PVP-based composite hydrogel towards the hMSC Cell line was investigated by the MTT assay method. Compared to negative control (cell control) the cell viability of the positive control is three times the minimum as shown in Figure 8. Hydrogels PVA/PVP and PVA/PVP/2HNr exhibit 89.71% and 92.32% Cell viability, respectively, and little enhancement in the cell viability observed in the composite hydrogel (PVA/PVP/2HNr) compared to pure PVA/PVPMaybe this enhancement is due to releasing bioactive ions (Ca^{2+} and PO_4^{3-}) from nanohydroxyapatite. The release of calcium and phosphate from nanohydroxyapatite increases the local concentration of Ca^{2+} and PO_4^{3-} ions, thus stimulating bone mineral formation on the counter surface. In addition, it helps to adsorb the extracellular matrix proteins, thus enhancing cell proliferation.
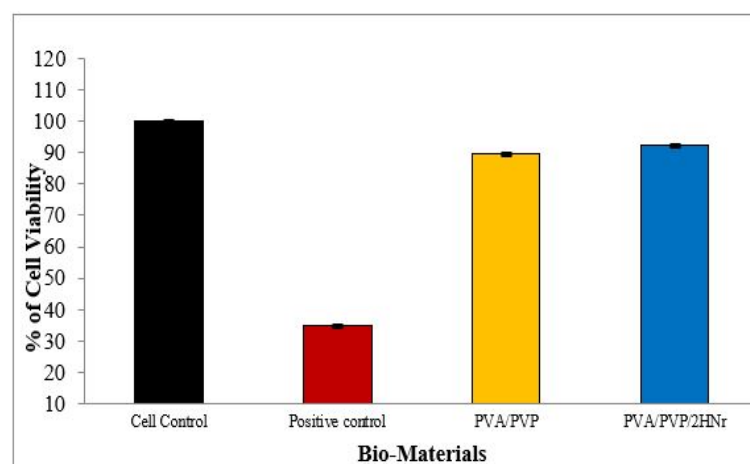
Figure 8. hMSC cell Viability of PVA/PVP and PVA/PVP/2HNr hydrogel after 72 h cell culture.

According to standards of biocompatibility evaluation, composite hydrogel did not show any apparent toxicity to hMSC cells, and its cell viability is more than 70%. These

cell lines exhibit fusiform morphology, as shown in Figure 9. All the cells are cultured and proliferated well in the culture plate after 72 h of incubation.
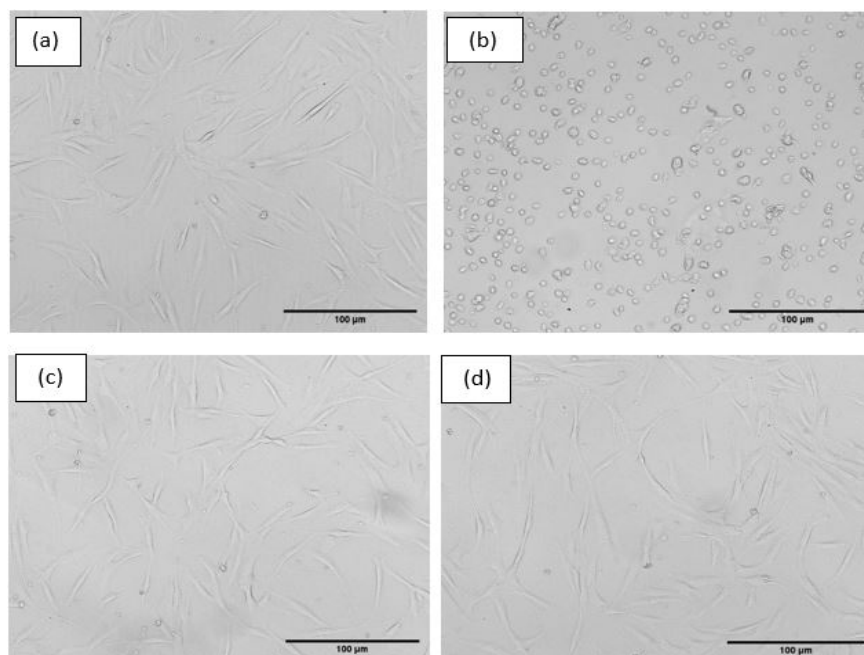
Figure 9. Inverted microscope images of hMSC Cells cultured for 72 h culture. (**a**) Untreated (**b**) Positive control, (**c**) PVA/PVP, and (**d**) PVA/PVP/2HNr.

3. Conclusions

In the present research, cuttlefish bone-derived hydroxyapatite was developed and hydroxyapatite reinforced PVA/PVP-based double network hydrogels were processed and characterized successfully to utilize as an engineered cartilage bioactive material. The hydroxyapatite shows one-dimensional rod-like morphology with a diameter ranging from 100 nm to 600 nm. All the developed hydrogels showed porous structure with interconnected porosity, which is an important index for cartilage scaffold. The swelling strength of the hydrogel is better than articular cartilage and has good hydrophilic properties. An important improvement in the mechanical property such as compression was found for composites having 2 wt% of nanohydroxyapatite and above 2 wt% of hydroxyapatite compressive strength decreases; this may be due to the agglomeration effect. The storage modulus value was much higher than the loss modulus, and the storage modulus value increases with an increase in the concentration of hydroxyapatite, implying that composites are dominant elastic hydrogels similar to mammalian soft tissues. The antimicrobial efficiency of the composite hydrogel was satisfactory and is nontoxic toward hMSC human mesenchymal stem cells, exhibiting more than 75% of cell viability after 72 h of culture. Agreeing with the above results and discussions, it can be concluded that the PVA/PVP/2%HNr composites are an excellent option in all prospective physical and mechanobiological properties. That could be a good candidate for next-generation biomaterial for articular cartilage and tissue engineering applications.

4. Materials and Methods

Polyvinyl alcohol hot water-soluble (Mw-60,000–125,000) was obtained from Himedia Ltd., Mumbai, India. Polyvinyl pyrrolidone K30 was obtained from Loba Chemie Pvt. Ltd., Mumbai, India. Cuttlefish bones were obtained from Blue Water Foods and Export Pvt. Ltd. in Mangalore, India, and orthophosphoric acid was obtained from India. The Human Mesenchymal Stem cells (Bone Marrow) cell line was obtained from Sigma Aldrich. All other chemicals and solvents were used as they were.

4.1. Hydroxyapatite Nano Rod Synthesis

The nanohydroxyapatite was prepared using cuttlefish bones. In brief, Cuttlefish bones were cleaned and boiled in water to remove fleshy residue attached over the surface and dried at 60 °C in an incubator for 10 h. Dried cuttlefish bones were crushed and powdered and sheived using a 100-micron siever 2 g of cuttlefish powder were weighed and added to 100 mL deionized water and stirred using a magnetic stirrer for 2 h at 60 °C. Orthophosphoric acid was added to uphold the stoichiometric ratio (Ca/P = 1.67). The stirring process continued for 10 h, and the obtained mixture was dried and calcined at 800 °C with a 5 °C/minute heating rate for 4 h [43]. Figure 1 shows the XRD and SEM of the hydroxyapatite.

4.2. PVA/PVP/HA Nanorods Hydrogel Sample Preparation

Hydrogels are synthesized by dissolving PVA and PVP separately in deionized water and stirring the solution with a magnetic stirrer until a clear solution is obtained. Later, both polymer solutions are mixed and stirred at 90 °C for 2 h to mix homogeneously. Meanwhile, hydroxyapatite nanorods with different mass fractions (1, 1.5, 2, 2.5, and 3 wt% HNr) were homogeneously distributed using a sonicator. Then it was mixed with a blended solution of PVA/PVP, and the stirring process was continued for the next 10 h at 80 °C. The gel was transferred to a Petri dish, and for cross-linking, prepared samples were processed for five freeze and thaw cycles at −23 °C for 10 h, freezing, and 4 h thawing at room temperature to produce PVA/PVP/HA hydrogels.

4.3. Morphological Analysis of PVA/PVP/Hap Nanorods Composite Hydrogel

Initially, hydrogels were lyophilized and fractured to study the hydrogel morphology. The cross-sectional section is used to determine the presence of porosity and the exact microstructure of the hydrogel. It is examined with a FESEM (HR-FESEM GEMINI 300, Carl Zeiss, Jena, Germany).

4.4. Swelling Studies

For the swelling study, lyophilized hydrogels weights were measured and noted as Initial weight (*Wi*) before immersing them in deionized water, and later weight of the hydrogel was measured after dipping them into deionized water until its weight reached an equilibrium state and the weight of the sample was measured for every 2 h till it reaches an equilibrium state. The swelling ratio can be calculated by considering the initial weight and final weight ratio mentioned below in Equation (1). The porosity of the hydrogel was evaluated as presented elsewhere. In brief, the samples were immersed in ethanol for 12 h, and the weight was measured (*W2*).then, the samples were removed, and the initial weight (*W1*) was measured by lyophilizing the swollen hydrogel. The porosity was calculated by Equation (2).

$$\text{Swelling rato} = \frac{(Wf - Wi)}{Wf} \times 100 \tag{1}$$

$$\text{Porosity} = \frac{(W2 - W1 - W3)}{(W2 - W3)} \times 100 \tag{2}$$

where *W3* is the weight of the ethanol remaining after removal of the swollen hydrogel sample.

4.5. Contact Angle Measurement

A contact angle analyzer was used to assess the wettability of the hydrogel samples, and 3 mm thick layered hydrogel samples were cast over the glass substrate to achieve flatness for the sample, which helps to measure the contact angle between the sample and droplet of the water. A liquid droplet was placed on a swollen flat hydrogel surface, and once the droplet reached an equilibrium, the contact angle was measured [44].

4.6. Compression Test

The unconfined compression strength was performed using a universal testing machine (Mec Mesin 10i–micro UTM) with 1 KN load cell, and the samples of size 10 mm in diameter and 7 mm in height were compressed up to 75% strain with the crosshead speed of 2 mm/min and stress vs. strain graph plotted for the test samples.

4.7. Rheological Study

The composite hydrogel was performed rheological testing at 37 °C using Anton and Par MCR 702 rheometer instrument. As well, an oscillatory frequency sweep analysis was performed at a frequency range of 0.1–100 Hz with a 1% fixed strain. The complex modulus of the components, such as storage and loss modulus, were investigated [45].

4.8. Antimicrobial Evaluation

The antimicrobial nature of the composite hydrogel against *E. coli* and *S. aureus* bacteria was evaluated by a growth inhibition assay. The bacterial culture was subcultured on a sterile broth, and the absorbance was measured (OD_i). Then 10 mg of the hydrogel sample was added to the appropriate well and incubated at 37 °C. After 24 h of incubation, the optical density of the inoculated culture was monitored (OD_f). The culture without the hydrogel was taken as a control, and the percentage inhibition of growth compared to the control was evaluated using Equation (3) [19].

$$Percentage\ growth\ inhibition = \frac{ODf}{ODi} \times 100 \tag{3}$$

4.9. Cytotoxicity Evaluation

The cytotoxicity of the gel sample was investigated by identifying the cell viability of the hMSC cell line using an MTT assay. In brief small 10 mm diameter discs 2 mm thick were sterilized using 70% ethanol and washed 3–4 times using water and PBS. Then samples were exposed to UV light for 20 min to ensure sterility of the sample. hMSC (Human Mesenchymal stem cells) 1000 µL of cell suspension containing 50,000 cells were seeded over the surface of the hydrogel and incubated on the plates for 72 h at 37 °C in 5% carbon dioxide media separately. Spent media was replaced by an MTT agent to the ultimate concentration of 0.5 mg/mL and incubated for a few hours. Reagents of MTT were removed, and add 100 µL of DMSO was gently stirred. The gyratory shaker will enhance the dissolution. In between, pipetting was done up and down to dissolve MTT formazan crystals in the dense culture. The cell viability was determined using the Equation (4) at 570 nm optical density.

$$\%\ of\ Cell\ Viability = \frac{Mean\ OD\ of\ sample\ @\ 570\ nm}{Mean\ OD\ of\ Control\ @\ 570\ nm} \times 100 \tag{4}$$

Statistics: All the quantitative results were obtained from three samples and data mean ± standard deviation. Statistical significance was calculated using the ANOVA Test. A value of $p < 0.05$ was considered as statistically significant.

References

1. Korah, L.V.; Anilkumar, G.; Thomas, S. Hydrogels, DNA, and RNA polypeptides for the preparation of biomaterials. In *Fundamental Biomaterials: Polymers*; Woodhead Publishing: Sawston, UK, 2018; pp. 85–104.
2. Mantha, S.; Pillai, S.; Khayambashi, P.; Upadhyay, A.; Zhang, Y. Smart Hydrogels in Tissue Engineering and Regenerative Medicine. *Materials* **2019**, *12*, 33. [CrossRef] [PubMed]
3. Li, L.; Yu, F.; Zheng, L.; Wang, R.; Yan, W.; Wang, Z.; Xu, J.; Wu, J.; Shi, D.; Zhu, L.; et al. Natural hydrogels for cartilage regeneration: Modification, preparation and application. *J. Orthop. Transl.* **2019**, *17*, 26–41. [CrossRef] [PubMed]
4. Joshi, A.; Fussell, G.; Thomas, J.; Hsuan, A.; Lowman, A.; Karduna, A.; Vresilovic, E.; Marcolongo, M. Functional compressive mechanics of a PVA/PVP nucleus pulposus replacement. *Biomaterials* **2006**, *27*, 176–184. [CrossRef]
5. Lee, Y.; Song, W.J.; Sun, J.Y. Hydrogel soft robotics. *Mater. Today Phys.* **2020**, *15*, 100258. [CrossRef]
6. Aswathy, S.H.; Narendrakumar, U.; Manjubala, I. Commercial hydrogels for biomedical applications. *Heliyon* **2020**, *6*, e03719. [CrossRef]
7. Bashir, S.; Hina, M.; Iqbal, J.; Rajpar, A.H.; Mujtaba, M.A.; Alghamdi, N.A.; Wageh, S.; Ramesh, K.; Ramesh, S. Fundamental concepts of hydrogels: Synthesis, properties, and their applications. *Polymers* **2020**, *12*, 2702. [CrossRef]
8. Kopecek, J. Hydrogel biomaterials: A smart future? *Biomaterials* **2007**, *28*, 5185–5192. [CrossRef]
9. Teodorescu, M.; Bercea, M.; Morariu, S. Biomaterials of Poly(vinyl alcohol) and Natural Polymers. *Polym. Rev.* **2018**, *58*, 247–287. [CrossRef]
10. Oliveira, A.S.; Seidi, O.; Ribeiro, N.; Colaço, R.; Serro, A.P. Tribomechanical comparison between PVA hydrogels obtained using different processing conditions and human cartilage. *Materials* **2019**, *12*, 3413. [CrossRef]
11. Teodorescu, M.; Bercea, M. Poly(vinylpyrrolidone)–A Versatile Polymer for Biomedical and Beyond Medical Applications. *Polym. Plast. Technol. Eng.* **2015**, *54*, 923–943. [CrossRef]
12. Gonzalez, J.S.; Alvarez, V.A. Mechanical properties of polyvinylalcohol/hydroxyapatite cryogel as potential artificial cartilage. *J. Mech. Behav. Biomed. Mater.* **2014**, *34*, 47–56. [CrossRef] [PubMed]
13. Li, F.; Wang, A.; Wang, C. Analysis of friction between articular cartilage and polyvinyl alcohol hydrogel artificial cartilage. *J. Mater. Sci. Mater. Med.* **2016**, *27*, 87. [CrossRef] [PubMed]
14. Chen, K.; Zhang, D.; Yang, X.; Cui, X.; Zhang, X.; Wang, Q. Research on torsional friction behavior and fluid load support of PVA/HA composite hydrogel. *J. Mech. Behav. Biomed. Mater.* **2016**, *62*, 182–194. [CrossRef] [PubMed]
15. Yan, X.; Yang, J.; Chen, F.; Zhu, L.; Tang, Z.; Qin, G.; Chen, Q.; Chen, G. Mechanical properties of gelatin/polyacrylamide/graphene oxide nanocomposite double-network hydrogels. *Compos. Sci. Technol.* **2018**, *163*, 81–88. [CrossRef]
16. Nurly, H.; Yan, Q.; Song, B.; Shi, Y. Effect of carbon nanotubes reinforcement on the polyvinyl alcohol–polyethylene glycol double-network hydrogel composites: A general approach to shape memory and printability. *Eur. Polym. J.* **2019**, *110*, 114–122. [CrossRef]
17. Gao, T.T.; Niu, N.; Liu, Y.D.; Liu, X.L.; Gao, G.; Liu, F.Q. Synthesis and characterization of hydrophobic association hydrogels with tunable mechanical strength. *RSC Adv.* **2016**, *6*, 43463–43469. [CrossRef]
18. Gierszewska, M.; Ostrowska-Czubenko, J. Chitosan-based membranes with different ionic crosslinking density for pharmaceutical and industrial applications. *Carbohydr. Polym.* **2016**, *153*, 501–511. [CrossRef]
19. Wei, Y.; Chen, K.; Wu, L. In situ synthesis of high swell ratio polyacrylic acid/silver nanocomposite hydrogels and their antimicrobial properties. *J. Inorg. Biochem.* **2016**, *164*, 17–25. [CrossRef]
20. Le Thi, P.; Lee, Y.; Thi, T.T.H.; Park, K.M.; Park, K.D. Catechol-rich gelatin hydrogels in situ hybridizations with silver nanoparticles for enhanced antibacterial activity. *Mater. Sci. Eng. C* **2018**, *92*, 52–60. [CrossRef]
21. Kumar, N.; Hazarika, S.N.; Limbu, S.; Boruah, R.; Deb, P.; Namsa, N.D.; Das, S.K. Microporous and Mesoporous Materials Hydrothermal synthesis of anatase titanium dioxide mesoporous microspheres and their antimicrobial activity. *Microporous Mesoporous Mater.* **2015**, *213*, 181–187. [CrossRef]
22. Dorozhkin, S. Calcium Orthophosphate-Containing Biocomposites and Hybrid Biomaterials for Biomedical Applications. *J. Funct. Biomater.* **2015**, *6*, 708–832. [CrossRef] [PubMed]
23. Plumlee, K.; Schwartz, C.J. Improved wear resistance of orthopedic UHMWPE by reinforcement with zirconium particles. *Wear* **2009**, *267*, 710–717. [CrossRef]
24. Jiang, H.; Zhang, G.; Feng, X.; Liu, H.; Li, F.; Wang, M.; Li, H. Room-temperature self-healing tough nanocomposite hydrogel crosslinked by zirconium hydroxide nanoparticles. *Compos. Sci. Technol.* **2017**, *140*, 54–62. [CrossRef]
25. Thomas, J.; Lowman, A.; Marcolongo, M. Novel associated hydrogels for nucleus pulposus replacement. *J. Biomed. Mater Res. A.* **2003**, *67*, 1329–1337. [CrossRef] [PubMed]

26. Kanca, Y.; Milner, P.; Dini, D.; Amis, A.A. Tribological properties of PVA/PVP blend hydrogels against articular cartilage. *J. Mech. Behav. Biomed. Mater.* **2018**, *78*, 36–45. [CrossRef]

27. Ma, R.; Xiong, D.; Miao, F.; Zhang, J.; Peng, Y. Friction properties of novel PVP/PVA blend hydrogels as artificial cartilage. *J. Biomed. Mater. Res. A* **2010**, *93*, 1016–1019. [CrossRef]

28. Turnbull, G.; Clarke, J.; Picard, F.; Riches, P.; Jia, L.; Han, F.; Li, B.; Shu, W. 3D bioactive composite scaffolds for bone tissue engineering. *Bioact. Mater.* **2018**, *3*, 278–314. [CrossRef]

29. NasiriTabrizi, B.; Fahami, A.; EbrahimiKahrizsangi, R.; Ebrahimi, F. New Frontiers in Mechanosynthesis: Hydroxyapatite– and Fluorapatite–Based Nanocomposite Powders. In *Nanocomposites: New Trends and Developments*; BoD–Books on Demand: Norderstedt, Germany, 2012.

30. Daryan, S.H.; Javadpour, J.; Khavandi, A.; Erfan, M. Morphological evolution on the surface of hydrothermally synthesized hydroxyapatite microspheres in the presence of EDTMP. *Ceram. Int.* **2018**, *44*, 19743–19750. [CrossRef]

31. Fiume, E.; Magnaterra, G.; Rahdar, A.; Verné, E.; Baino, F. Hydroxyapatite for biomedical applications: A short overview. *Ceramics* **2021**, *4*, 542–563. [CrossRef]

32. Patel, K.D.; Singh, R.K.; Lee, J.H.; Kim, H.W. Electrophoretic coatings of hydroxyapatite with various nanocrystal shapes. *Mater. Lett.* **2019**, *234*, 148–154. [CrossRef]

33. Patel, J.M.; Saleh, K.S.; Burdick, J.A.; Mauk, R.L. Bioactive Factors for Cartilage Repair and Regeneration:Improving Delivery, Retention, and Activity. *Acta Biomater.* **2019**, *93*, 222–238. [CrossRef]

34. Naahidi, S.; Jafari, M.; Logan, M.; Wang, Y.; Yuan, Y.; Bae, H.; Dixon, B.; Chen, P. biocompatibility of hydrogel-based scaffolds for tissue engineering applications. *Bio. Adv.* **2017**, *35*, 530–544. [CrossRef] [PubMed]

35. Sinha, A.; Guha, A. Biomimetic patterning of polymer hydrogels with hydroxyapatite nanoparticles. *Mater. Sci. Eng. C* **2009**, *29*, 1330–1333. [CrossRef]

36. Santosh Kumar, B.Y.; Isloor, A.M.; Anil, S.; Venkatesan, J.; Kumar, G.C.M. Calcium phosphate bioceramics with polyvinyl alcohol hydrogels for biomedical applications. *Mater. Res. Express* **2019**, *6*, 125404.

37. Nikolova, M.P.; Chavali, M.S. Recent advances in biomaterials for 3D scaffolds: A review. *Bioact. Mater.* **2019**, *4*, 271–292. [CrossRef] [PubMed]

38. Weizel, A.; Distler, T.; Schneidereit, D.; Friedrich, O.; Bräuer, L.; Paulsen, F.; Detsch, R.; Boccaccini, A.R.; Budday, S.; Seitz, H. Complex mechanical behavior of human articular cartilage and hydrogels for cartilage repair. *Acta Biomater.* **2020**, *118*, 113–128. [CrossRef]

39. Pan, Y.; Xiong, D.; Gao, F. Viscoelastic behavior of nano-hydroxyapatite reinforced poly(vinyl alcohol) gel biocomposites as an articular cartilage. *J. Mater. Sci. Mater. Med.* **2008**, *19*, 1963–1969. [CrossRef]

40. Mow, V.C.; Guo, X.E. Mechano-electrochemical properties of articular cartilage: Their inhomogeneities and anisotropies. *Annu. Rev. Biomed. Eng.* **2002**, *4*, 175–209. [CrossRef]

41. Siripatrawan, U.; Kaewklin, P. Food Hydrocolloids Fabrication and characterization of chitosan-titanium dioxide nanocomposite film as ethylene scavenging and antimicrobial active food packaging. *Food Hydrocoll.* **2018**, *84*, 125–134. [CrossRef]

42. Riaz, M.; Zia, R.; Ijaz, A.; Hussain, T.; Mohsin, M.; Malik, A. Synthesis of monophasic Ag doped hydroxyapatite and evaluation of antibacterial activity. *Mater. Sci. Eng. C* **2018**, *90*, 308–313. [CrossRef]

43. Chen, F.; Ni, Y.; Liu, B.; Zhou, T.; Yu, C.; Su, Y.; Zhu, X.; Yu, X.; Zhou, Y. Self-crosslinking and injectable hyaluronic acid/RGD-functionalized pectin hydrogel for cartilage tissue engineering. *Carbohydr. Polym.* **2017**, *166*, 31–44. [CrossRef] [PubMed]

44. Kumar, B.Y.; Isloor, A.M.; Kumar, G.C.; Asiri, A.M. Nanohydroxyapatite Reinforced Chitosan Composite Hydrogel with Tunable Mechanical and Biological Properties for Cartilage Regeneration. *Sci. Rep.* **2019**, *9*, 15957. [CrossRef] [PubMed]

45. Al-saud, L.M. Comparative evaluation of Rheological characteristics of Giomers and other Nano-flowable resin composites in vitro. *Biomater. Investig. Dent.* **2021**, *8*, 170–179. [CrossRef] [PubMed]

RGD-Functionalized Hydrogel Supports the Chondrogenic Commitment of Adipose Mesenchymal Stromal Cells

Cristina Manferdini [1,†] , Diego Trucco [1,2,3,†] , Yasmin Saleh [1], Elena Gabusi [1], Paolo Dolzani [1], Enrico Lenzi [1], Lorenzo Vannozzi [2,3] , Leonardo Ricotti [2,3] and Gina Lisignoli [1,*]

1 IRCCS Istituto Ortopedico Rizzoli, SC Laboratorio di Immunoreumatologia e Rigenerazione Tissutale, 40136 Bologna, Italy; cristina.manferdini@ior.it (C.M.); diego.trucco@santannapisa.it (D.T.); yasmin.saleh@ior.it (Y.S.); elena.gabusi@ior.it (E.G.); paolo.dolzani@ior.it (P.D.); enrico.lenzi@ior.it (E.L.)
2 The BioRobotics Institute, Scuola Superiore Sant'Anna, 56025 Pisa, Italy; lorenzo.vannozzi@santannapisa.it (L.V.); leonardo.ricotti@santannapisa.it (L.R.)
3 Department of Excellence in Robotics & AI, Scuola Superiore Sant'Anna, 56025 Pisa, Italy
* Correspondence: gina.lisignoli@ior.it
† These authors contributed equally to this work.

Abstract: Articular cartilage is known to have limited intrinsic self-healing capacity when a defect or a degeneration process occurs. Hydrogels represent promising biomaterials for cell encapsulation and injection in cartilage defects by creating an environment that mimics the cartilage extracellular matrix. The aim of this study is the analysis of two different concentrations (1:1 and 1:2) of VitroGel® (VG) hydrogels without (VG-3D) and with arginine-glycine-aspartic acid (RGD) motifs, (VG-RGD), verifying their ability to support chondrogenic differentiation of encapsulated human adipose mesenchymal stromal cells (hASCs). We analyzed the hydrogel properties in terms of rheometric measurements, cell viability, cytotoxicity, and the expression of chondrogenic markers using gene expression, histology, and immunohistochemical tests. We highlighted a shear-thinning behavior of both hydrogels, which showed good injectability. We demonstrated a good morphology and high viability of hASCs in both hydrogels. VG-RGD 1:2 hydrogels were the most effective, both at the gene and protein levels, to support the expression of the typical chondrogenic markers, including collagen type 2, SOX9, aggrecan, glycosaminoglycan, and cartilage oligomeric matrix protein and to decrease the proliferation marker MKI67 and the fibrotic marker collagen type 1. This study demonstrated that both hydrogels, at different concentrations, and the presence of RGD motifs, significantly contributed to the chondrogenic commitment of the laden hASCs.

Keywords: adipose mesenchymal stromal cells; hydrogels; chondrogenic differentiation; RGD motif; hydrogel characterization; cartilage regeneration

1. Introduction

The degeneration of articular cartilage due to trauma, osteoarthritis, or aging is a common joint disorder, with a high incidence worldwide [1,2]. It has been reported that the articular cartilage has limited intrinsic self-healing capacity, mainly due to its avascular and aneural nature [3]. Different clinical treatments, such as autologous chondrocyte implantation, mosaicplasty, and microfracture, have been used for inducing articular cartilage regeneration [4]. However, these techniques show limitations since they do not permit effective long-term cartilage regeneration and do not assure the formation of a fully differentiated articular cartilage structure, thus requiring the development of alternative strategies [5].

Tissue engineering approaches represent a promising alternative for cartilage regeneration and repair [6–8]. Hydrogels are among the most versatile kinds of materials used for various tissue engineering applications, since they can be engineered into almost any shape and size [9,10]. They can also be functionalized or enriched with micro/nanofillers

for building composite hydrogels, giving them improved properties tailored to specific applications [11,12]. In general, hydrogels represent hydrophilic 3D networks composed of water-soluble natural (e.g., polysaccharides and proteins) and/or synthetic polymers crosslinked by chemical or physical methods to form a water-insoluble matrix [13,14]. Different from hydrogels, aerogels are porous materials obtained when the liquid phase of a hydrogel is replaced by a gas, while preserving the internal structure and the surface area of the initial hydrogel [15–17]. They have been proven to provide highly desirable 3D environments for the regeneration of the cartilaginous tissue, as shown by in vitro and in vivo studies [18–21]. Hydrogels are viscoelastic materials, and their mechanical properties are an important requirement for engineering cell functions, since their tuning can improve mechanosensitive signaling. In fact, matrix stiffness, permeability, swelling ability, and degradation provide a peculiar biomimetic environment able to create a niche suitable to drive cell migration, adhesion, proliferation, and chondrogenic differentiation [22]. These properties, associated with other factors (i.e., seeding conditions, hypoxia), modulate the differentiation processes [23–25].

The use of injectable and in situ-forming hydrogels enables the treatment of irregular cartilage defects and a proper alignment with the surrounding tissues, characteristics that make them superior to 3D-structured scaffold-based approaches [26,27]. Meanwhile, from the clinical viewpoint, implantation surgery can be avoided and replaced by a simple, minimally invasive injection [26,28]. Moreover, bioactive molecules or cultured cells can simply be incorporated into the hydrogel precursors before they are ready for injection, or 3D bioprinted [29–31].

Mesenchymal stromal cells (MSCs) have shown interesting results in the field of cartilage regeneration, mainly due to their accessibility, immunomodulatory and pro-regenerative capabilities, and chondrogenic differentiation potential [32–35]. It has been shown that MSCs from various origins, combined with scaffold materials, have great potential in the regeneration of cartilage, in both animal models and in humans, as suggested by recent clinical trials [27,28,30,36]. It has been recognized that MSCs, laden in natural or synthetic hydrogels, create a suitable environment for inducing their cellular differentiation [37].

Recently, it has been shown that VitroGel® (VG) hydrogels have the potential to mimic the cartilage extracellular matrix (ECM) [38]. This hydrogel can also provide binding sites for cell adhesion, thanks to the functionalization with arginine-glycine-aspartic acid (RGD) motifs, which is a well-known tri-peptide able to promote cell attachment and, at the same time, favor cell-matrix interactions by enhancing cellular function, like cell proliferation, migration, and differentiation [39,40]. It has been shown that the RGD motif is a crucial component of adhesive proteins in the ECM, working through integrin transmembrane receptors by transmitting the cell survival signaling within the cells [41]. However, it has been shown that this tri-peptide exerts controversial issues in cartilage tissue engineering [42]. It has been demonstrated that the hydrogel modified with RGD peptide (VG-RGD) can be easily injected for the treatment of the intervertebral disc in rats, promoting the proliferation and differentiation of nucleus pulposus (NP)-derived MSCs (NPMSCs), and also promoting the NPMSC's long-term retention and survival in the degenerated intervertebral disc, with the formation of a neo-ECM [38].

The chondrogenic commitment of human adipose-derived mesenchymal stromal cells (hASCs) in VG hydrogels has been never investigated before. The novelty of the study is to gain new insight into the microenvironment fostered by natural hydrogels, by investigating the 3D hydrogel environment created by VG without (VG-3D) and with RGD (VG-RGD) motif on the chondrogenic differentiation of encapsulated hASCs for the potential treatment of cartilage defects.

2. Materials and Methods

2.1. Materials

VG-3D and VG-RGD hydrogels were both purchased from Well Bioscience (North Brunswick, NJ, USA) and prepared following the manufacturer's protocol. Briefly, the VG-3D and VG-RGD solutions were directly mixed at room temperature (RT) with the Dilution Solution Type 1® (The Well Bioscience, North Brunswick, NJ, USA) at the ratio of 1:1 and 1:2 to obtain two different hydrogel formulation. Then, Dulbecco Modified Eagle Medium (DMEM) (Life Technologies, Bleiswijk, The Netherlands) was added to each pre-crosslinked solution at the ratio of 4:1 (pre-crosslinked solution: DMEM) at RT. Four different combinations (VG-3D 1:1, VG-3D 1:2, VG-RGD 1:1, VG-RGD 1:2) were analyzed. Sodium alginate powder (Sigma-Aldrich Merck, Saint Louis, MO, USA) was used as the control hydrogel.

2.2. Experimental Plan

The experimental workflow for this study is shown in Figure 1. Briefly, the VG hydrogels raw materials (Figure 1a) were characterized through FTIR analysis. Then, the rheological and mechanical properties of hydrogels (Figure 1b) were evaluated and the protein diffusivity was tested. hASCs were analyzed in terms of antigenic profile and differentiation capabilities (Figure 1c). Then, hASC-laden hydrogels (Figure 1d) were analyzed at two different time points to assess cell distribution, viability, cytotoxicity, and metabolic activity. Finally, the chondrogenic differentiation of hASCs encapsulated in hydrogels (Figure 1d) was evaluated through molecular biology assays and immunohistochemical staining.
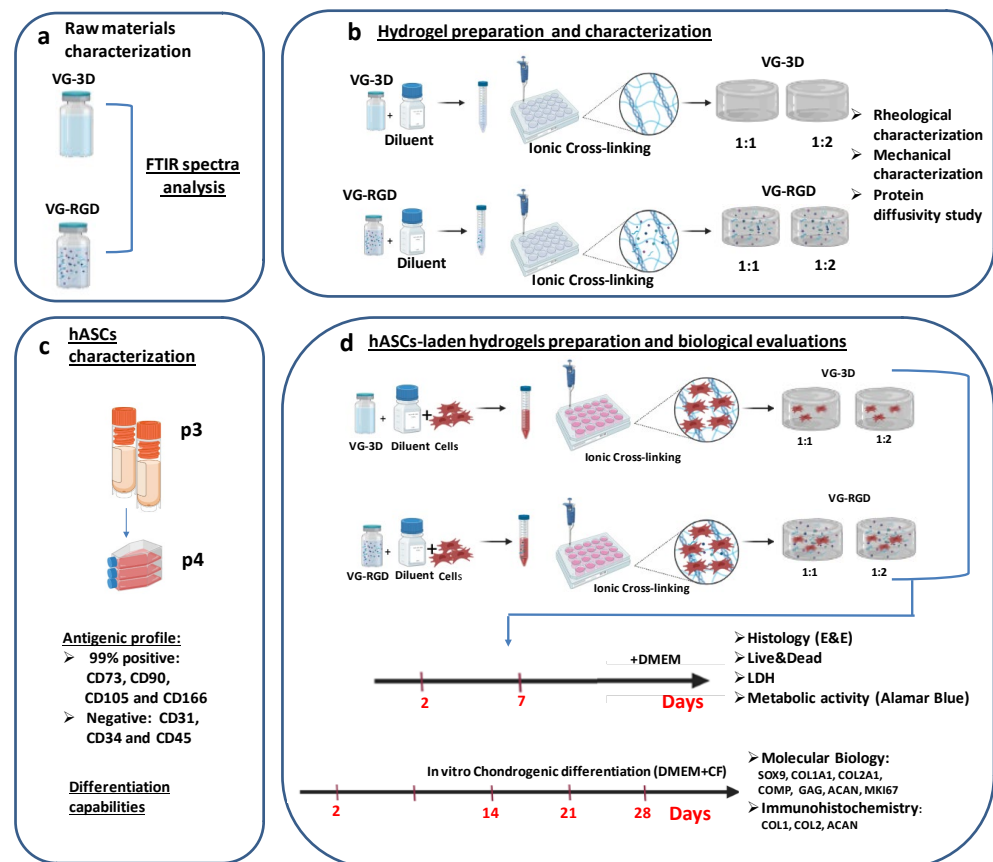
Figure 1. Depiction of the experimental plan: (**a**) characterization of raw materials through FTIR analysis; (**b**) evaluation of the rheological and mechanical properties of hydrogels and protein diffusivity

evaluation; (**c**) characterization of the hASCs in terms of antigenic profile and differentiation capabilities; (**d**) biological analysis to assess cell distribution, viability, cytotoxicity and metabolic activity, and chondrogenic assessment evaluated through molecular biology assays and immunohistochemical staining.

2.3. Raw Materials Characterization

2.3.1. FTIR Analysis

Fourier Transform Infrared Spectroscopy (FTIR) was used to characterize the presence of specific chemical groups in the VG-3D and VG-RGD hydrogels (Figure 1a). VG-3D and VG-RGD (300 μL) solutions were dehydrated using a freeze dryer (Labconco, FreeZone 2.5 Plus, Kansas City, MO, USA) for two days. VG-based material powders were analyzed and compared with sodium alginate powder. All FTIR spectra were obtained in the wavenumber range from 4000 to 600 cm^{-1} during 64 scans, with 4 cm^{-1} resolutions (Shimadzu IRAffinity-1, Duisburg, Germany). The FTIR spectra were plotted using OriginPro 8.5 (OriginLab, Northampton, MA, USA).

2.3.2. Hydrogel Preparation and Characterization

Rheological Characterization

The rheological properties of VG-3D and VG-RGD hydrogels were measured at 25 °C using a rheometer (Anton Paar MCR-302, Graz, Austria) with a plate-plate geometry (diameter: 25 mm, distance gap: 1 mm). The flow behavior was measured on all blends immediately after mixing with DMEM for shear rates ranging from 0.1 to 1000 s^{-1} in rate-controlled mode by selecting 10 points for each decade. The viscosity was investigated to model the viscosity of the materials according to the following power law [43]:

$$\eta = K\dot{\gamma}^{n-1} \tag{1}$$

where η is the dynamic viscosity, $\dot{\gamma}$ is the fluid shear rate, and K and n are the consistency index and the flow behavior index, respectively. Through linear interpolation, K and n for both VG-3D and VG-RGD hydrogels were determined and used to model the shear stress applied to cells during the injection (e.g., using a 26 G needle) following the model for non-Newtonian fluids [44].

Mechanical Characterization

To assess mechanical properties, 300 μL of VG-3D and VG-RGD solutions were gently poured into polydimethylsiloxane (PDMS) molds (diameter: 10 mm, height: 3 mm). After 20 min of stabilization at RT to let the solution crosslink, a further 200 μL of DMEM was placed over the hydrogels. Then, samples were incubated overnight at 37 °C and 5% CO_2. The mechanical characterization was performed the day after the samples' preparation on all four groups of crosslinked hydrogels (n = 6/group). The elastic modulus was measured by performing uniaxial compression with an Instron Mechanical Testing System (model 2444, Instron, Norwood, MA, USA) equipped with ±10 N load cell at a compression rate of 1 mm/min until reaching the hydrogel breaking point, as previously reported [45].

Protein Diffusivity Study

Albumin from bovine serum (BSA) conjugated with FITC (Invitrogen, FITC-BSA, Carlsbad, CA, USA) was tested to investigate the protein diffusion in VG-3D and VG-RGD hydrogels. FITC-BSA solution (1 mL, concentration: 100 μg/mL) was poured onto the upper surface of each crosslinked hydrogel. After 30 min, the hydrogels were washed with phosphate buffer saline (PBS 1x, Corning) 3 times for 5 min at 37 °C to remove the residual fluorescent dye. Controls (CTR-3D and CTR-RGD) without FITC-BSA were also used to verify the hydrogel autofluorescence. The cross-sectioned surface was observed with a confocal laser scanning microscope (Nikon Eclipse Ti, Tokyo, Japan) at the FITC wavelength (488 nm).

2.4. hASCs Characterization

2.4.1. Cell Culture and Phenotypic Characterization of hASCs

hASCs were purchased from Lonza (Morrisville, NC, USA (n = 5) and were expanded by seeding 7500 cells/cm^2 in T150 culture flask and culturing in α-MEM containing 5% isogrowth (IsoCellsGROWTH, Euroclone, Pero, Italy) and 1% penicillin/streptomycin (Life Technologies) at 37 °C in 5% CO$_2$ incubator. Before hydrogel encapsulation (Figure 1c), hASCs were phenotypically characterized for the CD markers CD31, CD34, CD45, CD73, CD90, CD105, and CD166, as we previously reported [46], and were analyzed for differentiation capabilities by using specific osteogenic and chondrogenic mediums, as we previously described [34,46] to check that they satisfied the "minimal criteria for defining multipotent MSCs," as previously reported [47].

2.4.2. hASCs-Laden Hydrogel Preparation and Biological Evaluations

VG-3D and VG-RGD hydrogels were prepared according to the VitroGel$^®$ protocol guidelines indicated by the company and following a defined workflow (Figure 1d). Briefly, both hydrogels were first diluted with the Dilution Solution Type 1$^®$ (1:1 and 1:2) at RT. Then, the hydrogel dilution was mixed with the ASCs (2×10^6 cell/mL) at a 4:1 ratio. Next, 300 μL of the mixture was gently transferred into the cell crown (Scaffdex, Finland), and inserted into the 24-well plates. After 20 min of stabilization at RT, a further 200 μL of DMEM was placed over the hydrogel.

Before testing the chondrogenic differentiation, hydrogels-loaded hASCs were cultured for 2 and 7 days in DMEM and evaluated for cell distribution, cell viability, cytotoxicity, and metabolic activity.

2.4.3. Histology

On days 2 and 7, VG-3D and VG-RGD hydrogel-loaded ASC were fixed in 10% formaldehyde in DPBS for 40 min, washed in DPBS, dehydrated in ethanol, and embedded in paraffin. Sections of 5 μm were cut and stained with hematoxylin-eosin (Bioptica, Milan, Italy), and slides were analyzed using a light microscope, according to the manufacturer instructions.

2.4.4. Live/Dead Viability Assay

The viability of hASC encapsulated in VG-3D and VG-RGD was evaluated using the Live/Dead kit (Life Technologies). Hydrogels were washed in D-PBS (Aurogene Srl, Rome, Italy) and incubated with Live/Dead solution for 35 min at 37 °C. After staining, hydrogels were washed again with DPBS and evaluated, with living cells showing green and the nuclei of dead cells showing red when viewed with a fluorescence microscope (Nikon Instruments Europe BW, Amsterdam, The Netherlands).

2.4.5. LDH Assay

The cytotoxicity of different hydrogel concentrations on hASCs was detected using the LDH assay kit (Roche, Mannheim, Germany). The supernatant was collected after 2 and 7 days and tested for the absorbance values at 490 nm using a microplate reader TECAN Infinite$^®$ 200 PRO (Tecan Italia S.r.l., Cernusco Sul Naviglio, Italy).

2.4.6. Metabolic Activity Test

Cell metabolic activity was analyzed at day 2 and 7 using the Alamar blue test. Briefly, the samples were incubated with 10% Alamar blue (Life Technologies), and after 5 h, the absorbance was read at 570 and 600 nm using an automated spectrophotometric plate reader TECAN Infinite$^®$ 200 PRO (Tecan). The results were expressed as percentages of AlamarBlue reduction, as indicated by the manufacturer's data sheet (BioRad Laboratories, Hercules, CA, USA).

2.4.7. Chondrogenic Differentiation

hASCs laden both in VG-3D and VG-RGD (1:1 and 1:2) were treated with chondrogenic medium (high-glucose DMEM supplemented with 50 mg/mL ITS + premix, 10^{-7} M dexamethasone, 50 μg/mL ascorbate–2phosphate, 1-mM sodium pyruvate, and 100 U/mL–100 μg/mL penicillin–streptomycin, Sigma Aldrich, St. Louis, MO, USA) containing chondrogenic factors (+CF) TGF-β3 10 ng/mL and BMP6 10 ng/mL (both from Miltenyi Biotech, Auburn, CA, USA). The cell culture medium was changed three times a week. Each construct was analyzed on day 2, 14, 21, and 28 to test the chondrogenic markers.

2.4.8. Molecular Biology

Total RNA was extracted from all chondrogenic samples at day 2, 14, 21, and 28. Each construct sample was treated with 1 mL of Eurogold RnaPure (EuroClone S.p.a.), immediately snap frozen in liquid nitrogen (-196 °C), and stored in a freezer at -80 °C. RNA extraction was performed by homogenizing samples and following the Eurogold manufacturer's instruction. The samples were then treated with DNase I (DNA-free Kit) and RNA quantified using a Nanodrop® spectrophotometer (EuroClone S.p.a). Reverse transcription was performed using a Super Script® Vilo™ cDNA synthesis kit (Life Technologies), according to the manufacturer's protocol. Real-time polymerase chain reaction (PCR) was performed using LightCycler®2.0 [48] (Roche Molecular Biochemicals, Mannheim, Germany) for the quantification of the following genes: SRY-Box Transcription Factor 9 (*SOX9*), collagen type 1 alpha 1 chain (*COL1A1*), collagen type 2 alpha 1 chain (*COL2A1*), cartilage oligomeric matrix protein (*COMP*), glycosaminoglycan (*GAG*), aggrecan (*ACAN*), and the cellular marker of proliferation Ki-67 (*MKI67*) (Table S1). The efficiency of all primers was confirmed to be high (>90%) and comparable (Table S1). For each target gene, mRNA levels were calculated, normalized to the housekeeping gene Glyceraldehyde-3-Phosphate Dehydrogenase (*GAPDH*) according to the formula $2^{-\Delta Ct}$, and expressed as a percentage of the reference gene.

2.4.9. Immunohistochemistry Staining

On day 28, both concentrations of VG-3D and VG-RGD hydrogel-loaded ASC were fixed in 10% formaldehyde in DPBS for 40 min, washed in PBS, dehydrated in ethanol, and embedded in paraffin. Immunohistochemistry techniques were used to evaluate collagen type 1, collagen type 2, and aggrecan expression. Serial sections of 5 μm were incubated for 60 min at RT with monoclonal mouse anti-human collagen type 1 (diluted 1:40), anti-human collagen type 2 (diluted 1:20), and anti-human aggrecan (diluted 1:50, all from Chemicon International, Temecula, CA, USA), rinsed, and then sequentially incubated at RT for 20 min with multilinker biotinylated secondary antibody and alkaline phosphatase-conjugated streptavidin (Biocare Medical, Walnut Creek, CA, USA). The colorimetric reactions were developed using fast red (Biocare Medical), counterstained with hematoxylin, and mounted with glycerol jelly. The sections were evaluated with a bright field microscope (Nikon Instruments Europe BW). Negative and isotype matched control sections were tested.

2.4.10. Statistical Analysis

Statistical analysis was done using CSS Statistical Software (Statsoft Inc., Tulsa, OK, USA). Non-parametric tests were performed, since the data did not have normal or strongly asymmetric distribution. The Kruskal–Wallis with Dunn's multiple comparisons test was used and values of $p < 0.05$ were considered statistically significant. Values were expressed either as the median and minimum and maximum, or as mean $\pm$ SD.

3. Results and Discussion

3.1. Raw Materials Characterization: FTIR Analysis

Firstly, the FTIR spectra analysis of both commercial VG-3D and VG-RGD solutions was performed to identify the functional groups present in these materials. This assessment was also performed on the sodium alginate, which was found to be similar in terms of

functional groups, as a comparison. As indicated by the manufacturer, both VG hydrogels are xeno-free synthetic polysaccharide-based hydrogel systems, with or without RGD motif, that can be crosslinked using ions present in DMEM solution. Therefore, we chose to compare alginate, which is a natural polysaccharide that normally crosslinks using magnesium or calcium ions (both present in the datasheet of the DMEM solution), used in many scientific studies related to tissue engineering and regenerative medicine [49]. For these reasons, we used this compound as a control for FTIR analysis to verify and discuss if differences existed in the presence of specific functional groups with a well-known polysaccharide. As shown in Figure 2a, all materials exhibited typical peaks at 3430 cm^{-1}, 2916 cm^{-1}, 1424 cm^{-1}, and 1025 cm^{-1}. Moreover, in VG-based materials, we found signal peaks around 1623 cm^{-1} and 1075 cm^{-1}, but absent in the sodium alginate. The peak at 3430 cm^{-1}, attributed to the O–H stretching vibration, was present in all materials. Interestingly, the peak at 2916 cm^{-1} in VG-based materials, indicative of the stretching vibration of all saturated C–H bonds, was more evident than in sodium alginate. As shown in Figure 2a, the signal, due to the presence of the tripeptide Arg-Gly-Asp (RGD) (peptides peak around 1670 cm^{-1}), is also noticeable (yellow band) on the VG-RGD spectrum, which identifies the minimal sequence to recognize the fibronectin that mediates cell attachment [27,28]. In particular, the signal overlapped with the peak around 1670–1623 cm^{-1}, which is attributed to the stretching vibration of the COO− groups. Moreover, the second C–N stretching vibration peak at 1385 cm^{-1} was common for all materials, not just for the VG-RGD hydrogel [29]. As for the sodium alginate, the peak at 1424 cm^{-1} for the symmetric stretching of the COO− groups and the peak at 1025 cm^{-1} attributed to the OC–O–CO stretching vibrations were also present in VG-based hydrogels. However, the peak at 1075 cm^{-1} attributed to C–O–C was not found in both VG-based materials, while it was found in sodium alginate's spectrum [30]. Overall, the FTIR analysis indicates that both VG-3D and VG-RGD formulations feature signal peaks similar to those of sodium alginate, which is known to support the chondrogenic differentiation of MSCs [34].
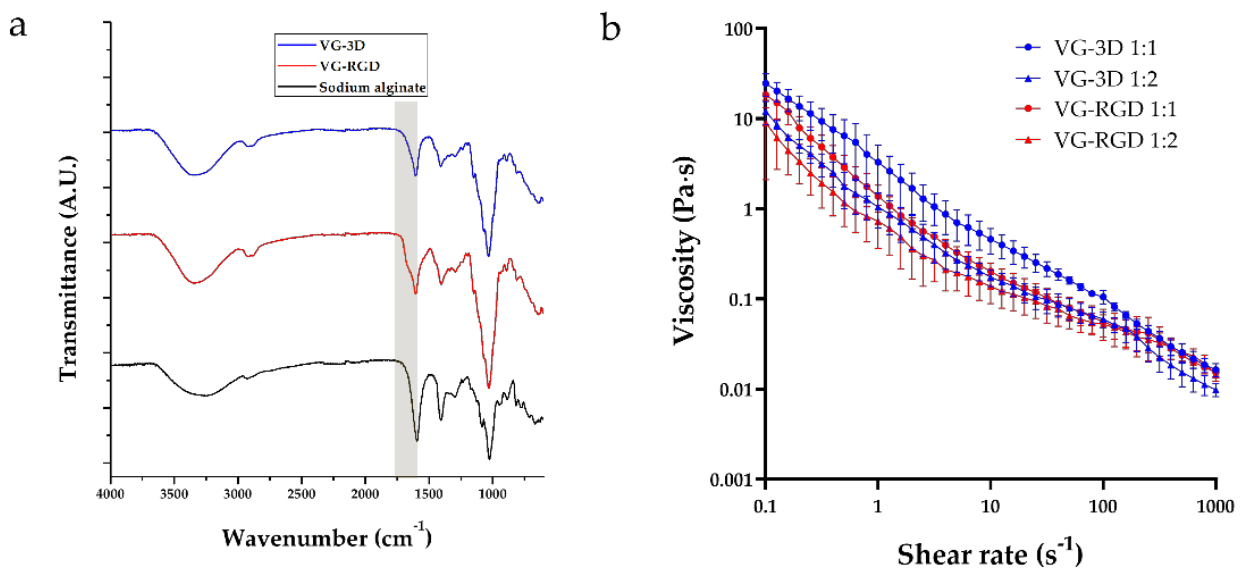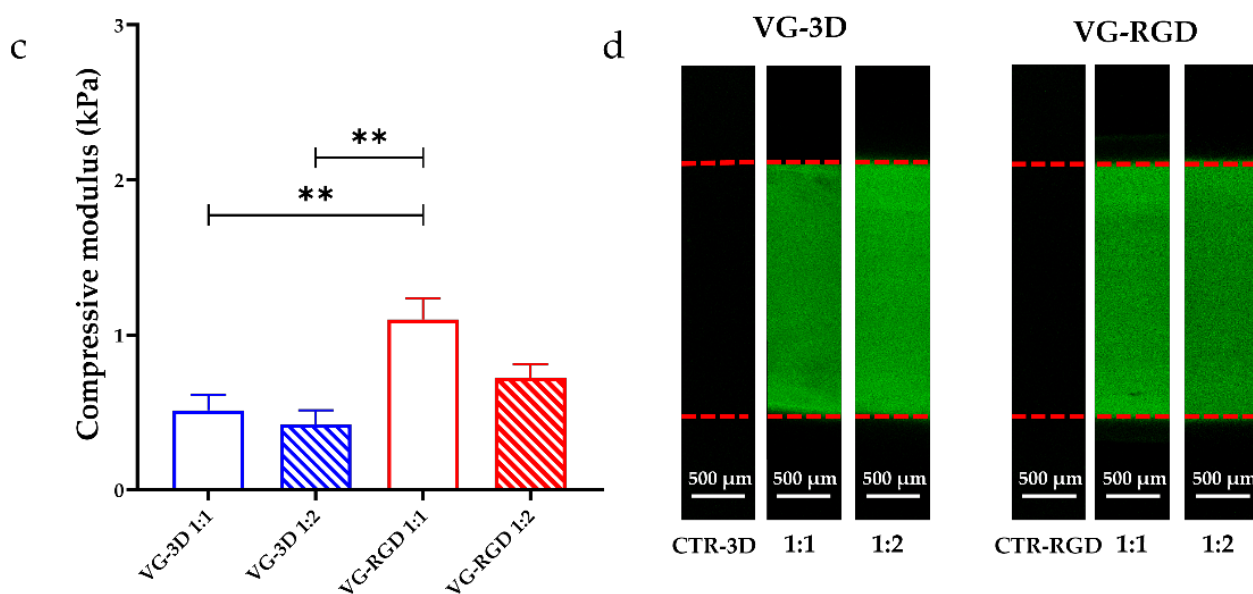

Figure 2. *Cont.*

Figure 2. (**a**) FTIR analysis of lyophilized VG-3D (blue), VG-RGD (red), and control sodium alginate powder (black) obtained in the range of wavenumber from 4000 to 600 cm^{-1}; (**b**) rheological characterization of VG-3D and VG-RGD materials regarding viscosity (flow curves); (**c**) mechanical characterization of VG-3D and VG-RGD hydrogels in terms of compressive modulus; (**d**) confocal images of cross-sectioned VG-3D (**left**) and VG-RGD (**right**) crosslinked hydrogels (1:1 and 1:2 dilutions) after treatment with FITC-conjugated albumin to evaluate the protein diffusivity through 3D constructs. The controls (CTR-3D, CTR-RGD) represent both hydrogels, not treated with FITC-conjugated albumin. The red dashed lines represent the hydrogel's thickness. Data are presented as mean ± SD, n = 5; *p*-values are calculated by the Kruskal–Wallis method with Dunn's multiple comparisons test, as indicated in the statistical section, ** *p* < 0.001.

3.2. Hydrogel Preparation and Characterization

3.2.1. Rheological Properties

The rheological properties (Figure 2b) of all solutions, immediately after mixing the components (thus in the pre-crosslinked formulation), were evaluated to analyze the flow curve and the relative shear stress applied to cells during injection. Figure 2b shows the flow curves of VG-3D and VG-RGD at both dilutions tested (1:1 and 1:2). At 1 s^{-1}, the viscosity of both VG-based hydrogels showed similar values. In particular, the viscosity of VG-3D 1:1 and 1:2 was 3.29 ± 1.79 Pa·s and 1.60 ± 0.67 Pa·s, respectively, and the viscosity of VG-RGD 1:1 and 1:2 was 1.37 ± 0.45 Pa·s and 1.77 ± 0.76 Pa·s, respectively.

The rheological indexes typical of non-Newtonian fluids (n and K) were extracted by the flow curves shown in Figure 2b, and the corresponding shear stresses (τ) were calculated, hypothesizing the delivery of the hydrogels through a 26 G needle (Table 1).

Table 1. Rheological indexes (**n**, **K**) extracted by flow curves of VG-3D and VG-RGD for dilution 1:1 and 1:2, and used to calculate shear stresses on cells during injection with 26 G (inner diameter: 0.25 mm) needles. Data are reported as mean ± SD, n = 5.

	VG-3D 1:1	**VG-3D 1:2**	**VG-RGD 1:1**	**VG-RGD 1:2**
K [Pa·s^n]	3.36 ± 0.69	1.56 ± 0.52	2.03 ± 0.38	1.12 ± 0.36
n	0.21 ± 0.02	0.22 ± 0.09	0.20 ± 0.03	0.29 ± 0.04
τ [Pa]	27.12 ± 9.01	15.38 ± 8.24	21.33 ± 8.48	15.93 ± 5.12

All VG-based hydrogels showed a shear-thinning behavior (**n** < 1), a relatively low consistency index, and a viscosity that decreased when the shear rate increased [31]. These

results suggest that all combinations can be injected (also directly in situ), as previously suggested elsewhere [24]. The VG-3D hydrogels showed a higher consistency index than VG-RGD ones, and we noticed a difference in both VG-based hydrogels while varying the dilution factor from 1:1 to 1:2 (Table 1). The results showed that the shear stress applied to cells encapsulated in all solutions during an injection step through a 26 G needle was lower than the safety threshold equal to 5 kPa, calculated as previously reported [32].

3.2.2. Mechanical Properties

The compressive modulus of all VG-based hydrogels is shown in Figure 2c. After crosslinking, VG-3D (1:1 and 1:2) showed a compressive modulus equal to 0.51 ± 0.10 kPa and 0.41 ± 0.09 kPa, respectively, and no statistical differences were found. VG-RGD 1:1 showed an elastic modulus of 1.10 ± 0.13 kPa, significantly higher than both VG-3D hydrogels (** $p < 0.01$), and VG-RGD 1:2 showed a value of 0.72 ± 0.08 kPa, not statistically significant compared to VG-3D. Interestingly, in this case, the higher viscosity of pre-crosslinked VG-based hydrogels reflected the higher modulus after the addition of ions.

Our results are far from the compressive modulus of the cartilage, because our hydrogel is thought to safely embed stem cells and let them differentiate into cartilage-like tissue over time (after a minimum of 28 days). For this reason, the mechanical properties of VG-based hydrogel do not have to be comparable with those of the cartilage. In fact, the mechanical properties of the cartilage are different, based on the zone considered: the mechanical properties of superficial and deep cartilage in terms of Young's modulus are 280 ± 160 and 730 ± 260 kPa, respectively [50]. The goal of this work is to obtain a one-zone hydrogel that is able to host stem cells and keep them viable for a cartilage regeneration strategy, which aims to recreate the ECM typical of the cartilage by using stem cells in the long-term. However, to achieve the mechanical properties of cartilage tissue, the strategy must be changed to obtain a complete substitution of the tissue with a biocompatible construct. For example, this type of construct can also be designed using synthetic materials (i.e., PEGDA) to improve the stiffness and the toughness of the substitute, but that may severely compromise the viability and differentiation potential of the stem cells in the long-term. We have followed this strategy in our previous work [45].

3.2.3. Protein Diffusivity Analysis

Confocal images on cross-sectioned VG-3D and VG-RGD crosslinked hydrogels at both concentrations (1:1 and 1:2) are reported in Figure 2d. The unmarked controls (CTR-3D for VG-3D, CTR-RGD for VG-RGD) hydrogels did not show any relevant autofluorescence signal when not incubated with FITC-conjugated albumin. Results show that all hydrogel formulations let the protein diffusion all along with their thickness (detected by red dashed lines) in the incubation period. In fact, both VG-based hydrogels (for both 1:1 and 1:2 dilutions) revealed the protein diffusivity in the whole 3D constructs, suggesting their suitability for being embedded with cells [23,37]. It is well known that the rheological and mechanical properties of the hydrogels, as well as the nutrients diffusivity, represent crucial cues on the cell behavior by affecting cell proliferation and differentiation [37,51].

3.3. hASCs Characterization

Human ASCs antigenic characteristics and differentiation potential were proven, according to internationally accepted criteria for defining MSCs [47]. The antigenic profile of expanded hASCs at passages 3 and 4 confirmed that cells were more than 99% positive for CD73, CD90, CD105, and CD166, and negative for CD31, CD34, and CD45 (Figure S1a). By using a specific differentiating medium, hASCs proved osteogenic and chondrogenic differentiation capabilities (Figure S1b,c).

3.3.1. Biological Evaluations of hASCs-Laden Hydrogels

Different hASCs characteristics in terms of morphology, distribution, viability, cytotoxicity, and metabolic activity were analyzed at days 2 and 7 after their encapsulation in the

hydrogels. As shown in Figure 3a, we found that the cells were homogeneously distributed in all layers analyzed in VG-3D and VG-RGD hydrogels at both concentrations tested (1:1 and 1:2), suggesting a uniform material structure that promoted cell adhesion. These results confirmed the suitability of the hydrogel systems for the long-term maintenance of cells. After 7 days of culture, we observed a morphological change of hASCs in VG-RGD with respect to VG-3D hydrogels (Figure 3b). The cells displayed a fibroblast-like morphology in VG-RGD, while in VG-3D, they showed a more rounded shape, independent from the hydrogel concentration. A reproducible specific dimension (diameter: 10 mm, height: 2 mm) of the hydrogels was selected to assure a good comparison among the biological tests and good diffusion of the nutrients, as we showed in Figure 2d. Moreover, preliminary experiments were performed to select the hASCs density that better showed a uniform distribution of the cells inside the hydrogels, with defined dimensions and the best chondrogenic differentiation (data not shown).

These pre-defined conditions showed that hASCs showed a high percentage of viable cells (Figure 2b) until day 7, confirming that the chosen hydrogels size did not negatively affect the cell viability. Live/dead staining showed a high number of viable cells in both VG-3D and VG-RGD hydrogels (1:1 and 1:2) from day 2 to day 7 (Figure 3c). This observation was confirmed by the low number of dead cells (red) found in all hydrogels.

A lactate dehydrogenase (LDH) assay was used to assess the hydrogel cytotoxicity on hASCs, and we found that the detected enzyme was lower or equal to 10% in all hydrogels (Figure 3d), supporting the non-toxic nature of the hydrogel matrices. Both formulations, with and without the RGD motifs, confirmed that the microenvironment created by the hydrogels did not negatively affect the encapsulated hASCs.

Moreover, the analysis of metabolic activity (Figure 3e) showed that at day 2 and 7, the number of metabolically active cells in the VG-RGD hydrogel (1:1 and 1:2) was similar to that found in the VG-3D hydrogels.

These results indicated that all hydrogel properties (both mechanical and biochemical) were favorable to maintain positive hASCs characteristics. Our results are in line with previous studies [52,53], showing different cell types (like immune, epithelial, and stem cells) encapsulated in VG-based hydrogels. The results demonstrated that these hydrogels were interesting matrices able to create a cell-friendly environment. In fact, the cell viability and phenotype were not affected in these in vitro 3D models. Results revealing the optimal cell viability and low cytotoxicity of hASCs encapsulated in both VG hydrogels represented an important pre-requisite that encouraged further tests focused on chondrogenic differentiation.

3.3.2. RGD-Based Hydrogels Favor the Chondrogenic Processes

The chondrogenic commitment of hASCs was analyzed at different time points (2, 14, 21, and 28 days) to check both the role of RGD motif and of the hydrogel concentrations (Figure 4). The analysis of the proliferating gene M*KI67* showed a significant decrease (indicated by *) from 2 to 28 days only in VG-3D 1:2, while no modulation was found in the other hydrogels analyzed. By contrast, we found a significant increase in M*KI67* in VG-RGD 1:1 compared to VG-3D 1:1 from day 21 to day 28, while a significant increase (indicated by °) was found in VG-RGD 1:2 compared to VG-3D 1:2 from day 14 to day 21. Interestingly, on day 28, the M*KI67* gene showed a significant decrease (indicated by ˆ) in VG-RGD 1:2 compared to 1:1.
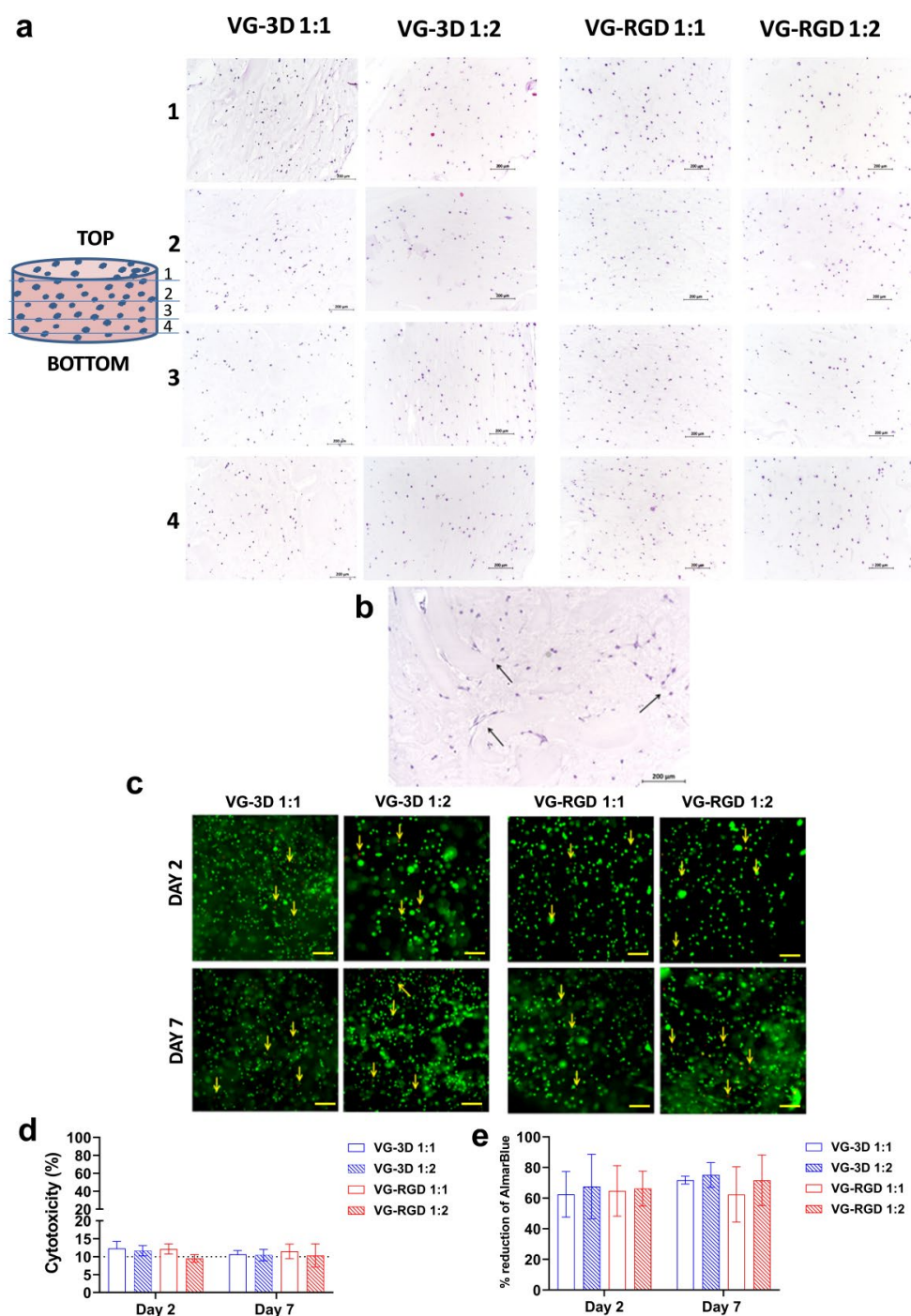
Figure 3. Histological analysis (hematoxylin-eosin staining): (**a**) Representative images of encapsulated-hASCs in VG-3D and VG-RGD hydrogels at day 7, scale bars = 200 μm. (**b**) Higher magnification of VG-RGD hydrogel 1:2, black arrows show hASCs cells. (**c**) Live/dead assay performed on hASCs encapsulated in VG-3D and VG-RGD hydrogels at days 2 and 7. Viable cells are shown in green; dead cells are shown in red (and indicated by yellow arrows); scale bars = 100 μm. (**d**) LDH analysis of hASCs embedded in VG-3D and VG-RGD hydrogels at days 2 and 7. Data are expressed as percentages of cytotoxicity. (**e**) AlamarBlue analysis of hASCs embedded in VG-3D and VG-RGD hydrogels at days 2 and 7. Data are expressed as percentage of reduction of alamarBlue. Data presented as mean $\pm$ SD, n = 5; *p*-values are calculated by Kruskal–Wallis with Dunn's multiple comparisons test, as indicated in the statistical section.
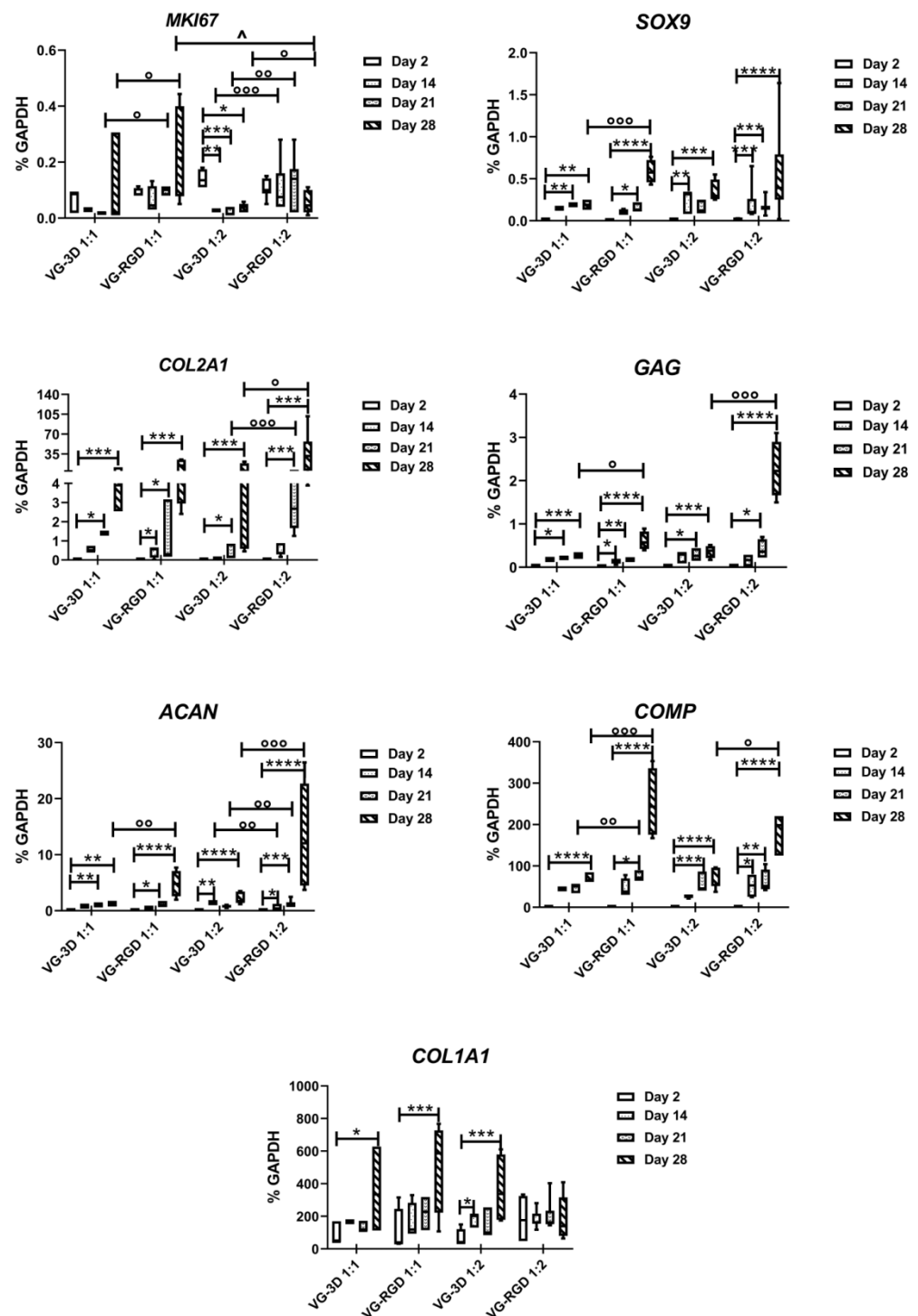
Figure 4. Real-time PCR analysis of M*Ki67, SOX9, COL2A1, GAG, ACAN, COMP,* and *COL1A1* genes of VG-3D and VG-RGD at day 2, 14, 21, and 28. Data were expressed as % *GAPDH* (housekeeping gene) and represented as a box-plot showing the median, minimum, and maximum values. The Kruskal–Wallis with Dunn's multiple comparisons test was used for statistical analysis: * indicates differences along time points (day 2 to day 28) for each hydrogel (VG-3D and VG-RGD), ° indicates significant differences between different hydrogels (VG-3D versus VG-RGD) at the same concentration (1:1 or 1:2); ˆ indicates differences between the same hydrogel at two different concentrations; n = 5, *, or ° or ˆ *p* < 0.05, ** or °° *p* < 0.005, *** or °°° *p* < 0.0005, **** *p* < 0.0001.

The expression of the *SOX9* transcription factor gene showed an increase (indicated by *) from 2 to day 28 for all the hydrogels analyzed. On day 28, we also found a significant

increase (indicated by °) in VG-RGD 1:1 compared to VG-3D 1:1. The analysis of typical chondrogenic *COL2A1*, *GAG*, and *ACAN* genes showed a significant increase (indicated by *) starting from day 14 or 21 until day 28 in all the hydrogels tested. However, of these three genes compared to the other formulations, only VG-RGD 1:2 showed the highest expression (indicated by °) on day 28. Interestingly, the expression of these three genes in VG-RGD 1:2 was also significantly higher (indicated by °) than in VG-3D 1:2. The *COMP* gene also significantly increased (indicated by *) from day 2 until day 28 in all formulations tested; however, on day 28, we saw a significant increase (indicated by °) in both VG-RGD 1:1 and 1:2 compared to VG-3D 1:1 and 1:2. The fibrotic *COL1A1* gene showed a significant increase (indicated by *) from day 2 to day 28 for all hydrogels tested, except for VG-RGD 1:2.

The analysis of the proliferating gene *MKI67* found that the presence of RGD motifs in the hydrogel favored cell proliferation; however, the 1:2 formulation was significantly decreased on day 28 compared to the 1:1 formulation, suggesting that this formulation better counteracted cell proliferation compared to the other conditions and better induced cell differentiation. In fact, we demonstrated that the VG-RGD 1:2 formulation showed the highest expression of *COL2A1*, *GAG*, and *ACAN*, the three major chondrogenic genes, on day 28, indicating that the presence of the RGD motif positively influenced the chondrogenic commitment of the hASCs. In the ECM of the articular cartilage, we distinguish two supramolecular compartments, the fibrillar collagen network, with the main collagen type 2, and the extrafibrillar matrix network, with proteoglycan and aggrecan [54]. The two networks are interconnected by non-collagenous perifibrillar adapter matrix protein-like COMP [55,56]. The positive increase in the VG-RGD 1:2 formulation of different ECM genes that provide different functions to the cartilage, such as tensile strength and swelling pressure, clearly showed that this formulation facilitates the formation of a very close cartilage-like tissue. Interestingly, not only the presence of the RGD motif, but also the lower concentration (1:2) of the hydrogel positively contributed to the chondrogenic differentiation of hASCs, suggesting that both culture conditions and hydrogel microenvironment at a defined stiffness were important for providing a positive in vitro effect on cell differentiation and ECM production.

The different effect of RGD motif on hASCs chondrogenesis was then investigated at day 28 by analyzing the modulation of collagen type 1, collagen type 2, and aggrecan proteins, which are typical fibrotic and chondrogenic markers (Figure 5). It was observed that chondrogenic treatment associated with VG-RGD 1:2 caused, in each sample analyzed, higher positive staining to both aggrecan and collagen type 2 with respect to VG-3D 1:1 and 1:2 (Figure 5). The presence of positive areas, mainly in the VG-RGD 1:2, confirmed that this formulation and not the other which also tested positively, pushed the differentiation of the hASCs. It has been shown that the concentration of the -RGD motif in the hydrogels could be detrimental to or supportive of cell differentiation [38–40,43]. In our in vitro system, we demonstrated that the presence of the RGD motif in the hydrogel significantly contributed to the commitment of hASCs, as reported by other authors using different hydrogel types [40,41,44]. It has been suggested that defined RGD concentration [57] and nanoscale spatial distribution [58] associated with appropriate mechanical stimulation [59] are effective at inducing the chondrogenic phenotype of the cells.

Conversely, chondrogenic differentiated areas were almost completely nonresponsive to collagen type 1. Therefore, despite the heterogeneity of the cell population, the embedded hASCs showed a very similar trend of response to chondrogenic commitment. A time response of RGD to cell differentiation [60,61] has been shown, contributing to the confirmation of the important role of this tri-peptide in inducing chondrogenic differentiation.
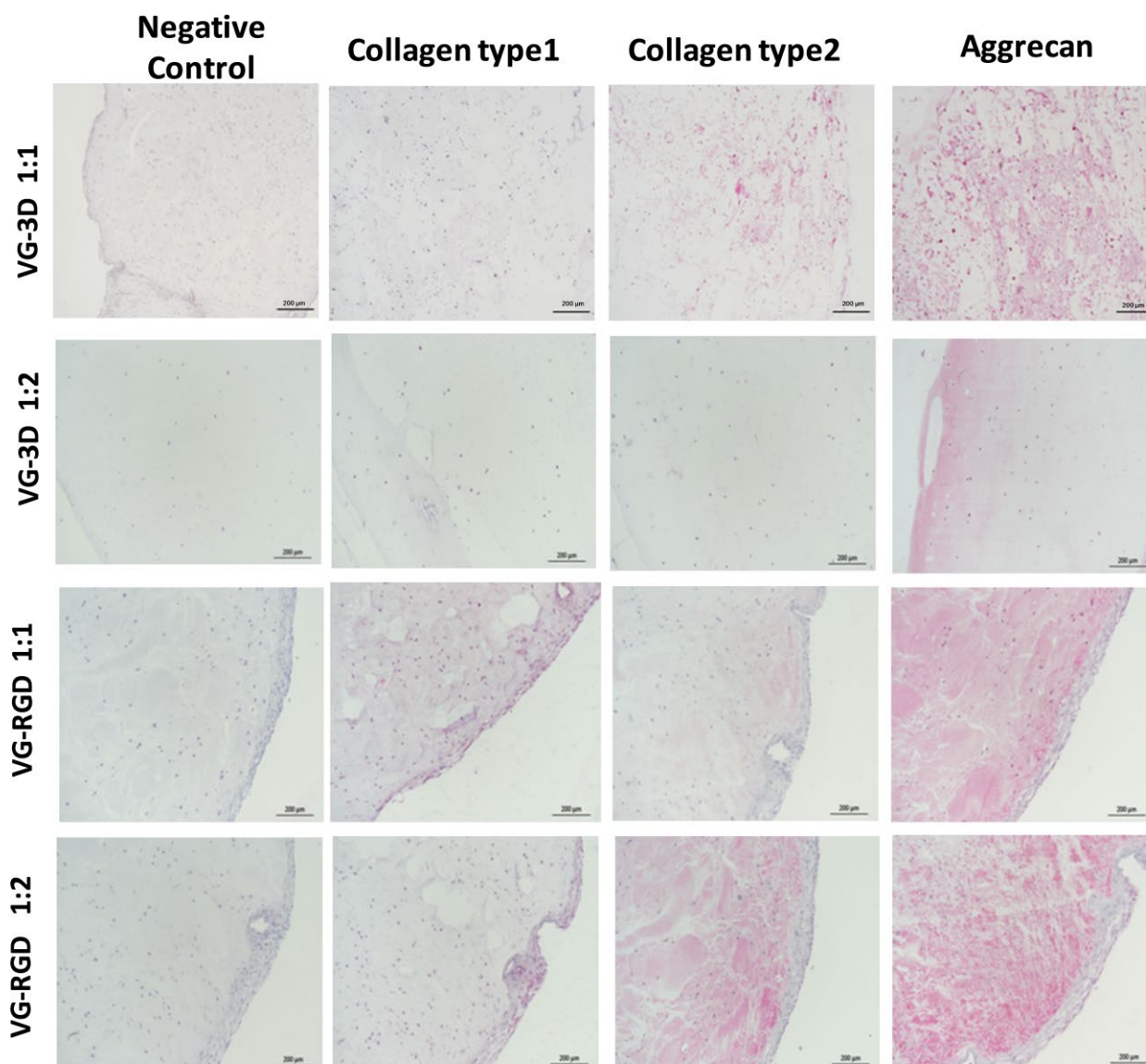
Figure 5. Immunohistochemical analysis of collagen type 1, collagen type 2, and aggrecan on encapsulated hASCs in VG-3D and VG-RGD hydrogels (1:1 and 1:2) at day 28. The negative control was included. Pink areas = positive immunostaining; scale bars = 200 μm.

4. Conclusions

In the field of cartilage tissue engineering, an ideal injectable hydrogel should be able to reproduce the complex functionalities of the cartilaginous ECM, thus providing specific cell adhesion and the subsequent control of cellular functions directing new tissue formation. Natural polysaccharides from different sources are potentially exciting candidates for cartilage regeneration. The RGD motif represents a crucial component of the adhesive proteins in the ECM, and via the $\alpha_v\beta3$ integrin receptors, favor cellular attachment that leads to the activation of focal adhesion kinase (FAK), well known to transmit the adhesion-dependent cell survival signal within the cell [41]. This study demonstrates that VG-RGD hydrogels at the concentration of 1:2 significantly contribute to guaranteeing the chondrogenic commitment of the hASCs laden in the hydrogel. Both the rheological and biochemical characteristics of this hydrogel formulation, with respect to other counterparts, positively influenced hASCs chondrogenic differentiation. Future studies may focus on the role of the hydrogel formulations in a broader panel of integrin markers of hASCs to define

which is the integrin signaling directly involved in the control of the hASCs chondrogenic differentiation, as previously reported for specific integrins [41,62].

Institutional Review Board Statement: Not applicable.

Informed Consent Statement: Not applicable.

Data Availability Statement: The data presented in this study are available on request from the corresponding author. The data are not publicly available due to issues of privacy.

Conflicts of Interest: The authors declare that there is no conflict of interest.

References

1. Huey, D.J.; Hu, J.C.; Athanasiou, K.A. Unlike bone, cartilage regeneration remains elusive. *Science* **2012**, *338*, 917–921. [CrossRef] [PubMed]
2. Cui, A.; Li, H.; Wang, D.; Zhong, J.; Chen, Y.; Lu, H. Global, regional prevalence, incidence and risk factors of knee osteoarthritis in population-based studies. *EClinicalMedicine* **2020**, *29–30*, 100587. [CrossRef] [PubMed]
3. Krishnan, Y.; Grodzinsky, A.J. Cartilage diseases. *Matrix Biol.* **2018**, *71–72*, 51–69. [CrossRef] [PubMed]
4. Kwon, H.; Brown, W.E.; Lee, C.A.; Wang, D.; Paschos, N.; Hu, J.C.; Athanasiou, K.A. Surgical and tissue engineering strategies for articular cartilage and meniscus repair. *Nat. Rev. Rheumatol.* **2019**, *15*, 550–570. [CrossRef]
5. Izadifar, Z.; Chen, X.; Kulyk, W. Strategic design and fabrication of engineered scaffolds for articular cartilage repair. *J. Funct. Biomater.* **2012**, *3*, 799–838. [CrossRef]
6. Armiento, A.R.; Stoddart, M.J.; Alini, M.; Eglin, D. Biomaterials for articular cartilage tissue engineering: Learning from biology. *Acta Biomater.* **2018**, *65*, 1–20. [CrossRef]
7. Yang, J.; Zhang, Y.S.; Yue, K.; Khademhosseini, A. Cell-laden hydrogels for osteochondral and cartilage tissue engineering. *Acta Biomater.* **2017**, *57*, 1–25. [CrossRef]
8. Bhattacharjee, M.; Coburn, J.; Centola, M.; Murab, S.; Barbero, A.; Kaplan, D.L.; Martin, I.; Ghosh, S. Tissue engineering strategies to study cartilage development, degeneration and regeneration. *Adv. Drug Deliv. Rev.* **2015**, *84*, 107–122. [CrossRef]
9. Wei, W.; Ma, Y.; Yao, X.; Zhou, W.; Wang, X.; Li, C.; Lin, J.; He, Q.; Leptihn, S.; Ouyang, H. Advanced hydrogels for the repair of cartilage defects and regeneration. *Bioact. Mater.* **2021**, *6*, 998–1011. [CrossRef]
10. Lin, H.; Yin, C.; Mo, A.; Hong, G. Applications of Hydrogel with Special Physical Properties in Bone and Cartilage Regeneration. *Materials* **2021**, *14*, 235. [CrossRef]
11. Radhakrishnan, J.; Subramanian, A.; Krishnan, U.M.; Sethuraman, S. Injectable and 3D Bioprinted Polysaccharide Hydrogels: From Cartilage to Osteochondral Tissue Engineering. *Biomacromolecules* **2017**, *18*, 1–26. [CrossRef] [PubMed]
12. Naghieh, S.; Sarker, M.; Sharma, N.K.; Barhoumi, Z.; Chen, X. Printability of 3D Printed Hydrogel Scaffolds: Influence of Hydrogel Composition and Printing Parameters. *Appl. Sci.* **2020**, *10*, 292. [CrossRef]
13. Zhu, J.; Marchant, R.E. Design properties of hydrogel tissue-engineering scaffolds. *Expert Rev. Med. Devices* **2011**, *8*, 607–626. [CrossRef] [PubMed]
14. Seidi, K.; Ayoubi-Joshaghani, M.H.; Azizi, M.; Javaheri, T.; Jaymand, M.; Alizadeh, E.; Webster, T.J.; Yazdi, A.A.; Niazi, M.; Hamblin, M.R.; et al. Bioinspired hydrogels build a bridge from bench to bedside. *Nano Today* **2021**, *39*, 101157. [CrossRef]
15. Long, L.-Y.; Weng, Y.-X.; Wang, Y.-Z. Cellulose Aerogels: Synthesis, Applications, and Prospects. *Polymers* **2018**, *10*, 623. [CrossRef]
16. Wei, Z.; Wu, C.; Li, R.; Yu, D.; Ding, Q. Nanocellulose based hydrogel or aerogel scaffolds for tissue engineering. *Cellulose* **2021**, *28*, 7497–7520. [CrossRef]

17. Yahya, E.B.; Amirul, A.A.; Abdul Khalil, H.P.S.; Olaiya, N.G.; Iqbal, M.O.; Fauziah Jummaat, A.S.A.; Adnan, A.S. Insights into the Role of Biopolymer Aerogel Scaffolds in Tissue Engineering and Regenerative Medicine. *Polymers* **2021**, *13*, 1612. [CrossRef]

18. Sánchez-Téllez, D.A.; Téllez-Jurado, L.; Rodríguez-Lorenzo, L.M. Hydrogels for Cartilage Regeneration, from Polysaccharides to Hybrids. *Polymers* **2017**, *9*, 671. [CrossRef]

19. Nikolova, M.P.; Chavali, M.S. Recent advances in biomaterials for 3D scaffolds: A review. *Bioact. Mater.* **2019**, *4*, 271–292. [CrossRef]

20. Zhao, T.; Wei, Z.; Zhu, W.; Weng, X. Recent Developments and Current Applications of Hydrogels in Osteoarthritis. *Bioengineering* **2022**, *9*, 132. [CrossRef]

21. Lin, X.; Tsao, C.T.; Kyomoto, M.; Zhang, M. Injectable Natural Polymer Hydrogels for Treatment of Knee Osteoarthritis. *Adv. Healthc. Mater.* **2022**, *11*, e2101479. [CrossRef] [PubMed]

22. Hafezi, M.; Nouri Khorasani, S.; Zare, M.; Esmaeely Neisiany, R.; Davoodi, P. Advanced Hydrogels for Cartilage Tissue Engineering: Recent Progress and Future Directions. *Polymers* **2021**, *13*, 4199. [CrossRef]

23. Vega, S.L.; Kwon, M.; Mauck, R.L.; Burdick, J.A. Single Cell Imaging to Probe Mesenchymal Stem Cell N-Cadherin Mediated Signaling within Hydrogels. *Ann. Biomed. Eng.* **2016**, *44*, 1921–1930. [CrossRef]

24. Foyt, D.A.; Taheem, D.K.; Ferreira, S.A.; Norman, M.D.A.; Petzold, J.; Jell, G.; Grigoriadis, A.E.; Gentleman, E. Hypoxia impacts human MSC response to substrate stiffness during chondrogenic differentiation. *Acta Biomater.* **2019**, *89*, 73–83. [CrossRef]

25. Amann, E.; Wolff, P.; Breel, E.; van Griensven, M.; Balmayor, E.R. Hyaluronic acid facilitates chondrogenesis and matrix deposition of human adipose derived mesenchymal stem cells and human chondrocytes co-cultures. *Acta Biomater.* **2017**, *52*, 130–144. [CrossRef]

26. Van Tomme, S.R.; Storm, G.; Hennink, W.E. In situ gelling hydrogels for pharmaceutical and biomedical applications. *Int. J. Pharm.* **2008**, *355*, 1–18. [CrossRef] [PubMed]

27. Jeong, B.; Kim, S.W.; Bae, Y.H. Thermosensitive sol-gel reversible hydrogels. *Adv. Drug Deliv. Rev.* **2002**, *54*, 37–51. [CrossRef]

28. Mandal, A.; Clegg, J.R.; Anselmo, A.C.; Mitragotri, S. Hydrogels in the clinic. *Bioeng. Transl. Med.* **2020**, *5*, e10158. [CrossRef]

29. Huang, J.; Xiong, J.; Wang, D.; Zhang, J.; Yang, L.; Sun, S.; Liang, Y. 3D Bioprinting of Hydrogels for Cartilage Tissue Engineering. *Gels* **2021**, *7*, 144. [CrossRef] [PubMed]

30. Yu, L.; Ding, J. Injectable hydrogels as unique biomedical materials. *Chem. Soc. Rev.* **2008**, *37*, 1473–1481. [CrossRef]

31. Neves, S.C.; Moroni, L.; Barrias, C.C.; Granja, P.L. Leveling Up Hydrogels: Hybrid Systems in Tissue Engineering. *Trends Biotechnol.* **2020**, *38*, 292–315. [CrossRef]

32. Boeuf, S.; Richter, W. Chondrogenesis of mesenchymal stem cells: Role of tissue source and inducing factors. *Stem Cell Res. Ther.* **2010**, *1*, 31. [CrossRef] [PubMed]

33. Jorgensen, C.; Noël, D. Mesenchymal stem cells in osteoarticular diseases. *Regen. Med.* **2011**, *6*, 44–51. [CrossRef] [PubMed]

34. Maumus, M.; Manferdini, C.; Toupet, K.; Peyrafitte, J.A.; Ferreira, R.; Facchini, A.; Gabusi, E.; Bourin, P.; Jorgensen, C.; Lisignoli, G.; et al. Adipose mesenchymal stem cells protect chondrocytes from degeneration associated with osteoarthritis. *Stem Cell Res.* **2013**, *11*, 834–844. [CrossRef] [PubMed]

35. Manferdini, C.; Maumus, M.; Gabusi, E.; Piacentini, A.; Filardo, G.; Peyrafitte, J.A.; Jorgensen, C.; Bourin, P.; Fleury-Cappellesso, S.; Facchini, A.; et al. Adipose-derived mesenchymal stem cells exert antiinflammatory effects on chondrocytes and synoviocytes from osteoarthritis patients through prostaglandin E2. *Arthritis Rheumatol.* **2013**, *65*, 1271–1281. [CrossRef]

36. Zoetebier, B.; Schmitz, T.; Ito, K.; Karperien, M.; Tryfonidou, M.A.; Paez, J. Injectable hydrogels for articular cartilage and nucleus pulposus repair: Status quo and prospects. *Tissue Eng. Part A*, 2022; *ahead of print*. [CrossRef]

37. Yang, J.; Li, Y.; Liu, Y.; Li, D.; Zhang, L.; Wang, Q.; Xiao, Y.; Zhang, X. Influence of hydrogel network microstructures on mesenchymal stem cell chondrogenesis in vitro and in vivo. *Acta Biomater.* **2019**, *91*, 159–172. [CrossRef]

38. Wang, F.; Nan, L.-P.; Zhou, S.-F.; Liu, Y.; Wang, Z.-Y.; Wang, J.-C.; Feng, X.-M.; Zhang, L. Injectable Hydrogel Combined with Nucleus Pulposus-Derived Mesenchymal Stem Cells for the Treatment of Degenerative Intervertebral Disc in Rats. *Stem Cells Int.* **2019**, *2019*, 8496025. [CrossRef]

39. Li, Z.; Cao, B.; Wang, X.; Ye, K.; Li, S.; Ding, J. Effects of RGD nanospacing on chondrogenic differentiation of mesenchymal stem cells. *J. Mater. Chem. B* **2015**, *3*, 5197–5209. [CrossRef]

40. Chen, F.; Ni, Y.; Liu, B.; Zhou, T.; Yu, C.; Su, Y.; Zhu, X.; Yu, X.; Zhou, Y. Self-crosslinking and injectable hyaluronic acid/RGD-functionalized pectin hydrogel for cartilage tissue engineering. *Carbohydr. Polym.* **2017**, *166*, 31–44. [CrossRef]

41. Ruoslahti, E. RGD and other recognition sequences for integrins. *Annu. Rev. Cell Dev. Biol.* **1996**, *12*, 697–715. [CrossRef]

42. Yang, M.; Zhang, Z.C.; Liu, Y.; Chen, Y.R.; Deng, R.H.; Zhang, Z.N.; Yu, J.K.; Yuan, F.Z. Function and Mechanism of RGD in Bone and Cartilage Tissue Engineering. *Front. Bioeng. Biotechnol.* **2021**, *9*, 773636. [CrossRef] [PubMed]

43. Denier, J.P.; Dabrowski, P.P. On the boundary–layer equations for power–law fluids. *Proc. R. Soc. Lond. Ser. A Math. Phys. Eng. Sci.* **2004**, *460*, 3143–3158. [CrossRef]

44. Blaeser, A.; Duarte Campos, D.F.; Puster, U.; Richtering, W.; Stevens, M.M.; Fischer, H. Controlling Shear Stress in 3D Bioprinting is a Key Factor to Balance Printing Resolution and Stem Cell Integrity. *Adv. Healthc. Mater.* **2016**, *5*, 326–333. [CrossRef] [PubMed]

45. Trucco, D.; Vannozzi, L.; Teblum, E.; Telkhozhayeva, M.; Nessim, G.D.; Affatato, S.; Al-Haddad, H.; Lisignoli, G.; Ricotti, L. Graphene Oxide-Doped Gellan Gum–PEGDA Bilayered Hydrogel Mimicking the Mechanical and Lubrication Properties of Articular Cartilage. *Adv. Healthc. Mater.* **2021**, *10*, 2001434. [CrossRef]

46. Manferdini, C.; Gabusi, E.; Sartore, L.; Dey, K.; Agnelli, S.; Almici, C.; Bianchetti, A.; Zini, N.; Russo, D.; Re, F.; et al. Chitosan-based scaffold counteracts hypertrophic and fibrotic markers in chondrogenic differentiated mesenchymal stromal cells. *J. Tissue Eng. Regen. Med.* **2019**, *13*, 1896–1911. [CrossRef]

47. Dominici, M.; Le Blanc, K.; Mueller, I.; Slaper-Cortenbach, I.; Marini, F.; Krause, D.; Deans, R.; Keating, A.; Prockop, D.; Horwitz, E. Minimal criteria for defining multipotent mesenchymal stromal cells. The International Society for Cellular Therapy position statement. *Cytotherapy* **2006**, *8*, 315–317. [CrossRef]

48. Lisignoli, G.; Manferdini, C.; Lambertini, E.; Zini, N.; Angelozzi, M.; Gabusi, E.; Gambari, L.; Penolazzi, L.; Lolli, A.; Facchini, A.; et al. Chondrogenic potential of Slug-depleted human mesenchymal stem cells. *Tissue Eng. Part A* **2014**, *20*, 2795–2805. [CrossRef]

49. Jin, M.; Shi, J.; Zhu, W.; Yao, H.; Wang, D.-A. Polysaccharide-Based Biomaterials in Tissue Engineering: A Review. *Tissue Eng. Part B Rev.* **2020**, *27*, 604–626. [CrossRef]

50. O'Connell, G.; Garcia, J.; Amir, J. 3D Bioprinting: New Directions in Articular Cartilage Tissue Engineering. *ACS Biomater. Sci. Eng.* **2017**, *3*, 2657–2668. [CrossRef]

51. Lee, H.-P.; Gu, L.; Mooney, D.J.; Levenston, M.E.; Chaudhuri, O. Mechanical confinement regulates cartilage matrix formation by chondrocytes. *Nat. Mater.* **2017**, *16*, 1243–1251. [CrossRef]

52. Cherne, M.D.; Sidar, B.; Sebrell, T.A.; Sanchez, H.S.; Heaton, K.; Kassama, F.J.; Roe, M.M.; Gentry, A.B.; Chang, C.B.; Walk, S.T.; et al. A Synthetic Hydrogel, VitroGel®ORGANOID-3, Improves Immune Cell-Epithelial Interactions in a Tissue Chip Co-Culture Model of Human Gastric Organoids and Dendritic Cells. *Front. Pharmacol.* **2021**, *12*, 707891. [CrossRef] [PubMed]

53. Baltazar, T.; Jiang, B.; Moncayo, A.; Merola, J.; Albanna, M.Z.; Saltzman, W.M.; Pober, J.S. 3D bioprinting of an implantable xeno-free vascularized human skin graft. *Bioeng. Transl. Med.* **2022**, e10324. [CrossRef]

54. Firner, S.; Zaucke, F.; Michael, J.; Dargel, J.; Schiwy-Bochat, K.H.; Heilig, J.; Rothschild, M.A.; Eysel, P.; Brüggemann, G.P.; Niehoff, A. Extracellular Distribution of Collagen II and Perifibrillar Adapter Proteins in Healthy and Osteoarthritic Human Knee Joint Cartilage. *J. Histochem. Cytochem.* **2017**, *65*, 593–606. [CrossRef] [PubMed]

55. Heinegård, D. Fell-Muir Lecture: Proteoglycans and more—From molecules to biology. *Int. J. Exp. Pathol.* **2009**, *90*, 575–586. [CrossRef]

56. Chen, F.H.; Herndon, M.E.; Patel, N.; Hecht, J.T.; Tuan, R.S.; Lawler, J. Interaction of cartilage oligomeric matrix protein/thrombospondin 5 with aggrecan. *J. Biol. Chem.* **2007**, *282*, 24591–24598. [CrossRef]

57. Liu, S.Q.; Tian, Q.; Wang, L.; Hedrick, J.L.; Hui, J.H.P.; Yang, Y.Y.; Ee, P.L.R. Injectable Biodegradable Poly(ethylene glycol)/RGD Peptide Hybrid Hydrogels for in vitro Chondrogenesis of Human Mesenchymal Stem Cells. *Macromol. Rapid Commun.* **2010**, *31*, 1148–1154. [CrossRef]

58. Li, S.; Wang, X.; Cao, B.; Ye, K.; Li, Z.; Ding, J. Effects of Nanoscale Spatial Arrangement of Arginine-Glycine-Aspartate Peptides on Dedifferentiation of Chondrocytes. *Nano Lett.* **2015**, *15*, 7755–7765. [CrossRef]

59. Villanueva, I.; Weigel, C.; Bryant, S. Cell–matrix interactions and dynamic mechanical loading influence chondrocyte gene expression and bioactivity in PEG-RGD hydrogels. *Acta Biomater.* **2009**, *5*, 2832–2846. [CrossRef]

60. Salinas, C.N.; Anseth, K.S. The enhancement of chondrogenic differentiation of human mesenchymal stem cells by enzymatically regulated RGD functionalities. *Biomaterials* **2008**, *29*, 2370–2377. [CrossRef]

61. Kloxin, A.M.; Kasko, A.M.; Salinas, C.N.; Anseth, K.S. Photodegradable hydrogels for dynamic tuning of physical and chemical properties. *Science* **2009**, *324*, 59–63. [CrossRef]

62. Di Maggio, N.; Martella, E.; Frismantiene, A.; Resink, T.J.; Schreiner, S.; Lucarelli, E.; Jaquiery, C.; Schaefer, D.J.; Martin, I.; Scherberich, A. Extracellular matrix and $\alpha(5)\beta(1)$ integrin signaling control the maintenance of bone formation capacity by human adipose-derived stromal cells. *Sci. Rep.* **2017**, *7*, 44398. [CrossRef] [PubMed]

Tuning Myogenesis by Controlling Gelatin Hydrogel Properties through Hydrogen Peroxide-Mediated Cross-Linking and Degradation

Wildan Mubarok [ID], Kelum Chamara Manoj Lakmal Elvitigala [ID] and Shinji Sakai *[ID]

Department of Materials Engineering Science, Graduate School of Engineering Science, Osaka University, Toyonaka 560-8531, Japan; wildanmubarok@cheng.es.osaka-u.ac.jp (W.M.); kelum@cheng.es.osaka-u.ac.jp (K.C.M.L.E.)
* Correspondence: sakai@cheng.es.osaka-u.ac.jp

Abstract: Engineering skeletal muscle tissue in vitro is important to study the mechanism of myogenesis, which is crucial for regenerating muscle cells. The physicochemical properties of the cellular microenvironment are known to govern various cell behaviours. Yet, most studies utilised synthetic materials to model the extracellular matrix that suffers from cytotoxicity to the cells. We have previously reported that the physicochemical property of hydrogels obtained from horseradish peroxidase (HRP)-catalysed cross-linking could be controlled by a simple adjustment to the exposure time to air containing H_2O_2. In this study, we evaluated the influence of physicochemical properties dynamics in the gelatin possessing phenol groups (Gelatin-Ph) hydrogel to regulate the myogenesis in vitro. We controlled the Young's modulus of the Gelatin-Ph hydrogel by tuning the air containing 16 ppm H_2O_2 exposure time for 15–60 min. Additionally, prolonged exposure to air containing H_2O_2 also induced Gelatin-Ph degradation. Myoblasts showed higher adhesion and myotube formation on stiff hydrogel (3.53 kPa) fabricated through 30 min of exposure to air containing H_2O_2 compared to those on softer hydrogel (0.77–2.79 kPa) fabricated through 15, 45, and 60 min of the exposure. These results demonstrate that the myogenesis can be tuned by changes in the physicochemical properties of Gelatin-Ph hydrogel mediated by H_2O_2.

Keywords: horseradish peroxidase; myoblast; skeletal muscle; tissue engineering; gelatin

1. Introduction

Skeletal muscle is the largest component of the human body, accounting for 30–40% of body mass [1,2]. In the occurrence of traumatic injuries or degenerative diseases, skeletal muscle can be damaged, which causes a physiological impairment. To rescue the physiological function, the formation of new muscle cells (myogenesis) is needed. While native cells could regenerate the muscle tissue, controlling the fate of these cells to differentiate into muscle cells is difficult due to the complex interaction between the intrinsic factors of the cells and external factors, including their microenvironment. The tissue engineering approach has garnered great interest since it provides an in vitro model to study the physiological phenomenon regulating myogenesis that could improve the efficiency of cell therapy [3,4].

Among the important factors that govern myogenesis are the materials comprising the extracellular matrix (ECM) and the physicochemical properties of the ECM. To study the physicochemical effect of the substrate on myoblasts, most studies utilised synthetic materials such as poly(ethylene glycol) diacrylate (PEGDA), poly(vinyl alcohol) (PVA) gels, and poly(acrylamide) [5,6]. Zahari et al. utilised laminin-coated poly(methyl methacrylate) nanofiber scaffold [7], while Shin et al. reported the use of poly(lactic-co-glycolic acid) [8]. Additionally, the graphene oxide-based matrix is also widely used to control myoblast

differentiation [9,10]. However, these materials are not components of natural ECM and suffer from the toxicity of the uncross-linked monomers and photo-crosslinkers [5,6].

To model the native ECM environment, gelatin is widely used due to its excellent biocompatibility and biodegradability [11]. In recent years, several studies have reported the application of gelatin-based hydrogels to control myoblasts' behaviour. Hayashi et al. reported gelatin-conjugated supramolecular hydrogels with a switchable stiffness [12]. While C2C12 adhesion showed dynamic changes according to the stiffness, this study does not report the myoblasts differentiation. Denes et al. fabricated micropatterned gelatin hydrogels to study the myotube orientation [13]. Du et al. also successfully achieved directed cell migration and myotube formation using 3D-printed gelatin methacrolyl (GelMA) micropatterns on a surface coated with thermo-responsive material poly(*N*-isopropylacrylamide) [14]. However, these studies do not consider the effect of the physico-chemical properties of the gelatin hydrogel, which also play a key role in myogenesis.

Recently, we have reported that hydrogen peroxide (H_2O_2) could be used to control the physicochemical property of gelatin derivatives possessing phenolic hydroxyl moieties (Gelatin-Ph) hydrogel obtained from horseradish peroxidase (HRP)-catalysed cross-linking [15]. This system exploits the contradictory effect of H_2O_2 that simultaneously induces the HRP-catalysed cross-linking as an electron donor while degrading the polymer as an oxidant (Figure 1a) [15]. The advantage of this system is that the mechanical property and molecular weight of the hydrogel can be controlled by a simple adjustment of the air containing H_2O_2 exposure time. Using this system, the adhesion of stem cells and fibroblasts can be controlled [15]. However, there are no reports that study the effect of the dynamics of the physicochemical properties of the Gelatin-Ph hydrogel by H_2O_2 to control the myogenesis.
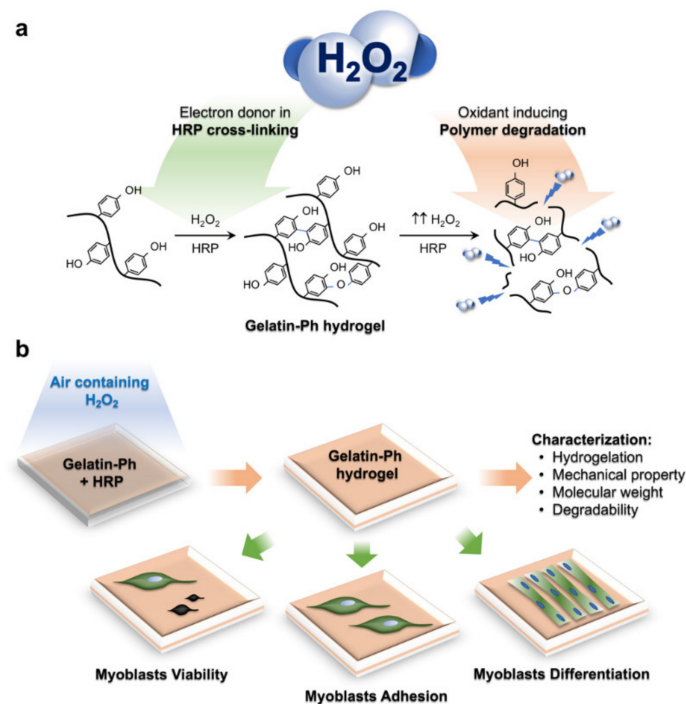
Figure 1. (**a**) The conceptual scheme of the contradictory function of hydrogen peroxide (H_2O_2) to induce horseradish peroxidase (HRP)-catalysed cross-linking and polymer degradation of the Gelatin-Ph. (**b**) Experimental scheme of this study. Gelatin-Ph hydrogels fabricated by tuning air containing H_2O_2 exposure time were characterised, and the effect on myoblasts' viability, adhesion, and differentiation was studied.

In this study, we aimed to investigate the effect of the H_2O_2–mediated control of the physicochemical properties of Gelatin-Ph on modulating myogenesis. To address this, we

fabricated the Gelatin-Ph hydrogel by exposing air containing H_2O_2 at different exposure times, and the hydrogel properties were characterised. The modulatory effect of these physicochemical changes of Gelatin-Ph on myoblast behaviour is studied to the myoblast adhesion and viability. In addition, we also report the influence of the H_2O_2 contradicting effect on the formation of myotubes on the Gelatin-Ph hydrogel (Figure 1b).

2. Results and Discussion

2.1. Gelatin-Ph Hydrogel Characterisation

Gelatin-Ph was successfully prepared by conjugating the gelatin with HPPA via WSCD/NHS chemistry in a DMF buffer pH 4.7 (Figure 2a). UV-Vis observation showed the peak at 275 nm corresponding to the phenol (Ph) group (Figure S1). The Ph-content was measured at 2.3×10^{-4} mol-Ph g-Gelatin-Ph^{-1} based on the tyramine standard. Next, we investigated the hydrogelation of Gelatin-Ph. In this study, hydrogelation is induced by HRP-catalysed cross-linking in the presence of air containing H_2O_2 (Figure 2b). Exposing air containing 16 ppm H_2O_2 to a PBS solution containing 3.0% *w/v* Gelatin-Ph and 0.1, 0.5, and 1.0 U mL^{-1} HRP resulted in hydrogel formation within 35 s. Additionally, the increase in the HRP concentration resulted in a shorter gelation time (Figure 2c). The shorter gelation time could be mediated by the higher phenolic radical generation in the higher HRP concentration [16].

The effect of air containing H_2O_2 exposure time on the properties of the Gelatin-Ph hydrogel was then investigated. The hydrogel was fabricated by exposing a PBS solution containing 3.0% *w/v* Gelatin-Ph and 1 U mL^{-1} HRP with air containing H_2O_2 for 15, 30, 45, and 60 min. We selected these parameters considering the ease of handling in room temperature. At 5.0% *w/v*, the Gelatin-Ph solution quickly forms hydrogel at room temperature, while at 1.0% *w/v*, the resultant hydrogels are too weak to handle for experiments. In addition, 1 U mL^{-1} HRP is used, since previous studies have reported an H_2O_2-mediated dynamic of the stiffening and softening of the hydrogels using a similar setup [15,17]. The scanning electron microscope (SEM) observation on the cross-section of the hydrogels showed a porous structure with a pore diameter of 28–42 μm (Figure S2). The mechanical property of the hydrogel was investigated by measuring the Young's modulus. The Young's modulus of the Gelatin-Ph hydrogels increased as the exposure time was extended from 0.77 ± 0.07 kPa at 15 min and peaked at 30 min at 3.53 ± 0.55 kPa. Further extending the exposure time to 45 and 60 min led to gradual decreases in the Young's modulus of the hydrogel to 2.79 ± 0.10 kPa and 1.97 ± 0.21 kPa, respectively (Figure 2d). The enzymatic degradation by collagenase showed a shorter time for the complete degradation on softer hydrogel obtained from 15 and 30 min of the exposure (Figure 2e).

The dynamic trend in the mechanical property of the hydrogel that shows an initial increase, which peaked at 30 min, followed by a reduction in the Young's modulus in prolonged exposure time (Figure 2d) is consistent with our previous studies on Gelatin-Ph hydrogel and Gelatin-Ph/HA-Ph composite hydrogel [15,17]. The decreased Young's moduli of Gelatin-Ph hydrogel in prolonged exposure to air containing 16 ppm H_2O_2 could be a consequence of cross-linking inhibition due to HRP inactivation. The prolonged exposure increased the concentration of H_2O_2 that generated excess phenoxy radicals. The attack of these excess radicals induces side reactions in the peroxidase catalytic cycle that inhibit cross-linking [18–21]. Further inactivation in higher H_2O_2 could also have occurred due to HRP denaturation [20].

Additionally, the decreasing Young's modulus at 45–60 min exposure time could also be caused by the degradation of Gelatin-Ph by H_2O_2. Molecular weight measurements showed a decreasing molecular weight of Gelatin-Ph following exposure with air containing H_2O_2 for 15–60 min (Figure 2f and Figure S3), demonstrating the Gelatin-Ph degradation in extended H_2O_2 exposure. H_2O_2 produced free radicals such as H·, O·, and OH· that could induce cleavage to degrade the polymer [22]. Indeed, previous studies have reported that H_2O_2 could degrade a variety of materials, including gelatin, via oxidation [23–25].
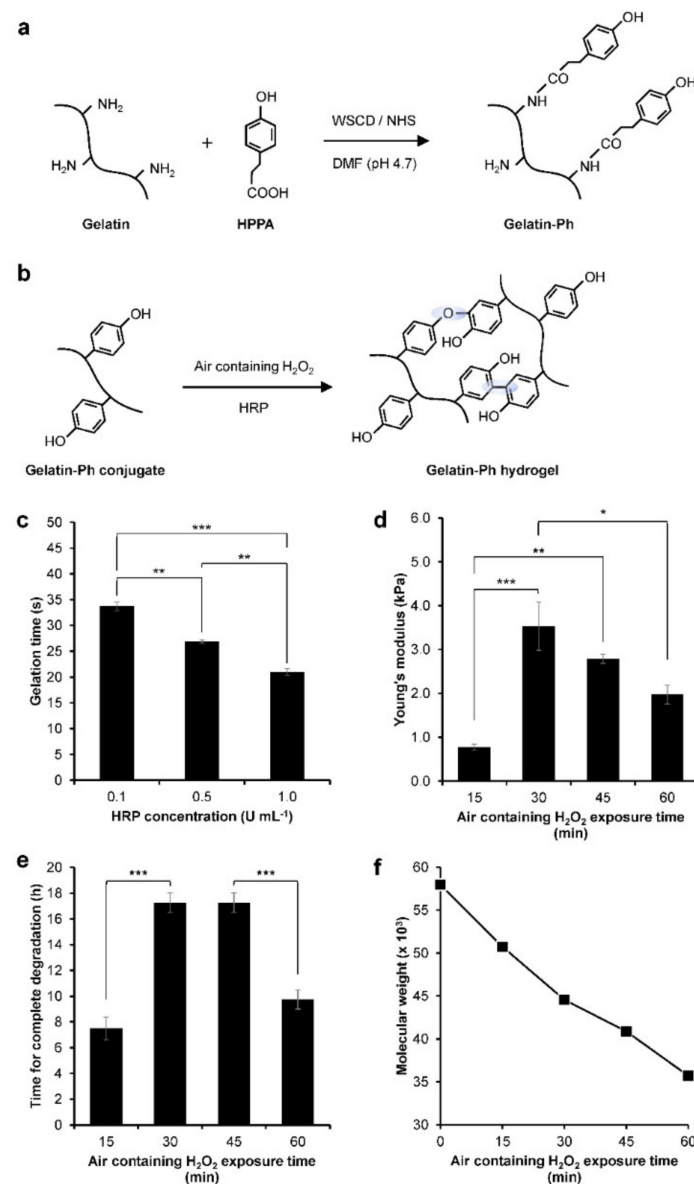
Figure 2. Characterisation of gelatin derivatives containing phenol groups (Gelatin-Ph) hydrogel. (**a**) Schematic of Gelatin-Ph preparation by conjugating gelatin with 3-(4-hydroxyphenyl) propionic acid (HPPA) using WSCD/NHS reaction in a DMF buffer (pH 4.7). (**b**) Schematic of HRP-catalysed cross-linking. (**c**) Gelation time of Gelatin-Ph hydrogel. Bar: S.E. (*n* = 3). (**d**) Young's modulus of Gelatin-Ph hydrogel obtained through exposing 16 ppm air containing H_2O_2 for 15–60 min. Bar: S.E. (*n* = 5). (**e**) Degradability of Gelatin-Ph hydrogel by collagenase. Bar: S.E. (*n* = 4). (**f**) Molecular weight of Gelatin-Ph exposed with air containing H_2O_2 for 0–60 min. * $p < 0.05$, ** $p < 0.005$, *** $p < 0.0005$, Tukey's HSD.

2.2. Myoblasts Viability

Cell-substrate interaction is important in the formation of muscle cells (myogenesis) during embryonic development and post-injury. In addition, understanding the effect of the physicochemical properties of the microenvironment is also important for studying muscle regeneration in vitro, which provides a crucial foundation for developing functional artificial tissues and in vivo or translational studies [3,4]. Therefore, we investigated the effect of the Young's moduli and molecular weight changes of the Gelatin-Ph hydrogel by air containing H_2O_2 to regulate myoblasts' behaviour.

In this study, we used C2C12 cells as the well-established myoblast cell line, which has been widely used as a skeletal muscle model [13,26–28]. Initially, we confirmed that the cells could attach to the hydrogel (Figure S4). Then, we investigated the viability of C2C12 myoblasts on the Gelatin-Ph hydrogels. The viability was analysed based on Calcein-AM/propidium iodide (PI) staining, which stained live and dead cells, respectively (Figure 3a). C2C12 cells showed the high viability (>94%) of the cells, independent of the exposure time to air containing H_2O_2 (Figure 3b). This result showed that, while the air containing H_2O_2 used in this study might intuitively be thought to induce cell death, the removal by catalase is sufficient to minimise or remove the toxic effect on cells. Additionally, the high viability of the cells could also be mediated by the well-known biocompatibility of Gelatin-Ph [29,30].
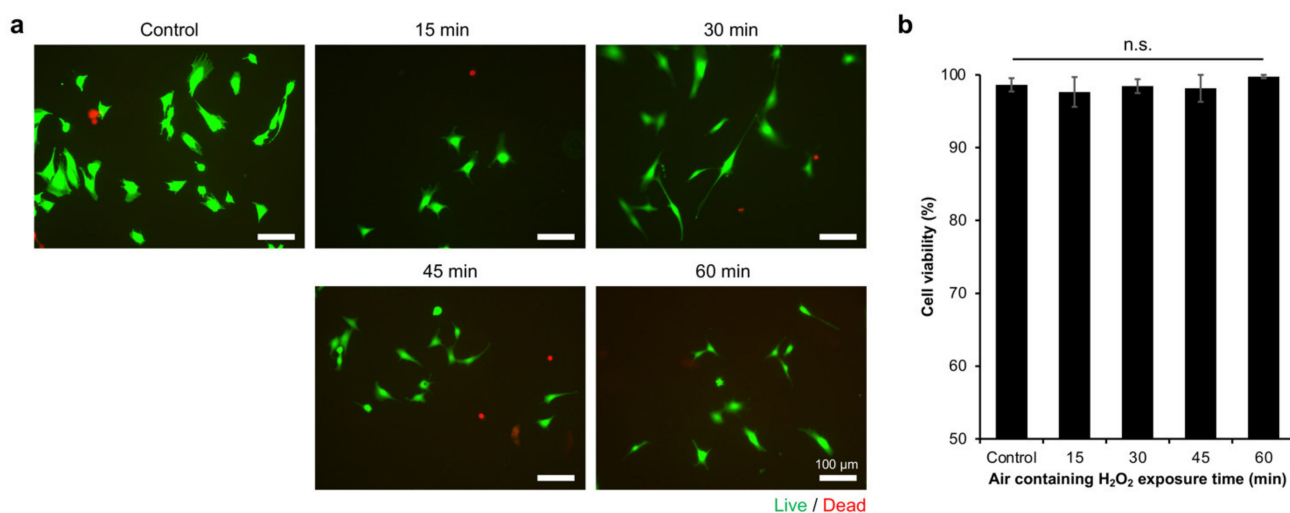
Figure 3. The viability of C2C12 myoblasts on Gelatin-Ph hydrogels obtained through varying air containing H_2O_2 exposure times. (**a**) Fluorescence micrograph of C2C12 myoblasts on day 2 of culture stained with Calcein-AM and propidium iodide (PI), which stained live and dead cells, respectively. (**b**) Viability of C2C12 myoblasts on the Gelatin-Ph hydrogels. Cells cultured on the culture well plate were used as the control. The data are presented as the means $\pm$ S.E. ($n = 6$). n.s.: $p > 0.05$, Tukey's HSD.

2.3. Myoblasts Adhesion

Based on the Calcein-AM staining during the viability analysis, it was observed that the cells had different morphologies on the hydrogels (Figure 3a). Previous studies have also reported that the Calcein, which stained the cytoplasm, allows for the observation of the cell morphology [31,32]. The difference in cell morphology could reflect the cell adhesion on the hydrogel. Therefore, the adhesion of myoblasts was investigated by analysing the morphology of the Calcein-AM-stained cells on the resultant Gelatin-Ph hydrogel. The myoblasts showed different morphologies on the Gelatin-Ph hydrogels obtained through different H_2O_2 exposure times (Figure 4a). The cells cultured on the hydrogel obtained through 30 min of the exposure, which has the highest mechanical property, had a large and elongated morphology, as shown by the largest cell area (Figure 4b) and lowest cell circularity (Figure 4c). In contrast, the cells cultured on the hydrogels obtained through air containing H_2O_2 exposure times of 15 min and 60 min had a more circular morphology, as shown by the lower cell area and higher circularity.
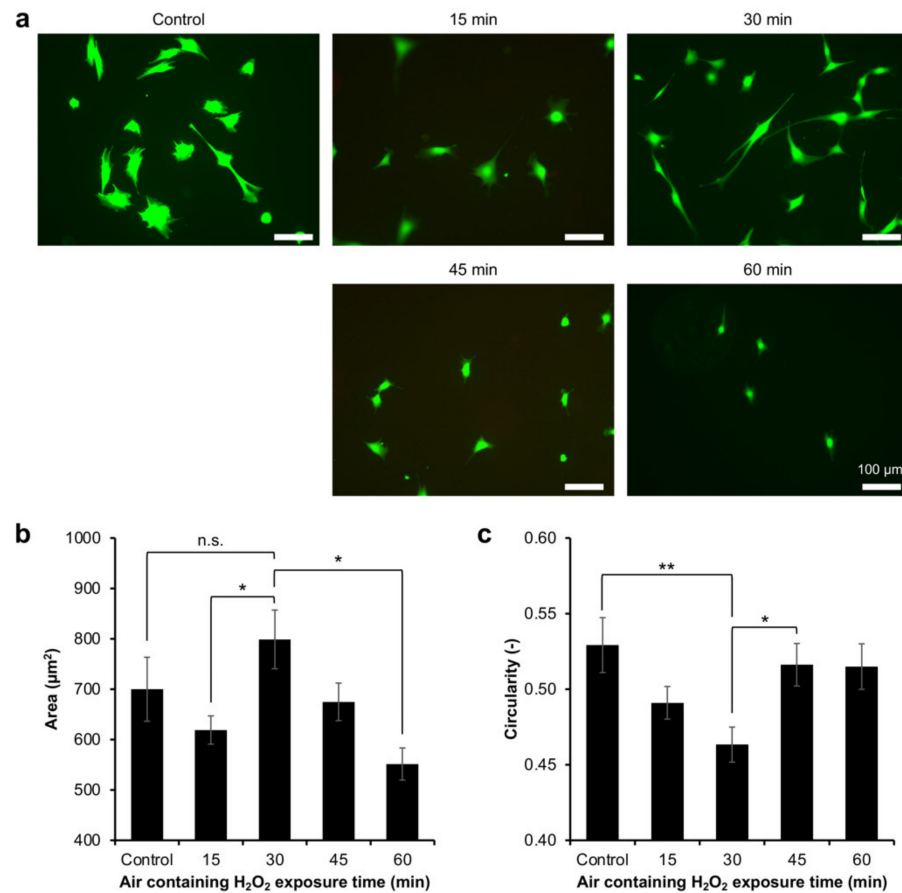
Figure 4. Adhesion of C2C12 myoblasts on Gelatin-Ph hydrogels obtained through exposure to air containing 16 ppm H_2O_2 for 15 to 60 min. (**a**) Fluorescence observation of C2C12 myoblasts stained with Calcein-AM cultured on the hydrogel for 2 days. As the control, the cells were cultured on the culture well plate. (**b**) Cell area and (**c**) circularity of C2C12 cells cultured on the resultant hydrogel. The data are presented as the means $\pm$ S.E. ($n \geq 114$ cells). N.s.: $p > 0.05$, * $p < 0.05$, ** $p < 0.005$, Tukey's HSD.

These results show that the adhesion of myoblasts depends on the stiffness of the Gelatin-Ph hydrogel. This phenomenon is similar to previous studies that cultured human mesenchymal stem cells, human adipose-derived stem cells, and fibroblasts on Gelatin-Ph hydrogel [15,33]. Additionally, smooth muscle cells and myoblasts also showed stiffness-dependent cell spreading on collagen-coated polyacrylamide gels and alginate hydrogel [34–36]. For adherent cells, including myoblasts, the adhesion dynamic depends on actin polymerisation and tension. A stiffer substrate allows actin polymerisation and assembly to occur and the cells to maintain the cytoskeletal tension, which results in the cell elongation [37,38]. In contrast, the cells cultured on the soft substrate cannot form F-actin bundles and stress fibres; thus, the cells appear in a round morphology [17,39].

Interestingly, we also found that the cells cultured on Gelatin-Ph hydrogel obtained through 30 min of exposure time have a more elongated shape than the cells on the plastic surface of the culture well plate, as observed from the significantly lower circularity ($p < 0.005$, Tukey's HSD) (Figure 4c). The stiffness of the culture well plate is much higher (~1 GPa) [40], than that of the Gelatin-Ph hydrogel (0.77–3.53 kPa). Therefore, despite having a lower stiffness, the cell-adhesive property of Gelatin-Ph could be beneficial to controlling the elongation of the myoblasts. This phenomenon is possibly mediated by the focal adhesion kinase (FAK), the regulator of the cell elongation that is activated by the interaction between the Arg-Gly-Asp (RGD) tripeptide of the Gelatin-Ph and the integrins [41].

2.4. Myoblasts Differentiation

Finally, we investigated myoblasts' differentiation into myotubes on the Gelatin-Ph hydrogels obtained from different exposures to H_2O_2. First, we seeded the cells on the culture well plate (control) and Gelatin-Ph hydrogels. After 1 day in the growth medium (DMEM + 10% fetal bovine serum), the cells' density had reached > 80% confluency. Therefore, the medium was changed to a differentiation medium consisting of DMEM supplied with 2% horse serum (Figure 5a). After 6 days, the myotube formation was determined by observing the multinucleated cells, in which the F-actin and nuclei of the cells were stained with Phalloidin and DAPI, respectively.
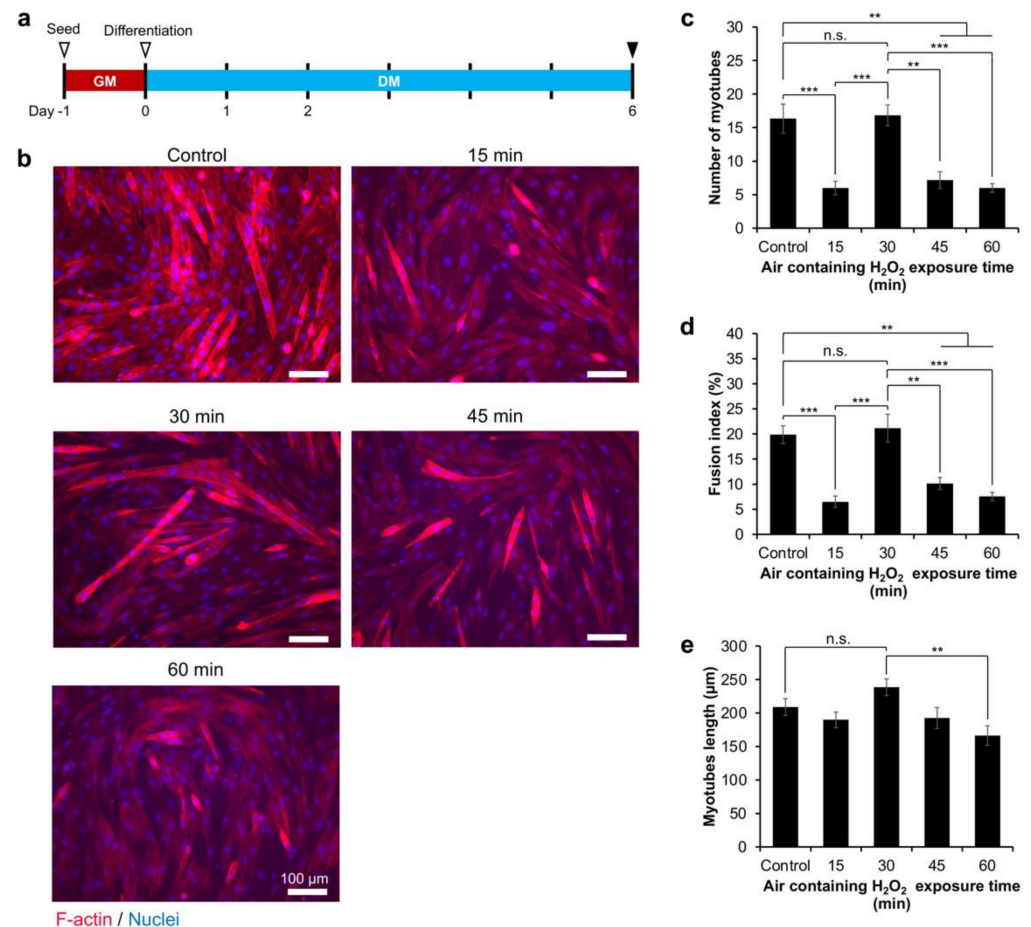
Figure 5. The differentiation of myoblasts to myotubes on the Gelatin-Ph hydrogel fabricated by altering the exposure time to air containing 16 ppm H_2O_2 for 15–60 min. (**a**) Experimental setup for inducing differentiation. After seeding, the cells were cultured in a growth medium (GM: DMEM + 10% fetal bovine serum). After 1 day in the GM, the medium was changed to a differentiation medium (DM: DMEM + 2% horse serum). (**b**) Fluorescence observation of C2C12 cells after 6 days in the differentiation medium stained with phalloidin and DAPI, staining F-actin and nuclei, respectively. (**c**) Number of myotubes ($n = 6$), (**d**) fusion index ($n = 6$), and (**e**) myotubes length ($n \geq 24$). Bar: S.E. n.s.: $p > 0.05$, ** $p < 0.005$, *** $p < 0.0005$, Tukey's HSD.

The fluorescence observations showed different myoblasts differentiation trends based on air containing H_2O_2 exposure times to fabricate Gelatin-Ph hydrogel (Figure 5b). The cells cultured on the Gelatin-Ph hydrogel obtained through 30 min of H_2O_2 exposure showed the highest myotube formation, similar to the control on the culture well plate, as shown by the highest number of myotubes (Figure 5c) and the fusion index (Figure 5d). In contrast, on the hydrogels fabricated through 15, 45, and 60 min of exposure to air containing H_2O_2, C2C12 showed a significantly lower number of myotubes (Figure 5c) and

a lower fusion index (Figure 5d). Furthermore, the myotubes cultured on hydrogel obtained through 30 min of the exposure also showed the longest myotube lengths (Figure 5e). These results showed that the myotube formation is also governed by the stiffness of the Gelatin-Ph hydrogel.

In this study, the myogenesis was studied on hydrogel with a stiffness range of 0.77–3.53 kPa. This stiffness range is lower than that in previous studies, in which Tomasch et al. used 5–20 kPa fibrin hydrogels [42], Boonen et al. used Matrigel-coated polyacrylamide gels with a stiffness of 3–80 kPa [43], and Romanazzo et al. used 0.9–133.2 MPa poly-ε-caprolactone film [44]. However, the stiffness of the Gelatin-Ph hydrogel in this study is within the range of the reported stiffnesses of an intact (~0.5 kPa) and damaged skeletal muscle tissue (2–5 kPa) [45–47]. The stiffness-dependent myotube formation observed in this study is in accordance with previous reports [42–44]. A possible explanation for the higher myogenesis in the stiffness of 3.53 kPa than that in the stiffness of 0.77 kPa in this study is that, similar to the native skeletal muscle tissue [45], higher myoblast proliferation and differentiation are observed in damaged tissue compared to those in intact tissue. A similar conclusion was also reported by Trensz et al., who modelled intact and damaged tissue stiffness using polyacrylamide gels [47]. Mechanically, the lower myogenesis on the softer substrate could also be explained by the deformation or collapse of the substrate under cell contraction forces, which inhibits the myotubes formation [48].

Taken together, our study demonstrates that the contradictory effect of H_2O_2 on inducing cross-linking and degrading the polymer of the Gelatin-Ph hydrogel could modulate the adhesion and differentiation of myoblasts. However, future studies should be conducted to address the limitations of our current study. In the future, myogenesis studies on higher stiffness that better reflect the optimum stiffness to induce myogenesis (~12 kPa) should be conducted [34]. Myogenesis analysis based on specific markers such as MyoD or MF20 also should be used to further confirm the myoblasts differentiation. More importantly, the intricate details of the mechanotransduction of the myoblasts in response to the physicochemical changes of the Gelatin-Ph hydrogel also need to be studied. The interaction between the RGD sequence of the gelatin and the myoblasts receptor, e.g., the integrins, could be the key regulator [49–51]. Integrins could affect the YAP/TAZ pathway, which is reported to play a role in cell adhesion [39,52] and differentiation [53].

Additionally, there is a possibility that the physicochemical changes in the Gelatin-Ph hydrogel also affect the cell–cell communication that triggers myoblast fusion to form myotubes. During myogenesis, myotubes are formed by the fusion between myoblasts or the myoblast-myotube. Hindi et al. reported that the myoblast fusion could be mediated by integrins that increase the expression of the β1D integrin and caveolin-3 via focal adhesion kinase (FAK) [54]. Alternatively, a gelatin-based scaffold could also regulate the Intercellular Adhesion Molecule-1 (ICAM-1) [55] that plays role in myoblast fusion [56,57]. Further studies should be conducted to address the details of these pathways. We believe that our findings are useful in the field of biomedical engineering aimed at the regeneration of muscular tissue, which requires the knowledge of cell-substrate interaction [3]. Additionally, our findings could also be applied in the development of scaffolds with tuneable physicochemical and biological properties for biomedical applications [58,59].

3. Conclusions

The modulatory effect of H_2O_2 in HRP-catalysed cross-linking and the polymer degradation of the Gelatin-Ph hydrogel on controlling the myogenesis is reported. The myoblasts showed a high viability on the Gelatin-Ph hydrogel. The myoblasts showed a stiffness-dependent adhesion and differentiation, with higher elongation and myotube formation observed in higher stiffnesses. Taken together, these results showed that the H_2O_2-mediated changes in the properties of the Gelatin-Ph could govern the myogenesis. We believe that our findings could be useful for skeletal muscle tissue engineering to control the cell fate to form new muscle cells.

4. Materials and Methods

4.1. Materials

Gelatin from bovine (type B, ~226 g Bloom) was purchased from Sigma-Aldrich (St. Louis, MO, USA). *N*-hydroxysuccinimide (NHS), *N*,*N*-Dimethylformamide (DMF), 3-(4-hydroxyphenyl) propionic acid (HPPA), aqueous hydrogen peroxide (H_2O_2, 31% *w/w*), horseradish peroxidase (HRP, 190 U mg^{-1}), catalase (bovine liver), collagenase, and 4% *w/v* paraformaldehyde in PBS were purchased from FUJIFILM Wako Pure Chemical (Osaka, Japan). Water-soluble carbodiimide hydrochloride (WSCD·HCl) was purchased from the Peptide Institute (Osaka, Japan). Dulbecco's Modified Eagle Medium (DMEM) was purchased from Nissui (Tokyo, Japan). Calcein-AM was purchased from Nacalai Tesque Inc., Kyoto, Japan). Propidium iodide (PI) was purchased from Dojindo, Kumamoto, Japan). Phalloidin-iFluor 647 Reagent (ab176759) was purchased from Abcam (Cambridge, UK), and -Cellstain®- DAPI solution was obtained from Dojindo (Kumamoto, Japan).

4.2. Gelatin-Ph Preparation

Gelatin-Ph was prepared based on the previously reported methods [60,61]. Briefly, the gelatin was conjugated with HPPA in the DMF buffer (pH 4.7) via WSCD/NHS chemistry. After 20 h, the solution was dialysed in dH_2O to remove the remaining HPPA, followed by freeze-drying. The presence of the Ph group introduced to the Gelatin-Ph was observed based on the peak at 275 nm using a UV-Vis spectrometer (UV-2600, Shimadzu, Kyoto, Japan).

4.3. Scanning Electron Microscope Observation

An aqueous solution containing 3.0% *w/v* Gelatin-Ph and 1 U mL^{-1} HRP in PBS was added to a polydimethylsiloxane (PDMS) mould (diameter: 8 mm, height: 4 mm). Air containing H_2O_2 was then exposed for 15, 30, 45, and 60 min. The resultant hydrogel was then frozen at -80 °C, immersed in 70% and 100% ethanol, and vacuum dried. The porous structure of the hydrogel was then observed using a scanning electron microscope (SEM, JCM-6000 plus, JEOL, Tokyo, Japan). The pore size was measured using ImageJ (1.53f51, NIH, Bethesda, MD, USA).

4.4. Gelation Time Measurement

The gelation time was measured based on previous reports [15,62]. A phosphate-buffered solution (PBS, pH 7.4) containing 3.0% *w/v* Gelatin-Ph and 0.1, 0.5, and 1 U mL^{-1} HRP was added to a well of a 48-well plate at 200 μL well^{-1}. Air containing H_2O_2 (16 ppm), which was prepared by blowing air into 1 M H_2O_2 solution, was then exposed to the polymer solution, which was continuously stirred with a magnetic stirrer. Gel formation was indicated by the swelling of the surface and the hindrance of the magnetic stirrer.

4.5. Mechanical Property Measurement

Air containing H_2O_2 was exposed for 15–60 min to 600 μL PBS solution containing 3.0% *w/v* Gelatin-Ph and 1 U mL^{-1} HRP in a 12-well plate. The Young's modulus of the fabricated Gelatin-Ph hydrogel was measured using a material tester (EZ-SX, Shimadzu, Kyoto, Japan). The hydrogels were compressed with a probe (ø: 8 mm) at a compression rate of 6.0 mm min^{-1}. The Young's modulus was calculated based on the stress–strain curve with a compression strain of 1–3% (Figure S5).

4.6. Enzymatic Degradation

The Gelatin-Ph hydrogels were immersed in the PBS solution for 24 h in order to reach an equilibrium state. The PBS solution was then changed to PBS containing 120 μg mL^{-1} collagenase. The time for the complete degradation of the hydrogel was observed using OLYMPUS Provi CM20 (Olympus, Tokyo, Japan).

4.7. Molecular Weight Measurement

The PBS solution containing 3.0% w/v Gelatin-Ph was exposed with air containing H_2O_2 for 0, 15, 30, 45, and 60 min. The molecular weights of the Gelatin-Ph were then measured using HPLC (LC-20AD, Shimadzu, Kyoto, Japan) and an RI detector (RID-20A, Shimadzu, Kyoto, Japan).

4.8. Cell Culture

The mouse muscle myoblasts C2C12 cell line was obtained from the RIKEN Cell Bank (Ibaraki, Japan). The C2C12 was cultured in a growth medium consisting of low glucose DMEM supplied with 10% v/v fetal bovine serum (FBS). The cells were cultured at a 37 °C incubator supplied with 5% CO_2.

4.9. Cell Viability and Adhesion Analysis

The hydrogel was fabricated by exposing 600 μL well^{-1} PBS solution containing 3.0% w/v Gelatin-Ph and 1 U mL^{-1} HRP to air containing H_2O_2 for 15–60 min. One millilitre of the growth medium containing 1 mg mL^{-1} catalase was added to the hydrogel to remove the remaining H_2O_2. After overnight incubation in the medium containing catalase, the hydrogels were washed with the PBS and growth medium. The C2C12 cells were then seeded on the hydrogel or culture well plate as the control at 3.6×10^3 cells cm^{-2}. The viability of the cells was observed after 2 days of culture by staining the cells with 3.3 μg mL^{-1} Calcein-AM/3.3 μg mL^{-1} propidium iodide (PI) in the PBS for 10 min, which stained the viable and dead cells, respectively. The Calcein-AM/PI-stained cells were observed using a fluorescence microscope (BZ-9000, Keyence, Osaka, Japan). The viability of the cells was calculated as the percentage of the number of viable cells/the total number of cells. Cell adhesion was analysed based on the morphological characteristics of the cells observed on day 2 of the culture. The cells' morphological parameters, including the cell area and circularity, were measured using ImageJ. The circularity was calculated as $4\pi \times (\text{area/perimeter}^2)$.

4.10. Cell Differentiation Analysis

The C2C12 cells were seeded onto the culture well plate (control) and the Gelatin-Ph hydrogels at a density of 2.6×10^4 cells cm^{-2}. After one day, the growth medium was changed to a differentiation medium consisting of DMEM containing 2% v/v horse serum. The differentiation medium was replenished every two days, and the multinucleated myotubes were observed on day 6 post-induction [63,64]. The myotubes were observed by staining the cells with Phalloidin-iFluor 647 Reagent and -Cellstain®- DAPI solution. Briefly, the cells were fixed with 4% paraformaldehyde in the PBS for 30 min, permeabilised in 4-(2-hydroxyethyl)-1-piperazineethanesulfonic acid (HEPES) pH 5.5 for 10 min, and stained with Phalloidin (1×) in the PBS for 60 min and with DAPI (100 nM) in the PBS for 30 min. The number of myotubes and nuclei, as well as the myotube lengths, were analysed using ImageJ. The fusion index was calculated as the percentage of the number of nuclei in the myotubes/the total number of nuclei.

4.11. Statistical Analysis

The data were analysed using Microsoft® Excel® 2019 version 1808 (Microsoft Corp., Redmond, WA, USA). The statistical analysis was conducted using a one-way analysis of variance (ANOVA). A post hoc t-test was conducted using Tukey's HSD; a p-value <0.05 was considered significantly different.

with air containing H_2O_2 for 0–60 min; Figure S4: Confocal laser-scanning microscope observation of the C2C12 myoblasts on the culture well plate (control) and the Gelatin-Ph hydrogel obtained through exposure to air containing H_2O_2 for 15, 30, 45, and 60 min.; Figure S5: Stress-strain curve of the Gelatin-Ph hydrogel fabricated by exposing the solution containing 3.0% w/v Gelatin-Ph and 1 U mL^{-1} HRP with air containing H_2O_2 for 15, 30, 45, and 60 min.

Author Contributions: Conceptualisation: S.S. and W.M.; Methodology: S.S.; Investigation: W.M. and K.C.M.L.E.; Data curation: W.M.; Formal analysis: W.M. and K.C.M.L.E.; Validation: W.M. and K.C.M.L.E.; Writing—original draft: W.M. and K.C.M.L.E.; Writing—review & editing: W.M., K.C.M.L.E., and S.S.; Project administration: S.S.; Funding acquisition: S.S.; Supervision: S.S. All authors have read and agreed to the published version of the manuscript.

Institutional Review Board Statement: Not applicable.

Informed Consent Statement: Not applicable.

Data Availability Statement: All data generated or analysed during this study are included in this published article and its supplementary files.

Conflicts of Interest: The authors declare no conflict of interest.

References

1. Kim, J.; Wang, Z.M.; Heymsfield, S.B.; Baumgartner, R.N.; Gallagher, D. Total-body skeletal muscle mass: Estimation by a new dual-energy X-ray absorptiometry method. *Am. J. Clin. Nutr.* **2002**, *76*, 378–383. [CrossRef]
2. Csapo, R.; Gumpenberger, M.; Wessner, B. Skeletal Muscle Extracellular Matrix—What Do We Know About Its Composition, Regulation, and Physiological Roles? A Narrative Review. *Front. Physiol.* **2020**, *11*, 253. [CrossRef]
3. Alarcin, E.; Bal-öztürk, A.; Avci, H.; Ghorbanpoor, H.; Guzel, F.D.; Akpek, A.; Yesiltas, G.; Canak-ipek, T.; Avci-adali, M. Current strategies for the regeneration of skeletal muscle tissue. *Int. J. Mol. Sci.* **2021**, *22*, 5929. [CrossRef]
4. Rossi, C.A.; Pozzobon, M.; De Coppi, P. Advances in musculoskeletal tissue engineering: Moving towards therapy. *Organogenesis* **2010**, *6*, 167–172. [CrossRef]
5. Maleiner, B.; Tomasch, J.; Heher, P.; Spadiut, O.; Rünzler, D.; Fuchs, C. The importance of biophysical and biochemical stimuli in dynamic skeletal muscle models. *Front. Physiol.* **2018**, *9*, 1130. [CrossRef]
6. Narasimhan, B.N.; Horrocks, M.S.; Malmström, J. Hydrogels with Tunable Physical Cues and Their Emerging Roles in Studies of Cellular Mechanotransduction. *Adv. NanoBiomed Res.* **2021**, *1*, 2100059. [CrossRef]
7. Zahari, N.K.; Idrus, R.B.H.; Chowdhury, S.R. Laminin-coated poly(Methyl methacrylate) (PMMA) nanofiber scaffold facilitates the enrichment of skeletal muscle myoblast population. *Int. J. Mol. Sci.* **2017**, *18*, 2242. [CrossRef]
8. Shin, Y.C.; Lee, J.H.; Jin, L.; Kim, M.J.; Kim, C.; Hong, S.W.; Oh, J.W.; Han, D.W. Cell-adhesive matrices composed of RGD peptide-displaying M13 bacteriophage/poly(lactic-co-glycolic acid) nanofibers beneficial to myoblast differentiation. *J. Nanosci. Nanotechnol.* **2015**, *15*, 7907–7912. [CrossRef]
9. Kumar, S.; Parekh, S.H. Linking graphene-based material physicochemical properties with molecular adsorption, structure and cell fate. *Commun. Chem.* **2020**, *3*, 8. [CrossRef]
10. Shin, Y.C.; Lee, J.H.; Jin, L.; Kim, M.J.; Kim, Y.J.; Hyun, J.K.; Jung, T.G.; Hong, S.W.; Han, D.W. Stimulated myoblast differentiation on graphene oxide-impregnated PLGA-collagen hybrid fibre matrices matrices. *J. Nanobiotechnol.* **2015**, *13*, 21. [CrossRef]
11. Jaipan, P.; Nguyen, A.; Narayan, R.J. Gelatin-based hydrogels for biomedical applications. *MRS Commun.* **2017**, *7*, 416–426. [CrossRef]
12. Hayashi, K.; Matsuda, M.; Mitake, N.; Nakahata, M.; Munding, N.; Harada, A.; Kaufmann, S.; Takashima, Y.; Tanaka, M. One-Step Synthesis of Gelatin-Conjugated Supramolecular Hydrogels for Dynamic Regulation of Adhesion Contact and Morphology of Myoblasts. *ACS Appl. Polym. Mater.* **2022**, *4*, 2595–2603. [CrossRef]
13. Denes, L.T.; Riley, L.A.; Mijares, J.R.; Arboleda, J.D.; McKee, K.; Esser, K.A.; Wang, E.T. Culturing C2C12 myotubes on micro-molded gelatin hydrogels accelerates myotube maturation. *Skelet. Muscle* **2019**, *9*, 17. [CrossRef]
14. Du, W.; Hong, S.; Scapin, G.; Goulard, M.; Shah, D.I. Directed Collective Cell Migration Using Three-Dimensional Bioprinted Micropatterns on Thermoresponsive Surfaces for Myotube Formation. *ACS Biomater. Sci. Eng.* **2019**, *5*, 3935–3943. [CrossRef]
15. Mubarok, W.; Qu, Y.; Sakai, S. Influence of Hydrogen Peroxide-Mediated Cross-Linking and Degradation on Cell-Adhesive Gelatin Hydrogels. *ACS Appl. Bio Mater.* **2021**, *4*, 4184–4190. [CrossRef]
16. Ren, K.; He, C.; Xiao, C.; Li, G.; Chen, X. Injectable glycopolypeptide hydrogels as biomimetic scaffolds forcartilage tissue engineering. *Biomaterials* **2015**, *51*, 238–249. [CrossRef]

17. Mubarok, W.; Elvitigala, K.C.M.L.; Nakahata, M.; Kojima, M.; Sakai, S. Modulation of Cell-Cycle Progression by Hydrogen Peroxide-Mediated Cross-Linking and Degradation of Cell-Adhesive Hydrogels. *Cells* **2022**, *11*, 881. [CrossRef]

18. Huang, Q.; Huang, Q.; Pinto, R.A.; Griebenow, K.; Schweitzer-Stenner, R.; Weber, W.J. Inactivation of horseradish peroxidase by phenoxyl radical attack. *J. Am. Chem. Soc.* **2005**, *127*, 1431–1437. [CrossRef]

19. Ogushi, Y.; Sakai, S.; Kawakami, K. Phenolic hydroxy groups incorporated for the peroxidase-catalyzed gelation of a carboxymethylcehulose support: Cellular adhesion and proliferation. *Macromol. Biosci.* **2009**, *9*, 262–267. [CrossRef]

20. Carvalho, R.H.; Lemos, F.; Lemos, M.A.N.D.A.; Vojinović, V.; Fonseca, L.P.; Cabral, J.M.S. Kinetic modelling of phenol co-oxidation using horseradish peroxidase. *Bioprocess Biosyst. Eng.* **2006**, *29*, 99–108. [CrossRef]

21. Reihmann, M.; Ritter, H. Synthesis of phenol polymers using peroxidases. In *Enzyme-Catalyzed Synthesis of Polymers*; Springer: Berlin/Heidelberg, Germany, 2006; Volume 194, pp. 1–49. [CrossRef]

22. Chen, H.; Qin, J.; Hu, Y. Efficient degradation of high-molecular-weight hyaluronic acid by a combination of ultrasound, hydrogen peroxide, and copper ion. *Molecules* **2019**, *24*, 617. [CrossRef]

23. Li, X.; Xu, A.; Xie, H.; Yu, W.; Xie, W.; Ma, X. Preparation of low molecular weight alginate by hydrogen peroxide depolymerization for tissue engineering. *Carbohydr. Polym.* **2010**, *79*, 660–664. [CrossRef]

24. Takahashi, S.; Itoh, N.; Kawamura, Y.; Hayashi, R. Physical and Chemical Changes of Gelatins by Oxidation Treatment. *Bull. Soc. Sci. Photogr. Jpn.* **1998**, *51*, 22–28. (In Japanese) [CrossRef]

25. Chang, K.L.B.; Tai, M.C.; Cheng, F.H. Kinetics and products of the degradation of chitosan by hydrogen peroxide. *J. Agric. Food Chem.* **2001**, *49*, 4845–4851. [CrossRef]

26. Burattini, S.; Ferri, R.; Battistelli, M.; Curci, R.; Luchetti, F.; Falcieri, E. C2C12 murine myoblasts as a model of skeletal muscle development: Morpho-functional characterization. *Eur. J. Histochem.* **2004**, *48*, 223–233.

27. McMahon, D.K.; Anderson, P.A.W.; Bunting, J.B.; Saba, Z.; Oakeley, E.; Carolina, N.; Anderson, P.A.W.; Bunting, J.B.; Saba, Z.; Oakeley, A.E.; et al. C2C12 cells: Biophysical, biochemical and immunocytochemical properties. *Am. J. Physiol.-Cell Physiol.* **1994**, *266*, C1795–C1802. [CrossRef]

28. Ikeda, K.; Ito, A.; Imada, R.; Sato, M.; Kawabe, Y.; Kamihira, M. In vitro drug testing based on contractile activity of C2C12 cells in an epigenetic drug model. *Sci. Rep.* **2017**, *7*, 44570. [CrossRef]

29. Kondo, D.; Ogino, Y.; Ayukawa, Y.; Sakai, S.; Kawakami, K.; Koyano, K. Bone Regeneration of Tibial Defects in Rats with Enzymatic Hydrogelation of Gelatin Derivative and Recombinant Human Platelet-Derived Growth Factor-BB Complex. *Int. J. Oral Maxillofac. Implant.* **2013**, *28*, 1377–1385. [CrossRef]

30. Le Thi, P.; Lee, Y.; Nguyen, D.H.; Park, K.D. In situ forming gelatin hydrogels by dual-enzymatic cross-linking for enhanced tissue adhesiveness. *J. Mater. Chem. B* **2017**, *5*, 757–764. [CrossRef]

31. Agarwal, V.; Tjandra, E.S.; Iyer, K.S.; Humfrey, B.; Fear, M.; Wood, F.M.; Dunlop, S.; Raston, C.L. Evaluating the effects of nacre on human skin and scar cells in culture. *Toxicol. Res.* **2014**, *3*, 223–227. [CrossRef]

32. Catelas, I.; Sese, N.; Wu, B.M.; Dunn, J.C.Y.; Helgerson, S.; Tawil, B. Human mesenchymal stem cell proliferation and osteogenic differentiation in fibrin gels in vitro. *Tissue Eng.* **2006**, *12*, 2385–2396. [CrossRef]

33. Wang, L.S.; Boulaire, J.; Chan, P.P.Y.; Chung, J.E.; Kurisawa, M. The role of stiffness of gelatin-hydroxyphenylpropionic acid hydrogels formed by enzyme-mediated crosslinking on the differentiation of human mesenchymal stem cell. *Biomaterials* **2010**, *31*, 8608–8616. [CrossRef]

34. Engler, A.J.; Griffin, M.A.; Sen, S.; Bönnemann, C.G.; Sweeney, H.L.; Discher, D.E. Myotubes differentiate optimally on substrates with tissue-like stiffness: Pathological implications for soft or stiff microenvironments. *J. Cell Biol.* **2004**, *166*, 877–887. [CrossRef]

35. Engler, A.; Bacakova, L.; Newman, C.; Hategan, A.; Griffin, M.; Discher, D. Substrate Compliance versus Ligand Density in Cell on Gel Responses. *Biophys. J.* **2004**, *86*, 617–628. [CrossRef]

36. Boontheekul, T.; Hill, E.E.; Kong, H.J.; Mooney, D.J. Regulating myoblast phenotype through controlled gel stiffness and degradation. *Tissue Eng.* **2007**, *13*, 1431–1442. [CrossRef]

37. Parsons, J.T.; Horwitz, A.R.; Schwartz, M.A. Cell adhesion: Integrating cytoskeletal dynamics and cellular tension. *Nat. Rev. Mol. Cell Biol.* **2010**, *11*, 633–643. [CrossRef]

38. Iskratsch, T.; Wolfenson, H.; Sheetz, M.P. Appreciating force and shape-the rise of mechanotransduction in cell biology. *Nat. Rev. Mol. Cell Biol.* **2014**, *15*, 825–833. [CrossRef]

39. Dupont, S. Role of YAP/TAZ in cell-matrix adhesion-mediated signalling and mechanotransduction. *Exp. Cell Res.* **2016**, *343*, 42–53. [CrossRef]

40. Syed, S.; Karadaghy, A.; Zustiak, S. Simple polyacrylamide-based multiwell stiffness assay for the study of stiffness-dependent cell responses. *J. Vis. Exp.* **2015**, *2015*, 1–12. [CrossRef]

41. Katoh, K. FAK-Dependent Cell Motility and Cell Elongation. *Cells* **2020**, *9*, 192. [CrossRef]

42. Tomasch, J.; Maleiner, B.; Heher, P.; Rufin, M.; Andriotis, O.G.; Thurner, P.J.; Redl, H.; Fuchs, C.; Teuschl-Woller, A.H. Changes in Elastic Moduli of Fibrin Hydrogels Within the Myogenic Range Alter Behavior of Murine C2C12 and Human C25 Myoblasts Differently. *Front. Bioeng. Biotechnol.* **2022**, *10*, 836520. [CrossRef]

43. Boonen, K.J.M.; Rosaria-Chak, K.Y.; Baaijens, F.P.T.; Van Der Schaft, D.W.J.; Post, M.J. Essential environmental cues from the satellite cell niche: Optimizing proliferation and differentiation. *Am. J. Physiol.-Cell Physiol.* **2009**, *296*, 1338–1345. [CrossRef]

44. Romanazzo, S.; Forte, G.; Ebara, M.; Uto, K.; Pagliari, S.; Aoyagi, T.; Traversa, E.; Taniguchi, A. Substrate stiffness affects skeletal myoblast differentiation in vitro. *Sci. Technol. Adv. Mater.* **2012**, *13*, 064211. [CrossRef]

45. Lacraz, G.; Rouleau, A.J.; Couture, V.; Söllrald, T.; Drouin, G.; Veillette, N.; Grandbois, M.; Grenier, G. Increased stiffness in aged skeletal muscle impairs muscle progenitor cell proliferative activity. *PLoS ONE* **2015**, *10*, e0136217. [CrossRef]

46. Silver, J.S.; Günay, K.A.; Cutler, A.A.; Vogler, T.O.; Brown, T.E.; Pawlikowski, B.T.; Bednarski, O.J.; Bannister, K.L.; Rogowski, C.J.; McKay, A.G.; et al. Injury-mediated stiffening persistently activates muscle stem cells through YAP and TAZ mechanotransduction. *Sci. Adv.* **2021**, *7*, eabe4501. [CrossRef]

47. Trensz, F.; Lucien, F.; Couture, V.; Söllrald, T.; Drouin, G.; Rouleau, A.J.; Grandbois, M.; Lacraz, G.; Grenier, G. Increased microenvironment stiffness in damaged myofibers promotes myogenic progenitor cell proliferation. *Skelet. Muscle* **2015**, *5*, 5. [CrossRef]

48. Levy-Mishali, M.; Zoldan, J.; Levenberg, S. Effect of scaffold stiffness on myoblast differentiation. *Tissue Eng.-Part A* **2009**, *15*, 935–944. [CrossRef]

49. Wang, P.Y.; Thissen, H.; Tsai, W.B. The roles of RGD and grooved topography in the adhesion, morphology, and differentiation of C2C12 skeletal myoblasts. *Biotechnol. Bioeng.* **2012**, *109*, 2104–2115. [CrossRef]

50. Gribova, V.; Gauthier-Rouvière, C.; Albigès-Rizo, C.; Auzely-Velty, R.; Picart, C. Effect of RGD functionalization and stiffness modulation of polyelectrolyte multilayer films on muscle cell differentiation. *Acta Biomater.* **2013**, *9*, 6468–6480. [CrossRef]

51. Robinson, P.A.; Brown, S.; McGrath, M.J.; Coghill, I.D.; Gurung, R.; Mitchell, C.A. Skeletal muscle LIM protein 1 regulates integrin-mediated myoblast adhesion, spreading, and migration. *Am. J. Physiol.-Cell Physiol.* **2003**, *284*, 681–695. [CrossRef]

52. Nardone, G.; Oliver-De La Cruz, J.; Vrbsky, J.; Martini, C.; Pribyl, J.; Skládal, P.; Pešl, M.; Caluori, G.; Pagliari, S.; Martino, F.; et al. YAP regulates cell mechanics by controlling focal adhesion assembly. *Nat. Commun.* **2017**, *8*, 15321. [CrossRef]

53. Van Putten, S.; Shafieyan, Y.; Hinz, B. Mechanical control of cardiac myofibroblasts. *J. Mol. Cell. Cardiol.* **2016**, *93*, 133–142. [CrossRef]

54. Hindi, S.M.; Tajrishi, M.M.; Kumar, A. Signaling mechanisms in mammalian myoblast fusion. *Sci. Signal.* **2013**, *6*, re2. [CrossRef]

55. Nosenko, M.A.; Maluchenko, N.V.; Drutskaya, M.S.; Arkhipova, A.Y.; Agapov, I.I.; Nedospasov, S.A.; Moisenovich, M.M. Induction of ICAM-1 expression in mouse embryonic fibroblasts cultured on fibroin-gelatin scaffolds. *Acta Nat.* **2017**, *9*, 89–93. [CrossRef]

56. Pizza, F.X.; Martin, R.A.; Springer, E.M.; Leffler, M.S.; Woelmer, B.R.; Recker, I.J.; Leaman, D.W. Intercellular adhesion molecule-1 augments myoblast adhesion and fusion through homophilic trans-interactions. *Sci. Rep.* **2017**, *7*, 5094. [CrossRef]

57. Goh, Q.; Dearth, C.L.; Corbett, J.T.; Pierre, P.; Chadee, D.N.; Pizza, F.X. Intercellular adhesion molecule-1 expression by skeletal muscle cells augments myogenesis. *Exp. Cell Res.* **2015**, *331*, 292–308. [CrossRef]

58. Zhang, Y.; Li, S.; Xu, Y.; Zhang, M.; Huang, Y.; Liang, Y.; Chen, Y.; Ji, W.; Kim, J.R.; Song, W.; et al. Engineering of hollow polymeric nanosphere-supported imidazolium-based ionic liquids with enhanced antimicrobial activities. *Nano Res.* **2022**, *15*, 5556–5568. [CrossRef]

59. Zhang, Y.; Song, W.; Lu, Y.; Xu, Y.; Wang, C.; Yu, D.G.; Kim, I. Recent Advances in Poly(α-L-glutamic acid)-Based Nanomaterials for Drug Delivery. *Biomolecules* **2022**, *12*, 636. [CrossRef]

60. Hu, M.; Kurisawa, M.; Deng, R.; Teo, C.M.; Schumacher, A.; Thong, Y.X.; Wang, L.; Schumacher, K.M.; Ying, J.Y. Cell immobilization in gelatin-hydroxyphenylpropionic acid hydrogel fibers. *Biomaterials* **2009**, *30*, 3523–3531. [CrossRef]

61. Wang, L.S.; Chung, J.E.; Pui-Yik Chan, P.; Kurisawa, M. Injectable biodegradable hydrogels with tunable mechanical properties for the stimulation of neurogenesic differentiation of human mesenchymal stem cells in 3D culture. *Biomaterials* **2010**, *31*, 1148–1157. [CrossRef]

62. Peng, H.T.; Blostein, M.D.; Shek, P.N. Experimental optimization of an in situ forming hydrogel for hemorrhage control. *J. Biomed. Mater. Res.-Part B Appl. Biomater.* **2009**, *89*, 199–209. [CrossRef]

63. Asano, T.; Ishizua, T.; Yawo, H. Optically controlled contraction of photosensitive skeletal muscle cells. *Biotechnol. Bioeng.* **2012**, *109*, 199–204. [CrossRef]

64. Asano, T.; Ishizuka, T.; Morishima, K.; Yawo, H. Optogenetic induction of contractile ability in immature C2C12 myotubes. *Sci. Rep.* **2015**, *5*, 8317. [CrossRef]

Antioxidant, Anti-Inflammatory and Attenuating Intracellular Reactive Oxygen Species Activities of *Nicotiana tabacum* var. Virginia Leaf Extract Phytosomes and Shape Memory Gel Formulation

Chuda Chittasupho [1,2], Kunyakorn Chaobankrang [1], Araya Sarawungkad [1], Weerasak Samee [3], Sudarshan Singh [1], Kirachuda Hemsuwimon [4], Siriporn Okonogi [1,2], Kantaporn Kheawfu [1,2], Kanokwan Kiattisin [1] and Wantida Chaiyana [1,2,*]

1   Department of Pharmaceutical Sciences, Faculty of Pharmacy, Chiang Mai University, Mueang, Chiang Mai 50200, Thailand
2   Research Center of Pharmaceutical Nanotechnology, Faculty of Pharmacy, Chiang Mai University, Chiang Mai 50200, Thailand
3   Department of Pharmaceutical Chemistry, Faculty of Pharmacy, Srinakharinwirot University, Ongkharak, Nahonnayok 26120, Thailand
4   Tobacco Authority of Thailand, Leaf Department, Maejo Tobacco Experiment Station, Chiang Mai 50290, Thailand
*   Correspondence: wantida.chaiyana@cmu.ac.th

Abstract: Oxidative stress is one of the major causes of skin aging. In this study, the shape memory gels containing phytosomes were developed as a delivery system for *Nicotiana tabacum* var. Virginia fresh (VFL) and dry (VDL) leaf extracts. The extracts were loaded in the phytosomes by a solvent displacement method. The physical and chemical characteristics and stability of phytosomes were evaluated by dynamic light scattering and phytochemistry, respectively. The in vitro antioxidant activity and intracellular reactive oxygen species reduction of phytosomes and/or extracts were investigated by the DPPH and ABTS radical scavenging assays, FRAP assay, and DCFH-DA fluorescent probe. The cytotoxicity and anti-inflammatory activity of VDL and VFL phytosomes were studied by an MTT and a nitric oxide assay, respectively. Here, we first reported the total phenolic content in the dry leaf extract of *N. tabacum* var. Virginia was significantly greater than that of the fresh leaf extract. The HPLC analysis results revealed that VDL and VFL extracts contained 4.94 ± 0.04 and 3.13 ± 0.01 µg/mL of chlorogenic acid and 0.89 ± 0.00 and 0.24 ± 0.00 µg/mL of rutin, respectively. The phytosomes of the VDL and VFL extracts displayed stable size, polydispersity index, zeta potential values, and good chemical stability. VDL and VDL phytosomes showed higher phenolic and flavonoid contents which showed stronger DPPH and ABTS radical scavenging effects and reduced the intracellular ROS. The results suggested that the phenolic compounds are the main factor in their antioxidant activity. Both VDL and VFL phytosomes inhibited nitric oxide production induced by LPS, suggesting the anti-inflammatory activity of the phytosomes. The shape memory gel containing VDL and VFL phytosomes had good physical stability in terms of pH and viscosity. The VDL and VFL phytosomes dispersed in the shape memory gels can be considered as a promising therapeutic delivery system for protecting the skin from oxidation and reactive oxygen species.

Keywords: phytosomes; tobacco leaf; polyurethane-62; reactive oxygen species; shape memory gel

1. Introduction

Skin aging can be caused by internal and external factors [1]. The internal factors include chronological aging and hormonal deficiency, resulting in the deterioration of tissues in the dermis and epidermis. The decrease in the number of fibroblasts synthesizing collagen, elastin fiber, and glycosaminoglycan leads to an increase in laxity and wrinkles [2].

The external factors are ultraviolet radiation (UVR), nutrition, smoking, and air pollution, causing increased free radicals and oxidative stress in the skin [3]. Oxidative stress can cause skin wrinkling and is linked to human skin diseases, including skin cancer. Reactive oxygen species (ROS) are involved in the pathogenesis of several allergic and inflammatory skin diseases. Intracellular and extracellular oxidative stress-initiated ROS promote skin aging. ROS disrupt gene and protein function, change intracellular and extracellular homeostasis, and impair skin function [4]. The prolonged accumulation of ROS can result in cellular aging and may adversely affect health. These reactions involve the damage of lipids, proteins, and DNA, thus, causing cellular damage that can eventually lead to cell death [5].

Antioxidants resist or slow down the aging of the skin. Several formulations have been developed to deliver antioxidants to prevent or delay the deterioration of skin cells. Antioxidants in nature are usually phenolic compounds, flavonoids, and tannins. In this study, the biological activity, and phytochemical constituents of tobacco dry leaf extract (VDL) and fresh leaf extract (VFL) from *Nicotiana tabacum* var. Virginia, especially phenolic compounds and flavonoids, were investigated. Although these phytochemicals have good antioxidative activity due to their ability to bind free radicals with the hydroxyl functional group (-OH) in the chemical structure, most effective natural extracts have limited water solubility [6–11]. Therefore, the delivery system must be developed to increase the solubility and stability of the bioactive compounds in the extracts.

The phytosome is a type of drug delivery system. The phytosome encapsulates natural bioactive constituents by forming hydrogen bonds with the polar head of the phytosome. The phytosome and bioactive compound complexes are formed in which the phospholipids' head group is anchored. In contrast, the fatty acid chains of phospholipids encapsulate the polar part of complexes to form a lipophilic surface [12]. Phytosomes can be prepared by various methods, including solvent evaporation, co-solvent lyophilization, and anti-solvent precipitation [13]. In this study, the solvent displacement method was applied to fabricate phytosomes. Generally, a polar aprotic solvent was used to dissolve the drug and phytosome component to support an optimal bonding environment. The extract was encapsulated in the phytosomes by forming hydrogen bonds with phospholipids to improve drug retention, enhance the stability of the formulation, increase the permeability and drug absorption through the skin, and strengthen the bioactive compound efficiency [14–16]. Numerous studies have shown the success of developing phytosome formulations for the delivery of natural substances such as apigenin, *Centella asiatica* extract, and grape seed (*Vitis vinifera* L.) extract [15–17]. Phytosomes stabilized and increased the bioavailability and permeability of the bioactive compounds.

Natural antioxidants, whether in the form of raw extracts or chemical constituents, are extremely effective at preventing the damaging processes caused by oxidative stress [18]. Despite the fact that the toxicity profile of most medicinal plants has not been thoroughly evaluated, it is widely accepted that medicines derived from a plant extract are safer than their synthetic counterparts [19,20]. The search for novel natural antioxidants of plant origin has intensified. The antioxidant activity of plant extract plays a significant role in protecting against the non-communicable diseases caused by oxidative stress. The current study was designed to investigate the possibility of *N. tabacum* var. Virginia dry and fresh leaf extracts for preventing skin aging caused by oxidative stress. Therefore, the total phenolic content and total flavonoids and the antioxidant activities of ethanol extract of *N. tabacum* var. Virginia dry and fresh leaf were investigated. The VDL and VFL phytosomes were successfully formulated with good colloidal stability. We found that the storage temperature and phytosome formulation including phospholipids, cholesterol, and poloxamers played significant roles in the stability of the VDL and VFL phytosomes. Pearson correlation coefficients revealed the very high correlation between the total phenolic content and antioxidant activity of the extract and phytosomes. The effective and non-toxic concentrations of VDL and VFL phytosomes in reducing inflammation and intracellular reactive oxygen species in keratinocytes were reported. The gels containing phytosomes were developed to make

phytosomes feasible for topical application. The method to prepare the shape memory gel containing phytosome developed in this study was simple and was achievable for scaling up commercially.

2. Results and Discussion

2.1. Physical Characterization and Colloidal Stability of VDL and VFL Phytosomes, Phytosomes w/o Chloresterol, Phytosomes w/o Poloxamer, and Nanoparticles

The average particle size and stability of the VDL and VFL phytosomes with and without cholesterol or poloxamer, and VDL and VFL nanoparticles are shown in Figure 1. The size of the VDL phytosome with cholesterol, VDL phytosome without cholesterol, VDL phytosome without poloxamer, and VDL nanoparticles were 198.17 ± 6.63 nm, 248.63 ± 1.33 nm, 311.00 ± 5.21 nm, and 249.30 ± 1.56 nm, respectively. The size of the VFL phytosome with cholesterol, VFL phytosome without cholesterol, VFL phytosome without poloxamer, and VFL nanoparticles shown in Figure 2 were 163.40 ± 0.26 nm, 203.83 ± 1.44 nm, 191.43 ± 1.19 nm, and 178.67 ± 0.82 nm, respectively.
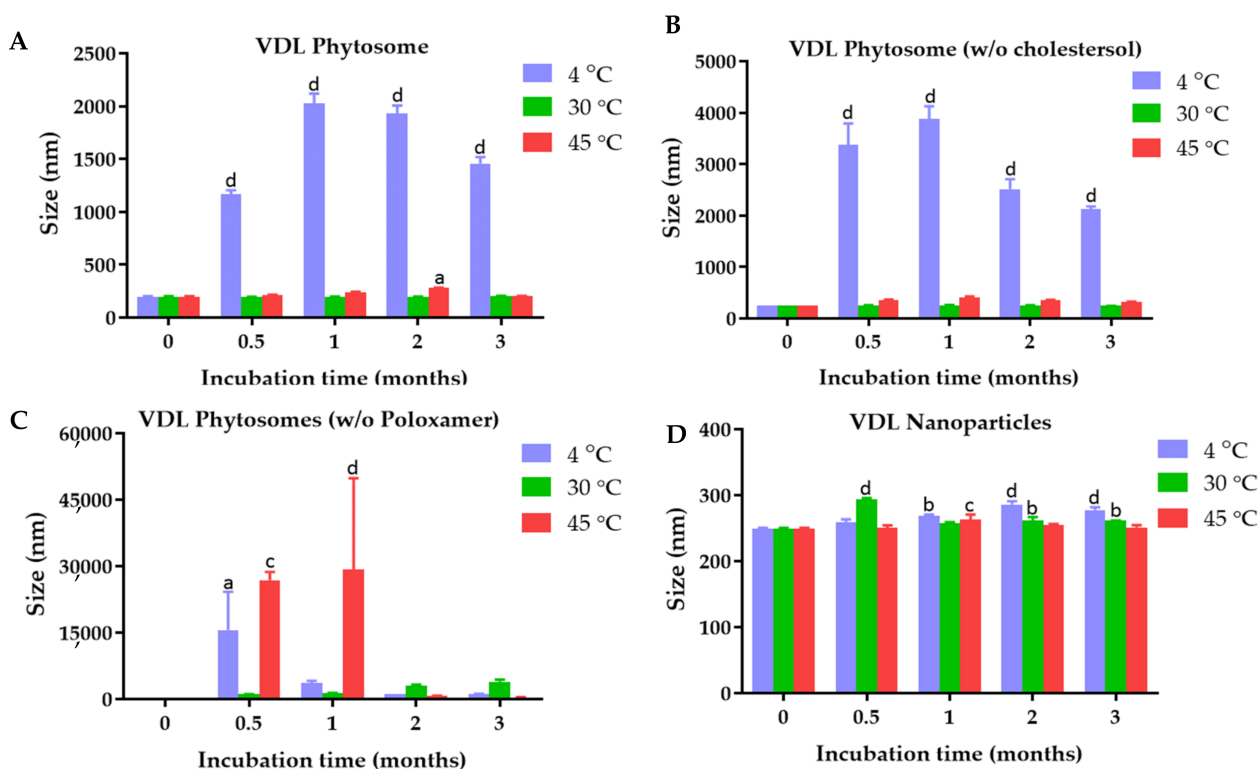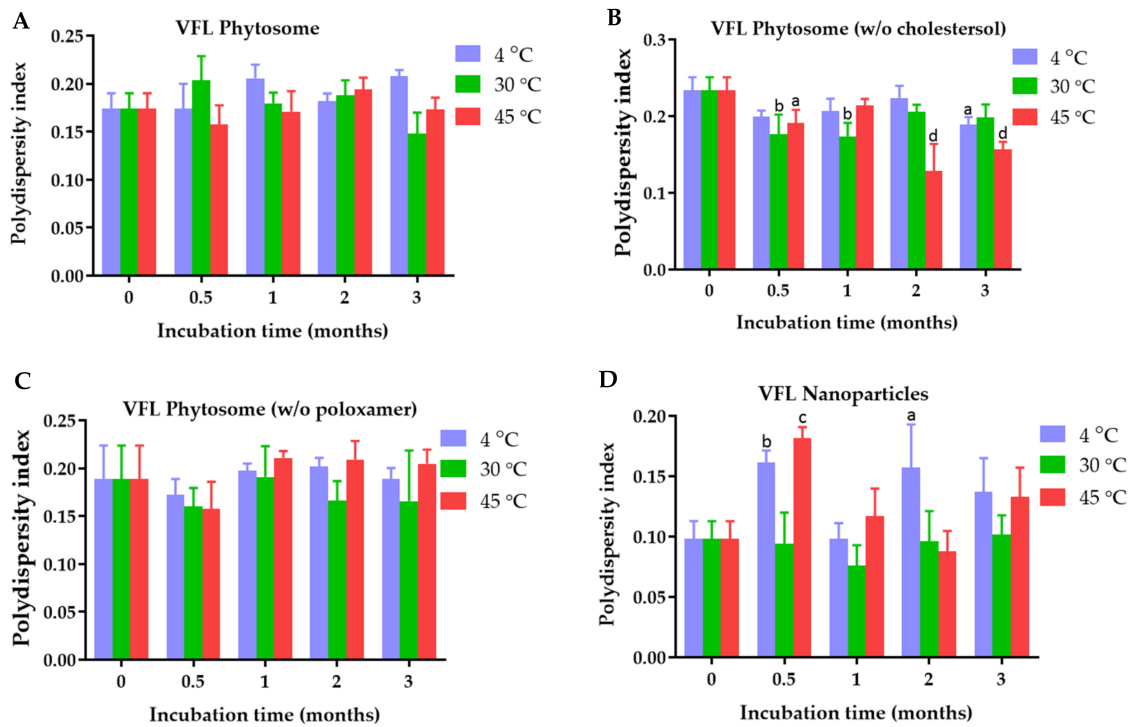

Figure 1. Size of (**A**) VDL phytosomes, (**B**) VDL phytosomes (w/o cholesterol), (**C**) VDL phytosomes (*w/o* poloxamer), and (**D**) VDL nanoparticles after fresh preparation and storage for 0.5, 1, 2, and 3 months at 4 °C, 30 °C, and 45 °C. The letters a, b, c, and d indicate *p*-values < 0.05, 0.01, 0.001, and 0.001, respectively.

The results showed that the particle size significantly increased in the absence of cholesterol in both VDL and VFL phytosome formulations. The importance of cholesterol in liposomes was reported. The solidity of the liposomes depended on the content of cholesterol. Numerous studies used cholesterol as a stabilizer of liposomes because it helped the packing of phospholipid molecules, reduced bilayer permeability, prevented liposome aggregation, and increased the rigidity and resistance to shear stress of the lipid bilayer [21]. Here, 0.9% *w/w* of cholesterol was used and was considered optimal for VDL and VFL phytosome formulations. In the absence of 0.1% *w/v* poloxamer 407, the VDL and VFL phytosomes were also significantly larger than the phytosomes stabilized with poloxamer. Poloxamer was assumed to be attached to the phytosome by adsorp-

tion. Minnelli et al. showed that combining poloxamer 407 with liposome increased liposome stability by hindering liposome aggregation, shielding the colloidal surface with the hydrophilic portions of the polymer, and decreasing the fusion of phosphatidylcholine multilamellar vesicles [22]. The size of the phytosomes significantly increased when samples were stored at 4 °C. Generally, the size of the liposome/phytosome is influenced by the elasticity modulus of the lipid bilayer, which depends on the temperature below the phase transition. Most membrane compositions form larger liposomes/phytosomes close to or below the gel-to-liquid crystalline phase transition temperature, where the membrane elasticity modulus is much larger [23]. The colloidal stability study results suggested that VDL and VFL phytosomes and nanoparticles should be stored at 30 °C to maintain the size of the particles. Interestingly, the effects of membrane stiffness of phytosomes were not found to significantly affect the size of VFL phytosomes when stored at 4 °C. This result suggested that the stability of phytosomes was mostly dependent on the zeta potential values of the phytosomes, which defeated the effect of the membrane elasticity [24].
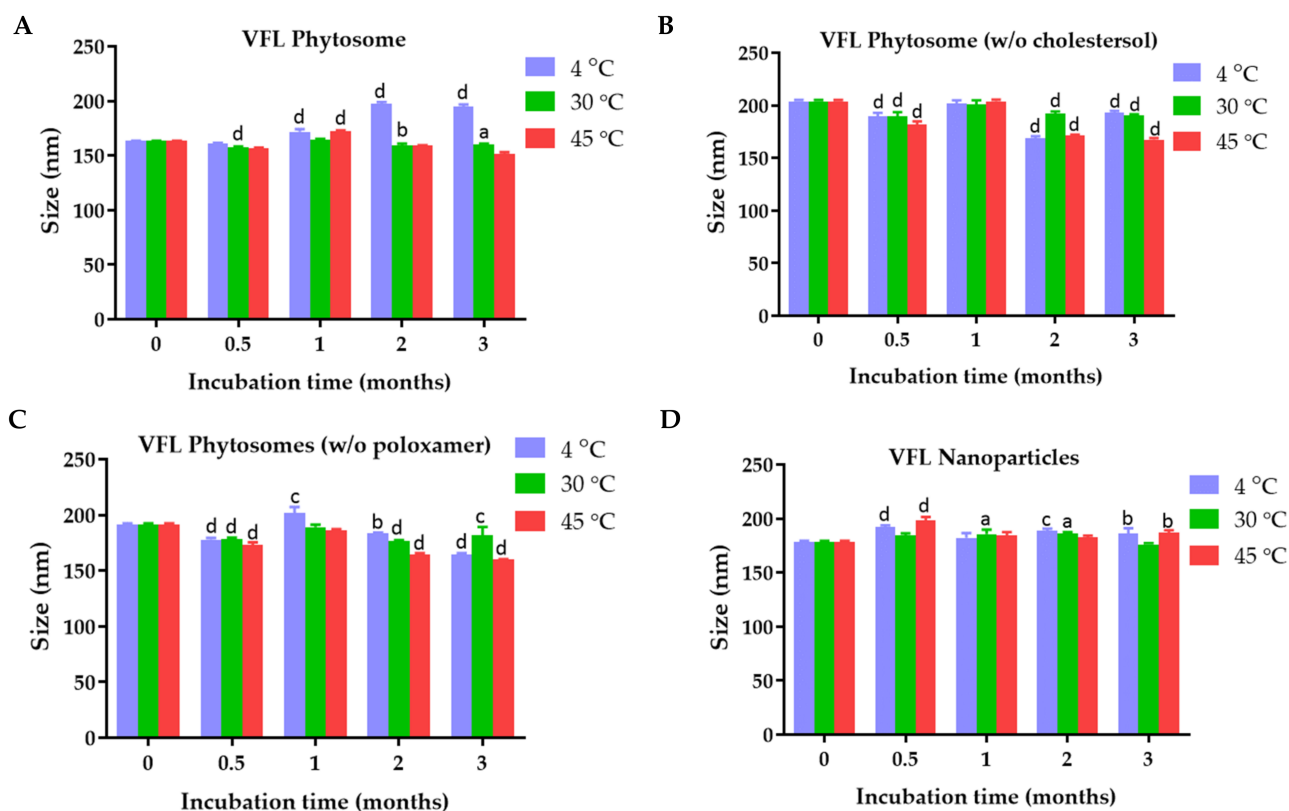
Figure 2. Size of (**A**) VFL phytosomes, (**B**) VFL phytosomes (*w/o* cholesterol), (**C**) VFL phytosomes (*w/o* poloxamer), and (**D**) VFL nanoparticles after fresh preparation and storage for 0.5, 1, 2, and 3 months at 4 °C, 30 °C, and 45 °C. The letters a, b, c, and d indicate *p*-value < 0.05, 0.01, 0.001, and 0.001, respectively.

The polydispersity index of VDL phytosome with cholesterol, VDL phytosome without cholesterol, VDL phytosome without poloxamer, and VDL nanoparticles were 0.136 ± 0.019, 0.128 ± 0.024, 0.169 ± 0.040, and 0.164 ± 0.027, respectively (Figure 3). The polydispersity index of VFL phytosome with cholesterol, VFL phytosome without cholesterol, VFL phytosome without poloxamer, and VFL nanoparticles were 0.174 ± 0.016, 0.234 ± 0.017, 0.189 ± 0.035, and 0.098 ± 0.015, respectively (Figure 4).
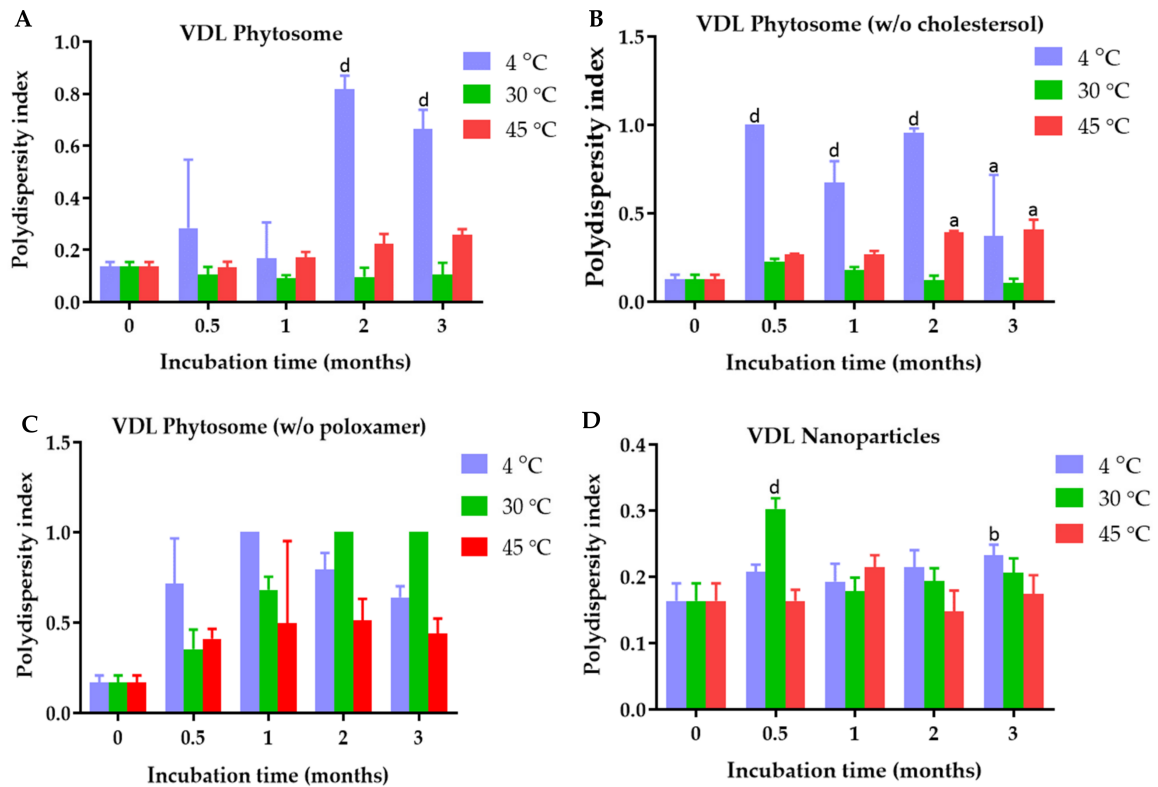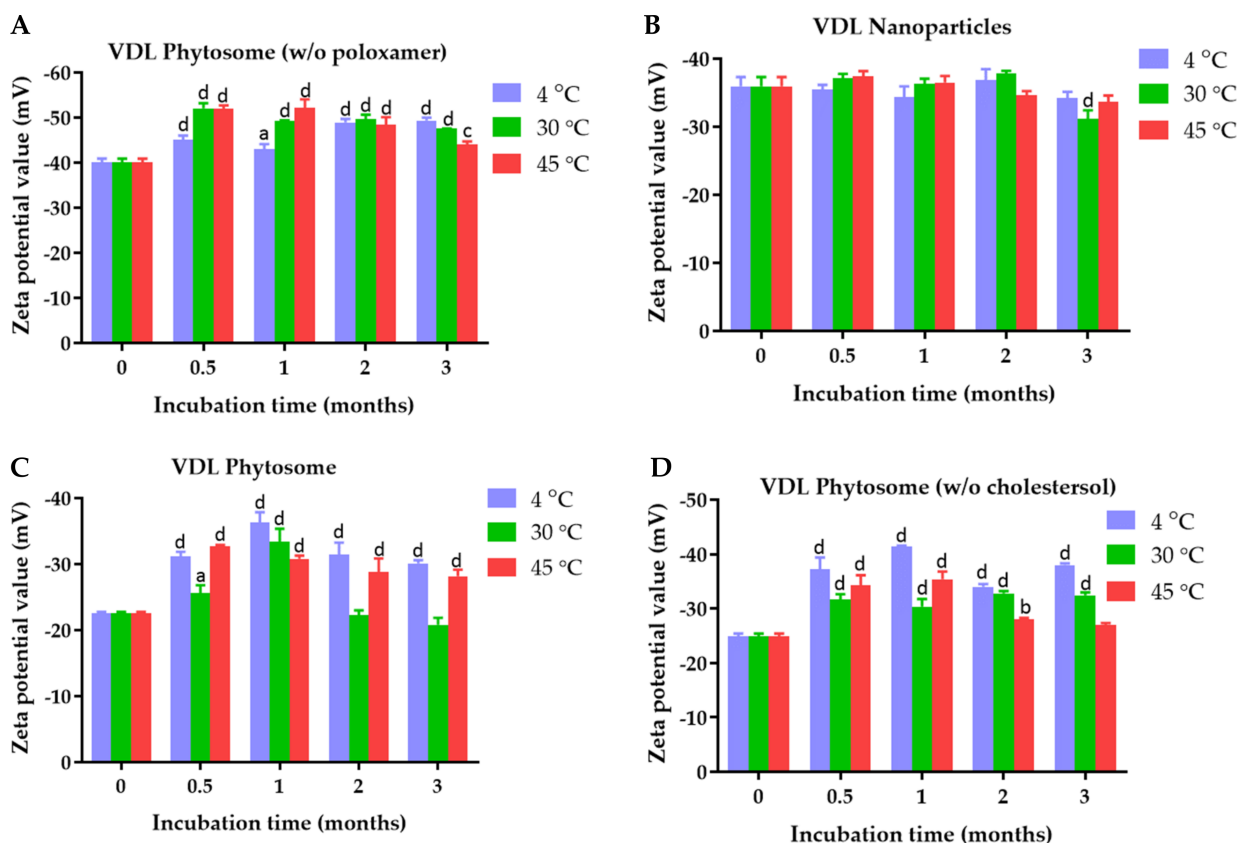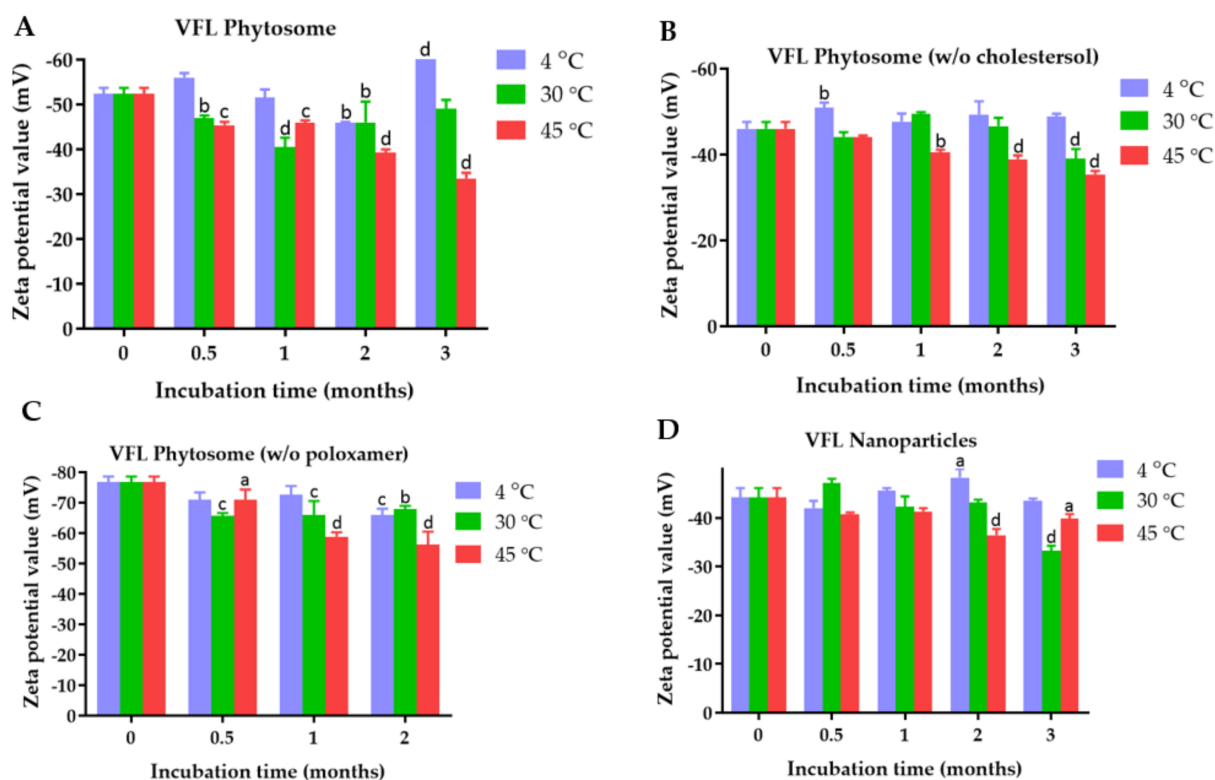
Figure 3. Polydispersity index of (**A**) VDL phytosomes, (**B**) VDL phytosomes (*w/o* cholesterol), (**C**) VDL phytosomes (*w/o* poloxamer), and (**D**) VDL after fresh preparation and storage for 0.5, 1, 2, and 3 months at 4 °C, 30 °C, and 45 °C. The letters a, b, and d indicate *p*-values < 0.05, 0.01, and 0.001, respectively.

Figure 4. Polydispersity index of (**A**) VFL phytosomes, (**B**) VFL phytosomes (*w/o* cholesterol), (**C**) VFL phytosomes (*w/o* poloxamer), and (**D**) VFL nanoparticles after fresh preparation and storage for 0.5, 1, 2, and 3 months at 4 °C, 30 °C, and 45 °C. The letters a, b, c, and d indicate *p*-values < 0.05, 0.01, 0.001, and 0.001, respectively.

The phytosome and nanoparticle size distribution can be articulated through the polydispersity index value. The nanoparticles with PDI values less than 0.3 are considered monodisperse, while a PDI value higher than 0.7 indicates a polydisperse system [25]. All VDL and VFL phytosomes and nanoparticles had PDI values less than 0.2, suggesting the uniformity of a sample based on the size. Heterogenicity can occur due to phytosome or nanoparticle aggregation. The polydispersity index of VDL phytosomes without poloxamer significantly increased to be higher than 0.4 when the phytosomes were stored at 4 °C, 30 °C, and 45 °C. VDL phytosomes containing poloxamers with and without cholesterol showed higher PDI values when they were kept at 4 °C. These results might be due to the aggregation of phytosomes at low temperatures. The poloxamer increased colloidal stability by forming hydrophilic layers of polyoxyethylene oxide at the surface of phytosomes and nanoparticles, hence preventing particle aggregation attributed to van der Waals forces between phytosomes and nanoparticles [26].

The zeta potential values of VDL phytosome with cholesterol, VDL phytosome without cholesterol, VDL phytosome without poloxamer, and VDL nanoparticles were -22.57 ± 0.23 mV, -24.93 ± 0.49 mV, -40.07 ± 0.86 mV, and -35.97 ± 01.36 nm, respectively (Figure 5). The zeta potential values of VFL phytosome with cholesterol, VFL phytosome without cholesterol, VFL phytosome without poloxamer, and VFL nanoparticles were -52.33 ± 1.40 mV, -46.00 ± 1.65 mV, -76.93 ± 1.71 mV, and -44.23 ± 1.86 mV, respectively (Figure 6).

Figure 5. Zeta potential values of (**A**) VDL phytosomes, (**B**) VDL phytosomes (*w/o* cholesterol), (**C**) VDL phytosomes (*w/o* poloxamer), and (**D**) VDL nanoparticles after fresh preparation and storage for 0.5, 1, 2, and 3 months at 4 °C, 30 °C, and 45 °C. The letters a, b, c, and d indicate *p*-values < 0.05, 0.01, 0.001, and 0.001, respectively.

Figure 6. Zeta potential values of (**A**) VFL phytosomes, (**B**) VFL phytosomes (*w/o* cholesterol), (**C**) VFL phytosomes (*w/o* poloxamer), and (**D**) VFL nanoparticles after fresh preparation and storage for 0.5, 1, 2, and 3 months at 4 °C, 30 °C, and 45 °C. The letters a, b, c, and d indicate *p*-values < 0.05, 0.01, 0.001, and 0.001, respectively.

Figures 5 and 6 show the results of the zeta potential measurements of VDL and VFL phytosomes and nanoparticles as a function of the storage time and temperature. The zeta potential value higher than ±30 mV suggested high colloidal stability of the phytosomes and nanoparticles.

Zeta potential results showed that all VDL and VFL formulations exhibited a negative charge with values ranging from 22.57 ± 0.23 mV to −40.07 ± 0.86 mV, and −44.23 ± 01.86 mV to 76.93 ± 1.71 mV, respectively. The negative charge value was due to the presence of phosphate and carbonyl groups of phosphatidylcholines. Compared with phytosomes coated with poloxamer, a more negative charge of phytosomes and nanoparticles was observed with phytosomes prepared without poloxamer. This could be because poloxamer adsorption on the phytosome or nanoparticle surface forms a coating layer, shielding the negative surface charge and shifting the plane of shear away from the particle surface. Overall, phytosomes containing cholesterol and poloxamer encapsulating VDL and VFL were the best formulation with optimal size, PDI, and zeta potential values. Both formulations were recommended to store at 30 °C.

Phytosomes of herbal extracts have been developed and characterized. Tiwari et al. developed herbal extract-loaded phytosomes. They showed that the encapsulation of herbal extract in the phytosomes did not change the chemical structure due to an FTIR analysis [27]. Direito et al. reported that the size of phytosomes depends on the amount of lipid composition in the formulation. It has been reported that increasing phospholipids in the phytosome increased the tendency of agglomeration [28]. The surface charge expressed as the zeta potential is an important physicochemical parameter that influences the stability of nanosuspensions which may also influence the biodistribution, pharmacokinetics, cellular affinity, and drug internalization [29]. When compared to a positive surface charge, the negative zeta potential is generally associated with higher biocompatibility [30,31].

2.2. Total Phenolic and Flavonoid Contents of VDL and VFL Phytosomes, Phytosomes w/o Cholesterol, Phytosomes w/o Poloxamer, and Nanoparticles

The total phenolic content in the VDL and VFL ethanolic extracts using the Folin–Ciocalteu reagent was expressed in terms of the gallic acid equivalent. The standard curves plotted between the absorbance, and gallic acid reacted with the Folin–Ciocalteau reagent are shown in Figure S1A. The total phenolic contents in the VDL and VFL extracts were 265 ± 0.67 and 258.56 ± 0.81 mg gallic acid equivalent/mL crude extract, respectively. The phytosomes of VDL and VFL contained 260.35 ± 2.29 and 238.54 ± 1.86 mg gallic acid equivalent/mL (Figure 7A). Here, we first reported the total phenolic content in the dry leaf extract of *N. tabacum* var. Virginia was significantly greater than that of the fresh leaf extract.
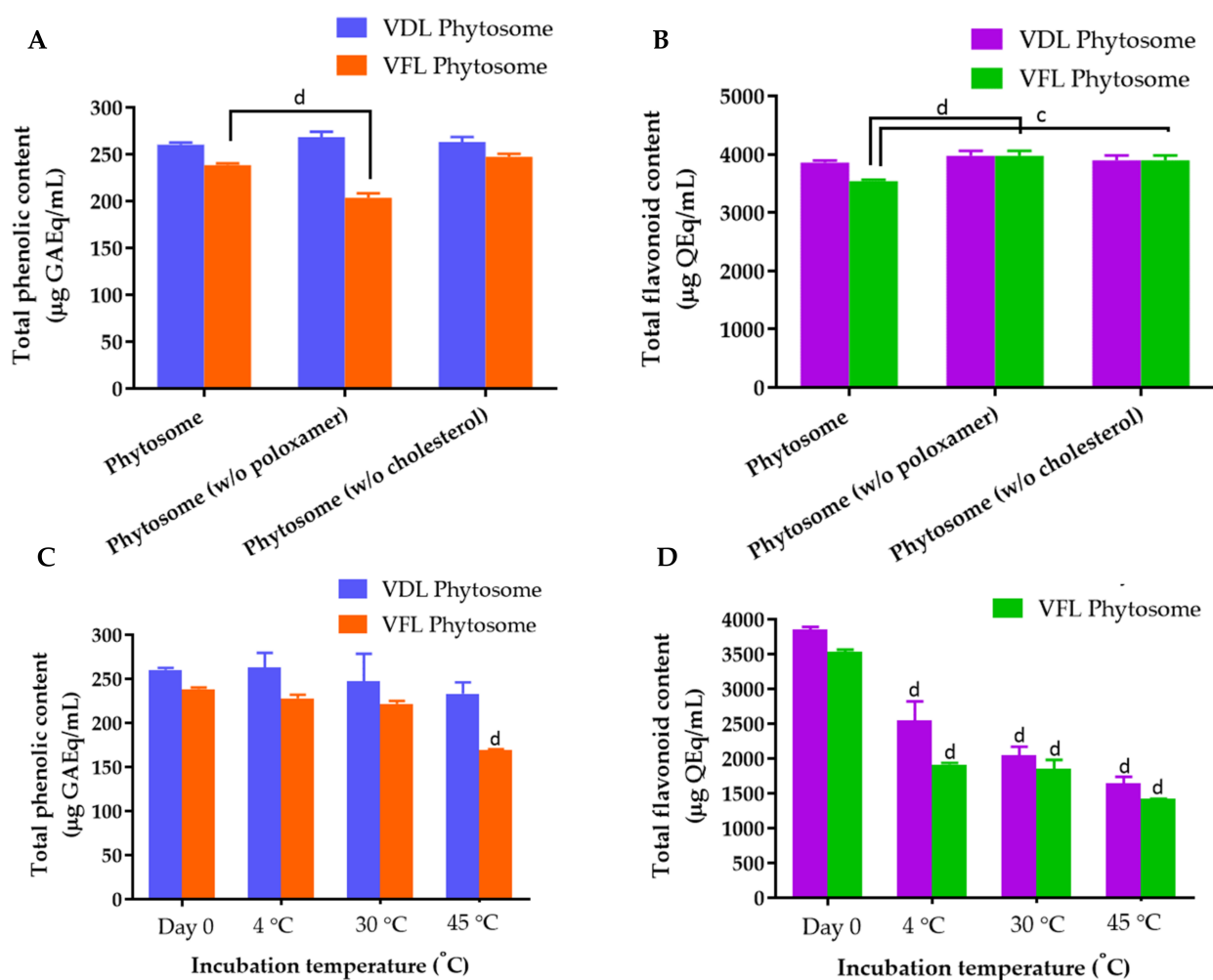
Figure 7. (**A**) Total phenolic content in various concentrations of VDL and VFL phytosomes. (**B**) Total flavonoid content in various concentrations of VDL and VFL phytosomes. (**C**) Total phenolic content and (**D**) total flavonoid content in VDL and VFL phytosomes upon storage at 4, 30, and 45 °C for 3 months. The letters a, b, c, and d indicate *p*-values < 0.05, 0.01, 0.001, and 0.001, respectively.

The standard curves of quercetin and EGCG reacted with the aluminum chloride reagent were presented in Figures S1B and 1C, respectively. The total flavonoid contents in the VDL and VFL extracts were 3620.52 ± 106.01 mg and 2836.44 ± 232.99 mg quercetin equivalent/mL crude extract, respectively. VDL and VFL extracts contained 3966.09 ± 388.49 mg and 2656.71 ± 247.24 mg EGCG equivalent/mL crude extract, respectively. The phytosomes of VDL and VFL contained 3858.19 ± 33.64 mg and 3538.41 ± 27.29 mg quercetin equivalent/mL phytosome, and 4343.46 ± 37.84 mg and 3938.71 ± 30.70 mg EGCG equivalent/mL phyto-

some, respectively (Figure 7B). The results suggested that the VDL extract and phytosome contained a larger amount of flavonoids compared with the VFL extract and phytosome. The component of VDL phytosomes did not affect the encapsulation of the total phenolic and total flavonoids, but the encapsulation of the total phenolic and total flavonoids of VFL was affected by the VFL phytosome formulation. The stability of the total phenolic and total flavonoids in VDL and VFL phytosomes was temperature dependent. The total phenolic and flavonoid contents significantly reduced when the phytosomes were stored at 45 °C (Figure 7C). The total flavonoids were prone to degrade more easily compared with total phenolic compounds encapsulated in the phytosomes (Figure 7D).

2.3. Antioxidant Activities of VDL and VFL Extracts and Phytosomes

The antioxidant activities of VDL and VFL phytosomes were determined by DPPH and ABTS radical scavenging assays. The scavenging activity of the extract and phytosomes was compared to that of gallic acid, quercetin, ascorbyl glucoside, and EGCG. The IC_{50} values obtained from the DPPH method were 5.40 µg/mL, 17.39 µg/mL, 19.74 µg/mL, and 4.82 µg/mL for gallic acid, quercetin, ascorbyl glucoside, and EGCG, respectively (Figure 8A). The IC_{50} values for VDL extract, VFL extract, VDL phytosomes, and VFL phytosomes were 693.70 µg/mL, 3363 µg/mL, 2146 µg/mL, and 4377 µg/mL, respectively (Figure 8A). The IC_{50} values obtained from the ABTS radical scavenging capacity of gallic acid, quercetin, ascorbyl glucoside, EGCG, VDL extract, VFL extract, VDL phytosomes, and VFL phytosomes were 7.87 µg/mL, 29.11 µg/mL, 46.3 µg/mL, 9.39 µg/mL, 1400 µg/mL, 2733 µg/mL, 1528 µg/mL, and 4154 µg/mL, respectively (Figure 8B).

The FRAP method measured the antioxidant and reduction ability of samples according to Fe^{3+} to Fe^{2+} reducing activity. Gallic acid, quercetin, ascorbyl glucoside, and EGCG at 250 µg/mL reduced Fe^{3+} to 4206.15 µM, 4097.15 µM, 711.72 µM, and 3721.07 µM of Fe^{2+}, respectively (Figure 8C). The VDL extract, VDL phytosomes, VFL extract, and VFL phytosomes at 250 µg/mL exhibited 306.61 µM, 195.36 µM, 169.76 µM, and 139.80 µM, respectively, suggesting the higher reducing power capacity of VDL compared with VFL (Figure 8D).

The results revealed that both the VDL extract and phytosomes had higher DPPH and ABTS radical scavenging activity and ferric reducing power than the VFL extract and phytosomes. Our results indicated that the VDL extract and VDL phytosomes demonstrated stronger DPPH and ABTS radical scavenging effects, probably because they contained higher amounts of phenolic and flavonoid contents, compared with VFL and VFL phytosomes. These results suggested that phenolic compounds are the main factor in their antioxidant activity.

2.4. Correlation between the Total Phenolic and Total Flavonoid Content and Antioxidant Activities

The correlation between the phenolic and flavonoid contents and antioxidant activities was evaluated by the Pearson's correlation test shown in Table 1. The total phenolic and total flavonoids in the VDL phytosomes, VFL extract, and VFL phytosomes showed a very high correlation with all three antioxidant activities. The total flavonoids in the VDL extract showed a high correlation with the DPPH free radical scavenging activity. These results supported the fact that the phenolic and flavonoids in the VDL and VFL extracts and phytosomes could scavenge free radicals and reduce ferric ions.

The total phenolic content and total flavonoid contents reported by Yati et al. were lower than our findings [32]. This might be due to the fact that the solvent used for polyphenol extraction is different. The higher effectiveness of ethanol in extracting phenolic compounds and flavonoids was shown in previous studies [33–36]. The ethanol extracts also exhibited a higher activity than the aqueous extract [33–35]. The extracts containing more polyphenols had higher antioxidant activity. Therefore, the 95% ethanol solvent might be more suitable to extract phenolic and flavonoids from *Nicotiana tabacum* var. Virginia.
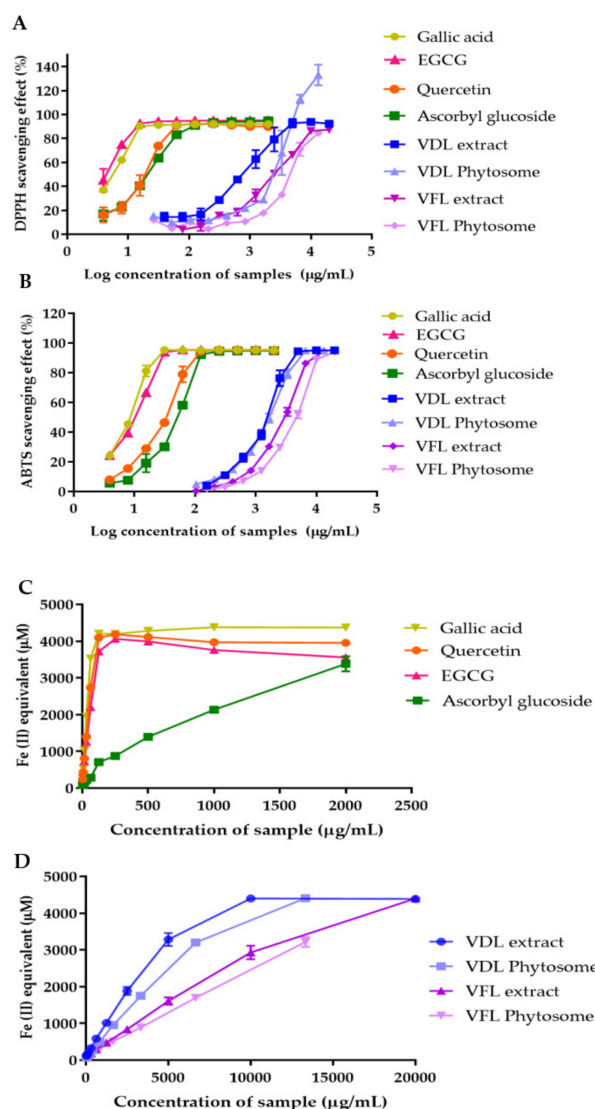
Figure 8. The DPPH scavenging activity of gallic acid, quercetin, epigallocatechin, ascorbyl glucoside, VDL and VFL extract and phytosomes determined by (**A**) DPPH free radical scavenging assay; (**B**) ABTS free radical scavenging assay; (**C**) ferric reducing antioxidant power assay for gallic acid, quercetin, and ascorbyl glucoside; (**D**) ferric reducing antioxidant power assay for VDL and VFL extracts and phytosomes.

Table 1. Pearson correlation coefficients of total phenolic content and total flavonoid content, and antioxidant activities of VDL, VFL, VDL phytosomes, and VFL phytosomes measured by DPPH, ABTS, and FRAP assays.

Antioxidant Assay	Total Phenolic Content (Gallic Acid Equivalent)				Total Flavonoid Content (Quercetin Equivalent)			
	VDL	VDL Phytosome	VFL	VFL Phytosome	VDL	VDL Phytosome	VFL	VFL Phytosome
DPPH assay	0.9090 ****	0.9823 ****	0.9557 ****	0.9773 ****	0.7717 *	0.9733 ****	0.9166 ****	0.9682 ****
ABTS assay	0.9259 ****	0.9422 ****	0.9862 ****	0.9830 ****	0.8013 *	0.9094 **	0.9663 ****	0.9015 **
FRAP assay	0.9907 ****	0.9932 ****	0.9901 ****	0.9697 ****	0.9192 **	0.9876 ****	0.9995 ****	0.9982 ****

* indicated $p < 0.05$, ** indicated $p < 0.01$, and **** indicated $p < 0.0001$.

2.5. HPLC Analysis of VDL and VFL Extracts

Chlorogenic acid and rutin have been reported as the main phenolic compounds in tobacco leaves. Chen et al. have shown that chlorogenic acid and rutin concentration were the highest among the other polyphenol compounds in tobacco leaves [37]. A reverse-phased HPLC was applied to analyze polyphenols in the VDL and VFL extracts. The HPLC profiles of the standard chlorogenic acid and rutin are presented in Figure 9. Chlorogenic acid and rutin were detected with high concentrations in the VDL and VFL extracts. The VDL and VFL extracts contained 4.94 ± 0.04 and 3.13 ± 0.01 µg/mL of chlorogenic acid, respectively, and 0.89 ± 0.00 and 0.24 ± 0.00 µg/mL of rutin, respectively. According to the literature, the peak at a retention time of 9.5 min might be assigned for nicotine [38]. At a retention time of 10.87 min and 11.13 min, the peaks might be identified as isomers of chlorogenic acid (3-caffoylquinic acid), such as 4-caffoylquinic acid and 5-caffoylquinic acid, respectively [39].
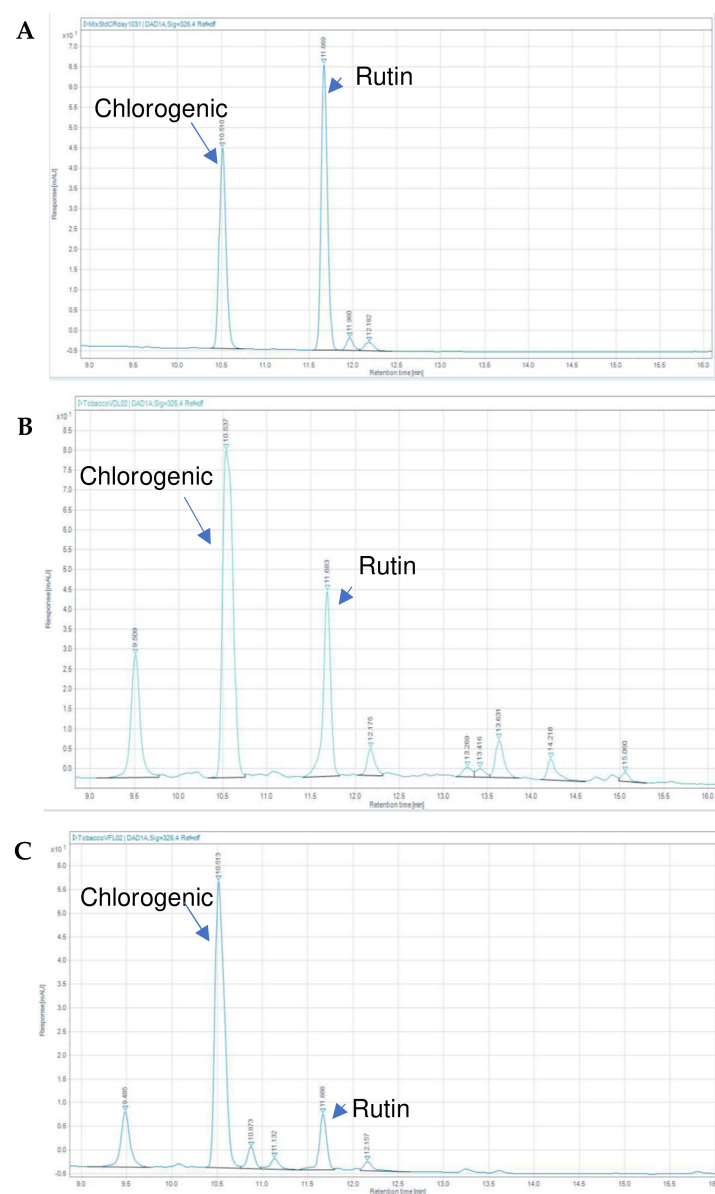
Figure 9. HPLC chromatograms of (**A**) chlorogenic acid and rutin standards at a retention time of 10.51 min and 11.68 min, respectively. (**B**) VDL extract and (**C**) VFL extract.

2.6. Effects of VDL and VFL Extracts and Phytosomes on Keratinocyte Cell Viability

The IC_{50} values of the VDL extract, VFL extract, VDL phytosomes, and VFL phytosomes after exposure to HaCaT cells for 24 h were 1137 µg/mL, 164.8 µg/mL, 15,741 µg/mL, and 910.5 µg/mL, respectively (Figure 10A). The IC_{50} values of the VDL extract, VFL extract, VDL phytosomes, and VFL phytosomes increased upon exposure with HaCaT cells for 48 h to 1222 µg/mL, 166 µg/mL, 28,671 µg/mL, and 916.4 µg/mL, respectively (Figure 10B). After 72 h, the IC_{50} values of the VDL extract, VFL extract, VDL phytosomes, and VFL phytosomes were 10,326 µg/mL, 1528 µg/mL, 139,737 µg/mL, and 7805 µg/mL, respectively (Figure 10C). The IC_{50} values of the VFL extract and VFL phytosomes were less than that of the VDL extract and VDL phytosomes, indicating the higher cytotoxicity against human keratinocyte cells. The IC_{50} values of all extracts and phytosomes increased with the incubation time, suggesting that VDL and VFL extracts and their phytosomes were safe to apply on skin. Phytosomes had higher IC_{50} values compared to the extract, indicating that they can protect cells from cytotoxic agents in the extracts.
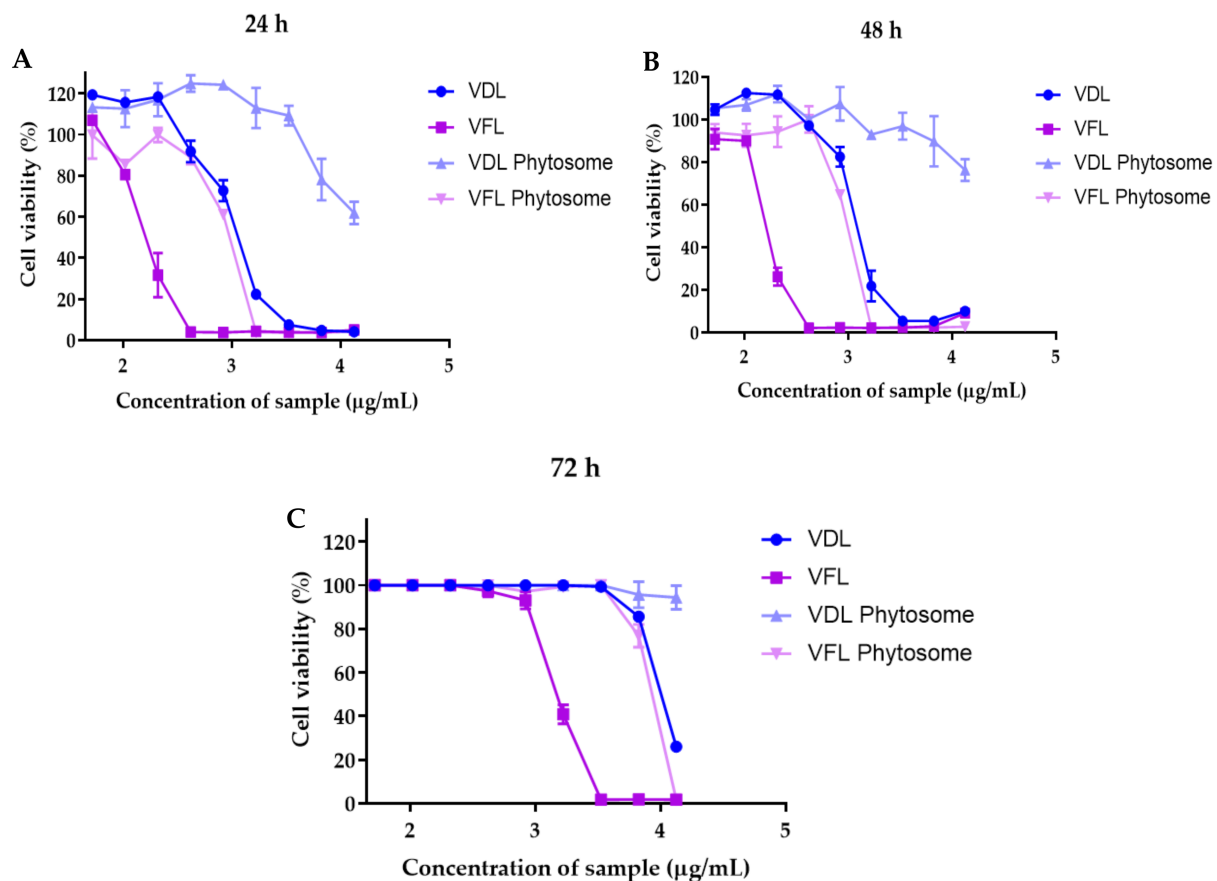
Figure 10. The viability and growth of HaCaT cells treated with various concentrations of the VDL and VFL extracts and phytosomes for (**A**) 24 h, (**B**) 48 h, and (**C**) 72 h.

2.7. Reactive Oxygen Species' Levels in HaCaT Cells Exposed to VDL and VFL Phytosomes

Intracellular ROS were assayed using fluorescent probe DCFH-DA, which can cross cell membranes and oxidize to a fluorescent DCF by intracellular ROS. Compared with the hydrogen peroxide-induced HaCaT cells, the fluorescent intensity of cells treated with VDL and VFL phytosomes was significantly decreased, indicating that the intracellular ROS level was significantly decreased (Figure 11). The results suggested that VDL and VFL phytosomes reduced the intracellular ROS, probably due to the total phenolic and total flavonoid compounds acting as an antioxidant in the extract.
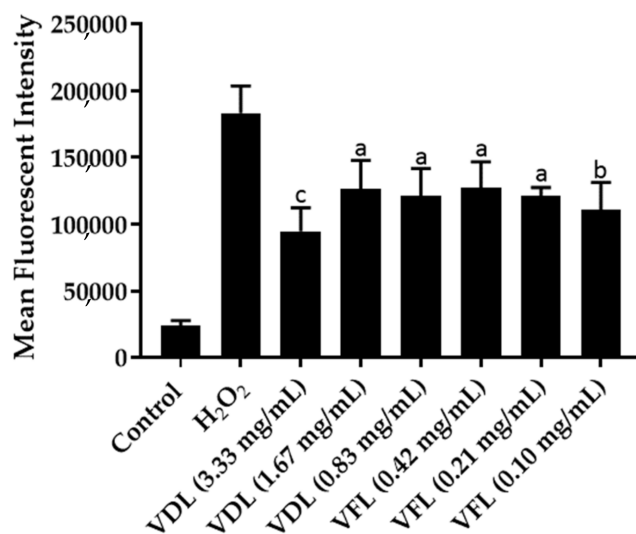
Figure 11. Intracellular ROS levels assayed with DCFH-DA fluorescent probe HaCaT cells treated with VDL and VFL phytosomes. The letters a, b, and c indicate p-values < 0.05, 0.01, and 0.001, respectively.

Free radicals and other ROS such as the oxygen singlet free radical, hydroxyl radical, peroxyl radical, and nitric oxide free radical are continuously formed at low concentrations during normal essential metabolic processes [40]. The natural antioxidant system regulates the amount of these free radical species to maintain redox hemostasis [41]. Polyphenols are strong antioxidants that can neutralize free radicals by donating an electron or hydrogen atom to a free radical through the H-atom transfer mechanism [42]. Tobacco leaves contain significant concentrations of polyphenols and carotenoids, which are important naturally occurring antioxidants [43,44]. Although we are the first to show the intracellular ROS suppression of *N. tabacum* leaves, the antioxidant activities of *N. tabacum* leaves were expressed in several studies by scavenging activities on hydroxyl, superoxide anion, DPPH and ABTS radicals, ferric thiocyanate forming complex, and reducing power [32,45,46]. These results supported the intracellular ROS inhibition of *N. tabacum* leaves firstly presented in our study.

2.8. Inhibition of LPS-Induced Nitric Oxide Production

The effects of VDL and VFL phytosomes on RAW264.7 cell viability are shown in Figure 12A. The viability of RAW264.7 cells treated with 7.8–500 µg/mL was not significantly reduced, indicating that phytosomes at this concentration range showed no cytotoxic effect on RAW264.7 cells. Natural polyphenols have demonstrated anti-inflammatory activity in vitro and in vivo, highlighting their therapeutic applications in a variety of diseases. Numerous studies have shown the anti-inflammatory and immune modulation activities of polyphenols [15,21]. The ability of these natural compounds to modulate the expression of several pro-inflammatory genes such as multiple cytokines, lipoxygenase, nitric oxide synthases, and cyclooxygenase, in addition to their antioxidant properties such as ROS scavenging, helps to regulate inflammatory signaling [22,23]. Thus, VDL and VFL phytosomes at 15.6–500 µg/mL were further used to study the anti-inflammatory effect of the phytosomes by inhibiting nitric oxide production. RAW264.7 cells were stimulated with LPS with or without co-treatment with VDL and VFL phytosomes. As shown in Figure 12B, both VDL and VFL phytosomes inhibited the NO production induced by LPS. The VFL phytosome inhibited LPS-induced NO production in RAW264.7 cells to a greater extent than the VDL phytosome. The viability of RAW264.7 cells treated with LPS and samples were not changed during the experiment (Figure 12C). A previous study on the phytoconstituent isolated from *N. tabacum* demonstrated significant inhibition of COX-2 by the downregulation of COX-2 mRNA [47]. Therefore, our data suggested that phytosomes

that incorporated *N. tabacum* Virginia leaf extract can be considered as a potential candidate for the mitigation of dermal inflammations.
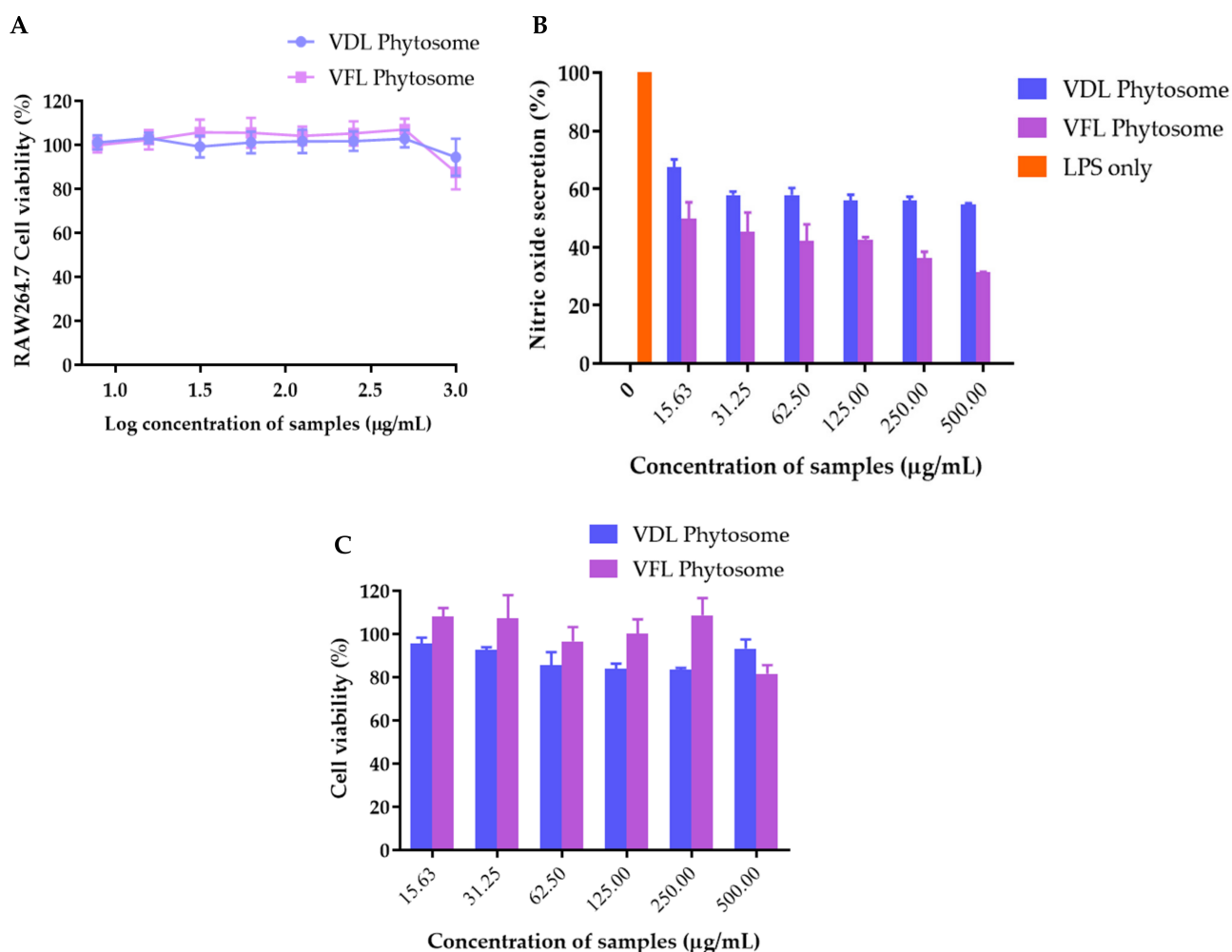
Figure 12. (**A**) RAW264.7 cell viability after the treatment with VDL and VFL phytosomes. (**B**) Effect of VDL and VFL phytosomes on NO production in LPS-stimulated RAW 264.7 cells. (**C**) RAW264.7 cell viability after the nitric oxide inhibition experiment.

2.9. Characterization of Shape Memory Gel Containing VDL and VFL Phytosomes

The physical stability of the shape memory gel containing VDL and VFL phytosomes was confirmed by the maintained appearance, viscosity, and pH. The appearance of gels is shown in Figure S2. Figure 13 exhibits the change in viscosity for gels containing 0.1% *w/w* VDL and VFL phytosomes as a function of shear rate. All samples showed a similar trend of change in viscosity. Initially, the gel showed high viscosity, followed by a gradual decrease in viscosity as the shear rate was applied, and followed by a plateau region. These results suggested that the gel exhibited pseudoplastic rheology behavior. The viscosity of gels containing VDL and VFL phytosomes was not significantly changed after the six heating–cooling cycles of the accelerated stability study (Figure 13A), and after 1 month-storage at 4 °C, 30 °C, and 45 °C (Figure 13B,C). The pH of VDL and VFL phytosome gels was not changed during the accelerated and long-term (1-month) stability studies (Figure 14).
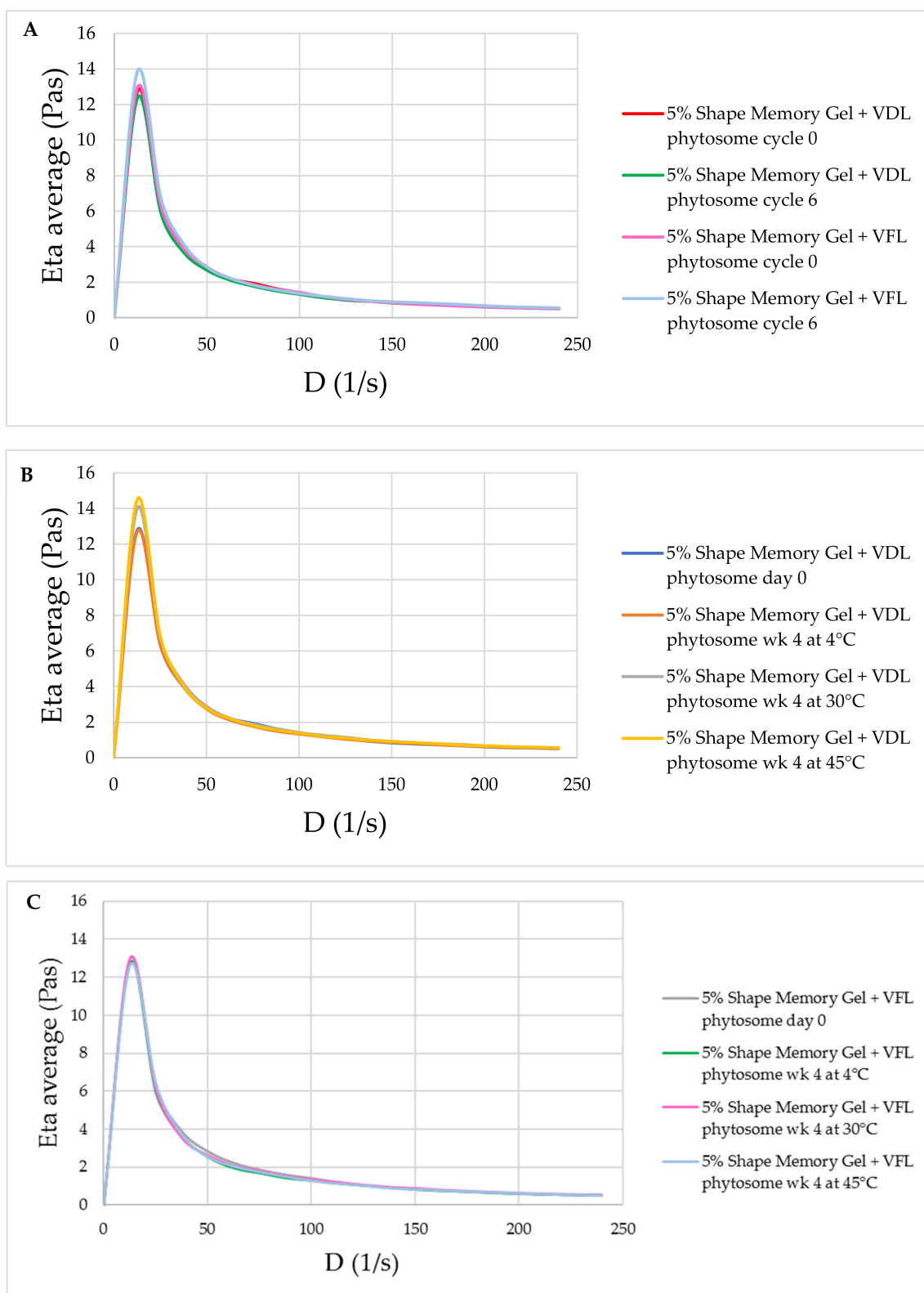
Figure 13. Rheology profile of the gels. (**A**) Flow curves of gels containing 1% *w/w* VDL and VFL phytosomes after six heating–cooling cycles of stability study. Flow curves of gels containing 1% *w/w* (**B**) VDL and (**C**) VFL phytosomes after 1 month-storage at 4 °C, 30 °C, and 45 °C, expressed as viscosity and shear rate.
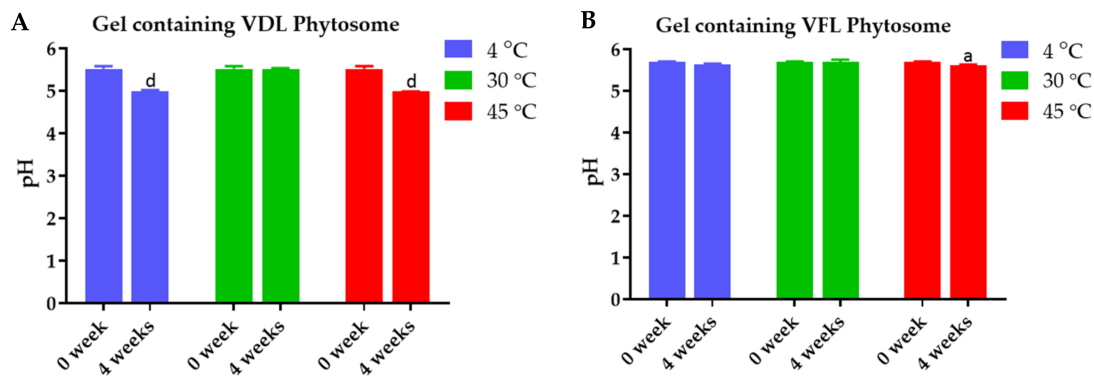
Figure 14. pH the gels. (**A**) pH of gels containing 1% *w/w* VDL phytosome after 1 month-storage at 4 °C, 30 °C, and 45 °C of stability study. (**B**) pH of gels containing 1% *w/w* VFL phytosome after 1 month-storage at 4 °C, 30 °C, and 45 °C of stability study. The letters a and d indicate *p*-values < 0.05 and 0.01, and 0.001, respectively.

The sustained release behavior of the total phenolic content from VDL and VFL extracts, phytosomes, and gels was observed (Figure 15). The VDL extract, VDL phytosome, and VDL gel released the total phenolic content up to $73.76 \pm 3.73\%$, $66.98 \pm 5.33\%$, and $38.04 \pm 2.59\%$, respectively, within 24 h. The VFL extract, VFL phytosome, and VFL gel released $13.92 \pm 2.26\%$, $55.78 \pm 3.86\%$, and $21.44 \pm 5.81\%$ of total phenolic content, respectively, in 24 h. The results suggested that the VDL extract contained a higher amount of hydrophilic polyphenols compared with the VFL extract, hence releasing the phenolic compounds at a higher rate. The VDL extract entrapped in the phytosomes gradually released total phenolic compounds from the phytosomes. The shape memory gel released phenolic compounds to a lesser extent compared with VDL extract and phytosomes. Interestingly, the VFL phytosome released the phenolic compounds faster than that of the extract and the gel. These results indicated that phytosomes enhanced the water solubility of the VFL extract. Alshahrani et al. showed that phytosomes loaded with *Cuscuta reflexa* extract released $96.3 \pm 3.7\%$ of the polyphenol and flavonoids phytoconstituents from phytosomes in 12 h, compared to $49.3 \pm 2.5\%$ in the plain extract. Therefore, the phytosomal nanocarriers have the potential to increase the bioavailability of the extract [48]. The release of the phenolic compounds in the gel-loading phytosomes occurred in several steps. The release was initiated by the penetration of the PBS medium into the gel, which created pores and degraded polymers. Then, the phenolic compounds diffused from the gel matrix to the medium, followed by the dissolution of the phenolic compounds in the medium [49].
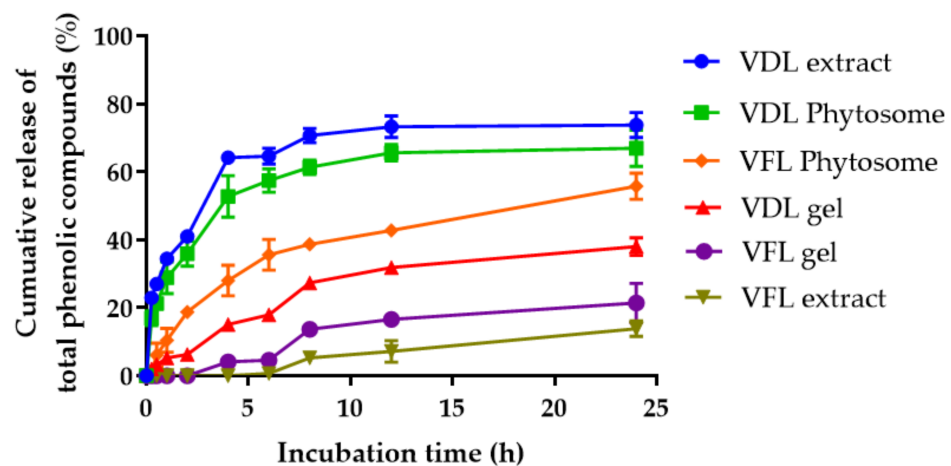
Figure 15. In vitro release curves of VDL and VFL extracts, phytosomes, and shape memory gel loaded with VDL or VFL phytosomes in phosphate buffer saline (PBS) within 24 h.

Shape memory gel is one of the new materials that can fulfill drug delivery and cosmetic application. Polyurethane-62 is a copolymer comprised, in part, of the carbamate (i.e., urethane) linkages that can form hydrogen bonds to yield its high mechanical strength. Combining hydrophobic polyurethane with butylene glycol generates a swellable copolymer network that is robust and durable [50]. Polyurethane-butylene glycol serves as a shape memory polymer. This stimuli-responsive material can memorize its original shape, which occurs during the gelation process when an appropriate stimulus is applied. Biocompatibility and cytotoxicity of the shape memory polymer are crucial concerns for drug delivery. It was suggested that polyurethane could be used for implanted medical devices with shape memory requirements. Peng et al. reported that the polyurethane grafted with poly-lactic acid had biocompatibility comparable to pure PLA [51]. Polyurethane-62 has been widely used in cosmetics, including moisturizers, sunscreens, serums, and water gel lotions. The Australian Industrial Chemicals Introduction Scheme (AICIS) determined that polyurethane-62 was not considered to pose an unreasonable risk to the health of workers and the public [52]. Polyurethan-62 is a high molecular weight polymer. The molecular weight is approximately 100,000 Da, which is not expected to penetrate the skin.

3. Conclusions

The phytosomes composed of phosphatidyl choline and cholesterol coated with poloxamer were successfully developed and suitable for the delivery of *N. tabacum* var. Virginia fresh and dry leaf extract to the skin. The phytosomes with different formulars were fabricated and the physical stability was compared. Both phosphatidyl choline and cholesterol played an important role in the physical stability of the phytosomes but did not affect the encapsulation efficiency of the phenolic compounds. VDL and VDL phytosomes had higher phenolic and flavonoid contents and displayed stronger DPPH and ABTS radical scavenging effects, suggesting that phenolic compounds are the main factor in their antioxidant activity. VDL and VFL phytosomes reduced the intracellular ROS and inhibited the NO production induced by LPS. The viscosity and pH of gels containing VDL and VFL phytosomes were not significantly changed after the six heating–cooling cycles of the accelerated stability study and after 1 month storage at 4 °C, 30 °C, and 45 °C.

4. Materials and Methods

4.1. Materials

Gallic acid, Griess reagent, DPPH (2,2-diphenyl-1-picrylhydrazyl), TPTZ (2,4,6-Tris(2-pyridyl)-s-triazine, and ABTS (2,2′-azino-bis(3-ethylbenzothiazoline-6-sulfonic acid)) were purchased from Sigma-Aldrich, St. Louis, USA. Absolute ethanol, dimethyl sulfoxide, sodium bicarbonate, sodium nitrate, acetic acid, and sodium hydroxide were purchased from RCI Labscan, Bangkok, Thailand. Iron (III) chloride hexahydrate and 37% hydrochloric acid were purchased from Qrec, New Zealand. The Folin–Ciocalteu phenol reagent, aluminum chloride, sodium acetate trihydrate, ferrous sulfate heptahydrate (99% purity), and potassium persulfate were obtained from Loba Chemie, Mumbai, India. Quercetin (98% purity), epigallocatechin (EGCG) (98% purity), ascorbyl glucoside, phosphatidylcholine, cholesterol, poloxamer 407, and polyurethane-62 were purchased from Chanjao Longevity Co., Ltd., Bangkok, Thailand. Dulbecco's Modified Eagle's Medium (DMEM) with high glucose, fetal bovine serum (FBS), penicillin-streptomycin, and trypsin-EDTA were purchased from Gibco (Waltham, MA, USA).

4.2. Methods

4.2.1. Preparation of VDL and VFL Phytosomes and Nanoparticles

Tobacco leaf extract (VDL or VFL) in 95% ethanol (0.5 g/mL, 400 μL) was mixed with phosphatidylcholine (30 mg in 1900 μL 95% ethanol). Cholesterol (2 mg) in acetone solution (200 μL) was added to the above solution and mixed thoroughly. Then, the mixture was added dropwise into 15 mL of 0.1% *w/v* poloxamer 407 at a rate of 1 mL/h with a stirring speed of 700 rpm. The obtained phytosome was named "VDL phytosome" or

"VFL phytosome" [53]. "VDL phytosomes (*w/o* cholesterol)" and "VFL phytosomes (*w/o* cholesterol)" were prepared by the following method, where cholesterol was not included. Tobacco leaf extract (VDL or VFL) in 95% ethanol (0.5 g/mL, 400 μL) was mixed with phosphatidylcholine (30 mg in 1900 μL 95% ethanol). The mixture was added dropwise into 15 mL of 0.1% *w/v* poloxamer 407 at a rate of 1 mL/h with a stirring speed of 700 rpm. To prepare "VDL phytosome (*w/o* poloxamer)" and "VFL phytosome (*w/o* poloxamer)", mixtures of VDL or VFL (0.5 g/mL, 400 μL) with phosphatidylcholine (30 mg in 1900 μL), 95% ethanol, and cholesterol (2 mg in 200 μL acetone) were infused into 15 mL of de-ionized water at a rate of 1 mL/h with a stirring speed of 700 rpm.

"VDL nanoparticles" and "VFL nanoparticles" were prepared by the infusion of VDL or VFL extracts (0.5 g/mL, 400 μL) into 0.1% poloxamer 407 solution at a rate of 1 mL/h with a stirring speed of 700 rpm [54–56]. The obtained VDL and VFL phytosomes and nanoparticles were washed three times with de-ionized water and characterized.

4.2.2. Characterization and Stability Study of VDL and VFL Phytosomes and VDL and VFL Nanoparticles

The freshly prepared VDL and VFL phytosomes or nanoparticles were measured for the size, PDI, and zeta potential values using the Zetasizer (Malvern Instruments, Worcestershire, UK). The colloidal stability of VDL and VFL phytosomes or nanoparticles was studied by storing phytosomes or nanoparticles at 4 °C, 30 °C, and 45 °C for 0.5, 1, 2, and 3 months. At the end of the incubation time, the particle size, PDI, and zeta potential of VDL and VFL phytosomes and nanoparticles were analyzed.

4.2.3. Quantitative Analysis of Total Phenolic Compounds in VDL and VFL Phytosomes

VDL and VFL extracts and phytosomes and gallic acid standard solution (3.9–125 μg/mL) were placed in a 96-well plate (50 μL/well). A Folin–Ciocalteau reagent (10% *v/v*, 100 μL) was added to the wells, mixed well, and incubated for 4 min at room temperature. Then, the sodium carbonate solution (10% *w/v*, 50 μL) was added to the mixture and incubated in the dark for 60 min at room temperature [57]. The absorbance was measured at a wavelength of 765 nm using a UV-Vis spectrophotometer microplate reader. The total phenolic contents in phytosomes were calculated by constructing a standard curve between the absorbance and the concentration of the gallic acid standard solution. The total phenolic content was expressed as the gallic acid equivalent (GAE).

4.2.4. Quantitative Analysis of Total Flavonoid Content in VDL and VFL Phytosomes

The VDL and VFL extracts and phytosomes, quercetin standard solution (7.8–500 μg/mL), and EGCG standard solution (7.8–1000 μg/mL) were placed in a 96-well plate (50 μL/well). Sodium nitrate (5% *w/v*, 30 μL) was added to the wells, mixed well, and incubated for 5 min at room temperature. Then, the aluminum chloride solution (2% *w/v*, 50 μL) was added to the mixture and incubated for 6 min at room temperature [57]. Sodium hydroxide (1 N, 50 μL) was added to the wells and incubated for another 10 min at room temperature. The absorbance was measured at a wavelength of 510 nm using a UV-Vis spectrophotometer microplate reader. The total flavonoid contents in phytosomes were calculated by constructing a standard curve between the absorbance and the concentration of quercetin or the EGCG standard solution. The total phenolic content was expressed as the quercetin equivalent or EGCG equivalent.

4.2.5. Chemical Stability Study of VDL and VFL Phytosomes

The chemical stability of VDL and VFL phytosomes stored at 4 °C, 30 °C, and 45 °C for 3 months was investigated by a quantitative analysis of total phenolic and total flavonoid contents in VDL and VFL phytosomes.

4.2.6. DPPH Free Radical Scavenging Assay of VDL and VFL Phytosomes

The VDL and VFL extracts (3.9–20,000 μg/mL), VDL and VFL phytosomes (26.0–13,333 μg/mL), gallic acid solution (3.9–2000 μg/mL), quercetin solution (3.9–2000 μg/mL),

EGCG solution (3.9–2000 µg/mL), and ascorbyl glucoside solution (3.9–2000 µg/mL) were added to 96-well plates (100 µL/well). The DPPH solution (0.1 mM) was added to the samples (100 µL/well). The mixtures were incubated in the dark at room temperature for 30 min [56]. Then, the absorbance at a wavelength of 517 nm was measured. The DPPH radical scavenging activity of samples was calculated by the following equation.

$$DPPH\ radical\ scavenging\ activity\ (\%) = \frac{1 - A_{Sample}}{A_{Control}} \times 100$$

4.2.7. ABTS Free Radical Scavenging Assay of VDL and VFL Phytosomes

The VDL and VFL extracts (3.9–20,000 µg/mL), VDL and VFL phytosomes (26.0–13,333 µg/mL), gallic acid solution (3.9–2000 µg/mL), quercetin solution (3.9–2000 µg/mL), EGCG solution (3.9–2000 µg/mL), and ascorbyl glucoside solution (3.9–2000 µg/mL) were added to 96-well plates (20 µL/well). The ABTS•+ solution (0.1 mM) was added to the samples and standard solutions (180 µL/well) [56]. The mixtures were incubated in the dark at room temperature for 15 min. Then, the absorbance at a wavelength of 734 nm was measured. The ABTS•+ radical scavenging activity of the samples was calculated by the following equation.

$$ABTS\ radical\ scavenging\ activity\ (\%) = \frac{1 - A_{Sample}}{A_{Control}} \times 100$$

4.2.8. Ferric Reducing Antioxidant Power Assay of VDL and VFL Phytosomes

The VDL and VFL extracts (3.9–20,000 µg/mL), VDL and VFL phytosomes (26.0–13,333 µg/mL), gallic acid solution (3.9–2000 µg/mL), quercetin solution (3.9–2000 µg/mL), EGCG solution (3.9–2000 µg/mL), and ascorbyl glucoside solution (3.9–2000 µg/mL) were added to 96-well plates (20 µL/well). The FRAP reagent, consisting of the acetate buffer (300 mM, pH 3.6), ferric chloride (20 mM), and TPTZ (10 mM) mixture at a ratio of 10:1:1, was added to the sample solutions (180 µL/well). The mixture of samples and FRAP reagent was then incubated at 37 °C for 30 min before reading the absorbance at a wavelength of 595 nm (Spectramax M3, Molecular Devices, San Jose, CA, USA) [58]. The FRAP values were calculated from the linear equation of a standard curve plotted between the concentration of the ferrous sulfate standard solution (9.8–5000 µM) and the absorbance value at 595 nm.

4.2.9. HPLC Analysis of Bioactive Compounds in VDL and VFL Extracts

HPLC separation was achieved on the HPLC (Agilent, Santa Clara, CA, USA) equipped with the 1260 Infinity II quaternary pump, 1260 Infinity II autosampler, 1260 Infinity II multi-column thermostat, and 1260 Infinity II PDA detector. The separation was completed in an ACE 5 C18-AR column (4.6 × 250 mm i.d., 4.6 mm) with a C_{18} guard column. The mobile phases were (B) acetonitrile and (C) 0.085% phosphoric acid in water using the following gradient elution: 10% B in C to 30% B in C for 15 min; 10% B for 5 min before each analysis, and the flow rate was set at 0.7 mL/min with the controlled temperature at 25 °C. The UV detector was set at the wavelength of 326 nm for the chlorogenic acid analysis and 356 nm for the rutin analysis, and the injection volume was 10 µL for every sample and reference standard [38,39].

4.2.10. Cell Culture

HaCaT and RAW264.7 cell lines were obtained from Dr. Kanokwan Kiettisin and Dr. Natthachai Duangnin, respectively. Cells were cultured in Dulbecco's Modified Eagle's Medium (DMEM) with high glucose and supplemented with 10% FBS and 1% penicillin-streptomycin. Cells were incubated in 5% CO_2 at 37 °C for growing. Cells were subcultured by incubating with 0.25% trypsin-EDTA every three days.

4.2.11. Cytotoxicity Assay of VDL and VFL Phytosomes against HaCaT Keratinocyte Cells

In 96-well plates, HaCaT cells were seeded in a culture medium at 8×10^3 cells/well. Prior to an MTT assay, cells were allowed to adhere for 24 h. VDL and VFL extracts and VDL and VFL phytosomes were added to the cells and were incubated in 5% CO_2 at 37 °C for 24 h. After treatment for 24, 48, and 72 h, an MTT solution in the culture medium (0.5 mg/mL) was added to each well and incubated for 2 h at 37 °C [58]. The formazan products resulting from the viable cells' metabolism were dissolved in DMSO (100 µL/well). The absorbances were measured at 550 nm. The IC_{50} values were calculated using GraphPad Prism v.7.0 (La Jolla, CA, USA). Cell viability was calculated using the following equation.

$$Cell\ viability\ (\%) = \frac{A550\ sample}{A550\ control} \times 100\%$$

4.2.12. Flow Cytometry Analysis of Intracellular Reactive Oxygen Species (ROS)

HaCaT cells were trypsinized and added into the microcentrifuge tubes (1×10^6 cells/mL). Cells were co-incubated for 2 h at 37 °C with 20 mM hydrogen peroxide and VDL or VFL phytosomes at different concentrations. Cells were washed three times with PBS, pH 7.4, followed by incubation with 10 µM DCFH-DA at 37 °C for 30 min [59]. The fluorescent intensity was detected by flow cytometry (Accuri, BD, Franklin Lakes, NJ, USA). For each sample, 10,000 events were recorded.

4.2.13. In Vitro Anti-Inflammatory Assay of VDL and VFL Phytosomes

The viability of RAW264.7 cells after the 24 h incubation with VDL and VFL phytosomes (7.8–1000 µg/mL) was tested by the MTT assay. The anti-inflammatory effect of VDL and VFL phytosomes was determined from nitric oxide secretion against macrophage cells. RAW 264.7 cells (1×10^4 cells/well) were incubated with LPS (50 ng/mL) in the presence or absence of VDL and VFL phytosomes (15.6–500 µg/mL) for 18 h at 5% CO_2, 37 °C. After incubation, an equal medium volume was mixed with the Griess reagent, consisting of 20 mg/mL sulfanilamide and 1 mg/mL N-(1-naphthylethylenediamine in 5% phosphoric acid at a 1:1 ratio [60,61]. The absorbance of the cell supernatant was recorded at 540 nm to quantify the nitrite levels using a UV-Vis spectrophotometer microplate reader (Spectramax M3, Molecular Devices, San Jose, CA, USA) equipped with SoftMax® Pro 7 software. The amount of nitrite was calculated from the sodium nitrite standard curve. The treated cells were then tested for cell viability using an MTT assay. The medium was replaced with 0.5 mg/mL MTT reagent (100 µL/well) and incubated for 2 h. The formazan product was measured at 550 nm using a UV-Vis spectrophotometer microplate reader (Spectramax M3, Molecular Devices, San Jose, CA, USA).

4.2.14. Formulation of Shape Memory Gel Containing VDL and VFL Phytosomes

The shape memory gel was formulated by mixing polyurethane-62-butlyelene glycol (5%) in de-ionized water (89.4%) at 50 °C with a stirring rate of 1200 rpm for 1 h. Then, glycerin (5%), phenoxyethanol (0.5%), and VDL and VFL phytosomes (0.1 %) were added to the gel.

4.2.15. Characterization and Stability Study of Shape Memory Gel

The pH and rheology of the shape memory gel containing VFL and VFL phytosomes were measured using a pH meter and rheometer (AMETEK Brookfield, Middleboro, MA, USA) equipped with a plate and plate geometry, respectively [62]. The physical stability of the products was investigated by measuring the pH and rheology of the gel after six heating/cooling cycles and after storage at 4 °C, 30 °C, and 45 °C for 1 month.

4.2.16. Release Study of VDL and VFL Extracts, Phytosomes, and Shape Memory Gel

The release profile of the VDL and VFL extracts, VDL and VFL phytosomes, and shape memory gels containing VDL and VFL phytosomes were evaluated by the method described by Liu et al. [63]. Phytosomes containing the same concentration of VDL and VFL extracts (13.33 mg/mL, 200 μL) and gels containing 0.1% VDL and VFL phytosomes were put in the upper chamber of Transwell® (Corning, Glendale, AZ, USA), where the donor chamber contained the PBS buffer (1000 μL). The total phenolic compounds released from extracts, phytosomes, and gels were collected at predetermined time intervals, i.e., 15 min, 30 min, 1, 2, 4, 6, 8, 12, and 24 h. The total phenolic contents were measured by the Folin–Ciocalteau method.

4.2.17. Statistical Analysis

The data were statistically analyzed using a one-way ANOVA, followed by the Newman–Keuls method as a post hoc test to determine the significance of differences (GraphPad Prism 7.02, La Jolla, CA, USA). In all cases, $p < 0.05$, $p < 0.01$, $p < 0.001$, and $p < 0.0001$ were deemed statistically significant. Data were presented as the mean $\pm$ SD of the % cell viability ($n = 3$).

References

1. Lynch, B.; Pageon, H.; Le Blay, H.; Brizion, S.; Bastien, P.; Bornschlögl, T.; Domanov, Y. A mechanistic view on the aging human skin through ex vivo layer-by-layer analysis of mechanics and microstructure of facial and mammary dermis. *Sci. Rep.* **2022**, *12*, 849. [CrossRef] [PubMed]
2. Chaudhary, M.; Khan, A.; Gupta, M. Skin Ageing: Pathophysiology and Current Market Treatment Approaches. *Curr. Aging Sci.* **2020**, *13*, 22–30. [CrossRef] [PubMed]
3. Poljšak, B.; Dahmane, R. Free radicals and extrinsic skin aging. *Derm. Res. Pract.* **2012**, *2012*, 135206. [CrossRef] [PubMed]
4. Juan, C.A.; Pérez de la Lastra, J.M.; Plou, F.J.; Pérez-Lebeña, E. The Chemistry of Reactive Oxygen Species (ROS) Revisited: Outlining Their Role in Biological Macromolecules (DNA, Lipids and Proteins) and Induced Pathologies. *Int. J. Mol. Sci.* **2021**, *22*, 4642. [CrossRef] [PubMed]
5. Rinnerthaler, M.; Bischof, J.; Streubel, M.K.; Trost, A.; Richter, K. Oxidative stress in aging human skin. *Biomolecules* **2015**, *5*, 545–589. [CrossRef]
6. Mota, F.L.; Queimada, A.J.; Pinho, S.P.; Macedo, E.A. Aqueous Solubility of Some Natural Phenolic Compounds. *Ind. Eng. Chem. Res.* **2008**, *47*, 5182–5189. [CrossRef]
7. Souza, J.; Casanova, L.; Costa, S. Bioavailability of phenolic compounds: A major challenge for drug development? *Fitos* **2015**, *9*, 1–72.
8. Férriz, J.M.; Vinsová, J. Prodrug design of phenolic drugs. *Curr. Pharm. Des.* **2010**, *16*, 2033–2052. [CrossRef]
9. Chen, M.; Li, R.; Gao, Y.; Zheng, Y.; Liao, L.; Cao, Y.; Li, J.; Zhou, W. Encapsulation of Hydrophobic and Low-Soluble Polyphenols into Nanoliposomes by pH-Driven Method: Naringenin and Naringin as Model Compounds. *Foods* **2021**, *10*, 963. [CrossRef]

10. Atanacković, M.T.; Gojković-Bukarica, L.C.; Cvejić, J.M. Improving the low solubility of resveratrol. *BMC Pharmacol. Toxicol.* **2012**, *13*, A25. [CrossRef]

11. Hamad, H.A.M. Phenolic Compounds: Classification, Chemistry, and Updated Techniques of Analysis and Synthesis. In *Phenolic Compounds*; Farid, A.B., Ed.; IntechOpen: Rijeka, Croatia, 2021; Chapter 4.

12. Lu, M.; Qiu, Q.; Luo, X.; Liu, X.; Sun, J.; Wang, C.; Lin, X.; Deng, Y.; Song, Y. Phyto-phospholipid complexes (phytosomes): A novel strategy to improve the bioavailability of active constituents. *Asian J. Pharm. Sci.* **2019**, *14*, 265–274. [CrossRef]

13. Barani, M.; Sangiovanni, E.; Angarano, M.; Rajizadeh, M.A.; Mehrabani, M.; Piazza, S.; Gangadharappa, H.V.; Pardakhty, A.; Mehrbani, M.; Dell'Agli, M.; et al. Phytosomes as Innovative Delivery Systems for Phytochemicals: A Comprehensive Review of Literature. *Int. J. Nanomed.* **2021**, *16*, 6983–7022. [CrossRef]

14. Vu, H.T.H.; Hook, S.M.; Siqueira, S.D.; Müllertz, A.; Rades, T.; McDowell, A. Are phytosomes a superior nanodelivery system for the antioxidant rutin? *Int. J. Pharm.* **2018**, *548*, 82–91. [CrossRef]

15. Telange, D.R.; Patil, A.T.; Pethe, A.M.; Fegade, H.; Anand, S.; Dave, V.S. Formulation and characterization of an apigenin-phospholipid phytosome (APLC) for improved solubility, in vivo bioavailability, and antioxidant potential. *Eur. J. Pharm. Sci.* **2017**, *108*, 36–49. [CrossRef]

16. Freag, M.S.; Elnaggar, Y.S.; Abdallah, O.Y. Lyophilized phytosomal nanocarriers as platforms for enhanced diosmin delivery: Optimization and ex vivo permeation. *Int. J. Nanomed.* **2013**, *8*, 2385–2397. [CrossRef]

17. Ju Ho, P.; Jun Sung, J.; Ki Cheon, K.; Jin Tae, H. Anti-inflammatory effect of Centella asiatica phytosome in a mouse model of phthalic anhydride-induced atopic dermatitis. *Phytomedicine* **2018**, *43*, 110–119. [CrossRef]

18. Hoang, H.T.; Moon, J.-Y.; Lee, Y.-C. Natural Antioxidants from Plant Extracts in Skincare Cosmetics: Recent Applications, Challenges and Perspectives. *Cosmetics* **2021**, *8*, 106. [CrossRef]

19. Rasoanaivo, P.; Wright, C.W.; Willcox, M.L.; Gilbert, B. Whole plant extracts versus single compounds for the treatment of malaria: Synergy and positive interactions. *Malar. J.* **2011**, *10* (Suppl. S1), S4. [CrossRef]

20. Ekor, M. The growing use of herbal medicines: Issues relating to adverse reactions and challenges in monitoring safety. *Front Pharm.* **2014**, *4*, 177. [CrossRef]

21. Briuglia, M.L.; Rotella, C.; McFarlane, A.; Lamprou, D.A. Influence of cholesterol on liposome stability and on in vitro drug release. *Drug Deliv. Transl. Res.* **2015**, *5*, 231–242. [CrossRef]

22. Minnelli, C.; Moretti, P.; Fulgenzi, G.; Mariani, P.; Laudadio, E.; Armeni, T.; Galeazzi, R.; Mobbili, G. A Poloxamer-407 modified liposome encapsulating epigallocatechin-3-gallate in the presence of magnesium: Characterization and protective effect against oxidative damage. *Int. J. Pharm.* **2018**, *552*, 225–234. [CrossRef] [PubMed]

23. Zook, J.M.; Vreeland, W.N. Effects of temperature, acyl chain length, and flow-rate ratio on liposome formation and size in a microfluidic hydrodynamic focusing device. *Soft Matter* **2010**, *6*, 1352–1360. [CrossRef]

24. Pistone, S.; Rykke, M.; Smistad, G.; Hiorth, M. Polysaccharide-coated liposomal formulations for dental targeting. *Int. J. Pharm.* **2017**, *516*, 106–115. [CrossRef] [PubMed]

25. Danaei, M.; Dehghankhold, M.; Ataei, S.; Hasanzadeh Davarani, F.; Javanmard, R.; Dokhani, A.; Khorasani, S.; Mozafari, M.R. Impact of Particle Size and Polydispersity Index on the Clinical Applications of Lipidic Nanocarrier Systems. *Pharmaceutics* **2018**, *10*, 57. [CrossRef]

26. Seo, J.W.; Kim, K.J.; Kim, S.H.; Hwang, K.M.; Seok, S.H.; Park, E.S. Effect of Process Parameters on Formation and Aggregation of Nanoparticles Prepared with a Shirasu Porous Glass Membrane. *Chem. Pharm. Bull.* **2015**, *63*, 792–798. [CrossRef]

27. Tiwari, R.; Tiwari, G.; Sharma, S.; Ramachandran, V. An Exploration of herbal extracts loaded phyto-phospholipid complexes (Phytosomes) against polycystic ovarian syndrome: Formulation considerations. *Pharm. Nanotechnol.* **2022**, *10*, 36121090. [CrossRef]

28. Direito, R.; Reis, C.; Roque, L.; Gonçalves, M.; Sanches-Silva, A.; Gaspar, M.M.; Pinto, R.; Rocha, J.; Sepodes, B.; Rosário Bronze, M.; et al. Phytosomes with Persimmon (*Diospyros kaki* L.) Extract: Preparation and Preliminary Demonstration of In Vivo Tolerability. *Pharmaceutics* **2019**, *11*, 296. [CrossRef]

29. Kraft, J.C.; Freeling, J.P.; Wang, Z.; Ho, R.J. Emerging research and clinical development trends of liposome and lipid nanoparticle drug delivery systems. *J. Pharm. Sci.* **2014**, *103*, 29–52. [CrossRef]

30. El Badawy, A.M.; Silva, R.G.; Morris, B.; Scheckel, K.G.; Suidan, M.T.; Tolaymat, T.M. Surface Charge-Dependent Toxicity of Silver Nanoparticles. *Environ. Sci. Technol.* **2011**, *45*, 283–287. [CrossRef]

31. Honary, S.; Zahir, F. Effect of Zeta Potential on the Properties of Nano-Drug Delivery Systems—A Review (Part 2). *Trop. J. Pharm. Res.* **2013**, *12*, 265–273. [CrossRef]

32. Kori, Y.; Misri, G.; Mardiastuti; Vivi, A.; Rini, P.; Mahdi, J. Phytochemical Evaluation and Antioxidant Activity of Virginia tobacco Leaves (*Nicotiana tabacum* L. var virginia) Fractions with DPPH and FTC Methods. *Pharmacogn. J.* **2022**, *14*, 544–548.

33. Sun, C.; Wu, Z.; Wang, Z.; Zhang, H. Effect of Ethanol/Water Solvents on Phenolic Profiles and Antioxidant Properties of Beijing Propolis Extracts. *Evid.-Based Complement. Altern. Med.* **2015**, *2015*, 595393. [CrossRef]

34. Chew, K.K.; Ng, S.Y.; Thoo, Y.Y.; Khoo, M.Z.; Aida, W.W.; Ho, C.W. Effect of ethanol concentration, extraction time and extraction temperature on the recovery of phenolic compounds and antioxidant capacity of Centella asiatica extracts. *Int. Food Res. J.* **2011**, *18*, 571–578.

35. Alara, O.R.; Abdurahman, N.H.; Olalere, O.A. Ethanolic extraction of flavonoids, phenolics and antioxidants from Vernonia amygdalina leaf using two-level factorial design. *J. King Saud Univ.-Sci.* **2020**, *32*, 7–16. [CrossRef]

36. Mello, B.C.B.S.; Petrus, J.C.C.; Hubinger, M.D. Concentration of flavonoids and phenolic compounds in aqueous and ethanolic propolis extracts through nanofiltration. *J. Food Eng.* **2010**, *96*, 533–539. [CrossRef]

37. Chen, Y.; Jimmy Yu, Q.; Li, X.; Luo, Y.; Liu, H. Extraction and HPLC Characterization of Chlorogenic Acid from Tobacco Residuals. *Sep. Sci. Technol.* **2007**, *42*, 3481–3492. [CrossRef]

38. Kınay, A.; Kurt, D. Chemical Content and Quality of Sun Cured Tobacco Lines. *Anadolu J. Agric. Sci.* **2021**, *36*, 282–292. [CrossRef]

39. Li, Z.; Wang, L.; Yang, G.; Shi, H.; Jiang, C.; Liu, W.; Zhang, Y. Study on the determination of polyphenols in tobacco by HPLC coupled with ESI-MS after solid-phase extraction. *J. Chromatogr. Sci.* **2003**, *41*, 36–40. [CrossRef]

40. Lobo, V.; Patil, A.; Phatak, A.; Chandra, N. Free radicals, antioxidants and functional foods: Impact on human health. *Pharm. Rev.* **2010**, *4*, 118–126. [CrossRef]

41. He, L.; He, T.; Farrar, S.; Ji, L.; Liu, T.; Ma, X. Antioxidants Maintain Cellular Redox Homeostasis by Elimination of Reactive Oxygen Species. *Cell. Physiol. Biochem.* **2017**, *44*, 532–553. [CrossRef]

42. Kruk, J.; Aboul-Enein, B.H.; Duchnik, E.; Marchlewicz, M. Antioxidative properties of phenolic compounds and their effect on oxidative stress induced by severe physical exercise. *J. Physiol. Sci.* **2022**, *72*, 19. [CrossRef] [PubMed]

43. Rodu, B.; Ou, B. The Antioxidant Properties of Tobacco. *Tob. Sci.* **2000**, *44*, 71–73. [CrossRef]

44. Zou, X.; Bk, A.; Rauf, A.; Saeed, M.; Al-Awthan, Y.S.; Al-Duais, M.A.; Bahattab, O.; Hamayoon Khan, M.; Suleria, H.A.R. Screening of Polyphenols in Tobacco (*Nicotiana tabacum*) and Determination of Their Antioxidant Activity in Different Tobacco Varieties. *ACS Omega* **2021**, *6*, 25361–25371. [CrossRef] [PubMed]

45. Ru, Q.M.; Wang, L.J.; Li, W.M.; Wang, J.L.; Ding, Y.T. In vitro antioxidant properties of flavonoids and polysaccharides extract from tobacco (*Nicotiana tabacum* L.) leaves. *Molecules* **2012**, *17*, 11281–11291. [CrossRef] [PubMed]

46. Zou, X.; Bk, A.; Abu-Izneid, T.; Aziz, A.; Devnath, P.; Rauf, A.; Mitra, S.; Emran, T.B.; Mujawah, A.A.H.; Lorenzo, J.M.; et al. Current advances of functional phytochemicals in Nicotiana plant and related potential value of tobacco processing waste: A review. *Biomed. Pharm.* **2021**, *143*, 112191. [CrossRef]

47. Akinloye, O.A.; Akinloye, D.I.; Onigbinde, S.B.; Metibemu, D.S. Phytosterols demonstrate selective inhibition of COX-2: In-vivo and in-silico studies of *Nicotiana tabacum*. *Bioorganic. Chem.* **2020**, *102*, 104037. [CrossRef]

48. Alshahrani, S.M. Optimization and Characterization of Cuscuta reflexa Extract Loaded Phytosomes by the Box-Behnken Design to Improve the Oral Bioavailability. *J. Oleo. Sci.* **2022**, *71*, 671–683. [CrossRef]

49. Zarzycki, R.; Modrzejewska, Z.; Nawrotek, K.; Leków, U.; Hydrożeli, Z. Drug release from hydrogel matrices. *Ecol. Chem. Eng. S* **2010**, *17*, 117–136.

50. Speidel, A.T.; Chivers, P.R.A.; Wood, C.S.; Roberts, D.A.; Correia, I.P.; Caravaca, A.S.; Chan, Y.K.V.; Hansel, C.S.; Heimgärtner, J.; Müller, E.; et al. Tailored Biocompatible Polyurethane-Poly(ethylene glycol) Hydrogels as a Versatile Nonfouling Biomaterial. *Adv. Healthc. Mater.* **2022**, *11*, 2201378. [CrossRef]

51. Ping, P.; Wang, W.; Zhang, P.; Chen, X.; Jing, X. Shape-memory and biocompatibility properties of segmented polyurethanes based on poly(L-lactide). *Front. Chem. China* **2007**, *2*, 331–336. [CrossRef]

52. Burnett, C.L.; Bergfeld, W.F.; Belsito, D.V.; Hill, R.A.; Klaassen, C.D.; Liebler, D.C.; Marks, J.G.; Shank, R.C.; Slaga, T.J.; Snyder, P.W.; et al. Safety Assessment of Polyene Group as Used in Cosmetics. *Int. J. Toxicol.* **2020**, *39*, 59S–90S. [CrossRef]

53. Nur Aini, D.; Ganet, E.; Muhamad, D. Development of the Myricetin Nano-Phytosome Formula with Phosphatidylcholine Variations. In Proceedings of the 2nd Bakti Tunas Husada-Health Science International Conference (BTH-HSIC 2019), Tasikmalaya, Indonesia, 5–6 October 2019; pp. 272–275.

54. Chittasupho, C.; Athikomkulchai, S. Nanoparticles of Combretum quadrangulare leaf extract induce cytotoxicity, apoptosis, cell cycle arrest and anti-migration in lung cancer cells. *J. Drug Deliv. Sci. Technol.* **2018**, *45*, 378–387. [CrossRef]

55. Buranasukhon, W.; Athikomkulchai, S.; Tadtong, S.; Chittasupho, C. Wound healing activity of *Pluchea indica* leaf extract in oral mucosal cell line and oral spray formulation containing nanoparticles of the extract. *Pharm Biol* **2017**, *55*, 1767–1774. [CrossRef]

56. Chiangnoon, R.; Samee, W.; Uttayarat, P.; Jittachai, W.; Ruksiriwanich, W.; Sommano, S.R.; Athikomkulchai, S.; Chittasupho, C. Phytochemical Analysis, Antioxidant, and Wound Healing Activity of *Pluchea indica* L. (Less) Branch Extract Nanoparticles. *Molecules* **2022**, *27*, 635. [CrossRef]

57. Tunit, P.; Thammarat, P.; Okonogi, S.; Chittasupho, C. Hydrogel Containing Borassus flabellifer L. Male Flower Extract for Antioxidant, Antimicrobial, and Anti-Inflammatory Activity. *Gels* **2022**, *8*, 126. [CrossRef]

58. Chittasupho, C.; Thongnopkoon, T.; Burapapisut, S.; Charoensukkho, C.; Shuwisitkul, D.; Samee, W. Stability, permeation, and cytotoxicity reduction of capsicum extract nanoparticles loaded hydrogel containing wax gourd extract. *Saudi Pharm J.* **2020**, *28*, 1538–1547. [CrossRef]

59. Zhong, Y.; Qi, A.; Liu, L.; Huang, Q.; Zhang, J.; Cai, K.; Cai, C. Shikonin attenuates H_2O_2-induced oxidative injury in HT29 cells via antioxidant activities and the inhibition of mitochondrial pathway-mediated apoptosis. *Exp. Ther. Med.* **2021**, *22*, 1118. [CrossRef]

60. Chittasupho, C.; Ditsri, S.; Singh, S.; Kanlayavattanakul, M.; Duangnin, N.; Ruksiriwanich, W.; Athikomkulchai, S. Ultraviolet Radiation Protective and Anti-Inflammatory Effects of Kaempferia galanga L. Rhizome Oil and Microemulsion: Formulation, Characterization, and Hydrogel Preparation. *Gels* **2022**, *8*, 639. [CrossRef]

61. Singh, S.; Nwabor, O.F.; Sukri, D.M.; Wunnoo, S.; Dumjun, K.; Lethongkam, S.; Kusolphat, P.; Hemtanon, N.; Klinprathum, K.; Sunghan, J.; et al. Poly (vinyl alcohol) copolymerized with xanthan gum/hypromellose/sodium carboxymethyl cellulose dermal dressings functionalized with biogenic nanostructured materials for antibacterial and wound healing application. *Int. J. Biol. Macromol.* **2022**, *216*, 235–250. [CrossRef]

62. Chittasupho, C.; Junmahasathien, T.; Chalermmongkol, J.; Wongjirasakul, R.; Leesawat, P.; Okonogi, S. Suppression of Intracellular Reactive Oxygen Species in Human Corneal Epithelial Cells via the Combination of Quercetin Nanoparticles and Epigallocatechin Gallate and In Situ Thermosensitive Gel Formulation for Ocular Drug Delivery. *Pharmaceuticals* **2021**, *14*, 679. [CrossRef]

63. Liu, Z.; Li, Y.; Li, W.; Lian, W.; Kemell, M.; Hietala, S.; Figueiredo, P.; Li, L.; Mäkilä, E.; Ma, M.; et al. Close-loop dynamic nanohybrids on collagen-ark with in situ gelling transformation capability for biomimetic stage-specific diabetic wound healing. *Mater. Horiz.* **2019**, *6*, 385–393. [CrossRef]

Multi-Responsive Optimization of Novel pH-Sensitive Hydrogel Beads Based on Basil Seed Mucilage, Alginate, and Magnetic Particles

Natwat Srikhao [1], Korrapat Chirochrapas [1], Nessaraporn Kwansanei [1], Pornnapa Kasemsiri [1,*],
Artjima Ounkaew [1], Manunya Okhawilai [2,3,*], Chutiwat Likitaporn [4], Somnuk Theerakulpisut [5]
and Hiroshi Uyama [6]

1   Department of Chemical Engineering, Faculty of Engineering, Khon Kaen University,
    Khon Kaen 40002, Thailand; natwat_s@kkumail.com (N.S.); korrapatchi@gmail.com (K.C.);
    nessaraporn.k@kkumail.com (N.K.); artjima.o@kkumail.com (A.O.)
2   Center of Excellence in Responsive Wearable Materials, Chulalongkorn University, Bangkok 10330, Thailand
3   Metallurgy and Materials Science Research Institute, Chulalongkorn University, Bangkok 10330, Thailand
4   International Graduate Program of Nanoscience & Technology, Chulalongkorn University,
    Bangkok 10330, Thailand; 6388315520@student.chula.ac.th
5   Energy Management and Conservation Office, Faculty of Engineering, Khon Kaen University,
    Khon Kaen 40000, Thailand; somthe@kku.ac.th
6   Department of Applied Chemistry, Graduate School of Engineering, Osaka University, Suita 565-0871, Japan;
    uyama@chem.eng.osaka-u.ac.jp
*   Correspondence: pornkas@kku.ac.th (P.K.); manunya.o@chula.ac.th (M.O.)

Abstract: Conventional drug delivery systems often cause side effects and gastric degradation. Novel drug delivery systems must be developed to decrease side effects and increase the efficacy of drug delivery. This research aimed to fabricate hydrogel beads for use as a drug delivery system based on basil seed mucilage (BSM), sodium alginate (SA), and magnetic particles (MPs). The Taguchi method and Grey relational analysis were used for the design and optimization of the hydrogel beads. Three factors, including BSM, SA, and MPs at four levels were designed by L-16 orthogonal arrays. BSM was the main factor influencing bead swelling, drug release rate at pH 7.4, and release of antioxidants at pH 1.2 and 7.4. In addition, SA and MPs mainly affected drug loading and drug release rate in acidic medium, respectively. Grey relational analysis indicated that the composition providing optimal overall properties was 0.2 vol% BSM, 0.8 vol% SA, and 2.25 vol% MPs. Based on the findings of this work, BSM/SA/MPs hydrogel beads have the potential to be used as a pH-sensitive alternative material for drug delivery in colon-specific systems.

Keywords: hydrogel beads; Taguchi's method; Grey relational analysis; drug delivery system

1. Introduction

Engineered materials that can control drug release have received a great deal of attention from researchers. These materials overcome disadvantages in drug delivery due to deterioration in the digestion system or to drug residues in the stomach affecting liver function. These problems cause the organs to work harder to remove residues; therefore, there is a need for new materials to control and optimize drug release in both dosage and time. This could reduce side effects of medication [1] such as damage to non-target cell tissues during delivery and excessive drug intake causing residues in the body [2].

Hydrogels are 3D structured materials that can easily retain and deliver drugs due to their high absorption ability and good compatibility with human tissues [1,3–5]. Hydrogels can be natural or synthetic polymers in a variety of forms, such as films [6], nanoparticles [7], microparticles [8], and beads [9]. Mucilage is a natural products of plant metabolism with low toxicity and high viscosity [1]. Consequently, mucilages can be suitable for use in

gel-forming and as stabilizers in the food and pharmaceutical industries. Basil (*Ocimum basilicum* L.) is a plant native to Iran that is commonly grown in Thailand. Basil seeds are used in traditional medicine to treat inflammation, diarrhea, indigestion, and other diseases [2]. In addition, basil slime has been used in pharmaceuticals via preparation as a capsule laxative [10]. When it comes into contact with water, the outer layer of a basil seed quickly swells and forms a gelatinous substance, basil seed mucilage (BSM). BSM has two main components, i.e., 43% glucomannan and 24% (1,4)-linked xylan, along with 6% uronic acid, which forms hydrogen bonds with water molecules. These components provide a large amount of water storage. When water is retained, mucilage forms a chain of polysaccharides to absorb water in its structure. Basil seeds are easy to obtain and inexpensive. Therefore, they are suitable for producing drugs such as anticancer drugs [11], nanocomposites [12], etc. Yari et al. [1] studied the synthesis of hydrogel beads using BSM and sodium alginate (SA) to improve the encapsulation efficiency and optimal control of the release of metformin. They reported that increased amounts of BSM increased encapsulation efficacy. On the contrary, drug release ability decreased due to the stronger structure of the polymer. To prepare hydrogel beads, a biopolymer such as SA can rapidly form hydrogel beads with cations (for example, Zn^{2+}, Ca^{2+}, and Ba^{2+}) at a neutral pH [13]. Hua et al. [14] reported that the encapsulation efficiency improved to 99.46% when using PVA mixed with SA at a ratio of 3:1 to form hydrogel beads. At a concentration of SA lower than this ratio, the bead form was imperfect.

Magnetic particles (MPs) have attracted a great deal of attention due to their potential for incorporation into hydrogel bead drug carriers [15]. MPs have a high surface area and low toxicity [16,17]. Furthermore, they can control the amount of drug released in different tissues in the body. This is because the human body has different pH levels in each organ; for example, the stomach has a pH of 1.2, while the intestine has a pH of 7.4 [2]. Supramaniam et al. [18] synthesized iron into magnetic nanoparticles in nanocellulose crystals (m-CNCs) to enhance mechanical strength and controlled release of ibuprofen from hydrogel tablets. A scanning electron microscope (SEM) micrograph revealed an increase in surface roughness with an increasing number of m-CNCs, resulting in a more porous structure and increased drug loading efficiency. The release of ibuprofen could be controlled at pH 1.2, 7.0, and 7.4. Moreover, the highest release, $3.2\% \pm 0.2\%$, and drug encapsulation, $38.2\% \pm 0.1\%$, were obtained from the sample with 3 wt% m-CNCs of SA solution. The pH-sensitive hydrogel was investigated for oral anticancer drug delivery based on magnetic particles [19]. The swelling ratio of the carboxymethylcellulose/polyacrylic acid/starch-modified Fe_3O_4 was affected by different contents of Fe_3O_4; i.e., the values increased at lower concentrations of Fe_3O_4, then decreased. Moreover, the results demonstrated the effect of pH on the swelling behavior of the hydrogel beads due to the shrinkage of the polymeric network under acidic conditions.

Our literature review indicated that using BSM and SA in optimal proportions can enhance drug encapsulation due to the stronger structure of the hydrogel beads and polymer chain, thus reducing drug release. An increase in MPs with a suitable content results in a rougher surface and more porosity, and can control the amount of drug release for body tissues with different pH values. Hence, to design a drug carrier with required properties, the design of the experiment (DOE) should analyze the impacts of individual components and their interactions [20]. Taguchi's method is a well-known method for DOE, and is used to design the optimum mix proportions of polymer composites while requiring a minimal number of experiments [17]. The Taguchi method has been used to both optimize a single response and to determine the main factors responsible for the response. In the case of multi-response optimization problems, the Taguchi method can be coupled with Grey relational analysis to optimize multi-responses by converting the multi-responses to a single relational grade. Recently, the mix proportion of various biopolymer composites has successfully been designed and optimized using the Taguchi method and Grey relational analysis, for example, in the context of bioactive starch foam composites [21], bioactive film composites [22], and drug delivery systems [23].

The objective of this study was to optimize hydrogel beads as a drug carrier composed of BSM, SA, and MPs. The experiment in this study was designed using the Taguchi method and Grey relational analysis. The experimental design involved three factors, including BSM, SA, and MPs, with four levels of values to find the appropriate volume percentage of individual factors. The prepared samples had their mix proportions optimized for swelling, drug loading, drug release in different pH values, and antioxidant activity in different pH values. Kinetic drug release was investigated as well. The chemical and physical properties of the beads were examined using a scanning electron microscope (SEM), X-ray diffraction (XRD) analysis, and Fourier Transform Infrared Spectroscopy (FT-IR).

2. Results and Discussion

2.1. Morphology of the BSM/SA/MPs Hydrogel Beads

SEM investigation was considered to observe the morphology of the BSM/SA/MPs hydrogel beads as they act as drug carriers, which is one of the most important factors affecting the administration route and drug release behavior. Figure 1 shows SEM micrographs of the cross-sectional hydrogel beads of the sample BSM/SA with and without MPs. Figure 1a,b shows the morphology of BSM/SA. A smooth surface and a porous structure with cavities were observed. Incorporation of MPs in the hydrogel beads led to a rougher surface and greater number of cavities inside compared to those without MPs, as shown in Figure 1c,d. The increase in cavities allowed the drug solution to be entrapped in the micro-environmental cavities and diffused into the hydrogel bead carrier more easily due to the capillary effect [1]. This structure was suitable for higher amounts of drug loading into hydrogel beads.
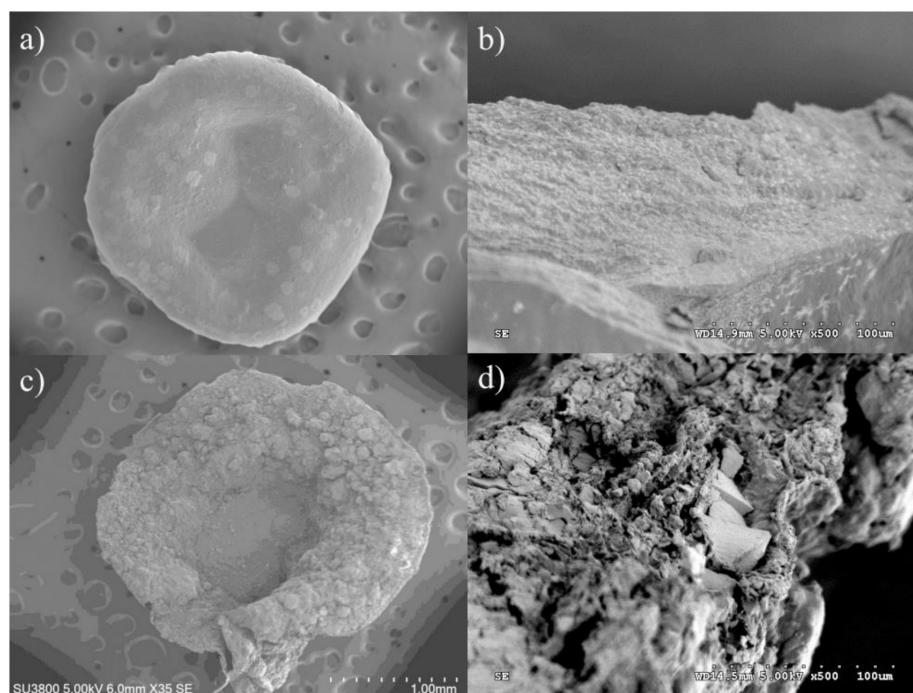

Figure 1. SEM images of hydrogel beads: (**a**) surface of sample from experimental design No. 4; (**b**) cross-section of sample from experimental design No. 4; (**c**) surface of sample from experimental design No. 16; and (**d**) cross-section of sample from experimental design No. 16.

2.2. Chemical Functionality of the BSM/SA/MPs Hydrogel Beads

The chemical structures of the hydrogel beads were studied using the ATR-FTIR technique. From Figure 2a, for BSM the broad peaks appeared around 3000–3500 cm^{-1} due to vibrational stretching of O-H molecule and at 870–1150 cm^{-1}, representing the C-O bond of the carbohydrate group. A small peak of BSM at 2850–3000 cm^{-1} related to the hydroxyl CH-bond oscillations, while the peak at 1593 cm^{-1} corresponded to C=C

stretching for non-condensed alkanes [24]. The peak positions at 1025 cm^{-1} were due to CH stretching, 1404 and 1593 cm^{-1} were assigned to stretching of carboxyl groups, and the broad peak at 3000–3600 relating to the O-H group was observed in the SA [25]. The characteristic peak position of MPs was observed at a wavelength of 558 cm^{-1}, indicating MP formation [19,26,27]. For the BSM/SA/MPs hydrogel beads, all characteristic peaks of BSM, SA, and MPs were observed and showed small changes in peak position, indicating physical interaction of the components [6,28,29].

The loading of diclofenac into hydrogel beads was confirmed by FTIR [30]. Figure 2b shows the characteristic peaks of diclofenac and hydrogel beads loaded with diclofenac. The principle FTIR spectra of diclofenac appeared at 1630 cm^{-1} (C=O stretching vibration of the carboxyl group), 1418 cm^{-1} (C=C vibration of aromatic ring), 1127 cm^{-1}, and 1083 cm^{-1} (C-H deformation vibration of aromatic ring), and band in the range of 3000–3300 cm^{-1} (N-H vibration) [31]. After loading diclofenac into hydrogel beads, all the principal characteristic peaks of diclofenac were observed in the hydrogel beads.
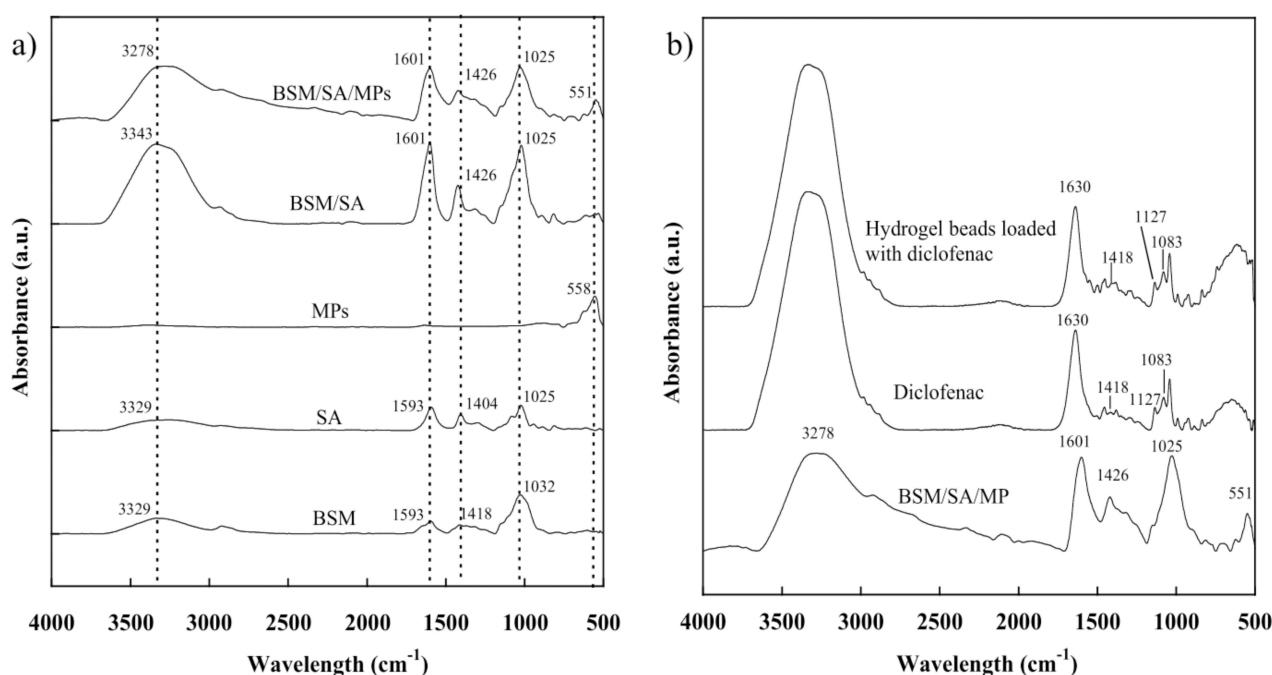
Figure 2. FTIR spectra of (**a**) chemical components and the BSM/SA/MPs hydrogel and (**b**) hydrogel beads loaded with diclofenac.

2.3. XRD Pattern of the BSM/SA/MPs Hydrogel Beads

There are several methods of synthesizing MPs. In this research, co-precipitation was used, as it is a simple and easy technique. The successful preparation of MPs is evidenced by XRD observation. As shown in Figure 3a, 2θ peaks were found at 30.34°, 35.58°, 43.52°, 53.63°, 56.70°, and 62.84°, and were assigned to (220), (311), (222), (422), (511), and (440) corresponding to the standard XRD format of International Center for Diffraction Data (ICDD) No. 019-0629 of Fe$_3$O$_4$ with a cubic crystal structure [32–34]. After adding MPs into hydrogel beads, the peaks of other iron oxides could not be observed. This observation confirmed that the MPs were successfully incorporated into hydrogel beads without oxidization. Figure 3b shows a particle-sized distribution of MPs in the range of 0.42–1.01 μm.
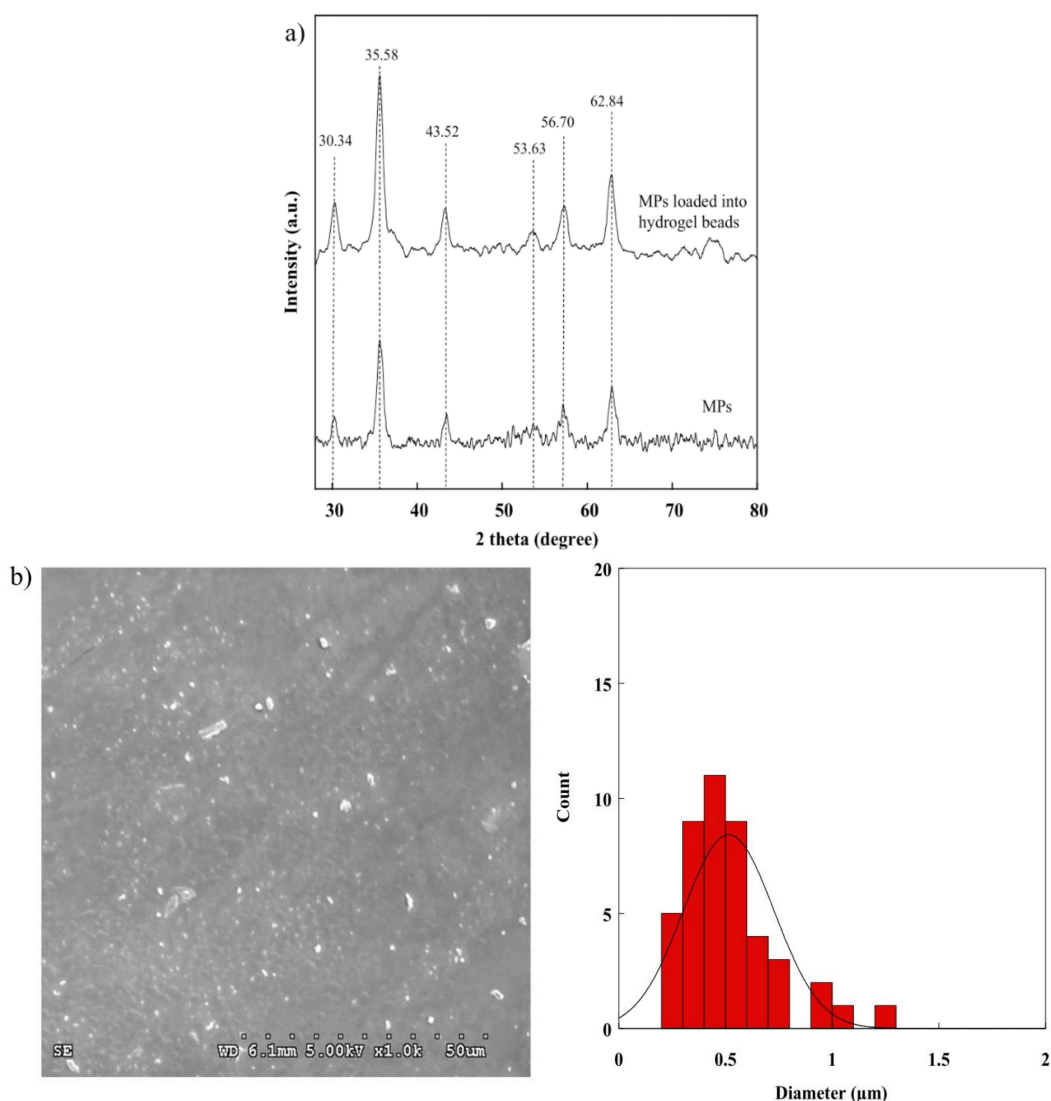
Figure 3. (**a**) XRD pattern of MPs and (**b**) SEM images of MPs.

2.4. Swelling Study of the BSM/SA/MPs Hydrogel Beads

The swelling property is one most important properties for drug delivery, as it affects the release rate of the drug to the medium [13]. Consequently, the effects of various compositions of BSM, SA, and MPs on the swelling property of the hydrogel beads were investigated in order to better understand each component's role in the release mechanism. Upon immersion, all of the hydrogels took up water, and the dimensions of the hydrogels changed due to the interaction of water molecules with the functional ionic groups of hydrogel beads and electrostatic repulsion between charges on a polymer chain, thus leading to an increase in swelling [6]. Figure 4 shows that the swelling value of the BSM/SA/MPs hydrogel beads increased sharply with increasing BSM concentration. This was attributable to the fact that BSM exhibits hydrophilicity due to its heteropolysaccharide structures of glucomannan and xylan, which have large amounts of hydroxyl groups [35]. In comparison, the swelling values of BSM/SA/MPs were in the range of 130–560%, higher than those reported in SA/BSM beads, which had values in the range of 150–250% [1]. The hydrophilic property of materials enhances the swelling efficiency, resulting in good diffusion of drugs from hydrogel beads into media solution. In contrast, the swelling value tended to decrease as the percentage of MPs and SA increased. The intermolecular chain of SA and BSM might create a tight structure, whereas MPs could create interaction with the polymer matrix and interaction between magnetic particles [36,37]. Moreover, this

was related to osmotic pressure and an increased intermolecular electrostatic repulsion force, resulting in water penetrating into the internal structure of the hydrogel [38]. A high S/N ratio indicates high swelling of hydrogel beads. The S/N ratio values were in good agreement with the larger-the-better criterion. The amount of BSM is the main factor affecting the hydrogel beads' swelling properties, with a contribution of 68.17%, as summarized in Table 1. The optimum composition of the BSM/SA/MPs hydrogel providing the highest swelling ratio was at 0 %vol of MPs, 0.8 %vol of BMS, and 0.2 %vol of SA. The multi-linear regression technique was applied to obtain the relationship between the swelling and the composition of hydrogel beads, as expressed in Equation (1):

$$\text{Swelling} = -0.01X_1 + 0.01X_2 + 0X_3 + 1.15 \tag{1}$$

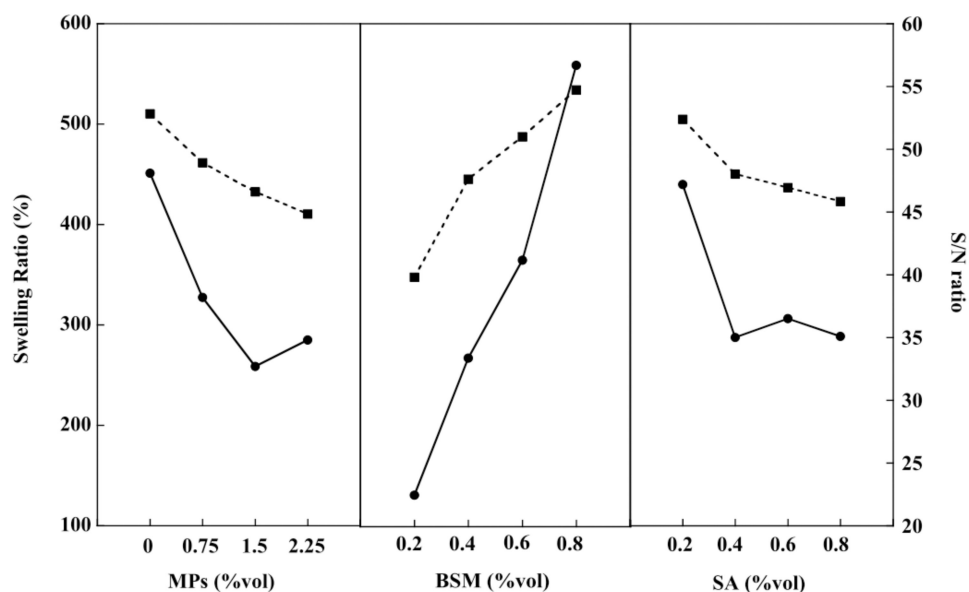where X_1 is MPs (%vol), X_2 is BSM (%vol), and X_3 is SA (%vol).

Figure 4. Swelling (–●–) and S/N (–■–) ratios of the BSM/SA/MPs hydrogel beads.

Table 1. ANOVA analysis results.

Factor	DF [a]	SS [b]	MS [c]	F-Value	*p*-Value	Contribution (%)
Swelling						
MPs	3	87,231.00	29,077	5.97	0.031	15.33
BSM	3	387,831.00	129,277	26.56	0.001	68.17
SA	3	64,681.00	21,560	4.43	0.058	11.37
Error	6	29,200.00	4867	-	-	5.13
Total	15	568,944.00	-	-	-	100.00
Drug loading						
MPs	3	0.0014	0.0005	0.29	0.830	3.31
BSM	3	0.0051	0.0017	1.07	0.429	12.14
SA	3	0.0259	0.0086	5.47	0.038	61.91
Error	6	0.0095	0.0016	-	-	22.64
Total	15	0.0418	-	-	-	100.00
Release rate at pH 1.2						
MPs	3	5.2066	1.7355	49.41	0.000	87.95
BSM	3	0.2119	0.0706	2.01	0.214	3.58
SA	3	0.2906	0.0969	2.76	0.134	4.91
Error	6	0.2108	0.0351	-	-	3.56
Total	15	5.9199	-	-	-	100.00

Table 1. *Cont.*

Factor	DF [a]	SS [b]	MS [c]	F-Value	*p*-Value	Contribution (%)
Release rate at pH 7.4						
MPs	3	7.9350	2.6450	0.86	0.513	16.58
BSM	3	10.8010	3.6000	1.16	0.398	22.56
SA	3	10.5900	3.5300	1.14	0.405	22.12
Error	6	18.5460	3.0910	-	-	38.74
Total	15	47.8720	-	-	-	100.00
Antioxidant activity at pH 1.2						
MPs	3	22.4500	7.4850	0.20	0.894	2.83
BSM	3	328.2000	109.4010	2.89	0.125	41.31
SA	3	216.6000	72.2010	1.91	0.230	27.26
Error	6	227.2300	37.8710	-	-	28.60
Total	15	794.4800	-	-	-	100.00
Antioxidant activity at pH 7.4						
MPs	3	126.9000	42.3000	0.510	0.690	12.10
BSM	3	280.3000	93.4200	1.12	0.411	26.73
SA	3	143.0000	47.6700	0.57	0.653	13.63
Error	6	498.7000	83.1100	-	-	47.55
Total	15	1048.8000	-	-	-	100.00

[a] Degree of freedom, [b] Sum of squares, [c] Mean square.

2.5. Drug Loading of the BSM/SA/MPs Hydrogel Beads

Consistent with Ecke et al., this study used diclofenac, a drug for relief of inflammation, pain, and intumescence, as a drug model to simulate drug transport and investigate drug loading of the BSM/SA/MPs hydrogel beads [39]. Drug loading of the hydrogel beads tended to decrease with increasing amounts of BSM and MPs, whereas the values gradually increased with SA content, as shown in Figure 5. This was attributed to the hydrophilicity of SA as a polymer matrix that facilitated the formation of hydrogel beads. Moreover, the structure of SA, containing a carboxylate group (–COO–) exhibited, an electrical attraction to the drug, thus allowing the drug to be contained and causing greater drug loading [40]. The increase of BSM enhanced the connection between BSM and SA. This phenomenon might have reduced the cavities inside the beads [1,36]. Similarly, the swelling property of hydrogel beads decreased when MP content increased. Mahdavinia et al. [37] suggested that adding MPs to hydrogel beads could create interaction with the polymer matrix, decreasing hydrophilicity. From Table 1, it can be seen that SA was the main factor, accounting for 61.91% of the drug loading value. The composition of BSM/SA/MPs providing the maximum drug loading was at 0 %vol of MPs, 0.2 %vol of BSM, and 0.8 %vol of SA. The value of drug loading of the BSM/SA/MPs was in the range of 99.3 to 99.7%, which was higher than that reported in micelles/sodium alginate composite gel beads [41]. A multi-linear regression analysis was used to formulate the relationship between drug loading and hydrogel bead components, as expressed in Equation (2):

$$\text{Drug loading} = 6.61X_1 + 2.67X_2 + 30.04X_3 - 3916.691 \tag{2}$$

where X_1 is MPs (%vol), X_2 is BSM (%vol), and X_3 is SA (%vol).

2.6. In Vitro Drug Release of the BSM/SA/MPs Hydrogel Beads

Drug release studies of the BSM/SA/MPs hydrogel beads were conducted in acid and neutral PBS solution at 37 °C to investigate the effect of pH on the drug release rate, similar to Yin et al. [42]. The PBS solution at pH 1.2 was prepared to simulate gastric fluid in the human stomach, and the release behavior of diclofenac was investigated [43]. As shown in Figure 6, it was found that the release of the drug from the BSM/SA/MPs hydrogel beads slightly increased with BSM. The drastic increase of drug release from the sample with a large number of MPs was observed due to the repulsion force between positive

charges of MPs and the drug [44]. The diclofenac release tended to decrease when SA increased. The carboxylic group (–COO–) in SA exhibited a negative charge and formed an attractive force to the positive charge of the drug [45]. The results of drug release in pH 1.2 corresponded to the S/N ratio with the smaller-the-better criteria. Table 1 shows that MPs influenced drug release at pH 1.2, accounting for 87.75%. The most suitable composition of the BSM/SA/MPs hydrogel beads providing the lowest release rate of diclofenac in PBS at pH 1.2 was at 0 %vol of MPs, 0.2 %vol of BSM, and 0.6 %vol of SA.
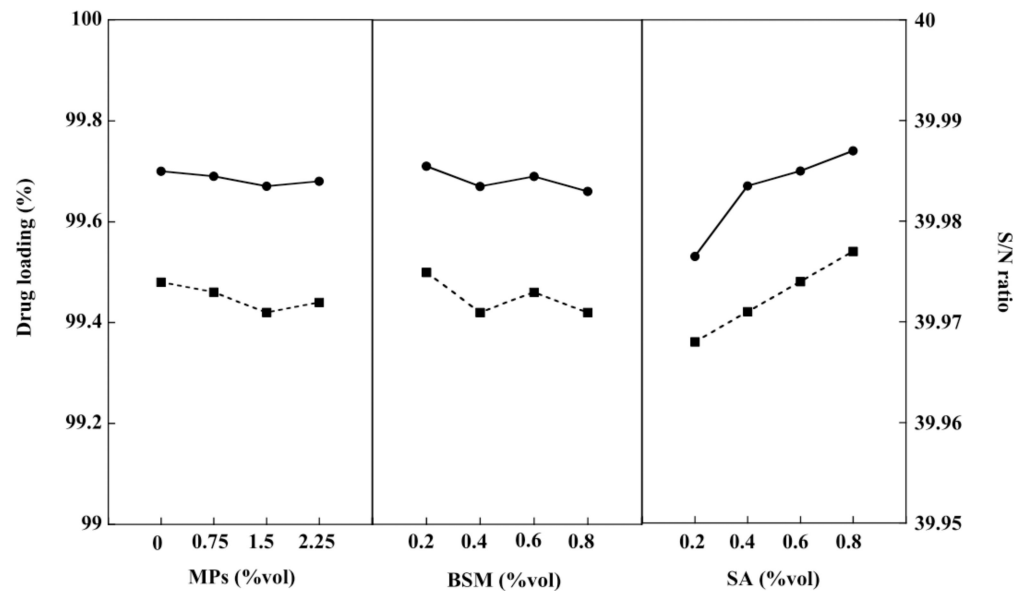
Figure 5. Drug loading (–●–) and S/N ratio (–■–) of the BSM/SA/MPs hydrogel beads.
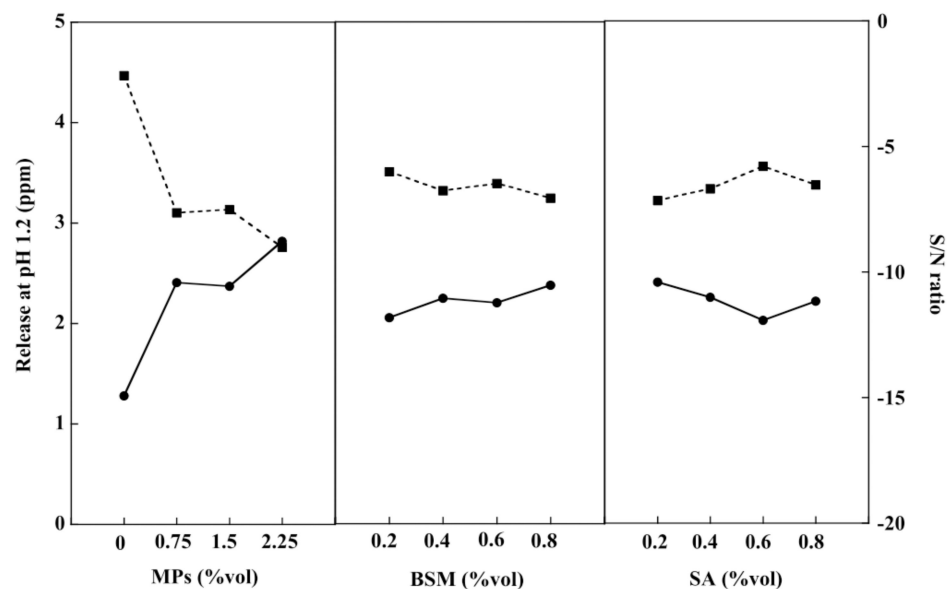
Figure 6. Drug release at pH 1.2 (–●–) and S/N ratio (–■–) of the BSM/SA/MPs hydrogel beads.

The swelling ratio of the hydrogel beads at pH 1.2 after 3 h of incubation was less than 0.6% due to the pKa of SA being about 3.2 [46], and the formation of insoluble alginic acid resulted in protonation of carboxyl groups (–COOH) in SA. However, ionization of the carboxyl groups of SA (–COO–) took place at pH 7.4. Due to osmotic pressure and increased intermolecular electrostatic repulsion forces, water penetration occurred on the internal structure of the hydrogel [1,41].

A PBS solution at pH 7.4 was prepared to simulate human intestinal fluid and the release rate of the drug from the BSM/SA/MPs hydrogel bead was studied. From Figure 7, it can be seen that the release of the drug tended to increase with a greater amount of BSM and MPs. However, an increase in SA content resulted in a reduction in drug release. This was attributed to the carboxylic groups of SA being neutralized at pH 7.4, leading to the repulsion force acting on the drug, then the release rate of the drug increasing with SA content. Moreover, it could be related to the opened pores caused by ionic repulsion of the constituted ions, which can be formed via ionization of carboxyl groups of BSM and hydroxyl groups on the SA chain [6]. BSM and SA were the major components affecting the release of the drug at pH 7.4. The hydrogel beads containing 2.25 %vol of MPs, 0.6 %vol of BSM, and 0.2 %vol of SA had the most suitable composition, providing the highest drug release at pH 7.4. Similarly, per multi-linear regression analysis drug release at pH 1.2 and pH 7.4 was formulated as a function of hydrogel bead components, as expressed in Equations (3) and (4), respectively:

$$\text{Drug release at pH1.2} = -5.34X_1 + 29.55X_2 - 8.99X_3 - 31.25 \tag{3}$$

$$\text{Drug release at pH7.4} = 0.73X_1 + 0.9X_2 + 0.06X_3 - 31.25 \tag{4}$$

where X_1 is MPs (%vol), X_2 is BSM (%vol), and X_3 is SA (%vol).
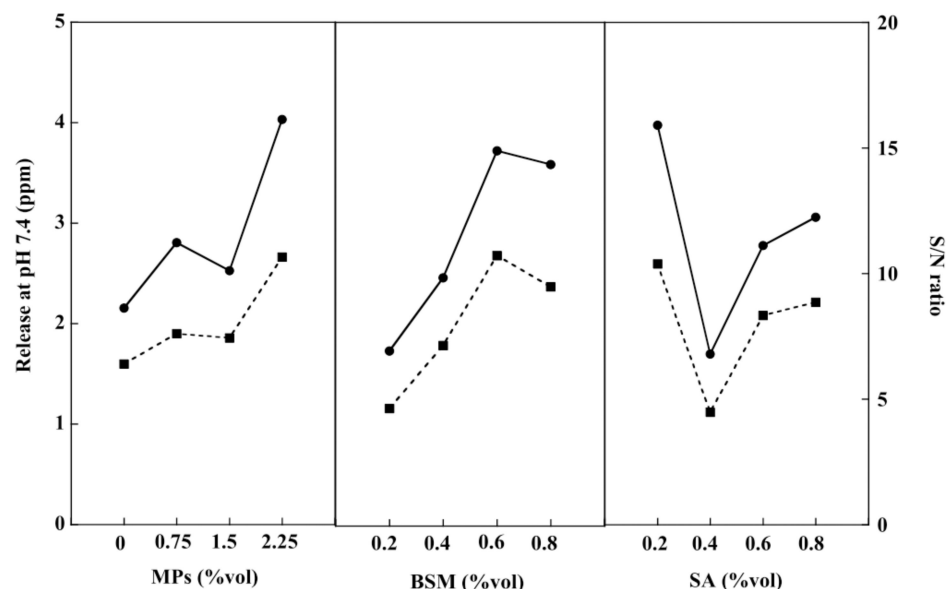
Figure 7. Drug release at pH 7.4 (–•–) and S/N ratio (–■–) of the BSM/SA/MPs hydrogel beads.

2.7. Release of Antioxidants from Hydrogel Beads

An antioxidant is an important chemical compound for humans because it helps the immune system work more efficiently. The human body eliminates waste products in the form of free radicals. These cause damage to the immune system, resulting in various diseases including heart disease, vascular disease, and cancer [47]. BSM contains nutrients such as vitamin E, an important substance that helps the body produce free antioxidants [48]. Consequently, the antioxidant activities of the BSM/SA/MPs hydrogel beads were studied at pH 1.2 and pH 7.4. Figure 8 shows that the release of antioxidants at pH 1.2 tended to increase with the increasing amount of all components in the hydrogel. BSM was the main contributor to the release of antioxidants at pH 1.2, accounting for 41.31%, followed by SA with a 27.26% contribution. According to the smaller-the-better criterion, the best composition providing the least antioxidant activity at pH 1.2 was at 0 %vol of MPs, 0.8 %vol of BSM, and 0.2 %vol of SA.
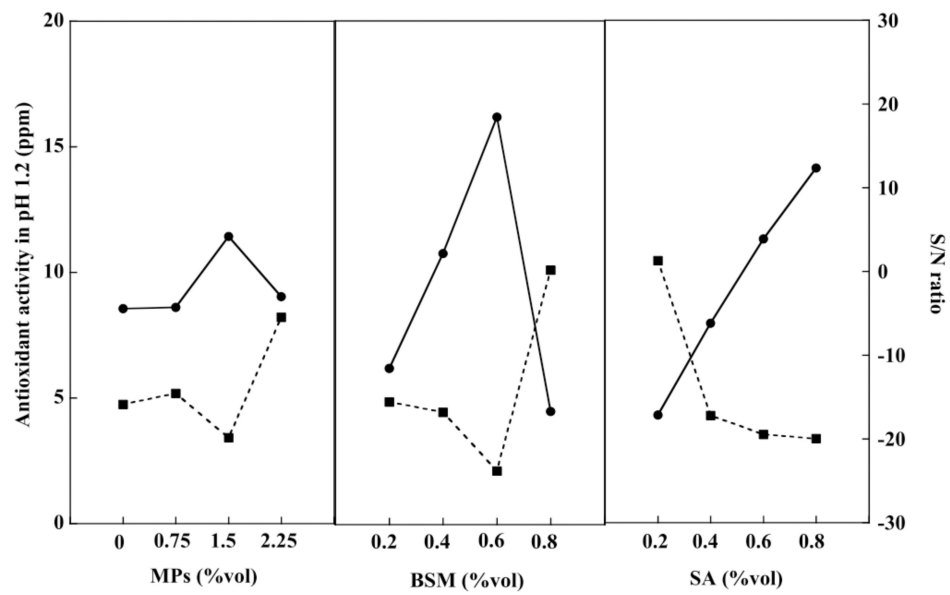
Figure 8. Release of antioxidant at pH 1.2 (–●–) and S/N ratio (–■–) of the BSM/SA/MPs hydrogel beads.

Figure 9 shows the antioxidant activity of the hydrogel beads at pH 7.4. The value tended to increase with an increasing amount of BSM, SA, and MPs. BSM was the major factor, contributing about 26.73% to the antioxidant activity, whereas SA and MPs contributed almost equally to the release of antioxidants. The relationship of antioxidant release was obtained by the regression method, as expressed in Equation (5):

$$\text{Values of antioxidant release} = -0.5X_1 + 0.3X_2 + 0.31X_3 + 1.33 \tag{5}$$

where X_1 is MPs (%vol), X_2 is BSM (%vol), and X_3 is SA (%vol).
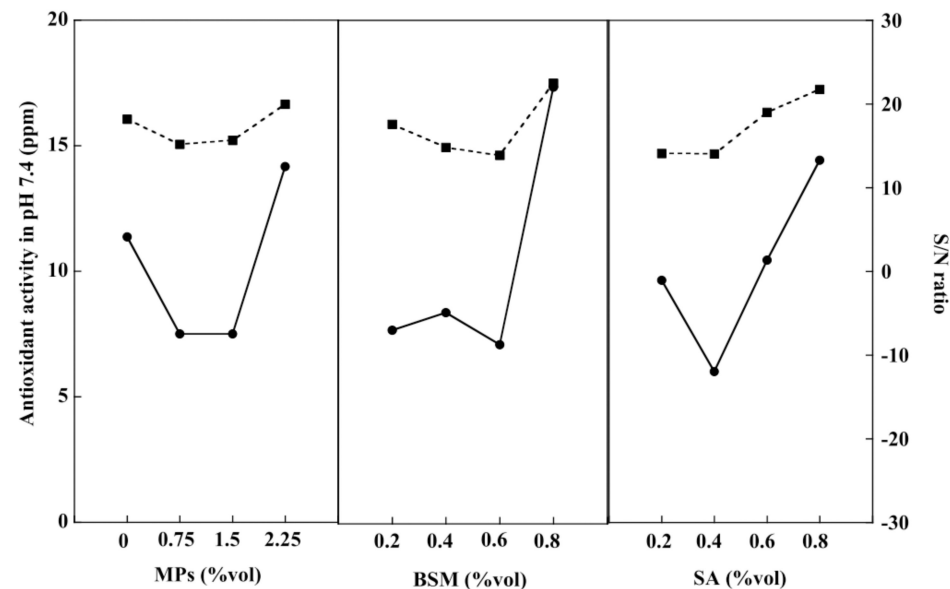
Figure 9. Release of antioxidant at pH 7.4 (–●–) and S/N ratio (–■–) of the BSM/SA/MPs hydrogel beads.

2.8. Optimization of the Hydrogel Bead Compositions Using Grey Relational Analysis

Grey relational analysis was used in conjunction with Taguchi's experimental method in this study. The optimal composition of the BSM/SA/MPs hydrogel beads with the best overall properties was determined as shown in Table S1. Grey relational coefficient calculation properties for the L-16 comparability sequence included drug release at pH 1.2 and 7.4, antioxidant release at pH 1.2 and 7.4, drug loading, and swelling of the hydrogel

beads. The highest concentration of Grey relational grade was 0.704, which contained 2.25 %vol MPs, 0.8 %vol BSM, and 0.2 %vol SA. The maximum value of the response results of the Grey relational analysis indicates the suitability of each factor affecting overall properties [49].

A confirmation test was conducted to determine the accuracy of the optimal combination. The predicted optimal properties of the BSM/SA/MPs hydrogel beads were calculated as shown in Equation (6):

$$\hat{\gamma} = \gamma_m + \sum_{i=1}^{q} (\gamma_i - \gamma_m) \tag{6}$$

where γ_m is the total mean of Grey relational grade, γ_i is the mean of the Grey relational grade at the optimal level, and q is a number matching the parameters that significantly affected multiple performance characteristics. As seen in Table 2, the experimental value agreed with the predicted value.

Table 2. Results of confirmation experiment.

	Predicted	**Experiment**
Grey relational grade	0.720	0.584

2.9. Effect of pH on Drug Release of the BSM/SA/MPs Hydrogel Beads

Regarding the most suitable composition, the BSM/SA/MPs hydrogel beads containing 2.25 %vol of MPs, 0.8 %vol of BSM, and 0.2 %vol of SA were selected to further study the kinetic release of drug from the hydrogel beads. The pH environment in the gastrointestinal tract varies from acidic to slightly alkaline. Therefore, the kinetic release study was carried out at pH 1.2 and again at pH 7.4. Figure 10 shows that the cumulative release amount of diclofenac from the BSM/SA/MPs hydrogel beads was significantly influenced by pH value. It was demonstrated that the drug release at pH 7.4 was higher than at pH 1.2. The drug release in an acidic medium slightly increased within 2 h and drastically increased when the hydrogel was transferred into a medium with pH 7.4. This can be explained by the minimum swelling of the hydrogel beads under acidic conditions. It was reported that the alginate polymer chain was catalytically hydrolyzed under acidic conditions to low molecular alginic acid [36]. It was additionally related to the shrinkage of the polymeric network due to the physical crosslinker generated from H-bonding among protonation of carboxylic group of the polymer under acidic conditions [19], and moreover because the carboxylate group (–COO–) of SA forms an attraction force with the drug, resulting in slower release of drug by the hydrogel beads [50–52]. A rapid drug release rate was observed at pH 7.4 because of the deprotonation of the carboxylate group of SA, resulting in an electrostatic repulsion force between the carboxylate group and the SA. Therefore, the drug was released rapidly. In the final stage, small molecules of alginic acid cannot retain the hydrate structure, and the hydrogel beads start to lose their overall structure. Consequently, the BSM/SA/MPs hydrogel beads showed changes in swelling properties in response to the pH of the medium, and can thus be used as a pH-responsive drug delivery system.

Mathematical modeling of drug release kinetics provides a basis for the study of mass transport mechanisms that are involved in the control of drug release. There are several comprehensive reviews on mathematical modeling for bioerodible polymeric delivery systems, dissolution-controlled drug delivery systems, microsphere delivery systems, and hydrogel networks. In general, diffusion, erosion, and degradation are the most important mechanisms for drug transport from polymeric matrices [53]. The release kinetics of diclofenac from the BSM/SA/MPs hydrogel beads into PBS at pH 7.4 were studied using four different release mathematical models, zero-order, hirst-order, Higuchi, and Korsmeyer–Peppas. For the kinetic study, the following relationships were plotted: %cumulative drug release vs. time (zero-order kinetic model); % log cumulative drug

remaining vs. time (first-order kinetic model); %cumulative drug release vs. square root of time (Higuchi model); % log cumulative drug release vs. log time (Korsmeyer–Peppas model). The zero-order behavior reflects the release of the drug at fixed rates at all investigated intervals and involves no effect on its concentration as a loaded drug. The first-order behavior involves a significant role of drug concentration during its release from the carriers. The Higuchi kinetic behavior demonstrates the diffusion of the drug as the release mechanism considering the reported assumptions of the model. The obtained kinetic curves and parameters are presented in Figure S1 and Table 3. The optimal fitting model was determined based on the highest correlation coefficient (R^2) obtained from regression analysis.
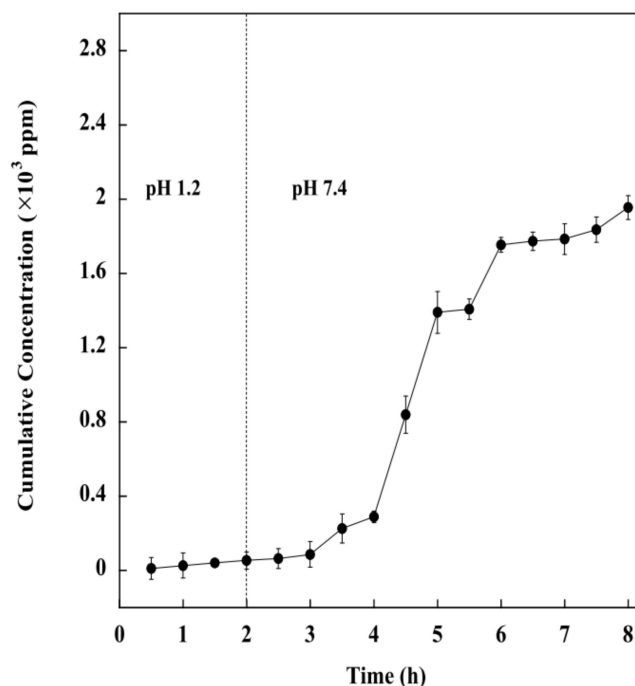
Figure 10. Release of drug from hydrogel at pH 1.2 and 7.4.

Table 3. The fitting data of model drug release obtained with different mathematical models.

Models	Parameters	PBS at pH 7.4
Zero order	k_0	387.400 ± 0.092
	R^2	0.957 ± 0.076
First order	k_1	1.106 ± 0.081
	R^2	0.783 ± 0.109
Higuchi	k_H	0.495 ± 0.095
	R^2	0.875 ± 0.103
Kormeyer-Peppas	k_{KP}	0.215 ± 0.087
	n	0.207 ± 0.098
	R^2	0.989 ± 0.097

It was found that Korsmeyer–Peppas was the model that best agreed with kinetic release of the model drug in PBS at PH 7.4, providing the highest R^2 value of 0.989 ± 0.097. From the Korsmeyer–Peppas model, the release value n for the hydrogel beads was lower than 0.5. The mathematical result indicated that the levels of diclofenac release rate from the hydrogel during the release time are probably related to drug diffusion near the hydrogel surfaces, and further revealed that the release of drug from the hydrogel took place through the quasi-Fickian diffusion mechanism, which is associated with a concentration gradient, diffusion distance, as well as with the degree of swelling.

3. Conclusions

This study developed BSM/SA/MPs hydrogel beads by optimizing their components. The experiment was designed using a Taguchi experimental design in combination with Grey relational analysis. The results indicated that BSM contributed most to the swelling behavior of the hydrogel beads, while drug loading was most affected by the addition of SA. The hydrogel beads were demonstrated to be pH sensitive to diclofenac release rate, with MPs being the principal components affecting the release rate in an acidic medium. In contrast, BSM and SA influenced the release rate in a neutral or mildly alkaline medium. The BSM/SA/MPs hydrogel beads exhibited antioxidant activity in media with different pH values, with BSM the major contributing factor. Using Grey relational analysis, the composition that provided the best properties in terms of swelling ratio, drug loading, release of diclofenac at pH 1.2 and 7.4 and antioxidant activity at pH 1.2 and 7.4 consisted of 2.25% MPs, 0.8% BSM, and 0.2% SA. It can be concluded that BSM/SA/MPs could be applied for pH sensitive intestine-specific drug delivery systems.

4. Materials and Methods

4.1. Materials

SA (91%–106%, LOBA CHEMIV PVT. Ltd., Mumbai, India), sodium hydroxide (99%, FW 40 RCI LabScan Limited, Bangkok, Thailand), Iron (III) chloride hexahydrate (97–102%, $FeCl_3 \cdot 6H_2O$; MW 270.32, KEMAUS, New South Wales, Australia), Iron (II) sulfate heptahydrate ($FeSO_4 \cdot 7H_2O$; 99.5–104.5%, MW 278.02, KEMAUS, New South Wales, Australia), Calcium chloride, hydrochloric acid (97%, Mw. 110.99, KEMAUS, New South Wales, Australia), dipotassium phosphate (K_2HPO_4; 99%, MW 174.18, KEMAUS, New South Wales, Australia), Potassium dihydrogen phosphate (KH_2PO_4; 99.5%, MW 136.09, RCI LabScan Limited, Bangkok, Thailand), 2,2-diphenyl-2-picryl-hydrazyl (DPPH) (MW. 394.32, Sigma-Aldrich, Singapore), and PVA with a DP of 1700–1800 were supplied by RCI Labscan Limited, Bangkok, Thailand. Diclofenac sodium was purchased from Lincoln Parenterals Pvt. Ltd, Gujarat, India.

4.2. Preparation of BSM

Basil seeds were soaked in deionized water (DI water) at a mass ratio of 1:50 for 2 h. The basil seeds were then spun with an overhead stirrer and heated to 70 °C for 12 h, using reflux equipment to prevent the water from evaporating. The BSM solution was centrifuged at 7000 rpm for 15 min, then BSM was filtered from the water. The BSM was poured into a petri dish and incubated at a temperature of 60 °C for 12 h to obtain dried BSM powder.

4.3. Preparation of MPs

$FeCl_3 \cdot 6H_2O$ was stirred into 125 mL DI water at 550 rpm at a temperature of 90 °C for 10 min. Then, 2.7 g of $FeSO_4 \cdot 7H_2O$ was added to the mixture and further stirred for 10 min. NaOH solution was prepared separately by dissolving 10 g of NaOH in 40 mL DI water. NaOH solution was added to $FeSO_4 \cdot 7H_2O$ solution. The dark precipitate was obtained and heated at a temperature of 90 °C for 1 h. After being cooled to room temperature, it was filtered, washed with DI water until pH 7.0–7.5 was reached, and dried at room temperature for 6 h.

4.4. Hydrogel Bead Preparation

Dried BSM was added to 40 mL of DI water and stirred for 2 h. The BMS/SA was prepared by adding SA solution to the basil seed mixture. The iron particles were added to obtain BSM/SA/MPs. The BSM/SA/MPs were added dropwise into the prepared $CaCl_2$ solution under continuous stirring. The resulting hydrogel beads were then rinsed several times and dried at a temperature of 40 °C for 6 h. The overall steps in hydrogel bead preparation are exhibited in Scheme S1.

The sol fraction of hydrogel beads was analyzed according to Nawaz et al. [54]. The sol part implied the unreacted portion of the formulation in the hydrogel. Based on previous reports, the sol fraction was reported to be 5–25% [51,54–57]. The sol fraction of the sixteen formulations of hydrogel beads was 7.07–49.55%, as shown in Supplemental Table S2.

4.5. Characterizations

The FTIR of hydrogel beads was carried out using a Bruker TENSOR27 (Billerica, United State), FTIR. The spectrum was analyzed at 4000–600 cm^{-1} with a resolution of 2 cm^{-1} for 64 scans.

The X-ray diffraction (XRD) of Fe_3O_4 was tested using an EMPYREAN X-ray diffractometer (Malvern, UK) provided with a Cu Kα radiation source operated at 45 kV and 40 mA. The sample was scanned at diffraction angles of $20° \leq 2θ \leq 80°$.

The structures of hydrogel beads were observed using scanning electron microscopy (SEM) (Hitachi SU-4800, Tokyo, Japan). The field emission scanning electron microscope was accelerated at a voltage of 3.0 kV and an emission current of 10 mA. The surfaces of the samples were sputter-coated with gold before measurement.

Kinetic drug release from the hydrogel beads was studied. The prepared hydrogel beads were loaded into a dialysis bag and suspended in 0.01 M of PBS at a temperature of 37 °C under magnetic stirring at 80 rpm. The release kinetics analysis was carried out in PBS at pH 1.2 for 2 h (as the average gastric empty time is about 2 h), and again at pH 7.4 for a predetermined time. The PBS solution was taken every 30 min for 3 h, and the same amount of fresh PBS was added to the system. The sample was then measured using a UV-Visible spectrophotometer (Agilent Cary 60, Santa Clara, CA, USA) at 222 nm.

The drug release mechanism from the hydrogel was studied by fitting the experimental result using four different release kinetic models, zero order, first order, Higuchi, and Korsmeyer–Peppas. Their equations are presented in Equations (7)–(10). These models were selected because they are widely used to explain drug release from polymers when several types of release mechanisms are involved. The model with the highest R^2 value was the most suitable model to describe the released kinetic of the hydrogel beads.

$$\text{Zero order model}: \ C = k_o \, t, \tag{7}$$

where C is the amount of diclofenac released at time t, k_0 is the zero-order rate constant, and t is the time.

$$\text{First} - \text{order model}: \ \ln C_t = \ln C_o - k_1 \, t \tag{8}$$

where C is the amount of diclofenac released at time t, k_1 is the zero-order rate constant, and t is the time.

$$\text{Higuchi model}: \ M = kt^{(1/2)} \tag{9}$$

where M is the diclofenac release amount at time t and k is the diffusion rate constant.

$$\text{Korsmeyer–Peppas model}: \ \frac{M_t}{M_\infty} = kt^n, \tag{10}$$

where M_t is the amount of diclofenac released at time t, M_∞ represents the amount of diclofenac released at equilibrium state, n is the release exponent, and k is the constant value of the drug–composite system.

The value of n is determined to identify the mechanism:

$n < 0.5$; quasi-Fickian diffusion

$n = 0.5$; normal Fickian diffusion

$n = 0.5–1.0$; non-Fickian or preposterous transport

$n = 1.0$; Case II diffusion.

The DPPH radical scavenging activity of nanocomposite film was studied using the method proposed by Brand Williams et al. [58]. The hydrogel beads were crushed and mixed with ethanol solution, and the sample was then ultrasonicated at 500 W at a

temperature of 37 °C for 30 min. The ethanol solution mixed with 0.4 mM methanolic DPPH was blended with the samples under a dark atmosphere and incubated for 30 min. The absorbance of the blend was assessed utilizing UV-spectrometer at a wavelength of 517 nm. The films' DPPH free radical scavenging activity was determined using Equation (11).

$$\text{DPPH free radical scavenging activity (\%)} = \frac{\text{Abs}_{\text{DPPH}} - \text{Abs}_{\text{Extract}}}{\text{Abs}_{\text{DPPH}}} \quad (11)$$

where Abs_{DPPH} is the absorbance at 517 nm of the DPPH solution and $\text{Abs}_{\text{Extract}}$ represents the absorbance of the extracted sample.

Swelling of the hydrogel beads was measured in DI water at pH levels of 1.2 and 7.4 for 24 h. The swelling (%) was calculated according to Equation (12)

$$\text{Swelling (\%)} = \frac{W_s - W_i}{W_i} \times 100 \quad (12)$$

where W_s and W_i represent the weight of the hydrogel beads after swelling and before swelling, respectively.

The percentage of drug loading on the hydrogel beads was determined based on Equation (13)

$$\text{Drug loading (\%)} = \frac{C_i - C_s}{C_i} \times 100 \quad (13)$$

where C_i represents the initial drug concentration and C_s is the concentration of free drug in the supernatant [59].

The Taguchi method, containing three factors and four levels, was used to optimize the conditions of the properties of hydrogel beads for drug delivery in terms of single response and multiple responses. The conditions and their variation levels are shown in Tables 4 and 5. The signal to noise ratio (S/N) was used to evaluate the effect of each parameter level for single response optimization with the help of ANOVA.

The S/N ratios were classified into three classes: (1) nominal-the-better, (2) smaller–the-better, and (3) larger-the-better, which were applied for optimization [60]. In this study, all responses, including drug release at pH 1.2 and release of antioxidants at pH 1.2, were minimized, corresponding to "smaller-the-better." Swelling (%), drug loading (%), drug release at pH 7.4, and release of antioxidants at pH 7.4 were maximized, corresponding to "larger-the-better", and the S/N ratio was analyzed based on Equations (14) and (15), respectively.

$$(\text{S/N}) = -10 \log \left[1/R \sum_{f=1}^{R} y_i^2 \right] \quad (14)$$

$$(\text{S/N}) = -10 \log \left[1/R \sum_{f=1}^{R} 1/y_i^2 \right] \quad (15)$$

where R is the number of all data points and y_i is the value of ith data point.

Grey relational analysis was used to convert multiple optimization responses into a single response optimization by calculating S/N ratios. The obtained results from the Taguchi method were then calculated to determine the highest overall Grey relational, which represents the optimal parametric combination. Prior to Grey relational analysis, data preprocessing is normally required to transfer the original sequence to a comparable sequence that is normalized within the range of zero to one [61]. The reference sequence and comparable sequence can be denoted by $x_o(k)$ and $x_i(k)$ for $i = 1, 2, \ldots , m; k = 1, 2, \ldots , n$, respectively, where m is the total number of experiments to be considered and n is the total number of observation data. The appropriate equation for this normalization depends on the type of the quality characteristic. In this work, smaller-the-better and

larger-the-better quality characteristics were applied to normalize all the responses, as expressed in Equations (16) and (17), respectively

$$x_i(k) = \frac{\max y_i(k) - y_i(k)}{\max y_i(k) - \min y_i(k)} \tag{16}$$

$$x_i(k) = \frac{y_i(k) - \min y_i(k)}{\max y_i(k) - \min y_i(k)} \tag{17}$$

where $x_i(k)$ is the value after Grey relational generation, $\min y_i(k)$ is the smallest value of $y_i(k)$ for kth response, and $y_i(k)$ max $y_i(k)$ is the largest value of $y_i(k)$ for kth response.

The Grey relational coefficient can be calculated using Equation (18)

$$\gamma(x_o^*(k), x_i^*(k)) = \frac{\Delta_{\min} + \zeta\Delta_{\max}}{\Delta_{0i}(k) + \zeta\Delta_{\max}} \tag{18}$$

$$0 < \gamma(x_o^*(k), x_i^*(k)) \leq 1$$

where

$$\Delta_{0i}(k) = |x_0^*(k) - x_i^*(k)|$$

$$\Delta_{\max} = \forall j \in i \overset{\max.}{\forall k} \overset{\max.}{\left|x_0^*(k) - x_j^*(k)\right|}$$

$$\Delta_{\min} = \forall j \in i \overset{\min.}{\forall k} \overset{\min.}{\left|x_0^*(k) - x_j^*(k)\right|}$$

x_0^* is the reference sequence, x_i^* is given sequence, x_j^* is comparison sequence and ζ is the distinguishing coefficient, $\zeta \in [0, 1]$.

If all process parameters have equal weighting, ζ is set to be 0.5. The Grey relational grade is the average of all Grey relational coefficients determined using Equation (19)

$$\gamma(x_o^*, x_i^*) = \frac{1}{n}\sum_{k=1}^{R} \beta_k \gamma(x_o^*(k), x_i^*(k)) \tag{19}$$

Finally, the optimal condition of the BSM/SA/MPs hydrogel beads is the level corresponding to the highest value of the average Grey relational grade of each factor. Tables 4 and 5 show the factors and their levels, including the Taguchi experimental design.

Table 4. Factors and their levels.

Parameter	Level 1	Level 2	Level 3	Level 4
BSM (%vol)	0.2	0.4	0.6	0.8
SA (%vol)	0.2	0.4	0.6	0.8
MP (%vol)	0.0	0.75	1.50	2.25

Table 5. Taguchi experimental design.

No.	Composition (%vol)		
	BSM	SA	MPs
1	0.2	0.2	0.0
2	0.4	0.4	0.0
3	0.6	0.6	0.0
4	0.8	0.8	0.0
5	0.4	0.2	0.75
6	0.2	0.4	0.75
7	0.8	0.6	0.75
8	0.6	0.8	0.75

Table 5. *Cont.*

No.	Composition (%vol)		
	BSM	SA	MPs
9	0.6	0.2	1.50
10	0.8	0.4	1.50
11	0.2	0.6	1.50
12	0.4	0.8	1.50
13	0.8	0.2	2.25
14	0.6	0.4	2.25
15	0.4	0.6	2.25
16	0.2	0.8	2.25

References

1. Yari, K.; Akbari, I.; Yazdi, S.A.V. Development and evaluation of sodium alginate-basil seeds mucilage beads as a suitable carrier for controlled release of metformin. *Int. J. Biol. Macromol.* **2020**, *159*, 1–10. [CrossRef]
2. Rayegan, A.; Allafchian, A.; Abdolhosseini Sarsari, I.; Kameli, P. Synthesis and characterization of basil seed mucilage coated Fe(3)O(4) magnetic nanoparticles as a drug carrier for the controlled delivery of cephalexin. *Int. J. Biol. Macromol.* **2018**, *113*, 317–328. [CrossRef]
3. Singh, A.K.; Nutan, B.; Raval, I.H.; Jewrajka, S.K. Self-assembly of partiall alkylated dextran-graft-poly[(2-dimethylamino)ethyl methacrylate] copolymer facilitating hydrophobic/hydrophilic drug delivery and improving conetwork hydrogel properties. *Biomacromoleculus* **2018**, *19*, 1142–1153. [CrossRef]
4. Nutan, B.; Chandel, A.K.; Bhanlani, D.V.; Jewrajka, S.K. Synthesis and tailoring the degradation of multi-responsive amphiphilic conetwork gels and hydrogels fo poly(β-amino ester) and poly(amido amine). *Polymer* **2017**, *111*, 265–274. [CrossRef]
5. Chandel, A.K.S.; Bera, A.; Nutan, B.; Jewrajka, S.K. Reactive compatibilizer mediated precise synthesis and application of stimuli responsive polysaccharides-pollycaprolactone amphiphilic co-network gels. *Polymer* **2016**, *99*, 470–479. [CrossRef]
6. Hosseini, M.S.; Nabid, M.R. Synthesis of chemically cross-linked hydrogel films based on basil seed (*Ocimum basilicum* L.) mucilage for wound dressing drug delivery applications. *Int. J. Biol. Macromol.* **2020**, *163*, 336–347. [CrossRef]
7. Khampieng, T.; Wongkittithavorn, S.; Chaiarwut, S.; Ekabutr, P.; Pavasant, P.; Supaphol, P. Silver nanoparticles-based hydrogel: Characterization of material parameters for pressure ulcer dressing applications. *J. Drug Deliv. Sci. Technol.* **2018**, *44*, 91–100. [CrossRef]
8. Choi, Y.H.; Kim, S.-H.; Kim, I.-S.; Kim, K.; Kwon, S.K.; Hwang, N.S. Gelatin-based micro-hydrogel carrying genetically engineered human endothelial cells for neovascularization. *Acta Biomater.* **2019**, *95*, 285–296. [CrossRef]
9. Javanbakht, V.; Shafiei, R. Preparation and performance of alginate/basil seed mucilage biocomposite for removal of eriochrome black T dye from aqueous solution. *Int. J. Biol. Macromol.* **2020**, *152*, 990–1001. [CrossRef]

10. Tosif, M.M.; Najda, A.; Bains, A.; Kaushik, R.; Dhull, S.B.; Chawla, P.; Walasek-Janusz, M. A Comprehensive Review on Plant-Derived Mucilage: Characterization, Functional Properties, Applications, and Its Utilization for Nanocarrier Fabrication. *Polymer* **2021**, *13*, 1066. [CrossRef]

11. Akbari, I.; Ghoreishi, S.M.; Habibi, N. Generation and precipitation of paclitaxel nanoparticles in basil seed mucilage via combination of supercritical gas antisolvent and phase inversion techniques. *J. Supercrit. Fluids* **2014**, *94*, 182–188. [CrossRef]

12. Maqsood, H.; Uroos, M.; Muazzam, R.; Naz, S.; Muhammad, N. Extraction of basil seed mucilage using ionic liquid and preparation of AuNps/mucilage nanocomposite for catalytic degradation of dye. *Int. J. Biol. Macromol.* **2020**, *164*, 1847–1857. [CrossRef]

13. Wang, H.; Gong, X.; Guo, X.; Liu, C.; Fan, Y.-Y.; Zhang, J.; Niu, B.; Li, W. Characterization, release, and antioxidant activity of curcumin-loaded sodium alginate/ZnO hydrogel beads. *Int. J. Biol. Macromol.* **2019**, *121*, 1118–1125. [CrossRef]

14. Hua, S.; Ma, H.; Li, X.; Yang, H.; Wang, A. pH-sensitive sodium alginate/poly(vinyl alcohol) hydrogel beads prepared by combined Ca2+ crosslinking and freeze-thawing cycles for controlled release of diclofenac sodium. *Int. J. Biol. Macromol.* **2010**, *46*, 517–523. [CrossRef]

15. Sharifianjazi, F.; Irani, M.; Esmaeilkhanian, A.; Bazli, L.; Asl, M.S.; Jang, H.W.; Kim, S.Y.; Ramakrishna, S.; Shokouhimehr, M.; Varma, R.S. Polymer incorporated magnetic nanoparticles: Applications for magnetoresponsive targeted drug delivery. *Mater. Sci. Eng. B* **2021**, *272*, 115358. [CrossRef]

16. Aisida, S.O.; Akpa, P.A.; Ahmad, I.; Zhao, T.; Maaza, M.; Ezema, F.I. Bio-inspired encapsulation and functionalization of iron oxide nanoparticles for biomedical applications. *Eur. Polym. J.* **2020**, *122*, 109371. [CrossRef]

17. Dacrory, S.; Moussa, M.; Turky, G.; Kamel, S. In situ synthesis of Fe3O4@ cyanoethyl cellulose composite as antimicrobial and semiconducting film. *Carbohydr. Polym.* **2020**, *236*, 116032. [CrossRef]

18. Supramaniam, J.; Adnan, R.; Mohd Kaus, N.H.; Bushra, R. Magnetic nanocellulose alginate hydrogel beads as potential drug delivery system. *Int. J. Biol. Macromol.* **2018**, *118*, 640–648. [CrossRef]

19. Mohammadi, R.; Saboury, A.; Javanbakht, S.; Foroutan, R.; Shaabani, A. Carboxymethylcellulose/polyacrylic acid/starch-modified Fe3O4 interpenetrating magnetic nanocomposite hydrogel beads as pH-sensitive carrier for oral anticancer drug delivery system. *Eur. Polym. J.* **2021**, *153*, 110500. [CrossRef]

20. Tavares Luiz, M.; Santos Rosa Viegas, J.; Palma Abriata, J.; Viegas, F.; Testa Moura de Carvalho Vicentini, F.; Lopes Badra Bentley, M.V.; Chorilli, M.; Maldonado Marchetti, J.; Tapia-Blácido, D.R. Design of experiments (DoE) to develop and to optimize nanoparticles as drug delivery systems. *Eur. J. Pharm. Biopharm.* **2021**, *165*, 127–148. [CrossRef]

21. Janaum, N.; Butsiri, T.; Kasemsiri, P.; Souvanh, M.; Pongsa, U.; Theerakulpisut, S.; Hiziroglu, S.; Okhawilai, M. Multi Response Optimization of Bioactive Starch Foam Composite Using Taguchi's Method and Grey Relational Analysis. *J. Polym. Environ.* **2020**, *28*, 1513–1525. [CrossRef]

22. Ounkaew, A.; Kasemsiri, P.; Pongsa, U.; Hiziroglu, S.; Pasuwan, P.; Boonlai, Y.; Theerakulpisut, S. Multiple Response Optimization of Poly(vinyl alcohol)/Starch Based Bioactive Composite Films for Antimicrobial Packaging Applications. *J. Polym. Environ.* **2022**, *30*, 1787–1802. [CrossRef]

23. Shafiee, S.; Ahangar, H.A.; Saffar, A. Taguchi method optimization for synthesis of Fe3O4 @chitosan/Tragacanth Gum nanocomposite as a drug delivery system. *Carbohydr. Polym.* **2019**, *222*, 114982. [CrossRef]

24. Tantiwatcharothai, S.; Prachayawarakorn, J. Characterization of an antibacterial wound dressing from basil seed (*Ocimum basilicum* L.) mucilage-ZnO nanocomposite. *Int. J. Biol. Macromol.* **2019**, *135*, 133–140. [CrossRef]

25. Glukhova, S.A.; Molchanov, V.S.; Chesnokov, Y.M.; Lokshin, B.V.; Kharitonova, E.P.; Philippova, O.E. Green nanocomposite gels based on binary network of sodium alginate and percolating halloysite clay nanotubes for 3D printing. *Carbohydr. Polym.* **2022**, *282*, 119106. [CrossRef]

26. Pooresmaeil, M.; Javanbakht, S.; Nia, S.B.; Namazi, H. Carboxymethyl cellulose/mesoporous magnetic graphene oxide as a safe and sustained ibuprofen delivery bio-system: Synthesis, characterization, and study of drug release kinetic. *Colloids Surf. A Physicochem. Eng. Asp.* **2020**, *594*, 124662. [CrossRef]

27. Amini-Fazl, M.S.; Mohammadi, R.; Kheiri, K. 5-Fluorouracil loaded chitosan/polyacrylic acid/Fe3O4 magnetic nanocomposite hydrogel as a potential anticancer drug delivery system. *Int. J. Biol. Macromol.* **2019**, *132*, 506–513. [CrossRef]

28. Kurd, F.; Fathi, M.; Shekarchizadeh, H. Basil seed mucilage as a new source for electrospinning: Production and physicochemical characterization. *Int. J. Biol. Macromol.* **2017**, *95*, 689–695. [CrossRef]

29. Ounkaew, A.; Janaum, N.; Kasemsiri, P.; Okhawilai, M.; Hiziroglu, S.; Chindaprasirt, P. Synergistic effect of starch/polyvinyl alcohol/citric acid films decorated with in-situ green-synthesized nano silver on bioactive packaging films. *J. Environ. Chem. Eng.* **2021**, *9*, 106793. [CrossRef]

30. Ray, S.; Banerjee, S.; Maiti, S.; Laha, B.; Barik, S.; Sa, B.; Bhattacharyya, U.K. Novel interpenetrating network microspheres of xanthan gum–poly(vinyl alcohol) for the delivery of diclofenac sodium to the intestine—In vitro and in vivo evaluation. *Drug Deliv.* **2010**, *17*, 508–519. [CrossRef]

31. Bi, L.; Chen, Z.; Li, L.; Kang, J.; Zhao, S.; Wang, B.; Yan, P.; Li, Y.; Zhang, X.; Shen, J. Selective adsorption and enhanced photodegradation of diclofenac in water by molecularly imprinted TiO2. *J. Hazard. Mater.* **2021**, *407*, 124759. [CrossRef]

32. Pan, X.; Cheng, S.; Su, T.; Zuo, G.; Zhao, W.; Qi, X.; Wei, W.; Dong, W. Fenton-like catalyst Fe3O4@polydopamine-MnO2 for enhancing removal of methylene blue in wastewater. *Colloids Surf. B Biointerfaces* **2019**, *181*, 226–233. [CrossRef]

33. Javanbakht, S.; Shadi, M.; Mohammadian, R.; Shaabani, A.; Ghorbani, M.; Rabiee, G.; Amini, M.M. Preparation of Fe₃O₄@SiO₂@Tannic acid double core-shell magnetic nanoparticles via the Ugi multicomponent reaction strategy as a pH-responsive co-delivery of doxorubicin and methotrexate. *Mater. Chem. Phys.* **2020**, *247*, 122857. [CrossRef]

34. Yang, L.; Tian, J.; Meng, J.; Zhao, R.; Li, C.; Ma, J.; Jin, T. Modification and Characterization of Fe₃O₄ Nanoparticles for Use in Adsorption of Alkaloids. *Molecules* **2018**, *23*, 562. [CrossRef]

35. Tantiwatcharothai, S.; Prachayawarakorn, J. Property improvement of antibacterial wound dressing from basil seed (*O. basilicum* L.) mucilage- ZnO nanocomposite by borax crosslinking. *Carbohydr. Polym.* **2020**, *227*, 115360. [CrossRef]

36. Reddy, S.G.; Pandit, A.S. Biodegradable sodium alginate and lignosulphonic acid blends: Characterization and swelling studies. *Polimeros* **2013**, *23*, 13–18. [CrossRef]

37. Mahdavinia, G.R.; Rahmani, Z.; Karami, S.; Pourjavadi, A. Magnetic/pH-sensitive κ-carrageenan/sodium alginate hydrogel nanocomposite beads: Preparation, swelling behavior, and drug delivery. *J. Biomater. Sci. Polym. Ed.* **2014**, *25*, 1891–1906. [CrossRef]

38. Chen, S.-C.; Wu, Y.-C.; Mi, F.-L.; Lin, Y.-H.; Yu, L.-C.; Sung, H.-W. A novel pH-sensitive hydrogel composed of N,O-carboxymethyl chitosan and alginate cross-linked by genipin for protein drug delivery. *J. Control. Release* **2004**, *96*, 285–300. [CrossRef]

39. Ecke, A.; Westphalen, T.; Hornung, J.; Voetz, M.; Schneider, R.J. A rapid magnetic bead-based immunoassay for sensitive determination of diclofenac. *Anal. Bioanal. Chem.* **2022**, *414*, 1563–1573. [CrossRef]

40. Cong, Z.; Shi, Y.; Wang, Y.; Wang, Y.; Niu, J.; Chen, N.; Xue, H. A novel controlled drug delivery system based on alginate hydrogel/chitosan micelle composites. *Int. J. Biol. Macromol.* **2018**, *107*, 855–864. [CrossRef]

41. Huang, X.; Xiao, Y.; Lang, M. Micelles/sodium-alginate composite gel beads: A new matrix for oral drug delivery of indomethacin. *Carbohydr. Polym.* **2012**, *87*, 790–798. [CrossRef]

42. Yin, Z.-C.; Wang, Y.-L.; Wang, K. A pH-responsive composite hydrogel beads based on agar and alginate for oral drug delivery. *J. Drug Deliv. Sci. Technol.* **2018**, *43*, 12–18. [CrossRef]

43. Xie, C.-X.; Tian, T.-C.; Yu, S.-T.; Li, L. pH-sensitive hydrogel based on carboxymethyl chitosan/sodium alginate and its application for drug delivery. *J. Appl. Polym. Sci.* **2019**, *136*, 46911. [CrossRef]

44. Naderi, Z.; Azizian, J.; Moniri, E.; Farhadyar, N. Synthesis and Characterization of Carboxymethyl Cellulose/β-Cyclodextrin/Chitosan Hydrogels and Investigating the Effect of Magnetic Nanoparticles (Fe₃O₄) on a Novel Carrier for a Controlled Release of Methotrexate as Drug Delivery. *J. Inorg. Organomet. Polym. Mater.* **2020**, *30*, 1339–1351. [CrossRef]

45. Omer, A.M.; Ahmed, M.S.; El-Subruiti, G.M.; Khalifa, R.E.; Eltaweil, A.S. pH-Sensitive Alginate/Carboxymethyl Chitosan/Aminated Chitosan Microcapsules for Efficient Encapsulation and Delivery of Diclofenac Sodium. *Pharmer* **2021**, *13*, 338. [CrossRef]

46. Guo, T.; Pei, Y.; Tang, K.; He, X.; Huang, J.; Wang, F. Mechanical and drug release properties of alginate beads reinforced with cellulose. *J. Appl. Polym. Sci.* **2017**, *134*. [CrossRef]

47. Tungmunnithum, D.; Thongboonyou, A.; Pholboon, A.; Yangsabai, A. Flavonoids and Other Phenolic Compounds from Medicinal Plants for Pharmaceutical and Medical Aspects: An Overview. *Medicines* **2018**, *5*, 93. [CrossRef]

48. Calderón Bravo, H.; Vera Céspedes, N.; Zura-Bravo, L.; Muñoz, L.A. Basil Seeds as a Novel Food, Source of Nutrients and Functional Ingredients with Beneficial Properties: A Review. *Foods* **2021**, *10*, 1467. [CrossRef]

49. Pandya, V.J.; Rathod, P.P. Optimization of Mechanical Properties of Green Composites by Gray Relational Analysis. *Mater. Today Proc.* **2020**, *27*, 19–22. [CrossRef]

50. Tan, L.S.; Tan, H.L.; Deekonda, K.; Wong, Y.Y.; Muniyandy, S.; Hashim, K.; Pushpamalar, J. Fabrication of radiation cross-linked diclofenac sodium loaded carboxymethyl sago pulp/chitosan hydrogel for enteric and sustained drug delivery. *Carbohydr. Polym. Technol. Appl.* **2021**, *2*, 100084. [CrossRef]

51. Suhail, M.; Khan, A.; Rosenholm, J.M.; Minhas, M.U.; Wu, P.C. Fabrication and characterization of diclofenac sodium loaded hydrogels of sodium alginate as sustained release carrier. *Gels* **2021**, *7*, 10. [CrossRef]

52. Li, Y.; Wang, C.; Luan, Y.; Liu, W.; Chen, T.; Liu, P.; Liu, Z. Preparation of pH-responsive cellulose nanofibril/sodium alginate based hydrogels for drug release. *J. Appl. Polym. Sci.* **2022**, *139*, 51647. [CrossRef]

53. Sadri, M.; Mohammadi, A.; Hosseini, H. Drug release rate and kinetic investigation of composite polymeric nanofibers. *Nanomed. Res. J.* **2016**, *1*, 112–121.

54. Nawaz, S.; Khan, S.; Farooq, U.; Haider, M.S.; Ranjha, N.M.; Rasul, A.; Nawaz, A.; Arshad, N.; Hameed, R. Biocompatible hydrogels for the controlled delivery of anti-hypertensive agent: Development, characterization and in vitro evaluation. *Des. Monomers Polym.* **2018**, *21*, 18–32. [CrossRef]

55. Suhail, M.; Vu, Q.L.; Wu, P.-C. Formulation, Characterization, and In Vitro Drug Release Study of β-Cyclodextrin-Based Smart Hydrogels. *Gels* **2022**, *8*, 207. [CrossRef]

56. Anwar, H.; Ahmad, M.; Minhas, M.U.; Rehmani, S. Alginate-polyvinyl alcohol based interpenetrating polymer network for prolonged drug therapy, Optimization and in-vitro characterization. *Carbohydr. Polym.* **2017**, *166*, 183–194. [CrossRef]

57. Khan, M.A.; Azad, A.K.; Safdar, M.; Nawaz, A.; Akhlaq, M.; Paul, P.; Hossain, M.K.; Rahman, M.H.; Baty, R.S.; El-kott, A.F.; et al. Synthesis and Characterization of Acrylamide/Acrylic Acid Co-Polymers and Glutaraldehyde Crosslinked pH-Sensitive Hydrogels. *Gels* **2022**, *8*, 47. [CrossRef]

58. Brand-Williams, W.; Cuvelier, M.E.; Berset, C. Use of a free radical method to evaluate antioxidant activity. *LWT-Food Sci. Technol.* **1995**, *28*, 25–30. [CrossRef]

59. Dharmalingam, K.; Anandalakshmi, R. Fabrication, characterization and drug loading efficiency of citric acid crosslinked NaCMC-HPMC hydrogel films for wound healing drug delivery applications. *Int. J. Biol. Macromol.* **2019**, *134*, 815–829. [CrossRef]

60. Kasemsiri, P.; Dulsang, N.; Pongsa, U.; Hiziroglu, S.; Chindaprasirt, P. Optimization of Biodegradable Foam Composites from Cassava Starch, Oil Palm Fiber, Chitosan and Palm Oil Using Taguchi Method and Grey Relational Analysis. *J. Polym. Environ.* **2017**, *25*, 378–390. [CrossRef]

61. Arifeen, W.U.; Kim, M.; Choi, J.; Yoo, K.; Kurniawan, R.; Ko, T.J. Optimization of porosity and tensile strength of electrospun polyacrylonitrile nanofibrous membranes. *Mater. Chem. Phys.* **2019**, *229*, 310–318. [CrossRef]

Development of Growth Factor Releasing Hyaluronic Acid-Based Hydrogel for Pulp Regeneration: A Preliminary Study

Mi Sun Kim [1] , Yu-Shik Hwang [2] , Hyo-Seol Lee [3] , Ok Hyung Nam [3] and Sung Chul Choi [3,*]

1   Department of Pediatric Dentistry, Kyung Hee University College of Dentistry, Kyung Hee University Hospital at Gangdong, 892 Dongnam-ro, Gangdong-gu, Seoul 05278, Republic of Korea
2   Department of Maxillofacial Biomedical Engineering, Kyung Hee University College of Dentistry, 26 Kyungheedae-ro, Dongdaemoon-gu, Seoul 02447, Republic of Korea
3   Department of Pediatric Dentistry, Kyung Hee University College of Dentistry, Kyung Hee University Medical Center, 26 Kyungheedae-ro, Dongdaemoon-gu, Seoul 02447, Republic of Korea
*   Correspondence: pedochoi@khu.ac.kr; Tel.: +82-2-958-9371

Abstract: Growth factors play essential roles as signaling molecules in pulp regeneration. We investigated the effect of a hyaluronic acid (HA)-collagen hybrid hydrogel with controlled release of fibroblast growth factor (FGF)-2 and platelet-derived growth factor (PDGF)-BB on human pulp regeneration. The cell interaction and cytotoxicity of the HA-collagen hybrid hydrogel, the release kinetics of each growth factor, and the effects of the released growth factors on pulp cell proliferation were examined. The vitality of pulp cells was maintained. The amounts of FGF-2 and PDGF-BB released over 7 days were 68% and 50%, respectively. Groups with a different concentration of growth factor (FGF-2: 100, 200, 500, and 1000 ng/mL; PDGF-BB: 10, 50, 100, 200, and 500 ng/mL) were experimented on days 1, 3, 5, and 7. Considering FGF-2 concentration, significantly increased pulp cell proliferation was observed on days 1, 3, 5, and 7 in the 100 ng/mL group and on days 3, 5, and 7 in the 200 ng/mL group. In the case of PDGF-BB concentration, significantly increased pulp cell proliferation was observed at all four time points in the 100 ng/mL group and on days 3, 5, and 7 in the 50, 200, and 500 ng/mL groups. This indicates that the optimal concentration of FGF-2 and PDGF-BB for pulp cell proliferation was 100 ng/mL and that the HA-collagen hybrid hydrogel has potential as a controlled release delivery system for FGF-2 and PDGF-BB.
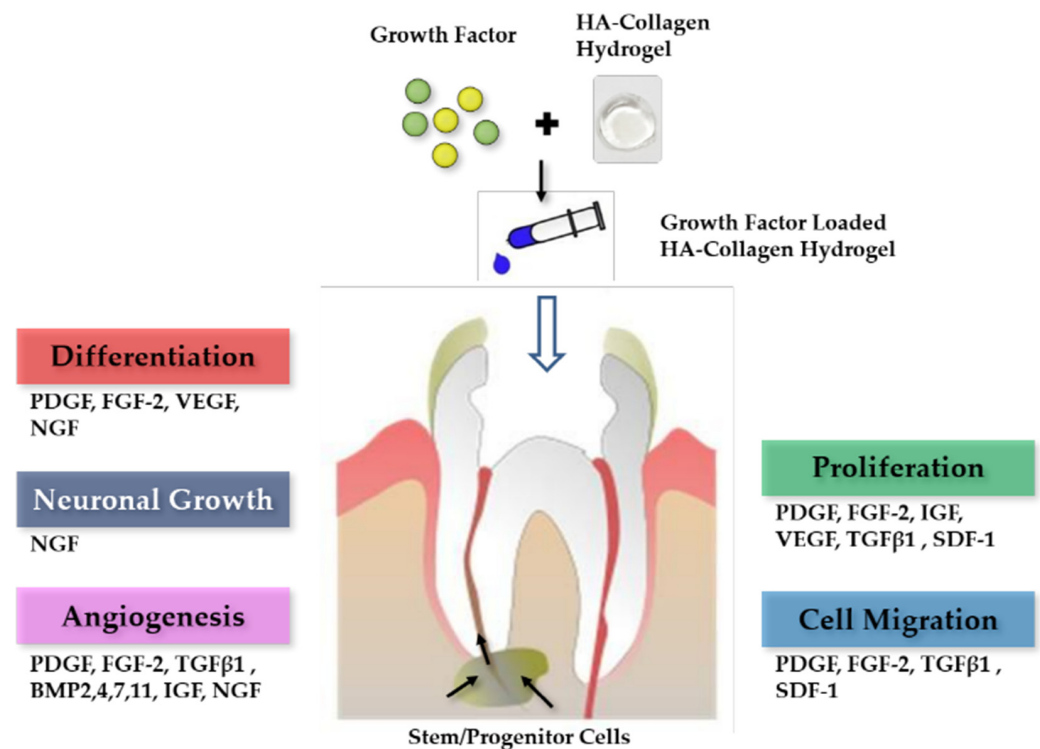
Keywords: fibroblast growth factor-2; growth factor; hyaluronic acid-collagen hybrid hydrogel; platelet-derived growth factor-BB; pulp regeneration

1. Introduction

The traditional root canal therapy technique involves devitalization of a tooth, which predisposes it to reinfection and fracture. Recently, regenerative endodontics has gained much attention as a promising biologically based alternative treatment. The ultimate goal of pulp regeneration is to reconstitute the vitality and function of the dental pulp due to trauma or infection [1]. For ingrowth of new regenerated tissues, advances in tissue engineering research have focused on three key elements for regeneration: stem cells, which have the ability to proliferate and differentiate; scaffold, which is a three-dimensional structure that supports the integrity of the tissue; and growth factors, which are signals governing morphogenesis and differentiation [2,3].

Growth factors are secreted polypeptides or proteins that control various cellular responses, such as cell migration, proliferation, differentiation, angiogenesis, neural growth, and apoptosis [1] (Figure 1). Growth factors act as signaling molecules in cellular activities by binding to receptors present on the cell membranes of target cells [4]. After injury to

dental pulp tissue, various growth factors participate in tissue repair. Therefore, growth factors are being increasingly considered to induce pulp regeneration.


Figure 1. Signaling molecules for pulp regeneration. PDGF, platelet-derived growth factor; FGF, fibroblast growth factor; VEGF, vascular endothelial growth factor; NGF, nerve growth factor; TGF, transforming growth factor; BMP, bone morphogenetic protein; IGF, insulin-like growth factor; SDF, stromal cell-derived factor [1].

Fibroblast growth factor (FGF)-2 is a multifunctional heparin-binding protein that stimulates and modulates cell growth, differentiation and migration [5]. Among the 22 FGF types identified in humans, FGF-2 was recently demonstrated to stimulate the regenerative potential of the dentin-pulp complex, increase proliferation and migration and regulate the cytodifferentiation of odontoblasts [6,7] (Table 1). Platelet-derived growth factor (PDGF) exerts a growth-promoting activity in human platelet α-granules and is a 30-kDa dimeric molecule with disulfide bonded A- and B-polypeptide chains [8,9]. PDGF has homodimeric (PDGF-AA, PDGF-BB, PDGF-CC, and PDGF-DD) and heterodimeric (PDGF-AB) isoforms [10]. It is a potent chemotactic, mitogenic, and activating agent for cells that are essential in soft tissue repair [11–13]. PDGF also stimulates the proliferation of fibroblasts in human dental pulp and angiogenesis at the site of dental pulp injury [14,15] (Table 1). Hence, although several growth factors appear to be involved in pulp regeneration, two key growth factors (FGF and PDGF) were investigated in this study.

Table 1. Primary effects of FGF-2 and PDGF-BB for pulp regeneration.

| Growth Factors	Target Cells	Primary Effects
PDGF	dental pulp cells	cell proliferation [14,16,17]
		dentin matrix synthesis [14,16,17]
		odontogenic differentiation
		dentinogenesis [18]
FGF-2	dental pulp stem cells	chemotaxis [19]
		cell proliferation [20]
	dental pulp cells	cell proliferation [21–23]
		dentinogenesis [21–23]

A suitable delivery system is essential for sustained release of the growth factors with progression of dentine dissolution in caries lesions or from the injured pulp cells. Because growth factors could be denatured easily in aqueous solutions at 37 °C, their biological activity should be preserved for effective application over extended periods [16]. Therefore, bioactive molecule delivery systems have been extensively investigated. To date, numerous synthetic and naturally derived polymers have been used as depots and delivery vehicles for protein growth factors [24]. Among them, hydrogels are one of the most extensively studied and frequently used forms of naturally derived biomaterials in tissue engineering [25]. The development of scaffolds from biomaterials, such as hyaluronic acid (HA) and collagen with improved mechanical stability against degradation and with better biochemical function can help deliver growth factors to promote regeneration [26] (Figure 2). The physiological activities of HA and collagen have a virtue in various applications in tissue engineering [27].
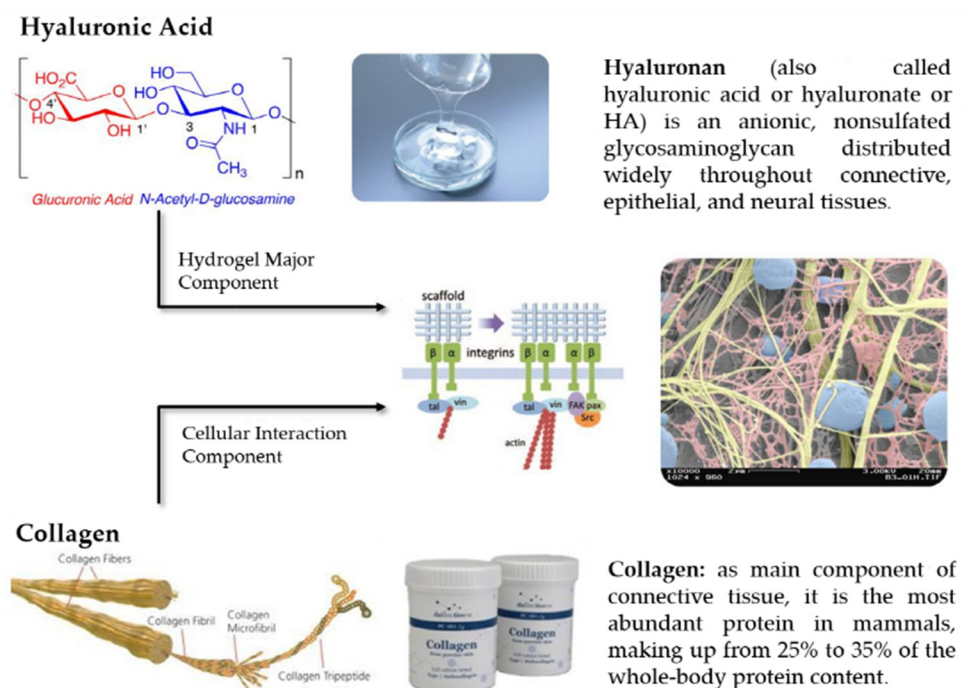
Figure 2. Hyaluronic acid and collagen are two of the most extensively studied and frequently used forms of naturally derived biomaterials in tissue engineering.

Based on these findings, FGF-2 and PDGF-BB loaded HA-collagen hybrid hydrogels were developed as a sustained release delivery system to maintain the biological activity of growth factors. The hypothesis of this study was that the effective proliferation of the human pulp cells can be achieved by using growth factor loaded HA-collagen hybrid hydrogels. To test this hypothesis, we investigated the effect of these HA-collagen hybrid hydrogels with controlled release of FGF-2 and PDGF-BB on human pulp cells (Figure 3).
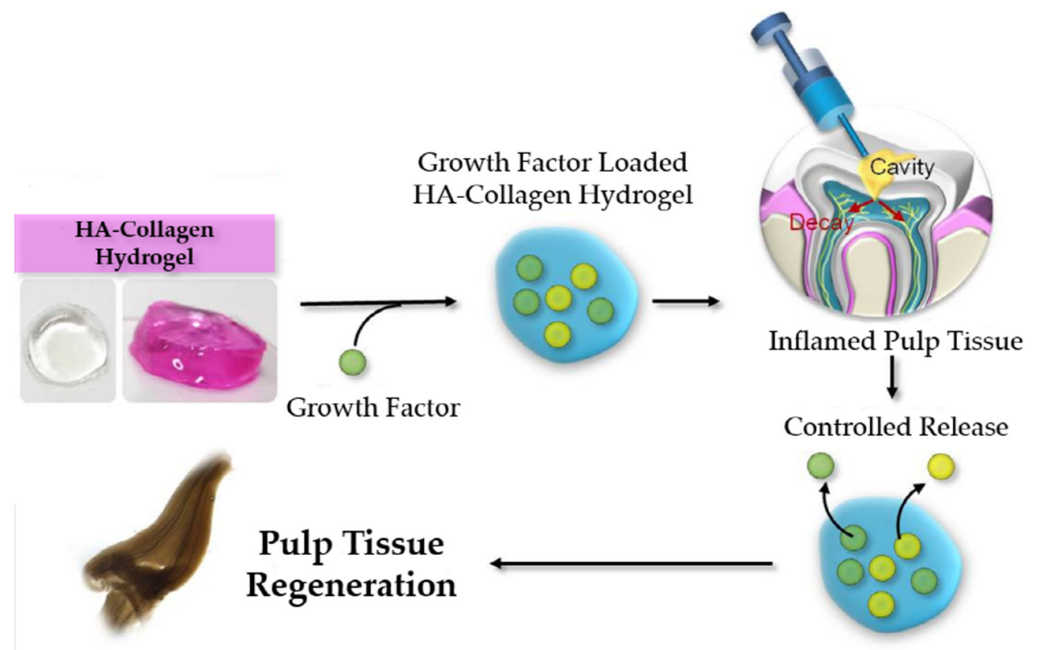
Figure 3. A schematic description of the use of growth factors released from HA-collagen hydrogel for pulp tissue regeneration.

2. Results and Discussion

2.1. Characterization of the HA + Collagen Hybrid Hydrogel

The mechanical integrity of the HA-collagen hydrogel was higher than that of the HA hydrogel alone (Figure 4). Infrared spectrometry was performed to determine the chemical modifications to the HA during the crosslinking reaction (Figure 5). The presence of amide bonds, which are the result of adipic dihydrazide (ADH) and oxidized HA reactions, was observed.
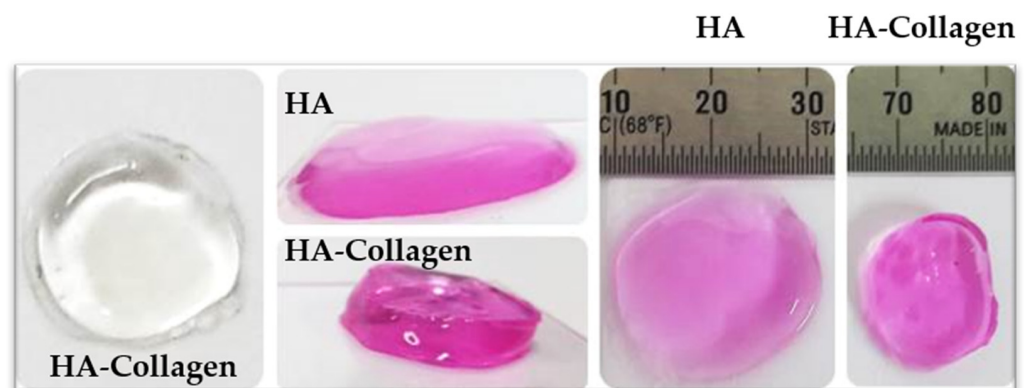
Figure 4. Optical images of HA-collagen hybrid gel and HA hydrogel. The mechanical integrity of HA-collagen hydrogel was increased compared with HA hydrogel. HA, hyaluronic acid.
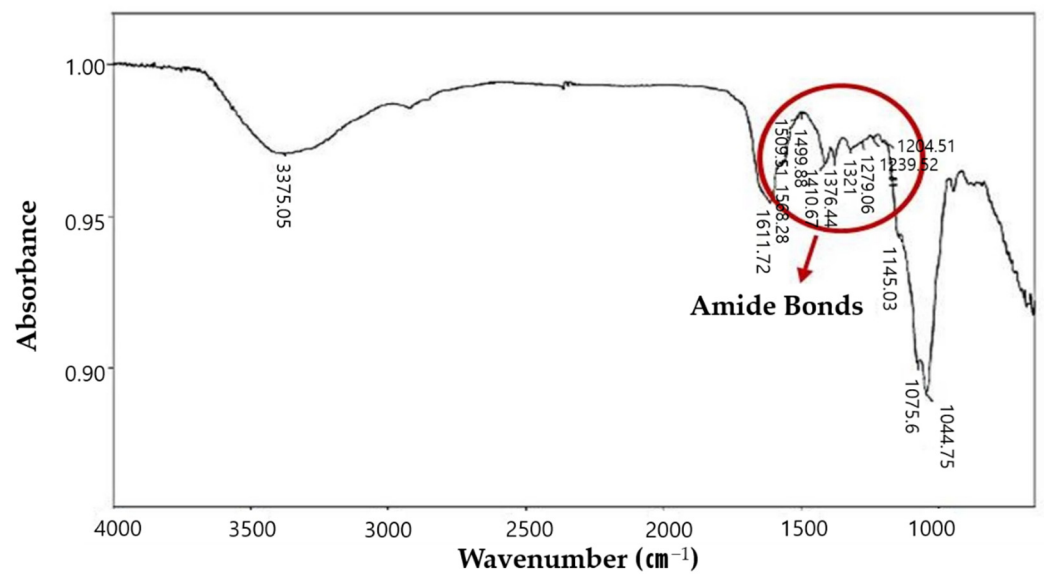
Figure 5. Fourier transform infrared spectroscopy. Spectrum of HA-collagen hydrogel. Infrared spectrometry showed the presence of amide bonds which are the reaction outcome of adipic dihydrazide (ADH) and oxidized HA. HA, hyaluronic acid.

2.2. Release Kinetics

The release kinetics of growth factors were quantified using an enzyme-linked immunosorbent assay (ELISA). The amount of FGF-2 released over 7 days was 68% (Figure 6). The amount of PDGF-BB released over 7 days was 50% (Figure 7). Sustained release of both FGF-2 and PDGF-BB was observed for 7 days, but significant release was observed during the first 24 h.
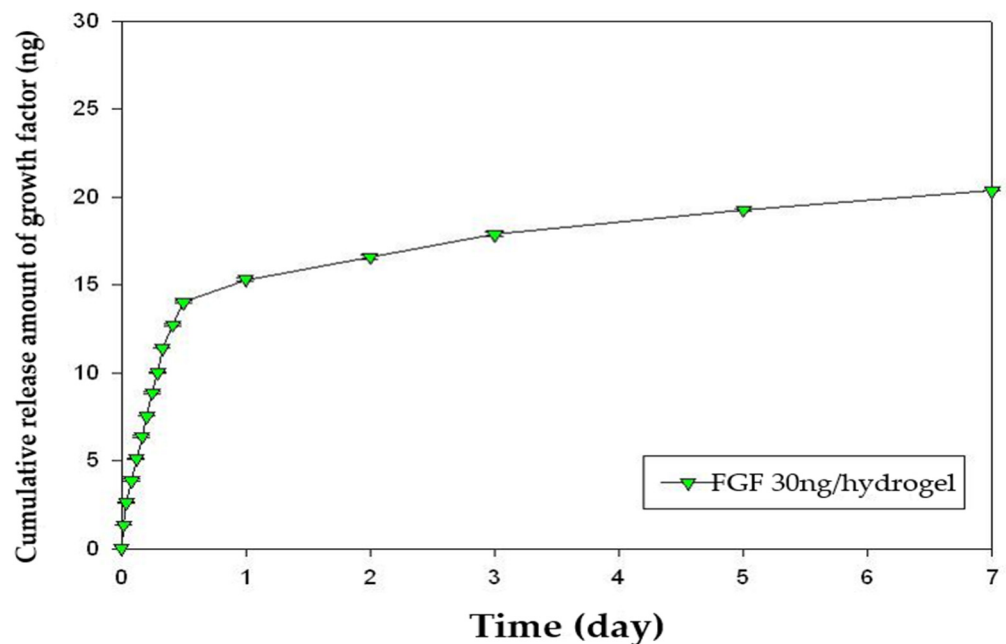
Figure 6. Cumulative release profile of FGF-2 over 7 days. The release kinetics of growth factors was quantified by an enzyme-linked immunosorbent assay (ELISA). FGF-2 was released sustainably for 7 days but significantly during the first 24 h. The released amount of FGF-2 for 7 days was 68%. FGF, fibroblast growth factor.
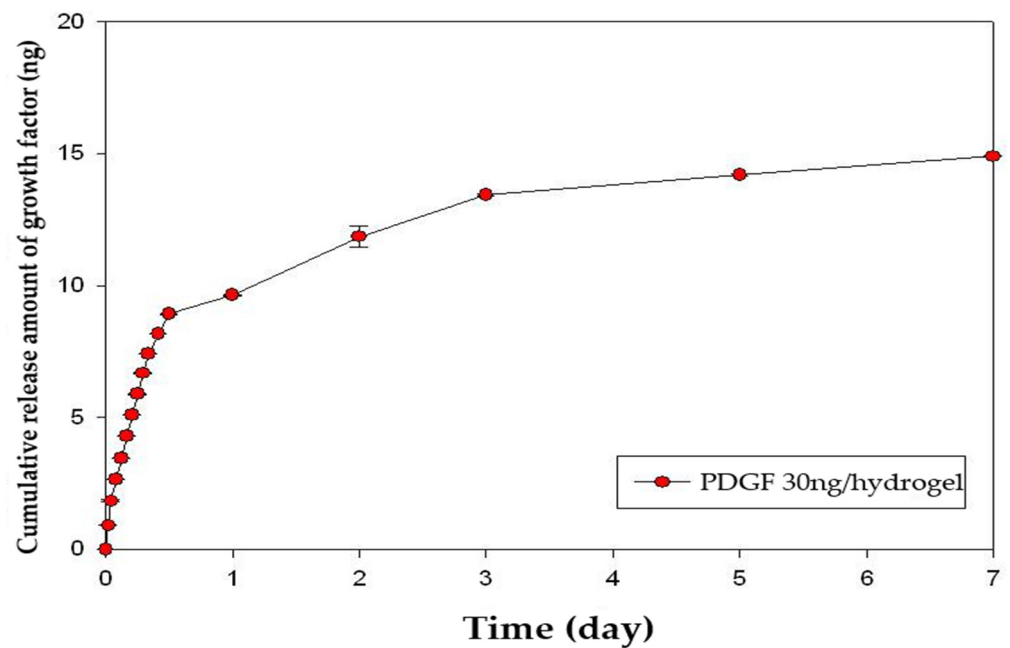
Figure 7. Cumulative release profile of PDGF-BB over 7 days. The release kinetics of growth factors was quantified by an enzyme-linked immunosorbent assay (ELISA). PDGF-BB was released sustainably for 7 days but significantly during the first 24 h. The released amount of PDGF-BB for 7 days was 50%. PDGF, platelet-derived growth factor.

2.3. Cellular Interaction and Cytotoxicity Test

The live and dead analysis, (Figure 8) revealed that dental pulp cells adhered well to the HA-collagen hydrogel, proliferated progressively, and maintained cell viability. Moreover, HA-collagen hydrogels did not exert significant cytotoxicity (Figure 9).
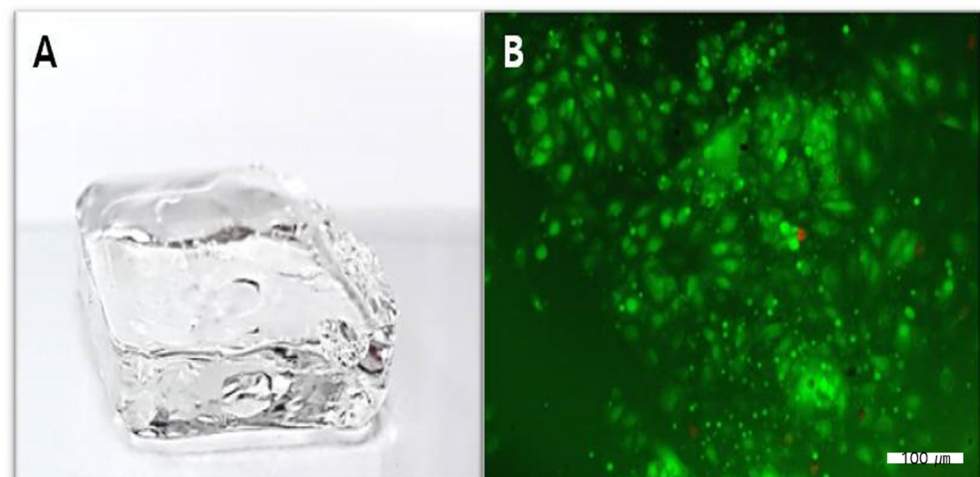

Figure 8. (**A**) Pulp cells in HA-collagen hydrogel (**B**) Live and dead analysis image shows that dental pulp cells adhered well to the HA-collagen hydrogel, proliferated progressively, and maintained cell viability with green fluorescence. HA, hyaluronic acid.
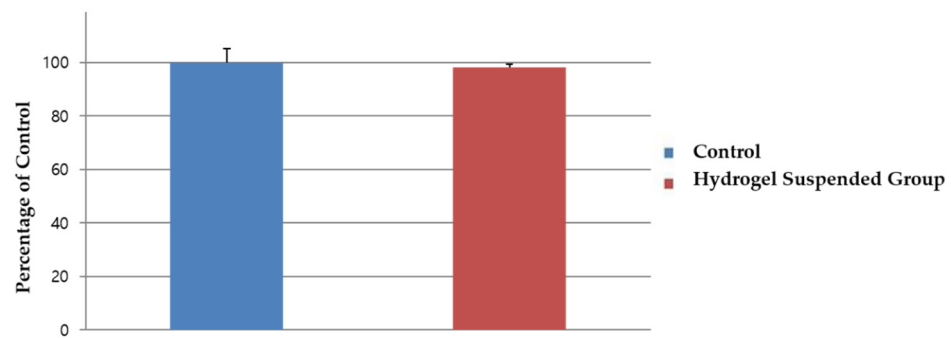
Figure 9. Findings of the cell viability test performed using a cell counting kit (CCK)-8 kit. The cell viability was not affected by the presence of the hydrogel.

2.4. Effect of Growth Factors on Cell Proliferation

Different concentrations of growth factor (FGF-2: 100, 200, 500, and 1000 ng/mL; PDGF-BB: 10, 50, 100, 200, and 500 ng/mL) and increased incubation time (1, 3, 5, and 7 days) were applied to investigate the effect of growth factors on dental pulp cell proliferation. Considering FGF-2, 100, 200 and 1000 ng/mL concentrations showed significantly increased pulp cell proliferation rates in the 3-, 5-, and 7-day groups ($p < 0.05$), and 100 ng/mL concentration showed significantly increased pulp cell proliferation rates in all four groups ($p < 0.05$) (Figure 10). Moreover, in the case of PDGF-BB, 50, 100 and 500 ng/mL concentrations showed significantly increased pulp cell proliferation rates in the 3-, 5-, and 7-day groups ($p < 0.05$), and 100 ng/mL concentration showed significantly increased pulp cell proliferation rates in all four groups ($p < 0.05$) (Figure 11). The proliferation rate of both growth factors increased as the incubation time increased.
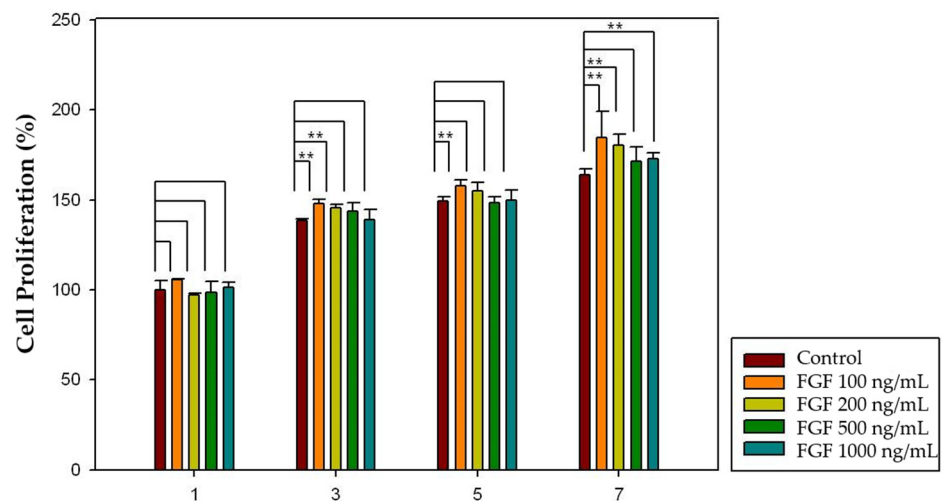
Figure 10. The effect of FGF-2 on pulp cell proliferation. The 100, 200 and 1000 ng/mL concentrations showed significantly increased pulp cell proliferation rates in the 3-, 5-, and 7-day groups ($p < 0.05$). The 100 ng/mL concentration showed significantly increased pulp cell proliferation rates in all four groups ($p < 0.05$). The results are expressed as mean values $\pm$ standard deviation. ** indicates the statistically significant differences ($p < 0.05$). FGF, fibroblast growth factor.
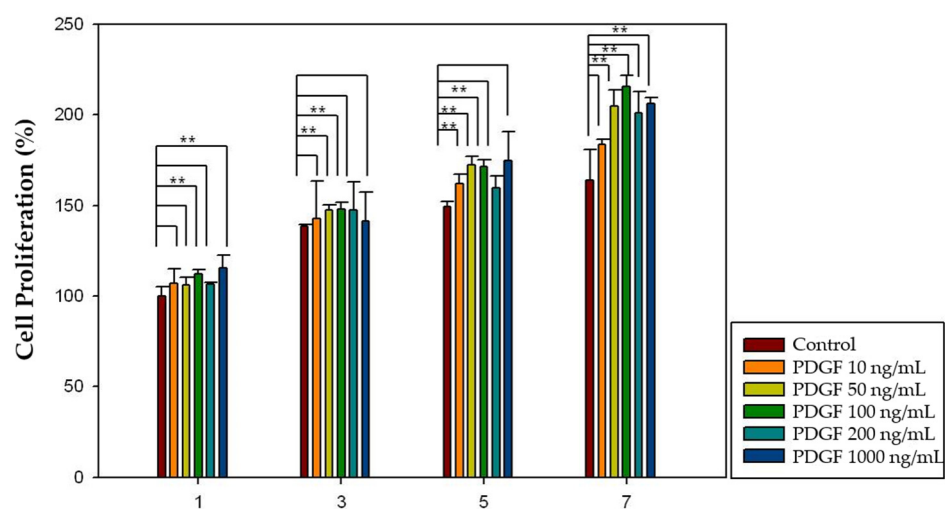
Figure 11. The effect of PDGF-BB on pulp cell proliferation. The 50, 100, and 500 ng/mL concentrations showed significantly increased pulp cell proliferation rates in the 3-, 5-, and 7-day groups ($p < 0.05$). The 100 ng/mL concentration showed significantly increased pulp cell proliferation rates in all four groups ($p < 0.05$). The results are expressed as mean values $\pm$ standard deviation. ** indicates the statistically significant differences ($p < 0.05$). PDGF, platelet-derived growth factor.
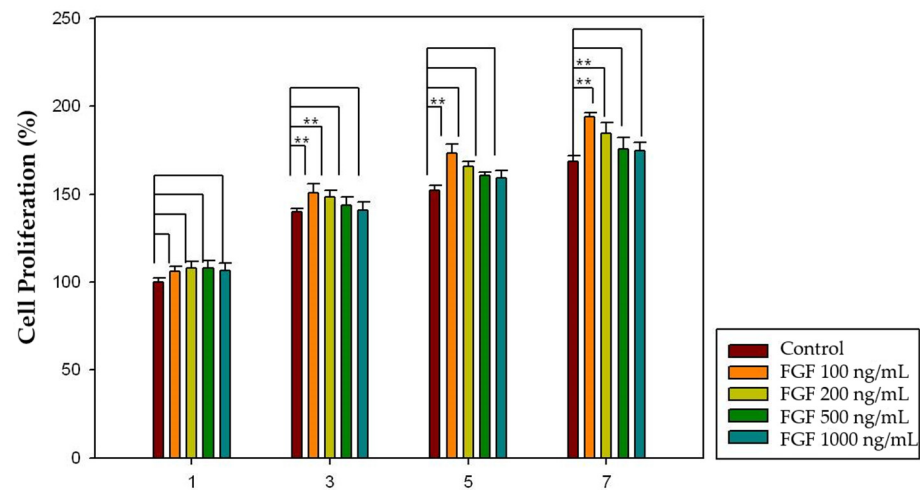
2.5. Effect of Growth Factors Released from HA-Collagen Hydrogel on Cell Proliferation

To determine the effect of growth factors released from the HA-collagen hydrogel on dental pulp cell proliferation, different concentrations of growth factor (FGF-2: 100, 200, 500, and 1000 ng/mL; PDGF-BB: 10, 50, 100, 200, and 500 ng/mL) and increased incubation time (1, 3, 5, and 7 days) were applied. In the case of FGF-2, 100 and 200 ng/mL concentrations showed significantly increased pulp cell proliferation rates in the 3-, 5-, and 7-day groups ($p < 0.05$), and 100 ng/mL concentration showed significantly increased pulp cell proliferation rates in all four groups ($p < 0.05$) (Figure 12). Moreover, in the case of PDGF-BB, 50, 100, 200 and 500 ng/mL concentrations showed significantly increased pulp cell proliferation rates in the 3-, 5-, and 7-day groups ($p < 0.05$) and 100 ng/mL concentration showed significantly increased pulp cell proliferation rates in all four groups ($p < 0.05$) (Figure 13). The proliferation rates of both growth factors increased as incubation time increased.

2.6. Discussion

To date, studies on dental pulp regeneration have been carried out by the typical tissue engineering approaches of delivering cells in biomaterial scaffolds with tooth slices or fragments for in vivo implantation [3,28,29]. Recently, an in vitro level cell-homing approach has been used to regenerate the pulp cells by the delivering growth factors [30]. Several growth factors, including FGF-2, vascular endothelial growth factor, nerve growth factor, PDGF, and bone morphogenetic protein-7, have been applied singularly or in combination into the root canal spaces. Dental pulp-like tissues can be regenerated with new blood vessels, indicating that these tissues can be regenerated without cell implantation [30]. This approach to dental pulp regeneration by applying multiple growth factors may accelerate the clinical translation of these findings.

Numerous growth factor delivery systems for the cell-homing approach have been investigated over the past decade. New approaches have been developed based on the molecular and cellular signaling pathways that regulate the regeneration process and their potential for clinical application [31]. In particular, hydrogels have numerous applications in tissue engineering and drug delivery. Hydrogels are structurally similar to the molecular components in the body and are considered biocompatible [32]. Moreover, hydrogels can be injected into the target sites. This approach enables clinicians to use hydrogels in a minimally invasive manner.

Figure 12. The effect of FGF-2 released from HA-collagen hydrogel on pulp cell proliferation. The 100 and 200 ng/mL concentrations showed significantly increased pulp cell proliferation rates in the 3-, 5-, and 7-day groups ($p < 0.05$). The 100 ng/mL concentration showed significantly increased pulp cell proliferation rates in all four groups ($p < 0.05$). The results are expressed as mean values $\pm$ standard deviation. ** indicates the statistically significant differences ($p < 0.05$). FGF, fibroblast growth factor.
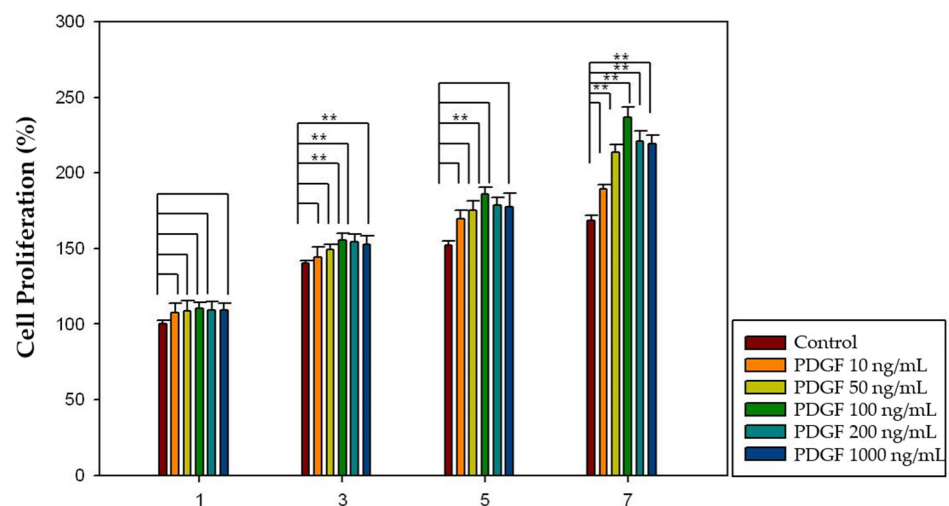
Figure 13. The effect of PDGF-BB released from HA-collagen hydrogel on pulp cell proliferation. The 50, 100, 200 and 500 ng/mL concentrations showed significantly increased pulp cell proliferation rates in the 3-, 5-, and 7-day groups ($p < 0.05$). The 100 ng/mL concentration showed significantly increased pulp cell proliferation rates in all four groups ($p < 0.05$). The results are expressed as mean values $\pm$ standard deviation. ** indicates the statistically significant differences ($p < 0.05$). PDGF, platelet-derived growth factor.

In tissue engineering, hydrogels have a number of design criteria to function appropriately and promote new tissue formation [33]. HA is a glycosaminoglycan component of natural extracellular matrices and is known to play a significant role in wound healing. However, HA hydrogels typically have poor mechanical properties and low stability against enzymatic degradation, which makes HA more suitable as an additive to another polymer such as collagen [34]. Therefore, HA-collagen hybrid hydrogels were prepared in this study. To investigate the cytotoxicity of the HA-collagen hybrid hydrogel with dental pulp cells, CCK-8 and live and dead assays were performed to ensure that they were not toxic. Our results showed that HA-collagen hydrogels can be used as a nontoxic delivery system for growth factors.

The release kinetics of FGF-2 and PDGF-BB showed that the HA-collagen hybrid hydrogel could be used as a controlled-release delivery system for FGF-2 and PDGF-BB in the early steps of pulp regeneration. We observed sustained release for 7 days, and the biological effects of FGF-2 and PDGF-BB on pulp cell proliferation were maintained. Furthermore, there was a significant release during the first 24 h, which may be attributed to a burst effect [35]. The release rate of FGF-2 was greater than that of PDGF-BB. This difference in the release rates can be caused by the different molecular nature and affinity of these growth factors to the polymer, such as molecular weight, hydrophobicity and electro charge differences.

A cell proliferation assay using the CCK-8 kit was performed to investigate the effect of growth factors on pulp cell proliferation. The proliferation of dental pulp cells increased as the incubation time increased. Moreover, there was an optimal concentration of each growth factor that affected the proliferation of dental pulp cells. In the case of FGF-2, 100, 200, and 1000 ng/mL concentrations showed significantly increased pulp cell proliferation rates in the 3-, 5-, and 7-day groups ($p < 0.05$) and 100 ng/mL concentration showed significantly increased pulp cell proliferation rates in all four groups ($p < 0.05$) (Figure 12). Moreover, in the case of PDGF-BB, 50, 100, and 500 ng/mL concentrations showed significantly increased pulp cell proliferation rate in the 3-, 5-, and 7-day groups ($p < 0.05$) and 100 ng/mL concentration showed significantly increased pulp cell proliferation rates in all four groups ($p < 0.05$) (Figure 13).

Finally, a cell proliferation assay using the CCK-8 kit was performed to investigate the effect of the growth factors released from the HA-collagen hydrogel on pulp cell proliferation. The proliferation of dental pulp cells increased as the incubation time increased. Moreover, there was an optimal concentration of each growth factor that affected the proliferation of dental pulp cells. The results seem to be quite close to those of the growth factor only groups. In the case of FGF-2, 100 and 200 ng/mL concentrations showed significantly increased pulp cell proliferation rates in the 3-, 5-, and 7-day groups ($p < 0.05$) and 100 ng/mL concentration showed significantly increased pulp cell proliferation rates in all four groups ($p < 0.05$) (Figure 14). Moreover, in the case of PDGF-BB, 50, 100, 200 and 500 ng/mL concentrations showed a significantly increased pulp cell proliferation rate in the 3-, 5-, and 7-day groups ($p < 0.05$) and 100 ng/mL concentration showed significantly increased pulp cell proliferation rates in all four groups ($p < 0.05$) (Figure 15). The proliferation rates of both growth factors increased as the incubation time increased.
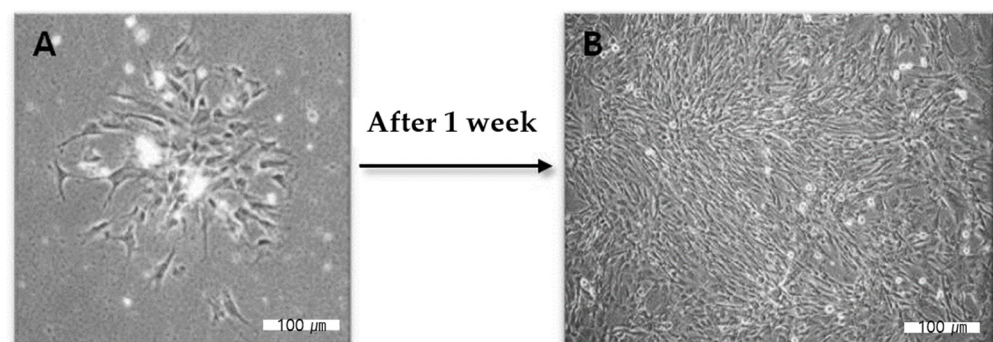
Figure 14. (**A**,**B**) Proliferation of human dental pulp cells over a week. Figures were taken from an optical microscope.

Because the price of growth factors is relatively high, it is important to determine the optimal concentration of growth factors to develop a clinically applicable delivery system for regenerative endodontics. A low concentration of growth factors showed less effect due to the inadequate amount, whereas a high concentration suppressed the proliferation because the excess of the growth factor might not participate in growth factor-receptor signaling responses. Although the optimal concentration of growth factors has been found

within the limits of this study, further evaluation of the subsequent effects on the pulp regeneration processes is needed. The limitation that hydrogel itself could act as a barrier or even an obstacle to pulp regeneration should also be considered. In this regard, it is important to investigate and use the optimal amounts of hydrogel to avoid these side effects. Moreover, many different kinds of hydrogels with various mechanical characteristics can be developed. Therefore, it is important to develop the most suitable hydrogel with the proper mechanical characteristics in need.
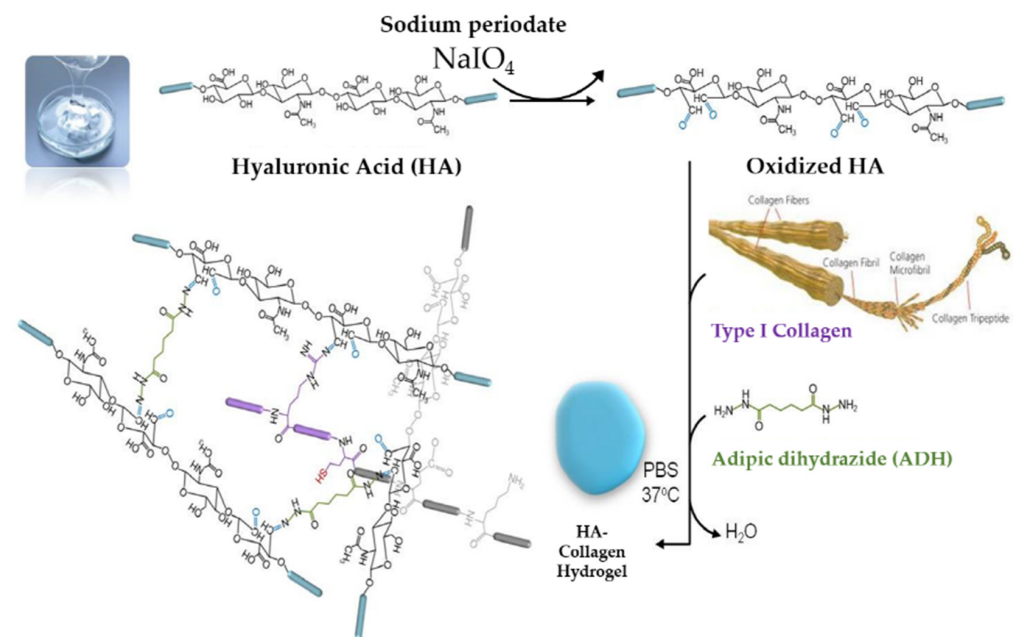
Figure 15. The synthetic scheme of hyaluronic acid (HA)-collagen hybrid hydrogel preparation. Oxidized HA was first formed by reacting sodium periodate and HA. Because adipic dihydrazide (ADH) works as a cross-linking agent, the hybrid-hydrogel was cured and hardened by mixing oxidized HA, collagen and ADH. Finally, the hydrogel with HA and collagen backbone at 37 °C was developed. Blue rod indicates the polymer of HA; purple rod indicates the polymer of collagen; grey rod indicates the polymer of ADH.

3. Conclusions

Although the findings of previous studies on pulp regeneration are very favorable, biologically and clinically complete pulp regeneration has not yet been achieved. The present study demonstrated that the HA-collagen hybrid hydrogel can be used as a controlled-release delivery system for FGF-2 and PDGF-BB. Moreover, within the limits of this study, the optimal concentration of both FGF-2 and PDGF-BB for the proliferation of dental pulp cells was found to be 100 ng/mL. Further research should focus on other ranges of cellular activities in pulp regeneration that growth factors can affect, including migration, differentiation, and apoptosis of all dental pulp cells and other growth factors involved in pulp regeneration.

4. Materials and Methods

4.1. Human Pulp Cells Preparation

Human dental pulp cells were purchased from Lonza Inc. (Walkersville, MD, USA) and cultured in 100-mm-diameter culture dishes (SPL Life Sciences, Seoul, Republic of Korea) containing alpha minimum essential medium (Gibco BRL, Eggenstein, Germany) supplemented with 10% fetal bovine serum (Gibco BRL Eggenstein, Germany), 1% penicillin-streptomycin (Gibco BRL Eggenstein, Germany), 100 μM ascorbic acid (Sigma aldrich, St. Louis, MO, USA), and 200 mM L-glutamine (Gibco BRL Eggenstein, Germany) in a humidified atmosphere containing 5% CO_2 at 37 °C. Confluent cultures were collected

by trypsinization and subcultured in 100-mm-diameter culture dishes (SPL Life Sciences, Seoul, Republic of Korea) (Figure 14).

4.2. HA + Collagen Hybrid-Hydrogel Preparation and Characterization

To develop HA and collagen hybrid-hydrogel with optimal mechanical properties, a pilot study on the proportion of HA to collagen was performed and the adequate ratio of HA to collagen was 4:1. Oxidized HA was first formed by the reaction of sodium periodate and HA. Because adipic dyhydrazide (ADH) works as a cross-linking agent, the hybrid-hydrogel was cured and hardened by mixing oxidized HA, collagen and ADH. Finally, a hydrogel with HA and a collagen backbone at 37 °C was developed (Figure 15). The developed hybrid-hydrogel was characterized using Fourier transform infrared spectroscopy (FT-IR).

4.3. Release Kinetics Study

To control the release of growth factors, the kinetics of HA-collagen hydrogels containing growth factors (30 ng/hydrogel) were dispersed into test tubes containing 3 mL Dulbecco's phosphate-buffered saline (DPBS) solution (Gibco BRL, Eggenstein, Germany). The suspension was gently stirred at room temperature in a release chamber. DPBS solutions in the tubes were collected 16 times at specific time points for 7 days and analyzed for growth factor secretion through an enzyme-linked immunosorbent assay (ELISA) in accordance with the manufacturer's instruction (Peprotech, Rocky Hill, NJ, USA). The experiments were conducted at least three times by one skilled operator.

4.4. Cellular Interaction and Cytotoxicity Test

To evaluate the cellular interaction of the HA-collagen hybrid hydrogel, a live and dead assay was performed. To check the toxicity of the hydrogel, a cell counting kit-8 (CCK-8; Dojindo Lab., Kumamoto, Japan) was used. Dental pulp cells were plated at 5000 cells/well in 96-well plates (SPL Life Sciences, Seoul, Republic of Korea). The 96-well dishes were then placed in a humidified incubator containing 5% CO_2 at 37 °C for 24 h before use. After 24 h, the medium from each well was removed and replaced with 100 μL of test or control medium. The hydrogel was suspended in 1 mL alpha-MEM culture medium without bovine serum for 24 h. The same medium without contact with the hydrogel was used as the control. The 96-well dishes were placed in a humidified incubator containing 5% CO_2 at 37 °C for 48 h. The CCK-8 solution was diluted to 1/10 with alpha-MEM without bovine serum. The medium was removed and replaced with 100 μL/well diluted CCK-8 solution. The 96-well dishes were placed in a humidified incubator containing 5% CO_2 at 37 °C for 2 h. The absorbance of each 96-well dish was determined using an automatic microplate spectrophotometer (Bio-Rad, Hercules, CA, USA) at 450 nm (OD 450). The experiments were conducted at least three times by one skilled operator.

4.5. Effect of Growth Factors on Cell Proliferation

Different concentrations of growth factors were suspended in alpha-MEM without bovine serum. (FGF-2: 100, 200, 500, and 1000 ng/mL; PDGF-BB: 10, 50, 100, 200, and 500 ng/mL). For the proliferation assay, the CCK-8 kit was used as described previously on days 1, 3, 5, and 7. Control groups without growth factors were used (100% viability). The results were normalized and expressed as a percentage of the optical density values of the control groups. The experiments were conducted at least three times by one skilled operator.

4.6. Effect of Growth Factors Released from HA-Collagen Hydrogel on Cell Proliferation

Different concentrations of growth factors loaded in the HA-collagen hybrid hydrogel (FGF-2: 100, 200, 500, and 1000 ng/mL; PDGF-BB: 10, 50, 100, 200, and 500 ng/mL) were placed in cell culture inserts (SPL Life Sciences), and the released growth factors were

diffused into alpha-MEM culture medium without bovine serum. For the proliferation assay, the CCK-8 kit was used as described previously on days 1, 3, 5, and 7. Unloaded hydrogels were used as the controls (100% viability). The results were normalized and expressed as a percentage of the optical density values of the control group. The experiments were conducted at least three times by one skilled operator.

4.7. Statistical Analysis

Statistical differences between the experimental groups were determined using the Student's *t* test. The threshold for statistical significance was set at $p < 0.05$.

References

1. Kim, S.G.; Zhou, J.; Solomon, C.; Zheng, Y.; Suzuki, T.; Chen, M.; Song, S.; Jiang, N.; Cho, S.; Mao, J.J. Effects of growth factors on dental stem/progenitor cells. *Dent. Clin. N. Am.* **2012**, *56*, 563–575. [CrossRef] [PubMed]
2. Tabata, Y. Tissue regeneration based on tissue engineering technology. *Congenit. Anom.* **2004**, *44*, 111–124. [CrossRef] [PubMed]
3. Murray, P.E.; Garcia-Godoy, F.; Hargreaves, K.M. Regenerative endodontics: A review of current status and a call for action. *J. Endod.* **2007**, *33*, 377–390. [CrossRef] [PubMed]
4. Lind, M. Growth factors: Possible new clinical tools: A review. *Acta. Orthop. Scand.* **1996**, *67*, 407–417. [CrossRef]
5. Nugent, M.A.; Iozzo, R.V. Fibroblast growth factor-2. *Int. J. Biochem. Cell Biol.* **2000**, *32*, 115–120. [CrossRef]
6. Shimabukuro, Y.; Ichikawa, T.; Takayama, S.; Yamada, S.; Takedachi, M.; Terakura, M.; Hashikawa, T.; Murakami, S. Fibroblast growth factor-2 regulates the synthesis of hyaluronan by human periodontal ligament cells. *J. Cell. Physiol.* **2005**, *203*, 557–563. [CrossRef]
7. Shimabukuro, Y.; Ueda, M.; Ozasa, M.; Anzai, J.; Takedachi, M.; Yanagita, M.; Ito, M.; Hashikawa, T.; Yamada, S.; Murakami, S. Fibroblast growth factor–2 regulates the cell function of human dental pulp cells. *J. Endod.* **2009**, *35*, 1529–1535. [CrossRef]
8. Rutherford, R.B.; TrailSmith, M.D.; Ryan, M.E.; Charette, M.F. Synergistic effects of dexamethasone on platelet-derived growth factor mitogenesis in vitro. *Arch. Oral. Biol.* **1992**, *37*, 139–145. [CrossRef]
9. Nakashima, M. Bone morphogenetic proteins in dentin regeneration for potential use in endodontic therapy. *Cytokine Growth Factor Rev.* **2005**, *16*, 369–376. [CrossRef]
10. Denholm, I.A.; Moule, A.J.; Bartold, P.M. The behaviour and proliferation of human dental pulp cell strains in vitro, and their response to the application of platelet-derived growth factor-BB and insulin-like growth factor-1. *Int. Endod. J.* **1998**, *31*, 251–258. [CrossRef]
11. Yokose, S.; Kadokura, H.; Tajima, N.; Hasegawa, A.; Sakagami, H.; Fujieda, K.; Katayama, T. Platelet-derived growth factor exerts disparate effects on odontoblast differentiation depending on the dimers in rat dental pulp cells. *Cell Tissue Res.* **2004**, *315*, 375–384. [CrossRef] [PubMed]
12. Suzuki, T.; Lee, C.H.; Chen, M.; Zhao, W.; Fu, S.Y.; Qi, J.J.; Chotkowski, G.; Eisig, S.B.; Wong, A.; Mao, J.J. Induced migration of dental pulp stem cells for in vivo pulp regeneration. *J. Dent. Res.* **2011**, *90*, 1013–1018. [CrossRef] [PubMed]
13. He, H.; Yu, J.; Liu, Y.; Lu, S.; Liu, H.; Shi, J.; Jin, Y. Effects of FGF2 and TGF-β1 on the differentiation of human dental pulp stem cells in vitro. *Cell Biol. Int.* **2008**, *32*, 827–834. [CrossRef] [PubMed]
14. Kitamura, C.; Nishihara, T.; Terashita, M.; Tabata, Y.; Washio, A. Local regeneration of dentin-pulp complex using controlled release of FGF-2 and naturally derived sponge-like scaffolds. *Int. J. Dent.* **2012**, *2012*, 190561. [CrossRef] [PubMed]
15. Bouletreau, P.J.; Warren, S.M.; Spector, J.A.; Steinbrech, D.S.; Mehrara, B.J.; Longaker, M.T. Factors in the fracture microenvironment induce primary osteoblast angiogenic cytokine production. *Plast. Reconstr. Surg.* **2002**, *110*, 139–148. [CrossRef]

16. Ishimatsu, H.; Kitamura, C.; Morotomi, T.; Tabata, Y.; Nishihara, T.; Chen, K.K.; Terashita, M. Formation of dentinal bridge on surface of regenerated dental pulp in dentin defects by controlled release of fibroblast growth factor–2 from gelatin hydrogels. *J. Endod.* **2009**, *35*, 858–865. [CrossRef]

17. Kikuchi, N.; Kitamura, C.; Morotomi, T.; Inuyama, Y.; Ishimatsu, H.; Tabata, Y.; Nishihara, T.; Terashita, M. Formation of dentin-like particles in dentin defects above exposed pulp by controlled release of fibroblast growth factor 2 from gelatin hydrogels. *J. Endod.* **2007**, *33*, 1198–1202. [CrossRef]

18. Ross, R.; Raines, E.W.; Bowen-Pope, D.F. The biology of platelet-derived growth factor. *Cell* **1986**, *46*, 155–169. [CrossRef]

19. Westermark, B.; Claesson-Welsh, L.; Heldin, C.H. Structural and functional aspects of the receptors for platelet-derived growth factor. *Prog. Growth Factor Res.* **1989**, *1*, 253–266. [CrossRef]

20. Alvarez, R.H.; Kantarjian, H.M.; Cortes, J.E. Biology of platelet-derived growth factor and its involvement in disease. *Mayo Clin. Proc.* **2006**, *81*, 1241–1257. [CrossRef]

21. Grotendorst, G.R.; Seppä, H.E.; Kleinman, H.K.; Martin, G.R. Attachment of smooth muscle cells to collagen and their migration toward platelet-derived growth factor. *Proc. Natl. Acad. Sci. USA* **1981**, *78*, 3669–3672. [CrossRef] [PubMed]

22. Seppä, H.; Grotendorst, G.; Seppä, S.; Schiffmann, E.; Martin, G.R. Platelet-derived growth factor in chemotactic for fibroblasts. *J. Cell Biol.* **1982**, *92*, 584–588. [CrossRef]

23. Deuel, T.F.; Senior, R.M.; Huang, J.S.; Griffin, G.L. Chemotaxis of monocytes and neutrophils to platelet-derived growth factor. *J. Clin. Investig.* **1982**, *69*, 1046–1049. [CrossRef]

24. Mark Saltzman, W.; Baldwin, S.P. Materials for protein delivery in tissue engineering. *Adv. Drug Deliv. Rev.* **1998**, *33*, 71–86. [CrossRef]

25. Jen, A.C.; Wake, M.C.; Mikos, A.G. Review: Hydrogels for cell immobilization. *Biotechnol. Bioeng.* **1996**, *50*, 357–364. [CrossRef]

26. Segura, T.; Anderson, B.C.; Chung, P.H.; Webber, R.E.; Shull, K.R.; Shea, L.D. Crosslinked hyaluronic acid hydrogels: A strategy to functionalize and pattern. *Biomaterials* **2005**, *26*, 359–371. [CrossRef] [PubMed]

27. Palma, P.J.; Ramos, J.C.; Martins, J.B.; Diogenes, A.; Figueiredo, M.H.; Ferreira, P.; Viegas, C.; Santos, J.M. Histologic Evaluation of Regenerative Endodontic Procedures with the Use of Chitosan Scaffolds in Immature Dog Teeth with Apical Periodontitis. *J. Endod.* **2017**, *43*, 1279–1287. [CrossRef]

28. Hargreaves, K.M.; Giesler, T.; Henry, M.; Wang, Y. Regeneration potential of the young permanent tooth: What does the future hold? *J. Endod.* **2008**, *30*, S51–S56. [CrossRef]

29. Sloan, A.J.; Smith, A.J. Stem cells and the dental pulp: Potential roles in dentine regeneration and repair. *Oral. Dis.* **2007**, *13*, 151–157. [CrossRef]

30. Kim, J.Y.; Xin, X.; Moioli, E.K.; Chung, J.; Lee, C.H.; Chen, M.; Fu, S.Y.; Koch, P.D.; Mao, J.J. Regeneration of dental-pulp-like tissue by chemotaxis-induced cell homing. *Tissue Eng. Part A* **2010**, *16*, 3023–3031. [CrossRef]

31. Tziafas, D. The future role of a molecular approach to pulp-dentinal regeneration. *Caries Res.* **2004**, *38*, 314–320. [CrossRef] [PubMed]

32. Jhon, M.S.; Andrade, J.D. Water and hydrogels. *J. Biomed. Mater. Res.* **1973**, *7*, 509–522. [CrossRef] [PubMed]

33. Lee, K.Y.; Mooney, D.J. Hydrogels for tissue engineering. *Chem. Rev.* **2001**, *101*, 1869–1879. [CrossRef] [PubMed]

34. Kawasaki, K.; Ochi, M.; Uchio, Y.; Adachi, N.; Matsusaki, M. Hyaluronic acid enhances proliferation and chondroitin sulfate synthesis in cultured chondrocytes embedded in collagen gels. *J. Cell. Physiol.* **1999**, *179*, 142–148. [CrossRef]

35. Lu, L.; Yaszemski, M.J.; Mikos, A.G. TGF-β1 release from biodegradable polymer microparticles: Its effects on marrow stromal osteoblast function. *J. Bone Jt. Surg.* **2001**, *83* (Suppl. S1), S82–S91. [CrossRef]